frontiers | Research Topics

Flexibility analysis and regulation technology of clean energy system

Edited by
Nantian Huang, Yingjun Wu, Dazhi Yang and
Zhaoyu Wang

Published in
Frontiers in Energy Research

ISSN 1664-8714
ISBN 978-2-8325-2478-7
DOI 10.3389/978-2-8325-2478-7

About Frontiers

Frontiers is more than just an open access publisher of scholarly articles: it is a pioneering approach to the world of academia, radically improving the way scholarly research is managed. The grand vision of Frontiers is a world where all people have an equal opportunity to seek, share and generate knowledge. Frontiers provides immediate and permanent online open access to all its publications, but this alone is not enough to realize our grand goals.

Frontiers journal series

The Frontiers journal series is a multi-tier and interdisciplinary set of open-access, online journals, promising a paradigm shift from the current review, selection and dissemination processes in academic publishing. All Frontiers journals are driven by researchers for researchers; therefore, they constitute a service to the scholarly community. At the same time, the *Frontiers journal series* operates on a revolutionary invention, the tiered publishing system, initially addressing specific communities of scholars, and gradually climbing up to broader public understanding, thus serving the interests of the lay society, too.

Dedication to quality

Each Frontiers article is a landmark of the highest quality, thanks to genuinely collaborative interactions between authors and review editors, who include some of the world's best academicians. Research must be certified by peers before entering a stream of knowledge that may eventually reach the public - and shape society; therefore, Frontiers only applies the most rigorous and unbiased reviews. Frontiers revolutionizes research publishing by freely delivering the most outstanding research, evaluated with no bias from both the academic and social point of view. By applying the most advanced information technologies, Frontiers is catapulting scholarly publishing into a new generation.

What are Frontiers Research Topics?

Frontiers Research Topics are very popular trademarks of the *Frontiers journals series*: they are collections of at least ten articles, all centered on a particular subject. With their unique mix of varied contributions from Original Research to Review Articles, Frontiers Research Topics unify the most influential researchers, the latest key findings and historical advances in a hot research area.

Find out more on how to host your own Frontiers Research Topic or contribute to one as an author by contacting the Frontiers editorial office: frontiersin.org/about/contact

Flexibility analysis and regulation technology of clean energy system

Topic editors
Nantian Huang — Northeast Electric Power University, China
Yingjun Wu — Hohai University, China
Dazhi Yang — Harbin Institute of Technology, China
Zhaoyu Wang — Iowa State University, United States

Citation
Huang, N., Wu, Y., Yang, D., Wang, Z., eds. (2023). *Flexibility analysis and regulation technology of clean energy system*. Lausanne: Frontiers Media SA.
doi: 10.3389/978-2-8325-2478-7

Table of contents

frontiers | Frontiers in Energy Research

TYPE Editorial
PUBLISHED 05 May 2023
DOI 10.3389/fenrg.2023.1161202

OPEN ACCESS

EDITED AND REVIEWED BY
ZhaoYang Dong,
Nanyang Technological University,
Singapore

*CORRESPONDENCE
Nantian Huang,
✉ huangnanian@126.com

RECEIVED 08 February 2023
ACCEPTED 24 April 2023
PUBLISHED 05 May 2023

CITATION
Huang N, Wu Y, Yang D and Wang Z (2023), Editorial: Flexibility analysis and regulation technology of clean energy system.
Front. Energy Res. 11:1161202.
doi: 10.3389/fenrg.2023.1161202

Editorial: Flexibility analysis and regulation technology of clean energy system

Nantian Huang[1]*, Yingjun Wu[2], Dazhi Yang[3] and Zhaoyu Wang[4]

[1]Key Laboratory of Modern Power System Simulation and Control and Renewable Energy Technology, Ministry of Education, Northeast Electric Power University, Jilin, China, [2]College of Energy and Electricity, Hohai University, Nanjing, China, [3]College of Electrical Engineering, Harbin Institute of Technology, Harbin, China, [4]College of Electrical Engineering, Iowa State University, Ames, IA, United States

KEYWORDS

operational flexibility, frequency regulation, power system, system uncertainty, technology index

Editorial on the Research Topic
Flexibility analysis and regulation technology of clean energy system

1 Introduction

Today's power system is facing various challenges brought by large-scale renewable energy integration, which puts forward higher requirements for flexibility. Therefore, it is an effective measure to actively build a clean, low-carbon, safe, and efficient energy system with renewable energy such as wind energy and solar energy as the core. The research topic (Flexibility Analysis and Regulation Technology of Clean Energy System) aims to achieve efficient control of clean energy systems in clean energy scenarios in new power systems and provide a communication platform.

2 Published papers

The research topic contains a total of 16 articles. Under the basic premise of energy security, with a strong smart grid as the hub platform, we will establish a clean, low-carbon, controllable, flexible, and efficient new power system based on renewable energy.The articles included in The Research are mainly divided into two directions: 1) Optimization control of distribution networks containing renewable energy generation 2) Power system load forecasting.

For the optimization control of distribution networks, a distribution network scheduling model is established based on the economic indicators, frequency, voltage, and other aspects of the power system.

Wang et al. proposed an evaluation method for quantifying the flexibility of distributed multi energy microgrids in order to effectively utilize their regulatory flexibility. Virtual establishment of flexible bus and assignment of flexible parameters to reflect flexible characteristics. To consider the impact of operational uncertainty on multi energy microgrids, a two-stage adaptive robust optimization model is proposed, which can be solved using the C&CG algorithm.

Yu et al. mainly evaluated and analyzed the economic and technical indicators of distributed power grids, and proposed the advantages and disadvantages, application scope, and objective functions of each indicator. By optimizing location and capacity, voltage quality can be improved, power grid losses can be reduced, and investment costs can be reduced. In addition, the investment cost can be recovered by actively participating in demand response based on the price control mechanism, and the investment cost can be recovered by appropriately increasing the electricity price.

Luo et al. proposed a cloud edge coordination fast adjustment strategy based on intelligent transformer power supply area edge consistency algorithm to address the problem of long-term prediction bias in distribution networks. The edge transformer power supply area cluster performs global initial optimal allocation, and then the cluster performs secondary collaborative optimal allocation for the edge area. A fast power interaction model within a cluster based on consistency algorithm was established, and the micro growth rate of scheduling cost was used as the consistency variable to optimally allocate the cluster adjustment amount to each transformer power supply area, minimizing the total scheduling cost of all transformer power supply areas.

Luo et al. designed an auction method to achieve low-carbon economic scheduling, using blockchain technology to reliably record the entire process data. According to the regional division of market entities, the Owen value method is used to allocate carbon emissions to regions and entities. In order to reduce the expected carbon emissions of the entity, an additional carbon price is added to the original quotation by allocating the results. Based on the typical output characteristics of wind and photovoltaic power generation in bilateral bidding markets, optimization control is conducted hourly.

Lu et al., established a combined wind energy and solar energy hydrogen electrolysis system, and assessed the hydrogen production potential of 31 provincial regions in China in 2050, taking into account the impact of regional wind energy solar load characteristics and transmission costs.

Kun et al., based on the external characteristics of photovoltaic cells, established a mathematical model of the equivalent circuit of distributed photovoltaic power supply and proposed the control mode of the distributed power grid when the distribution network fails.

Lv et al., to realize the efficient and economic operation of building a microgrid, put forward a multi-objective optimization method for planning and operating a microgrid considering virtual energy storage.

Wang et al. established a frequency regulation model of power systems including the primary operation dynamics of the wind turbines and proposed a dynamic integrated inertial control method according to the relationship between load, wind speed, and frequency.

Zhu et al., comprehensively analyzed the working principle of the charging process of electric vehicles, analyzed the relevant factors affecting the failure of power batteries and charging equipment from multiple perspectives, and summarized the relationship between power batteries and charging equipment.

Sun et al. proposed an emergency frequency control method based on deep reinforcement learning to solve the problem of controllable load-shedding response time. The method evaluates the emergency control response capability of the controlled load from three aspects: load response time, controllable load, and controllable load bus.

Su et al., taking the power battery energy storage configuration cost, voltage fluctuation, and load fluctuation as objectives, established a multi-objective optimization model for power battery energy storage configuration and solved it using non dominated sorting genetic algorithm.

Zhu et al. put forward a method for energy storage capacity allocation of wind farm groups. A two-layer model of shared energy storage allocation is established. The upper model optimizes the shared energy storage configuration of each wind farm group to minimize the risk of the out-of-limit output of the wind power base; The lower model calculates the out-of-limit output power of each wind farm group according to the energy storage capacity distribution and transfers the out of limit output power value to the upper model.

Hao et al. put forward a mechanism for evaluating the power balance and power trading potential of the Lancang Mekong countries and South China under long-term operation simulation. The mechanism analyzes the energy supply structure, energy utilization form, cross-border transmission capacity, and multi-regional power trading potential of Lancang Mekong countries and China Southern Power Grid.

For power system load forecasting, the included articles establish a load forecasting model for the power system based on the coupling relationship between loads.

Yang et al. proposed a multi load forecasting method that considers the coupling characteristics of multiple loads and the partitioning of load similar fluctuation sets.

Liu et al. provided a comprehensive review of power information fusion methods for the first time, providing the framework of power information fusion methods and the types of power data.

Li et al. proposed a charging demand prediction model based on real-time data of Baidu Maps. This model can explain the driving strategy and charging strategy of electric vehicle users based on the ability to generate strategy learning against imitative learning.

3 Perspectives

To sum up, 16 papers have been published, including the continuous research results of experts in related fields. These findings will help readers better understand and learn the latest knowledge in relevant fields.

Author contributions

All authors listed have made a substantial, direct, and intellectual contribution to the work and approved it for publication.

Conflict of interest

The authors declare that the research was conducted in the absence of any commercial or financial relationships that could be construed as a potential conflict of interest.

Publisher's note

frontiers | Frontiers in Energy Research

TYPE Original Research
PUBLISHED 02 September 2022
DOI 10.3389/fenrg.2022.1000582

OPEN ACCESS

EDITED BY
Nantian Huang,
Northeast Electric Power University,
China

REVIEWED BY
Yang Li,
Northeast Electric Power University,
China
Mingfei Ban,
Northeast Forestry University, China

*CORRESPONDENCE
Zhiyi Li,
zhiyi@zju.edu.cn

SPECIALTY SECTION
This article was submitted to Smart Grids,
a section of the journal
Frontiers in Energy Research

RECEIVED 22 July 2022
ACCEPTED 10 August 2022
PUBLISHED 02 September 2022

CITATION
Luo R, Wang H, Deng H, Jiang H, Xu C and Li Z (2022), Blockchain-based bilateral bidding market mechanism with carbon allocation on both supply and demand sides.
Front. Energy Res. 10:1000582.
doi: 10.3389/fenrg.2022.1000582

Blockchain-based bilateral bidding market mechanism with carbon allocation on both supply and demand sides

Renjie Luo[1], Hanyi Wang[1], Hui Deng[2], Haiyang Jiang[3], Chengwei Xu[2] and Zhiyi Li[1]*

[1]College of Electrical Engineering, Zhejiang University, Hang Zhou, China, [2]Electric Power Research Institute of State Grid Zhejiang Electric Power Co., Ltd., Hang Zhou, China, [3]Power Dispatching and Control Center, State Grid Heilongjiang Co., Ltd., Harbin, China

Recently, the interaction between power generation and load has been continuously strengthened, providing a new method for realizing the decarbonization of the power system. An auction method that enables a low-carbon economic dispatch is designed in this study, where blockchain technology is employed to record the whole process data credibly. According to the regional division of market entities, carbon emissions are allocated to regions and entities by using the Owen value method. In order to reduce the expected carbon emission of entities, an additional carbon price is added to the original quotation through the allocation results. Case studies are conducted based on the typical output characteristics of wind and photovoltaic power generation in the bilateral bidding market hourly. The results have validated that the proposed method can reduce expected carbon emissions in the power system by prioritizing zero-carbon and low-carbon generation units.

KEYWORDS

carbon allocation, cooperative game, low carbon electricity, Owen value, blockchain

1 Introduction

Global warming is becoming more obvious with the intensification of greenhouse gas emissions (Zhongming et al., 2021). Hence, how to reduce carbon is an important topic. Among the carbon emissions of energy, the power system accounts for about 40% so that electricity will play an increasingly important role in the future. In building a power system with a higher proportion of renewable energy, how to realize renewable energy consumption is also crucial. In the first 5 months of 2022, China's entire society consumed 3,352.6 billion kWh of electricity. As of the end of May 2022, coal-fired thermal power accounted for 49.3% of the installed capacity of power plants. At the same time, gas-fired power generation accounted for 4.8%, and grid-connected wind power and photovoltaic power generation accounted for only 15.1% and 9.3%, respectively. Currently, China has established a carbon market to meet the checks and balances on the proportion of renewable energy and thermal power units through carbon trading(Yue et al., 2021). The

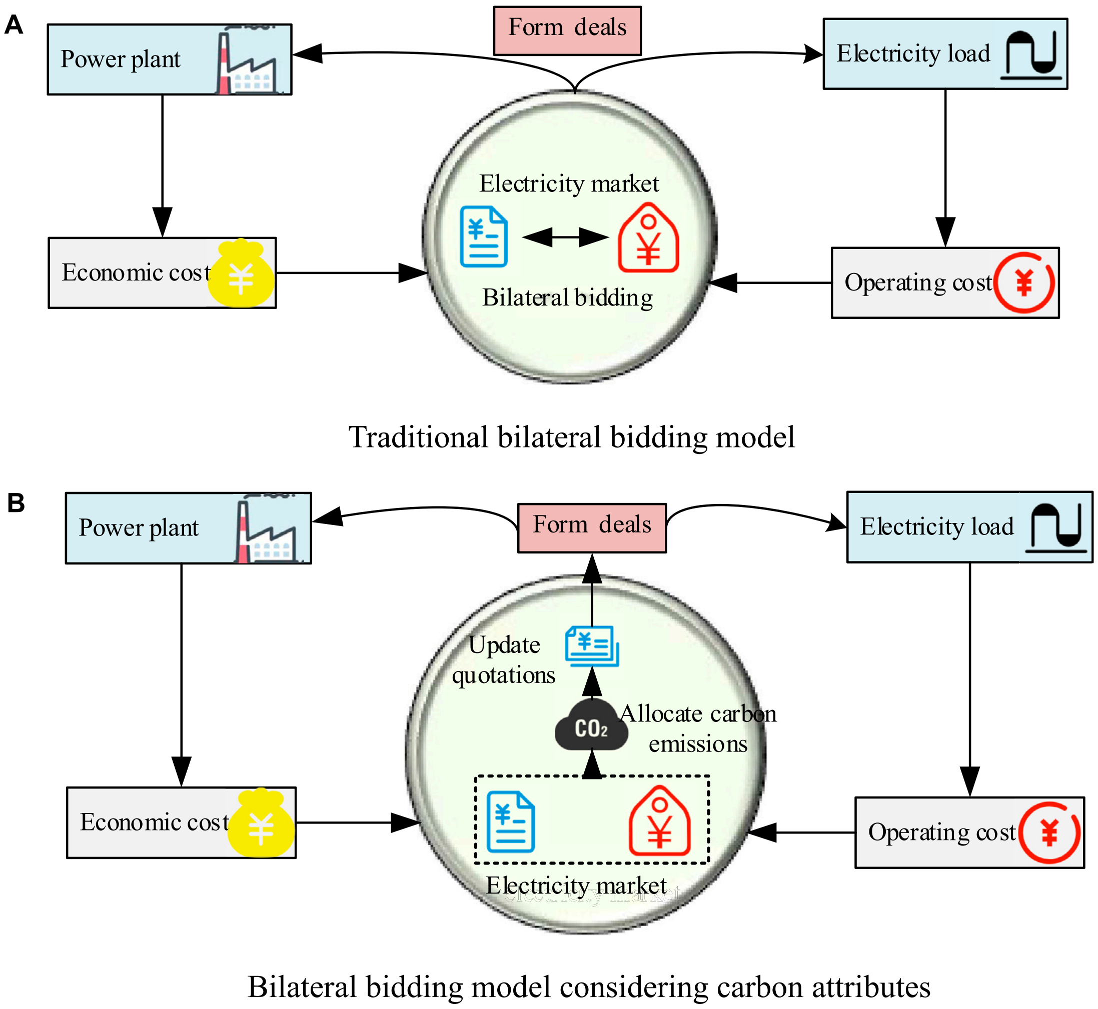

FIGURE 1
Schematic diagram of the change in the bilateral bidding model. **(A)** Traditional bilateral bidding model. **(B)** Bilateral bidding model considering carbon attributes.

emission reduction of the power industry is a vital and challenging task, and people are constantly exploring solutions (Wang and Feng, 2017; Zhang D et al., 2017; Zhang X et al., 2017; Zhang Y.-J et al., 2017; Cheng Z et al., 2018). Therefore, in this study, it is significant to allocate the carbon cost to each entity and guide each entity to reduce emissions and actively participate in renewable energy consumption by means of a market mechanism.

Since the power industry and carbon emissions coexist, figuring out how to achieve decoupling between power and carbon emissions is a critical step in evaluating carbon properties. Some of the methods currently start from the input–output model to track the emission flow through the power grid and quantify the pollution, which is reflected in the power production, exchange, and final consumption of the corresponding institutions (De Chalendar et al., 2019). Some studies use input–output analysis (EIOA) to calculate the implied emission intensity or use a top-down approach to assess the environmental footprint (Gao et al., 2022), while other studies convert electricity into emissions by using the EIA factor to convert fuel into emissions where energy carbon emissions are imputed (Goldstein et al., 2020). Furthermore, some studies decouple the two models by introducing the concept of carbon emission flow attached to the power flow (Kang et al., 2015; Tian et al., 2015). In addition, relevant operating scenarios also include quantifying carbon emissions related to energy transmission (Cheng Y et al., 2018) and conversion processes in multi-energy systems, coordinating energy generation, transmission, conversion, and utilization across different energy sectors, paths, and time scales, and implementing a hierarchical process (Huang et al., 2020). Some studies start from the perspective of cooperative games. At first, the

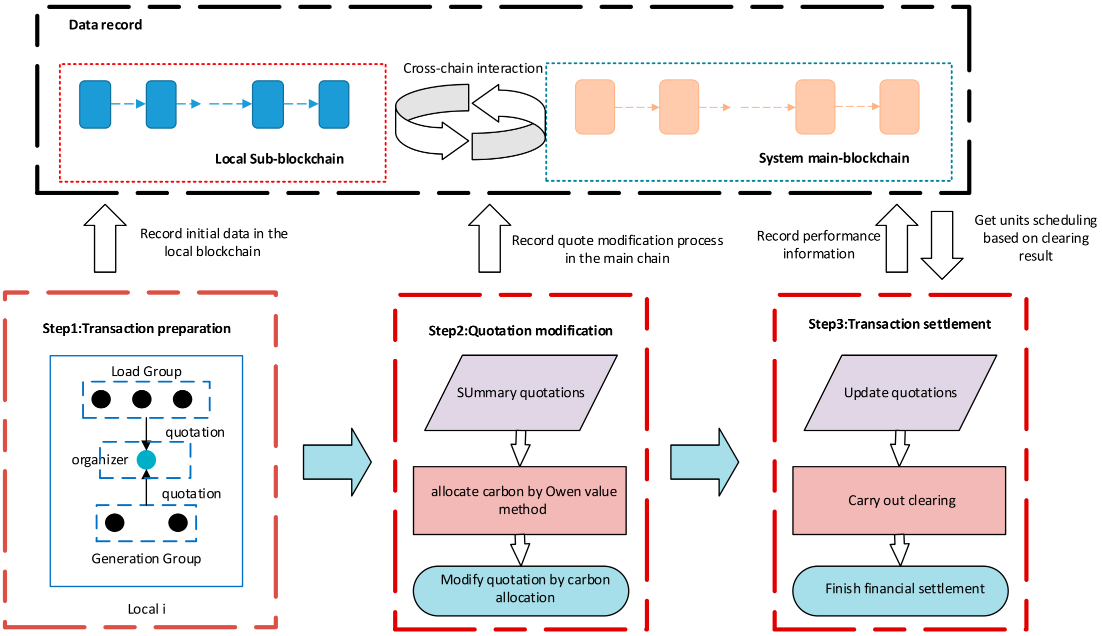

FIGURE 2
Schematic diagram of the overall framework.

Shapley value method can be used for the benefit distribution of internal members in the electricity market (Lei et al., 2020). Later studies regard the whole process of carbon allocation as a cost allocation process and use the Shapley value to share carbon emissions on the load and power generation sides (Chen et al., 2017). However, since the entire system is time-varying and carbon emissions are spatially and temporally different, a reasonable distribution cannot be achieved by simply describing them with fixed parameters.

At present, the existing research hardly allocates the carbon emissions to the power generations and loads. It changes the current trading cycle of quotations by considering the allocation to promote the realization of carbon reduction on both sides of power generation and loads. At the same time, in the current ideas of cooperative games, all market entities are regarded as the same class for cost allocation. However, due to the different geographical distribution of each entity as well as issues such as administrative divisions and policies, it does not take into account the impact of the division of the major leagues. Thus, they belong to cooperative games with coalition structure constraints, which is consistent with the characteristics of Owen's value method. The research (Fiestras-Janeiro et al., 2015) proves the hypothesis of the Owen value. Moreover, the design of a bilateral bidding mechanism considering carbon allocations on both sides starts from the problems mentioned previously by adopting the two-level structure of region-entity. According to the Owen value method and the rules of bilateral bidding, the carbon allocation is set for the entity in each game. The carbon allocation result is transmitted as a price signal to original quotations of entities, and the final transaction is cleared according to the quotation after considering the change of carbon allocations.

Due to the process of quotation changing in the middle, in order to guarantee the traceability of the data, blockchain technology is used to realize the whole process recording on the chain. At present, some research studies have designed the transaction and settlement framework in the electricity market by blockchain (Xu et al., 2021), as well as simplified the transaction process and realized mutual trust between users (Zhou et al., 2021). At the same time, a decentralized trading market is designed in the distribution market for bilateral energy trading (Morstyn et al., 2018). Due to the blockchain consensus mechanism, various information silos are connected (Hamouda et al., 2020), and the problem of information tampering in distributed energy transactions is prevented (Tonev and Nikolaev, 2020). Some studies use private key encryption to protect the privacy of the auctioneer in the bidding process (Zhang et al., 2019). At the same time, there is also a two-level structure of the agent and transaction settlement in the transaction (Luo et al., 2018). It also establishes a regional structure for many types of entities and realizes inter-regional and cross-regional transactions (Li et al., 2021). In order to fit with the aforementioned region-entity two-level structure, a two-level blockchain structure with the main chain of the whole system and sub-chains of each region is designed. Blockchain technology is used in the overall process,

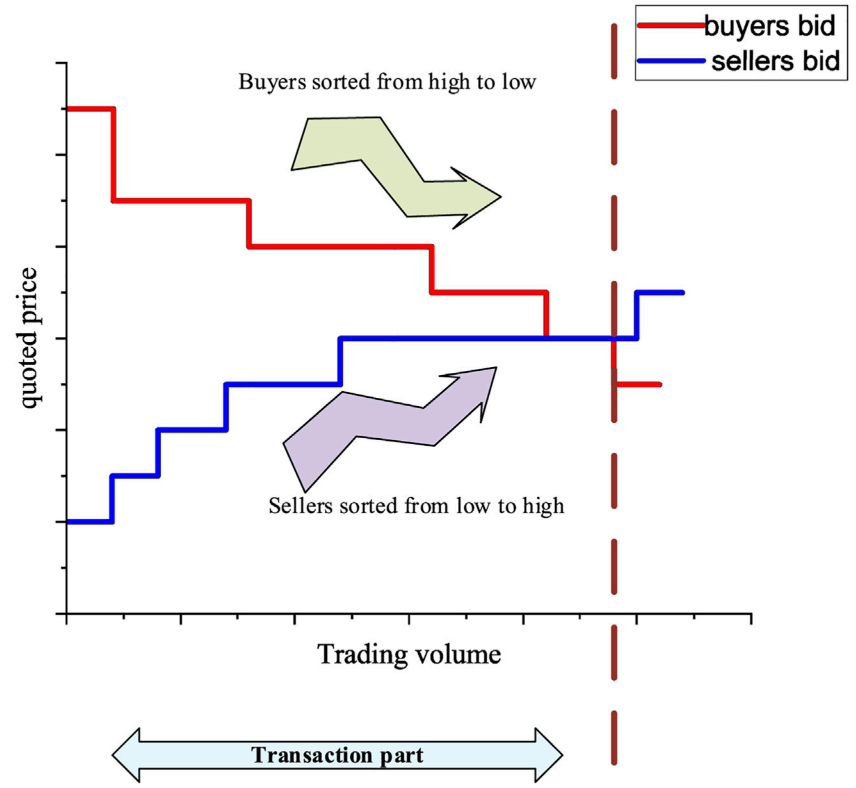

FIGURE 3
Bilateral bidding curve.

and cross-chain between multiple blockchains is used. A blockchain is set up in the overall system to realize the traceability record of regional data and critical data in the transaction, and the aforementioned method is written into the smart contract to transmit the optimal unit output across the chain to each regional blockchain for scheduling. The innovations are as follows:

1) The Owen value method is used to allocate carbon emissions in two levels. The Shapley method is used between regions, and the improved Shapley method is used for each entity in the region to achieve a reasonable allocation.
2) The process of carbon allocation is integrated into the quotations of the current trading bilateral market. In that case, the factor of carbon allocation can be fully considered while satisfying social welfare in the final transaction.
3) Blockchain technology is used to record the corresponding data of the whole process to the chain and realizes the operability and achievability of the process by adopting a two-level blockchain structure.

The remaining contents of this article are as follows: Section 2 introduces the operation process of the whole market mechanism. Section 3 introduces the main models and methods. Section 4 analyzes the results through simulation. Section 5 gives the conclusion and summarizes the whole article.

2 Bilateral electricity market framework with carbon emission allocation

The article follows the general idea of using carbon emissions as a price signal to change the auction before the completion of the current transaction. A cooperative game method is used to allocate carbon emissions to the power generation and load entities participating in the market. A new quotation is formed, taking into account the allocation results and the original quotation.

As shown in Figure 1, in the traditional bilateral bidding model in the electricity market, each entity quotes according to its economic cost while ignoring the environmental value, which is the impact of greenhouse gas emissions. In bilateral electricity trading considering carbon attributes, reasonable carbon allocation should be carried out according to the marginal effect of carbon emissions caused by the participation of each

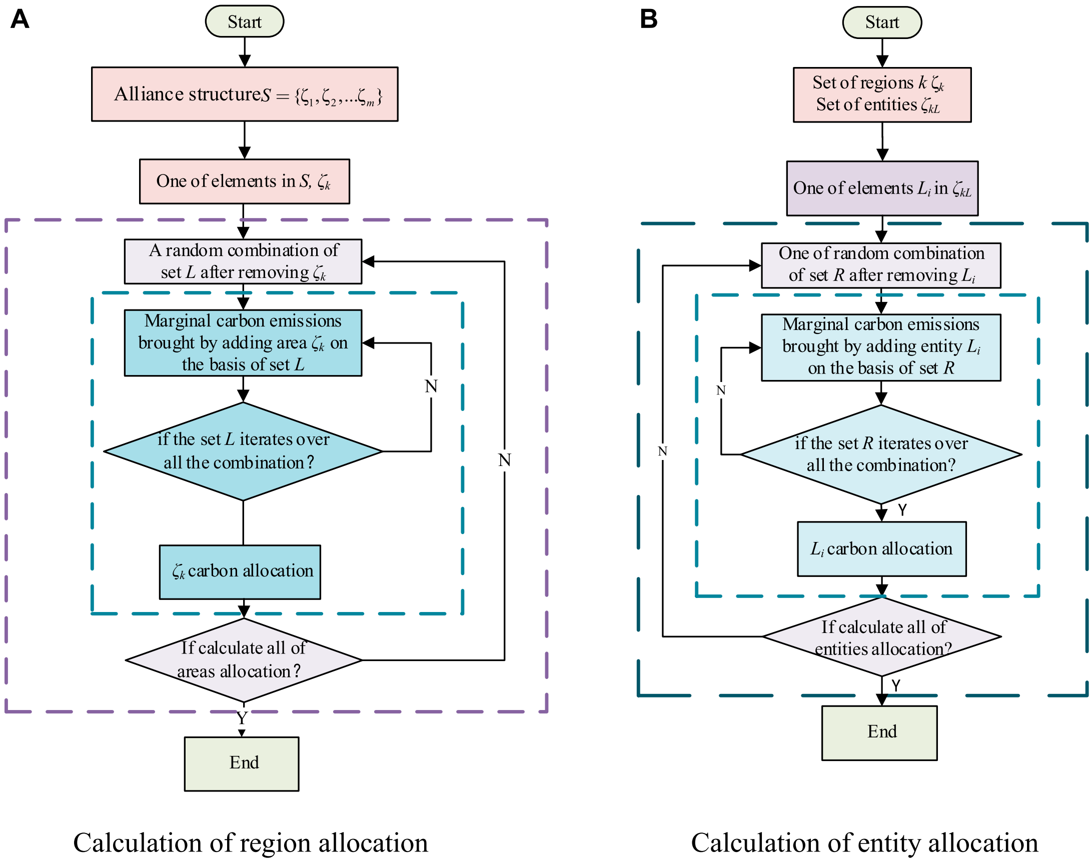

FIGURE 4
Flowchart of the Owen value method calculation process. **(A)** Calculation of region allocation. **(B)** Calculation of entity allocation.

entity in the market. Market organizers make revisions based on the original quotation and the allocation results before the transaction. It considers not only the physical value of electricity but also its environmental value, which can promote the development of low-carbon generation and make the entire system develop toward the goal of a low-carbon and economical operation.

The whole framework is divided into four parts, namely, transaction preparation, modification of quotations, final market transaction, and transaction data recording. The whole framework is shown in Figure 2.

In the transaction preparation process, each power generation entity reports data, including the upper and lower limits of output $\overset{\frown}{P}_{\mathrm{Gi}}P_{\mathrm{Gi}}$, corresponding quotation λ_{Gi}, the carbon emission intensity of generation its_i, and regional locations $local_i$. Each load entity reports data simultaneously, including the upper and lower limits of the load demand $\overset{\frown}{P}_{\mathrm{Li}}P_{Li}$, the corresponding quotation λ_{Li}, and the regional location $local_i$.

In the modification of the quotation process, the Owen value method is used to allocate carbon emissions to each market entity by integrating the previously reported data. The allocation is to divide regional carbon emissions on the basis that each market entity is divided into regions. Then, the entities are divided according to the regional division results, and a ladder carbon price is set according to the allocation results, so as to make a new quotation. At the same time, according to the characteristics of the bilateral bidding market mechanism, in order to promote the low-carbon economic dispatch of the whole system, the additional quotation of the load entities should be negatively correlated with their carbon allocation. The additional quotation of the power generation entities should have a positive correlation with their carbon allocation.

In the final market transaction process, the latest quotation can be obtained based on the quotation of the market entity in the first step and the revised quotation in the second step. Based on the latest quotation, clearing is carried out according to the bilateral bidding model, and the output of each generation and the consumption of each load are distributed.

In the transaction data recording process, its aim is to record the data of the previous three steps, respectively, and realize the

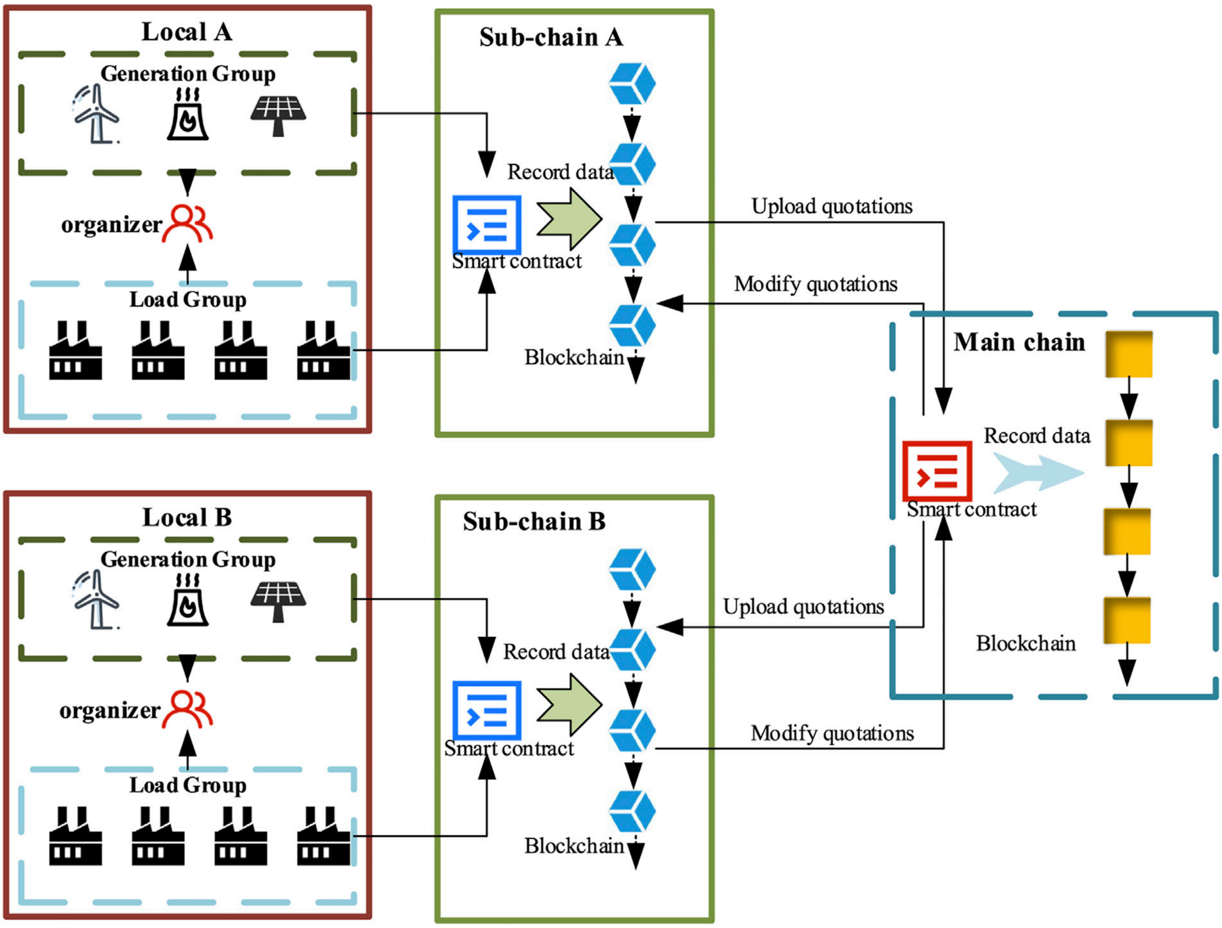

FIGURE 5
Schematic diagram of a two-level blockchain.

automatic implementation of the process through smart contracts. This process establishes a two-level blockchain system. First, the sub-chains in each region are used for the record of report data of market entities and the settlement after the final transaction. Then, the main chain for all regions is used to integrate the report data of each sub-chain to form and record a new quotation.

3 Model and methodology

In this section, detailed modeling regarding the whole mechanism is introduced.

3.1 Bilateral bidding market model

The electricity market clearing model based on bilateral bidding is as follows:

$$
\begin{aligned}
&\max_{P_G P_D}\left(\sum_{i=1}^{D} P_{Di}\bullet\lambda_{Di}-\sum_{j=1}^{G} P_{Gj}\bullet\lambda_{Gj}\right),\\
&\sum_{i=1}^{D} P_{Di}=\sum_{j=1}^{G} P_{Gj},\\
&s.t.\\
&\check{P}_{Gj}\le P_{Gj}\le\widehat{P}_{Gj},\\
&\check{P}_{Di}\le P_{Di}\le\widehat{P}_{Di},\\
&f_l\le\widehat{f}_l,
\end{aligned}
\tag{1}
$$

where P_{Di} represents the actual consumption of load i, the actual output of generation j, and, respectively, represent the quotations for load i and generation j, respectively, the minimum and maximum output of generation j and minimum and maximum consumption of load i.

Since in the bilateral bidding model, the buyer's quotations are sorted from high to low, the buyer can get more advantage in the auction if his bid is higher. The seller's quotation is sorted from low to high, so the lower the seller's quotation, the more the transaction will be prioritized, as shown in Figure 3.

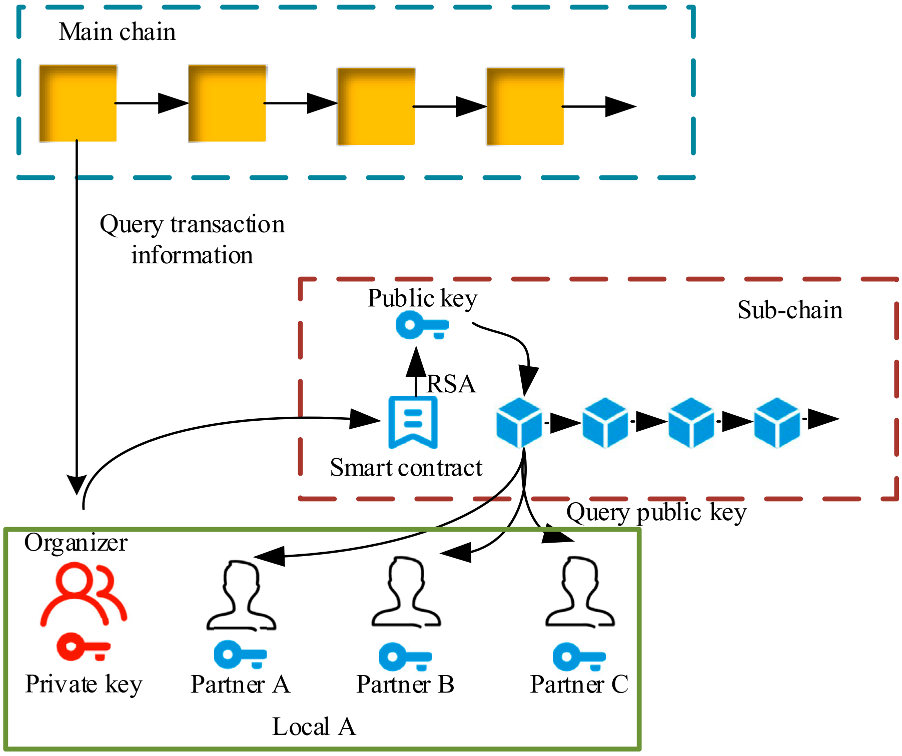

FIGURE 6
Schematic diagram of the first step.

3.2 Carbon allocation model based on the Owen value method

At present, the carbon emission allocation method is adopted from the perspective of a cooperative game. Under the premise of considering axiomatic standards, the Shapley method has good fairness and consistency. At the same time, considering that each entity is divided according to administrative regions, it follows the priority alliance's structure. Therefore, when allocating carbon emissions, it is necessary to separate them from the regional level first and then carry out the allocation of market entities according to the regional allocation results. In summary, this section adopts a two-level structure of the Owen value, and each level is allocated by the Shapley method. Each region can be treated as a priority alliance, and each market entity can be treated as a player in the game.

The carbon allocation of the entity is the additionally expected carbon emissions after the entity joins the bilateral market trading. However, the transaction is based on the modified quotations, which consider every allocation of the entity. The result of carbon allocation can be seen as a factor in the final transaction.

Assume that all market players form a set $N = \{L_1, L_2, ...L_{nl}, G_1, G_2, ...G_{ng}\}$. Different market players are located in different positions, thus forming different alliances. Therefore, the set of all market players can be divided into m parts according to the alliance structure S,

$$\begin{aligned} S &= \{\zeta_1, \zeta_2, ...\zeta_m\}, \\ \zeta_k &= \left\{L_{k1}, L_{k2}, ...L_{kl}, G_{k1}, G_{k2}, ...G_{kg}\right\}, \end{aligned} \tag{2}$$

where ζ_k represents the area k, which consists of loads and generations in the area k, which is the group $\{L_{k1}, L_{k2}, ...L_{kl}, G_{k1}, G_{k2}, ...G_{kg}\}$ Therefore, the calculation of the Owen value method is divided into two steps as follows:

1) First, use the Shapley value method to allocate carbon among regions, which is a priority alliance. The method is as follows:

$$x_{\zeta_k} = \sum_{L\subset (S\setminus\{\zeta_k\})} P(L)(c(L\cup\{\zeta_k\}) - c(L)), \tag{3}$$

where x_{ζ_k} represents the carbon allocation in the local k, L represents a subset of the set S with ζ_k removed, $c(A)$ represents a function which calculates the carbon emissions when the market consists of entities in the alliance structure A , and $c(L\cup\{\zeta_k\}) - c(L)$ represents the

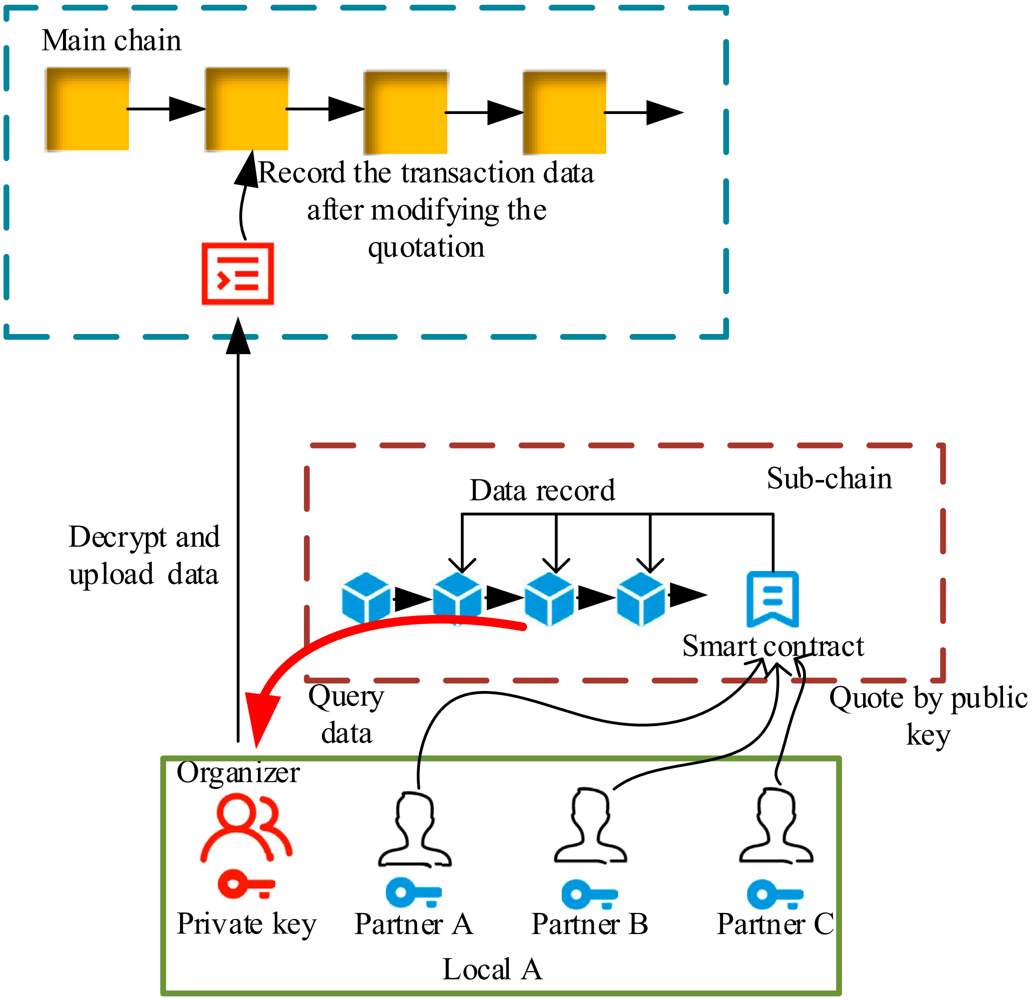

FIGURE 7
Schematic diagram of the quotation modification step.

additional carbon emissions caused when joining in the market.

When considering that all regions are randomly arranged, the probability of the region L is as follows:

$$P(L) = \frac{n_L!(m - n_L - 1)!}{m!}, \tag{4}$$

where m represents the number of alliance structures and n_L represents the number of the probability of forming subset L.

2) According to the idea of the first step, the market players in a certain regional structure are first considered. The Shapley value method is used to calculate the marginal effect of additional allocation to the area when an entity joins the area. The method is as follows:

$$x_{ci} = \sum_{R\subset(\zeta_k/\{ci\})} P(R)\cdot(s(R\cup\{ci\}) - s(R)), \tag{5}$$

where x_{ci} represents the entities ci in the area k alliance structure, which is the load entity or generation entity; R represents a subset of the set ζ_k with ci removed; and $s(R)$ represents carbon allocation in the area k when the market entities in area k only have all the elements in R. When considering that all entities are randomly arranged, the probability of the subset R is as follows:

$$P(R) = \frac{n_R!(n_k - n_R - 1)!}{n_k!}, \tag{6}$$

where n_k represents the number of entities in the area k and n_R represents the number of the entities in the subset R.

Specifically, the combinations of entities need to be considered in order to calculate all the marginal effects. When

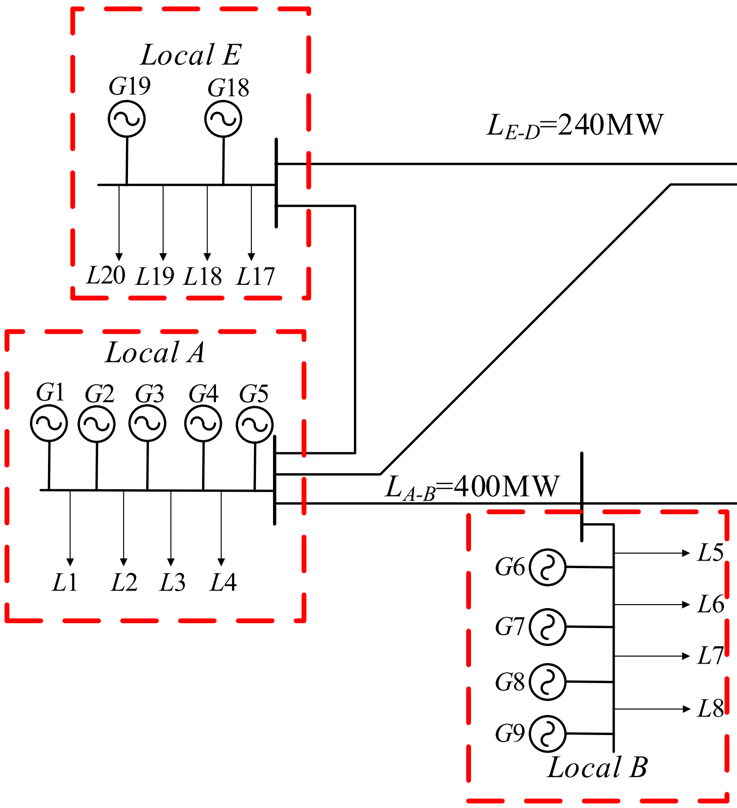

FIGURE 8
PJM-5 node system.

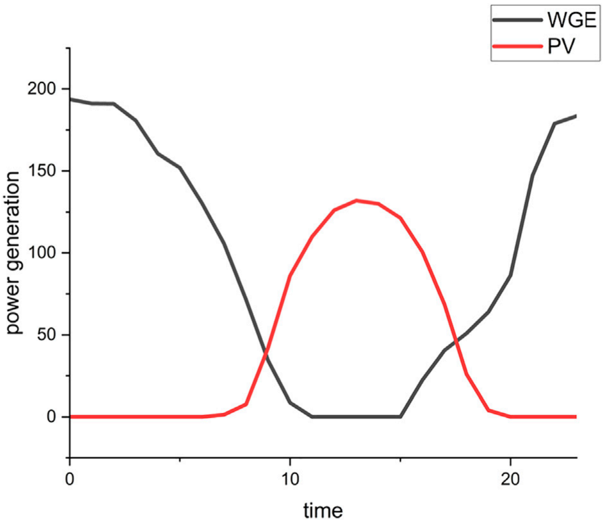

FIGURE 9
Output characteristic curve of the renewable energy unit.

calculating the carbon allocation of the entity C_i, it also needs to be carried out in two steps by the improved Shapley method as follows:

1) Since the carbon allocation of the target entity is calculated by the marginal effect of the region when the entity participates in each combination, we need to calculate the carbon allocation of the region ζ_k in each combination of the entities. When some combination of set L after removing ζ_k is chosen, we can get the total carbon emissions of the system if a bilateral transaction is carried out in this combination. When we add the region ζ_k to the set L, we can get the total carbon emissions of the system again. In this way, the marginal effect of one combination case is obtained. Finally, we can get all the case results and add them to get the region of the target entity allocation, shown in Figure 4A.

2) When some combination R is chosen, the distribution of the entities in the region will change. Thus, Eq. 3 is used to calculate the allocation of the region, which is where the

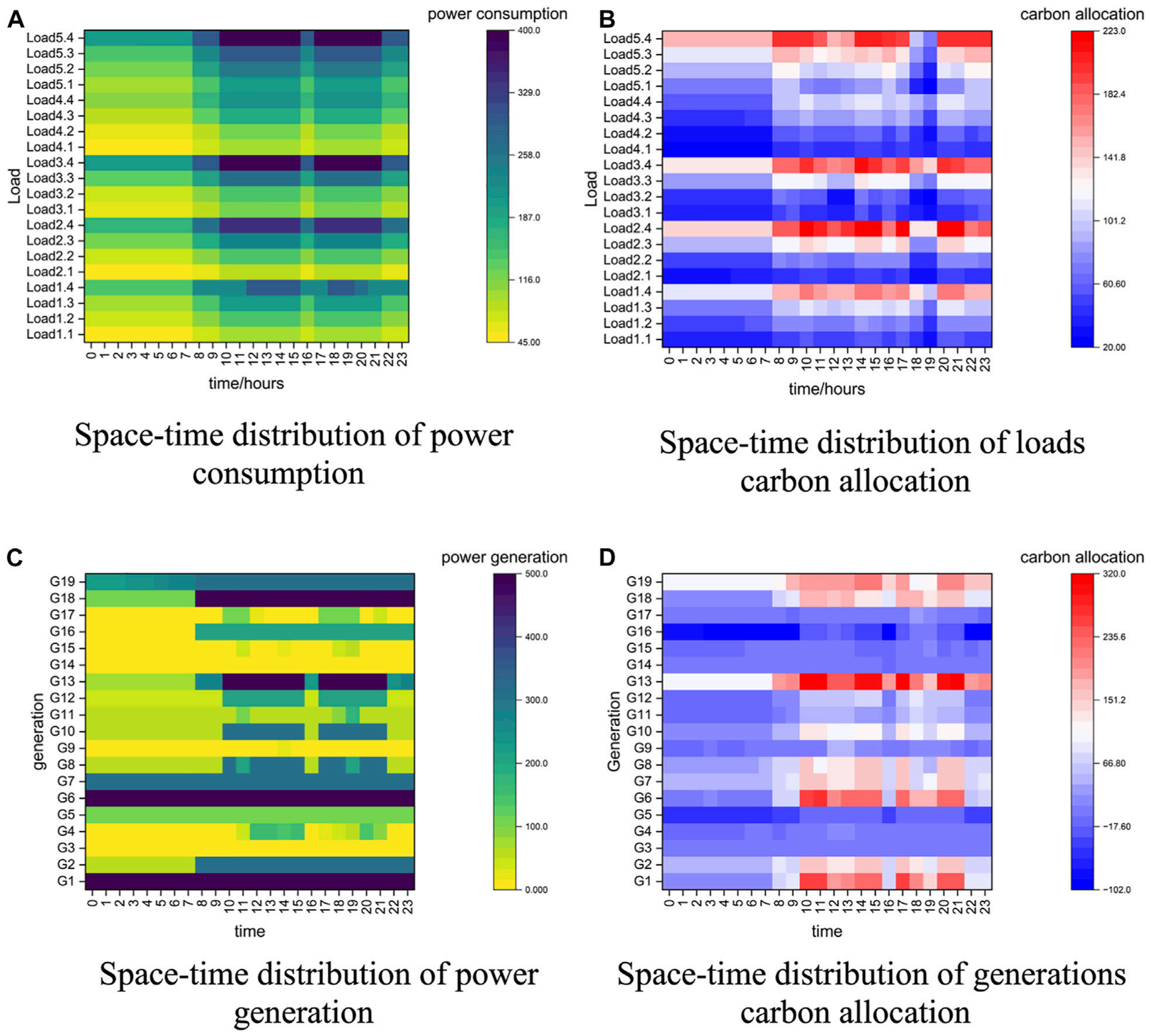

FIGURE 10
Consumption or generation of entity and carbon allocation result comparison. **(A)** Space-time distribution of power consumption. **(B)** Space-time distribution of load carbon allocation. **(C)** Space-time distribution of power generation. **(D)** Space-time distribution of generation carbon allocation.

target entity is located. Then, since the previous combinations did not contain the target entity, the combination R is mixed with the target entity C_i and the new combination is obtained. Finally, Eq. 3 is used to calculate the allocation of the region with further distribution of the combination. In this way, the marginal effect of a combined case can be obtained. The final carbon allocation is obtained when we add all the cases together by Eq. 5. The whole process of this step is shown in Figure 4B.

In calculating the marginal effect, this method needs to consider all the combinations of the entities and the marginal effect of the target entity in each combination. However, in the calculation steps of the Owen method, it needs to consider combinations of regions and entities in the region. It means that minimum supply exceeds maximum demand or minimum demand exceeds maximum supply. Hence, the improved Shapley method will exclude the inappropriate combination to reduce computational complexity. The improved method adds a filter function of combinations compared with the original method.

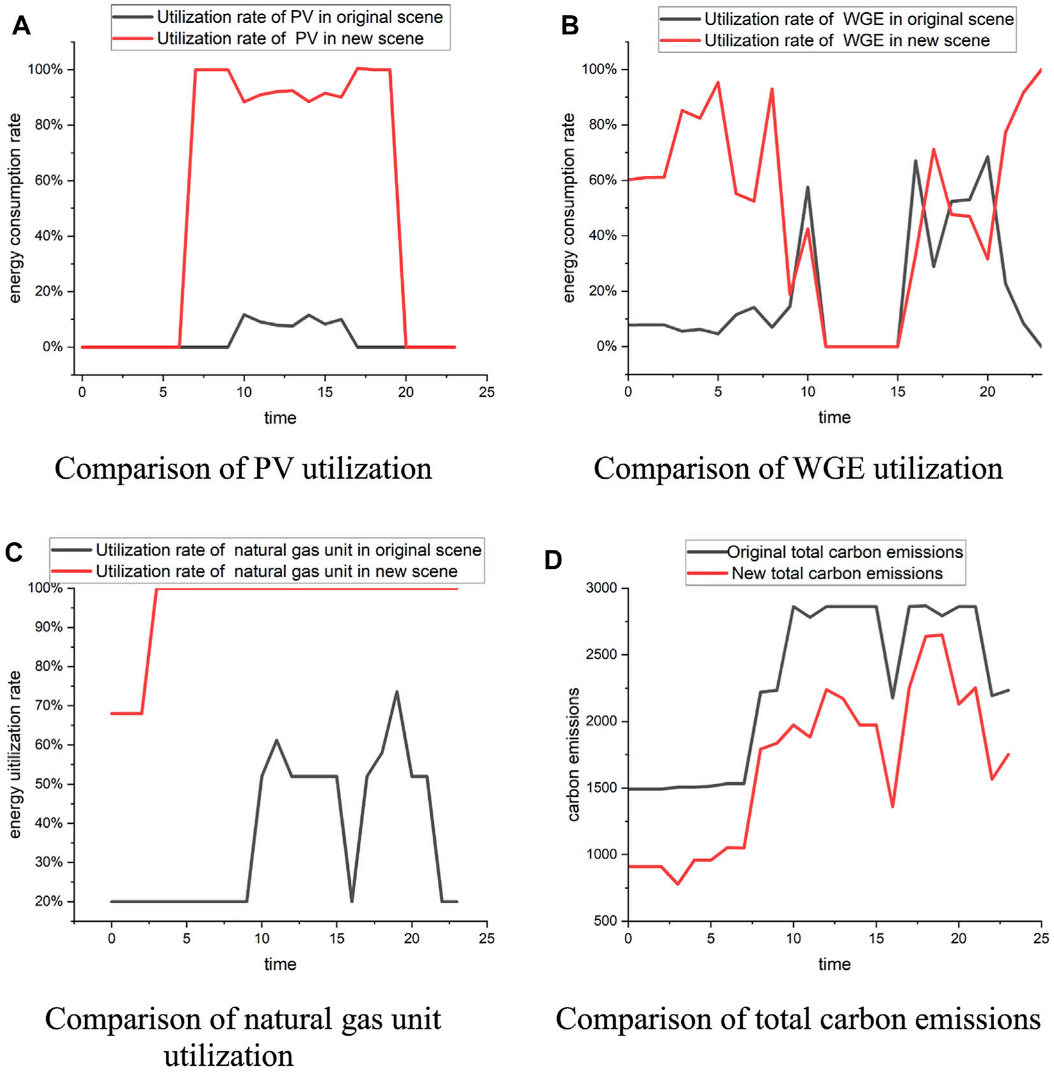

Comparison of PV utilization

Comparison of WGE utilization

Comparison of natural gas unit utilization

Comparison of total carbon emissions

FIGURE 11
Parameters after considering carbon attributes and the initial market. **(A)** Comparison of PV utilization. **(B)** Comparison of WGE utilization. **(C)** Comparison of natural gas unit utilization. **(D)** Comparison of total carbon emissions.

3.3 Design of auction rules

This subsection introduces a method to add the carbon cost based on the allocation of the Owen value method on the quotation in the bilateral market. This mechanism changes the clearing sequence to make low-carbon generations or loads preferentially traded. Considering the characteristics of bilateral auction market clearing, it is necessary to design the quotations of load and power generation entities accordingly.

Then, considering the carbon emissions of load allocation and the additional carbon price, there is a negative correlation, so that the load with more carbon emissions will be ranked lower in the auction, which is consistent with the original goal. The expected additional carbon price for the carbon emissions shared by power generation is positively correlated, so that the units with fewer carbon emissions will accumulate less additional carbon price, and the rank will be relatively high.

The total amount is first calculated through the stepped carbon price in the extra carbon price setting. The carbon price is set to transmit the carbon price of the entity's allocation to its quotation. In this way, the quotation in the final transaction includes economic and environmental factors. If the carbon price is too low, it is impossible to achieve low carbon by changing the quotation order. Therefore, the setting of carbon price should satisfy such that the low-allocation entity can gain an advantage in the quotation. In Section 3.3, the carbon price(40$/t) is a relatively acceptable empirical value obtained

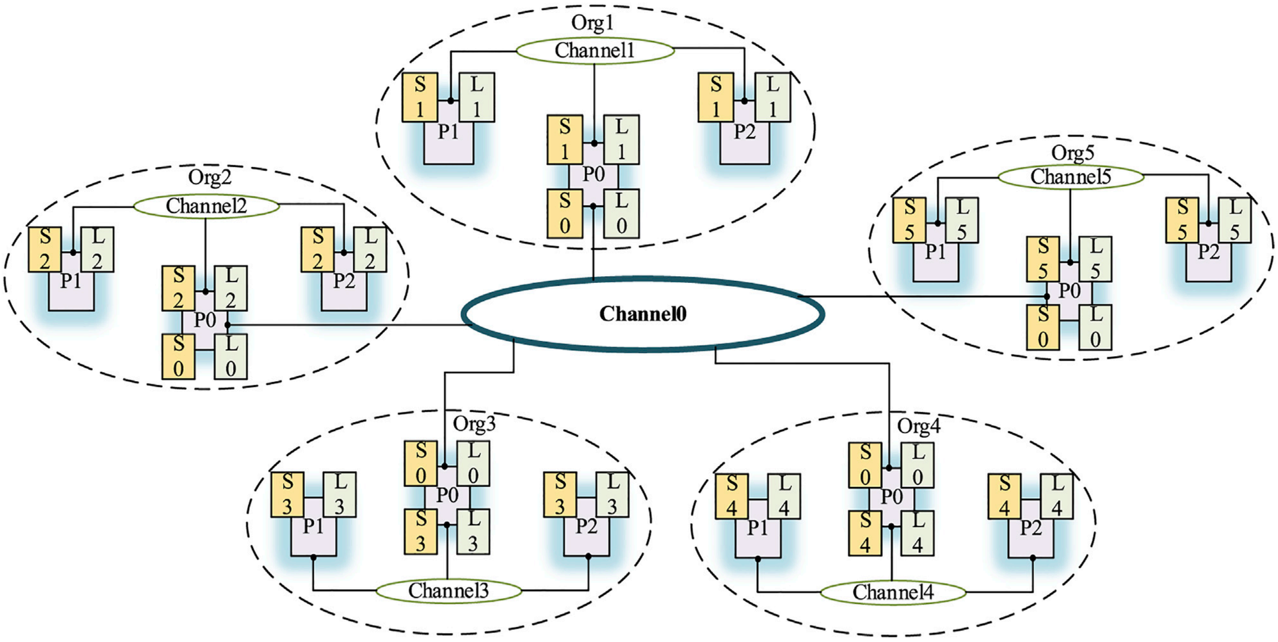

FIGURE 12
Schematic diagram of the blockchain network structure.

by many experiments, which is close to the international carbon price. The detailed method is as follows:

$$\begin{cases} c = 5 \times (x_{ci} - x_{\min}), & x_{ci} \le x_{avg}, \\ c = 5 \times \left(x_{avg} - x_{\min}\right) + 10 \times \left(x_{ci} - x_{avg}\right), & x_{\min} \le x_{ci} \le x_{avg}, \end{cases} \tag{7}$$

where c represents the whole cost for the carbon allocation, x_{ci} represents the carbon allocation of generation or load entity, $x_{\min}$ represents the minimum allocation in generation or load entities, and x_{avg} represents the average allocation of generation or load entities. Then, the additional carbon price is set to

$$\lambda_{ci} = \frac{c}{p_{ci}}, \tag{8}$$

where p_{ci} represents the output or load allocated in the original bilateral bidding scenario. Then, the latest quotation of the load entity is $\lambda_{Di} = \lambda_{Di0} - \lambda_{Li}$, and the latest quotation of the power generation entity is $\lambda_{Gi} = \lambda_{Gi0} + \lambda_{Gi}$.

TABLE 1 Configuration of each node port.

Entity_name	Container_name	Port
Organizer	peer0.org1.example.com	7051
G1	peer1.org1.example.com	7151
G2	peer2.org1.example.com	7251
G3	peer3.org1.example.com	7351
G4	peer4.org1.example.com	7451
G5	peer5.org1.example.com	7551
L1	peer6.org1.example.com	7651
L2	peer7.org1.example.com	7751
L3	peer8.org1.example.com	7851
L4	peer0.org1.example.com	7951

3.4 Application of blockchain technology

In the market transaction of the proposed model, blockchain technology is used in the whole transaction process. Since the transaction process involves multiple regions, many transaction entities, steps, and blockchain technology makes the whole process traceable and simple while preventing tampering, which is suitable for the intermediate quotation change step.

Due to the previous calculation of the Owen value method, the blockchain application is divided into a two-level structure. The target of the sub-chain is to collect the quotation information and deliver the transaction results. Thus, it is aimed at the primary users, such as generation or load entities. The target of the main chain is to evaluate the allocation and supervise the performance of the users. Thus, it is aimed at the market organizers. Meanwhile, it can

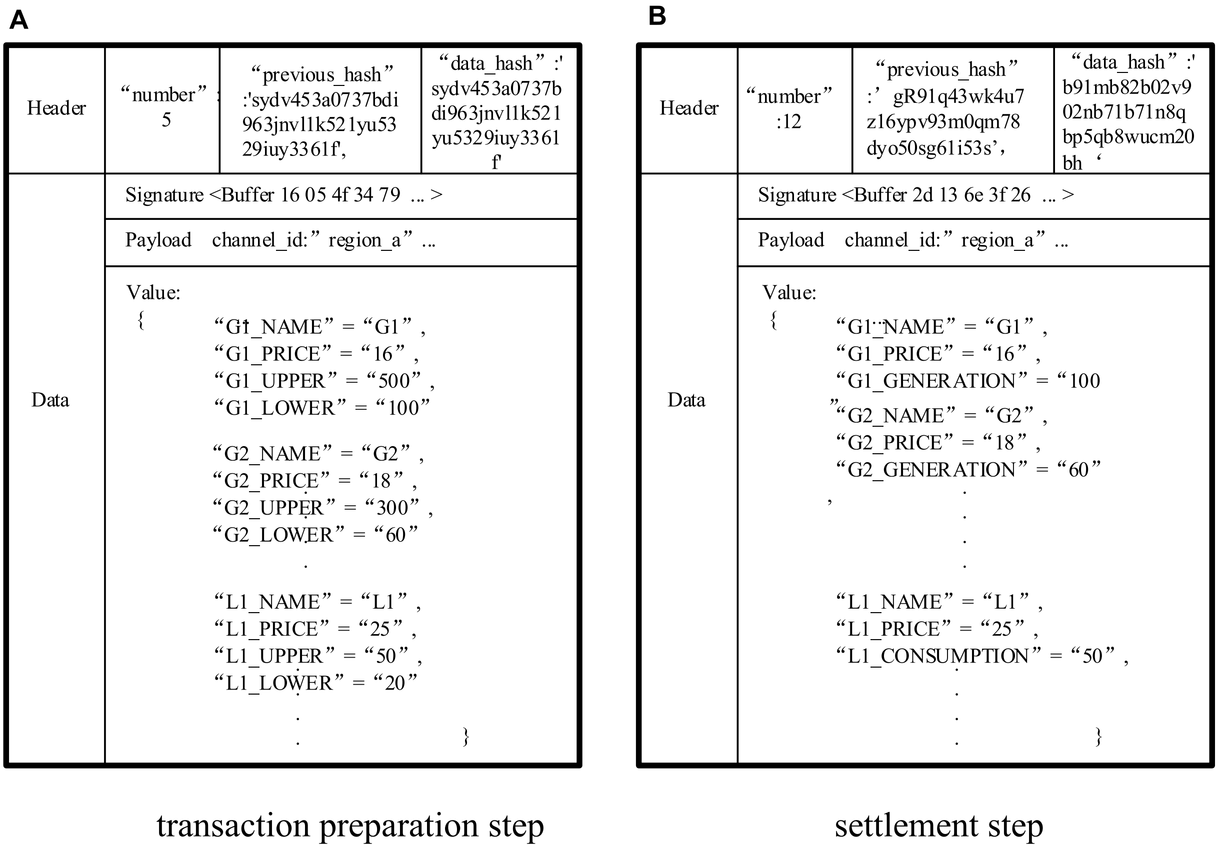

FIGURE 13
Schematic diagram of block information. **(A)** Transaction preparation step. **(B)** Settlement step.

reduce the risk by setting up a separate sub-chain in each region when some sub-chain encounters a mistake.

Therefore, when building the blockchain and establishing a two-level structure, the main chain of the total area and the sub-chain of a single region are set, respectively, as shown in Figure 5. The members of the sub-chain consist of load entities, generation entities, and market organizers in the region, while the members of the main chain consist of market organizers of all regions. They all have a set of the ledger separately and, by using a consensus mechanism, all the members keep the ledgers identical when the transaction is finished. The Kafka algorithm used in the Fabric 1.4 version of the consensus mechanism is adopted. After the peer node requests endorsement, all transaction information is sorted through the Kafka cluster, and then the block is packaged through the order node. Finally, each peer node verifies the correctness of the block (Androulaki et al., 2018).

In the sub-chain of each region, each market entity represents a node in the blockchain system. At the same time, a super node is saved, which is the market organizer of every region for the information interaction with the main chain and the supervision and management of the sub-chain. The functions in the smart contract of the sub-chain are as follows:

1) Record the public key of the market organizer on the sub-chain.
2) Realize the quotations and relevant data of users reporting and record the information after encrypting the aforementioned data with the public key.
3) Record the modification quotation and the transaction results on the chain.
4) Realize query of final results for all users and decoding of quotations for market organizers through their private key.

The main chain comprises market organizers, mainly used to record the data interacted through the cross-chain and change the quotation through the smart contract in the main chain. Since market organizers join both blockchains, they can be seen as the bridge between the main chain and sub-chain. Relevant operations are implemented through smart contracts. The functions in the smart contract of the main chain are as follows:

1) Record the quotations of all regions on the main chain through market organizers.
2) Calculate the carbon allocation of all entities according to the reporting data through the Owen method and modify the quotation based on allocation.
3) Fulfill the final transaction by the modification quotations.
4) Realize the query of final results for market organizers.

The process is divided into three steps: the quotation report, the quotation modification, and the transaction settlement.

In the first step as shown in Figure 6, by querying transaction notifications in the main chain, the information is transmitted to each market entity in the sub-chain through cross-chain operations of market organizers. The organizers in each region use the RSA algorithm to generate a new public and private key and broadcast the public key to the region by sub-chain. Each market entity reports the quotation and the maximum and minimum values of its demand or output according to its situation and encrypts it with the public key of the super node.

In the second step as shown in Figure 7, the super node of each regional sub-chain decrypts the reporting data by the market entity through its private key and uploads it to the main chain. The smart contract in the main chain uses the data to modify the quotation and record those in the main chain. Then, the transaction is carried out according to the new quotation. Finally, super nodes will transmit the clearing result and the changed quotation to the sub-chain.

In the last step, the clearing results are transferred from the main chain to each sub-chain. Each market entity on the sub-chain finishes the settlement of electricity or funds according to the final result. Relevant power generation entities are dispatched according to requirements. The settlement of the final electricity and the funds' performance is written into each region's blockchain.

4 Case study

The example analysis in this section is divided into two parts. The first part is in the PJM-5 system simulation, using five nodes to simulate five areas. Then, each power generation entity and load entity are set up in different groups. Carbon allocation is carried out through the Owen value method and transmitted to the quotations of each entity as a price signal. Considering the typical daily output characteristics of renewable energy units, the transactions of 24 times a day are simulated. After adopting this method, the impact on the overall carbon emissions and the changes in the dispatch of low-carbon or zero-carbon units are analyzed. The second part implements the aforementioned process in the blockchain by using the Hyperledger Fabric and verifies the practicability of blockchain technology by setting up a two-level structure of the main chain and sub-chain.

4.1 PJM-5 node example

The network structure of the PJM-5 system is shown in Figure 8, where each node is regarded as a region. G3 and G14 are photovoltaic power generation; G4, G9, and G15 are wind power generation; and G11 and G12 are natural gas generators. The remaining units are conventional thermal power units. The AB and ED lines' capacity is 400 and 240 MW, respectively. There is no capacity limit on other lines.

The capacity of two photovoltaic power generations is 200 MW; and the capacity of three wind power generations is 200 MW. Their typical day output curves are shown in Figure 9.

Within 24 h, the load and power generations declare the quotations separately. If the transaction is formed according to the bilateral bidding mode, the consumption of each load and the output of each unit are shown in Figures 10A, C and through the Owen value method, carbon allocation is carried out on 24 trading points. The results are shown in Figures 10B, D. It can be seen that the carbon allocation result is positively correlated with the assumed original bilateral market clearing result. Loads with higher power consumption have higher carbon allocation results, and thermal power units with higher power generation also have higher carbon allocations. The results show that the hydropower units have a negative allocation lower than the photovoltaic or wind power. The reason is that the calculation of carbon allocation is based on the marginal carbon effect in the hypothetical bilateral bidding scenario. Due to the lower quotation of hydropower units, hydropower units are easier to be traded in the bilateral market. The participation of the hydropower unit will reduce the carbon emissions of the entire system, so its allocation is lower. However, due to their high quotations of renewable units, they are not easily traded in the bilateral market. Its participation will not change the output distribution of units, so its allocation is higher than that of hydropower units.

Next, each entity will tier carbon prices based on the Owen value allocation in each trading period. A ladder carbon price of 40$/t, 20$/t, and 0$/t is set according to the maximum allocation, average allocation, and minimum allocation among entities of the same type, respectively. The subsequent clearing is carried out by adding the ladder carbon price to the original quotation. The change in carbon emissions of the entire system is shown in Figure 11. It can be seen that this method can promote the utilization rate of the low-carbon and zero-carbon units and reduce the carbon emissions of the system effectively. The results show that calculating the carbon allocation and considering it as a cost to loads and power generations. On the one hand, an additional carbon price is added to the quotation of power generations so that the environmental value of zero-carbon or low-carbon generators can be exerted and their priority dispatch can be realized. On the other hand, after allocating carbon to loads and attaching a carbon price, according to the results of their quotations, the expected usage of loads with excessively allocated carbon emissions will be reduced in the bilateral market, so as to guide load entities to energy conservation and emission reduction.

4.2 Implementation based on blockchain technology

Hyperledger Fabric 1.4 version is used in the process of building a blockchain. The operating environment is Linux CentOS 7.5. According to the operation characteristics of the fabric, the smart contract and ledger in each channel will be shared. Therefore, different nodes will be grouped into other channels to realize the construction of different blockchains. As shown in Figure 12, P1 represents the nodes of the power generation entity, P2 represents the nodes of the load entity, and the number of entities determines the number of nodes. P0 represents the organizational nodes in each region. Channels 1–5 represent the sub-chains of five regions; Channel 0 represents the total chain for the entire region. At the same time, because the market organizer in each region is located in the sub-chain of its region and the general chain of the whole region, it has not only the account book of its region but also the account book of the general chain. So it acts as a bridge between the total chain and the sub-chain.

In the application of the sub-chain, it mainly involves the transaction information reporting step and the last transaction step. Therefore, region *A* was taken as an example to display the relevant results. In region *A*, there are five power generation nodes, four load nodes, and an organizer's super node. The simulation method is a single machine with a multi-node network. Each node port is set as follows in Table 1.

Two blocks representing two steps in the sub-chain are selected, as shown in Figure 13. A block consists of a header, data, and metadata in blockchain technology. The relevant hash value and block number are displayed in the header. The data in the middle show the signature and value, etc., where the value is parsed by converting the relevant data into the JSON format. Metadata have little effect on the application, which is not shown in the figure.

According to the analysis of the results, it can be seen that the adoption of blockchain technology can automate the entire process. The process involves multiple steps, but it can be finished quickly. In addition, the data of the whole process are recorded on the blockchain. This makes the entire quote change process traceable and credible. Finally, due to the consensus mechanism, all data are tamper-proof, thus ensuring the secure and smooth operation of the market.

5 Conclusion

This article proposes a method to allocate the carbon emissions of the power system to the power generation entities and load entities according to the Owen value method region-entity principle and establish a model that can realize the transaction of the allocation result as a price signal in the bilateral trading market in this period. Based on the example analysis, the following conclusions are drawn:

1) The allocation results of the Owen value method show that its allocation to the power generation and load sides is more reasonable. For different generation units The allocation results correspond to the different generation units' carbon emissions from electricity generation. For other loads, the allocations are consistent with their consumption behavior. At the same time, the difference in carbon emissions caused by geographical factors caused by line capacity is also considered.
2) In the bilateral bidding scene, the allocation calculated by the Owen value method is used as a price signal to update entity quotations, which can realize the combination of policy and market mechanisms to realize the dispatch of low-carbon and zero-carbon generators so as to realize the low-carbon economic operation of the whole system.
3) The two-level blockchain structure can fit with the entire process. On the one hand, it realizes the contract by a code during the entire process, thereby simplifying the process. On the other hand, during changes in the quotation, it realizes the record of the overall data on the chain to ensure the credibility and traceability of the entire process.

Data availability statement

The raw data supporting the conclusion of this article will be made available by the authors, without undue reservation.

Author contributions

RL and ZL contributed to the conception and design of the study. RL organized the simulation, analyzed the results, and wrote parts of the manuscript. HW gave suggestions to technical support. HD and HJ contributed to writing parts of the manuscript. CX contributed to the improvement of the study design.

Funding

This work was supported by the Zhejiang Provincial Public Welfare Technology Application Research Project (LGJ21E070001).

Conflict of interest

Authors HD and CX was employed by the company Electric Power Research Institute of State Grid Zhejiang

Electric Power Co., Ltd., Hangzhou, China. HJ was employed by the company Power Dispatching and Control Center, State Grid Heilongjiang Co., Ltd., Harbin, China.

The remaining authors declare that the research was conducted in the absence of any commercial or financial relationships that could be construed as a potential conflict of interest.

Publisher's note

References

Androulaki, E., Barger, A., Bortnikov, V., Cachin, C., Christidis, K., De Caro, A., et al. (2018). "Hyperledger fabric: A distributed operating system for permissioned blockchains," in Proceedings Of The Thirteenth Eurosys Conference, Portugal, April 23–26, 2018, 1–15.

Chen, L., Sun, T., Zhou, Q., and Feng, D. (2017). "A Shapley value based method for allocating carbon obligation between generation side and demand side in power system," in Iecon 2017-43rd Annual Conference Of The Ieee Industrial Electronics Society, China, 29 Oct-01 Nov, 56–60.

Cheng, Y., Zhang, N., Wang, Y., Yang, J., Kang, C., and Xia, Q. (2018). Modeling carbon emission flow in multiple energy systems. *IEEE Trans. Smart Grid* 10, 3562–3574. doi:10.1109/tsg.2018.2830775

Cheng, Z., Li, L., and Liu, J. (2018). Industrial structure, technical progress and carbon intensity in China's provinces. *Renew. And Sustain. Energy Rev.* 81, 2935–2946. doi:10.1016/j.rser.2017.06.103

De Chalendar, J. A., Taggart, J., and Benson, S. M. (2019). Tracking emissions in the us electricity system. *Proc. Natl. Acad. Sci. U. S. A.* 116, 25497–25502. doi:10.1073/pnas.1912950116

Fiestras-Janeiro, M. G., Gallardo, J. M., Jiménez-Losada, A., and Mosquera, M. A. (2015). Cooperative games and coalition cohesion indices: The choquet–owen value. *IEEE Trans. Fuzzy Syst.* 24, 444–455. doi:10.1109/tfuzz.2015.2459761

Gao, T., Jin, P., Song, D., and Chen, B. (2022). Tracking the carbon footprint of China's coal-fired power system. *Resour. Conservation And Recycl.* 177, 105964. doi:10.1016/j.resconrec.2021.105964

Goldstein, B., Gounaridis, D., and Newell, J. P. (2020). The carbon footprint of household energy use in the United States. *Proc. Natl. Acad. Sci. U. S. A.* 117, 19122–19130. doi:10.1073/pnas.1922205117

Hamouda, M. R., Nassar, M. E., and Salama, M. (2020). A novel energy trading framework using adapted blockchain technology. *IEEE Trans. Smart Grid* 12, 2165–2175. doi:10.1109/tsg.2020.3045662

Huang, W., Zhang, N., Cheng, Y., Yang, J., Wang, Y., and Kang, C. (2020). Multienergy networks analytics: Standardized modeling, optimization, and low carbon analysis. *Proc. IEEE* 108, 1411–1436. doi:10.1109/jproc.2020.2993787

Kang, C., Zhou, T., Chen, Q., Wang, J., Sun, Y., Xia, Q., et al. (2015). Carbon emission flow from generation to demand: A network-based model. *IEEE Trans. Smart Grid* 6, 2386–2394. doi:10.1109/tsg.2015.2388695

Lei, R., Zhou, M., Wu, Z., Sha, Y., Zhang, Y., and Liu, X. (2020). "The optimal operation and revenue allocation method of virtual power plant considering carbon trading," in 2020 Ieee 4th Conference On Energy Internet And Energy System Integration (Ei2)China, Oct 30-Nov 1, 2396–2402.

Li, J.-F., Lu, X., Zhang, D., and Sheng, J. (2021). "A review on the blockchain technique applied in cloud energy storage power system," in 2021 Ieee 6th International Conference On Cloud Computing And Big Data Analytics (Icccbda), China, Apr 24 26, 415–422.

Luo, F., Dong, Z. Y., Liang, G., Murata, J., and Xu, Z. (2018). A distributed electricity trading system in active distribution networks based on multi-agent coalition and blockchain. *IEEE Trans. Power Syst.* 34, 4097–4108. doi:10.1109/tpwrs.2018.2876612

Morstyn, T., Teytelboym, A., and Mcculloch, M. D. (2018). Designing decentralized markets for distribution system flexibility. *IEEE Trans. Power Syst.* 34, 2128–2139. doi:10.1109/tpwrs.2018.2886244

Tian, D., Li, Y., Cai, Y., Cao, Y., Xin, J., and Fan, R. (2015). "A hierarchical and partition low-carbon evaluation model for active power distribution grid," in 2015 Ieee 15th International Conference On Environment And Electrical Engineering (Eeeic), Rome, June 10-13, 1448–1452.

Tonev, I., and Nikolaev, N. (2020). "Review on blockchain applications for electric power systems," in 2020 21st International Symposium On Electrical Apparatus & Technologies (Siela), Balgaria, June 3-6, 1–4.

Wang, M., and Feng, C. (2017). Decomposition of energy-related Co2 emissions in China: An empirical analysis based on provincial panel data of three sectors. *Appl. Energy* 190, 772–787. doi:10.1016/j.apenergy.2017.01.007

Xu, Y., Hu, J., and Zhou, H. (2021). "Blockchain-based trading and settlement framework for electricity markets," in 2021 International Conference On Communications, Information System And Computer Engineering (Cisce), China, May 27-29, 243–246.

Yue, B., Guo, C., Guo, Y., Feng, B., Ding, X., and Wang, S. (2021). "Review on the development of carbon transaction in China and analysis on the participation strategy of electric power industry," in 2021 Ieee Sustainable Power And Energy Conference (Ispec), China, Dec 23-25, 717–724.

Zhang, D., Wang, J., Lin, Y., Si, Y., Huang, C., Yang, J., et al. (2017). Present situation and future prospect of renewable energy in China. *Renew. and Sustain. Energy Rev.* 76, 865–871. doi:10.1016/j.rser.2017.03.023

Zhang, S., Pu, M., Wang, B., and Dong, B. (2019). A privacy protection scheme of microgrid direct electricity transaction based on consortium blockchain and continuous double auction. *Ieee Access* 7, 151746–151753. doi:10.1109/access.2019.2946794

Zhang, X., Zhao, X., Jiang, Z., and Shao, S. (2017). How to achieve the 2030 Co2 emission-reduction targets for China's industrial sector: Retrospective decomposition and prospective trajectories. *Glob. Environ. Change* 44, 83–97. doi:10.1016/j.gloenvcha.2017.03.003

Zhang, Y.-J., Peng, Y.-L., Ma, C.-Q., and Shen, B. (2017). Can environmental innovation facilitate carbon emissions reduction? Evidence from China. *Energy Policy* 100, 18–28. doi:10.1016/j.enpol.2016.10.005

Zhongming, Z., Linong, L., Xiaona, Y., Wangqiang, Z., and Wei, L. (2021). *New climate predictions increase likelihood of temporarily reaching 1.5°C in next 5 years*. Available at: http://119.78.100.173/C666/handle/2XK7JSWQ/328222.

Zhou, K., Chong, J., Lu, X., and Yang, S. (2021). Credit-based peer-to-peer electricity trading in energy blockchain environment. *IEEE Trans. Smart Grid* 13, 678–687. doi:10.1109/tsg.2021.3111181

frontiers | Frontiers in Energy Research

TYPE Opinion
PUBLISHED 14 September 2022
DOI 10.3389/fenrg.2022.1019352

EDITED BY
Nantian Huang,
Northeast Electric Power University,
China

REVIEWED BY
Xiaoshuna Zhang,
Northeastern University, China
Yiyan Sang,
Shanghai University of Electric Power,
China

*CORRESPONDENCE
Xiaowei Yu,
1261481464@qq.com
Kui Li,
61145986@qq.com

SPECIALTY SECTION
This article was submitted
to Smart Grids,
a section of the journal
Frontiers in Energy Research

RECEIVED 15 August 2022
ACCEPTED 23 August 2022
PUBLISHED 14 September 2022

CITATION
Yu X, Ling X, Zhou X, Li K and Feng X (2022), Flexibility evaluation and index analysis of distributed generation planning for grid-source coordination. *Front. Energy Res.* 10:1019352.
doi: 10.3389/fenrg.2022.1019352

Flexibility evaluation and index analysis of distributed generation planning for grid-source coordination

Xiaowei Yu[1]*, Xu Ling[1], Xiaogang Zhou[1], Kui Li[2]* and Xiaoxia Feng[2]

[1]Central China Branch of State Grid Corporation of China, Wuhan, China, [2]Central Southern China Electric Power Design Institute Co.,Ltd., Wuhan, China

KEYWORDS

flexibility evaluationl, distributed generation, demand response, technology index, economic index

1 Introduction

Electric energy has a critical impact on the consumer's life, which is mostly based on centralized generation at present. However, the centralized generation has caused high power transmission and distribution losses. Meanwhile, the high combustion cost of fossil fuels and the environmental pollution caused by the greenhouse effect has become the problems that have to face. Reasonable planning sizing and location of distributed generations (DGs) to the distribution network (DN) may overcome the above limitations such as reducing power loss and environmental pollution. Therefore, access to DGs at the DN has been widely adopted (Rana et al., 2017; Ali and Qiang, 2018). Nowadays, due to the ability to maximize the use of renewable energy such as wind, solar, wave, hydro, and hydrogen the penetration rate of DGs has increased.

The optimal location and capacity of DGs properly may reduce power loss, cost and enhance the reliability of the power grid. A large number of DG connections have a great impact on DN such as power flow, voltage profile, power loss, and power grid stability of the DN. Therefore, it is valuable to quantitatively evaluate the comprehensive impact of DG connections on the DN (Francisco et al., 2020; Li et al., 2021). In order to evaluate whether the location and capacity of the DGs connected to the power grid are correct, various evaluation indexes are proposed mainly including economy, technology, and environment. Reference (Wang et al., 2019) has defined the voltage stability index based on the power flow calculation results of the DN and studied the influence of the DG connection on the voltage stability of the DN. Literature (Su, 2010) has considered the uncertainty of the operation of the distribution system, including the daily variable load, the random DG generation, the grid configuration, and the voltage control device, and analyzes the influence of the distributed power supply connected to the distribution network on the voltage deviation. Currently, various literatures proposed several methods for optimal location and capacity of DGs, literature (Koutsoukis et al., 2014; Magadum and Kulkarni, 2015) separately proposed tabu search (TS), and fuzzy logic to minimize power loss and cost of DGs. Moreover, artificial neural networks (ANN) have either been designed to minimize energy loss, and it no need for flow calculations (Semic et al., 2019).

However, the above literature both ignores the users' demand response (DR) about the DGs accessing, and just consider the DGs' impact on the grid. Meanwhile, there is no review paper evaluating and analyzing the index of DGs. Hence, this paper has mainly evaluated and analyzed the economic index, and technology index of DGs. Furthermore, the advantages/limitations, applications, and objective function of each index have been proposed. Finally, valuable perspectives and challenges for future researchers are proposed.

2 Analysis of economic indexes

Generally, to decrease the environmental pollution and power loss caused by the traditional centralized generators, installing DGs in DN as far as possible is a conventional method to solve. However, how to not only decrease the investment, operation, and maintenance cost but enhance the reliability of the power grid is a critical challenge for the current researchers. Currently, several approaches have been proposed to solve this problem, as follows:

- By optimizing the location and capacity, the voltage quality can be improved and the loss of the grid will be reduced with less investment cost. Moreover, investment costs can be recovered by actively participating in DN management based on a price control mechanism, and investment costs can be recovered by appropriately increasing electricity prices. Meanwhile, by adding robots to make equipment intelligent to reduce operation and maintenance costs;
- Establish an incentive scheme to help the company and government to install DGs. These incentive plans may include government subsidies on the generator side and taxes on customers (e.g., environmental taxes);
- Active DN (ADN) mechanism should be more widely used in the current new power system. Based on the resident DR, combine the resident and generation to create more ADN.

The cost of the DG is a complex problem, which includes several uncertain paraments such as the price of the fuel cell, labor cost, inflation rate, tax, raw material cost, government subsidy, and DGs types. Literature (Yang et al., 2020) has comprehensively summarized the types of DGs which are divided into four types including only active power DGs (type-I), reactive power generators (type-II), which generate both active and reactive power DGs (type-III), and generate active power and consume reactive power (type-VI). A variety of uncertain parameters will lead to a very complex problem in calculating the investment and operation cost of the system. In addition to the investment and operation costs, the environmental benefits generated by installing DGs on the DN side should also be considered, which not only alleviates the pollution but better use of renewable energy (Priyanka et al., 2014). Because of its benefit, several researchers have chosen the minimized cost of DGs as the objective to optime the capacity and location. Table 1 comprehensively summarizes the typical economic indexes and analyzes their application, benefits, and limitations.

Drawn from Table 1, typical economic indexes have been adopted for various types of DGs, and most of them are tested in experimental models. However, many researchers ignore the labor cost, tax, and fuel costs at present. Meanwhile, DGs planning is based on experimental models and has not been applied to the real model. Besides, in future research, DGs should be planned based on user experience. The demand side is extremely important. Future researchers should consider how to not only meet the users' power consumption feeling but also reduce the investment and operation costs. In the small-scale power grid, the load on the user side and the daily load fluctuation are relatively low, while in the large-scale power grid, the daily load fluctuation is large and more DGs are required, so it is difficult to ensure the economy. Hence, in the large-scale power grid, the reliability index such as load fluctuation and voltage profile are more important. Moreover, as the increasing penetration of electric vehicles (EVs) has increased, it will cause load fluctuation. The design and selection of economic indexes will face difficulties.

3 Analysis of technology indexes

3.1 Power loss

Before the DGs are connected to DN, the power flow of the DN simply flows from the substation side to the load side. However, with the incorporation of the DGs, the direction and magnitude of the system power flow will be affected, thus changing the power loss of the DN. To minimize the power loss, the most ideal method is to install DGs locally at each power node. However, due to the investment cost and the limitation of the number of generators installed, this method is not feasible. In general, the value of DGs power factor is equal to the total load of the electric power system network, but there are equality constraints to prevent power flow reversal. In practice, the power factor of most DGs operates according to their rated power value, reducing power loss on the premise of maintaining voltage stability. The value of DGs power factor will be different in different periods (Quezada et al., 2006; Hengsritawat and Tayjasanant, 2012). During the peak off hour, to limit voltage fluctuation and reduce active power loss, the value of DGs power factor is generally chosen as the leading power factor. Besides, during the peak hour, to compensate for voltage drop and enhance reactive power, the value of DGs power factor is supposed to be chosen for the lagging power factor.

The access of DGs makes the DN change from a simple radiation network to a multi-power supply system. Before DGs are connected, the direction of feeder power flow is always unidirectional. When DN is connected to the DGs, the unidirectional power flow mode of the system is changed. The power flow of the system is not necessarily unidirectional, and the reverse flow of the power flow may occur. The access to DGs may

TABLE 1 Summary and analyze the evaluation indexes of DGs.

Evaluation index	Objective	Objective function	Type of DG	Parameters	Application	Benefits	Limitations
Economic index	Maximize benefits (He et al., 2019)	$F = f_{\mathrm{Inc}} - f_{\mathrm{Inv}} - f_{\mathrm{Ope}}$	Type-I; Type-III; Type-IV.	f_{Inc} : income of company; f_{Inv} : investment of DG; f_{Ope} : operation cost.	Small-scale power grid.	Consider three types of DG.	Ignore the labor cost, government subsidy, and environmental impact; Ignore DR.
	Minimize system cost (Jabr and Pal, 2009)	$C_{\mathrm{DG}} = \sum_{i=1}^{n} P_{\mathrm{DG},i} + C_{\mathrm{L}}\left[P_{\mathrm{L(target)}} - P_{\mathrm{L(actual)}}\right]$	Type-I.	C_{L} : incentive penalty; $P_{\mathrm{DG},i}$: power output; $P_{\mathrm{L(target)}}$: target power loss; $P_{\mathrm{L(actual)}}$: actual power loss.	Small-scale power grid.	Consider the power loss of DN.	Only single-objective; Ignore labor cost, environmental influence and DR.
	Minimize cost and maximize the benefit (Porkar et al., 2011)	$C = \left(\frac{s}{h}\right) = C_{\mathrm{DG}} + C_{\mathrm{OM,DG}} + C_{\mathrm{SC}} + C_{\mathrm{OMSC}}$ $+ C_{\mathrm{E}} + C_{\mathrm{loss}} + C_{\mathrm{ENS}}$ $TSB() = C_{\mathrm{DGsave}} + A \cdot \sum_{t=1}^{8760} \left[C_{\mathrm{Esave}}(t) + C_{\mathrm{losssave}}(t) C_{\mathrm{ENS}}(t)\right]$	All types.	C_{DG} : DG investment cost; C_{OMDG} : DG operation and maintenance cost; C_{SC} : synchronous condense (SC) cost; C_{OMSC} : SC operation and maintenance cost; C_{E}: cost of fuel cell; C_{loss} : energy loss cost; C_{ENS} : energy is not supplied cost.	Small-scale power grid.	Consider many uncertain parameters; Not only include cost but consider profit.	High complexity; Ignore the resident response; Ignor e labor cost, government subsidy, and environmental influence.
Technology index	Power loss	$S_{\mathrm{loss}} - S_{\mathrm{loss}}^{\mathrm{DG}} = (U_{\mathrm{G}} - U_{\mathrm{L}}) \cdot I_{\mathrm{DG}}$	Type-III reduces power loss most.	U_{G} : main grid voltage; U_{L}: load voltage; I_{DG} current through t DG.	Long distance and large-scale power grid.	Reduce power loss and improve system reliability.	Related to power factor, types and location of DGs; Only install type-IV on DN, the high penetration may cause greater power loss.
	Voltage profile	$U_{\mathrm{s}} = \sum_{i=1}^{K} \frac{\lvert U_i - U_{\mathrm{R}} \rvert}{U_{\mathrm{R}} \cdot K}$	Type-III improves voltage profile most.	U_{R} : reference voltage of electric power system; U_i: ith node voltage; K : number of nodes.	Long distance and large-scale power grid.	Primary substation voltage reduced; Voltage quality improved.	Shut down DGs during small-scale power grid.

lead to the increase or decrease of power flow along the feeder line. The power flow of DN will change, and the power loss of DN will change accordingly. The power loss may increase or decrease, depending on various factors. Furthermore, in the large-scale grid, due to the long transmission distance, the installation of DGs with improper capacity at the end of the line will reduce the power loss. Generally, the power loss may be reduced by the penetration level of DGs. Meanwhile, note that the location of DGs installed on the DN must cause a different effect on the power loss. The equations of the power loss with DGs and without DGs are as follows:

$$S_{\mathrm{loss}} = S_{\mathrm{G}} - S_{\mathrm{L}} = (U_{\mathrm{G}} - U_{\mathrm{L}}) \cdot I_{\mathrm{link}} \tag{1}$$

$$S_{\mathrm{loss}}^{\mathrm{DG}} = S_{\mathrm{G}} - S_{\mathrm{L}} + S_{\mathrm{DG}} = (U_{\mathrm{G}} - U_{\mathrm{L}}) \cdot (I_{\mathrm{link}} - I_{\mathrm{DG}}) \tag{2}$$

where S_{G}, S_{L} and S_{DG} separately mean the power of the main grid, load, and DG; U_{G} and U_{L} denote the voltage of the main grid and load; I_{link} and I_{DG} are the current through the link and DG. The power loss reduced by DG is as follows:

$$S_{\mathrm{loss}} - S_{\mathrm{loss}}^{\mathrm{DG}} = (U_{\mathrm{G}} - U_{\mathrm{L}}) \cdot I_{\mathrm{DG}} \tag{3}$$

Furthermore, as concluded from the literature (Ufa et al., 2022), all types of DGs can reduce power loss. However, the power loss reduced by different types of DGs connected to DN is different. The installation type of type-III has the most obvious effect on the reduction of power loss. The types of DGs that reduce power loss are sorted in the order of type-III, type-I, type-II, and type-IV, respectively. When DGs can deliver both active and reactive power, which have the most obvious effect on power loss reduction. In addition, DGs type-III and type-II can generate reactive power (improve voltage profile), which also has a great impact on the reduced power loss. Finally, when there is only type-IV installed on the DN, the high penetration level of the DGs will cause greater power loss than that without DGs (Prakash and Lakshminarayana, 2018).

3.2 Voltage profile

The allowable deviation of the three-phase power supply voltage of 10 kV and below is ± 7% of the nominal voltage (Li et al., 2021), and the smaller the absolute value, the better. Therefore, the system voltage profile index is defined as the average value of the absolute value of the voltage profile of each node to represent the overall voltage deviation level of the system. The calculation formula is as follows:

$$U_{\mathrm{s}} = \sum\nolimits_{i=1}^{K} \frac{|U_i - U_{\mathrm{R}}|}{U_{\mathrm{R}} \cdot K} \tag{4}$$

where U_{R} means the reference voltage of the electric power system; U_i is the ith node voltage; K denotes the number of the node.

Similar to the power loss, the voltage profile is related to the power factor, location, capacity, and penetration level of DGs. However, for small-scale load systems, DG integration may lead to voltage overrun and other problems. Therefore, before the DGs have been connected to the power grid, a large number of experimental analyses should be conducted.

4 Discussion and conclusion

To research the comprehensive impact of DGs access on DN, this paper comprehensively evaluated and analyzed the economic indexes and technical indexes of DG, and summarized their advantages and disadvantages and applicable scenarios in Table 1. Besides, two valuable conclusions about the DGs evaluation index have been proposed, as follows:

a) Economic indexes are generally applicable to small-scale grids because the load fluctuation of residents with low load in small-scale grids will not be large. Large-scale grids, not only consider the benefits and investment costs of the power grid but also consider the demand side response. Meanwhile, in the large-scale power grid, the load fluctuation is high. The most significant to configuring DGs is to maintain the stability of the power grid, so minimizing the cost and maximizing the benefits are suitable for small-scale power grids.
b) Reasonable access to DGs will reduce the power loss and improve the voltage profile of the power grid, especially in the large-scale power grid. The power loss and voltage profile are related to the power factor and location penetration level of DGs. In small-scale power grids, it is better not to connect DGs under light load conditions, otherwise voltage quality may reduce.

Generally speaking, according to the scale of the power grid, it is very important to flexibly coordinate the grid-source and reasonably select the evaluation indexes to maintain the stability of the power grid and ensure the economy.

Author contributions

XY: writing the manuscript; XL: discussion of the economic index; XZ: discussion of the technology index; KL: editing; XF: discussion of the topic.

Funding

Grid-source coordination development-based power sources planning evaluation index system research (5214GH210011).

Conflict of interest

XY, XL, XZ, KL, XF was employed by Central China Branch of State Grid Corporation of China, Central Southern China Electric Power Design Institute Co., Ltd.

Publisher's note

References

Ali, E., and Qiang, Y. (2018). Optimal integration and planning of renewable distributed generation in the power distribution networks: A review of analytical techniques. *Appl. Energy* 210, 44–59. doi:10.1016/j.apenergy.2017.10.106

Francisco, C. R. C., Wesley, P., Ivo, C., and Bruno, H. (2020). Empirical continuous metaheuristic for multiple distributed generation scheduling considering energy loss minimization, voltage and unbalance regulatory limits. *IET Generation,Transmission Distribution* 14 (16), 3301–3309. doi:10.1049/iet-gtd.2019.1860

He, S., Gao, H., Liu, J., and Liu, J. (2019)"Distributionally robust optimal DG allocation model considering flexible adjustment of demand response," in Paper presented at: 2019 IEEE Power & Energy Society General Meeting (PESGM), Atlanta, GA, USA, August 4-8, 2019, 1–5. doi:10.1109/PESGM40551.2019.8973569

Hengsritawat, V., and Tayjasanant, T. (2012). Impacts of load models and power factor control on optimal sizing of photovoltaic distributed generators in a distribution system. *IEEJ Trans. Elec. Electron. Eng.* 7 (6), 567–573. doi:10.1002/tee.21774

Jabr, R., and Pal, B. (2009). Ordinal optimisation approach for locating and sizing of distributed generation. *IET Generation Transm. Distribution* 3 (8), 713–723. doi:10.1049/iet-gtd.2009.0019

Koutsoukis, N. C., Georgilakis, P. S., and Hatziargyriou, N. D. (2014)"A Tabu search method for distribution network planning considering distributed generation and uncertainties," in Paper presented at: 2014 International Conference on Probabilistic Methods Applied to Power Systems (PMAPS), Durham, England, July 7-10, 2014, 1–6. doi:10.1109/PMAPS.2014.6960627

Li, G. D., Wang, Z., Shuai, H., Zhao, F., Zhang, Q., Liu, C., et al. (2021). Evaluation of the impact of distributed generation access on distribution network operation index. *Electr. Energy Manag. Technol.* 6, 79–85. doi:10.16628/j.cnki.2095-8188.2021.06.014

Magadum, R. B., and Kulkarni, D. (2015)"Power loss reduction by optimal location of DG using fuzzy logic," in Paper presented at: 2015 International Conference on Smart Technologies and Management for Computing, Communication, Controls, Energy and Materials (ICSTM), Chennai, India, May 6-8, 2015, 338–343. doi:10.1109/ICSTM.2015.7225438

Porkar, S., Poure, P., Abbaspour-Tehrani-fard, A., and Saadate, S. (2011). Optimal allocation of distributed generation using a two-stage multi-objective mixed-integer-nonlinear programming. *Euro. Trans. Electr. Power* 21 (1), 1072–1087. doi:10.1002/etep.497

Prakash, D. B., and Lakshminarayana, C. (2018). Multiple DG placements in radial distribution system for multi objectives using whale optimization algorithm. *Alexandria Eng. J.* 57, 2797–2806. doi:10.1016/j.aej.2017.11.003

Priyanka, P., Patidar, N. P., and Nema, R. K. (2014). Planning of grid integrated distributed generators: A review of technology, objectives and techniques. *Renew. Sustain. Energy Rev.* 40 (2014), 557–570. doi:10.1016/j.rser.2014.07.200

Quezada, V. H. M., Abbad, J. R., and Roman, T. G. S. (2006). Assessment of energy distribution losses for increasing penetration of distributed generation. *IEEE Trans. Power Syst.* 21, 533–540. doi:10.1109/TPWRS.2006.873115

Rana, H. A. Z., Geev, M., Haile-Selassie, R., Aghaei, J., Niknam, T., and Pillai, P. (2017). Operation and planning of distribution networks with integration of renewable distributed generators considering uncertainties: A review. *Renew. Sustain. Energy Rev.* 72 (2017), 1177–1198. doi:10.1016/j.rser.2016.10.036

Semic, E., Hubana, T., and Šaric, M. (2019)"Distributed generation allocation in low voltage distribution network using artificial neural network," in Paper presented at: IEEE Eurocon 2019-18th International Conference on Smart Technologies, Novi Sad, Serbia, July 1-4, 2019, 1–6. doi:10.1109/EUROCON.2019.8861816

Su, C. (2010). Stochastic evaluation of voltages in distribution networks with distributed generation using detailed distribution operation models. *IEEE Trans. Power Syst.* 25 (2), 786–795. doi:10.1109/TPWRS.2009.2034968

Ufa, R. A., Malkova, Y. Y., Rudnik, V. E., Boriov, V. A., and Borisov, V. (2022). A review on distributed generation impacts on electric power system. *Int. J. Hydrogen Energy* 47, 20347–20361. doi:10.1016/j.ijhydene.2022.04.142

Wang, X. L., Hao, C. C., Li, X. M., Sun, S. X., and Shi, W. C. (2019). The vulnerability analysis of distribution network with distributed generation. *Electr. Meas. Instrum.* 56 (6), 38–43. doi:10.19753/j.issn1001-1390.2019.06.007

Yang, B., Yu, L., Chen, Y. X., Ye, H., Shao, R., Shu, H., et al. (2020). Modelling, applications, and evaluations of optimal sizing and placement of distributed generations: A critical state-of-the-art survey. *Int. J. Energy Res.* 45 (3), 3615–3642. doi:10.1002/er.6104

frontiers | Frontiers in Energy Research

TYPE Original Research
PUBLISHED 20 September 2022
DOI 10.3389/fenrg.2022.1019349

OPEN ACCESS

EDITED BY
Nantian Huang,
Northeast Electric Power University,
China

REVIEWED BY
Wenxia Liu,
North China Electric Power University,
China
Chengmin Wang,
Shanghai Jiao Tong University, China

*CORRESPONDENCE
Jifeng Liang,
ljifeng@126.com
Junming Lin,
ljm121618233462319@126.com

SPECIALTY SECTION
This article was submitted to Smart Grids,
a section of the journal
Frontiers in Energy Research

RECEIVED 15 August 2022
ACCEPTED 22 August 2022
PUBLISHED 20 September 2022

CITATION
Luo P, Liang J, Fan H, Zeng S, Yang G and Lin J (2022), Real-time distributed dispatch strategy for distribution transformer supply zone cluster based on cloud-edge collaboration architecture.
Front. Energy Res. 10:1019349.
doi: 10.3389/fenrg.2022.1019349

Real-time distributed dispatch strategy for distribution transformer supply zone cluster based on cloud-edge collaboration architecture

Peng Luo[1], Jifeng Liang[1]*, Hui Fan[2], Siming Zeng[1], Guangjie Yang[3] and Junming Lin[4]*

[1]Electric Power Research Institute of State Grid Hebei Electric Power Co, Ltd., Shijiazhuang, China, [2]State Grid Hebei Electric Power Co, Ltd., Shijiazhuang, China, [3]Handan Power Supply Branch of State Grid Hebei Electric Power Co, Ltd., Handan, China, [4]Key Lab of Power Electronics for Energy Conservation and Motor Drive of Hebei Province (School of Electrical Engineering, Yanshan University), Qinhuangdao, China

Aiming at the problem of long-timescale prediction deviation in the distribution network, a fast regulation strategy of cloud-edge coordination based on an intelligent transformer supply zones edge consistency algorithm is proposed. The cloud makes the global initial optimal allocation to the edge transformer supply zone clusters, and then the cluster makes the secondary collaborative optimal allocation to the edge zones. A fast power interaction model within a cluster based on a consensus algorithm is established, and the micro-increase rate of dispatching cost is used as the consistency variable so that the cluster adjustment amount is optimally allocated to each transformer supply zone, and the total dispatch cost of all transformer supply zones is minimized. The simulation example verifies the effectiveness of the cloud-edge collaborative fast control strategy based on the intelligent station cluster edge consensus algorithm in this article.

KEYWORDS

transformer supply zone, coordinate the edge sides, power deviation, distributed dispatch, consensus algorithm

1 Introduction

Under the background of the “double-carbon” goal, China has accelerated the construction of the new electric power system with new energy as the main body. The wide access to a high proportion of distributed new energy and the participation of large-scale resources such as energy storage and flexible load in the regulation and control of the distribution network have affected the safe and stable operation of the system (Peng et al., 2022); how to use the abovementioned resources to coordinate and dispatch is one of the key issues that need to be solved urgently at present (Fang et al., 2019; Zhao et al., 2019).

There have been many studies on the scheduling of using distributed resources. Tofighi-Milani et al. (2022), in order to promote the distributed scheduling of multi-agent systems, proposed a P2P resource management scheme considering network constraints, which can realize that each agent can independently schedule local resources to maximize its own interests. Huang et al. (2022), to manage multiple distributed resources in a microgrid, proposed a two-stage interactive retail electricity market based on interactive energy, which can effectively exploit the flexibility potential of each distributed resource. Huang et al. (2021), in order to promote the free competition of electric energy retailers with multiple distributed resources in the retail market, proposed a transactional retail market mechanism, which reduces the impact of clean energy uncertainty and improves market efficiency. Yang et al. (2021), in order to fully coordinate and utilize flexible resources, proposed a three-timescale coordinated scheduling framework, which can effectively improve the economy of active distribution networks.

With the vigorous development of the Internet of energy (Liu. et al., 2020), he automation and digital transformation of low-voltage distribution transformer supply zone as a unit is gradually carried out in China, and a new generation of intelligent distribution transformer supply zone based on the concept of cloud-edge collaboration and edge computing of the distribution Internet of Things has become one of the construction paths. Cloud-side collaboration can reasonably allocate complex computing tasks. Edge computing implements local data collection and analysis on the side near the data (Gong et al., 2018), and then uploads to the end. The cloud collects the data transmitted from the edges, makes the optimization decision of the whole system, and then sends the control task to each edge. The cloud-edge cooperative dispatching mode fits the distribution characteristics of new energy in the distribution network (Li. and Song, 2021), and is applied to the optimal regulation of the distribution network (Ren et al., 2019), which can effectively solve the problem of a large amount of computing and communication data caused by the access of a high proportion of distributed resources.

There have been some research works on the cloud-edge cooperative dispatching strategy. Peng et al. (2022) proposed the dispatching operation mode of two-level fusion of “cloud brain-edge neuron.” Liu et al. (2020), aiming at the problem of peak regulation in virtual power plants, constructed a multi-energy virtual power plant dispatching technical framework of cloud-edge-end hierarchical cooperation. Si et al. (2020) established the physical architecture of Power Internet of Things based on cloud-edge collaboration, built a CPPS unified computing mathematical model based on edge computing and the idea of cooperative autonomy among clusters and cloud-edge collaborative control, and applied the dispatching calculation of virtual power plants. In order to promote the synergistic interaction between distributed resources and distribution network, Zhou et al. (2022) proposed the Power Internet of Things 5G cloud-edge-end multi-level coordination framework and a cloud-side-end collaborative resource regulation method based on semi-distributed artificial intelligence to achieve collaborative optimization of cloud-side/side-side computing resource allocation. Zhang and Wang (2022) proposed a real-time demand response dispatching strategy of cloud-side collaboration for electric vehicles, and a task unloading strategy of cloud-side collaboration was proposed. A dispatching decision model was established with the goal of minimizing the load difference of the central cloud and maximizing the response benefit of the edge cloud.

Random fluctuation and unpredictability of new energy bring power deviation to distribution network regulation (Bian et al., 2021; Li et al., 2022). Although the cloud-side cooperative regulation strategy can effectively improve the problems of computation and communication, it is difficult to correct the power deviation in time due to the communication delay in the cloud-edge cooperative control. Therefore, it is necessary to seek an efficient and fast dispatch decision-making method (Gong et al., 2018). Compared with remote computing in the cloud, edge computing performs data analysis near the device. Compared with cloud-edge information transmission, it is more convenient and faster to directly exchange data between adjacent edges.

A consensus algorithm is a distributed optimization algorithm to solve the task concentration. It only needs the communication data between local and adjacent units, and completes the iterative optimization between each unit, which can effectively reduce the computation and communication burden. At present, the consensus algorithm has been applied to the coordinated control of the distribution network (Zeraati et al., 2019). Zhang et al. (2020) proposed a distributed energy storage optimization control strategy based on a consensus algorithm for the economic dispatch of autonomous microgrid clusters, and used the consensus algorithm to distribute the output power of energy storage. Pu et al. (2017) proposed a distributed optimization scheduling method based on consistency theory to solve the problem of regional autonomous optimal scheduling in an active distribution network. The incremental cost of distributed power supply was taken as a consistency variable to realize the optimization of power generation cost in the autonomous region. Li et al. (2018), to solve the problem of DC micro-power grid in the centralized control, proposed the multi-objective control strategy based on a consistency algorithm, to realize the voltage stability and power generation cost minimum. Yang et al. (2020) proposed a distributed control strategy based on a consensus algorithm to solve the problem of unbalanced power between photo-voltaic power generation and load in a DC microgrid composed of multiple photovoltaic and battery energy storage units. Taking the control power of batteries as a consistency variable, the unbalanced power can be distributed among batteries according to the real-time state of SoC, avoiding the phenomenon of mutual charging and discharging between batteries. Lv et al. (2019) established a dynamic economic dispatching model of an independent microgrid with energy storage and controllable loads, and proposed a distributed solution algorithm based on a consensus algorithm to realize the optimal power distribution of distributed power and energy storage.

The abovementioned research applies the consensus algorithm to realize the distributed control of the microgrid or adopts the completely distributed scheme to realize the coordinated regulation of the distribution network. However, due to the lack of coordination of centralized links, the distributed scheme is generally only suitable for distributed control with relatively fixed rules, which is difficult to adapt to changes in the power grid environment, and it is difficult to convert complex optimization problems into distributed algorithms. In this article, aiming at correcting the long-term prediction deviation, combined with the characteristics of the cloud and the edge, a real-time dispatch strategy for distribution transformer supply zone cluster based on cloud-edge collaboration architecture is proposed. Multiple zones with adjacent communication functions are formed into a transformer supply zone cluster. The leader of the transformer supply zone cluster sends the power deviation and dispatching cost signals of the cluster to the cloud, and the cloud optimizes the total power deviation of the distribution network to each cluster based on long-term global control. The study aims to minimize the deviation amendment cost; a real-time power interaction model was established based on the consensus algorithm. The micro-increase rate of the cost was taken as the consistency variable of the transformer supply zone cluster, and the consistency iteration was carried out within the cluster, so the power deviation signal of the cluster was optimally allocated to each zone cluster. When cloud-side communication is interrupted, each cluster can independently implement consistent dispatch according to its own power deviation within the cluster, with autonomous ability. The simulation example verifies the effectiveness of the coordinated control strategy of the transformer supply zone cluster based on the consensus algorithm of the edge nodes of the intelligent transformer supply zones.

The main contributions of this article are as follows:

A distributed real-time control scheme of cloud-edge cooperation is proposed, in which the intelligent terminals of the zones are used as the edge computing nodes, and the cloud-edge cooperation is carried out among multiple zones with adjacent communication functions. The cloud allocates the total dispatch amount to the transformer supply zone clusters for the initial allocation. The transformer supply zone cluster then collaboratively distributes the initial dispatching quantity to each transformer zone for secondary allocation. When the communication between the cloud and the edge is interrupted, the transformer supply zone cluster independently performs secondary optimal allocation according to the scheduling amount of the cluster to achieve independent operation.

A centralized-distributed scheduling method based on a consensus algorithm is proposed. The cloud optimally distributes the dispatching volume of the distribution network to the transformer supply zone clusters. With the micro-increase rate of dispatching cost as the consistency variable, the consistency iteration is carried out within the cluster, and the dispatch quantity of the cluster is optimally allocated to each transformer supply zone.

2 Distributed fast power regulation strategy for transformer area clusters under the cloud-edge collaboration architecture

2.1 Cloud-side collaborative power dispatching framework

In the cloud-side collaborative control architecture of a new energy distribution network, the cloud is the control center responsible for the global control of the distribution network system. Its main functions include collecting and processing information transmitted by the edge side, making optimization decisions for the whole system, and issuing control instructions to edge side and assisting edge computing. The edge side is each transformer supply zone, equipped with intelligent distribution transformer terminals, which is mainly responsible for intelligent sensing and aggregation of distributed power, energy storage and controllable load in the transformer supply zones, communication with cloud and adjacent side, executing of edge calculation, load dispatching ability of evaluation and control, *etc.* The information exchange between the cloud and the side is carried out through the public channel to realize the cloud-edge cooperation; each transformer supply zone is equipped with an independent local controller to exchange information with adjacent stations to realize edge cooperation.

Based on the flexible load, energy storage, and distributed generation resources output, the day-ahead dispatching is carried out with the objective of minimizing the operation cost of the transformer supply zone. According to the forecast of distributed generation resources output and flexible load, to determine the power generation plan of this transformer supply zone cluster, divide 24 h of a day into T periods, assuming that the power of the constituent unit remains basically unchanged in each period. The objective function of the day ahead dispatching is (Huang et al., 2017)

$$\min F = \sum_{t=1}^{T} \left\{ \sum_{i=1}^{n} \left[C_{DR,i}(t) + C_{ESS,i}(t) + C_{dr,i}(t) \right] \right\} \tag{1}$$

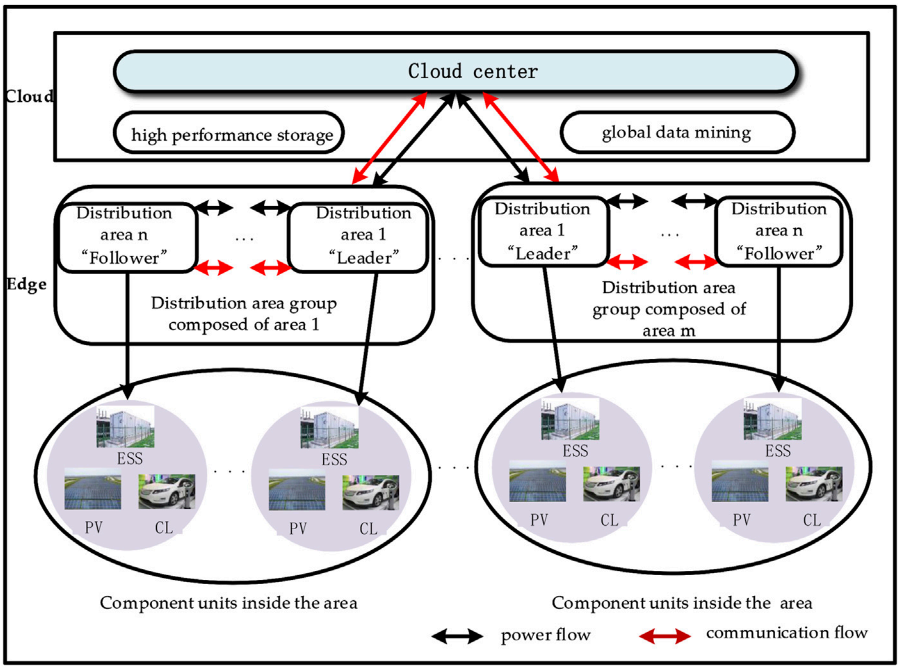

FIGURE 1
Real-time dispatch framework for distribution transformer supply zone cluster based on cloud-edge collaboration architecture.

where $C_{DR,i}(t)$, $C_{ESS,i}(t)$, and $C_{dr,i}(t)$ are, respectively, the operating costs of distributed generation resources, energy storage, and flexible load in transformer i during period t.

In the previous dispatch stage, the cloud performs centralized optimization calculations with the goal of minimizing the cost and optimally allocates the regulation amount to each transformer supply zone cluster because the prediction accuracy decreases with the increase of timescale, and the day ahead scheduling often cannot meet the requirements of power balance. This study takes the optimization value of the long timescale as the reference value to correct the deviation of regulation power from the short timescale. In this study, combined with the characteristics of cloud edge, multiple transformer supply zones with adjacent communication functions are formed into transformer supply zone clusters to form edge nodes, and uses edge computing to adjust and correct the power deviation in real time on a short timescale. Figure 1 shows the real-time dispatch framework for the distribution transformer supply zone cluster based on the cloud-edge collaboration architecture. The "Leader-Follower" distributed dispatching method is adopted within each transformer supply zone cluster (Zhang and Chow, 2011), and the "Leader" of the cluster sends the power deviation and dispatching cost signal of the cluster to the cloud; the cloud summarizes the data information uploaded by all leaders, on a long-term scale; the global centralized dispatch optimization calculation is carried out with the goal of economical optimization, and distributes the optimized power deviation value to the "leaders" of each transformer supply zone cluster for initial distribution; the transformer supply zone clusters then cooperatively allocate the scheduling amount obtained from the initial allocation to each transformer supply zone for secondary allocation. When the communication between cloud and edges is interrupted, the transformer supply zone cluster can optimize the allocation according to the scheduling volume of the cluster to realize independent operation.

According to the scheduling results of different stages at the transformer supply zone level, the internal resources of the transformer supply zone are finely controlled, and then the ending resources are optimized and managed according to the target dispatching power of the transformer supply zone. With the best global cost as the goal, the resources in the transformer supply zone are classified and participate in the dispatch in stages. The integrated regulation and control requirements of end transformer supply zones are realized.

The total power deviation of the distribution network is

$$\Delta P = \sum_{j=1}^{m} \Delta P_j \;\; (j = 1, 2, ...m), \tag{2}$$

$$\Delta P = \sum_{j=1}^{m} \Delta P_j \;\; (j = 1, 2, \dots m), \tag{3}$$

where ΔP refers to the total power deviation of the distribution network, ΔP_j represents the power deviation of the jth power distribution cluster being uploaded to the cloud, and $\Delta P_{j,\min}$ and $\Delta P_{j,\max}$are the upper and lower limits of the regulated power of thejth transformer supply zone cluster, respectively.

According to the power deviation uploaded by the leader of each transformer supply zone cluster, the cloud performs optimization calculations based on the slight increase rate of equal cost. When the equation shown in Eq. 4 is satisfied, the purpose of optimizing power deviation distribution to each power transformer supply zone cluster can be achieved with the goal of economy.

$$\frac{\partial C_1}{\partial(\Delta P_1)}=\frac{\partial C_2}{\partial(\Delta P_2)}=\mathrm{L}=\frac{\partial C_m}{\partial(\Delta P_m)} \tag{4}$$

where C_m is the control cost of the mth transformer supply zone cluster and ΔP_m is the power deviation of the mth transformer supply zone cluster.

When the micro-increase rate of cost of all transformer supply zone clusters is consistent, the optimal power deviation value to be corrected for each cluster under the lowest dispatch cost is obtained; that is, it meets the relationship shown in Eq. 5.

$$\sum_{j=1}^{m}\Delta P_j=\sum_{j=1}^{m}\Delta P_j^{'}, \tag{5}$$

where ΔP_j represents the power deviation of the jth transformer supply zone cluster and $\Delta P_j^{'}$represents the power deviation of the jth transformer supply zone cluster after optimization calculation of the cloud equal incremental rate.

2.2 Distribution zone cluster members and functions

There are multiple transformer supply zones in the transformer supply zone cluster, and each transformer supply zone has the resources that can participate in the dispatch. Considering that the type and quantity of distributed power supply, energy storage, and flexible load may be different in each transformer supply zone, for the convenience of expression, the units inside the zone are no longer distinguished here; each transformer supply zone is regarded as an edge node, and in order to ensure that the distribution transformer supply zones cluster has high communication reliability (Zhang and Chow, 2012), the transformer supply zone with good communication and computing capabilities is selected as the “Leader,” and the rest of the transformer supply zones are selected as “followers.”

Leader: As the most important transformer supply zone in the transformer supply zone cluster, it is required to have high communication reliability and good computing capability. It can interact with the cloud for data and information, upload the power deviation of the local transformer supply zone cluster to the cloud, and receive the optimized power deviation value from the cloud; it can carry out communication exchange with adjacent transformer supply zones, obtain the information transmitted by adjacent transformer supply zones, and update the dispatching information of transformer supply zone in the cluster based on the consensus algorithm.

Follower: All transformer supply zones except “Leader”; they do not need to communicate with the cloud, only interact with adjacent transformer supply zones, and update the dispatching information of the transformer supply zone based on the consensus algorithm.

3 Consistent distributed control method for transformer area cluster

3.1 Consistency theory

3.1.1 Distributed topological graph theory

In this article, optimization is carried out with the goal of minimizing the dispatch cost of all transformer supply zones. It is necessary to coordinate control among multiple zones so that the cost micro-increase rate in the multi-distribution transformer supply zones system tends to a stable common value, which belongs to the consistency of the transformer supply zones.

In the problem of real-time dispatching consistency in transformer supply zones cluster, information is interacted through the communication network between the transformer supply zones, forming a distributed topology, so that can be described by graph theory. The communication relationship between the transformer supply zones of a transformer supply zone cluster can be represented by a directed graph $\boldsymbol{G}=(\boldsymbol{V},\boldsymbol{E})$, where $\boldsymbol{V}=\{1,\cdots,n\}$ is the set of nodes of the directed graph $\boldsymbol{G}$ and each transformer supply zone can be represented by a node in the directed graph, and $\boldsymbol{E}\subseteq\boldsymbol{V}\times\boldsymbol{V}$ is the set of edges of the directed graph $\boldsymbol{G}$. Two connected nodes are said to be “neighbors” if and only if there is an information transmission channel between node i and node j. $\boldsymbol{A}$ graph $\boldsymbol{G}$ is said to be a strongly connected graph if, for any two nodes $i,j\,(i\neq j)$, there exist directed paths from i to j and from j to i.

Define the matrix $\boldsymbol{A}=[a_{ij}]$ as the adjacency matrix of $\boldsymbol{G}$ with diagonal elements of 0 and non-diagonal elements a_{ij} as the number of edges from node i to node j. $\boldsymbol{D}=[d_{ij}]$ is a degree matrix, which is a diagonal matrix of $n\times n$, $d_1,d_2,\cdots,d_n$ is the number of degrees corresponding to each node, and the degrees are the number of neighboring nodes of a node. $\boldsymbol{L}=\boldsymbol{D}-\boldsymbol{A}=[l_{ij}]$ is a Laplacian matrix reflecting the topological structure of the power distribution zone, where l_{ij} satisfies the relationship shown in Eq. 6.

$$l_{ij}=\begin{cases}\sum\limits_{j\in N_i}a_{ij}, & (i=j)\\ -a_{ij}, & (i\neq j)\end{cases} \tag{6}$$

3.1.2 Consensus algorithm

In order to effectively reduce the computational and communication burden of cloud-side coordinated control of distribution networks, a centralized-distributed dispatch method based on a consensus algorithm is proposed in this article. In the day-ahead stage, the centralized optimization calculation is performed by the cloud, and in the real-time stage, the coordinated regulation of each transformer supply zone is transformed into a distributed control in the distribution transformer supply zones cluster. The consistency algorithm exchanges information between the local controller and adjacent controllers, and performs iterative calculations in each controller to make the selected consistency variables tend to a common value (Zheng et al., 2022). The calculation process is distributed computing. Therefore, each distribution transformer supply zone can be linked by the consensus algorithm so as to realize the coordinated regulation of the distribution transformer supply zones cluster. The proposed centralized-distributed dispatch method based on the consensus algorithm can not only solve the problem of high computational pressure of the centralized control method but also overcome the global limitation of the distributed control method so that the proposed method combines the advantages of both and overcome the shortcomings of both.

Considering the transformer supply zone as a node, for node i, $x_i(k)$ represents the consistency state information of node i after k iterations, where $i = 1, 2, \cdots, n$ and n are the number of nodes, and k is the number of iterations. In the distributed system, using the discrete consensus algorithm, the consistency variables of each node are updated according to the consistency variables of its neighboring nodes. As the number of iterations gradually increases, the consistency variables $x_i(k)$、$x_j(k)$of any adjacent nodes tend to be consistent and satisfy $x_i(k) = x_j(k)$; at this point, all nodes in the system are considered to converge to a common value, and the first-order consensus algorithm is expressed as

$$x_i(k+1) = \sum_{j=1}^{n} d_{ij} x_j(k), \tag{7}$$

where $x_i(k+1)$ is the state information of node i after $k+1$ iterations, $x_j(k)$ is the state information of node j after k iterations; $\boldsymbol{D}(k)$ is the state transition matrix; if matrix $\boldsymbol{D}(k)$ satisfies two conditions, $\boldsymbol{D}(k)$ is a non-negative row random matrix and all the eigenvalues are not greater than 1. All intelligent bodies of the system will converge to the same value after enough iterations. d_{ij} are the elements of the i row and j column of the state transfer matrix $i \in n$, $j \in n$ determined by the topology of the communication network, which can be expressed as

$$d_{ij} = \frac{z_{ij}(k)\left|l_{ij}(k)\right|}{\sum_{j=1}^{n} z_{ij}(k)\left|l_{ij}(k)\right|}, \tag{8}$$

where z_{ij} represents the gain weight of node i to node j.

3.2 Consistent and distributed control model for transformer supply zone

3.2.1 Dispatching cost function of zone

For the transformer supply zone, the internal resource attributes are no longer distinguished. The dispatching target is to minimize the dispatching cost of each transformer supply zone in the transformer supply zone cluster, which can be expressed as

$$\min C_i(P_i), \tag{9}$$

where P_i refers to the dispatching power of the ith transformer supply zone and C_i represents the dispatching cost of the ith transformer supply zone.

The flexible resources involved in the real-time dispatch of the transformer supply zone mainly include distributed generation resources, flexible load, and energy storage. Among them, the power dispatch cost function of distributed generation resources can be expressed as (Rahbari-Asr et al., 2014)

$$C_{G,i}\left(P_{G,i}\right) = a_i P_{G,i}^2 + b_i P_{G,i} + c_i, \tag{10}$$

where $C_{G,i}$ is the dispatching cost of the ith distributed generation resources; $P_{G,i}$ is the power dispatched by the ith distributed generation resources; a_i, b_i, and c_i are corresponding cost coefficients, respectively.

The operating cost function of the energy storage device is expressed as (Rahbari-Asr et al., 2014)

$$\begin{cases} C_{ESS}(P_{ESS}) = a_c P_{ESS}^2, P_{ESS} < 0 \\ C_{ESS}(P_{ESS}) = a_d P_{ESS}^2, P_{ESS} > 0 \end{cases}, \tag{11}$$

where P_{ESS} is the power dispatched by the energy storage device, $P_{\mathrm{ESS}} < 0$ indicates charging the energy storage, $P_{\mathrm{ESS}} > 0$ indicates discharging the energy storage, a_c, a_d are corresponding cost coefficients, respectively.

The cost function of flexible load is usually expressed by quadratic function (Liu et al., 2021):

$$C_{dr}(P_{dr}) = -a_{dr} P_{dr}^2 + b_{dr} P_{dr} + c_{dr} \tag{12}$$

where $C_{\mathrm{dr}}$is the control cost of flexible load; $P_{\mathrm{dr}}$is the power consumed by the flexible load; $a_{\mathrm{dr}}, b_{\mathrm{dr}}, c_{\mathrm{dr}}$ are corresponding coefficients, respectively.

According to Eqs 10–12, the dispatching cost function of the ith transformer supply zone can be regarded as the linear convex combination of each component unit in the transformer supply zone:

$$C_i(P_i) = a_i(P_i)^2 + b_i P_i + c_i, \tag{13}$$

where P_i refers to the dispatched power of the ith transformer supply zone, a_i, b_i, and, c_i are the corresponding cost coefficients, respectively, which are comprehensively calculated by Eqs 10–12.

The abovementioned calculation method is suitable for the case where the number of distributed resources in the transformer supply zone is small. When the number of distributed resources in the transformer supply zone is large, the K-means algorithm is used to cluster resources with the same response characteristics, which can significantly reduce the amount of calculation.

The power balance constraint of the distribution network is expressed as

$$\sum_{i=1}^{n} P_i = \sum_{i=1}^{n} P_L, \tag{14}$$

where P_i refers to the dispatched power of the distribution network and P_L refers to the actual load demand power.

The upper and lower limit constraints of distribution network dispatch power are expressed as

$$P_{i,\min} \le P_i \le P_{i,\max}, \tag{15}$$

where $P_{i,\min}$ and $P_{i,\max}$ represent the upper and lower limits, respectively, of the regulated power of the distribution network.

3.2.2 Consistent power dispatching method

According to the principle of the equal cost increment rate, when the adjustment cost increment rate of all stations tends to be the same, the total control cost of the station group can be minimized, and the optimal distribution of the station area control power can be achieved.

According to the equal micro-increase rate of cost, when the micro-increase rate of dispatching cost in all zones tends to be the same, the total control cost of the transformer supply zone cluster can be minimized, and the optimal distribution of the transformer supply zones cluster dispatch power can be achieved. Based on the abovementioned analysis, this article selects the micro-increase rate of cost of each transformer supply zone as the consistency variable, and uses the consistency algorithm to continuously update the consistency variable and update the dispatching power of the transformer supply zone at the same time. When the consistency variables of each transformer supply zone tend to be consistent, the optimal distribution of dispatching power in each transformer supply zone will be realized.

$$\lambda_i = \frac{\partial C_i}{\partial P_i} \quad i = 1, 2, \ldots n \tag{16}$$

It can be obtained from Eq. 17:

$$\lambda_i = 2a_i P_i + b_i \tag{17}$$

The slight increase rate of control cost of station i at $k+1$ is expressed as

$$\lambda_i(k+1) = \begin{cases} \sum_{j=1}^{n} d_{ij}(k)\lambda_j(k) + \mu\Delta P_d & \Delta P > 0, Leader \\ \sum_{j=1}^{n} d_{ij}(k)\lambda_j(k) - \mu\Delta P_d & \Delta P < 0, Leader \\ \sum_{j=1}^{n} d_{ij}(k)\lambda_j(k) & , Follower \end{cases} \tag{18}$$

where μ is the power regulation coefficient, ΔP is the power deviation optimally allocated to the transformer supply zone cluster by the cloud, ΔP_d is the deviation between the control amount allocated by cloud optimization to the transformer supply zone and the actual control amount, $\lambda_j(k)$ is the micro-increase rate of cost of the jth station at the k time, and $\lambda_i(k+1)$ is the micro-increase rate of cost of the ith transformer at the time.

ΔP_d is represented as

$$\Delta P_d = \Delta P - \sum_{i=1}^{n} \Delta P_i. \tag{19}$$

According to the micro-increase rate of dispatching cost at $k+1$ time in the ith transformer supply zone, the dispatching power at $k+1$ time in the ith transformer supply zone is obtained.

$$P_i(k+1) = \begin{cases} P_{i,\min} & , \frac{\lambda_i(k+1) - b_i}{2a_i} \le P_{i\min} \\ \frac{\lambda_i(k+1) - b_i}{2a_i} & , P_{i\min} \le \frac{\lambda_i(k+1) - b_i}{2a_i} \le P_{i\max} \\ P_{i,\max} & , \frac{\lambda_i(k+1) - b_i}{2a_i} \ge P_{i\max} \end{cases}, \tag{20}$$

where $P_i(k+1)$ is the dispatched power of the ith transformer supply zone at $k+1$ time, and $P_{i,\min}$ and $P_{i,\max}$ are the upper and lower limits of power dispatch in the ith transformer supply zone, respectively.

In the iterative calculation process of the consensus algorithm, ΔP_d is taken as the convergence condition. When $|\Delta P_d| < \varepsilon$, the consistency calculation reaches convergence, and ε is the convergence error.

Iteratively updating λ_i, respectively, until$\lambda_i$tends to the same valueλ_i^*, the system reaches uniform convergence, and the optimal dispatching cost of each transformer supply zone under this convergence value is obtained. According to the consensus algorithm, the value of the consistency variable of each transformer supply zone is obtained; thus, the optimal value of the active power output of the transformer supply zone under the minimum control cost is

$$P_i = \frac{\lambda_i^* - b_i}{2a_i} \tag{21}$$

3.3 Proof of convergence of consistency algorithm

The proof of the convergence of the consensus algorithm with the micro-increase rate of cost as the consensus variable is shown below.

After repeated iterative calculation using the consistency algorithm, the micro-increase rate of cost of each transformer supply zone can be achieved:

$$\begin{cases} \dfrac{\partial C_1\left(P_1^k\right)}{\partial P_1} = \dfrac{\partial C_2\left(P_2^k\right)}{\partial P_2} = \mathrm{L} = \dfrac{\partial C_n\left(P_n^k\right)}{\partial P_n} \\ P_1^k + P_2^k + \mathrm{L} + P_n^k = P_1^{k+1} + P_2^{k+1} + \mathrm{L} + P_n^{k+1} \end{cases}, \tag{22}$$

where k is the number of iterations, $C_i(P_i)$ is the control cost function of transformer supply zone i, and P_i is the control power of transformer supply zone i.

The transformer area dispatching cost function $C_i(P_i)$ is a univariate continuous differentiable convex function; its definition domain is $R = [P_i{}^{\min}, P_i{}^{\max}]$ and meets the characteristics of convex function in its definition domain:

$$C_i\left(P_i^{k+1}\right) \ge C_i\left(P_i^k\right) + \frac{\partial C_i\left(P_i^k\right)}{P_i^k}\left(P_i^{k+1} - P_i^k\right). \tag{23}$$

A Lyapunov multivariate function about the dispatching power of each transformer supply zone is defined V; its definition domain is the vector composed of the limit value of dispatch power in each transformer supply zone, and V can be expressed as

$$V\left(P_i^k\right) = V\left(P_1^k, P_2^k, P_3^k, \mathrm{L}\, P_n^k\right) = \sum_{i\in v} C_i\left(P_i^k\right), \tag{24}$$

where P_i^k represents the dispatching power calculated by the kth iteration of transformer supply zone i.

Assuming that in the *kth* iteration calculation all transformer supply zones reach the state shown in Eq. 25, the following relationship exists:

$$\begin{aligned} &V\left(P_i^{k+1}\right) - V\left(P_i^k\right) = \sum_{i\in v} C_i\left(P_i^{k+1}\right) - \sum_{i\in v} C_i\left(P_i^k\right) \le \\ &\left[C_1\left(P_1^{k+1}\right) + C_2\left(P_2^{k+1}\right) + \mathrm{L}\, C_n\left(P_n^{k+1}\right)\right] - \\ &\left[C_1\left(P_1^{k+1}\right) + \frac{\partial C_1\left(P_1^{k+1}\right)}{\partial P_1^{k+1}}\left(P_1^k - P_1^{k+1}\right)\right] - L - \\ &\left[C_n\left(P_n^{k+1}\right) + \frac{\partial C_n\left(P_n^{k+1}\right)}{\partial P_n^{k+1}}\left(P_n^k - P_n^{k+1}\right)\right] = 0 \end{aligned} \tag{25}$$

.

That is, $V(P_i^{k+1}) - V(P_i^k) \to 0$; therefore, the cost incremental rate consistency algorithm is convergent.

The solution process of real-time dispatch of transformer supply zone cluster

Flowchart of the power dispatch strategy in edge-side cooperative transformer supply zone based on the consensus algorithm is shown in Figure 2. The specific steps are as follows:

Step 1: The “Leader” transformer supply zone obtains the power deviation allocated after cloud optimization calculation and carries out information interaction with adjacent zones to calculate the consistent state variable value of each transformer supply zone;

Step 2: Obtain Laplace matrix $\boldsymbol{L}$ according to the topology of the transformer supply zone cluster, and then obtain state transition matrix $\boldsymbol{D}$;

Step 3: Update the consistency variable of each transformer supply zone cluster according to Eq. 18 and obtain the dispatched power of the transformer supply zone in this state according to Eq. 20;

Step 4: Judge whether the updated dispatch power value meets the constraint conditions. If not, update the network topology again, find the state transition matrix again, and repeat Step 3.

Step 5: Determine whether $|\Delta P_d| < \varepsilon$ is satisfied; if yes, the dispatched power value of the transformer supply zone will be output; if not, the power deviation of the transformer supply zone cluster will be recalculated.

4 Example analysis

4.1 Illustration of the calculation

To verify the effectiveness of the strategy proposed in this article, a typical active distribution network demonstration project in a city is used as an example for calculation and analysis. The network topology of the transformer supply zone cluster is shown in Figure 3. The transformer supply zone cluster consists of six zones, with zone 1 as the “Leader” and zone 2 to zone 6 as the “Followers.” The voltage level of each transformer zone is 10 kV/380 V and the frequency is 50 Hz in the model of the transformer supply zone cluster built in this article.

The categories of constituent units contained in each transformer supply zone cluster are shown in Table 1; zone 1 contains distributed generation resources, energy storage devices, and flexible loads; zone 2 contains distributed generation resources and flexible loads; zone 3 contains energy storage devices and flexible loads; zone 4 contains only distributed generation resources; zone 5 contains only energy storage devices; zone 6 contains only flexible loads.

We have to synthesize the control resources in the transformer supply zone, and perform linear convex combination to obtain the total cost parameters of the transformer supply zone. The parameters for each transformer

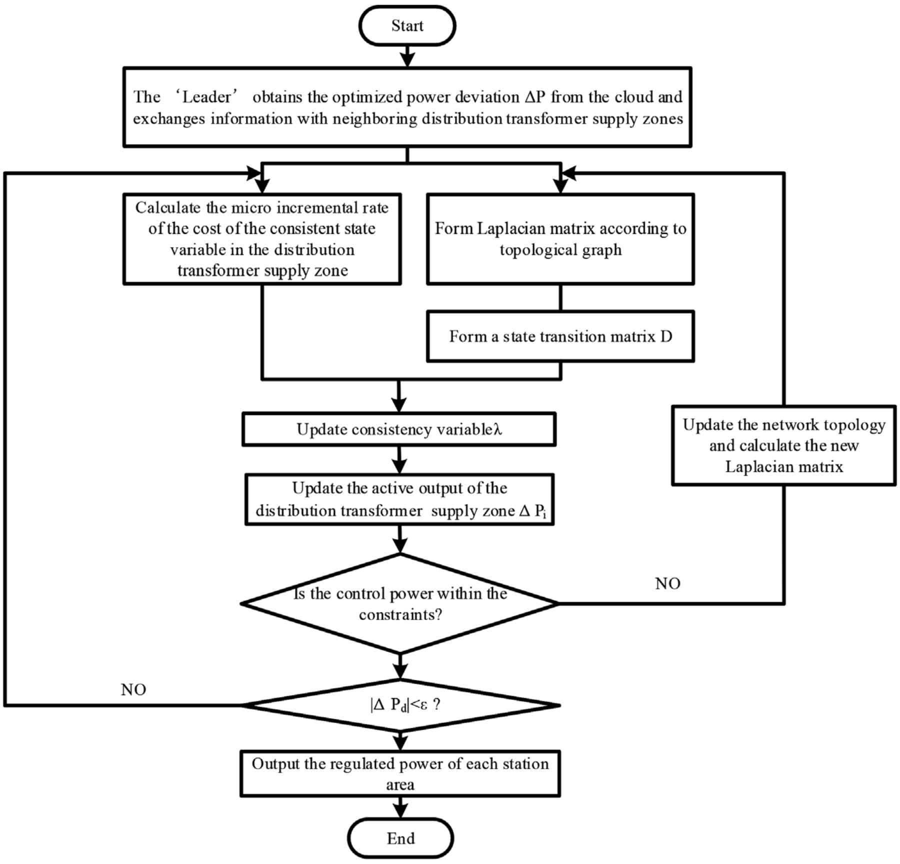

FIGURE 2
Flowchart of the power dispatch strategy in edge-side cooperative distribution transformer supply zone based on the consensus algorithm.

supply zone are set as shown in Table 2, which contains the cost coefficient for each transformer supply zone and the upper and lower active output limits.

4.2 Analysis of example results

The real-time power dispatch simulation analysis of the transformer supply zone cluster is carried out with a dispatch period of 15 min, and the total duration is 24 h; then a total of 96 dispatch plans are included. The power dispatching coefficient of the consistency algorithm $\mu = 0.02$, the convergence error $\varepsilon = 0.7$, the deviation of the power allocated by the cloud optimization for this transformer supply zone cluster is$\Delta P = -450$ kW, and the weighting coefficient matrix $Z = [1]$.

The whole-day total power deviation curve is obtained from the predicted value and the actual value of the previous power regulation, as shown in Figure 4, which shows that the power imbalance mainly occurs between 11:00–22:00. The maximum positive power deviation occurs at 14:00, and the power deviation value is 630 kW. The main reason is that due to the large photovoltaic output at noon, there is excess electric energy. At this time, the generated power shall be reduced, energy storage should be charged, and the load should be increased; the maximum negative power deviation occurs at 18:00 with a power deviation value of −450 kW, which is mainly due to the power shortage caused by the peak load in the evening; at this time, we should increase the power generation, discharge energy, and cut the load.

Based on the analysis of historical data in the region, the controllable active power prediction value of the transformer supply zone on a long-term scale of a typical day in the zone obtained from the distribution network management center is shown in Figure 5.

Applying a cloud-edge collaborative real-time control strategy based on the edge consistency algorithm of the intelligent transformer supply zone cluster to this power transformer supply zones, the simulation results can be obtained as shown in Figures 6, 7.

It can be seen from Figure 6 that the initial value of the micro-increase rate of cost of each transformer zone is different. The value of the micro-increase rate of cost of zone 3 is the highest,

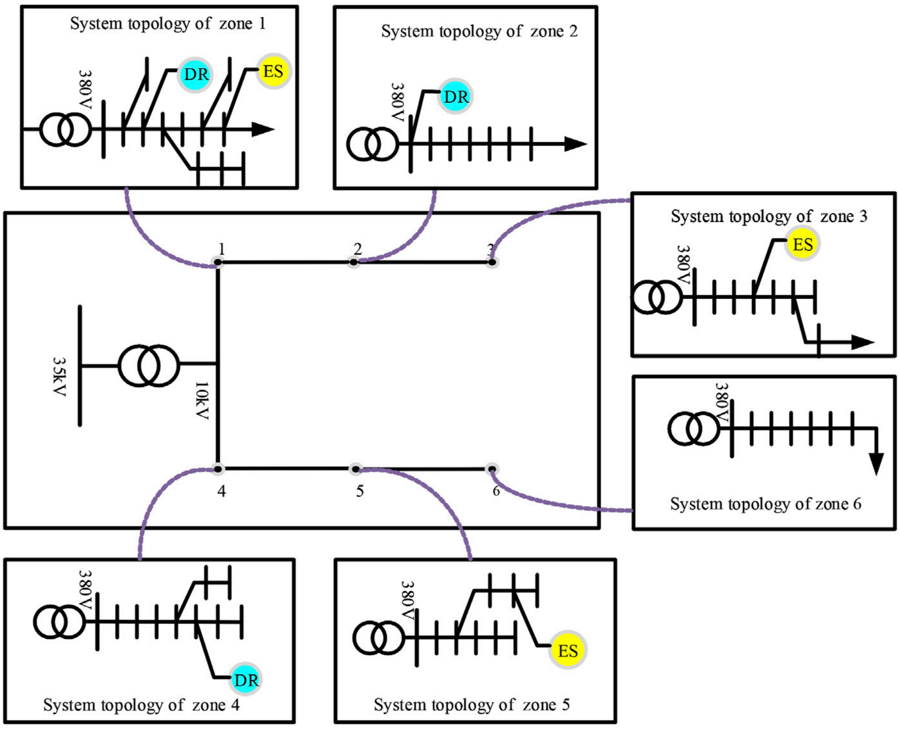

FIGURE 3
Network topology of distribution transformer supply zone cluster.

TABLE 1 Components inside the transformer supply zone.

Zone number	Distributed generation resource	Energy storage device	Flexible load
1	√	√	√
2	√	×	√
3	×	√	√
4	√	×	×
5	×	√	×
6	×	×	√

TABLE 2 Cost parameters and generation constraints.

Zone number	a_i	b_i	c_i	$P_{i,min}/kW$	$P_{i,max}/kW$
1	3.2	2.1	0.0085	10	300
2	2.8	1.8	0.0055	10	250
3	2.3	2.0	0	0	200
4	2.5	2.3	0.0073	20	150
5	2.2	0	0	0	80
6	1.8	2.5	0	10	80

the value of the micro-increase rate of cost of zone 6 is the lowest, and its growth rate is the fastest. After the consensus algorithm of the iterative update calculation, the micro-increase rate of cost for zone 1 and zone 2 gradually increases after the first decrease, and the cost incremental rate for zone 3 to zone 6 gradually increases, and when the number of iterations reaches 40, the value of cost incremental rate in all zones tends to be the same, which is 330.57 ¥/kWh.

As can be seen from Figure 7, after the iterative update calculation of the consensus algorithm, in the initial stage, the

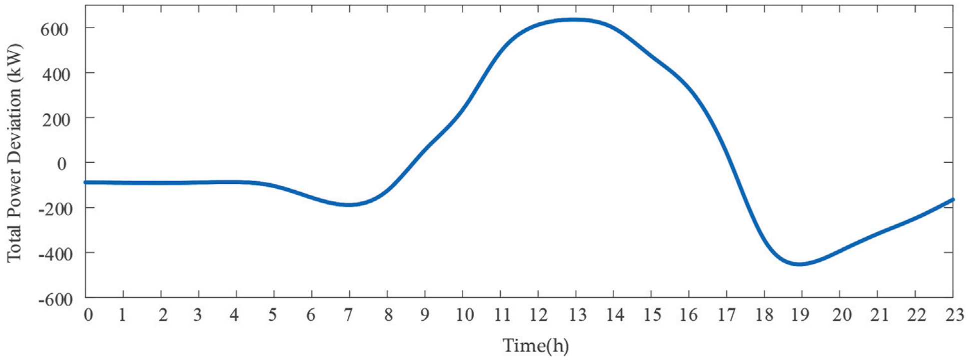

FIGURE 4
All-day power deviation curve.

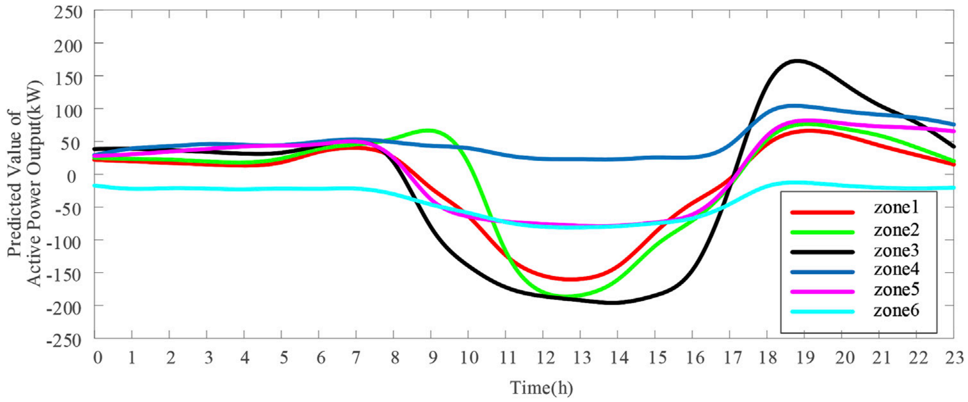

FIGURE 5
Adjustable active power prediction value of each distribution transformer supply zone on a long timescale.

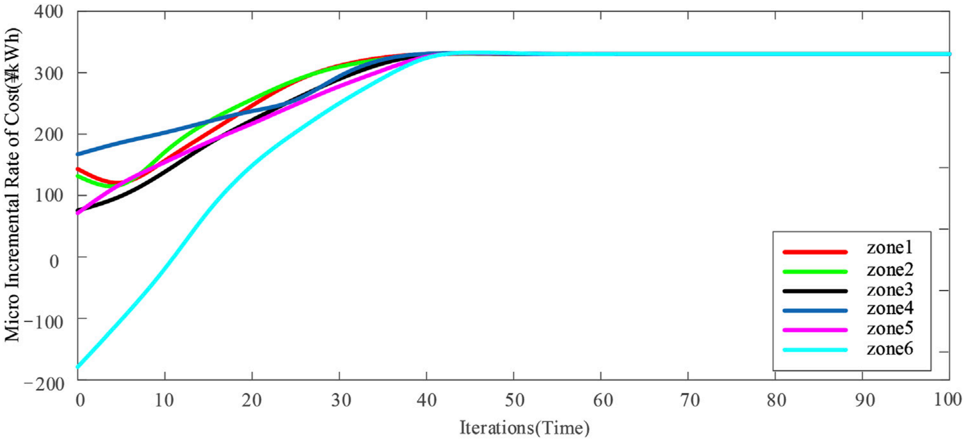

FIGURE 6
Consistent convergence process of the micro-increase rate of cost at 18:00.

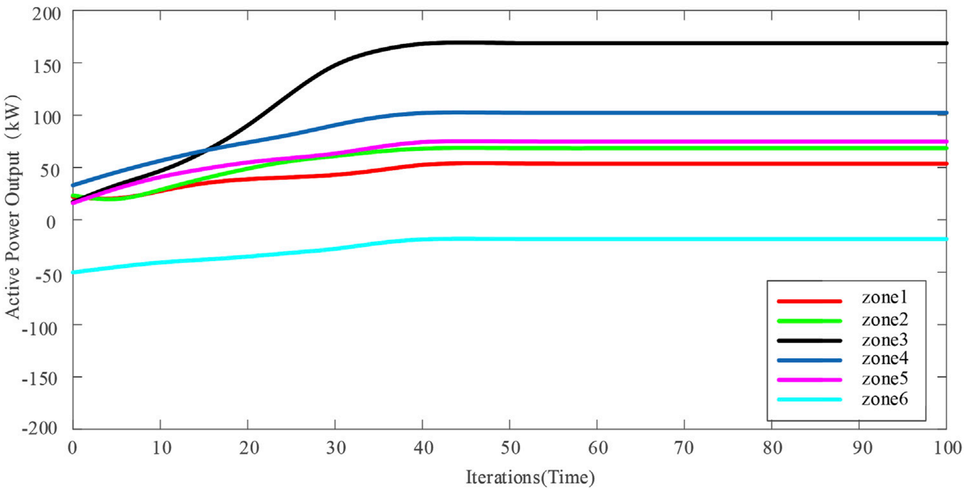

FIGURE 7
Iterative process of the active power output of each distribution transformer supply zone at 18:00.

active power output of zone 1 and zone 2 first decreases and then gradually increases; the active power output of zone3 to zone 6 gradually increases. At the 40*th* iteration, the active power output of all zones stabilizes. The active power output from transformer supply zone 1 to transformer supply zone 6 tends to be stable, respectively: P_1 = 53.75 kW, P_2 = 68.45 kW, P_3 = 168.85 kW, P_4 = 102.31 kW, P_5 = 74.89 kW, and P_6 = -18.25 kW, which shows that the active power outputs values of all transformer supply zones are within the operational constraints.

4.3 Comparative analysis of different control methods

In order to verify the effectiveness and economy of the dispatching strategy proposed in this article, the following three control methods are used for the transformer supply zone cluster for comparative analysis.

Mode 1: No information interaction between transformer supply zones; each transformer supply zone operates independently.

Mode 2: Information interaction between transformer supply zones, with each transformer supply zone giving priority to autonomy and taking the initiative to exchange power with the cluster to maintain the cluster's power balance when its own power command differs from the power command of the transformer supply zone cluster.

Mode 3: Information interaction between each transformer supply zone is controlled according to the cloud-edge collaborative fast control strategy based on the intelligent transformer supply zone edge consensus algorithm proposed in this article.

TABLE 3 Dispatching costs of the three control methods.

Zone number	Cost of dispatch/million		
	Mode1	Mode 2	Mode 3
1	1.79	1.19	0.91
2	2.01	1.88	1.65
3	7.24	6.89	6.28
4	3.29	2.76	2.53
5	1.98	1.56	1.20
6	0.26	0.13	0.064
Total	16.57	14.41	12.63

Simulation and analysis of these three control methods were carried out separately, and the total dispatching cost of the transformer supply zone cluster and the dispatching cost of each transformer zone are shown in Table 3.

Table 3 shows that with Mode 3 control, the dispatching cost of each transformer zone is less than those of Mode 1 and Mode 2 control. The total dispatching cost is "Mode 1 > Mode 2 > Mode 3," and the total dispatching cost of Mode 3 is 23.8% lower than that of Mode 1 and 12.35% lower than that of Mode 2, indicating that the proposed strategy can achieve the optimal economic dispatch of the active output.

In Mode 1, each zone operates independently, and when power deviation occurs, it can only rely on its own internal regulation to make power balance, which will result in more abandoned generation and load shedding; in Mode 2, each transformer zone gives priority to self-governance, and when

TABLE 4 Transmission characteristics of information branch.

Zone number	Cloud computing latency/ms	Edge computing latency/ms
1	158.84	95.23
2	158.84	87.26
3	158.84	85.49
4	158.84	69.25
5	158.84	67.58
6	158.84	65.69

TABLE 5 Comparison of model effects of different control methods.

Different control method	Model size	Transmission delay/ms
Centralized control	22×35	87.56
Distributed control	25×36	88.75
Centralized-distributed control	25×42	182.55

self-governance still cannot make system power balance, then it relies on information interaction with neighboring zones for dispatching; Mode 3 adopts the cloud-edge coordination real-time control strategy based on the intelligent transformer supply zone cluster edge consensus algorithm proposed in this study to control, and for each transformer zone, the active power is allocated based on the micro-increase rate of cost, which can achieve real-time and economic power dispatch.

4.4 Experimental results

In this experiment, RT-Lab is used to physically model the distribution network transformer supply zone cluster in the example, and the semi-physical simulation of the real-time dispatching of the distribution transformer supply zone cluster with cloud-edge coordination is carried out. According to the distribution network structure in the calculation example, a cloud center computing data pool and 6 edge computing groups quantitatively analyze the transmission delay advantage of the centralized-distributed control method in the scheduling process, so as to illustrate the establishment and use of the model in this article , and to verify the rationality and versatility of the model. Table 4 shows the computing delays on the cloud and edge sides. Table 5 shows the comparison of model effects of different control methods.

It can be seen from Table 5 that the computing speed of the centralized-distributed cooperative control method based on cloud-side collaboration is not much different from that of the distributed control method. Compared with the traditional centralized control method, it has a lower communication time. The calculation speed is significantly faster than that of the centralized control method.

5 Conclusion

In order to correct the long-timescale prediction bias in the distribution network, this article proposes a fast cloud-side coordinated dispatching strategy based on the edge consistency algorithm of intelligent transformer areas cluster, in which the cloud makes the first global optimal allocation and the transformer area makes the second coordinated optimal allocation on the edge side. Based on the consensus algorithm, each area uses the micro-increase rate of dispatching cost as a consistent variable and performs consistent iterations to achieve the optimal distribution of the dispatching power in the transformer area. The main advantages of this article are as follows:

1) The burden of the cloud is reduced. The cloud is responsible for optimizing the calculation of the cluster power deviation information uploaded by the leaders of each cluster and the dispatching cost, which reduces the calculation amount. The iterative calculation is distributed in each edge transformer area, which reduces the communication delay and ensures the rapid power dispatch of the transformer areas cluster.
2) Only the adjacent distribution station areas in the cluster exchange information, which reduces the communication burden of the communication network and improves the reliability of communication.
3) The cost micro-increase rate is selected as the consistency variable. When the cost micro-increase rate tends to be consistent, it can ensure that the power distribution transformer supply zone cluster can perform power regulation at a lower cost.

There are still some deficiencies in the work done in this article. This article only considers the cooperative power interaction between the distribution stations and does not consider the information interaction between groups. This problem will continue to be studied in the next work.

Data availability statement

The raw data supporting the conclusions of this article will be made available by the authors, without undue reservation.

Author contributions

JIL and JUL contributed to framework establishment and manuscript writing; PL and HF contributed to provide theoretical support; SZ and GY contributed to model solving.

Funding

The work has been supported by the Science and Technology Program of Hebei Province (20314301D).

Conflict of interest

Authors PL and JL were employed by the company Electric Power Research Institute of State Grid Hebei Electric Power Co, Ltd. Author HF was employed by the company State Grid Hebei Electric Power Co, Ltd. Author GY was employed by the company Handan Power Supply Branch of State Grid Hebei Electric Power Co, Ltd.

The remaining author declares that the research was conducted in the absence of any commercial or financial relationships that could be construed as a potential conflict of interest.

Publisher's note

References

Bian, X., Sun, M., Zhao, J., Lin, S., Zhou, B., and Li, D. (2021). Distributed coordinative optimal dispatch and control of source and load based on consensus algorithm. *Proc. CSEE* 41 (04), 1334–1347+1540. doi:10.13334/j.0258-8013.pcsee.200416

Fang, X., Hodge, B.-M., Jiang, H., and Zhang, Y. (2019). Decentralized wind uncertainty management: Alternating direction method of multipliers based distributionally-robust chance constrained optimal power flow. *Appl. Energy* 239, 938–947. doi:10.1016/j.apenergy.2019.01.259

Gong, G., Luo, A., Chen, Z., Luan, J., An, X., and Wang, X. (2018). Cyber physical system of active distribution network based on edge computing. *Power Syst. Technol.* 42 (10), 3128–3135. doi:10.13335/j.1000-3673.pst.2018.0119

Huang, C., Wang, C., Zhang, M., Xie, N., and Wang, Y. (2021). A transactive retail market mechanism for active distribution network integrated with large-scale distributed energy resources. *IEEE Trans. Smart Grid* 12 (5), 4225–4237. doi:10.1109/TSG.2021.3087720

Huang, C., Zhang, M., Wang, C., Xie, N., and Yuan, Z. (2022). An interactive two-stage retail electricity market for microgrids with peer-to-peer flexibility trading. *Appl. Energy* 315, 119085. doi:10.1016/j.apenergy.2022.119085

Huang, W., Li, N., Tian, Y., and Zhang, Z. (2017). Research on day-ahead and real-time schedule strategy for ADN. *Mod. Electr.* 34 (03), 52–59. doi:10.19725/j.cnki.1007-2322.2017.03.008

Li, X., Han, X., and Yang, M. (2022). Day-ahead optimal dispatch strategy for active distribution network based on improved deep reinforcement learning. *IEEE Access* 10, 9357–9370. doi:10.1109/ACCESS.2022.3141824

Li, Y., Dong, P., Liu, M., and Lin, Y. (2018). Distributed coordinated control of DC microgrid based on finite-time consensus algorithm. *Automation Electr. Power Syst.* 42 (16), 96–103. doi:10.7500/AEPS20170907003

Li, Z., Song, K., Ding, M., Ni, R., Wang, J., Qu, L., et al. (2021). Comparative analysis of three data mining techniques in diagnosis of lung cancer. *Eur. J. Cancer Prev.* 40 (06), 15–20. doi:10.1097/CEJ.0000000000000598

Liu, H., Li, Z., Cheng, Q., Yao, T., Yang, X., and Hu, Y. (2020). Construction of the evaluation index system of the regional integrated energy system compatible with the hierarchical structure of the energy Internet." in. IEEE 4th Conference on Energy Internet and Energy System Integration (EI2), Wuhan, China, October 30–November 1, 2020, 342–348. doi:10.1109/EI250167.2020.9346665

Liu, T., Han, D., Wang, Y., and Dong, X. (2021). Strategies of market game behavior of virtual power plants based on Q-learning with augmented Lagrange function. *Power Syst. Technol.* 45 (10), 4000–4008. doi:10.13335/j.1000-3673.pst.2020.1932

Lv, P., Zhao, J., Su, D., and Chen, G. (2019). Consensus-based distributed dynamic economic dispatching for islanged microgrids. *Automation Electr. Power Syst.* 43 (05), 22–29. doi:10.7500/AEPS20180214001

Peng, C., Liu, Y., Zhou, H., Liu, F., Zhang, K., and Hu, R. (2022). Power ecosystem operation based on cloud-edge collaboration: Theoretical framework. *Proc. CSEE* 42 (09), 3204–3214. doi:10.13334/j.0258-8013.pcsee.202422

Pu, T., Liu, W., Chen, N., Wang, X., and Dong, L. (2017). Distributed optimal dispatching of active distribution network based on consensus algorithm. *Proc. CSEE* 37 (06), 1579–1590. doi:10.13334/j.0258-8013.pcsee.160937

Rahbari-Asr, N., Ojha, U., Zhang, Z., and Chow, M. (2014). Incremental welfare consensus algorithm for cooperative distributed generation/demand response in Smart grid. *IEEE Trans. Smart Grid* 5 (6), 2836–2845. doi:10.1109/TSG.2014.2346511

Ren, J., Yu, G., He, Y., and Li, G. Y. (2019). Collaborative cloud and edge computing for latency minimization. *IEEE Trans. Veh. Technol.* 68 (5), 5031–5044. doi:10.1109/TVT.2019.2904244

Si, Y., Tan, Y., Wang, F., Kang, W., and Liu, S. (2020). Cloud-edge collaborative structure model for power Internet of Things. *Proc. CSEE* 40 (24), 7973–7979+8234. doi:10.13334/j.0258-8013.pcsee.191532

Tofighi-Milani, M., Fattaheian-Dehkordi, S., Fotuhi-Firuzabad, M., and Lehtonen, M. (2022). Decentralized active power management in multi-agent distribution systems considering congestion issue. *IEEE Trans. Smart Grid* 13, 3582–3593. doi:10.1109/TSG.2022.3172757

Yang, Q., Huang, Y., Shi, M., Zhou, J., Chen, X., and Wen, J. (2020). Consensus based distributed control for multiple PV-battery storage units in DC microgrid. *Proc. CSEE* 40 (12), 3919–3928. doi:10.13334/j.0258-8013.pcsee.190444

Yang, X., Xu, C., Zhang, Y., Yao, W., Wen, J., and Cheng, S. (2021). Real-time coordinated scheduling for ADNs with soft open points and charging stations. *IEEE Trans. Power Syst.* 36 (6), 5486–5499. doi:10.1109/TPWRS.2021.3070036

Zeraati, M., Hamedani Golshan, M. E., and Guerrero, J. M. (2019). A consensus-based cooperative control of PEV battery and PV active power curtailment for voltage regulation in distribution networks. *IEEE Trans. Smart Grid* 10 (1), 670–680. doi:10.1109/TSG.2017.2749623

Zhang, B., Wang, J., Liang, D., and Han, X. (2020). Optimization control strategy of distributed energy storage in autonomous microgrid cluster on consensus algorithm. *Power Syst. Technol.* 44 (05), 1705–1713. doi:10.13335/j.1000-3673.pst.2019.1968

Zhang, W., and Wang, D. (2022). Real-time demand response scheduling strategy for electric vehicles based on cloud edge collaboration. *Power Syst. Technol.* 46 (04), 1447–1458. doi:10.13335/j.1000-3673.pst.2021.0581

Zhang, Z., and Chow, M.-Y. (2012). Convergence analysis of the incremental cost consensus algorithm under different communication network topologies in a Smart grid. *IEEE Trans. Power Syst.* 27 (4), 1761–1768. doi:10.1109/TPWRS.2012.2188912

Zhang, Z., and Chow, M.-Y. (2011). "The leader election criterion for decentralized economic dispatch using incremental cost consensus algorithm," in *IECON 2011-37th annual conference of the IEEE industrial electronics society* (Raleigh: IEEE), 2730–2735. doi:10.1109/IECON.2011.6119743

Zhao, Y., Wu, Z., Qian, Z., Gu, W., Li, D., and Liu, Y. (2019). Distributed optimal dispatch of active distribution network considering source-load temporal and spatial correlations. *Automation Electr. Power Syst.* 43 (19), 68–76. doi:10.7500/AEPS20190423003

Zheng, J., Wang, J., Sun, Z., and Wu, F. (2022). Improved droop control of optical storage DC microgrid based on consensus algorithm. *Proc. CSUEPSA* 34 (04), 116–125. doi:10.19635/j.cnki.csu-epsa.000859

Zhou, Z., Wang, Z., Liao, H., Wang, Y., and Zhang, H. (2022). 5G cloud-edge-end collaboration framework and resource scheduling method in power Internet of Things. *Power Syst. Technol.* 46 (05), 1641–1651. doi:10.13335/j.1000-3673.pst.2021.2427

frontiers | Frontiers in Energy Research

TYPE Original Research
PUBLISHED 06 January 2023
DOI 10.3389/fenrg.2022.1067896

OPEN ACCESS

EDITED BY
Nantian Huang,
Northeast Electric Power University,
China

REVIEWED BY
Kenneth E. Okedu,
National University of Science and
Technology (Muscat), Oman
Yingwei Wang,
Harbin Institute of Technology, China

*CORRESPONDENCE
Hanbo Wang,
✉ wanghb@smail.sut.edu.cn

SPECIALTY SECTION
This article was submitted to Smart
Grids,
a section of the journal
Frontiers in Energy Research

RECEIVED 12 October 2022
ACCEPTED 18 November 2022
PUBLISHED 06 January 2023

CITATION
Wang H, Liu Y, Wang X, Guo G and
Wang L (2023), Dynamic synthetic
inertial control method of wind turbines
considering fatigue load.
Front. Energy Res. 10:1067896.
doi: 10.3389/fenrg.2022.1067896

Dynamic synthetic inertial control method of wind turbines considering fatigue load

Hanbo Wang[1]*, Yingming Liu[1], Xiaodong Wang[1], Guoxian Guo[1] and Liming Wang[2]

[1]Institute of Electrical Engineering, Shenyang University of Technology, Shenyang, China, [2]Institute of Electrical Engineering, Shenyang Institute of Engineering, Shenyang, China

This paper proposes a dynamic synthetic inertia control method, considering the fatigue loads of the wind turbine. The control objectives include reducing the rate of change of frequency and frequency nadir of the power system and the fatigue load of the shaft and tower of the wind turbine. A frequency regulation model of the power system containing the primary operating dynamics of the wind turbine is established. The dynamic synthetic inertia control method is proposed according to the relationship between fatigue load, wind velocity, and frequency. Case studies are conducted with a wind turbine fatigue load under a synthetic inertia control with different weights for different wind velocities and system loads. Therefore, the dynamic weights are obtained. Comparing the rate of change of frequency and frequency nadir and equivalent damage load, the efficacy of the proposed method is verified.

KEYWORDS

wind turbine, frequency regulation, fatigue load, synthetic inertia, power system

Introduction

In recent years, with the rapid development of renewable energy technology, wind power constitutes an increasing proportion of the power system (Wu et al., 2021a; Shamlou et al., 2021; Huang et al., 2022). However, as the wind turbine (WT) does not contribute to the inertia of the power system, the total equivalent inertia of the power system will become smaller (Mahish and Pradhan, 2019; Wu et al., 2021b; Lin et al., 2022; Wu et al., 2022). Therefore, large-scale grid connection of the WT brings considerable challenges to the frequency stability of the power system (Arani and El-Saadany, 2013; Mohammad et al., 2017). Although the current WT inertia control methods can improve the inertia of the power system (Ma et al., 2021), these methods do not focus on the fatigue load of the WT. Studies show that participating in inertia control will increase the fatigue load of the WT drivetrain (Ye et al., 2015), which will greatly shorten its service life. Therefore, studying the inertia control method of the WT, considering the fatigue load, can not only improve the inertia of the power system but also extend the service life of the WT.

For a long time, researchers have conducted a series of studies on reducing the frequency nadir (FN) and the rate of change of frequency (ROCOF) of the power system based on the introduction of inertial control (Mandal and Chatterjee, 2021) (Xu et al., 2019). In order to get rid of the inherent adverse effects of the inertial control strategy with constant parameters, Hwang et al. (2016), Pradhan et al. (2018), Wu et al. (2018), and Yang et al. (2020) proposed an inertial control method based on dynamic gain to improve the frequency stability of the system under fixed wind conditions. Sato et al. (2022) designed a novel virtual inertia control strategy based on fuzzy logic controller (FLC) to reduce the FN. Lu et al. (2021) performed a comprehensive analysis of the existing inertia and droop controllers applicable to offshore WT. However, the aforementioned references only consider the stability of frequency of the system itself and completely ignores the fatigue load of the low-speed shaft and tower of the WT that participate in the system frequency adjustment, which will pose a certain threat to the stability of the WT itself.

The fatigue load of the low-speed shaft and tower of WT has significant influence on its service life (Zhao et al., 2017). The fatigue load of the low-speed shaft is particularly sensitive to the change in energy, and the active power reference value of WT with inertia control will frequently change according to the change in system frequency, thus aggravating the fatigue load of the low-speed shaft (Zhang et al., 2020). The study showed the following: 1) both the droop and virtual inertia methods can expose the shaft of a wind generator to forces capable of stimulating its natural resonance frequencies. 2) The mechanical resonance in a frequency-regulating wind generator should be studied as a part of the integrated power system dynamics. The time-domain simulation results verified the analytical results and discussion (Arani and Mohamed, 2016).

In addition, studies have pointed out that the instantaneous torque response may stimulate the tower of WT, resulting in tower resonance (Attya and Dominguez-Garcia, 2018). It can be seen from the aforementioned analysis that participation in frequency response may lead to the increase in the WT fatigue load. However, there is no inertia control method that considers the WT fatigue load.

It can be seen from the aforementioned analysis that few studies can take into account the ROCOF, FN, and fatigue load simultaneously. Therefore, in this study, the main goal of the control scheme is to minimize these three indicators at the same time. However, since the WT participating in the frequency regulation must frequently change the power reference value to adapt to the frequency change in the power system, it is not easy to reduce the aforementioned three control indicators. Therefore, the following two control results are also acceptable: one is to minimize the ROCOF and FN of the system without affecting the fatigue load; and the other is to minimize the fatigue load without affecting the ROCOF and FN.

Therefore, a WT dynamic synthetic inertia control (DSIC) method, considering fatigue load, is proposed:

1) The frequency regulation model is established. The model includes a WT with central operating dynamics, considering shaft torque and tower bending moment.
2) The WT fatigue load is analyzed under different turbulent winds and active power reference values.
3) The changes in the ROCOF and FN of the system and fatigue load under different inertia gains are analyzed.

Based on the analysis result, the dynamic gain range is determined. By simulating the model and method, the advantages of the proposed DSIC method are verified.

The main contributions are as follows:

The fatigue loads of the WT drivetrain and tower caused by frequency response are analyzed, which can help guide the construction of corresponding methods for WT and frequency control. The DSIC control method is proposed, which can simultaneously reduce the ROCOF and FN of the power system and the fatigue loads of the WT.

General system description

In this section, the power system and WT models are established, which can be used for the analysis of fatigue load and the establishment of the inertia control method. The research mainly focuses on a doubly fed induction generator (DFIG), so the DFIG is mainly described.

Electrical power system model

Under normal operation of the power system, the load fluctuates only in a small range. Compared with the dynamic characteristics of voltage and power angle, the dynamic response characteristics of system frequency are relatively slow. Therefore, when studying the long period behavior of the power system frequency under small disturbances (such as primary frequency regulation and secondary frequency regulation), the research on the dynamic characteristics of voltage and power angle is usually ignored. The frequency of the whole power system is considered to be uniform. In order to study the relationship between the frequency change of the power system, the wind turbine inertia, and fatigue load, the model is established as shown in Figure 1. The researched system consists of wind power, hydropower, and thermal power. The selection of the model and parameters refers to Wang et al. (2020). The penetration rates of thermal, hydropower, and wind power are 60%, 20%, and 20%, respectively. Both thermal power and hydropower use power reserves to participate in the primary frequency regulation and secondary frequency regulation of the power system.

The main parameters of the power system are shown in Table 1. The main parameters of the wind turbine are shown in Table 2.

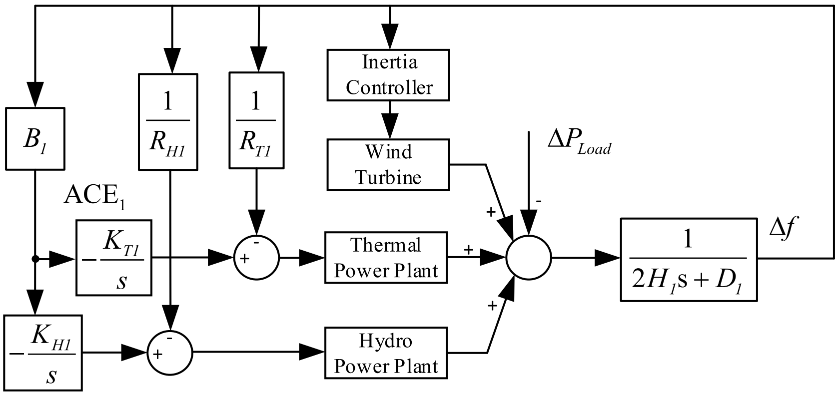

FIGURE 1
Frequency regulation model of the power system with the WT.

TABLE 1 Parameters for the frequency regulation model.

Parameter	Name	Value (p.u.)
R_{H1}	Speed droop for the hydropower model	0.05
R_{T1}	Speed droop for the thermal plant model	0.05
H_1	Equivalent inertia constant	5.994
D_1	Equivalent damping factor of the loads	1
B_1	Bias factor	0.425
K_{T1}	Integral controller for the thermal model	3
K_{H1}	Integral controller for the hydropower model	3

TABLE 2 Main parameters of the wind turbine.

Parameter	Name	Value
J_r	Rotor inertia	3.54×10^7 (kg m^2)
J_g	Generator inertia	5.34×10^2 (kg m^2)
η_g	Gear box ratio	97
τ_f	Filter time constant of ω_g	10
$\omega_{g\text{-rated}}$	Generator rated speed	122.91 (rad/s)
B	Main shaft viscous friction coefficient	6.22×10^6(Nm s/rad)
ρ	Air density	1.22 (kg/m^3)
R_{rotor}	Length of the blade	63(m)
τ_g	Filter time constant of T_{g_ref}	0.1

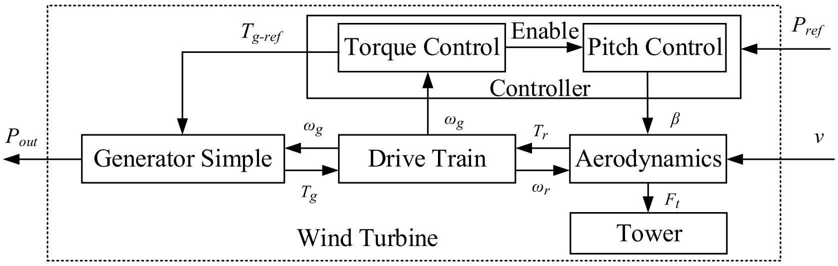

FIGURE 2
Wind turbine block diagram, considering the low-speed shaft torque M_s and the tower bending moment M_t.

Wind turbine model

Since this research considers the fatigue load of the low-speed shaft torque Ms and the tower bending moment Mt of the WT, the main dynamics need to be considered when modeling the WT. The WT model used in this paper can be simplified as shown in Figure 2, which is developed by NREL (Jonkman et al., 2009). The main dynamics of the wind turbine are simulated by the FAST (Fatigue, Aerodynamics, Structures, and Turbulence) Code (Jonkman et al., 2005).

The aerodynamic torque T_r can be expressed by:

$$T_r = \frac{0.5\pi R_{rotor}^2 \rho v^3 C_p}{\omega_r}, \tag{1}$$

where ρ is the air density, v is the wind speed, R_{rotor} is the length of the blade, C_p is the power coefficient, and ω_r is the rotor speed.

The tower thrust force F_t can be expressed by:

$$F_t = 0.5\pi R_{rotor}^2 \rho v^2 C_t, \tag{2}$$

where C_t is the thrust coefficient.

The tower bending moment M_t can be calculated by:

$$M_t = H_{tower} \cdot F_t, \tag{3}$$

where H_{tower} is the tower height.

In order to more accurately describe the dynamics of M_s, a dual mass model is used. The model can be expressed by:

$$\dot{\omega}_r \approx \frac{1}{J_r}\left(T_r - M_s - B\left(\omega_r - \frac{\omega_g}{\eta_g}\right)\right), \tag{4}$$

$$\dot{\omega}_g \approx \frac{1}{J_g}\left(\frac{1}{\eta_g}\left(M_s + B\left(\omega_r - \frac{\omega_g}{\eta_g}\right)\right) - T_g\right), \tag{5}$$

where ω_g is the generator speed, B is the main shaft viscous friction coefficient, M_s is the shaft torque, J_r is the rotor mass, and J_g is the generator mass.

The generator model can be expressed by:

$$P_{out} \approx T_{g-ref} \times \omega_g, \tag{6}$$

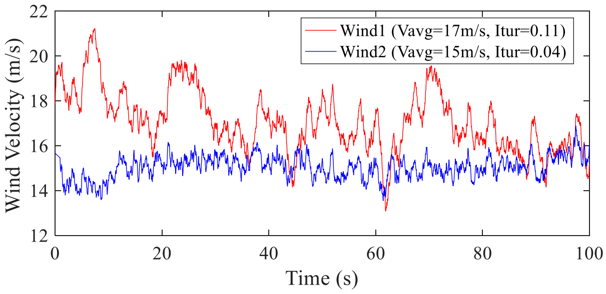

FIGURE 3
Two wind-velocity curves.

where $T_{g\text{-}ref}$ is the generator torque reference value. The maximum power of the generator is 5.3 MW, which can exceed the rated power by 6%.

It should be noted that in this research, the wind power only provides inertia frequency regulation without the power reserve. In addition, because the WT fatigue load is lower than the rated wind speed, this research only focuses on the fatigue load of the wind turbine higher than the rated wind speed.

Proposed control method of a DFIG

In this section, the fatigue loads caused by inertial response is discussed. First, the changes in the WT fatigue load under different wind speeds and power references are analyzed. The relationship between fatigue load, power reference, and wind velocity is clarified, which makes it clear that the influence of fatigue load can be used for the establishment of DSIC. The corresponding analysis was rarely reported in other research studies, so it is the first time to be analyzed. Then, the fixed-gain inertia control method is introduced. Also, the DSIC method is proposed, considering the wind turbine fatigue load. Finally, a

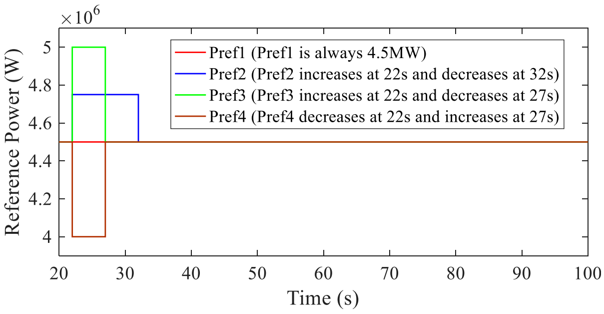

FIGURE 4
Four different reference power values used for testing under Wind1 and Wind2 conditions.

quantitative index that can evaluate the performance of the control method is proposed.

Effects of wind velocity and reference power on fatigue load

First, TurbSim is used to generate two wind-velocity curves. The curves are shown in Figure 3. The average wind velocity (V_{avg}) of Wind1 is 17 m/s, and the turbulence intensity (I_{tur}) is 0.11. The V_{avg} of Wind2 is 15 m/s, and the I_{tur} is 0.04. The simulation time is 100 s. Since the WT is mainly in the starting stage during the first 15 s, in order to accurately compare the results of different control methods, the fatigue load performance of the WT is mainly studied after 20 s. The dynamic behavior of the WT in a simulated wind field yields time series of loads or stresses. Through post-processing, the fatigue cycles based on the rainflow counting method are derived to evaluate the performance of the proposed scheme (TonyNickDavidErvin, 2011). In addition, the WT fatigue load is evaluated by DEL. DEL is calculated according to Miner's rule. The rule depends on the material properties specified by the slope of the S-N curve (Spudić et al., 2011). The DEL calculation is performed using the MCrunch code.

In the case of Wind2, four different reference powers shown in Figure 4 are used for this research. P_{ref2} has a smaller power change and slower recovery (called small positive changes). P_{ref3} has a larger power change and faster recovery (called large positive changes). The total energy of these two reference power changes is the same. The change of P_{ref4} is opposite to P_{ref3} (called large negative changes).

Figure 5 shows the cumulative rainflow cycle results of the WT shaft torque and tower bending moment under different wind velocities and reference power values. In a relatively stable wind speed, relative to the constant load P_{ref1}, a variable load will increase the fatigue load of the WT. It can be seen from the results of P_{ref2} and P_{ref3} that the cycles of P_{ref3} with large positive changes are larger than those of P_{ref2} with small positive changes, which implies that the fatigue load of P_{ref2} is smaller.

Therefore, under the same stable wind condition, the greater the load fluctuation, the greater the fatigue load of the shaft.

Compared with P_{ref3} with large positive changes, P_{ref4} with large negative changes would cause the shaft to have a great fatigue load. The main reason is that the WT controller will increase the pitch angle to release the obtained air kinetic energy after reducing the power reference value. Therefore, M_s will decrease, but its fluctuation is greater. The change curves of M_s are shown in Figure 6.

Figure 5 also shows the cumulative rainflow cycle results under Wind1 and P_{ref1}. It can be seen from the figure that under the same power reference value, the fatigue loads of M_s and M_t are 200% of those under Wind2. The main reason is that the fluctuation of Wind1 is greater.

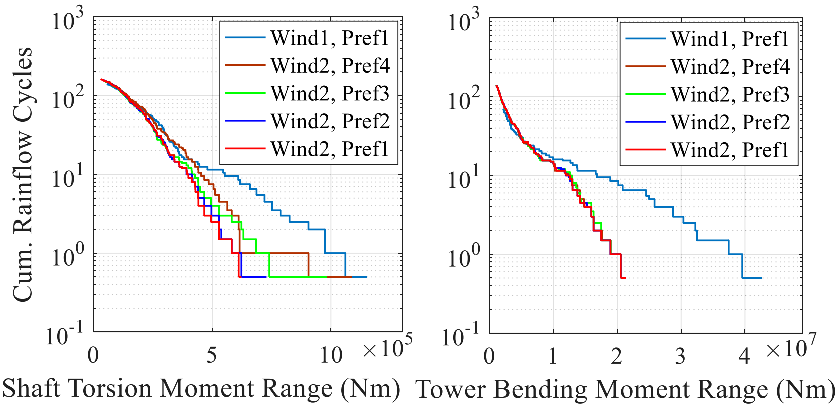

FIGURE 5
Cumulative rainflow cycle result of the WT shaft and tower under different wind velocity and reference power values.

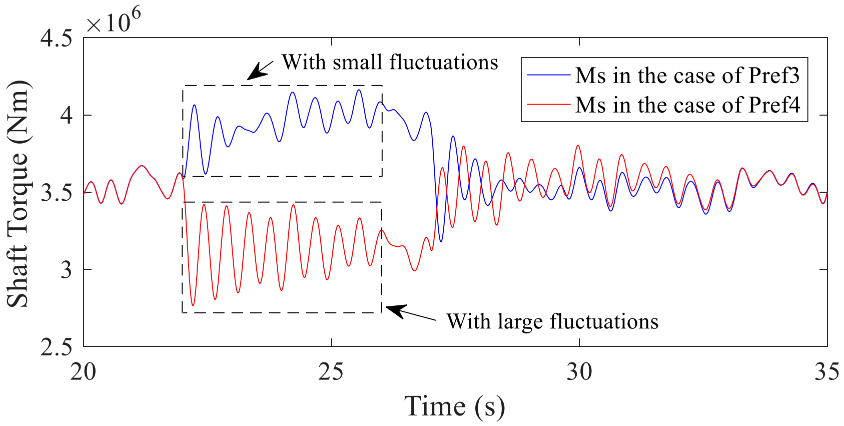

FIGURE 6
Change curves of M_s under different reference power values.

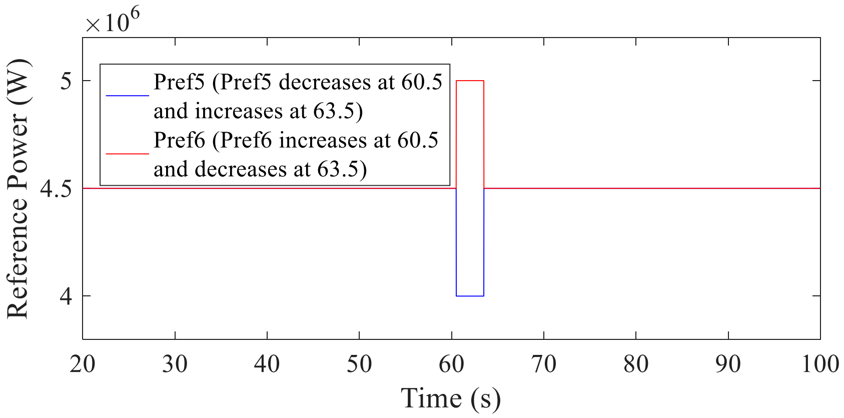

FIGURE 7
Two different reference power values used for testing under Wind1 conditions.

Therefore, under the same reference power value, the greater the average wind speed and turbulence, the greater the fatigue load. Therefore, it is necessary to pay more attention to the fatigue loads when the turbulence intensity is higher or wind velocity is increasing.

As shown in Figure 7, two different power reference values are used for testing under Wind1 conditions. Figure 8 shows cumulative rainflow cycle results of the WT shaft and tower under different reference power and wind velocity values. The difference from the case of Wind2 is that when the reference power fluctuates in the reverse direction (decreases first and then increases), the fatigue loads of the shaft and tower of the wind turbine both decrease instead of showing an increase. The reason is that Wind1 also undergoes significant changes. At this moment, the wind velocity falls first and then rises, consistent with the power change trend. If the power reference value increases at this time, it will cause the air kinetic energy to decrease relative to the steady wind speed. Therefore, the WT controller will reduce the pitch angle to obtain more energy, and shaft torque and tower bending moment will increase and fluctuate more.

Therefore, when the changing trend of the reference power is the same as the changing trend of the wind velocity, it is beneficial to reducing the fatigue load of the wind turbine. Some experience is obtained: 1) when the wind velocity decreases, the reference power of the WT should be reduced as much as possible, or the increased power of the WT should be reduced. 2) Similarly, when the wind velocity increases, the reference power should be increased, or the decreased power should be reduced.

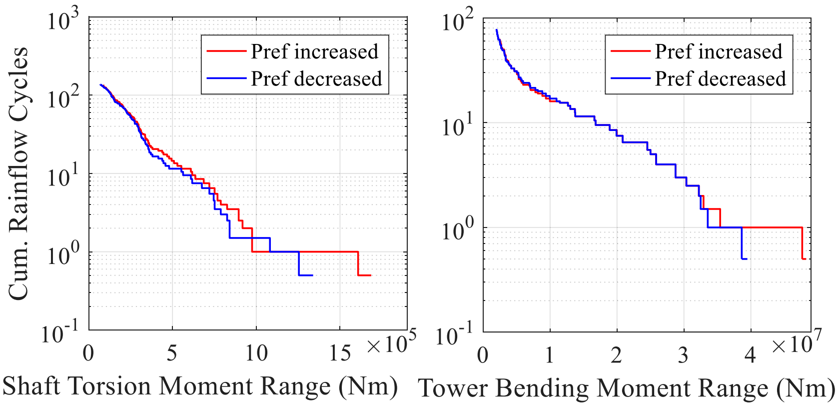

FIGURE 8
Cumulative rainflow cycle results of the WT shaft and tower under different reference power and wind velocity values.

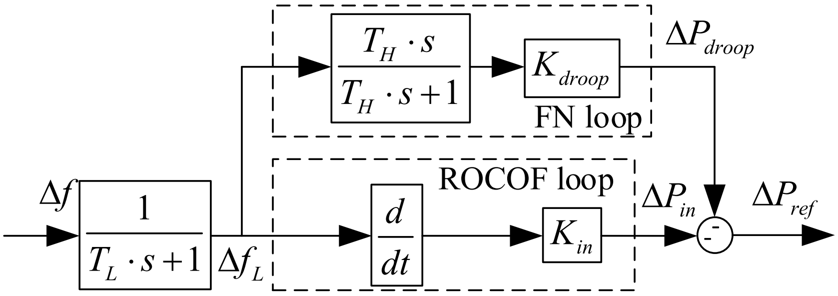

FIGURE 9
Conventional fixed-gain inertial control of a DFIG.

Conventional fixed-gain inertial control of a DFIG

This part mainly describes the fixed-gain inertia control method, as shown in Figure 9. In order to regulate the output of the wind turbine according to the power system frequency, the frequency of the power system must be measured and filtered through a low-pass filter to reject the measurement noise. Since the derivative of frequency is used for calculation, sufficient filtering is required. Differentiation of a noisy signal may lead to large variations in the value of ΔP_{in}, which is undesired because it may cause heavy torque pulsations in the WT drivetrain.

The inertial control scheme based on ROCOF and FN loops is used simultaneously in VDV et al. (2016). As shown in Figure 9, ΔP_{ref} consists of two terms: ΔP_{droop} and ΔP_{in}. In the initial stage of the disturbance, the ROCOF loop dominates and is proportional to the frequency change rate. In contrast, the FN loop dominates near the frequency nadir. The FN loop has two functions: 1) to counteract the control effect of MPPT and 2) to limit the frequency deviation by increasing the WT power output proportional to the frequency deviation. The WT should return to the operating point before the disturbance after the inertial response. Therefore, the period of overproduction during the inertial response period should be followed by a period of underproduction or recovery. To allow recovery of the WT, a high-pass filter, which prevents a contribution of the droop controller in a steady state, is added:

$$\lim_{t\longrightarrow\infty} \Delta P_{droop}(t) = \lim_{s\longrightarrow 0} s\frac{T_h s \cdot \Delta f_L}{T_h s + 1} = 0, \tag{7}$$

where T_h is the time constant of the high-pass filter.

The output of the droop loop ΔP_{droop} can be expressed by:

$$\Delta P_{droop} = K_{droop} \Delta f_L \frac{T_h s}{T_h s + 1}, \tag{8}$$

where K_{droop} is the weight coefficient of the FN loop.

The output of the ROCOF loop ΔP_{in} can be expressed by:

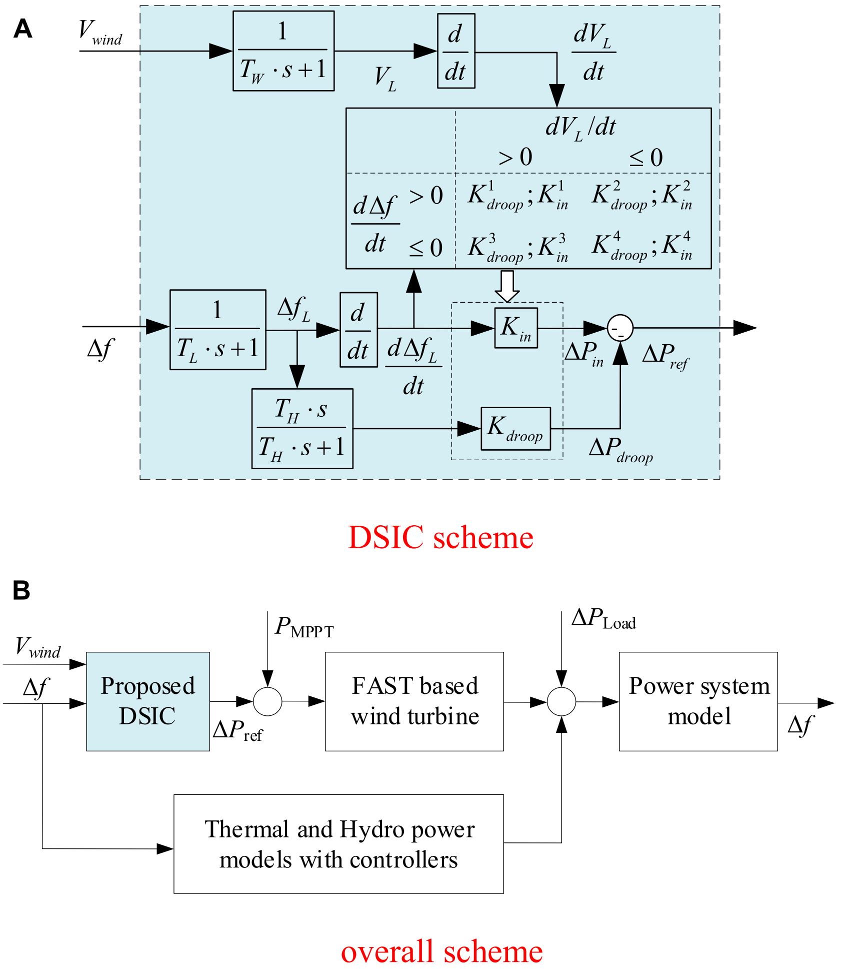

FIGURE 10
Proposed DSIC scheme for DFIG participating in the power system frequency regulation. **(A)** DSIC scheme. **(B)** Overall scheme.

$$\Delta P_{in} = K_{in}\frac{d\Delta f_L}{dt}, \tag{9}$$

where K_{in} is the weight coefficient of the ROCOF loop.

The loop gain of these schemes is fixed, so a more significant gain can ensure that the FN and ROCOF are reduced. However, it can be known from the analysis of Part 3.1 of this section that more extensive power changes may cause larger fatigue loads. Therefore, it is necessary to change the gains when the frequency regulation method has a more significant impact on the fatigue loads of the WT to minimize the effect of frequency regulation on the fatigue loads.

The proposed DSIC scheme

This DSIC scheme aims to: 1) reduce the FN and ROCOF; and 2) mitigate the fatigue loads of a DFIG caused by frequency regulation. This scheme dynamically adjusts the weight based on the wind velocity increase or decrease and the frequency deviation increase or decrease. The main reasons analyzed in Part 3.1 of this section are the following two points:

1) The fatigue load experienced by the shaft torque of WT is related to the wind speed and increase or decrease in the reference power change. The reference power of the WT participating in frequency regulation is mainly determined by the change in the power system frequency.
2) Under the exact reference power change, the fatigue load of the WT is related to the change in wind velocity and its increase or decrease. When the wind velocity is in the rising phase, the falling reference wind power should be reduced, and the increasing reference power should continue to increase. When the wind velocity decreases, the decreasing value should continue to decrease, and the increasing value should be reduced.

The proposed DSIC method is shown in Figure 10. Figure 10A shows the implementation method of DSIC. Figure 10B shows an overall block diagram of a control system. In the actual operation and control of the WT, it is not easy to accurately sample the wind speed with a shorter step length. Therefore, the increases or decreases in wind velocity and frequency are used to change the gains.

The following equation expresses the increase or decrease in wind velocity:

$$\frac{dV_L}{dt} = \frac{V_L(t) - V_L(t-1)}{\Delta t}, \tag{10}$$

where V_L is the filtered wind speed. The main function of the filter is to eliminate the interference of low-frequency wind fluctuations to judge the increase or decrease in the wind speed.

The increase or decrease in Δf is expressed by:

$$\frac{d\Delta f_L}{dt} = \frac{\Delta f_L(t) - \Delta f_L(t-1)}{\Delta t}, \tag{11}$$

where Δf_L is the filtered frequency deviation.

The weight of K (K is short for K_{droop} and K_{in}) depends on the increase or decrease in frequency deviation and the increase or decrease in wind velocity. Since the fatigue load is related to the speed of the power change, the weight cannot have rapid fluctuations. In this study, K changes every 1s. Moreover, different K values cannot differ too much. Otherwise, it would cause the reference power to change too much and increase the fatigue load experienced by the WT.

Evaluation method for control scheme performance

This study has three control objectives: FN, ROCOF, and fatigue load. A quantitative analysis of these three goals is needed when comparing controller performance. Since the ROCOF and FN constantly change during the simulation process, equations are needed to quantify. DEL mainly compares the fatigue load.

The quantification of ROCOF is mainly shown in Equation 12. The quantification method is to mainly evaluate the ROCOF integral during the simulation operation cycle to evaluate the ROCOF situation for a period of time.

$$\text{ROCOF} = \int_0^{\infty} \left| \frac{\Delta f(t) - \Delta f(t-1)}{\Delta t} \right| dt. \tag{12}$$

The quantization of FN mainly considers the absolute value of the maximum frequency deviation. Moreover, every time an extreme value occurs, it will be accumulated.

$$\text{FN} = \sum_{t=0}^{\infty} \left| \Delta f_{ext}(t) \right|, \tag{13}$$

where Δf_{ext} is the extremum of Δf. Every time an extremum value appears, it will be accumulated once.

The fatigue load of the tower and shaft is evaluated using DEL. Following the fatigue load evaluation method in Zhang et al. (2018), the fatigue loads of the tower and the shaft are combined, and the calculation method of the total DEL is as follows:

$$DEL_{tot} = K_{Ms} DEL_{Ms} + K_{Mt} DEL_{Mt}, \tag{14}$$

where DEL_{Ms} represents the equivalent damage load of M_s, which is used to evaluate the fatigue load of the shaft. DEL_{Mt} represents the equivalent damage load of M_t, which is used to evaluate the fatigue load of the tower. K_{Ms} and K_{Mt} are tunable weightings and can be tuned according to the costs and the designed lifetime of the shaft and the tower. In this paper, K_{Mt} is chosen as 1, and K_{Ms} is chosen as 2 (Zhang et al., 2016), since the shaft stress is higher than the tower stress when participating in frequency regulation. Since the DEL value of the tower is much larger than the DEL value of the shaft, the DELs of the tower are normalized with base 5×10^7, and the DELs of the shaft are normalized with base 2×10^6. In this way, the DEL values of both series are all transferred to per unit values.

Case studies

The effects of the controller parameter change on the system performance with Wind2

In the Wind2 scenario, the system load increases and decreases by 5% p. u. at 35 s. The control objectives are given in the following paragraphs. In the next two sections, we would focus on the influence of control variables on the WT fatigue load.

The ROCOF and FN of the system are shown in Figure 11. The same is that ROCOF and FN decrease with the increase in K, and the decreasing trend is the same. In addition, when the load increases, the decreasing trend of ROCOF and FN becomes insignificant after K increases to a certain level (such as (6, 10), (7, 9), and (8, 8)). This is due to the limitation of the wind power output. In this case, the benefit of continuing to increase K is not obvious to the system.

Figure 12 shows the results of DEL_{Ms} under this condition. It can be seen from the figure that under stable wind speed, the DEL_{Ms} increases no matter how the frequency changes. Also, the larger the K, the more obvious the increasing trend, and the maximum increase is 16.9% within the weight range. This is because the fatigue load of the shaft under this working condition mainly depends on the reference power fluctuation. The greater the K, the greater the fluctuation of the reference power under the same frequency fluctuation, which will cause an increase in the fatigue load.

Figure 13 shows the results of DEL_{Mt} under this condition. DEL_{Mt} shows a slight downward trend when the load

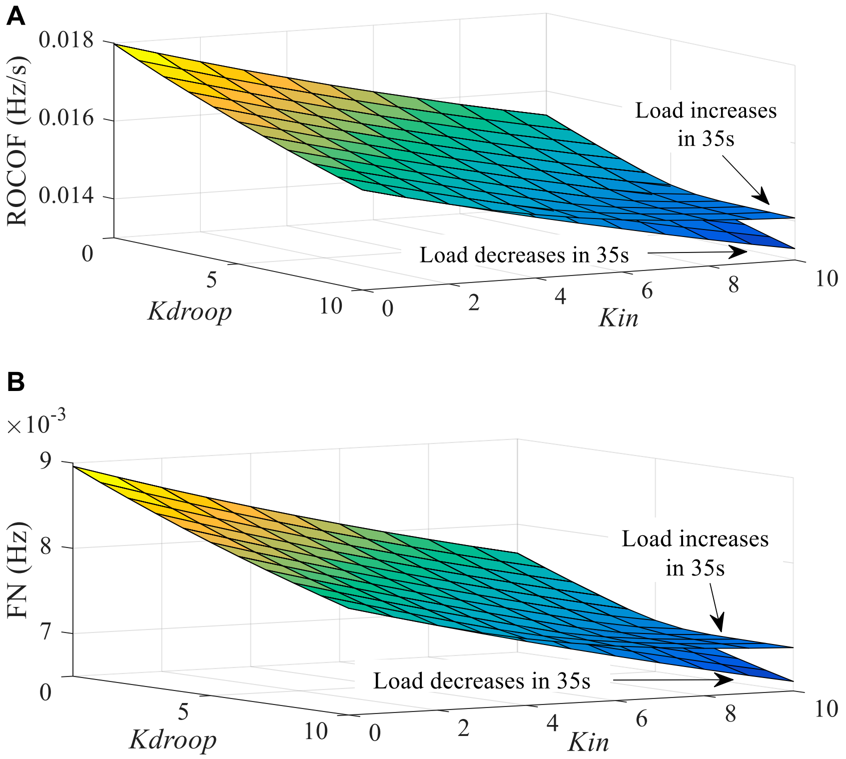

FIGURE 11
ROCOF and FN of the system. **(A)** ROCOF results under the change in *K* when the system load increases and decreases by 5% at 35 s. **(B)** FN results under the change in *K* when the system load increases and decreases by 5% at 35 s.

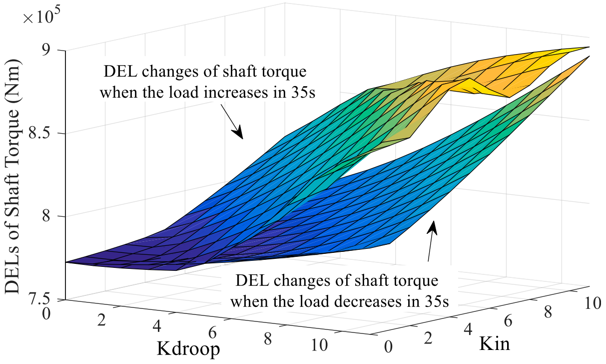

FIGURE 12
DEL_{Ms} results under the change in *K* when the system load increases and decreases by 5% at 35 s.

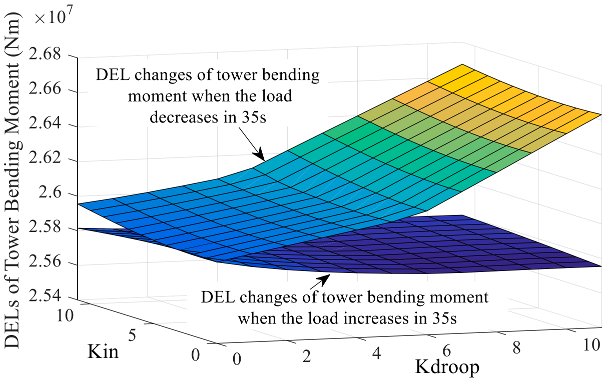

FIGURE 13
DEL_{Mt} results under the change in *K* when the system load increases and decreases by 5% at 35 s.

increases. When K is changed within the range of 11, the tower DEL is reduced by up to 0.4%. DEL_{Mt} increases with the increase in K_{droop} when the load decreases. Also, the more significant the K_{droop}, the more pronounced the increasing trend. Compared with K_{droop}, K_{in} has less effect on DEL_{Mt}, which implies that the FN loop has a more significant impact on tower fatigue than the ROCOF loop. Figure 14 shows the results of DELtot under this condition. Under this working condition, the evaluation result of DEL_{tot} shows that DEL_{tot} increases with the increase in K, which implies that the increase in K will increase the total fatigue load of the WT.

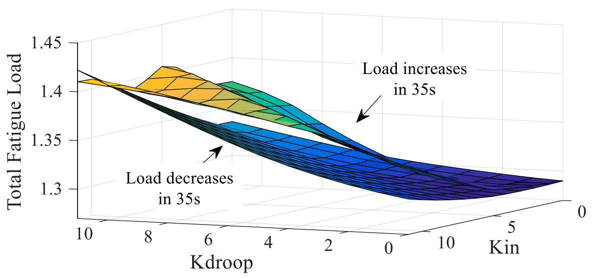

FIGURE 14
DEL_{tot} results under the change in K when the system load increases and decreases by 5% at 35 s.

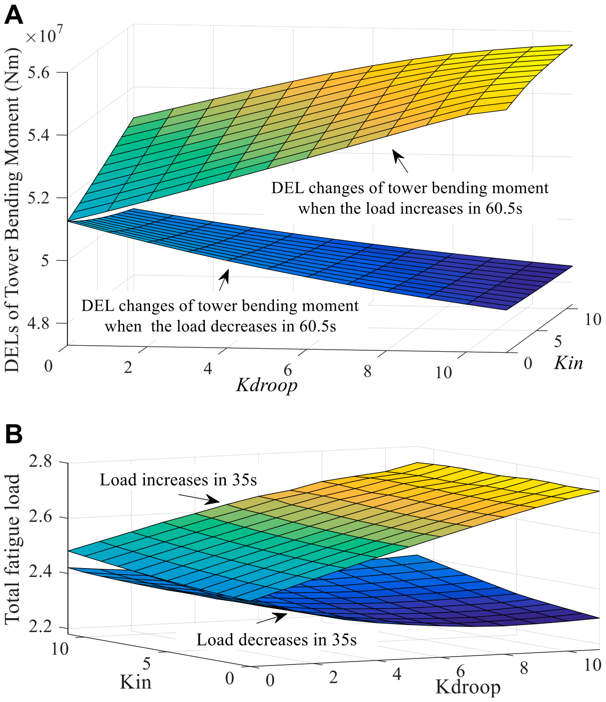

FIGURE 15
M_s under different K_{droop} values when the system load increases and decreases by 5% at 60.5 s.

According to the analysis in this part, K should not be too large or too small. If K is too large, the fatigue load will increase. If K is too small, the frequency regulation performance will be poor. Therefore, the range of K is set between 6 and 11 in this research.

The effects of the controller parameter change on the system performance with Wind1

In Wind1, the system load increases and decreases by 5% at 60.5 s (that is, the load also changes when the wind velocity is about to change significantly). In the study of this working condition, the changing trend of the ROCOF and FN is the same as in the previous section, so the analysis is not repeated.

TABLE 3 DEL_{Ms} **up to three different times under different** K_{droop} **values when the system load increases and decreases by 5%.**

Time (s)	DEL_{Ms} for different K_{droop} values		
	0	9	11
62.5	1.328	1.339	1.355
63	1.352	1.342	1.358
63.5	1.423	1.351	1.366

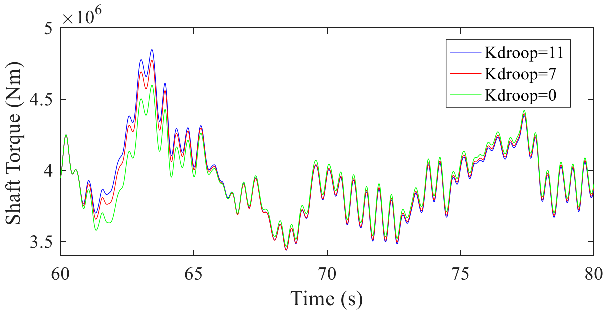

FIGURE 16
DEL_{Ms} results under the change in K when the system load increases and decreases by 5% at 60.5 s.

After the load decreases at 60.5 s, the frequency will increase to a specific value and decrease. The changing frequency trend will be opposite to the changing trend of wind velocity. At this time, DEL_{Ms} and DEL_{Mt} will decrease as K increases. Consistent with the results of the previous analysis, the changing trend of the reference power is the same as the wind speed change trend, reducing the fatigue load. Similarly, there is almost no effect on DEL_{Mt} by K_{in} after K_{droop} reaches a value greater than 8. Furthermore, DEL_{Mt} will decrease with the increase in K_{droop}.

Under the same K_{droop} condition, the changing trend of DEL_{Ms} increases with the increase in K_{in}. The reason is that K_{in} mainly limits the frequency change rate. The increase in K_{in} will make the power fluctuations become larger, which will cause the fluctuations in Ms to increase the fatigue load. However, in the case of the same K_{in}, DEL_{Ms} decreases first and then increases with the increase in K_{droop}. Ms under different K_{droop} values is shown in Figure 15.

Between 60.5 s and 65 s, M_s increases with the increase in K_{droop}. However, this does not mean that DEL_{Ms} increases with the increase in K_{droop} before 65 s. DEL_{Ms} up to three different times is shown in Figure 15.

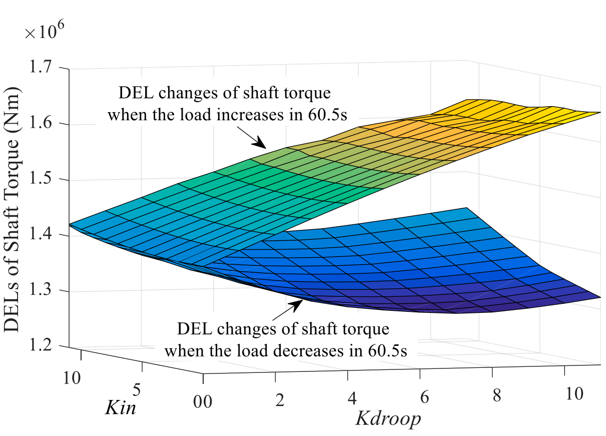

FIGURE 17
DEL_{Mt} and DEL_{tot} results under the change in K when the system load increases and decreases by 5% at 60.5 s. **(A)**DEL_{Mt} results under the change in K when the system load increases and decreases by 5% at 60.5 s. **(B)**DEL_{tot} results under the change in K when the system load increases and decreases by 5% at 60.5 s.

TABLE 4 K_{droop} **and** K_{in} **weights under different working conditions.**

$\frac{d\Delta f_L}{dt}$	$d\Delta V_L/dt$	
	>0	≤0
>0	$K^1_{droop} = 8$ $K^1_{in} = 11$	$K^2_{droop} = 11$ $K^2_{in} = 9$
≤0	$K^3_{droop} = 8$ $K^3_{in} = 7$	$K^4_{droop} = 9$ $K^4_{in} = 7$

It can be seen from Table 3 that only DEL_{Ms} values of the 0–62.5 s time period increase with the increase in K_{droop}. It shows that increasing K_{droop} leads to the increase in DEL_{Ms} when the load changes within 2 s. When K_{droop} increases to 9, DEL_{Ms} increases by 0.83%. However, due to the inertia of the power system and WT, it takes time for changes in the system load to be converted into the output power of WTs. For load changes exceeding 2 s, the fatigue load of M_s will still decrease first and then increase as K_{droop} increases. This is because the fluctuation in M_s will increase with the increase in K_{droop} after K_{droop} exceeds a certain value.

As shown in Figure 16 and Figure 17A, when the change trends of wind velocity and frequency are the same, the fatigue load of the shaft and tower will increase with the increase in K_{droop}. Considering the changing trends of FN and ROCOF, K_{droop} is selected as 8. Since the fatigue load of the shaft and the tower does not change much when K_{in} increases, K_{in} can be increased as much as possible when the wind speed decreases, and K_{in} is selected as 11. This does not increase the fatigue load. However, when the wind velocity increases, in order to reduce the burden on the shaft and tower, K_{in} should not be too large, and K_{in} is selected as 7 in this case. When the changing trend of wind speed is opposite to the changing trend of frequency, K_{in} should not be selected too large. So, when the wind speed increases, K_{in} is selected as 6. When the wind velocity decreases, K_{in} can be increased appropriately, and K_{in} is selected as 9. When the frequency increases, K_{droop} can be increased as much as possible, and K_{droop} is selected as 11. When the frequency decreases, K_{droop} is selected as 9. The K weights under different working conditions are shown in Table 4.

System performance for DSIC under random load fluctuations

In this case, the random system load that changes every 2 s is applied to Wind1 to verify the advantages of the proposed method. In addition, the performances of FN and ROCOF, and DEL under different fixed gains are compared. The choice of fixed gain mainly considers ROCOF, FN, and DEL, so values from 7 to 9 are selected, respectively. The load changes from 25 s to 100 s are shown in Figure 18A, and the K changes for DSIC are shown in Figure 18B. The ROCOF and FN and the fatigue loads are compared under the fixed gain and the DSIC methods, respectively. The results are shown in Table 5 and Table 6.

It can be seen from Table 5 that DEL_{Ms} and DEL_{Mt} under the DSIC method are lower than those of the inertia control based on a fixed gain. It can be seen from Table 6 that DEL_{tot} under the DSIC method is lower than that of the inertia control of fixed gain. The reduction range is about 4%, which can significantly mitigate the wind turbine drivetrain fatigue load. For the FN, the reduction ranges from −3.41% to 9.57%. The ROCOF decreases from 0 to 5.23%. It can be known from the aforementioned data that the proposed DSIC method can significantly reduce ROCOF and FN while reducing fatigue load. This shows that the proposed DSIC scheme has good performance in reducing fatigue load and ROCOF and FN at the same time.

Performance of wind turbine operation dynamics

In order to further clarify the dynamic behavior of wind turbine under different parameters, power output, rotor speed, and torque of drive chain are compared. Figure 19A shows the output power under different parameters. It can be seen that the rise in parameters increases the fluctuation of power output. The increase in output power is beneficial to the stability of system frequency. The DSIC method can have higher output power, so it can make the system frequency deviation and rate of change of frequency smaller.

The rotor speed under different parameters is shown in Figure 19B. It can be seen that the rotor speed difference is

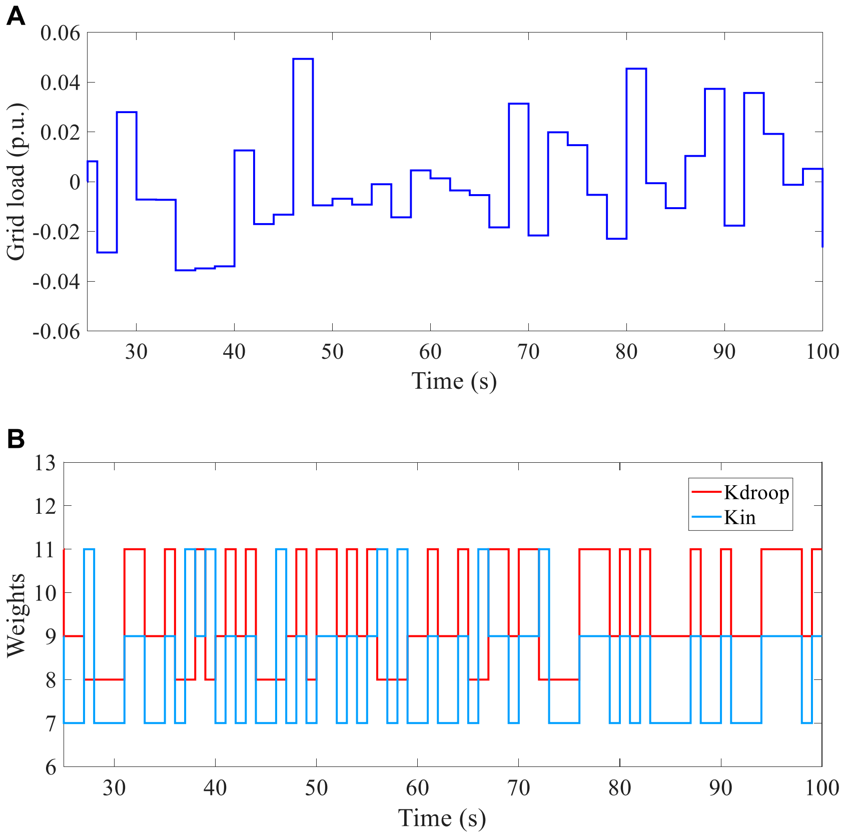

FIGURE 18
Load change from 25 s to 100 s, and K change in the corresponding DSIC scheme. **(A)** Random system load that changes every 2 seconds. **(B)** K_{droop} and K_{in} changes for the DSIC scheme when a random white noise system load appears.

TABLE 5 DELs of shaft torque and tower bending moment under the fixed gain and DSIC methods.

(K_{droop}, K_{in})	DEL_{Ms} (MNm)	DEL_{Mt} (MNm)
(7,7)	1.466	50.309
(8,8)	1.472	50.216
(9,9)	1.477	50.131
DSIC	1.463	50.021

TABLE 6 DEL_{tot} and ROCOF and FN under the fixed gain and DSIC methods.

(K_{droop}, K_{in})	DEL_{tot}	$ROCOF$ (Hz/s)	FN (Hz)
(7.7)	2.572	0.153	0.094
DSIC	2.464	0.145	0.085
Percentage	−4.20%	−5.23%	−9.57%
(8.8)	2.577	0.149	0.091
DSIC	2.464	0.145	0.085
Percentage	−4.39%	−2.68%	−6.59%
(9.9)	2.579	0.145	0.088
DSIC	2.464	0.145	0.085
Percentage	−4.50%	0.00%	−3.41%

small, which indicates that the proposed method will not affect the stable operation of the wind turbine. Figure 19C shows the drive chain torque. It can be seen that with the increase in the parameters of the traditional method, the torque fluctuation of the transmission chain increases. This is because larger parameters are easy to cause torsional vibration of the transmission chain. The proposed DSIC method further changes the generator torque by dynamically adjusting the output power, which can restrain the torsional vibration of the drive chain to a certain extent. Therefore, the proposed method can reduce the fatigue load of the WT. In conclusion, the results show that the proposed DSIC method can reduce the

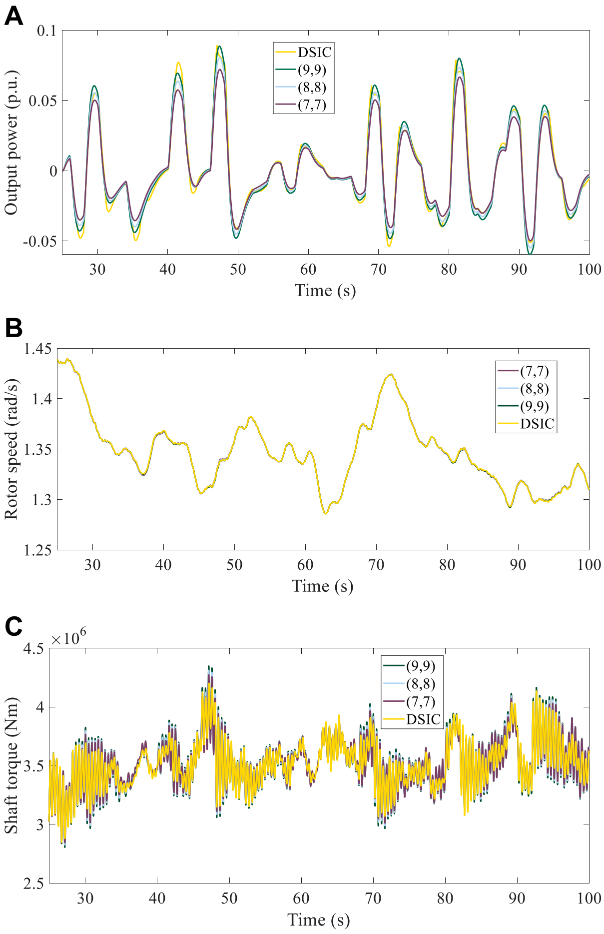

FIGURE 19
Dynamic behavior of the wind turbine. **(A)** Power output under different control parameters. **(B)** Rotor speed under different control parameters. **(C)** Shaft torque under different control parameters.

fatigue load of the wind turbine while improving the frequency regulation capability of the WT.

Conclusion

A WT DSIC method, considering fatigue load, is proposed. This method uses two loops of the ROCOF and FN, and the loop gain would change dynamically according to wind speed and frequency. This method can simultaneously reduce the system's FN and ROCOF and the wind turbine's fatigue load.

The analysis shows that the *K* weight under different working conditions should not be too different to prevent the power reference value from changing too much and causing the DEL to increase. For working conditions with significant changes in wind velocity, the FN loop has a more significant impact on the DEL than the ROCOF loop. When the changing trend of wind velocity is opposite to the changing trend of frequency, the weight of inertia control can be increased, which helps to reduce the DEL. The results show that compared with the conventional scheme, the proposed DSIC scheme can significantly reduce the FN and ROCOF while reducing the DEL. The reduction in DEL_{tot} is about 4%. The reduction in the ROCOF ranges from -5.23% to 0%. The reduction in the FN ranges from −9.57% to −3.41%.

Data availability statement

The original contributions presented in the study are included in the article/Supplementary Material; further inquiries can be directed to the corresponding author.

Author contributions

All authors listed have made a substantial, direct, and intellectual contribution to the work and approved it for publication.

Funding

This work was supported by the Development and Industrialization of Intelligent Wind Farm Holographic State Accurate Perception and Optimization Decision System Project (2021JH1/10400009) and Liaoning Provincial Central Government Guides Local Science and Technology Development Fund Projects (2021JH6/10500166).

Conflict of interest

The authors declare that the research was conducted in the absence of any commercial or financial relationships that could be construed as a potential conflict of interest.

Publisher's note

References

Arani, M., and El-Saadany, E. (2013). Implementing virtual inertia in DFIG-based wind power generation. *IEEE Trans. Power Syst.* 28, 1373–1384. doi:10.1109/TPWRS.2012.2207972

Arani, M. K. M., and Mohamed, Y-R. (2016). Analysis and mitigation of undesirable impacts of implementing frequency support controllers in wind power generation. *IEEE Trans. Energy Convers.* 31, 174–186. doi:10.1109/tec.2015.2484380

Attya, A. B. T., and Dominguez-Garcia, J. L. (2018). Insights on the provision of frequency support by wind power and the impact on energy systems. *IEEE Trans. Sustain. Energy* 99, 719–728. doi:10.1109/tste.2017.2759503

Huang, T., He, Q., Qi, J., Hu, Q., Wang, R., Cai, G., et al. (2022). Multinodes interval electric vehicle day-ahead charging load forecasting based on joint adversarial generation. *Int. J. Electr. Power & Energy Syst.* 143, 108404. doi:10.1016/j.ijepes.2022.108404

Hwang, M., Muljadi, E., Park, J. W., Sorensen, P., and Kang, Y. C. (2016). Dynamic droop–based inertial control of a doubly-fed induction generator. *IEEE Trans. Sustain. Energy* 7, 924–933. doi:10.1109/TSTE.2015.2508792

Jonkman, J. M., Buhl, J., Musial, w., and Scott, G. (2005). *FAST user's guide*. United States. doi:10.2172/15020796

Jonkman, J., Butterfield, S., Musial, W., and Scott, G. (2009). *Definition of a 5-MW reference wind turbine for offshore system development*. United States: National Renewable Energy Laboratory. NREL/TP-500-38060. doi:10.2172/947422

Lin, L., Cheng, C., Wei, B., Li, H., Shi, J., Zhang, J., et al. (2022). Residential electricity load scenario prediction based on transferable flow generation model. *J. Electr. Eng. Technol.* doi:10.1007/s42835-022-01172-6

Lu, G. L., Lin, C. H., and Yk, Wu. (2021). Comparison of communication-based and coordination-based frequency control schemes for HVDC-connected offshore wind farms. *IEEE Trans. Ind. Appl.* 57, 3352–3365. doi:10.1109/tia.2021.3079233

Ma, J., Gu, Y., Shen, Y., Zhou, Y., Phadke, A. G., and Cheng, P. (2021). Stability analysis of power grid connected with direct-drive wind farm containing virtual inertia based on integrated dissipation energy model. *IEEE Trans. Sustain. Energy* 12, 2378–2392. doi:10.1109/TSTE.2021.3095171

Mahish, P., and Pradhan, A. K. (2019). Distributed synchronized control in grid integrated wind farms to improve primary frequency regulation. *IEEE Trans. Power Syst.* 99, 362–373. doi:10.1109/TPWRS.2019.2928394

Mandal, R., and Chatterjee, K. (2021). Virtual inertia emulation and RoCoF control of a microgrid with high renewable power penetration. *Electr. Power Syst. Res.* 194, 107093. doi:10.1016/j.epsr.2021.107093

Mohammad, D., Mokhlis, H., and Mekhilef, S. (2017). Inertia response and frequency control techniques for renewable energy sources: A review. *Renew. Sustain. Energy Rev.* 69, 144–155. doi:10.1016/j.rser.2016.11.170

Pradhan, C., Bhende, C. N., and Samanta, A. K. (2018). Adaptive virtual inertia-based frequency regulation in wind power systems. *Renew. Energy* 115, 558–574. doi:10.1016/j.renene.2017.08.065

Sato, T., Alsharif, F., Umemura, A., Takahashi, R., and Tamura, J. (2022). Stability improvement of power system by cooperative virtual inertia control and reactive power control of pmsg wind generator and battery. *Electr. Eng. Jpn.* 1, 215. doi:10.1002/eej.23362

Shamlou, A., Feyzi, M. R., and Behjat, V. (2021). Winding deformation classification in a power transformer based on the time-frequency image of frequency response analysis using Hilbert-Huang transform and evidence theory. *Int. J. Electr. Power & Energy Syst.* 129, 106854. doi:10.1016/j.ijepes.2021.106854

Spudi´ c, V., Jelavi´ c, M., and Baoti´ c, M. (2011). Wind turbine power references in coordinated control of wind farms. *Automatika* 52, 82–94. doi:10.1080/00051144.2011.11828408

TonyNickDavidErvin, B. J. S. B. (2011). *Wind energy handbook*. Wiley Online Library. doi:10.1002/9781119992714

Vdv, Jan., Jdm, Kooning., Meersman, B., Vandevelde, L., and Vandoorn, T. L. (2016). Droop control as an alternative inertial response strategy for the synthetic inertia on wind turbines. *IEEE Trans. Power Syst.* 31, 1129–1138. doi:10.1109/TPWRS.2015.2417758

Wang, X., Wang, Y., and Liu, Y. (2020). Dynamic load frequency control for high-penetration wind power considering wind turbine fatigue load. *Int. J. Electr. Power & Energy Syst.* 117, 105696. doi:10.1016/j.ijepes.2019.105696

Wu, Y., Liang, X., Huang, T., and Zw Lin, M. F. Hossain (2021). A hierarchical framework for renewable energy sources consumption promotion among microgrids through two-layer electricity prices. *Renew. Sustain. Energy Rev.* 145, 111140. doi:10.1016/j.rser.2021.111140

Wu, Y., Lin, Z., Liu, C., Chen, Y., and Uddin, N. (2021). A demand response trade model considering cost and benefit allocation game and hydrogen to electricity conversion. *IEEE Trans. Ind. Appl.* 99, 2909–2920. doi:10.1109/TIA.2021.3088769

Wu, Y., Lin, Z., Liu, C., Huang, T., Chen, Y., Ru, Y., et al. (2022). Resilience enhancement for urban distribution network via risk-based emergency response plan amendment for ice disasters. *Int. J. Electr. Power & Energy Syst.* 141, 108183. doi:10.1016/j.ijepes.2022.108183

Wu, Y., Yang, W., Hu, Y., and Dzung, P. (2018). Frequency regulation at a wind farm using time-varying inertia and droop controls. *IEEE Trans. Ind. Appl.* 55, 213–224. doi:10.1109/TIA.2018.2868644

Xu, X., Huang, L., Wang, Z., He, J., and Xin, H. (2019). Analysis on impact of virtual inertia control of DFIG-based wind turbine on electromechanical oscillation of power system. *Automation Electr. Power Syst.* 43, 11–17. doi:10.7500/AEPS20180925001

Yang, D., Jin, E., You, J., and Hua, L. (2020). Dynamic frequency support from a DFIG-based wind turbine generator via virtual inertia control. *Appl. Sci. (Basel).* 10, 3376. doi:10.3390/app10103376

Ye, H., Pei, W., and Qi, Z. (2015). Analytical modeling of inertial and droop responses from a wind farm for short-term frequency regulation in power systems. *IEEE Trans. Power Syst.* 31, 3414–3423. doi:10.1109/TPWRS.2015.2490342

Zhang, B., Soltani, M., Hu, W., Hou, P., Huang, Q., and Chen, Z. (2018). Optimized power dispatch in wind farms for power maximizing considering fatigue loads. *IEEE Trans. Sustain. Energy* 99, 862–871. doi:10.1109/TSTE.2017.2763939

Zhang, X., He, W., and Hu, J. (2020). Impact of inertia control of DFIG-based WT on torsional vibration in drive train. *IEEE Trans. Sustain. Energy* 99, 2525–2534. doi:10.1109/TSTE.2020.2964837

Zhang, B., Mohsen, S., Hu, W., Hou, P., and Chen, Z. (2016). A wind farm active power dispatch strategy for fatigue load reduction. Proceedings of the American Control Conference. Boston, MA, USA, 5879–5884. doi:10.1109/ACC.2016.7526591

Zhao, H., Wu, Q., Huang, S., Shahidehpour, M., Guo, Q., and Sun, H. (2017). Fatigue load sensitivity-based optimal active power dispatch for wind farms. *IEEE Trans. Sustain. Energy* 99, 1247–1259. doi:10.1109/tste.2017.2673122

frontiers | Frontiers in Energy Research

TYPE Original Research
PUBLISHED 06 January 2023
DOI 10.3389/fenrg.2022.1021627

OPEN ACCESS

EDITED BY
Yingjun Wu,
Hohai University, China

REVIEWED BY
Zhao Liu,
Nanjing University of Science and Technology, China
Can Huang,
Lawrence Livermore National Laboratory (DOE), United States

*CORRESPONDENCE
Zhi Wu,
zwu@seu.edu.cn

SPECIALTY SECTION
This article was submitted to Smart Grids,
a section of the journal
Frontiers in Energy Research

RECEIVED 17 August 2022
ACCEPTED 02 September 2022
PUBLISHED 06 January 2023

CITATION
Wang J, Wu Z, Zhao Y, Sun Q and Wang F (2023), A robust flexibility evaluation method for distributed multi-energy microgrid in supporting power distribution system.
Front. Energy Res. 10:1021627.
doi: 10.3389/fenrg.2022.1021627

A robust flexibility evaluation method for distributed multi-energy microgrid in supporting power distribution system

Jingxuan Wang, Zhi Wu*, Yating Zhao, Qirun Sun and Fujue Wang

School of Electrical Engineering, Southeast University, Nanjing, China

Today's power system is facing various challenges brought by large-scale renewable energy (RE) integration, which brings higher demand for flexibility. With the energy network gradually showing its distributed structural characteristics, multi-energy microgrids (MEMG) become an important component to effectively utilize distributed energy sources and supplement the flexibility of power distribution system (PDS). To effectively harness the operational flexibility of distributed MEMGs, we propose in this paper an evaluation method to quantify the flexibility capability of MEMG. A virtually established MG flexibility bus (MG-FB) is endowed with MG flexibility parameters (MG-FPs), which can reflect the flexibility characteristics of MEMG. To consider the impact of operational uncertainty on MG-FPs, a two-stage adaptive robust optimization (ARO) model is proposed, which can be solved by the C&CG algorithm. The results of a typical test system show the influence of system configuration, operator's risk preference, and other factors on the values of MG-FPs. Besides, we illustrate the effectiveness and applicability of the proposed framework in modeling and quantifying the operational flexibility of MEMG to support the operation of the upstream network.

KEYWORDS

operational flexibility, multi-energy microgrid, system uncertainty, robust optimization, low-carbon

1 Introduction

In recent years, due to the practical need of alleviating the shortage of fossil fuels and environmental pollution, renewable energy (RE) generation forms dominated by wind power and photovoltaics have developed rapidly (Chen et al., 2016). Microgrid (MG), as an effective carrier of RE access, has been vigorously developed (Wu et al., 2021). MGs have several capital advantages, such as improving power quality, enhancing energy supply reliability, improving energy efficiency, etc. Future power grids can be pictured as systems of interconnected MGs (Parhizi et al., 2015). However, uncertainties from the RE and load-side pose some challenges to system operation. Many studies have focused on methods for forecasting RE output and load-side demand (Zang et al., 2020; Zang et al., 2021). In addition to this, increasing the operational flexibility of MGs is an unavoidable key aspect of dealing with uncertainties (Wang and Hodge, 2017; Ding et al., 2022). The application of multi-energy microgrid (MEMG) provides an important avenue to improve operational flexibility. It is inevitable to tap the flexibility potential of the MEMG system and fully plan the flexible resources in the scheduling process (Holttinen et al., 2013; Ma et al., 2013; Lund et al., 2015; Trovato et al., 2018), which implies the requirement of formulating a reasonable method to evaluate the flexibility margin of flexible resources in the MEMG system.

Flexibility can be explained as the ability of the system to cope with uncertainty. Some significant researches have been carried out, evaluating the flexibility level of power system (De Coninck and Helsen, 2016; Lu et al., 2018; Liu et al., 2021). It is proposed in (Makarov et al., 2009) the indicators for evaluating the technical operation flexibility of power system, namely power ramp-rate, power capacity, energy capacity, and ramp duration. The meaning of these indicators are further discussed in (Ulbig and Andersson, 2012). Based on these basic indicators, more research works have been conducted on evaluating the flexibility of power system. In (Lannoye et al., 2012, 2015), a probability metric called insufficient ramping resource expectation is proposed to evaluate the flexibility of the power system for use in long-term planning, which is derived from traditional generation adequacy metrics. A unified flexibility framework is proposed in (Zhao et al., 2016) to define and quantify power system flexibility in a systematic way which is based on four essential elements that are common to various applications of flexibility. In (Zhao et al., 2015), the concept of the do-not-exceed limit is introduced, which is the maximum renewable generation range that the power system can accommodate under the worst case. These studies focus on the flexibility of power system and provide basic research ideas for the flexibility evaluation of multi-energy systems.

The multi-energy coupling operation mode expands the regulation capacity of the single power system and plays a key role in emission reduction (Mancarella, 2014; Martinez Cesena et al., 2019; Wu et al., 2022). However, the complex energy conversion relationship and non-linear characteristics bring challenges to the operational flexibility evaluation. There have been several studies on the integrated operational flexibility of multi-energy systems from different perspectives. The flexible conversions of energy forms, large-scale heat and gas storage, load with different energy consumption characteristics on the demand side, etc. Are important flexibility resources in multi-energy systems. In (Wang et al., 2018), flexibility brought by energy conversion is analyzed and quantitatively evaluated based on the energy hub (EH) model. Flexibility brought by hybrid energy storage is researched in (Jiang and Hong, 2013) by assessing the benefits of smoothing out wind power fluctuations. Modeling and evaluation of flexible demand in heat and electricity integrated systems are researched in (Shao et al., 2018). A novel geometric approach is proposed in (Zhao L. et al., 2017) to characterize the aggregated flexibility of a population of thermostatically controlled loads. Besides, collaborative use of various units in multiple energy carrier operation can give play to the inherent advantages of various units' attributes. Literature (Ulbig and Andersson, 2014) researches the flexibility of combined equipment by solving the Minkowski sum. The results show that fast frequency regulation can be provided by combining the dynamic slow power plant with the dynamic fast but energy-limited storage unit. How to obtain the most beneficial aggregated operational flexibility within a pool of different units is still the content to be studied in the future. The researches above mainly focus on the flexibility capacity of a certain component or combination benefits of some links in the system, however, the synergy of components in the multi-energy systems is neglected and the integrated flexibility of multi-energy operation is not elaborately characterized. Moreover, the transmission constraints of the networks are not taken into account.

With the large-scale access of various distributed resources such as wind power and gas turbines (GT) in recent years, load-side users have gradually transformed into MEMGs that can operate independently, and their prosumer characteristics have brought possibilities for flexibility applications in supporting PDS. In reference (Holjevac et al., 2015), the flexibility of MEMG is analyzed from two perspectives: independent of the distribution grid and in interaction with the upstream system. In reference (Capuder and Mancarella, 2014), the flexibility of coupled operation of different components in MEMG is considered. A flexibility-oriented MEMG optimization scheduling model is proposed in (Majzoobi and Khodaei, 2017) to efficiently schedule MEMG resources to meet the flexible demand of the distribution network. To address the day-ahead self-scheduling problem of the MG flexibility resources, a two-stage stochastic optimization method is developed in (Bahramara et al., 2022). However, these studies lack specific modeling and quantification of the flexibility characteristics of the MEMG. In reference (Chen and Li, 2021), the flexibility of distributed energy resources is aggregated and characterized by a parameterized set, this method can be further applied to evaluate the flexibility of MEMG. However, the significant uncertainties that affect the operational flexibility are not considered, resulting in inaccurate assessment.

To address the challenges above, we propose an evaluation method to quantify the aggregate flexibility of MEMG. We consider MEMG components of several types to fully explore the flexibility of the MEMG and the synergy between the components. Significant operational uncertainties are

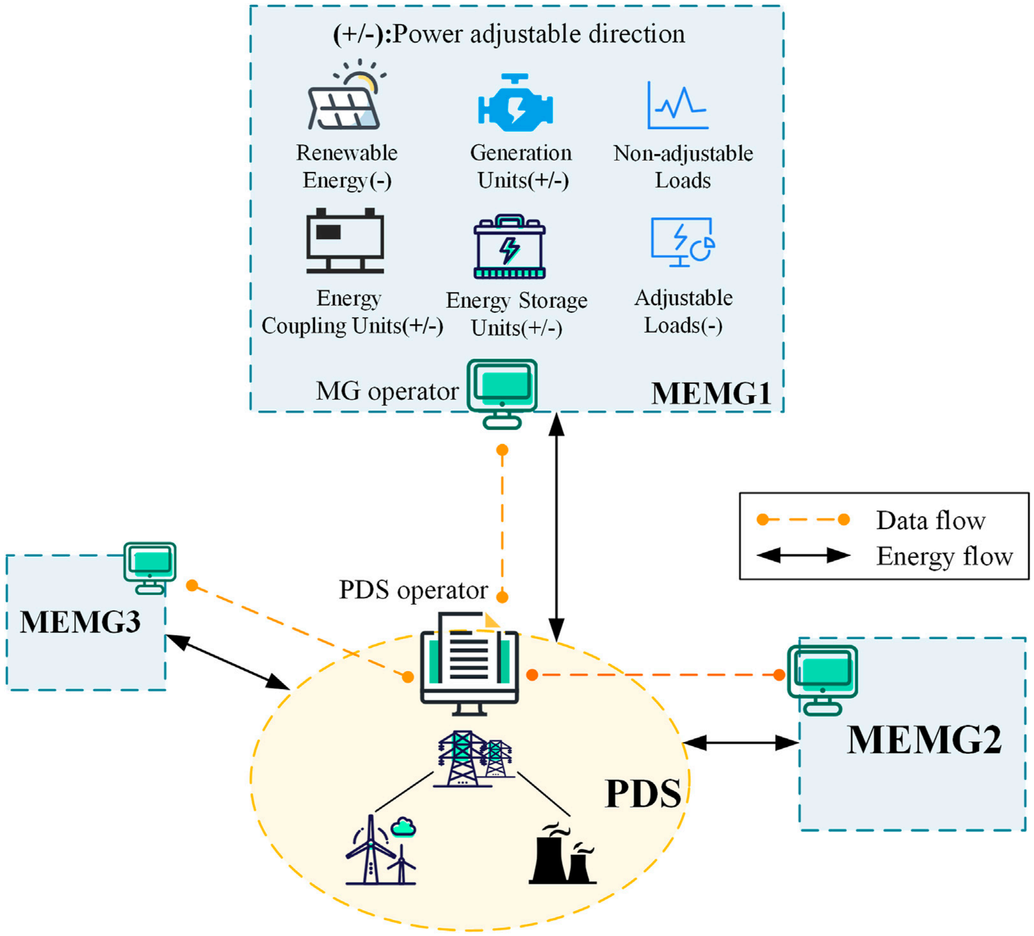

FIGURE 1
MG-PDS interactive structure.

considered in the evaluation process, making the results robust and capable of being realized by the MEMG in its actual operation. There is data and energy interaction between MEMG and PDS, as shown in Figure 1. The quantitative MEMG flexibility capability in power exchange with the upstream network in the grid-connected mode is the focus of this paper. With the proposed method in this paper, the flexibility of the MEMG is represented by a specific set of parameters, and the power exchange efficiency between the MEMG and the PDS can be improved. In order to consider operational uncertainties in evaluating the flexible level of MEMG, the two-stage adaptive robust optimization (ARO) method is adopted. The ARO method has been widely applied to power system, such as unit commitment (Zhang et al., 2019; Dehghan et al., 2021), economic dispatch (Baringo et al., 2019; Yan et al., 2019), DER capacity assessment (Zhao J. et al., 2017; Chen et al., 2018), Resilient dispatch (Xiang and Wang, 2019; Yan et al., 2021), Active/reactive power coordination (Wu and Conejo, 2020; Huang et al., 2022), etc., mature ARO solution methods, e.g. the column-constraint-generation (C&CG) algorithm (Zeng and Zhao, 2013; Ding et al., 2017), can be directly applied as an efficient solution.

The major contributions of this paper are threefold:

1) The flexibility-oriented model of MEMG is comprehensively proposed with consideration of energy generation-, conversion-, storage- and load-side, as well as the flexibility utility of gas and heat pipelines' storage effect.
2) Set virtual MG-FB between MEMG and PDS and specify its properties, which are recorded as MG-FPs. The flexibility capability of MEMG is quantified by the MG-FPs which reflect the energy support effect of MEMG on PDS. This aggregated flexibility model is developed in the form of conventional generator model, which incorporates attributes of various units into simplified parameters.
3) A two-stage ARO method is developed by which the MG-FPs can be obtained. To ensure the robustness of the results, a variety of uncertainties are considered, including the

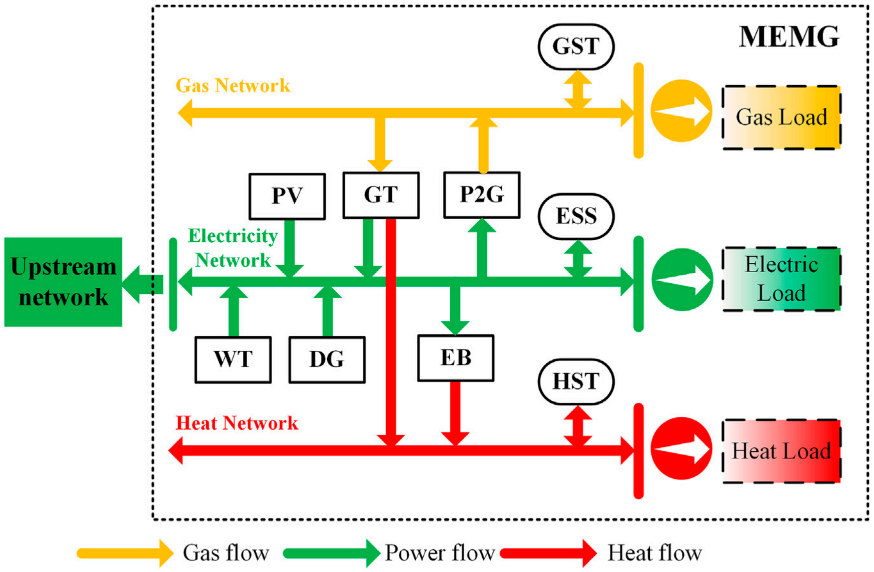

FIGURE 2
Typical MEMG structure incorporated with multiple components.

uncertainty of RE power, load profiles, and dispatch instructions from the PDS. Besides, the impact of several factors on the values of MG-FPs is researched based on case study results.

The remaining part of this paper is organized as follows: Section 2 proposes the operational flexibility model and operational uncertainty set of MEMG. Section 3 presents the detailed ARO model and the C&CG algorithm for obtaining MG-FPs. Section 4 verifies the effectiveness of the proposed method for obtaining MG-FPs and researches the impact of several factors on the values of MG-FPs. Finally, Section 5 concludes the paper.

2 Operational flexibility model of MEMG

In this paper, the operational flexibility of units or systems is embodied as power and ramping rate adjustment capability, specifically, $\Omega^{flex}: = \{\bar{P}, \bar{P}, \overline{RU}, \overline{RD}\}$. For MEMG, a virtually established MG flexibility bus (MG-FB) is endowed with these attributes, which are denoted by MG-FPs. We define the operational flexibility region in the form of time-decoupled intervals, which is simple and efficient for model analysis and practical applications. The typical MEMG structure including various types of units and multi-energy flow is shown in Figure 2. Photovoltaic (PV) unit, wind turbine (WT), diesel generator (DG), gas turbine (GT), power to gas (P2G), electric boiler (EB), energy storage cell (ESC), gas storage tank (GST) and heat storage tank (HST) are considered in the MEMG model.

2.1 Flexibility model of MEMG components

To obtain MG-FPs, we first propose the flexibility models of the MEMG components.

2.1.1 Renewable energy unit

WT and PV units in the MEMG are considered, and the related constraints are as follows:

$$\bar{P}_i^{WT} \le p_{i,t}^{WT} \le \min\left\{\bar{P}_i^{WT}, u_{i,t}^{WT}\right\}, \forall t \in \boldsymbol{T} \tag{1}$$

$$\bar{P}_i^{PV} \le p_{i,t}^{PV} \le \min\left\{\bar{P}_i^{PV}, u_{i,t}^{PV}\right\}, \forall t \in \boldsymbol{T} \tag{2}$$

$$v_{i,t}^{WT} = u_{i,t}^{WT} - p_{i,t}^{WT} \tag{3}$$

$$v_{i,t}^{PV} = u_{i,t}^{PV} - p_{i,t}^{PV} \tag{4}$$

where $p_{i,t}^{WT}$ and $p_{i,t}^{PV}$ are output of WT i and PV unit i at time t, respectively. $\bar{P}_i^{WT}$, $\bar{P}_i^{WT}$,$\bar{P}_i^{PV}$ and $\bar{P}_i^{PV}$ are output limits of WT i and PV unit i. $u_{i,t}^{WT}$ and $u_{i,t}^{PV}$ denote the available wind power and PV power of WT i and PV unit i at time t considering environmental factors. Curtailment of wind power and PV power of WT i and PV unit i at time t are denoted by $v_{i,t}^{WT}$ and $v_{i,t}^{PV}$. The output of RE units is restrained by the equipment properties and the environmental factors, as shown in Eqs.1, 2. Curtailment of RE are calculated as Eqs.3, 4.

2.1.2 Diesel generator

The operation constraints of diesel generator (DG) are as follows:

$$\bar{P}_i^{DG} x_{i,t}^{DG} \le p_{i,t}^{DG} \le \bar{P}_i^{DG} x_{i,t}^{DG}, \forall t \in \boldsymbol{T} \tag{5}$$

$$-\overline{RD}_i^{DG} \le p_{i,t}^{DG} - p_{i,t-1}^{DG} \le \overline{RU}_i^{DG}, \forall t \in \boldsymbol{T} \tag{6}$$

$$x_{i,\tau}^{DG} \ge x_{i,t}^{DG} - x_{i,t-1}^{DG}, \tau = t+1, \dots, \min\left(t + T_i^{DG,on} - 1, T^m\right), \forall t \in \boldsymbol{T} \tag{7}$$

where $p_{i,t}^{DG}$is the output of DG i at time t, $\bar{P}_i^{DG}$ and $\bar{P}_i^{DG}$ are the minimum and maximum output of DG i, and $x_{i,t}^{DG}$ is the state variable of DG i at time t. $\overline{RD}_i^{DG}$ and $\overline{RU}_i^{DG}$ are the maximum ramp-down rate and ramp-up rate of DG i. $T_i^{DG,on}$ is the minimum on-time of DG i. T^m is the time horizon of the optimization. Constraints Eqs. 5, 6 refers to the operating power constraint and ramping rate constraint of DG. Constraint Eq. 7 is the start-stop constraint of DG to avoid frequent startup and shutdown in a short time. It should be noted that the state variables are binary variables. When the state variable of DG is 1, the DG is turned on and the output power is between the maximum and minimum power output. When the state variable is 0, the DG is turned off and the power output is 0.

2.1.3 Gas turbine

The operation constraints of gas turbine (GT) are as follows:

$$p_{i,t}^{GT} = g_{i,t}^{GT} \eta_i^{GT}, \forall t \in \boldsymbol{T} \tag{8}$$

$$h_{i,t}^{GT} = p_{i,t}^{GT} \mu_i^{GT}, \forall t \in \boldsymbol{T} \tag{9}$$

$$\bar{P}_i^{GT} x_{i,t}^{GT} \le p_{i,t}^{GT} \le \bar{P}_i^{GT} x_{i,t}^{GT}, \forall t \in \boldsymbol{T} \tag{10}$$

$$-\overline{RD}_i^{GT} \le p_{i,t}^{GT} - p_{i,t-1}^{GT} \le \overline{RU}_i^{GT}, \forall t \in \boldsymbol{T} \tag{11}$$

$$x_{i,\tau}^{GT} \ge x_{i,t}^{GT} - x_{i,t-1}^{GT}, \tau = t+1, \dots, \min\left(t + T_i^{GT,on} - 1, T^m\right), \forall t \in \boldsymbol{T} \tag{12}$$

where $p_{i,t}^{GT}$,$h_{i,t}^{GT}$ and $g_{i,t}^{GT}$ are electric power output, heat power output, and gas input of GT i at time t, respectively. η_i^{GT}denotes the power efficiency of GT i, $\mu_i^{GT}$is the electrothermal ratio of GT i. $\bar{P}_i^{GT}$and $\bar{P}_i^{GT}$ are the minimum and maximum output of GT i, and $x_{i,t}^{GT}$ is the state variable of GT i at time t. $\overline{RD}_i^{GT}$ and $\overline{RU}_i^{GT}$ are the maximum ramp-down rate and ramp-up rate of GT i. $T_i^{GT,on}$ is the minimum on-time of GT i. Constraints Eqs. 8, 9 depict the energy conversion relationship of GT. Constraints Eqs. 10, 11 describe the output power constraint and ramping rate constraint of GT. The operating state constraint of GT is presented in (Eq. 12).

2.1.4 Power to gas

The operation constraints of power to gas (P2G) are as follows:

$$g_{i,t}^{P2G} = \delta_i^{P2G} p_{i,t}^{P2G}, \forall t \in \boldsymbol{T} \tag{13}$$

$$\bar{P}_i^{P2G} x_{i,t}^{P2G} \le p_{i,t}^{P2G} \le \bar{P}_i^{P2G} x_{i,t}^{P2G}, \forall t \in \boldsymbol{T} \tag{14}$$

$$x_{i,\tau}^{P2G} \ge x_{i,t}^{P2G} - x_{i,t-1}^{P2G}, \tau = t+1, \dots, \min\left(t + T_i^{P2G,on} - 1, T^m\right), \forall t \in \boldsymbol{T} \tag{15}$$

where$g_{i,t}^{P2G}$ and $p_{i,t}^{P2G}$are gas output and power input of P2G i at time t, respectively. $\delta_i^{P2G}$is the conversion efficiency of P2G i. $\bar{P}_i^{P2G}$ and $\bar{P}_i^{P2G}$ are the minimum and maximum output of P2G i, and $x_{i,t}^{P2G}$ is the state variable of P2G i at time t. $T_i^{P2G,on}$ is the minimum on-time of P2G i. Constraint (Eq. 13) depicts the energy conversion relationship of P2G. Constraint (Eq. 14) describes the output power limit of P2G. The operating state constraint of P2G is presented in (Eq. 15).

2.1.5 Electric boiler

The constraints of the electric boiler (EB) are as follows:

$$h_{i,t}^{EB} = \mu_i^{EB} p_{i,t}^{EB}, \forall t \in \boldsymbol{T} \tag{16}$$

$$\bar{P}_i^{EB} x_{i,t}^{EB} \le p_{i,t}^{EB} \le \bar{P}_i^{EB} x_{i,t}^{EB}, \forall t \in \boldsymbol{T} \tag{17}$$

$$-\overline{RD}_i^{EB} \le p_{i,t}^{EB} - p_{i,t-1}^{EB} \le \overline{RU}_i^{EB}, \forall t \in \boldsymbol{T} \tag{18}$$

$$x_{i,\tau}^{EB} \ge x_{i,t}^{EB} - x_{i,t-1}^{EB}, \tau = t+1, \dots, \min\left(t + T_i^{EB,on} - 1, T^m\right), \forall t \in \boldsymbol{T} \tag{19}$$

where $h_{i,t}^{EB}$ and $p_{i,t}^{EB}$are heat output and power input of EB i at time t, respectively. $\mu_i^{EB}$is the conversion efficiency of EB i. $\bar{P}_i^{EB}$ and $\bar{P}_i^{EB}$ are the minimum and maximum output of EB i, and $x_{i,t}^{EB}$ is the state variable of EB i at time t. $\overline{RD}_i^{EB}$ and $\overline{RU}_i^{EB}$ are the maximum ramp-down rate and ramp-up rate of EB i. $T_i^{EB,on}$ is the minimum on-time of EB i. Constraint (Eq. 16) depicts the energy conversion relationship of EB. Constraints (Eqs. 17, 18) describe the output power constraint and ramping rate constraint of EB. The operating state constraint of EB is presented in (Eq. 19).

2.1.6 Energy storage system

The constraints of the energy storage systems are as follows:

$$x_{i,t}^{ch,\theta} + x_{i,t}^{dis,\theta} \le 1, \forall t \in \boldsymbol{T} \tag{20}$$

$$0 \le e_{i,t}^{ch,\theta} \le x_{i,t}^{ch,\theta} \bar{E}_i^{ch,\theta}, \forall t \in \boldsymbol{T} \tag{21}$$

$$0 \le e_{i,t}^{dis,\theta} \le x_{i,t}^{dis,\theta} \bar{E}_i^{dis,\theta}, \forall t \in \boldsymbol{T} \tag{22}$$

$$\underline{E}_i^{s,\theta} \le e_{i,t}^{s,\theta} \le \bar{E}_i^{s,\theta}, \forall t \in \boldsymbol{T} \tag{23}$$

where $\theta = \{ESC, GST, HST\}$, denoting electricity storage cell (ESC), gas storage tank (GST) and heat storage tank (HST), respectively. $x_{i,t}^{ch,\theta}$ and $x_{i,t}^{dis,\theta}$ denote charge and discharge state of energy storage unit i at time t, respectively. $e_{i,t}^{ch,\theta}$ and $e_{i,t}^{dis,\theta}$ are charging rate and discharging rate of energy storage unit i at time t. $\bar{E}_i^{ch,\theta}$ and $\bar{E}_i^{dis,\theta}$ are maximum charging and discharging rate of energy storage unit i. $e_{i,t}^{s,\theta}$ is the current energy storage of energy storage unit i at time t. $\underline{E}_i^{s,\theta}$ and $\bar{E}_i^{s,\theta}$ are the minimum and maximum storage of energy storage unit i. Operating state of energy storage unit is constrained by (Eq 20). Constraints (Eq. 21, 21) represent the energy storage unit charging and discharging bounds, and current storage limit of energy storage unit is presented in (Eq. 23).

2.1.7 Load model

We consider four types of electric load in the flexibility model of MEMG, which are represented in (Eqs 24–(27).

1) Fixed load

$$L_{i,t}^{fix,oper} = r_i^{fix} u_{i,t}^e, \forall t \in \boldsymbol{T} \tag{24}$$

2) Translatable load

$$L_{i,t+\tau}^{trans,oper} = r_i^{trans} u_{i,t}^e, \forall t \in \boldsymbol{T} \tag{25}$$

3) Shiftable load

$$\sum_{t \in T} L_{i,t}^{sft,oper} = r_i^{sft} u_{i,t}^e, \forall t \in \boldsymbol{T} \tag{26}$$

4) Interruptible load

$$0 \le L_{i,t}^{int,oper} \le r_i^{int} u_{i,t}^e, \forall t \in \boldsymbol{T} \tag{27}$$

where $L_{i,t}^{fix,oper}$, $L_{i,t}^{trans,oper}$, $L_{i,t}^{sft,oper}$ and $L_{i,t}^{int,oper}$ are fixed load, translatable load, shiftable load and interruptible load supplied at bus i at time t, respectively. r_i^{fix}, r_i^{trans}, r_i^{sft} and r_i^{int} are the percentage of the four types of load at node i. $u_{i,t}^e$ is the value of electric load at bus i at time t.

$$r_i^{fix} + r_i^{trans} + r_i^{sft} + r_i^{int} = 1, \forall i \in \Omega^{eload} \tag{28}$$

$$L_{i,t}^{e,oper} = L_{i,t}^{fix,oper} + L_{i,t}^{trans,oper} + L_{i,t}^{sft,oper} + L_{i,t}^{int,oper} \tag{29}$$

$$v_{i,t}^{eload} = r_i^{int} u_{i,t}^e - L_{i,t}^{int,oper} \tag{30}$$

The percentage of the four types of load are constrained by (Eq. 28) and the collection of them is denoted by $\boldsymbol{r}^e = \{r^{fix}, r^{trans}, r^{sft}, r^{int}\}$. $L_{i,t}^{e,oper}$ is the load actually supplied at bus i at time t, which is constrained by (Eq. 29). The electric load that is not supplied at electric bus i at time t, denoted by $v_{i,t}^{eload}$, is calculated as (Eq. 30). Among these four types of load, 1) is non-adjustable load, b), c), and 4) belong to adjustable load.

2.2 Model of MEMG network

2.2.1 MEMG electricity network

Model of MEMG electricity network are shown as follow:

$$\begin{aligned} & p_{i,t}^{PDS} + \sum_{u \in i} p_{u,t}^{DG} + \sum_{v \in i} p_{v,t}^{CHP} + \sum_{w \in i} p_{w,t}^{PV} + \sum_{m \in i} p_{m,t}^{WT} + \sum_{c \in i} p_{c,t}^{ESC} \\ & = L_{i,t}^{e,equ} + \sum_{j \in i} p_{ij,t} - \sum_{j \in i} p_{ji,t}, \forall t \in \boldsymbol{T} \end{aligned} \tag{31}$$

$$\bar{P}_k \le p_{k,t} \le \bar{P}_k, \forall t \in \boldsymbol{T} \tag{32}$$

where $p_{i,t}^{PDS}$ denotes the power from PDS at electric bus i at time t. $p_{u,t}^{DG}/p_{v,t}^{CHP}/p_{w,t}^{PV}/p_{m,t}^{WT}/p_{c,t}^{ESC}$ is the power output of DG/CHP/PV/WT/ESC at electric bus i at time t. $L_{i,t}^{e,equ}$ denotes the equivalent electric load at electric bus i at time t. $p_{ij,t}$ is electric flow of the lines which start with electric bus i and $p_{ji,t}$ is electric flow of the lines which end with electric bus i. $p_{k,t}$ denotes the electric flow of line k at time t. $\bar{P}_k$ and $\bar{P}_k$ are limits of the electric flow of line k. MEMG electricity network constraints include nodal power balance constraint (Eq. 31) and electric power line transmission capacity constraint (Eq. 32).

2.2.2 MEMG gas network

We adopt Weymouth steady-state model in this paper:

$$\sum_{s \in i} g_{s,t}^{GS} + \sum_{n \in i} g_{n,t}^{P2G} + \sum_{z \in i} g_{z,t}^{GST} = L_{i,t}^{g,equ} + \sum_{j \in i} g_{ij,t} - \sum_{j \in i} g_{ji,t}, \forall t \in \boldsymbol{T} \tag{33}$$

$$V_{k,t} \left| V_{k,t} \right| = C_k \Delta pre_{k,t}, \forall t \in \boldsymbol{T} \tag{34}$$

$$\underline{V}_k \le V_{k,t} \le \bar{V}_k, \forall t \in \boldsymbol{T} \tag{35}$$

$$\underline{pre}_i \le pre_{i,t} \le \overline{pre}_i, \forall t \in \boldsymbol{T} \tag{36}$$

where $g_{s,t}^{GS}/g_{n,t}^{P2G}/g_{z,t}^{GST}$ is the gas output of gas source/P2G/GST at gas bus i at time t. $L_{i,t}^{g,equ}$ denotes the equivalent gas load at gas bus i at time t. $g_{ij,t}$ is gas flow of the pipelines which start with gas bus i at time t and $g_{ji,t}$is gas flow of the pipelines which end with gas bus i at time t. $V_{k,t}$ denotes the gas flow of pipeline k at time t. C_k is the flow-pressure correlation coefficient. $\Delta pre_{k,t}$ is the pressure difference between the start and the end of pipeline k. $\underline{V}_k$ and $\bar{V}_k$ are the minimum and maximum gas flow of pipeline k. $pre_{i,t}$ is the pressure at gas bus i at time t. $\underline{pre}_i$ and $\overline{pre}_i$ are minimum and maximum pressure at gas bus i. The nodal gas balance constraint is presented in (Eq. 33). The relationship between the gas flow and nodal pressure is shown in (Eq. 34). Constraint (Eqs. 35, 36) depict the gas flow limit and nodal pressure limit, respectively. It should be noted that constraint (34) is nonlinear, and it is piecewise linearized in the following optimization model for efficient solution.

The transmission rate of gas is slow, and the gas has inertia and compressibility, so the gas transmission pipeline has a certain storage capacity. This energy storage effect can alleviate the time and space mismatch between the natural gas supply and the gas load consumption demand to a certain extent. The more natural gas stored in the pipeline, the greater the pressure at both ends of the pipeline, which are constrained by (Eq. 36).

2.2.3 MEMG heating network

We use the steady-state model of the heat supply network in this paper:

$$\sum_{k \in \Omega_{sp,i-}} T_{k,t}^{sp,out} \cdot q_k^{sp} = T_{i,t}^{sn} \sum_{k \in \Omega_{sp,i-}} q_k^{sp}, \forall t \in \boldsymbol{T} \tag{37}$$

$$\sum_{k \in \Omega_{rp,i-}} T_{k,t}^{rp,out} \cdot q_k^{rp} = T_{i,t}^{rn} \sum_{k \in \Omega_{rp,i-}} q_k^{rp}, \forall t \in \boldsymbol{T} \tag{38}$$

$$T_{k,t}^{sp,in} = T_{i,t}^{sn}, \forall k \in \Omega_{sp,i+}, \forall t \in \boldsymbol{T} \tag{39}$$

$$T_{k,t}^{rp,in} = T_{i,t}^{rn}, \forall k \in \Omega_{rp,i+}, \forall t \in \boldsymbol{T} \tag{40}$$

$$T_{k,t}^{sp,out} = \left(T_{k,t}^{sp,in} - T_a\right)e^{-\frac{l_k}{Rc\rho f_k}} + T_{k,t}^{sp,in}, \forall k \in \Omega_{sp}, \forall t \in \boldsymbol{T} \tag{41}$$

$$T_{k,t}^{rp,out} = \left(T_{k,t}^{rp,in} - T_a\right)e^{-\frac{l_k}{Rc\rho f_k}} + T_{k,t}^{rp,in}, \forall k \in \Omega_{rp}, \forall t \in \boldsymbol{T} \tag{42}$$

$$T_{k,t}^{sp,out} = \left(T_a - T_{k,t}^{sp,in}\right)\frac{l_k}{Rc\rho f_k} + T_{k,t}^{sp,in}, \forall k \in \Omega_{sp}, \forall t \in \boldsymbol{T} \tag{43}$$

$$T_{k,t}^{rp,out} = \left(T_a - T_{k,t}^{rp,in}\right)\frac{l_k}{Rc\rho f_k} + T_{k,t}^{rp,in}, \forall k \in \Omega_{rp}, \forall t \in \boldsymbol{T} \tag{44}$$

$$\underline{T}^{sp} \le T_{k,t}^{sp,in} \le \bar{T}^{sp}, \forall k \in \Omega_{sp}, \forall t \in \boldsymbol{T} \tag{45}$$

$$\underline{T}^{sp} \le T_{k,t}^{sp,out} \le \bar{T}^{sp}, \forall k \in \Omega_{sp}, \forall t \in \boldsymbol{T} \tag{46}$$

$$\underline{T}^{rp} \le T_{k,t}^{rp,in} \le \bar{T}^{rp}, \forall k \in \Omega_{rp}, \forall t \in \boldsymbol{T} \tag{47}$$

$$\underline{T}^{rp} \le T_{k,t}^{rp,out} \le \bar{T}^{rp}, \forall k \in \Omega_{rp}, \forall t \in \boldsymbol{T} \tag{48}$$

$$\sum_{k\in\Omega_{sp,i-}} \left(C^h q_k^{sp}\left(T_{k,t}^{sp,out} - T_{k,t}^{rp,in}\right)\right) = L_{i,t}^{h,equ}, \forall t \in \boldsymbol{T} \tag{49}$$

where $\Omega_{sp,i-}$ and $\Omega_{rp,i-}$ represent the collection of water supply and return pipelines whose end point is heat bus *i*. $\Omega_{sp,i+}$ and $\Omega_{rp,i+}$ represent the collection of water supply and return pipelines whose end point is heat bus *i*. Ω_{sp} and Ω_{rp} represent the collection of water supply and return pipelines. $T_{k,t}^{sp,out}$ and $T_{k,t}^{rp,out}$ represent the temperature at the outlet of pipeline k in the water supply and return network at time *t*, respectively. q_k^{sp} and q_k^{rp} indicate the water outflowing from pipeline k in the water supply and return network, respectively. $T_{i,t}^{sn}$ and $T_{i,t}^{rn}$ are the temperature at node i within the water supply and return network at time *t*. $T_{k,t}^{sp,in}$ and $T_{k,t}^{rp,in}$ are the temperature at the inlet of the pipeline *k* in the supply and return network, respectively. The flow of heat medium in the pipeline will produce heat loss, which is related to ambient temperature T_a, pipeline length l_k, pipeline thermal resistance R, pipeline flow f_k, the specific heat capacity $c$of heat medium, and heat medium density ρ. $\underline{T}^{sp}$, $\bar{T}^{sp}$, $\underline{T}^{rp}$ and $\bar{T}^{rp}$are the temperature limits of water supply and return pipelines. C^h is the heat capacity of the water within the pipelines. $L_{i,t}^{h,equ}$ denotes the equivalent heat load at heat bus *i* at time *t*. Eqs. 37, 38 are the node temperature fusion constraint, which indicates that the node temperature is equal to the fusion temperature of the incoming heat medium. The temperature of the heat medium flowing out of the node is equal to the temperature of the node, as depicted in constraints (Eqs. 39, 40). The temperature relationship of the heat medium at the inlet and outlet of the pipelines is shown in constraints (Eqs. 41, 42). Considering that the exponential term is close to zero, its linearized form can be obtained by Taylor expansion and omitting the higher order terms, as shown in constraints (Eqs. 43, 44). Constraints (Eqs. 45–48) are the temperature limits of the heat supply and return pipelines. Heat balance constraint of heat load node is shown as (Eq. 49).

Since the temperature of the heat pipelines can fluctuate within a certain range, as shown in (Eqs. 45–(48), the heat pipelines have a certain heat storage capacity. Heat pipelines in MEMG are flexible resources with flexible capability that can be dispatched.

2.2.4 Coupling constraints of MEMG

The coupling constraints of different networks in MEMG are as follows:

$$L_{i,t}^{e,equ} = L_{i,t}^{e,oper} + \sum_{k\in\Omega_{ECU}^i} p_{k,t}, \forall t \in \boldsymbol{T} \tag{50}$$

$$L_{i,t}^{g,equ} = u_{i,t}^{g} + \sum_{k\in\Omega_{GCU}^i} g_{k,t}, \forall t \in \boldsymbol{T} \tag{51}$$

$$L_{i,t}^{h,equ} = u_{i,t}^{h}, \forall t \in \boldsymbol{T} \tag{52}$$

where $\Omega_{ECU}^i/\Omega_{GCU}^i$ is collection of power consuming units/gas consuming units at bus *i*, $p_{k,t}/g_{k,t}$ is the power consumption/gas consumption of unit *k* at time *t*. $u_{i,t}^{g}$ and $u_{i,t}^{h}$ are the value of gas load and heat load at bus *i* at time *t*. In the MEMG, in addition to the conventional user-side load, the input of the multi-energy coupling equipment is also considered as the load of the corresponding energy system. Therefore, the equivalent electric load and the equivalent gas load at node *i* at time *t* are expressed as (Eqs. 50, 51). The equivalent heat load at node *i* at time *t* is shown as (Eq. 52).

2.3 Operational uncertainty set of MEMG

MEMGs face many uncertainties in their operation and it is risky to reduce these uncertainties to predicted values. To consider these uncertain factors in evaluating the flexibility of MEMG, an ARO problem is proposed. In the ARO problem, it is important to construct a suitable uncertainty set. The uncertainty model of MEMG operation is given in this section.

2.3.1 RE output and load consumption

A way to capture RE output and load consumption uncertainty is as follows:

$$\begin{aligned}\boldsymbol{u}^{RE} = \Big\{&u^{WT}, u^{PV} \Big| u_{i,t}^{WT} = \hat{u}_{i,t}^{WT} + \varsigma_i^{WT} d_i^{WT}, \varsigma_i^{WT} \in [0,1], d_i^{WT}\Big/\hat{u}_{i,t}^{WT} \le \rho^{WT},\\ &u_{i,t}^{PV} = \hat{u}_{i,t}^{PV} + \varsigma_i^{PV} d_i^{PV}, \varsigma_i^{PV} \in [0,1], d_i^{PV}\Big/\hat{u}_{i,t}^{PV} \le \rho^{PV}, \forall t \in \boldsymbol{T}\Big\}\end{aligned} \tag{53}$$

$$\begin{aligned}\boldsymbol{u}^{load} &= \Big\{u^{\omega} \Big| u_{j,t}^{\omega} = \hat{u}_{j,t}^{\omega} + \varsigma_j^{\omega} d_j^{\omega}, \varsigma_j^{\omega} \in [0,1], d_j^{\omega}\Big/\hat{u}_{j,t}^{\omega} \le \rho^{\omega}, \omega\\ &= \{e, g, h\}\Big\}\end{aligned} \tag{54}$$

where $\hat{u}_{i,t}^{WT}$ and $\hat{u}_{i,t}^{PV}$ respectively represent the predicted available power of WT and PV at node *i* at time *t*. ω is a collection of energy forms in the MEMG system, including the energy form of electricity, gas and heat. $\hat{u}_{j,t}^{e}$, $\hat{u}_{j,t}^{g}$ and $\hat{u}_{j,t}^{h}$ represent the predicted electric, gas and heat load consumption at load node j at time t, respectively. These predicted values are obtained based on historical data. We use the product of the maximum deviation $d_i^{WT}/d_i^{PV}/d_j^{L,\omega}$ and the error coefficient $\varsigma_i^{WT}/\varsigma_i^{PV}/\varsigma_j^{\omega}$ to express the prediction deviation of WT output/PV output/load consumption. ρ^{WT}, $\rho^{PV}$and $\rho^{\omega}$are given constants, which are introduced to define the limit of uncertainty to control the conservative level.

2.3.2 Dispatch instructions from PDS operator with carbon emission target

The uncertainty set of the dispatch instructions from the PDS operator is modeled as follows:

$$\boldsymbol{u}^{DI} \supset \left\{P_t^{DI}, RR_t^{DI} \middle| \bar{P}^{MG} \le P_t^{DI} \le \bar{P}^{MG}, -\overline{RD}^{MG} \le RR_t^{DI} \le \overline{RU}^{MG}, RR_t^{DI} = P_{t+1}^{DI} - P_t^{DI}, \forall t \in \boldsymbol{T}\right\} \tag{55}$$

where P_t^{DI} and RR_t^{DI} are instructed power output and ramping rate at time *t* from the PDS. When MEMG is providing flexibility to PDS, the interaction power between MEMG and PDS is constrained by (Eqs.56, 57).

$$p_t^{PDS} = P_t^{DI}, \forall t \in \boldsymbol{T} \tag{56}$$

$$r_t^{PDS} = p_t^{PDS} - p_{t-1}^{PDS} = RR_t^{DI}, \forall t \in \boldsymbol{T} \tag{57}$$

where p_t^{PDS} and r_t^{PDS} are power output and ramping rate of MEMG at the MG-FB at time *t*.

Besides, based on the carbon reduction trend of the energy system, we add the carbon emission limits that need to be realized by MEMG to the uncertainty set of the model: $\boldsymbol{u}^{DI} = \{P_t^{DI}, RR_t^{DI}, CE_t^{DI}\}$. Thus, the energy supply units in the MEMG can be more preferably configured based on the environmental protection objectives. The relevant constraints are shown below.

$$CE_{m,t} = \psi_m p_{m,t}, \forall m \in \Omega_{emi} \tag{58}$$

$$CE_t = \sum_{m \in \Omega_{emi}} CE_{m,t} \tag{59}$$

$$CE_t \le CE_t^{DI} \tag{60}$$

$$\sum_{t \in T} CE_t^{DI} \le \Gamma \tag{61}$$

$$\underline{CE}^{DI} \le CE_t^{DI} \le \overline{CE}^{DI} \tag{62}$$

where Ω_{emi} is the collection of units with carbon emission in the MEMG. $CE_{m,t}$ and $p_{m,t}$ are the carbon emission and energy output of unit *m* at time *t*, respectively. ψ_m is the carbon emission factor of unit *m*. CE_t denotes the carbon emission of MEMG at time *t*. CE_t^{DI} is the carbon emission limit for MEMG at time *t* in dispatch instructions from the PDS. Γ, $\underline{CE}^{DI}$ and $\overline{CE}^{DI}$ are pre-given constants. Part of the units in the MEMG produce pollution when operating, and the carbon emission of the units is usually proportional to the production, i.e. constraint (Eq. 58). The carbon emission of the MEMG system is the total emission of all carbon emission generating units in the system, i.e. constraint (Eq. 59). To achieve an overall carbon emission reduction target, the PDS operator will add the carbon emission constraint (Eq. 60) to MEMG in the dispatch instructions, in which the boundary is shown as (Eqs. 61, 62), which ensures that the carbon emission range of the MEMG is always kept within a reasonable range.

Based on the discussion above, operational uncertainty set of MEMG is denoted by (Eq. 63).

$$\boldsymbol{u} = \left\{\boldsymbol{u}^{RE}, \boldsymbol{u}^{load}, \boldsymbol{u}^{DI}\right\} \tag{63}$$

3 ARO model for obtaining MG-FPs

3.1 ARO model

When considering the operational uncertainty, the acquisition of MG-FPs has the following steps. In step 1, the MEMG operator collects the operation parameters of various local units, and in step 2, solves the initial MG-FPs according to the MEMG flexibility model and network operation constraints. In step 3, the MEMG operator searches for possible dispatch instructions from PDS and possible operation scenarios. In step 4, the MEMG operator tries to track the dispatch instructions from PDS in different operation scenarios, and judges if these orders are realizable and whether the MG-FPs need to be adjusted. If an unrealizable scenario is found, the MEMG operator adjusts the MG-FPs in step 5. Repeat steps three to five until no infeasible scenario is found, and the MEMG operator submits the MG-FPs obtained in the latest iteration to the PDS operator.

Based on the steps above, we propose a two-stage ARO model to obtain the MG-FPs submitted by the MEMG to PDS. The upper stage problem is solved first to obtain the MG-FPs. The upper stage problem aims to maximize the MEMG's flexibility region, including the feasible range of power, and upward and downward ramping rate. Subsequently, the lower stage problem aims to identify the worst-case uncertainty vector that maximizes the power imbalance at the MG-FB and optimizes the post-contingency dispatch with the values of MG-FPs. The convergence speed of the ARO model is accelerated by adding the worst scenario set to the upper stage problem. In the iteration process, the scenarios that are difficult to realize in the MEMG are gradually discovered, and the obtained MEMG's flexibility domain is gradually shrinking. When no solution-free scenario can be found, the MEMG operator obtains the accurate MG-FPs.

By solving this robust problem, the obtained optimal MG-FPs results can immunize to any uncertainty within a reasonable range. When the uncertainty u^* happens, the deviation caused by u^* is tried to be accommodated by the MEMG post-contingency dispatch. The compact formulation of the proposed model is presented in (Eqs. 64–(70):

$$\min_{\boldsymbol{z}} \left\{-\boldsymbol{c}^T\boldsymbol{z} + \max_{\boldsymbol{u}} \min_{x,y \in \Omega(z,u)} \boldsymbol{d}^T\boldsymbol{y}\right\} \tag{64}$$

$$s.t. \boldsymbol{A}\boldsymbol{x} \le \boldsymbol{b} \tag{65}$$

$$\boldsymbol{D}\boldsymbol{y} \le \boldsymbol{a} \tag{66}$$

$$\boldsymbol{C}\boldsymbol{y} + \boldsymbol{E}\boldsymbol{x} + \boldsymbol{F}\boldsymbol{u} + \boldsymbol{G}\boldsymbol{z} \le \boldsymbol{h} \tag{67}$$

$$\Omega(\boldsymbol{z}, \boldsymbol{u}) = \{\boldsymbol{x}, \boldsymbol{y} | \boldsymbol{C}\boldsymbol{y} + \boldsymbol{E}\boldsymbol{x} \le \boldsymbol{h} - \boldsymbol{F}\boldsymbol{u} - \boldsymbol{G}\boldsymbol{z}\} \tag{68}$$

$$c^T \boldsymbol{z} = \kappa_1 \bar{P}^{MG} + \kappa_2 \bar{P}^{MG} + \lambda_1 \overline{RU}^{MG} + \lambda_2 \overline{RD}^{MG} \tag{69}$$

$$\kappa_1 > 0, \kappa_2 < 0, \lambda_1 > 0, \lambda_2 < 0 \tag{70}$$

$$\text{where } \boldsymbol{x} = \{x_t^{DG}, x_t^{GT}, x_t^{P2G}, x_t^{EB}, x_t^{ch,ESC}, x_t^{dis,ESC}, x_t^{ch,GST}, x_t^{dis,GST},$$

$$x_t^{ch,HST}, x_t^{dis,HST}, \forall t \in \boldsymbol{T}\}, \boldsymbol{y} = \{p_t^{WT}, p_t^{PV}, v_t^{WT}, v_t^{PV}, p_t^{DG}, g_t^{GT}, p_t^{GT}, h_t^{GT},$$

$$g_t^{P2G}, p_t^{P2G}, h_t^{EB}, p_t^{EB}, e_t^{ch,\theta}, e_t^{dis,\theta}, e_t^{s,\theta}, L_t^{fix,oper},$$

$$L_t^{trans,oper}, L_t^{sft,oper}, L_t^{int,oper}, L_t^{e,oper}, V_t, \Delta pre_t, T_t^{sp,in}, T_t^{sp,out}, T_t^{sn}, T_t^{rn}, T_t^{rp,in},$$

$$T_t^{rp,out}, L_t^{e,equ}, L_t^{g,equ}, L_t^{h,equ}, t \in \boldsymbol{T}\}, \boldsymbol{u} = \{u_t^{WT}, u_t^{PV}, u_t^{e}, \boldsymbol{r}^e, u_t^{g}, u_t^{h},$$

$$P_t^{DI}, RR_t^{DI}, CE_t^{DI}, \forall t \in \boldsymbol{T}\}$$

Constraint 65) refers to (7), (12), (15), (19), (20). Constraint 66) represents (6), (8)–(9), (11), (13), (16), (18), (23), (29), (31)–(50), (58)–(59). Constraint 67) denotes the constraints (1)–(5), (10), (14), (17), (21)–(22), (24)–(28), (30), (51)–(57), (60)–(62).

Weight coefficients κ_1, κ_2, λ_1, and λ_2 in constraint 69) are given in advance by the MEMG operators, which could reflect their decision preferences. When κ_1 ($|\kappa_2|$) is large, a higher power upper limit (lower power inferior limit) will be obtained, but it will lead to contraction of the ramping rate adjustable range. When λ_1 ($|\lambda_2|$) is large, MEMG will have a better upward (downward) ramping rate adjustment ability, but the power adjustment ability will become worse. By selecting the weight coefficients, MEMG operator finally obtains MG-FPs of different operational flexibility characteristics. For PDS, MEMGs with different MG-FPs are equivalent to different types of generation units or loads.

3.1.1 Master problem

The primal problem can be decoupled into a master problem (MP) and a subproblem (SP). The MP is presented in (Eqs. 71–(76), which optimizes the decision variables of MG-FPs.

$$MP:$$

$$\min_{z} \; (-\boldsymbol{c}^T \boldsymbol{z}) \tag{71}$$

$$s.t. \boldsymbol{A}\boldsymbol{x} \le \boldsymbol{b} \tag{72}$$

$$\boldsymbol{D}\boldsymbol{y} \le \boldsymbol{a} \tag{73}$$

$$\boldsymbol{C}\boldsymbol{y} + \boldsymbol{E}\boldsymbol{x} + \boldsymbol{G}\boldsymbol{z} \le \boldsymbol{h} - \boldsymbol{F}\boldsymbol{u}_{l-1}^*, \forall l \le k \tag{74}$$

$$c^T \boldsymbol{z} = \kappa_1 \bar{P}^{MG} + \kappa_2 \bar{P}^{MG} + \lambda_1 \overline{RU}^{MG} + \lambda_2 \overline{RD}^{MG} \tag{75}$$

$$\kappa_1 > 0, \kappa_2 < 0, \lambda_1 > 0, \lambda_2 < 0 \tag{76}$$

where k denotes the current iteration. $\boldsymbol{u}_{l-1}^*$ is identified by the SP in the previous iteration. The optimal result of the MP is recorded as $\boldsymbol{z}*$, and is passed to the SP as known parameters.

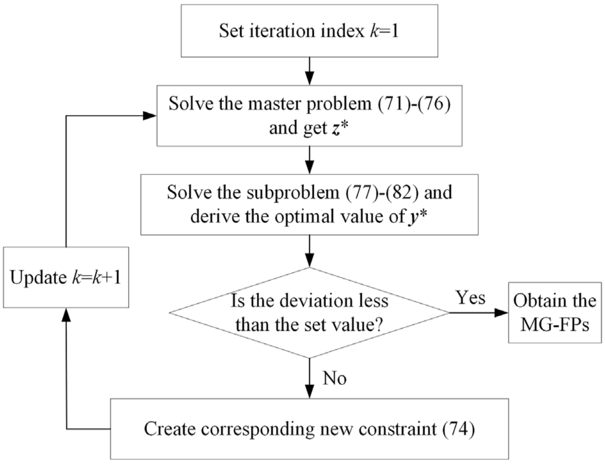

FIGURE 3
Solving procedures of C&CG algorithm.

3.1.2 Max-min subproblem

The SP identifies the most damaging uncertainty set for the determined MG-FPs obtained by the MP. The unsolvable scenarios are iteratively generated and added by solving the feasibility check SP. The compact form of the feasibility check SP in the kth iteration is formulated as (Eqs. 77–82). We reformulate the SP as an equivalent maximization problem (Eqs. 83–(86) using the duality principle for the initial bi-level model cannot be solved directly.

$$SP:$$

$$\max_{\boldsymbol{u}} \; \min_{\boldsymbol{x}, \boldsymbol{y} \in \Omega(\boldsymbol{z}, \boldsymbol{u})} \boldsymbol{d}^T \boldsymbol{y} \tag{77}$$

$$s.t. \; \boldsymbol{C}\boldsymbol{y} + \boldsymbol{E}\boldsymbol{x} + \boldsymbol{F}\boldsymbol{u} \le \boldsymbol{h} - \boldsymbol{G}\boldsymbol{z}_k^*: \; (\lambda) \tag{78}$$

$$\boldsymbol{d}^T \boldsymbol{y} = e_1 \sum_{t \in T} (\chi^+ + \chi^-) + e_2 \sum_{t \in T} (\delta^+ + \delta^-) \tag{79}$$

$$P_t^{DI} = p_t^{PDS} + \chi^+ - \chi^- \tag{80}$$

$$RR_t^{DI} = r_t^{PDS} + \delta^+ - \delta^- \tag{81}$$

$$\chi^+ \ge 0, \; \chi^- \ge 0, \; \delta^+ \ge 0, \; \delta^- \ge 0 \tag{82}$$

$$\max_{\boldsymbol{u}, \lambda} \lambda^T (\boldsymbol{h} - \boldsymbol{G}\boldsymbol{z}_k^* - \boldsymbol{F}\boldsymbol{u}) \tag{83}$$

$$s.t. \boldsymbol{\lambda}^T C \le d \tag{84}$$

$$\boldsymbol{\lambda}^T E \le 0 \tag{85}$$

$$\boldsymbol{\lambda} \le 0 \tag{86}$$

where λ is the dual variable vector of the MEMG dispatch problem in the inner level of SP. χ^+ and χ^- denote the deviation between actual power output p_t^{PDS} and the instructed P_t^{DI} at time t, δ^+ and δ^- denotes the deviation between actual ramping rate r_t^{PDS} and the instructed RR_t^{DI}. These deviations will be eliminated in the iteration procedure

TABLE 1 Main parameters of units in MEMG.

Type	$\bar{P}(kW)$	$\bar{P}(kW)$	$\Delta P(kW)$	$\overline{RU}$ $(kW/10\,\text{min})$	$\overline{RD}$ $(kW/10\,\text{min})$	ΔR $(kW/10\,\text{min})$
DG1	180	500	320	100	70	170
DG2	150	500	350	100	70	170
GT1	90	300	210	80	50	130
GT2	90	300	210	100	80	180
P2G1	100	300	200	-	-	-
P2G2	150	500	350	-	-	-
EB1	100	500	400	55	50	105
EB2	150	500	350	60	40	100
EB3	250	750	500	75	60	135
PV	0	550	550	-	-	-
WT	0	600	600	-	-	-

TABLE 2 Main parameters of energy storage units in MEMG.

Type	$\bar{P}$ $(kW)/(m^3/h)$	$\bar{P}$ $(kW)/(m^3/h)$	ΔP $(kW)/(m^3/h)$	$\underline{Cap}$ $(kWh)/(m^3)$	$\overline{Cap}$ $(kWh)/(m^3)$
ESS	0	100	100	10	300
GST	0	30	30	10	100
HST	0	120	120	50	400

to ensure that the MEMG can track these dispatch instructions from the PDS operator.

3.2 The detailed solution procedure of C&CG

The proposed MP and the max-min SP are both MILP models, which can be solved by several solvers. The two-stage ARO model is solved by the C&CG Algorithm 1, which is a cutting-plane-based method. The procedure is conducted iteratively, as shown in Figure 3. Detailed steps are shown as follows.

```
0. Initialization: A set of uncertain variables $\boldsymbol{u}^*$ is given as the initial scenario. Set k=1 and tolerance $\varepsilon^{ARO} > 0$.
1. while $deviation > \varepsilon^{ARO}$ do
    2. Solve MP (71)-(76), go to step3 with the optimal solutions of MG-FPs, denoted by $\{\overline{P}^{*MG}_{(k)}, \underline{P}^{*MG}_{(k)}, \overline{RU}^{*MG}_{(k)}, \overline{RD}^{*MG}_{(k)}\}$.
    3. Solve max-min SP (77)-(82) with $\{\overline{P}^{*MG}_{(k)}, \underline{P}^{*MG}_{(k)}, \overline{RU}^{*MG}_{(k)}, \overline{RD}^{*MG}_{(k)}\}$ from step 2, and find the worst-scenario set $\boldsymbol{u}^*_k$ that leads to the largest deviation.
    4. Generate new constraint (74) with $\boldsymbol{u}^*_k$, and pass the new constraint to MP. Update $k \leftarrow k+1$.
5. end while
6. Obtain the optimal feasible MG-FPs, denoted by $\{\overline{P}^{MG}, \underline{P}^{MG}, \overline{RU}^{MG}, \overline{RD}^{MG}\}$.
```

Algorithm 1. Column-and-Constraint Generation Algorithm.

4 Case study

The following cases are performed on a modified network that operates as a MEMG. Characteristics of the initial network are available in (Yang et al., 2020). The MEMG is connected to PDS for data and energy exchange. The MEMG includes 70 buses, 65 lines, and 32 loads. Besides, there are 2 DGs, 2 GTs, 2 P2G, 3 EBs, 1 PV, 1 WT, 1 ESC, 1 GST, and 1 HST. The main parameters of the units are shown in Tables 1, 2. Daily load, wind power and PV power are depicted in Figures 4, 5.

All tests are implemented on a computer with eight processors running at 3.60 GHz with 16 GB of memory. Programs are coded under MATLAB 2019b environment and programmed with YALMIP by calling cplex.

4.1 Comparison of MG-FPs' calculation methods

We first verify the effectiveness and accuracy of the proposed ARO model in obtaining MG-FPs. In addition to the proposed ARO method, we calculate the MG-FPs in a direct way for comparison. Table 3 shows the results of the optimized MG-FPs with the two methods. The basic equations of the direct method are as follows:

$$\bar{P}^{MG} = \sum_{k\in\Omega_{sup}} \bar{P}_k + \sum_{r\in\Omega_{co}} \Delta\bar{P}_r - \sum_{i\in\Omega_{EL}} L_i \tag{87}$$

$$\bar{P}^{MG} = \sum_{k\in\Omega_{sup}} \bar{P}_k + \sum_{r\in\Omega_{co}} \Delta\bar{P}_r - \sum_{i\in\Omega_{EL}} L_i \tag{88}$$

$$\overline{RU}^{MG} = \sum_{k\in\Omega_r} \overline{RU}_k \tag{89}$$

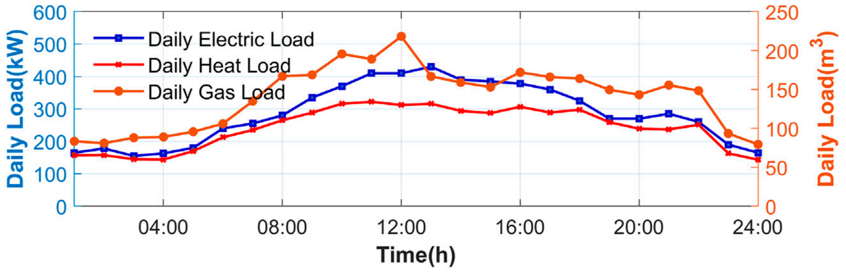

FIGURE 4
Daily load profiles of MEMG.

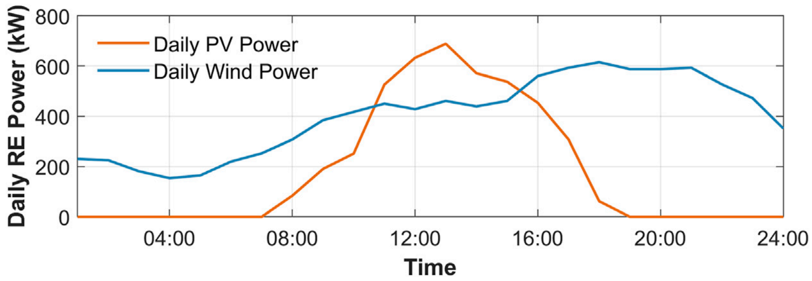

FIGURE 5
Daily RE power of MEMG.

TABLE 3 Results of MG-FPs from different methods.

Method	$\bar{P}^{MG}$ (kW)	$\bar{P}^{MG}$ (kW)	ΔP^{MG} (kW)	$\overline{RU}^{MG}$ $(kW/10\,\mathrm{min})$	$\overline{RD}^{MG}$ $(kW/10\,\mathrm{min})$	ΔR^{MG} $(kW/10\,\mathrm{min})$
Direct method	646.50	−891.2	1,537.7	669.12	570.00	1,239.12
ARO method	358.88	−838.28	1,197.16	461.10	428.91	890.01

$$\overline{RD}^{MG} = \sum_{k\in\Omega_r} \overline{RD}_k \tag{90}$$

where $\sum_{k\in\Omega_{sup}} \bar{P}_k$ and $\sum_{k\in\Omega_{sup}} \bar{P}_k$ denote the sum of maximum and minimum output of power supply units, $\sum_{r\in\Omega_{co}} \Delta\bar{P}_r$ and $\sum_{r\in\Omega_{co}} \Delta\bar{P}_r$ denote the sum of maximum and minimum power output of the energy coupling units while loads of other energy types meet their demand. $\sum_{i\in\Omega_{EL}} L_i$denotes the sum of electric load. $\sum_{k\in\Omega_r} \overline{RU}_k$ and $\sum_{k\in\Omega_r} \overline{RD}_k$ represent the sum of the maximum ramp-up rate and ramp-down rate of units in MEMG.

It is obvious that the MG-FPs obtained from the direct method have better flexibility benefits than the ARO method. But actually, these look-better parameters are hard to track for MEMGs because the direct method calculates the MG-FPs without consideration of line capacity limitation. In other words, the inaccuracy of the direct method comes mainly from the violation of network constraints when directly summing up the flexibility parameters of units. There is a possibility that the MEMG operator cannot realize the committed parameters in some scenarios without security violation.

When the power of the MEMG is negative, the PDS supplies electric power to the MEMG, MEMG is equivalent to the load of the PDS. This minimum power flexibility parameter is constrained by MEMG's energy consumption level and energy transmission capacity. The higher the MEMG energy consumption level and the greater the line transmission capacity, the greater the absolute value of the minimum power flexibility parameter, and vice versa. When the interaction power is positive, the MEMG supplies energy to the PDS on the basis of meeting its own load demand. The maximum power flexibility parameter is limited by the energy supply capacity of energy supply equipment, conversion capacity of energy conversion equipment, and energy transmission capacity of MEMG.

TABLE 4 Results of MG-FPs with different risk preferences in configuration case 1.

UP	$\bar{P}^{MG}$ (kW)	$\bar{P}^{MG}$ (kW)	ΔP^{MG} (kW)	$\overline{RU}^{MG}$ $(kW/10\,\text{min})$	$\overline{RD}^{MG}$ $(kW/10\,\text{min})$	ΔR^{MG} $(kW/10\,\text{min})$
DO	374.00	−843.50	1,217.50	461.56	421.91	883.47
0/0	374.00	−843.50	1,217.50	461.56	421.91	883.47
5%/5%	367.70	−841.33	1,209.03	461.10	421.91	883.01
12%/18%	358.88	−838.28	1,197.16	460.46	421.91	882.37
15%/20%	355.10	−836.98	1,192.08	460.19	421.90	882.09
30%/30%	336.20	−830.45	1,166.65	458.82	421.88	880.70

TABLE 5 Results of MG-FPs in different system configuration cases.

Case	$\bar{P}^{MG}$ (kW)	$\bar{P}^{MG}$ (kW)	ΔP^{MG} (kW)	$\overline{RU}^{MG}$ $(kW/10\,\text{min})$	$\overline{RD}^{MG}$ $(kW/10\,\text{min})$	ΔR^{MG} $(kW/10\,\text{min})$
case1	358.88	−838.28	1,197.16	460.46	421.91	882.37
case2	275.39	−748.72	1,024.11	387.76	372.24	760.00
case3	80.48	−546.49	626.97	337.76	322.24	660.00

TABLE 6 Results of MG-FPs from different optimization model.

Model	**DO**					
Item	$\bar{P}^{MG}$ (kW)	$\bar{P}^{MG}$ (kW)	ΔP^{MG} (kW)	$\overline{RU}^{MG}$ $(kW/10\,\text{min})$	$\overline{RD}^{MG}$ $(kW/10\,\text{min})$	ΔR^{MG} $(kW/10\,\text{min})$
	374.00	-843.50	1,217.50	461.56	421.91	883.47
Model	**ARO**					
Item	$\bar{P}^{MG}$ (kW)	$\bar{P}^{MG}$ (kW)	ΔP^{MG} (kW)	$\overline{RU}^{MG}$ $(kW/10\,\text{min})$	$\overline{RD}^{MG}$ $(kW/10\,\text{min})$	ΔR^{MG} $(kW/10\,\text{min})$
	358.88	-838.28	1,197.16	460.46	421.91	882.37

TABLE 7 System operation performance with MG-FPs from different optimization model.

Prediction error (Load/RE)	**DO**		**ARO**	
	RECR (%)	**LOL** (kWh)	**RECR (%)**	**LOL** (kWh)
6%/9%	98.22	268.05	98.87	0
12%/18%	96.25	563.54	96.92	0
18%/27%	94.21	649.65	95.91	265.4
24%/36%	92.16	735.27	94.68	412.5

4.2 Impact of MEMG Operator's risk preference and system configuration

Adopting the robust optimization framework proposed in this paper, we can change the MEMG operator's risk preference by changing the uncertainty parameters (UP). The UPs refer to ρ^{PV}, ρ^{WT} and ρ^{ω} in the MEMG operational uncertainty model. The deterministic optimization (DO), in which the uncertainty variables take the predicted values, is also solved for comparison. The results are listed in Table 4.

It is shown that the MEMG operator's risk preference does not have much impact on ramping rate flexibility parameters, but is influential on power flexibility parameters. When the UP is set to 0, the ARO model is equal to the DO model, the look-best MG-

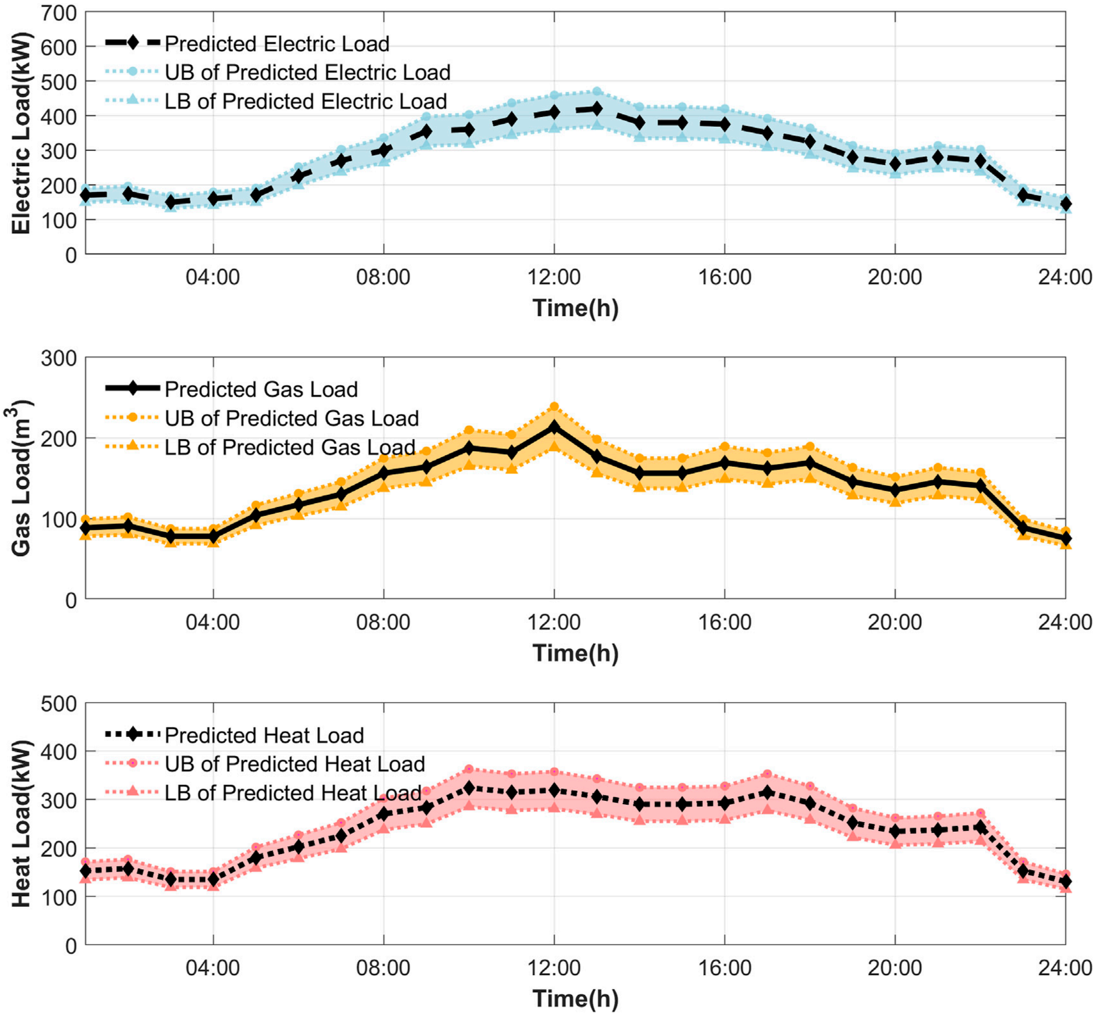

FIGURE 6
MEMG load profiles predicted, and uncertainty intervals.

FPs among these contrast sets are obtained. As UPs increase, MG-FPs tend to get worse to adapt to the worse scenarios. This indicates that the operators will give more consideration to the uncertainty they face when determining MG-FPs. Therefore, the parameters will be more conservative, which means that the MG-FPs of MEMG get worse. Conversely, when the operators consider more about the favorable scenarios, the UPs will be small, resulting in better MG-FPs values.

We can conclude that the evaluated flexibility level of the MEMG system is related to the risk preference of MEMG operators. When the MEMG operator is a conservative idea holder, the submitted MG-FPs are likely to be constrictive. Otherwise, if the MEMG operator is a risk-taker, the MEMG appears to be more effective in supporting the flexible operation of the main network although the actual flexibility capability of MEMG does not change.

In addition to the risk preference of the MEMG operator, the system configuration of the MEMG has a more significant impact on the assessment results. This impact may arise from the characteristics of the MEMG units and the synergies between them. The impact of system configuration on MG-FPs is researched through the following three configuration cases:

Case 1 All units in the MEMG are available in the scheduling.

Case 2 State variables of GT 1 and P2G 1 are set to 0, and other units in the MEMG are available.

Case 3 Only EB 1 and EB 3 are reserved as heat sources of the heat supply network, state variables of other units are set to 0.

The optimization results are presented in Table 5. With the reduction of units in the MEMG system, the flexibility parameters of MEMG become significantly worse in terms of power and ramping rate. The configuration of power-consuming equipment has a significant effect on the

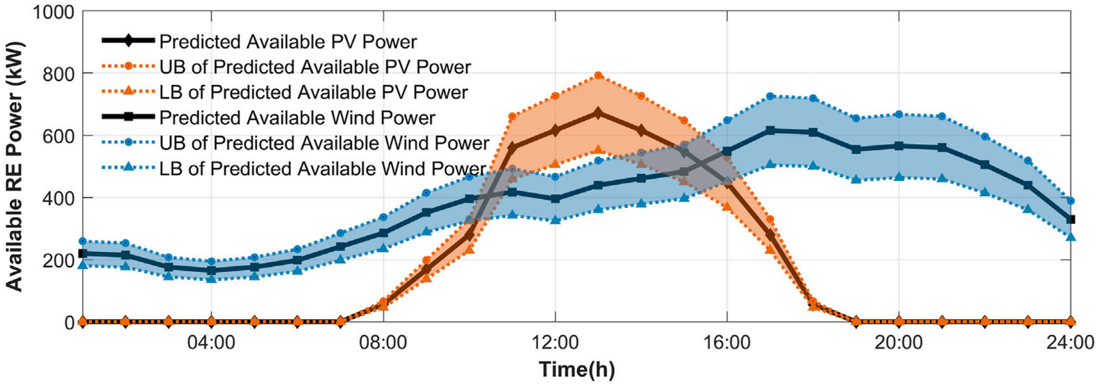

FIGURE 7
MEMG available RE power predicted, and uncertainty intervals.

minimum power parameter. Because in the MEMG, power-consuming units are regarded as the equivalent electric load, and the minimum power flexibility parameter is limited by the power consumption level. When the power generation equipment in the MEMG system halt, the maximum power parameters will be decreased.

4.3 Impact of the prediction error of MEMG operator

To verify that the MG-FPs obtained by the ARO model in this paper can withstand the worst scenarios, the optimization results of the DO model are compared with results of the ARO model in this section. Results of MG-FPs from the two models are presented in Table 6.

We compare the system's loss of load (LOL) and RE curtailment rate (RECR) under different prediction errors, as shown in Table 7. The prediction error refers to the degree to which the predicted value of load consumption and available RE deviate from the actual value. The proposed ARO model in the following comparative examples have the same risk preference coefficients of MEMG operator which are 12 and 18% for load and RE, as shown in Figures 6, 7.

It should be noted that when solving MG-FPs, MEMG operators do not regard reducible load as a flexible resource that can be curtailed. Therefore, when the prediction error is within the risk preference interval, the MEMGs which submit the MG-FPs of the ARO model will not have load shedding. When the prediction error exceeds MEMG operators' anticipation (e.g. the power consumption level of MEMG is higher than expected and PDS commands a certain large power output of MEMG, or the available RE output is lower than the lowest expected level), the loads will probably be shed to track the scheduling instructions.

There exists no provision for 100% RE consumption in the ARO model, thus, although the prediction error is expected, RE may not be completely absorbed in MEMG. The rejection of RE power may be due to the constraints of line transmission capacity, the low energy consumption level of MEMG, etc. When the prediction error exceeds the risk tolerance, the RE consumption rate may be further downward constrained by undesirable PDS orders, which are hard to track without RE abandonment (e.g. power instructions of certain low negative values).

The results show that the ARO model has more advantages when considering the prediction error. With the increase in prediction error, the results of the DO method get worse, because the results of DO method are not robust to operational uncertainties. There may occur load shedding or RE abandonment in MEMG, to track the scheduling orders from PDS which are formulated with submitted MG-FPs. The results indicate that the robust optimization framework we proposed to obtain MG-FPs possesses preponderance, especially in scenarios with large prediction error.

5 Conclusion

In this paper, we propose a specific evaluation method for the operational flexibility of distributed MEMG in supporting power distribution systems. The method has the following merits.

The flexibility-oriented model of MEMG is introduced, by systematically considering the flexibility resources of MEMG. The network constraints are considered as well, making the proposed evaluation method more applicable. The flexibility representation way we adopt, namely MG-FPs, determines that the main network can schedule the MEMGs as conventional units or loads in the primal scheduling model. Besides, the privacy problem can be avoided.

Several uncertainties are considered when assessing the flexibility of MEMG, making the assessment result robust. The MG-FPs obtained through the ARO model proposed in this paper can resist the influence of system operational uncertainty to a certain extent, which depends on the prediction error of the uncertainty set and the risk preference of the MEMG operator. The case studies show the effectiveness of the MG-FPs in representing the flexibility of MEMG. It can also be summarized that the flexibility capability of MEMG is related to equipment configuration, line transmission capacity, and energy consumption level.

Future works include 1) improving the model of MEMG components to meet the actual needs; 2) developing a reasonable pricing mechanism for the flexibility of the MEMG to encourage the MEMG to participate in the operation support of the main network.

Data availability statement

The original contributions presented in the study are included in the article/Supplementary Material, further inquiries can be directed to the corresponding author.

Author contributions

JW performed the statistical analysis and wrote the first draft of the manuscript. ZW contributed to the conception and design of the study. All authors contributed to manuscript revision and read and approved the submitted version.

Funding

This research was supported in part by the National Key R&D Program of China under Grant 2020YFE0200400, in part by the National Natural Science Foundation of China under Grant 52177077.

Conflict of interest

The authors declare that the research was conducted in the absence of any commercial or financial relationships that could be construed as a potential conflict of interest.

Publisher's note

References

Bahramara, S., Sheikhahmadi, P., Mazza, A., and Chicco, G. (2022). Day-ahead self-scheduling from risk-averse microgrid operators to provide reserves and flexible ramping ancillary services. *Int. J. Electr. Power. Energy Syst.* 142, 108381. doi:10.1016/j.ijepes.2022.108381

Baringo, A., Baringo, L., and Arroyo, J. M. (2019). Day-ahead self-scheduling of a virtual power plant in energy and reserve electricity markets under uncertainty. *IEEE Trans. Power Syst.* 34 (3), 1881–1894. doi:10.1109/tpwrs.2018.2883753

Capuder, T., and Mancarella, P. (2014). Techno-economic and environmental modelling and optimization of flexible distributed multi-generation options. *Energy* 71, 516–533. doi:10.1016/j.energy.2014.04.097

Chen, H., Xuan, P., Wang, Y., Tan, K., and Jin, X. (2016). Key technologies for integration of multitype renewable energy sources—research on multi-timeframe robust scheduling/dispatch. *IEEE Trans. Smart Grid* 7 (1), 471–480. doi:10.1109/tsg.2015.2388756

Chen, X., and Li, N. (2021). Leveraging two-stage adaptive robust optimization for power flexibility aggregation. *IEEE Trans. Smart Grid* 12 (5), 3954–3965. doi:10.1109/tsg.2021.3068341

Chen, X., Wu, W., and Zhang, B. (2018). Robust capacity assessment of distributed generation in unbalanced distribution networks incorporating ANM techniques. *IEEE Trans. Sustain. Energy* 9 (2), 651–663. doi:10.1109/tste.2017.2754421

De Coninck, R., and Helsen, L. (2016). Quantification of flexibility in buildings by cost curves – methodology and application. *Appl. Energy* 162, 653–665. doi:10.1016/j.apenergy.2015.10.114

Dehghan, S., Aristidou, P., Amjady, N., and Conejo, A. (2021). A distributionally robust AC network-constrained unit commitment. *IEEE Trans. Power Syst.* 36 (6), 5258–5270. doi:10.1109/tpwrs.2021.3078801

Ding, T., Li, C., Yang, Y., Jiang, J., Bie, Z., and Blaabjerg, F. (2017). A two-stage robust optimization for centralized-optimal dispatch of photovoltaic inverters in active distribution networks. *IEEE Trans. Sustain. Energy* 8 (2), 744–754. doi:10.1109/tste.2016.2605926

Ding, T., Zhang, X., Lu, R., Qu, M., Shahidehpour, M., He, Y., et al. (2022). Multi-stage distributionally robust stochastic dual dynamic programming to multi-period economic dispatch with virtual energy storage. *IEEE Trans. Sustain. Energy* 13 (1), 146–158. doi:10.1109/tste.2021.3105525

Holjevac, N., Capuder, T., and Kuzle, I. (2015). Adaptive control for evaluation of flexibility benefits in microgrid systems. *Energy* 92, 487–504. doi:10.1016/j.energy.2015.04.031

Holttinen, H., Tuohy, A., Milligan, M., Lannoye, E., Silva, V., Muller, S., et al. (2013). The flexibility workout: Managing variable resources and assessing the need for power system modification. *IEEE Power Energy Mag.* 11 (6), 53–62. doi:10.1109/mpe.2013.2278000

Huang, Z., Zhang, Y., and Xie, S. (2022). Data-adaptive robust coordinated optimization of dynamic active and reactive power flow in active distribution networks. *Renew. Energy* 188, 164–183. doi:10.1016/j.renene.2022.02.027

Jiang, Q., and Hong, H. (2013). Wavelet-based capacity configuration and coordinated control of hybrid energy storage system for smoothing out wind power fluctuations. *IEEE Trans. Power Syst.* 28 (2), 1363–1372. doi:10.1109/tpwrs.2012.2212252

Lannoye, E., Flynn, D., and O'Malley, M. (2012). Evaluation of power system flexibility. *IEEE Trans. Power Syst.* 27 (2), 922–931. doi:10.1109/tpwrs.2011.2177280

Lannoye, E., Flynn, D., and O'Malley, M. (2015). Transmission, variable generation, and power system flexibility. *IEEE Trans. Power Syst.* 30 (1), 57–66. doi:10.1109/tpwrs.2014.2321793

Liu, M. Z., Ochoa, L. N., Riaz, S., Mancarella, P., Ting, T., San, J., et al. (2021). Grid and market services from the edge: Using operating envelopes to unlock network-aware bottom-up flexibility. *IEEE Power Energy Mag.* 19 (4), 52–62. doi:10.1109/mpe.2021.3072819

Lu, Z., Li, H., and Qiao, Y. (2018). Probabilistic flexibility evaluation for power system planning considering its association with renewable power curtailment. *IEEE Trans. Power Syst.* 33 (3), 3285–3295. doi:10.1109/tpwrs.2018.2810091

Lund, P. D., Lindgren, J., Mikkola, J., and Salpakari, J. (2015). Review of energy system flexibility measures to enable high levels of variable renewable electricity. *Renew. Sustain. Energy Rev.* 45, 785–807. doi:10.1016/j.rser.2015.01.057

Ma, J., Silva, V., Belhomme, R., Kirschen, D. S., and Ochoa, L. F. (2013). Evaluating and planning flexibility in sustainable power systems. *IEEE Trans. Sustain. Energy* 4 (1), 200–209. doi:10.1109/tste.2012.2212471

Majzoobi, A., and Khodaei, A. (2017). Application of microgrids in supporting distribution grid flexibility. *IEEE Trans. Power Syst.* 32 (5), 3660–3669. doi:10.1109/tpwrs.2016.2635024

Makarov, Y. V., Loutan, C., Ma, J., and De Mello, P. (2009). Operational impacts of wind generation on California power systems. *IEEE Trans. Power Syst.* 24 (2), 1039–1050. doi:10.1109/tpwrs.2009.2016364

Mancarella, P. (2014). MES (multi-energy systems): An overview of concepts and evaluation models. *Energy* 65, 1–17. doi:10.1016/j.energy.2013.10.041

Martinez Cesena, E. A., Good, N., Panteli, M., Mutale, J., and Mancarella, P. (2019). Flexibility in sustainable electricity systems: Multivector and multisector nexus perspectives. *IEEE Electrific. Mag.* 7 (2), 12–21. doi:10.1109/mele.2019.2908890

Parhizi, S., Lotfi, H., Khodaei, A., and Bahramirad, S. (2015). State of the art in research on microgrids: A review. *IEEE Access* 3, 890–925. doi:10.1109/access.2015.2443119

Shao, C., Ding, Y., Wang, J., and Song, Y. (2018). Modeling and integration of flexible demand in heat and electricity integrated energy system. *IEEE Trans. Sustain. Energy* 9 (1), 361–370. doi:10.1109/tste.2017.2731786

Trovato, V., Teng, F., and Strbac, G. (2018). Role and benefits of flexible thermostatically controlled loads in future low-carbon systems. *IEEE Trans. Smart Grid* 9 (5), 5067–5079. doi:10.1109/tsg.2017.2679133

Ulbig, A., and Andersson, G. (2014). *Analyzing operational flexibility of electric power systems*. Power systems computation conference: Ieee.

Ulbig, A., and Andersson, G. (2012). *On operational flexibility in power systems*. IEEE Power and Energy Society General Meeting: IEEE

Wang, Q., and Hodge, B.-M. (2017). Enhancing power system operational flexibility with flexible ramping products: A review. *IEEE Trans. Ind. Inf.* 13 (4), 1652–1664. doi:10.1109/tii.2016.2637879

Wang, Y., Cheng, J., Zhang, N., and Kang, C. (2018). Automatic and linearized modeling of energy hub and its flexibility analysis. *Appl. Energy* 211, 705–714. doi:10.1016/j.apenergy.2017.10.125

Wu, X., and Conejo, A. J. (2020). Security-constrained ACOPF: Incorporating worst contingencies and discrete controllers. *IEEE Trans. Power Syst.* 35 (3), 1936–1945. doi:10.1109/tpwrs.2019.2937105

Wu, Y. J., Liang, X. Y., Huang, T., Lin, Z. W., Li, Z. X., and Hossain, M. F. (2021). A hierarchical framework for renewable energy sources consumption promotion among microgrids through two-layer electricity prices. *Renew. Sustain. Energy Rev.* 145, 111140. doi:10.1016/j.rser.2021.111140

Wu, Y., Shi, Z., Lin, Z., Zhao, X., Xue, T., and Shao, J. (2022). Low-carbon economic dispatch for integrated energy system through the dynamic reward and penalty carbon emission pricing mechanism. *Front. Energy Res.* 10, 843993. doi:10.3389/fenrg.2022.843993

Xiang, Y., and Wang, L. (2019). An improved defender–attacker–defender model for transmission line defense considering offensive resource uncertainties. *IEEE Trans. Smart Grid* 10 (3), 2534–2546. doi:10.1109/tsg.2018.2803783

Yan, M., Shahidehpour, M., Paaso, A., Zhang, L., Alabdulwahab, A., and Abusorrah, A. (2021). Distribution system resilience in ice storms by optimal routing of mobile devices on congested roads. *IEEE Trans. Smart Grid* 12 (2), 1314–1328. doi:10.1109/tsg.2020.3036634

Yan, M., Zhang, N., Ai, X., Shahidehpour, M., Kang, C., and Wen, J. (2019). Robust two-stage regional-district scheduling of multi-carrier energy systems with a large penetration of wind power. *IEEE Trans. Sustain. Energy* 10 (3), 1227–1239. doi:10.1109/tste.2018.2864296

Yang, W., Liu, W., Chung, C. Y., and Wen, F. (2020). Coordinated planning strategy for integrated energy systems in a district energy sector. *IEEE Trans. Sustain. Energy* 11 (3), 1807–1819. doi:10.1109/tste.2019.2941418

Zang, H., Cheng, L., Ding, T., Cheung, K. W., Wei, Z., and Sun, G. (2020). Day-ahead photovoltaic power forecasting approach based on deep convolutional neural networks and meta learning. *Int. J. Electr. Power. Energy Syst.* 118, 105790. doi:10.1016/j.ijepes.2019.105790

Zang, H., Xu, R., Cheng, L., Ding, T., Liu, L., Wei, Z., et al. (2021). Residential load forecasting based on LSTM fusing self-attention mechanism with pooling. *Energy* 229, 120682. doi:10.1016/j.energy.2021.120682

Zeng, B., and Zhao, L. (2013). Solving two-stage robust optimization problems using a column-and-constraint generation method. *Operations Res. Lett.* 41 (5), 457–461. doi:10.1016/j.orl.2013.05.003

Zhang, Y., Han, X., Yang, M., Xu, B., Zhao, Y., and Zhai, H. (2019). Adaptive robust unit commitment considering distributional uncertainty. *Int. J. Electr. Power. Energy Syst.* 104, 635–644. doi:10.1016/j.ijepes.2018.07.048

Zhao, J., Wang, J., Xu, Z., Wang, C., Wan, C., and Chen, C. (2017a). Distribution network electric vehicle hosting capacity maximization: A chargeable region optimization model. *IEEE Trans. Power Syst.* 32 (5), 4119–4130. doi:10.1109/tpwrs.2017.2652485

Zhao, J., Zheng, T., and Litvinov, E. (2016). A unified framework for defining and measuring flexibility in power system. *IEEE Trans. Power Syst.* 31 (1), 339–347. doi:10.1109/tpwrs.2015.2390038

Zhao, J., Zheng, T., and Litvinov, E. (2015). Variable resource dispatch through do-not-exceed limit. *IEEE Trans. Power Syst.* 30 (2), 820–828. doi:10.1109/tpwrs.2014.2333367

Zhao, L., Zhang, W., Hao, H., and Kalsi, K. (2017b). A geometric approach to aggregate flexibility modeling of thermostatically controlled loads. *IEEE Trans. Power Syst.* 32 (6), 4721–4731. doi:10.1109/tpwrs.2017.2674699

frontiers | Frontiers in Energy Research

TYPE Original Research
PUBLISHED 09 January 2023
DOI 10.3389/fenrg.2022.1013154

EDITED BY
Yingjun Wu,
Hohai University, China

REVIEWED BY
Yiyan Li,
North Carolina State University,
United States
Yan Qin,
Nanyang Technological University,
Singapore
Su Su,
Beijing Jiaotong University, China

*CORRESPONDENCE
Yun Zhou,
yun.zhou@sjtu.edu.cn

SPECIALTY SECTION
This article was submitted to Smart Grids,
a section of the journal
Frontiers in Energy Research

RECEIVED 06 August 2022
ACCEPTED 16 September 2022
PUBLISHED 09 January 2023

CITATION
Li H, Liang D, Zhou Y, Shi Y, Feng D and Shi S (2023), Spatiotemporal charging demand models for electric vehicles considering user strategies.
Front. Energy Res. 10:1013154.
doi: 10.3389/fenrg.2022.1013154

Spatiotemporal charging demand models for electric vehicles considering user strategies

Hengjie Li[1,2], Daming Liang[1], Yun Zhou[2]*, Yiwei Shi[2], Donghan Feng[2] and Shanshan Shi[3]

[1]School of Electrical and Information Engineering, Lanzhou University of Technology, Lanzhou, China, [2]Key Laboratory of Control of Power Transmission and Conversion, Ministry of Education, Shanghai Jiao Tong University, Shanghai, China, [3]Electric Power Research Institute, State Grid Shanghai Municipal Electric Power Company, Shanghai, China

As the number of urban electric vehicles continues to increase, accurate prediction of the electric vehicle (EV) spatial and temporal distribution charging demand is of great importance for safely operating the power grid. Due to the uncertainty and variability of EV user charging and discharging strategies, the strategic factors behind user behavior become the key to influencing whether the charging demand prediction results are reasonable. As a result, this paper proposes a charging demand prediction model based on real-time data from Baidu map that can interpret EV user driving strategies and charging strategies based on the strategy learning capability of generative adversarial imitation learning. This paper first analyzes the correlation between strategy factors and SOC in user charging and discharging data, then describes establishing a 24-hour SOC prediction model for a single vehicle, and finally discusses building a spatiotemporal model of charging demand in the region on this basis. The results demonstrate that, while it can be combined with real-time traffic data, the method has better prediction accuracy and robustness compared with the current mainstream prediction methods and high application value.

KEYWORDS

data-driven, charging demand, user strategies, imitative learning, spatiotemporal models

1 Introduction

In recent years, in order to reduce dependence on oil and fossil fuels, a number of countries and regions have developed policies to promote the development and market penetration of electric vehicles. Global electric vehicle sales reached 6.75 million units in 2021, an increase of 108% over 2020, while the global share of electric vehicles in global light vehicle sales was 8.3% compared to 4.2% in 2020 (EV volumes.com, 2021). The continued growth of scaled EV charging loads connected to the grid will certainly bring challenges to urban road traffic, as well as to the stable operation of the grid. Currently, research on EVs focuses on charging demand prediction, energy management and charging guidance, which can help reduce the negative impacts of EVs on the grid, where EV charging demand prediction is the basis for conducting an impact analysis of EV access on the grid, a distribution grid planning and control operation, a two-way interaction between EVs and the grid, and charging guidance (Chen and Zhang, 2019). However, with the increasing penetration of EVs and the increasing charging demand, the rationality and accuracy of the existing charging demand prediction methods can no longer meet the needs of grid dispatch and charging guidance well (Ge et al., 2020). Therefore, this paper discusses conducting a series of studies on electric vehicle charging demand prediction.

Contemporary research on EV charging demand prediction focuses on user behavior analysis and the coupling characteristics between user behavior, road networks, and EVs (Arias et al., 2017; Li et al., 2018; Liu et al., 2022). Charging demand is generated due to the lack of energy of electric vehicles, and user behavior is the dominant factor of electric vehicle battery energy change, where user behavior users include charging time selection, travel mileage selection and driving strategy; thus, user behavior analysis is the difficulty and key to charging demand prediction. In recent years, load prediction models based on IoT big data platforms for obtaining user psychological and behavioral characteristics to meet real-time charging demand have been the focus of research (Ge et al., 2020), (Ge et al., 2020) obtains regenerative feature data by obtaining historical travel information and using data mining and fusion techniques to analyze the distribution pattern of residential trips and charging behavior characteristics. (Xydas et al., 2016) starts with the analysis of real charging data to establish a framework of features for EV charging demands. The model uses data analysis methods to extract the information hidden behind charging events to characterize EV charging loads. (Arias et al., 2017) proposes a time-space EV charging-electricity demand prediction model based on real-time CCTV data in Seoul, Korea. Traffic data (i.e., arrival rates) and EV battery information (i.e., SOC levels and charging patterns) are used to calculate EV charging demands. (Jahangir et al., 2021) proposes a supervised EV demand prediction method called EVGANS, which was developed in a 3D environment based on generative adversarial networks that can represent different characteristics of EV charging demands. (Zhao et al., 2021) addresses the problem of prediction accuracy by developing a new data-driven prediction framework, which improves the application of charging demand prediction models and enhances the prediction accuracy in complex real-world scenarios. (Yang et al., 2020) proposes an analytical framework for EV charging demand, emphasizing that charging demand is mainly determined by users' travel behavior and bounded rational behavior. (Zang et al., 2020; Zang et al., 2021) analyze the information of user consumption behavior from practical load data from residential customers, and predict regional charging load based on deep learning algorithm.

Recent research methods show that researchers focus on individual user charging SOC feature mining and user charging strategy distribution based on model group behavior and its impact on charging demand prediction (Yang et al., 2017; Chaudhari et al., 2018; Calearo et al., 2019). A Marquardt (LM) training method based on a rough structure was developed using Levenberg's feedforward and recursive artificial neural network (ANN). The method considers the correlation between arrival time, departure time and trip length (Jahangir et al., 2019). (Yi et al., 2020) investigates the spatial and temporal distribution of an EV charging demand in different urban functional areas and temperatures. The method describes the variability of individual users and considers various objective factors, such as time, location, temperature, and road conditions. (Lin et al., 2019) establishes an agent-based travel chain model (ABTCM) to study the distribution of electric vehicle (EV) charging demand and its dynamic characteristics, where a large number of EV charging demand differentiation models are considered. (Majidpour et al., 2014; Yi and Bauer, 2015) links charging demand to the urgency coefficient of user charging behavior, which gave a mathematical model to describe charging demand behavior, but lacked a method to determine charging demand behavior. (Ge et al., 2020) predicts the future 24-hour SOC variation curve of a single EV based on user historical SOC data, but this is only applicable to the more regular user SOC historical data, while the method lacks a grasp of user behavior. Based on a large amount of literature, it is known that user behavior is a deterministic strategy made by users based on factors, such as current time and remaining SOC, and there is a lack of research on accurate mathematical models of user charging and discharging strategies in current research due to the large number of factors influencing user behavior.

In this paper, we study two problems. The first problem is building an accurate mathematical model of user charging and discharging policies. Currently, generative adversarial imitation learning (Ho and Ermon, 2016) can express user policies as a neural network, and thus, neural networks can fit user policies due to their good strategy learnability (Wang, 2003). Generative adversarial imitation learning improves on the original inverse reinforcement learning (Ng and Russell, 2000), which can extract policies directly from user data, while avoiding the problem of difficult definition of the reward function in inverse reinforcement learning. In this paper, user charging and discharging policies are divided into driving policies, travel target mileage policies, and charging duration selection policies, and then these three policies are learned using generative adversarial imitation learning. The second problem is perceiving the charging demand behavior on the single vehicle SOC prediction results. Here, we consider quantifying the perception of user charging demand based on the user charging urgency model and providing the method of determining charging demand.

In summary, this paper proposes a new EV charging demand prediction method that fully considers user charging and discharging strategies, and this paper makes the following contributions.

1) A user charging and discharging strategy model is established. Based on the MIC maximum information coefficient to prove the correlation between EV SOC variation and driving strategy and charging strategy, combined with the real-time traffic flow speed of Baidu map, we propose a strategy learning model based on the generative adversarial imitation learning (GAIL) hybrid proximal policy optimization algorithm (PPO).
2) A 24-hour SOC prediction model for a single electric vehicle is established. Based on the strategy learning model, the prediction method of single EV SOC is proposed based on the XGboost algorithm, and it is proven that the prediction method has good robustness and accuracy.
3) A spatiotemporal model of EV cluster charging demand in the region is established. Based on the individual EV SOC prediction curves and combined with the user charging urgency perception model, a spatiotemporal model of EV cluster charging demand in the region is established and demonstrated to describe the spatiotemporal characteristics of charging demand.

The rest of the paper is organized as follows: Chapter 2 demonstrates that the user charging and discharging strategy is the main factor in the SOC variation of EVs. Chapter 3 gives a detailed description of the approach in this paper, and Chapter 4 presents and discusses the results of the model simulation. Chapter 5 provides a summary and outlook of the work in this paper.

2 Analysis of charging and discharging strategies for EV users

From Chapter 1, it is clear that the core problem of EV charging demand prediction at this stage is to consider a single-user SOC prediction model based on the user's EV charging and discharging strategy. Since SOC variation is affected by many factors, including user strategy factors and environmental factors, it is necessary to demonstrate that charging and discharging strategies are the main factors of SOC variation. Thus, this proves the feasibility of a single EV SOC prediction model, followed by screening the strategy factors that are strongly related to SOC as the input features of the single vehicle SOC prediction model, where charging and discharging strategies include the user driving strategy, the user travel mileage selection strategy and the user charging duration selection strategy. Next, the correlation between user charging demand and user charging starting SOC distribution and user charging urgency is illustrated.

2.1 Strategic factors analysis of the charging and discharging process based on the MIC matrix

MIC is the maximal information coefficient (Zhang et al., 2014). MIC can measure the degree of correlation between two variables, and the value of MIC is between 0 and 1. The larger the value of MIC is, the stronger the correlation between the two. Meanwhile, MIC has good accuracy and robustness.

The charge-discharge characteristic analysis proves the correlation between the discharging SOC and the driving strategy based on the MIC matrix and illustrates the correlation between the charging SOC and the charging strategy. The MIC matrix values are distributed from 0 to 1; the closer to 1 the value is, the stronger the correlation between the horizontal and vertical factors.

2.1.1 Correlation analysis of discharging characteristics

The discharging process, i.e., the driving process, is a process with human factors involved, and its SOC is affected by numerous factors, not limited to those shown in the figure below, such as road conditions (slope, bumpiness). This paper mainly considers the influence of the user's driving strategy on the SOC variation. The discharging characteristic MIC matrix is shown on the left of Figure 1, and the results prove that the correlation between the discharging SOC and driving distance, speed and temperature is the strongestamong the subcorrelation factors of the discharging SOC, the correlation between the discharging SOC and total voltage and battery voltage is stronger, therefore, the user driving strategy is the main causal factor of SOC change in the discharging process. Meanwhile, temperature is also a major factor affecting SOC, which is due to the fact that electric vehicles are driven in situations where the outdoor temperature is low and the low temperature inhibits the performance of the battery (Qin et al., 2021). Here, a discharging SOC prediction model based on user driving strategy and real temperature data is considered.

2.1.2 Correlation analysis of charging characteristics

The charging stage has no human subjective factors involved, and each variable changes with the interaction process of EV and charging pile. The whole process is more regular than the discharging process, and the charging process is divided into fast charging and slow charging. The correlation of these two process features is basically unified. The MIC matrix is shown on

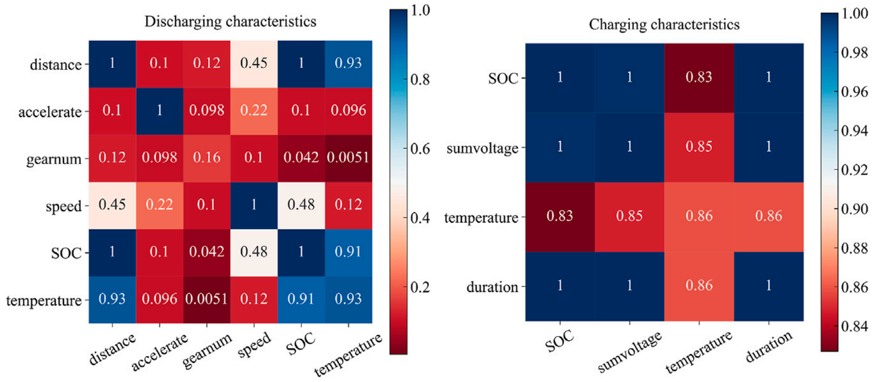

FIGURE 1
MIC matrix analysis of charging characteristics and discharging characteristics.

the right of Figure 1, and the results prove that the charging SOC and the user charging duration, charging voltage, and temperature are strongly correlated. As with the discharging process, a charging SOC prediction model based on user charging duration and real temperature data is considered here.

2.2 Correlation analysis of charging urgency and charging demand

The root cause of user charging demand generation is the reduction of battery energy, which affects the urgency of user charging, i.e., charging urgency (Yi and Bauer, 2015). The higher the charging urgency is, the higher the probability of that user signaling charging demand. Only the charging urgency determined by the battery SOC is considered here. When the depth of discharge (DOD) is deep and the remaining charge is less, the higher the charging probability of the user and the higher the charging urgency of the user, it becomes more urgent for the user to charge.

Here, we consider the general expression of the charging urgency function. Let the charging probability density function be $D(x)$ in Eq. 1, $D(x)$ is a function of depth of discharge DOD. The integral of $D(x)$ is the charging probability, then the closer the DOD is to 1, the greater the charging probability. Here, DOD = 1- SOC, $D(x)$ is determined by the functions $h_1(x)$ and $h_2(x)$, where x_1, x_2 and x_3 are determined by the battery capacity; the larger the battery capacity, the larger x_1, x_2, and x_3.

$$D(x) = \begin{cases} 0 & x \le x_1 \\ h_1(x) = k_1 x + m_1, & x_1 < x \le x_2 \\ h_2(x) = k_2 x + m_2, & x_2 < x \le x_3 \\ 0 & x_3 < x \le 1 \end{cases} \tag{1}$$

where $h_1(x_1) = 0$, $h_1(x_2) = h_2(x_2)$, $h_2(x_3) = 0$, k_1, m_1, k_2, and m_2 are calculated from x_1, x_2, and x_3, the charging urgency function $C_u(x)$ is the integral of $D(x)$ from 0 to x, i.e., charging probability, giving the following equation.

$$C_u(x) = \int_0^x D(t)dt \tag{2}$$

Here, $\int_0^{x_3} D(t)dt = 1$, while we express the charging urgency function:

$$C_u(x) = \begin{cases} 0 & x \le x_1 \\ f_1(x) = a_1 x^2 + b_1 x + c_1, & x_1 < x \le x_2 \\ f_2(x) = a_2 x^2 + b_2 x + c_2, & x_2 < x \le x_3 \\ 1 & x_3 < x \le 1 \end{cases} \tag{3}$$

where $f_1(x_1) = 0$, $f_1(x_2) = f_2(x_2)$, and $f_2(x_3) = 1$.

2.3 Correlation analysis of user charging starting SOC distribution and charging demand

The user charging starting SOC distribution reflects the user's dependence on the action of charging demand on the selection of starting charging SOC. If a user tends to choose to charge at a lower SOC, the probability of having a charging demand at a certain moment will also be lower, conversely, the probability of generating charging demand will increase. We consider fitting the charging start SOC distribution of different users using a normal distribution, and the method of determining the charging demand is as follows: when a user's real-time SOC approaches this user's historical charging starting SOC at moment t, i.e., when the real-time SOC drops to some user's charging demand interval, that user will generate charging demand, which is determined by the distribution of the user's charging urgency coefficient and that user's charging starting SOC.

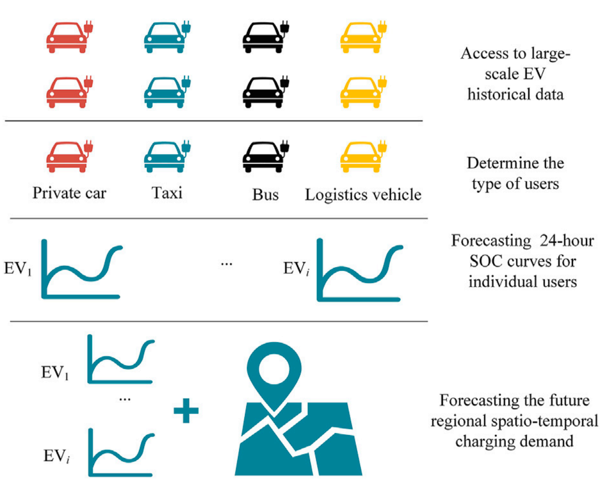

FIGURE 2
Spatial and temporal prediction framework for EV cluster charging demand.

Here, consider the case that when the charging starting SOC is smaller, the greater the probability of charging for a user. In order to obtain the charging start SOC distribution of a user, i.e. normal distribution $N(\mu, \sigma^2)$, we obtain the mean and variance of a user's historical charging start SOC data, which are extracted from the EV operating data introduced in Section 3.1.1, then draw the starting SOC value X from $N(\mu, \sigma^2)$, and let the user's SOC at moment t be X_t, at which time the user's charging urgency factor is $C_u(X_t)$. Then, the charging demand interval of that user is $[X, X + C_u(X_t)]$. It can be seen that the smaller X_t is and the larger $C_u(X_t)$ is, the wider the range of the charging demand interval and the greater the probability of that user generating charging demand.

3 Spatial and temporal prediction model for EV cluster charging demand

The analysis of the strategy factors of the charging and discharging process in Section 2.1 shows that there is a correlation between user strategy and SOC variation, as well as variability in different user behavior strategies, so it is necessary to establish a single-user 24-hour SOC curve and finally a regional EV cluster charging demand model. Strategy learning is performed using generative adversarial imitation learning (GAIL), and based on strategy learning; individual vehicle SOC curves are predicted based on the XGboost algorithm. The spatial and temporal prediction framework for EV cluster charging demand is shown in Figure 2, and the prediction process is divided into three steps, which are described in detail in Sections 3.3, 3.4, 3.5, followed by experimental data acquisition and algorithm introduction described in Sections 3.1, 3.2, respectively.

TABLE 1 Data attributes.

Property name	Range of values
Speed	0–220 km/h
Acceleration	−2.2305–2.7277 m/s^2
SOC	0–100%
Temperature	0–40°C
Longitudes	118.787731–121.962492°
Latitudes	30.698392–32.069602°

Step 1: Regional scale EV path planning and real-time traffic flow speed acquisition on the path.

Step 2: 24-hour individual EV SOC prediction.

Step 3: Regional EV cluster charging demand prediction.

3.1 Data acquisition

3.1.1 EV operating data

The experimental data in this paper are obtained from the Shanghai New Energy Electric Vehicle Monitoring Center for 1,000 tested EVs in a month (Shanghai Electric Vehicle Public Data Collecting, 2019), which contains the following EV operation parameters: speed, acceleration, SOC, temperature, latitudes and longitudes, with data points sampled every 10 s, with private cars, logistics vehicles, buses, and taxis accounting for 10%, 12%, 35%, and 43% of the data, and the data points for a single trip trajectory are approximately 2000. This article states: all vehicle information has been de-privatized. The data attributes are shown in Table 1.

3.1.2 Road network node data

The OSMnx library in Python was used to obtain information on the coordinates of all road nodes in the target prediction area and the distance between nodes (road nodes are the intersections of that path and other roads), and a sample road network is shown in Figure 3.

3.2 Algorithm description

3.2.1 Generative adversarial imitative learning algorithm

Generative adversarial imitation learning is an effective combination of imitation learning (Osa et al., 2018) and adversarial networks (Goodfellow et al., 2014). This paper is based on GAIL to fit user charging and discharging strategies.

FIGURE 3
Example of a path.

The generator network is the charging and discharging policy, where the discriminator and generator are multilayer fully connected neural networks. Here set the label of generated data by the generator to 1 and the real user data to 0. The above process is a game process between the discriminator and the generator. After several iterations of the above process, when the discriminator cannot distinguish the data generated by the generator from the real data, i.e., the generator and the discriminator reach Nash equilibrium, the generated data successfully matches the real data.

3.2.1.1 Discriminator network

First, we introduce the binary cross-entropy loss function:

$$H(q) = -\sum_{i=1}^{m}\left[y_i \cdot \log\left(p(y_i)\right) + (1 - y_i) \cdot \log\left(1 - p(y_i)\right)\right] \quad (4)$$

Eq. 4 is the loss function for training the binary classifier, $p(y_i)$ is the probability of y_i, where y_i is the data label (0 or 1), and $-\sum_{i=1}^{N} y_i \cdot \log(p(y_i))$ is the entropy of the distribution of y_i, while a smaller entropy indicates a closer approximation to the true distribution $q(y_i)$.

According to the principle of generative adversarial model, the discriminator performs a gradient descent update based on Eq. 5:

$$\nabla_{\theta_d}\frac{1}{m}\sum_{i=1}^{m}\left[\log D\left(x^{(i)}\right) + \log\left(1 - D\left(G\left(z^{(i)}\right)\right)\right)\right] \quad (5)$$

where $D(x^{(i)})$ is the discriminator's probabilistic determination of the real data and $D(G(z^{(i)}))$ is the probabilistic determination of the generated data.

3.2.1.2 Generator network

The loss function of the generative network is constructed using Eq. 4 as follows:

$$\nabla_{\theta_g}\frac{1}{m}\sum_{i=1}^{m}\log\left(1 - D\left(G\left(z^{(i)}\right)\right)\right) \quad (6)$$

3.2.2 Proximal policy optimization algorithm

The optimization of the parameters of the generator and the discriminator is performed by the PPO algorithm. This algorithm accelerates the convergence of the network parameters. The PPO algorithm has some of the advantages of trust region policy optimization (TRPO) (Schulman et al., 2015). The objective function of PPO is a first-order approximation taken over TRPO, so they are easier to implement, more general and have better sample complexity (Schulman et al., 2017). In this paper, certain improvements are made based on the original PPO algorithm as follows.

In order to make the generalization ability of the generator better, the generated samples collected from the environment are disrupted here, while the samples are divided into certain batches and sent to the PPO algorithm for multiple rounds of parameter updates, which can make full use of the sample information and also improve the learning efficiency and convergence speed of the generator. Here, the sample batches should not be too many, so as not to reduce the operation speed of the algorithm.

3.2.3 Extreme gradient boosting algorithm

XGBoost is an optimized distributed gradient boosting library (Chen and Guestrin, 2016) that performs well on regression problems. It is a machine learning algorithm based on the gradient boosting framework. The basic idea of XGBoost is the same as GBDT (Friedman, 2001).

3.3 Regional scaled EV path planning and real-time traffic flow speed acquisition on the path

3.3.1 Intraregional scaled EV pathway planning

Path planning uses the set of real path latitude and longitude coordinates in the dataset of Section 3.1.2, and all path latitude and longitude coordinates are processed through the data. Then, the OSMnx library in Python is used to visualize the path and extract information about the coordinates of road nodes and distance from the starting node (a path node is the intersection of that path and other roads). Let the dataset of each path node be:

$$\Omega^j = \left\{\left(x_1^j, y_1^j, s_1^j\right), \left(x_2^j, y_2^j, s_2^j\right), \dots, \left(x_n^j, y_n^j, s_n^j\right)\right\} \tag{7}$$

where Ω^j denotes the j trajectory $j = 1, 2, 3, \dots$ dataset and, (x_1^j, y_1^j) and s_1^j are the path node latitude and longitude coordinates and the distance from the starting node, respectively. Examples of path visualization are shown in Figure 3.

3.3.2 Path real-time traffic flow speed acquisition

Considering that the user's driving strategy is affected by the real-time traffic flow speed, it is necessary to obtain the real-time average speed of each road section based on the Baidu map real-time information platform (Baidu map open platform, 2022) to obtain the driving time T of the road section to which the current vehicle coordinates belong. Let the distance of the adjacent nodes from the starting node be l_1 and l_2. Then, the length of the current road section is $L = l_1 - l_2$, the time required to pass the current road section is T_t, and the real-time average traffic flow speed of this road section is v_t. Its real-time average traffic flow speed can be calculated according to the following expression:

$$v_t = \frac{L}{T_t} \tag{8}$$

3.4 24-hour individual EV SOC prediction model

The individual EV SOC is predicted on the path-based real-time traffic flow speed extraction in Section 3.3. The prediction flow diagram is shown in the dashed part of Figure 4, and the prediction model is divided into two submodels as follows.

3.4.1 User strategies learning model based on generative adversarial imitation learning

The dashed part of Figure 4 shows the policy model part, which consists of three upper-level policies and one lower-level policy. The state space is the current SOC and the current moment, and all upper layer strategies share the current state information and make actions according to the state, where the charging and discharging strategies make charging action 0 or travel action 1; the charging strategy outputs the single charging duration; the travel strategy outputs the single travel target distance; the lower driving strategy executes the output target of the upper-level strategy and outputs the acceleration, single mileage, and time of the next moment with an output interval of 10 s. Thus, the output after executing the policy network is a single EV 24-hour speed curve and a single mileage curve. The three policy networks use the same GAIL structure with a time scale of 24 h. The strategy learning flow chart is shown in Figure 5. The strategy learning model consists of a policy generation network, a discriminator network and a PPO network. The policy network uses the user history data as the learning sample and fits the user history policy distribution through the discriminator. The specific process is as follows.

Step 1: Trajectory sampling

The main program is a nested loop structure. The first layer loop is an iterative loop, traversing all expert trajectory data for one generation. The second layer is an expert trajectory loop, first

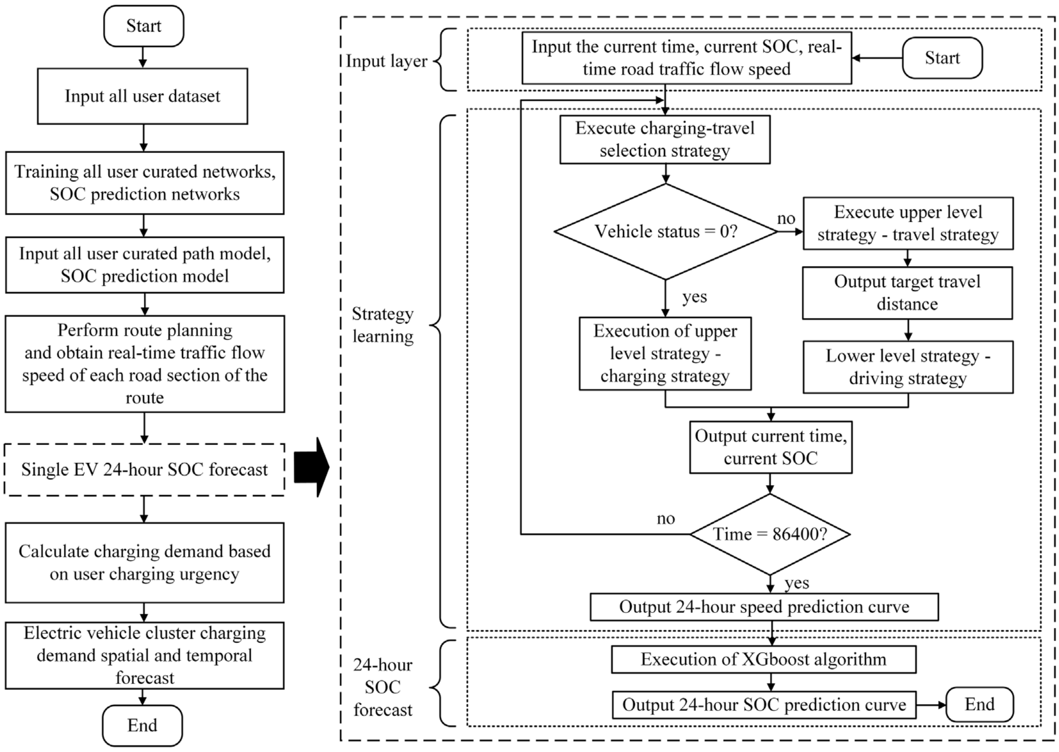

FIGURE 4
Flow chart of EV cluster charging demand spatial and temporal prediction.

generating the sampled trajectory after the policy network and then calculating the corresponding value function, advantage function, and the mixed logarithmic density of the sampled trajectory, before sending the expert strategy trajectory and sampled trajectory to the discriminator to update the discriminator parameters, and finally sending the value function, advantage function, and the mixed logarithmic density of the sampled trajectories to the PPO algorithm to update the policy network until all expert trajectories are traversed and the second level of the loop ends.

Step 2: PPO policy optimization

The structure is a nested two-layer loop; the first layer is an iterative loop, for each iteration, the order of the collected sample data (state set, reward value set, advantage estimation set, value estimation set, return estimation set, state-action mixed logarithmic probability set) is disordered, divided by certain batches and sent to the PPO algorithm for a parameter optimization update together with the policy network, value network; and the second layer is the network parameter update layer, traversing all sampled batches, i.e., the cycle is completed.

3.4.2 XGboost-based 24-hour SOC prediction model for a single EV

Based on the input feature analysis of the SOC prediction model in Section 2, the speed and mileage curves, as well as the charging duration curve, are calculated based on the 24-hour user speed curve generated by the learning strategy in Section 3.4.1, where the speed and mileage curves predict the discharging SOC and the charging duration curve predicts the charging SOC. Therefore, the driving SOC regression prediction model and the charging SOC regression prediction model are developed.

Here, the prediction algorithm is chosen as XGboost, and the prediction model flowchart is shown in the lower part of Figure 6, where the loop is a cross-validation process. The process divides the training dataset into n subsets and normalizes the training set by removing the mean and scaling to the unit variance, and each loop uses one of the subsets as the validation set and the remaining subsets as the training set until all subsets are traversed. This method ensures good generalization.

3.5 Regional EV cluster charging demand prediction model

As shown in Figure 4, based on the individual EV SOC prediction model in Section 3.4, a regional-scale EV charging energy demand prediction model is established, where the user charging urgency and charging starting SOC are used to predict the charging energy demand without using the user. According to the definition of the charging demand interval in Section 2.3,

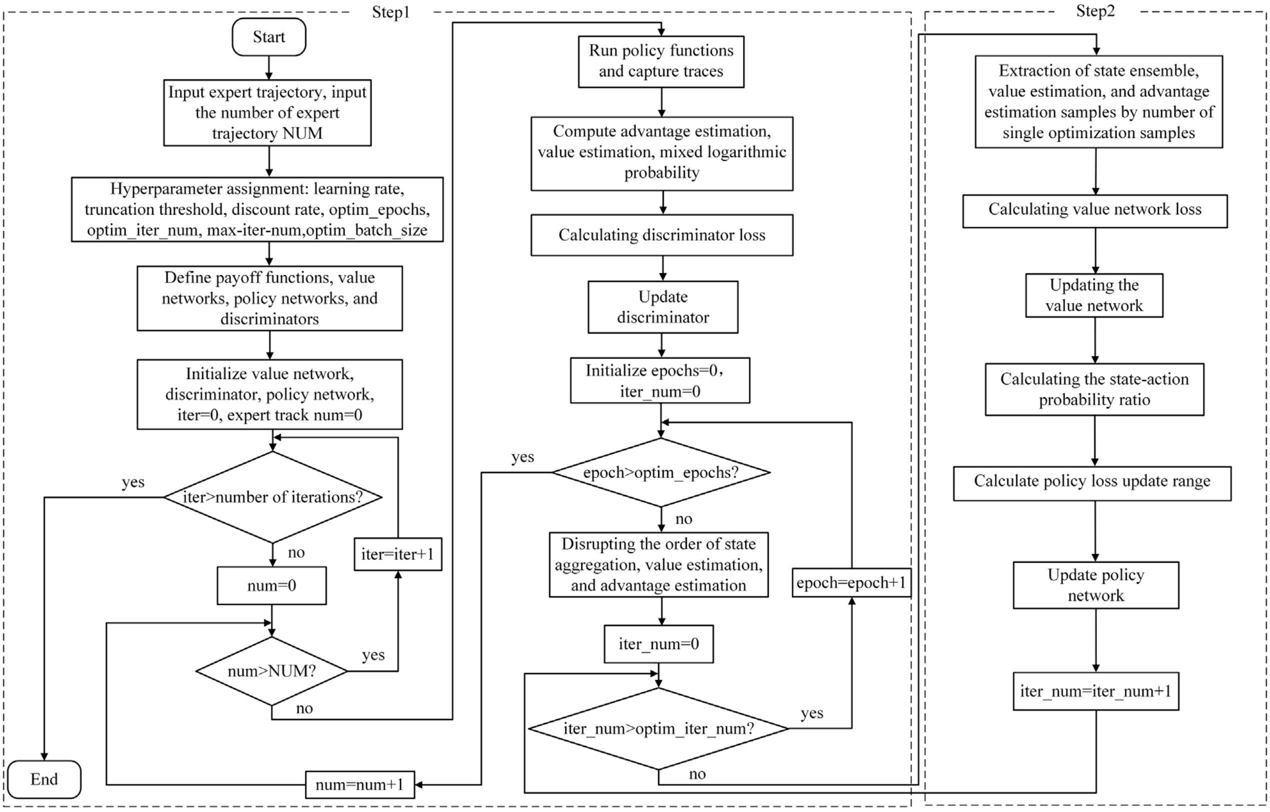

FIGURE 5
Flow chart of strategy learning based on the PPO algorithm.

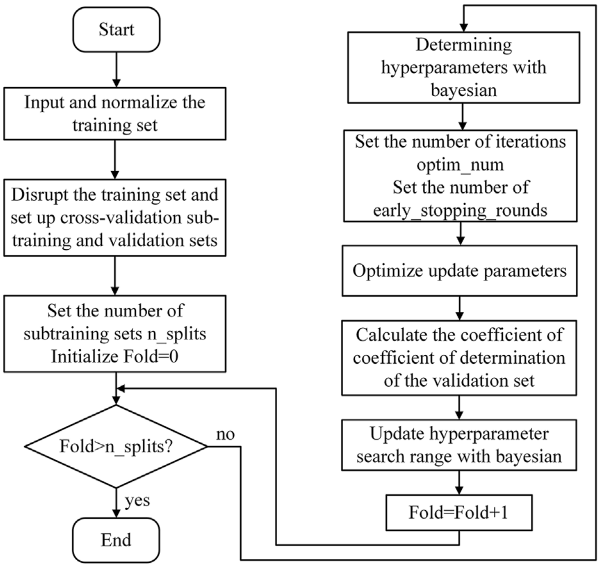

FIGURE 6
Flow chart of single vehicle 24-hour SOC prediction based on the XGboost algorithm.

when the user SOC enters within the charging demand interval, the user is considered to have charging demand, and the charging energy demand of this user is calculated, labeled on the map, then finally generated a heatmap for EV cluster charging demand prediction.

3.6 Hyper parameter optimization of strategy learning model and SOC prediction model

In order to make the strategy learning model and SOC prediction model in Section 3.4 converge in a shorter time to achieve better performance, the Bayesian optimization algorithm is utilized here for hyper parameter search. In the curated path model, the KL scatter of the true and predicted values is used as the objective function of Bayesian optimization, where the policy network and the discriminator network consist of multilayer fully connected neural networks, and the network hyper parameters are shown in Table 2, with the number of expert trajectories set to 10. In the SOC prediction model, the mean square error of the true and predicted values is used as the objective function of Bayesian

TABLE 2 Parameter settings.

Object	Parameter	Value or class
Discriminator network	Number of neural network layers	3
	Set the number of hidden layer dimensions	(3,128)
	Activation function	Hyperbolic tangent function
Policy network	Number of neural network layers	3
	Set the number of hidden layer dimensions	(3,128)
	Set the initial action variance	0
	Activation function	Hyperbolic tangent function
PPO algorithm	Optimization iteration number	100
	Optimize the number of single samples	128
	Discount rate	0.9581
	Truncation threshold	0.2234
Main program	Operating equipment	Tesla P100 GPU
	Maximum number of iterations	1,000
	Learning rate	$9.9234*10^{-5}$
XGboost algorithm	Learning rate	0.0696
	Gamma	2.3287
	The maximum depth of the tree	19.8345
	Subsample rate	0.8565
	L2 regularization	0
	L1 regularization	93.1137
	Maximum number of nodes	734.9243
	The sum of the minimum instance weights required in the child	66.9243
	Number of iterations of boosting	716.9243
	Bagging_fraction	0.9822

optimization, and the number of search generations is 50. The XGboost hyperparameters are shown in Table 2, and the hyperparameters are all accurate to 4 decimal places.

3.7 Evaluation metrics

3.7.1 Regression model metrics

1) Root mean square error (RMSE):

$$RMSE(y_i, \hat{y}_i) = \left[\frac{1}{n}\sum_{i=1}^{n}(y_i - \hat{y}_i)^2\right]^{\frac{1}{2}} \tag{9}$$

2) Mean square error (MSE):

$$MSE(y_i, \hat{y}_i) = \frac{1}{n}\sum_{i=1}^{n}(y_i - \hat{y}_i)^2 \tag{10}$$

3) Coefficient of determination (R-Squared):

$$R - Squared(y_i, \hat{y}_i) = 1 - \frac{\sum_{i=1}^{n}(y_i - \hat{y}_i)^2}{\sum_{i=1}^{n}(y_i - \bar{y})^2} \tag{11}$$

The R-squared is between 0 and 1; the closer it is to 1, the better the performance of the regression model.

4) Mean absolute error (MAE):

$$MAE(y_i, \hat{y}_i) = \frac{1}{n}\sum_{i=1}^{n}|y_i - \hat{y}_i| \tag{12}$$

3.7.2 Reinforcement learning metrics

3.7.2.1 Robustness

The size of the expert sample determines the amount of information that can be learned by the policy network, which in turn affects the stability of the policy network. Thus, the robustness of the reinforcement learning model is mainly reflected in the effect of the size of the data on the model's stability.

3.7.2.2 Kullback-Leibler divergence

KL divergence (Kullback-Leibler divergence), also known as relative entropy, is a way to describe the difference between two probability distributions, P and Q, where P denotes the true distribution and Q denotes the fitted distribution of P. For two probability distributions, P and Q, of a discrete random variable or a continuous random variable, the KL divergence is defined as follows:

$$D(P\|Q) = \log\left(\frac{P(i)}{Q(i)}\right) \times \sum_{i\in X} P(i) \tag{13}$$

$$D(P\|Q) = \log\left(\frac{P(i)}{Q(i)}\right) \times \int_{x} P(x) \tag{14}$$

The KL divergence is between 0 and $+\infty$. The smaller the KL divergence is, the closer a certain probability distribution is proven to be to the true distribution.

4 Results and discussion

The model simulation analysis is divided into several parts: first, the robustness and learnability of the policy network are evaluated, followed by a speed prediction model based on the policy model to illustrate the variability of user policies, comparing the speed prediction results for four types of users. Then, the single vehicle 24-hour SOC prediction results are shown and compared with historical SOC-based prediction methods, and finally, a spatiotemporal map of charging demand at key moments throughout the day in the main city of Shanghai is shown. The algorithm program is fully implemented by Python 3.7.

4.1 Analysis of the strategy learning model

4.1.1 Policy network robustness analysis

The robustness of the policy network reflects the stability of the policy network, therefore the stability of the policy network obtained by different policy optimization algorithms is different; thus, it is necessary to analyze the robustness of the policy optimization algorithm (PPO algorithm) based on this paper, and the comparison algorithm is the TRPO algorithm. As shown in Figure 7. Here, the total historical travel trajectories are supplied for 20, and the average returns of TRPO- and PPO-based policy networks are compared and analyzed under the conditions of 25%, 50%, 75%, and 100% historical travel trajectory data, respectively. 3 to 5 simulations are performed with the same random seeds. The dashed lines indicate the values of the reward functions corresponding to the expert policies, and the red color represents the TRPO-based return curves. The purple color represents the return curve based on PPO. The TRPO algorithm is less robust when the amount of data is less, while the average return is lower, and the PPO algorithm is more robust under each amount of data. Its average return fluctuation is less than 0.2%, while the average return is higher than the TRPO algorithm, and the average return value of the PPO algorithm is close to the expert strategy. Therefore, the robustness of the method in this paper is better, and the stability of the policy network is stronger.

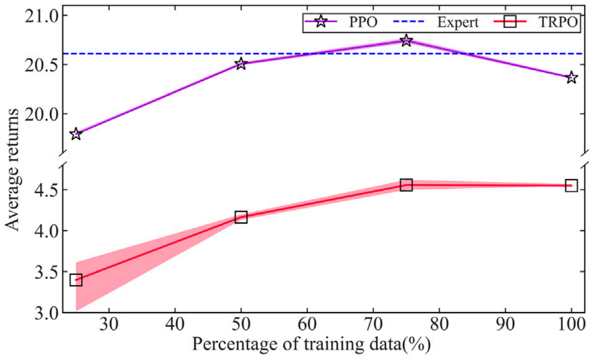

FIGURE 7
Comparison of PPO and TRPO robustness.

TABLE 3 Comparison of KL divergence of strategy learning results and expert data.

Data distribution	PPO	TRPO
Charging duration strategy	0.1052	0.8792
Traveling mileage strategy	0.1256	0.8254
Driving strategy	0.1123	0.8648

4.1.2 Kullback-Leibler divergence analysis of strategy distribution and real data

In order to prove that the method of this paper has good strategy learnability, the KL divergence of this paper's algorithm (PPO) and TRPO algorithm on strategy learning is compared and analyzed here, and the magnitude of KL divergence indicates the difference between the policy network generated data and the real data. The results are shown in Table 3. The results based on the PPO algorithm have the

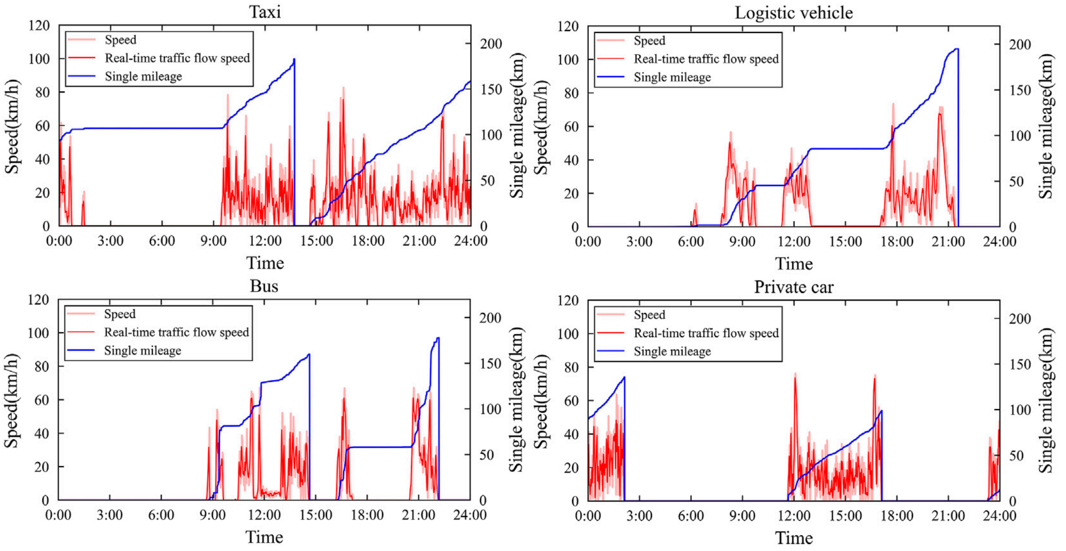

FIGURE 8
Single vehicle 24-hour speed and mileage prediction results.

lowest KL divergence among the three learning strategy results, which indicates that the PPO algorithm has better learnability for the policy path.

4.2 Real-time speed prediction for a single EV based on the policy model

We illustrate the effect of variability in the charging and discharging strategies of different users on the time distribution of charging demand and provide data for the subsequent prediction of the 24-hour SOC of a single vehicle. The results of the 24-hour speed prediction for a single vehicle are shown here. Here, four types of users are considered: private cars, logistics vehicles, buses, and taxis. Their respective charging and discharging strategies are learned, and then the 24-hour speed prediction curve of a single vehicle is predicted based on the real-time traffic flow speed, as shown by the red line in Figure 8. Finally, the single driving mileage is calculated based on the speed curve, and here, the starting mileage is obtained by averaging the user's historical data. As shown by the blue line in the figure, the following analysis shows the variability of user charging and discharging strategies.

As shown in Figure 8, taxis and buses travel the longest single mileage, and due to the functionality of logistics vehicles and buses, the charging demand for both is distributed between 9:00 p.m. and 8:00 a.m. the following day. Additionally, after 10:00 p.m., the operation basically stops, so both take slow charging in the evening. There is relatively no substantial regularity in the discharging time interval for taxis and private cars. Meanwhile, taxis have obvious charging behavior at approximately 1:00 p.m. Since taxis need to obtain more travel orders during the day, they mostly adopt fast charging, so the charging duration of taxis is approximately 1 h, while the charging demand of private cars is basically concentrated between 12:00 a.m. and 8:00 a.m., and private car users mostly adopt slow charging in the evening. Additionally, the driving speed of the four types of cars is basically positively correlated with the real-time traffic flow speed, and the learning results of the user's driving strategy are relatively substantial. In summary, the variability of the time distribution of charging demand for different users is relatively obvious due to different charging and discharging strategies.

4.3 24-hour SOC prediction for a single EV

Here, the user driving speed and mileage prediction results based on Section 4.2, i.e., the charging and discharging strategy, are used as the input features of the XGboost algorithm as a way to predict the 24-hour SOC curve of a single vehicle to demonstrate the superiority of the method in this paper. As shown in Figure 9, four types of EVs are selected by vehicle usage and compared with the prediction method based on historical SOC, where the red line represents the real SOC, the blue line

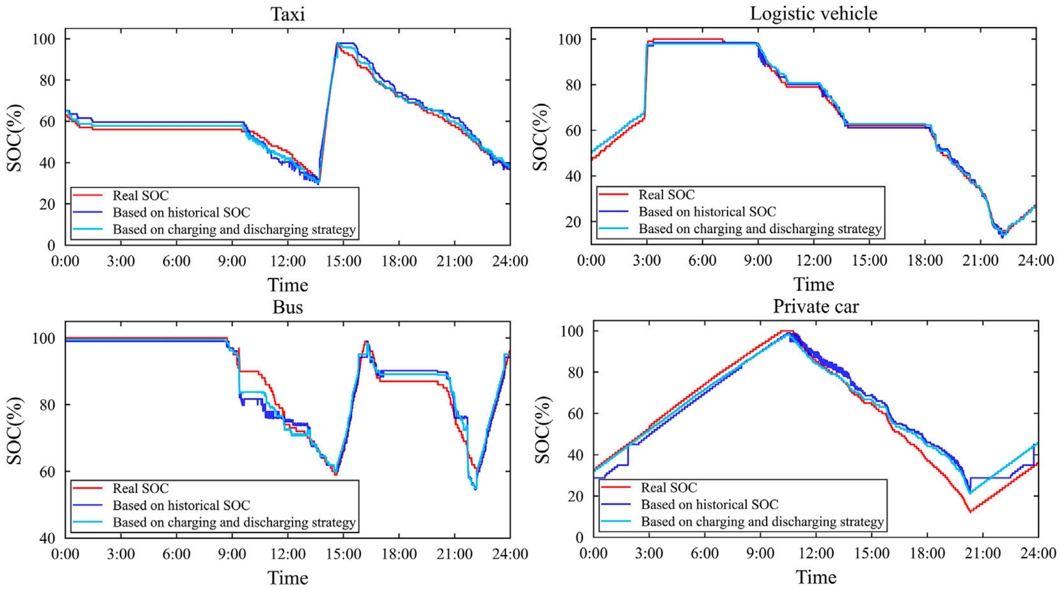

FIGURE 9
Single vehicle 24-hour SOC prediction results.

TABLE 4 Evaluation metrics.

Type of vehicle	Prediction methodology	MAE	RMSE	MSE	R-Squared
Logistics vehicle	Real-time traffic flow speed	1.3761	2.1281	4.5287	0.9924
	Historical SOC	1.6585	2.3239	5.3964	0.9923
Taxi	Real-time traffic flow speed	1.6732	2.4536	6.0201	0.9725
	Historical SOC	2.7492	3.1373	9.8429	0.9496
Bus	Real-time traffic flow speed	2.7218	3.3042	10.9176	0.9074
	Historical SOC	3.1527	4.4402	19.7158	0.8652
Private car	Real-time traffic flow speed	2.0627	2.6167	6.8472	0.9831
	Historical SOC	3.1424	3.8717	14.8005	0.8522

represents the prediction result based on historical SOC, and the sky blue line represents the prediction result based on the charging and discharging strategy. The prediction results of both methods for charging SOC are good, the prediction curves are relatively smooth, and the prediction results are stable. However, in SOC the prediction results of the discharging process, the two perform slightly differently. In the comparison of the prediction results for private car users, the prediction curves of the two methods are less stable and show obvious jitter, which may be related to the feature distribution of the data itself, but both have a good grasp of the overall trend of the SOC discharging process. In the prediction results for taxi users, the method in this paper performs well in the prediction results for taxi users. The method in this paper shows good stability in the prediction results of the discharging process, but the prediction results of the historical SOC-based method show obvious jitters and outliers in the second half of the discharging process, which is due to the inconspicuous characteristics of the historical data. In the prediction results of SOC for logistics vehicle users, both show better robustness and fit.

It also proves the good prediction accuracy of the method in this paper. According to Table 4, the four evaluation metrics of regression prediction in Section 3.7 are selected here, and the prediction accuracy of this paper's SOC prediction method and the historical SOC-based prediction method are compared according to these four indicators. Both methods use the same

FIGURE 10
Results of 24-hour charging demand prediction in Pudong.

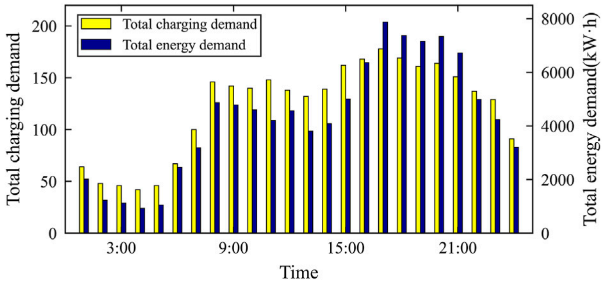

FIGURE 11
Total charging demand and total energy demand statistics by moment.

size training set to train the network, and the training set size is 5,000 data points. From the prediction results of the four types of vehicle SOCs, each of the prediction methods obtained from this paper's average mean square error is reduced by 37% and the average coefficient of determination is improved by 4%. The results demonstrate that the two methods perform basically equivalently for the logistics vehicle SOC prediction problem, while in the other three types of EV SOC prediction problems, the prediction accuracy of this paper's method is considerably higher than that of the traditional prediction method.

4.4 Regional EV cluster charging demand prediction

Spatial and temporal prediction of large-scale EV charging demand is considered here. The individual EV 24-hour SOC prediction results based on Section 4.3 and the definition of charging demand intervals in Section 2.3 are combined to predict the charging demand and energy demand for all users. The spatiotemporal distribution of charging demand in the region is then built on this basis. Here, it is specified that when a user generates charging demand, the difference between the current battery energy and 100% of the battery capacity is used as the charging energy demand. Let the charging energy demand be E_{pc}, let the current battery SOC be SOC_t, and let the user battery capacity be C_p, at which time the charging energy demand of a single user is calculated as follows:

$$E_{pc} = (1 - SOC_t)C_p \tag{15}$$

The battery capacity options are as follows: 135 kWh for buses, 48 kWh for private cars, 40.6 kWh for logistics vehicles, and 45 kWh for taxis.

Figure 10 selects the prediction area as the core area of Pudong New Area in Shanghai, which is divided into three functional areas: the main urban area, containing the central business district along Lujiazui and three subcenters (Huamu Road, Jinqiao, and Zhangjiang Town); the high-tech industrial area, centered on Tang Town and Zhuqiao Town; and the residential area, centered on Kangqiao and Zhoupu Town. The spatial distribution characteristics of charging demand for 1,000 tested EVs in a day are shown here, where 8 key time points in a day (3:00 a.m., 6:00 a.m., 9:00 a.m., 12:00 a.m., 3:00 p.m., 6:00 p.m., 9:00 p.m., and 12:00 p.m.) are intercepted in kWh, and only users with charging demand are shown in the figure, where each dot represents a vehicle with a charging demand, and the size and color shades of the dots represent the amount of energy demanded by the user. Figure 11 shows the total charging demand in each hour of a day. In order to prove the validity of the model in this paper, the spatiotemporal distribution characteristics of charging demand are analyzed based on the prediction results.

4.4.1 Analysis of the temporal characteristics of the charging demand

As seen in Figure 11, charging requests peak at approximately 12:00 p.m. and 6:00 p.m., reaching approximately 150 and 180, respectively. Charging energy demand also peaks at approximately 12:00 p.m. and 6:00 p.m., reaching approximately 4,000 kWh and 7000 kWh, respectively, with charging demand entering a trough at approximately 3:00 a.m. Overall, the temporal distribution of charging demand is relatively smooth, and the peak period lasts for a long time. This proves that the charging demand has the characteristics of time distribution.

4.4.2 Analysis of the spatial characteristics of charging demand

As shown in Figure 10, from the spatial distribution of charging demand, the charging load demand is in the low period from 12:00 a.m. to next day 6:00 a.m., and there is no obvious aggregated demand for charging. After 6:00 a.m., the charging demand gradually increases in the main urban area due to the emergence of the morning peak period, with Lujiazui, Zhangjiang town and Jinqiao town as the center in a radial distribution and less charging demand in the area of high-tech industrial zone and residential area. After 6:00 p.m., due to the emergence of the evening peak period, the charging demand in the high-tech industrial area appears to be aggregated, and the residential area also has an aggregated distribution. After 12:00 a.m., the charging demand in the sub center area and the industrial area decreases substantially. Other areas show a uniform distribution of a charging demand throughout the day. In summary, it is proven that the charging demand distribution is related to the functionality of the area, and therefore, the charging demand has spatial distribution characteristics.

From the distribution of charging energy demand throughout the day, most of the charging demand energy near the central business district is distributed below 30 kWh, so the charging users are mainly taxis and private cars, while the charging energy demand in the high-tech industrial area is distributed above 60 kWh, which indicates that the charging users are mainly public transport vehicles. This proves that the functionality of the vehicle and the charging demand distribution are related, and in the case of this paper, the users are dominated by taxis.

5 Conclusion

In this paper, first, to address the problem that the mathematical model of user charging and discharging strategies in the current literature is vague, a GAIL hybrid PPO-based strategy learning model is proposed. Then, a single-user SOC prediction model is built based on the strategy model. Second, a mathematical determination method of charging demand is given based on user charging urgency, and a regional EV cluster charging demand model is predicted based on the determination method. The model analysis demonstrated that the KL divergence of the policy network obtained based on the GAIL hybrid PPO algorithm is reduced by 77% compared to the GAIL hybrid TRPO algorithm. Thus, in strategy learning, this paper method has better learnability. Finally, in terms of single vehicle SOC prediction, this paper proposes that the prediction method using user behavior characteristics (speed, distance traveled, charging duration) has lower prediction error, as well as better robustness compared to the current historical SOC-based prediction methods with a 37% reduction in mean square error. The main contributions of this paper are as follows.

1) A 24-hour SOC prediction model is established for individual EVs based on real-time traffic flow rates that can elaborate on the variability of user policies.
2) A regional charging demand prediction model is established for charging EV clusters based on user charging urgency.

Future research work will make further improvements based on the above results. First, since the strategy learning model in this paper only considers real-time traffic flow speed information, the vehicle speed in real situations will be affected by more factors, such as the degree of road depression, the slope and the distance of the previous vehicle; thus, more complex driving environments need to be considered to portray the perfect EV SOC changes. Second, the charging demand urgency factor directly affects the reasonableness and accuracy of charging demand. In the future, more users need to be considered to perceive the overall charging requirements, and with the rapid development of telematics technology, more comprehensive user information can be fully obtained in the future. Finally, this paper focuses on the charging demand prediction of the whole urban area. However, it lacks the charging demand prediction of the charging station because the practical charging station model of the parking location is the key to estimating the charging demand, and at the same time, can provide more accurate data support for charging guidance, so the application value of the model in this paper needs to be improved.

Data availability statement

The datasets presented in this study can be found in online repositories. The names of the repository/repositories and accession number(s) can be found below: https://labs.shevdc.com/home.

Author contributions

HL: methodology, algorithm finding, experimental platform provision, editing, supervision, and review. DL: algorithm finding, programming, simulation, and writing-original draft preparation. YZ: methodology, experimental platform provision, algorithm refinement, editing, supervision, and review. YS: methodology, algorithm search, raw data provision, review, and article refinement. DF: methodology, algorithm refinement, editing, supervision, and review. SS: algorithm search, testing, and validation.

Funding

This work was sponsored in part by the National Natural Science Foundation of China (Nos. 52167014 and 52077139), in part by the Science and Technology Commission of Shanghai Municipality (Nos. 21DZ2204800 and 21YF1408600), in part by the Key Laboratory of Control of Power Transmission and Conversion (SJTU), Ministry of Education (2022AA04), and in part by the Science and Technology Project of State Grid Shanghai Municipal Electric Power Company of China (No. 52094022000G).

Conflict of interest

Author SS was employed by State Grid Shanghai Municipal Electric Power Company.

The remaining authors declare that the research was conducted in the absence of any commercial or financial relationships that could be construed as a potential conflict of interest.

Publisher's note

References

Arias, M. B., Kim, M., and Bae, S. (2017). Prediction of electric vehicle charging-power demand in realistic urban traffic networks. *Appl. Energy* 195, 738–753. doi:10.1016/j.apenergy.2017.02.021

Baidu map open platform (2022). Baidu map open platform. Available at https://lbsyun.baidu.com (Accessed March 15, 2022).

Calearo, L., Thingvad, A., Suzuki, K., and Marinelli, M. (2019). Grid loading due to EV charging profiles based on pseudo-real driving pattern and user behavior. *IEEE Trans. Transp. Electrif.* 5 (3), 683–694. doi:10.1109/TTE.2019.2921854

Chaudhari, K., Kandasamy, N. K., Krishnan, A., Ukil, A., and Gooi, H. B. (2018). Agent-based aggregated behavior modeling for electric vehicle charging load. *IEEE Trans. Ind. Informat.* 15 (2), 856–868. doi:10.1109/TII.2018.2823321

Chen, L., and Zhang, Y. (2019). Overview of charging and discharging load forcasting for electric vehicles. *Automat. Electr. Power Syst.* 43 (10), 177–197. doi:10.7500/AEPS20180814001

Chen, T., and Guestrin, C. (2016). "Xgboost: A scalable tree boosting system," in Proceedings of the 22nd ACM SIGKDD International Conference on Knowledge Discovery and Data Mining (KDD), San Francisco, CA, 785–794. doi:10.1145/2939672.2939785

EV volumes.com (2021). *Global EV sales for 2021*. Available at http://www.evvolumes.com (Accessed May 13, 2022).

Friedman, J. H. (2001). Greedy function approximation: A gradient boosting machine. *Ann. Stat.* 29 (5), 1189–1232. doi:10.1214/aos/1013203451

Ge, X., Shi, L., Fu, Y., Muyeen, S. M., Zhang, Z., and He, H. (2020). Data-driven spatial-temporal prediction of electric vehicle load profile considering charging behavior. *Electr. Power Syst. Res.* 187, 106469. doi:10.1016/j.epsr.2020.106469

Goodfellow, I., Pouget-Abadie, J., Mirza, M., Xu, B., Warde-Farley, D., Ozair, S., et al. (2014). Generative adversarial nets. *Adv. Neural Inf. Process. Syst.* 3, 2672–2680. doi:10.3156/jsoft.29.5_177_2

Ho, J., and Ermon, S. (2016). Generative adversarial imitation learning. *Adv. Neural Inf. Process.* 29, 4572–4580.

Jahangir, H., Gougheri, S. S., Vatandoust, B., Golkar, M. A., Golkar, M. A., Ahmadian, A., et al. (2021). A novel cross-case electric vehicle demand modeling based on 3D convolutional generative adversarial networks. *IEEE Trans. Power Syst.* 37 (2), 1173–1183. doi:10.1109/TPWRS.2021.3100994

Jahangir, H., Tayarani, H., Ahmadian, A., Golkar, M. A., Miret, J., Tayarani, M., et al. (2019). Charging demand of plug-in electric vehicles: Forecasting travel behavior based on a novel rough artificial neural network approach. *J. Clean Prod.* 229, 1029–1044. doi:10.1016/j.jclepro.2019.04.345

Li, M., Lenzen, M., Keck, F., McBain, B., Rey-Lescure, O., Li, B., et al. (2018). GIS-based probabilistic modeling of BEV charging load for Australia. *IEEE Trans. Smart Grid* 10 (4), 3525–3534. doi:10.1109/TSG.2018.2829917

Lin, H., Fu, K., Wang, Y., Sun, Q., Li, H., Hu, Y., et al. (2019). Characteristics of electric vehicle charging demand at multiple types of location-Application of an agent-based trip chain model. *Energy* 188, 116122. doi:10.1016/j.energy.2019.116122

Liu, Y., Liu, W., Gao, S., Wang, Y., and Shi, Q. (2022). Fast charging demand forecasting based on the intelligent sensing system of dynamic vehicle under EVs-traffic-distribution coupling. *Energy Rep.* 8, 1218–1226. doi:10.1016/j.egyr.2022.02.261

Majidpour, M., Qiu, C., Chu, P., Gadh, R., and Pota, H. R. (2014). Fast prediction for sparse time series: Demand forecast of EV charging stations for cell phone applications. *IEEE Trans. Ind. Informat.* 11 (1), 242–250. doi:10.1109/TII.2014.2374993

Ng, A. Y., and Russell, S. J. (2000). "Algorithms for inverse reinforcement learning," in Proceedings of the Seventeenth International Conference on Machine Learning (ICML), San Francisco, CA, 0, 663–670.

Osa, T., Pajarinen, J., Neumann, G., Bagnell, J. A., Abbeel, P., and Peters, J. (2018). An algorithmic perspective on imitation learning. *Found. Trends® Robotics* 7 (1-2), 1–179. doi:10.1561/2300000053

Qin, Y., Adams, S., and Yuen, C. (2021). Transfer learning-based state of charge estimation for lithium-Ion battery at Varying Ambient temperatures. *IEEE Trans. Ind. Informat.* 17 (11), 7304–7315. doi:10.1109/TII.2021.3051048

Schulman, J., Levine, S., Abbeel, P., Jordan, M., and Moritz, P. (2015). "Trust region policy optimization," in 32nd International Conference on Machine Learning (ICML), Lille, France, 1889–1897.

Schulman, J., Wolski, F., Dhariwal, P., Radford, A., and Klimov, O. (2017). Proximal policy optimization algorithms. Available at https://arxiv.org/abs/1707.06347.

Shanghai Electric Vehicle Public Data Collecting (2019). New energy vehicle operation data. Shanghai Electric Vehicle Public Data Collecting, Monitoring and Research Center. Available at https://labs.shevdc.com/home.

Wang, S. C. (2003). "Artificial neural network," in *Interdisciplinary computing in java programming* (Boston, MA: Springer), 81–100.

Xydas, E., Marmaras, C., Cipcigan, L. M., Jenkins, N., Carroll, S., and Barker, M. (2016). A data-driven approach for characterising the charging demand of electric vehicles: A UK case study. *Appl. Energy* 162, 763–771. doi:10.1016/j.apenergy.2015.10.151

Yang, J., Wu, F., Yan, J., Lin, Y., Zhan, X., Chen, L., et al. (2020). Charging demand analysis framework for electric vehicles considering the bounded rationality behavior of users. *Int. J. Electr. Power & Energy Syst.* 119, 105952. doi:10.1016/j.ijepes.2020.105952

Yang, W., Xiang, Y., Liu, J., and Gu, C. (2017). Agent-based modeling for scale evolution of plug-in electric vehicles and charging demand. *IEEE Trans. Power Syst.* 33 (2), 1915–1925. doi:10.1109/TPWRS.2017.2739113

Yi, T., Zhang, C., Lin, T., and Liu, J. (2020). Research on the spatial-temporal distribution of electric vehicle charging load demand: A case study in China. *J. Clean Prod.* 242, 118457. doi:10.1016/j.jclepro.2019.118457

Yi, Z., and Bauer, P. H. (2015). Spatiotemporal energy demand models for electric vehicles. *IEEE Trans. Veh. Technol.* 65 (3), 1030–1042. doi:10.1109/TVT.2015.2502249

Zang, H., Cheng, L., Ding, T., Cheung, K. W., Wei, Z., and Sun, G. (2020). Day-ahead photovoltaic power forecasting approach based on deep convolutional neural networks and meta learning. *Int. J. Electr. Power & Energy Syst.* 118, 105790. doi:10.1016/j.ijepes.2019.105790

Zang, H., Xu, R., Cheng, L., Ding, T., Liu, L., Wei, Z., et al. (2021). Residential load forecasting based on LSTM fusing self-attention mechanism with pooling. *Energy* 229, 120682. doi:10.1016/j.energy.2021.120682

Zhang, Y., Jia, S., Huang, H., Qiu, J., and Zhou, C. (2014). A novel algorithm for the precise calculation of the maximal in formation coefficient. *Sci. Rep.* 4 (1), 6662–6665. doi:10.1038/srep06662

Zhao, Y., Wang, Z., Shen, Z. J. M., and Sun, F. (2021). Data-driven framework for large-scale prediction of charging energy in electric vehicles. *Appl. Energy* 282, 116175. doi:10.1016/j.apenergy.2020.116175

Nomenclature

ε Truncation threshold

γ Reward discount rate

π_E Expert strategies

π_θ A policy with the parameter θ

$\prod$ Policy space

$\mathcal{C}$ Reward function space

τ_i Collection of sampled trajectories

ρ_{π_E} State-action probability distribution

$\hat{A}_t$ Advantage estimation at moment t

$c(s, a)$ Reward functions under status s and action a

DOD Depth of discharge

$D(x)$ Discriminator function

$D_\omega(s, a)$ The discriminator function with the parameter ω

$\mathcal{D}_k$ Trajectory space

d_{π_E} State probability distribution

$G(x)$ Policy generation functions

GAIL Generating adversarial imitation learning

$H(\pi)$ Policy π causal entropy function

IRL Inverse reinforcement learning

KL Kullback-Leibler divergence

MIC Maximal information coefficient

MSE Mean square error

MAE Mean absolute error

PPO Proximal policy optimization

$Q_\pi(s, a)$ Policy π under the state-action value function

RMSE Root mean square error

R-Squared Coefficient of determination

$\hat{R}_t$ Value of reward function at moment t

$r_t(\theta)$ State-to-action probability ratio at moment t

SOC State of charge

TRPO Trust region policy optimization

$V_\pi(s)$ Policy π under the state value function

XGboost Extreme gradient boosting algorithm

frontiers | Frontiers in Energy Research

TYPE Original Research
PUBLISHED 10 January 2023
DOI 10.3389/fenrg.2022.1099262

EDITED BY
Nantian Huang,
Northeast Electric Power University,
China

REVIEWED BY
Meng Song,
Southeast University, China
Chengcheng Shao,
Xi'an Jiaotong University, China

*CORRESPONDENCE
Zhiyi Li,
zhiyi@zju.edu.cn

SPECIALTY SECTION
This article was submitted to Smart Grids, a section of the journal Frontiers in Energy Research

RECEIVED 15 November 2022
ACCEPTED 22 November 2022
PUBLISHED 10 January 2023

CITATION
Zhu W, Song K, Gu Y, Luo Y, Shu J, Weng H and Li Z (2023), Allocating the capacity of shared energy storage for wind farm groups based on the over-limit power export risk.
Front. Energy Res. 10:1099262.
doi: 10.3389/fenrg.2022.1099262

Allocating the capacity of shared energy storage for wind farm groups based on the over-limit power export risk

Weijun Zhu[1], Kexuan Song[2], Yilei Gu[3], Yaogang Luo[4], Jing Shu[5], Hua Weng[1] and Zhiyi Li[2]*

[1]Zhejiang Huayun Electric Power Engineering Design & Consultation Co., Ltd, Hangzhou, China, [2]College of Electrical Engineering, Zhejiang University, Hangzhou, China, [3]State Grid Zhejiang Electric Power Co., Ltd., Hangzhou, China, [4]Institute of Economics and Tech Research, State Grid Ningbo Power Supply Co., Ningbo, China, [5]Yinzhou Branch, State Grid Ningbo Power Supply Co., Ningbo, China

Energy storage in wind farms can stabilize the fluctuation of wind power output. Shared energy storage can reduce the construction cost of energy storage devices and stimulate the enthusiasm of wind farms to invest in energy storage. The wind power base is composed of multiple wind farm groups. Existing research methods did not consider how to allocate shared energy storage among wind farm groups in the wind power base. This paper proposes an energy storage capacity allocation method for wind farm groups. Firstly, a bilevel model for the shared energy storage allocation is established. The upper-level model optimizes the shared energy storage allocation of each wind farm group with the goal of minimizing the over-limit power export risk in the wind power base; The lower-level model calculates the over-limit power export of each wind farm group according to the energy storage capacity allocation and transfers the value of over-limit power export to the upper-level model. The bilevel model can be converted to a two-stage model that can be solved sequentially; The wind power base in Belgium is used for numerical simulation to verify the effectiveness of the proposed model. Finally, the sensitivity of confidence level, total energy storage capacity, and risk preference factor are analyzed.

KEYWORDS

shared energy storage, capacity allocation, CVaR, wind volatility, over-limit power

1 Introduction

Integrating renewable energy into the power system makes the power system more environmentally friendly (Kong et al., 2019). However, the substantial volatility of renewable energy is one of the important factors limiting its large-scale grid connection, which directly affects the stable operation of the power system (Ju et al., 2019). In order to use large-scale renewable energy more effectively, researchers all over the world discuss solutions to reduce the threat of large-scale renewable energy to the power system. Some researchers design a dispatching strategy for wind farms with a multiple-stage hybrid energy storage system (Zhang et al., 2018), while other researchers discuss the optimal allocation of energy storage capacity for stabilizing wind power fluctuations (Zhu et al., 2020). Further, some studies reduce curtailed wind energy through energy storage and demand response (Bitaraf and Rahman, 2018). In addition, some studies propose the capacity allocation method using big data (Song et al., 2021). Some studies propose a power smoothing method by using a battery system using the fuzzy control strategy (Cong et al., 2018). The research (Zhang et al., 2019) enhances performances on wind power fluctuations mitigation by optimizing the operation schedule of battery energy storage systems with considerations of operation cost. In addition, some studies deal with the calculation of short and long-term energy storage needs and their dependence on the installed amount of solar energy and wind power (Weiss and Schulz., 2013). Later studies calculate the required energy storage capacity and charging/discharging power ratings for different desired operation scenarios (Lu et al., 2009).

The above studies all refer to the use of energy storage devices in a single wind farm to stabilize volatility, without considering the sharing of energy storage among wind farms. The operation efficiency of energy storage devices is low if the wind farm uses energy storage devices individually. In order to fully tap the application potential of energy storage, some studies propose the concept of shared energy storage (Zhao et al., 2020). Some studies propose a business model for utility-scale shared energy storage systems (Ben-Idris et al., 2021), while other studies analyze the complementary and controllable capabilities of energy storage that promote new energy consumption, and study the multiple energy storage sharing mechanism (Xv et al., 2022). Further, some studies use a hybrid storage system for energy sharing within the prosumers’ community (Mussadiq et al., 2022). In addition, some studies propose a capacity allocation method for photovoltaic microgrid energy storage systems based on time-sharing energy complementarity (Cong et al., 2021). Some studies propose a bi-level optimization problem aiming to improve the use of the shared energy storage for distribution system flexibility (Taşcıkaraoğlu et al., 2018). In addition, some studies propose a shared energy storage strategy among multiple wind farms based on wind power forecasting (Zhu et al., 2018). Later studies establish a cooperative game model in which prosumers and energy storage operators are the main participants to realize capacity optimization of renewable energy and energy storage systems (Tian et al., 2021). Some studies propose a novel shared energy storage planning method considering the correlation of renewable uncertainties on the supply side (Wang et al., 2022). However, how to reasonably allocate the shared energy storage capacity and reduce the over-limit power export risk of wind farm groups is still a problem to be solved.

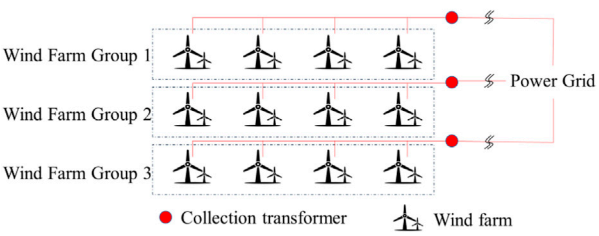

FIGURE 1
Large-scale wind power base.

TABLE 1 Guidelines for wind farm grid connection.

Capacity	Maximum output change (15 min)
<30 MW	10 MW
30–150 MW	1/3 Capacity
>150 MW	50 MW

Large-scale wind power base is the main form of wind power. Under the combined effect of multiple factors such as large-scale wind power equipment, cost reduction, and intensified market competition, the wind power base has entered a new stage of installation growth and expansion. Due to the large scale of the wind power base, the wind power base is usually divided into different wind farm groups and connected to the power grid through collection transformers as shown in Figure 1.

The fluctuation of wind power is the main limiting factor for the development of the wind power base. Based on the concept of shared energy storage, this paper proposes an allocation method of shared energy storage capacity for wind farm groups from the perspective of minimizing the over-limit power export risk in the wind power base. The innovations are as follows:

1) Conditional Value at Risk theory is used to characterize the over-limit power export risk of each wind farm group.
2) A bilevel optimization model for shared energy storage capacity allocation in wind farm groups is proposed, which provides a theoretical basis for the reasonable allocation of shared energy storage in wind farm groups.
3) A two-stage solution method for the bilevel optimization model of shared energy storage capacity allocation is proposed, and its equivalence is proved.

The remaining contents of this article are as follows: Section 2 introduces the shared energy storage for wind farm groups. Section 3 introduces the energy storage allocation models and the solution method. Section 4 analyzes the results through

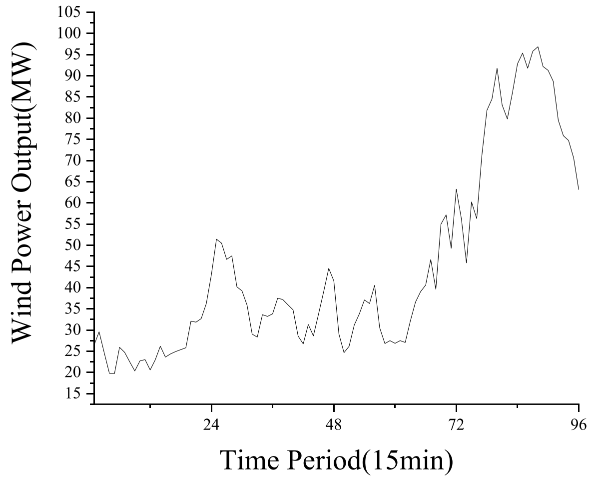

FIGURE 2
Wind farm group's output in Belgium.

simulation. Section 5 gives the conclusion and summarizes the whole article.

2 Sharing energy storage for wind farm groups

The fluctuation of wind power is a threat to the power grid operation. Generally speaking, the long, high-speed, and wide-range fluctuation process is more likely to pose a threat to the power grid operation. In order to reduce the impact of wind power fluctuations, State Grid proposed guidelines for wind farms connected to the power grid, as shown in Table 1.

The real data of the wind farm group's output in Belgium is shown in Figure 2. We can see that the wind farm group's output has exceeded the limit 8 times a day, and the most serious over-limit power is 14.78 MW. If grid connection is not allowed for the part of over-limit power, 25.5 MWh of wind power will be abandoned per day.

We define the over-limit power export risk in wind farms as follows:

$$R = \sum_{s=1}^{NS} \eta_s \left(\Delta P_s^{wind} - P_{\text{limit}} \right) \tag{1}$$

where, ΔP_s^{wind} represents power export change of adjacent periods in wind farms. P_{limit} represents the guideline of power export change shown in Table 1. NS represents the total number of possible scenarios of power export in wind farms. η_s represents the probability of occurrence of scenario s.

Energy storage can effectively reduce the power fluctuation of wind farm groups so that the power export can meet the guidelines. In other words, energy storage can effectively reduce the over-limit power export risk in wind farm groups and improve wind utilization. Large-scale wind power base usually contains multiple wind farm groups, and each wind farm group is composed of multiple wind farms. We define all wind farms connected to the same collection substation as one wind farm group. As shown in Figure 3, the wind farms inside the wind farm group are connected through the collection station, and then connected to the power grid. In order to reduce the over-limit power export risk, wind farm groups install distributed energy storage independently.

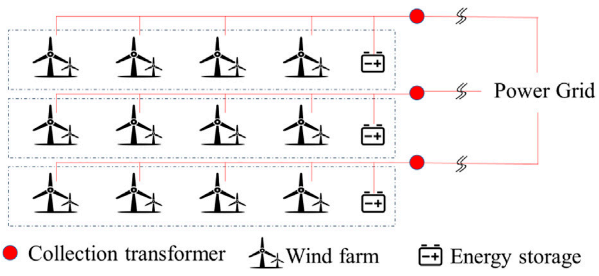

FIGURE 3
Distributed energy storage in the wind power base.

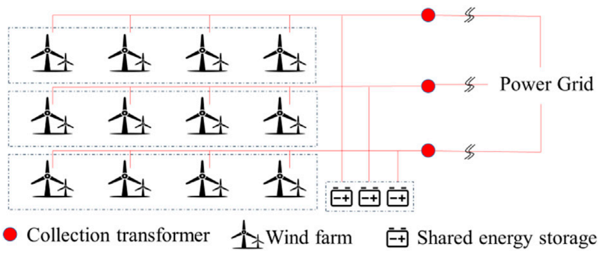

FIGURE 4
Shared energy storage in the wind power base.

However, the high investment cost of energy storage is the main obstacle for wind farm groups. Figure 4 shows the schematic diagram of shared energy storage in the wind power base. If each wind farm group constructs energy storage independently in the wind power base, the investment will be huge and the energy storage operation efficiency will be low. As wind farm groups belong to the same wind power base, there is only one single stakeholder in the wind power base. Using the concept of sharing energy storage, wind farm groups can jointly invest in energy storage equipment and coordinate operation, which is a new idea for wind farm groups to reduce power fluctuation. In the wind power base, the wind farm groups' output may vary greatly due to the wake effect. The wake effect refers to the wake area where wind turbines obtain

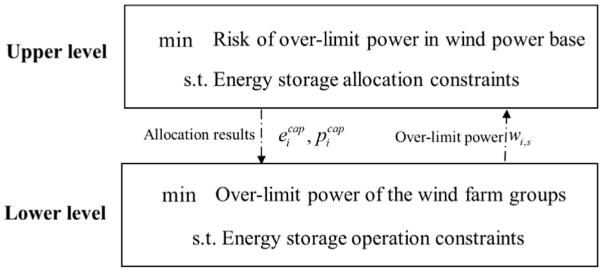

FIGURE 5
Model framework.

energy from the wind and wind speed decreases downstream. If a downstream wind turbine is located in the wake area, the input wind speed of the downstream wind turbine will be lower than that of the upstream wind turbine. Thus, wind farm groups can jointly use centralized energy storage devices to smooth the wind power output. By reasonably allocating shared energy storage in wind power groups, the wind power base can maximize the use of shared energy storage devices due to the difference of the output power in wind power groups.

In this way, the wind power base can reduce the over-limit power export risk in a more effective way. If we allocate the shared energy storage to each wind power group, it can be equivalent to that each wind power group has a distributed energy storage to reduce the power fluctuation. However, how to characterize the over-limit power export risk of wind farm groups, and how to reasonably allocate shared energy storage capacity among wind farm groups to minimize the over-limit power export risk of wind farm groups, have become new issues worth studying.

CVaR is an effective method for risk measurement. It can help us understand the expected risk of loss that exceeds a certain value at a certain confidence level. CVaR is widely used in the power system. Some studies use CVaR to describe the risk loss when the real wind power output is beyond the predefined uncertainty set (Zhang et al., 2018). Later studies use CVaR to help the distribution system operator (DSO) to balance the condition risk and the power generation dispatch cost in the power generation dispatch for the lowest total cost (Ren et al., 2019). The advantage of CVaR is that it is not a point probability value, but the weighted average expected value of all losses above the selected probability. In addition, CVaR can be optimized by using the linear programming algorithm. Thus, CVaR is very suitable to characterize the over-limit power export risk.

This paper will use CVaR to characterize the over-limit power export risk of wind farm groups, and allocate the shared energy storage in each wind farm group with the goal of minimizing the over-limit power export risk in the wind power base.

3 Model and methodology

In this section, we introduce a shared energy storage allocation model for wind farm groups in the wind power base based on CVaR. The goal of this model is to minimize the over-limit power export risk in the wind power base. The model framework is shown in Figure 5. The upper-level model minimizes over-limit power export risk in the wind power base with the constraints of energy storage allocation. The upper-level model optimizes the allocation of shared energy storage capacity in each wind farm group and obtains the allocation results of shared energy storage capacity. Then, the upper-level model transfers the allocation results to the lower-level model. The lower-level model minimizes the over-limit power export of each wind farm group according to the allocation results with the constraints of the energy storage operation. The lower-level model obtains the over-limit power export of each wind farm group and transfers it to the upper-level model.

3.1 Bilevel model for energy storage allocation

3.1.1 Upper-level model

The objective function of the upper-level model based on CVaR is as follows:

$$\min (1-\mu)F^c + \mu CVaR \tag{2}$$

where, μ represents the risk preference factor, F^c represents the over-limit power export of wind farm groups, $CVaR$ represents the over-limit power export risk. The calculation formula of F^c is as follows,

$$F^c = \frac{1}{NS}\sum_{s=1}^{NS}\sum_{i=1}^{NI}\sum_{t=1}^{NT} P_{ex,s,i,t} \tag{3}$$

where, $P_{ex,s,i,t}$ represents the over-limit power export of wind farm i at time t in scenario s. NS represents the number of scenarios. NI represents the number of wind farm groups. NT represents the total periods.

The calculation formula of $CVaR$ is as follows,

$$CVaR = \sum_{i=1}^{NI} CVaR_i \tag{4}$$

$$CVaR_i = \beta_i + \frac{1}{NS(1-\alpha)}\sum_{s=1}^{NS}\phi_{i,s}, \quad \forall i \in [1, \ldots, NI] \tag{5}$$

$$\phi_{i,s} \geq w_{i,s} - \beta_i, \quad \forall i \in [1, \ldots, NI]; \quad s \in [1, \ldots, NS] \tag{6}$$

$$\phi_{i,s} \geq 0, \quad \forall i \in [1, \ldots, NI]; \quad s \in [1, \ldots, NS] \tag{7}$$

where, $CVaR_i$ represents the over-limit power export risk of wind farm i. β_i represents the VaR value of wind farm i at α confidence level. $\phi_{i,s}$ is the auxiliary variable, which represents the over-limit power export risk over VaR of wind farm i in scenario s. $w_{i,s}$ represents the over-limit power export of wind farm i in scenario s.

The constrains of upper-level model is as follows:

$$e_i^{cap} \geq 0.1 \times e_i^N, \quad \forall i \in [1, ..., NI] \tag{8}$$

$$e_i^{cap} \geq 4 \times p_i^{cap}, \quad \forall i \in [1, ..., NI] \tag{9}$$

$$\sum_{i=1}^{NI} e_i^{cap} \leq E^{cap} \tag{10}$$

$$\sum_{i=1}^{NI} p_i^{cap} \leq P^{cap} \tag{11}$$

where, e_i^{cap} represents energy storage capacity allocated to wind farm i. e_i^N represents the energy storage capacity of wind farm i. p_i^{cap} represents max real power output of energy storage allocated to wind farm i. E^{cap} represents the shared energy storage capacity. P^{cap} represents the max real power output of shared energy storage.

In order to reduce the impact of wind fluctuations on grid stability, the wind farm is required to be equipped with 10% capacity energy storage, and the charging time should not less than 4 h. To ensure the above requirements, constraints (8)–(9) are added to the model (10)–(11) represents the constraints of the allocation of shared energy storage in wind farm groups.

3.1.2 Lower-level model

The lower-level model minimizes the over-limit power export of the wind farm groups. The objective function of the lower-level model is as follows:

$$\min \sum_{t=1}^{NT} \max\left(\left|P_{s,i,t} - P_{s,i,t-1}\right| - P_{i,\text{limit}}, 0\right) \tag{12}$$

where, $P_{s,i,t}$ represents the power export of wind farm i at time t in scenario s. $P_{i,\text{limit}}$ represents the power export fluctuation limit value to wind farm i. The specific definition of $P_{i,\text{limit}}$ are as follows:

$$P_{i,\text{limit}} = \begin{cases} 3 & e_i^N \leq 30 \\ \dfrac{e_i^N}{10} & 30 < e_i^N \leq 100 \\ 10 & 100 < e_i^N \end{cases} \tag{13}$$

There are two nonlinear terms in the objective function, absolute value and maximum value, which need to be linearized. Auxiliary variables $P_{ex,s,i,t}$ is introduced to equivalent the objective function to the following linearized form:

$$\min \sum_{t \in NT} P_{ex,s,i,t} \tag{14}$$

$$P_{ex,s,i,t} \geq P_{s,i,t} - P_{s,i,t-1} - P_{i,\text{limit}} \tag{15}$$

$$P_{ex,s,i,t} \geq P_{s,i,t-1} - P_{s,i,t} - P_{i,\text{limit}} \tag{16}$$

$$P_{ex,s,i,t} \geq 0 \tag{17}$$

The constraints of the lower-level model are as follows:

$$P_{s,i,t} = p_{s,i,t}^N + \left(p_{s,i,t}^D - p_{s,i,t}^C\right) \tag{18}$$

$$e_{s,i,t} = (1 - s_i)e_{s,i,t-1} + \left(\eta_i^C p_{s,i,t}^C - \frac{p_{s,i,t}^D}{\eta_i^D}\right), \quad \forall t \in [1, ..., NT] \tag{19}$$

$$0 \leq p_{s,i,t}^C \leq I_{s,i,t}^C p_i^{cap}, \quad \forall t \in [1, ..., NT] \tag{20}$$

$$0 \leq p_{s,i,t}^D \leq I_{s,i,t}^D p_i^{cap}, \quad \forall t \in [1, ..., NT] \tag{21}$$

$$SOC_{\min} e_i^{cap} \leq e_{s,i,t} \leq SOC_{\max} e_i^{cap}, \quad \forall t \in [1, ..., NT] \tag{22}$$

$$I_{s,i,t}^C + I_{s,i,t}^D \leq 1, \quad \forall t \in [1, ..., NT] \tag{23}$$

$$e_{s,i,1} = e_{s,i,T} \tag{24}$$

where, $p_{s,i,t}^N$ represents wind power output of wind farm i at time t in scenario s. $p_{s,i,t}^D$ represents discharging power of the energy storage of wind farm i at time t in scenario s. $p_{s,i,t}^C$ represents charging power of the energy storage of wind farm i at time t in scenario s. $e_{s,i,t}$ represents remaining power of the energy storage of wind farm i at time t in scenario s. s_i represents self-loss-rate of energy storage of wind farm i. η_i^C and η_i^D represent charging efficiency and discharging efficiency for energy storage. $SOC_{\min}$ and $SOC_{\max}$ represent minimum and maximum state-of-charge values for energy storage.

After the wind farm gets the allocated energy storage, its power export depends not only on the output of wind farm but also on the output of energy storage. The power balance constraint can be expressed as constraint (18). Constraints (19)–(24) are energy storage operation constraints.

Since the lower-level model is nonconvex, neither Karush–Kuhn–Tucker optimality conditions nor duality theory can be applied to transform the lower-level model into a set of constraints so as to convert the original bilevel model into an equivalent single-level model. Due to the difficulty in solving the bilevel model, a two-stage solution method is proposed for this bilevel model, which sequentially solve two models.

3.2 Equivalent two-stage model

3.2.1 First-stage model

The objective function of the first-stage model is as follows:

$$\min (1 - \mu)F^c + \mu CVaR \tag{25}$$

The constraints of the first-stage model are all the constraints of the upper-level model, that is, constraints (8)–(11). And all constraints of the lower-level model, that is, constraints (18)–(24). After solving the first-stage model, we obtain the optimal value $\bar{e}_i^{cap}$ and $\bar{p}_i^{cap}$.

3.2.2 Second-stage model

The objective function of the second-stage model is as follows:

$$\min \sum_{t\in NT} P_{ex,s,i,t} \tag{26}$$

The constraints of the second-stage model are all the constraints of the lower-level model, that is, constraints (18)–(24). In addition, the constraints of the second-stage model also include (27) and (28):

$$e_i^{cap} = \bar{e}_i^{cap} \tag{27}$$

$$p_i^{cap} = \bar{p}_i^{cap} \tag{28}$$

After solving the first-stage model and the second-stage model sequentially, the energy storage allocation result and the optimal value of CVaR are consistent with the results of the bilevel model in 3.1. The effectiveness of the proposed two-stage model is proved as follows.

3.3 Proof of effectiveness of two-stage model

This section will prove the equivalence of the solution results of the two-stage model and the bilevel model (Li et al., 2016).

Due to all the constraints in the first-stage problem are satisfied in the original bilevel problem, we can infer that any feasible solution to the original bilevel problem also corresponds to a feasible solution to this first-stage problem. The following equation is always true.

$$\hat{f}^{one}_{two-stage} \le \hat{f}_{bilevel} \tag{29}$$

Where $\hat{f}^{one}_{two-stage}$ represents the optimal value of objective function of the first-stage model. $\hat{f}_{bilevel}$ represents the optimal value of objective function of the bilevel model.

Since the objective function of the lower-level model in the bilevel model is the power export fluctuation, which is also a variable in constraint (6) in the upper-level model. The bilevel model can be converted into the following form:

$$\min (1-\mu)F^c + \mu CVaR \tag{30}$$

$$\begin{aligned} s.t.&(2)-(4)\\ &(6)-(10)\\ &(14)-(23)\end{aligned} \tag{31}$$

$$\phi_{i,s} \ge \min\left(\sum_{t\in NT} P_{ex,s,i,t}\right) - \beta_i, \quad \forall i \in [1,\ldots,NI];\ s \in [1,\ldots,NS] \tag{32}$$

Since the following inequality is always true:

$$\min\left(\sum_{t\in NT} P_{ex,s,i,t}\right) - \beta_i \le \sum_{t\in NT} P_{ex,s,i,t} - \beta_i \tag{33}$$

It can be seen from the above formula that the feasible region of the bilevel model is not smaller than that of the first-stage model. We can prove that the following inequality is always true:

$$\hat{f}^{one}_{two-stage} \ge \hat{f}_{bilevel} \tag{34}$$

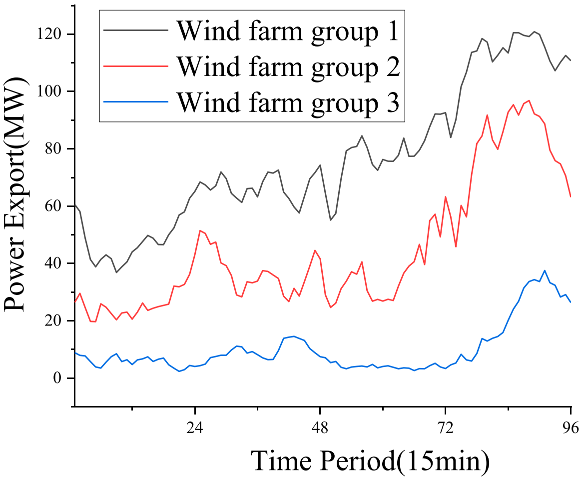

FIGURE 6
Historical data of wind power output.

Since (29) and (34) is always true, we can infer that the following equality is always true:

$$\hat{f}^{one}_{two-stage} = \hat{f}_{bilevel} \tag{35}$$

The above formula shows that the optimal objective function value of the two-stage model is equal to that of the bilevel model. The over-limit power export risk of wind farm groups is determined by the results of shared energy storage allocation. Since the optimal objective function of the first-stage model is the same as that of the bilevel model, and the over-limit power export risk of wind farm groups is the same, the results of optimal energy storage allocation of the first-stage model are also the same as those of the bilevel model.

Finally, after the optimal allocation of energy storage is obtained from the first-stage model, the second-stage model optimizes the power fluctuation of wind farm groups according to the energy storage allocation. Because the second-stage model and the lower-level model in the bilevel model have similar structures under the same energy storage allocation scheme, the optimal decision variable values obtained by solving the second-stage model and the lower-level model in the bilevel model must also be the same. This shows that after solving the first-stage model and the second-stage model in sequence, the energy storage allocation and the optimal value of CVaR are completely consistent with the results of the bilevel model. The proof is over.

4 Case study

The case studies are conducted based on the wind power base in Belgian. The wind power base contains three wind

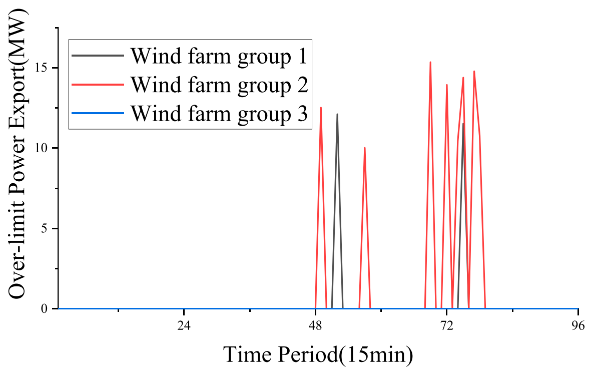

FIGURE 7
Over-limit power export.

TABLE 2 Solution results.

	VaR	CVAR	Energy storage capacity
Wind farm 1	0.00	2.45	25.00 MWh/6.25 MW
Wind farm 2	0.00	14.00	41.44 MWh/10.36 MW
Wind farm 3	2.54	13.85	33.56 MWh/8.39 MW
Total amount	2.54	30.30	100.00 MWh/25.00 MW

farm groups with installed capacity of 250, 150, and 100 MW respectively. Historical wind power output data of the wind power base in Belgian is used as the scenario in the above model, and the time interval is 15 min. The energy storage capacity of three wind farm groups is allocated by using the proposed energy storage allocation method. We use MATLAB with the mixed-integer programming solver Gurobi to solve all the optimization problems (Gurobi Optimizer Reference Manual, 2020).

Historical data of wind farm groups in Belgian is shown in Figure 6.

As shown in Figure 7, Wind farm 2 has the highest volatility, followed by wind farm 1, and wind farm 3 has the lowest volatility. The confidence level of over-limit power export risk is 0.9. The total scale of shared energy storage is 100 MWh/50 MW. The charging and discharging efficiency of energy storage is 90%. The self-discharging rate is 0.001.

4.1 Energy storage allocation results

The VaR and CVaR values of wind farm groups and the energy storage allocation results are shown in Table 2.

According to the historical output of the wind farm groups, wind farm 2 has the largest fluctuation (6 times out of the limit).

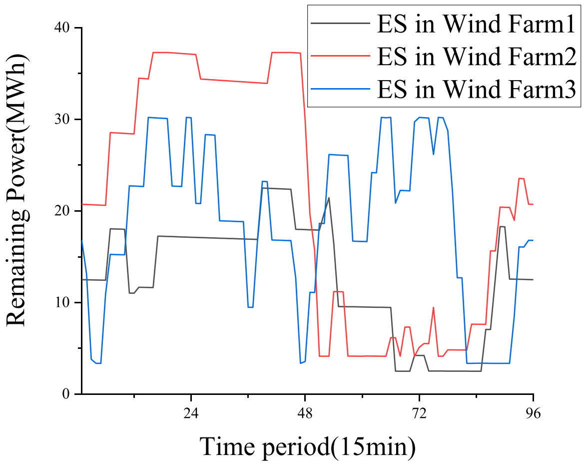

FIGURE 8
The remaining power of energy storage allocated to wind farm groups.

If energy storage is allocated only according to the principle of reducing fluctuation, wind farm 2 should get the largest energy storage capacity. However, we have the constraint that the wind farm must be equipped with energy storage with the capacity of 10% of the wind farm installation capacity. The energy storage capacity allocated to wind farm 1 is more than that of wind farm 2 only because the capacity of wind farm 1 is larger. Figure 8 shows the remaining power of energy storage shared by each wind farm.

If grid connection is not allowed for the part of power fluctuation exceeding the limit, the three wind farm groups can reduce the wind power curtailment of 7.2 MWh, 10.94 MWh, and 8.23 MWh respectively after energy distribution and storage.

4.2 Sensitivity analysis

4.2.1 Confidence level

The shared energy storage allocation results under different confidence levels are shown in Table 3. The value of VaR and CVaR under different confidence levels are shown in Figure 9.

It can be seen from the figure that, the value of CVaR increases with the increase of confidence level, and the value of VaR also increases. VaR is equal to CVaR when the confidence level is 0.99. This is because the total number of scenarios in the model is 100. When the value of CVaR exceeds the expectation of VaR at 99% confidence level, there is only one scenario representing tail risk, so the value of CVaR is equal to VaR.

TABLE 3 Solution results.

Confidence level	Energy storage capacity		
	Wind farm group 1	Wind farm group 2	Wind farm group 3
0.9	25.00 MWh/6.25 MW	18.82 MWh/4.705 MW	16.18 MWh/4.045 MW
0.95	25.00 MWh/6.25 MW	17.94 MWh/4.485 MW	17.06 MWh/4.265 MW
0.99	25.00 MWh/6.25 MW	19.18 MWh/4.795 MW	15.82 MWh/3.955 MW

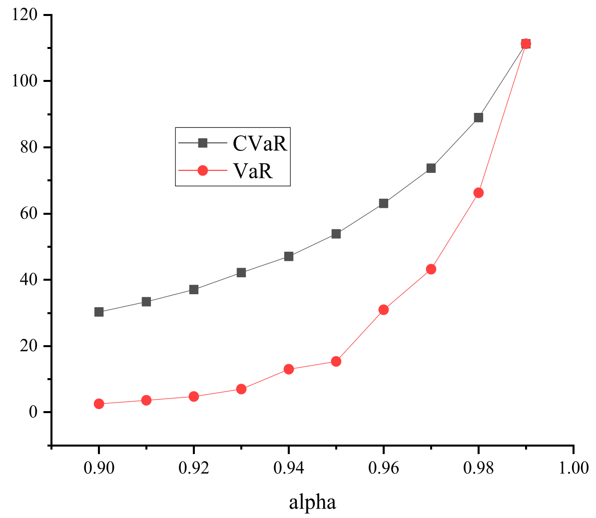

FIGURE 9
VaR and CVaR under different confidence levels.

4.2.2 Capacity of shared energy storage

In order to further investigate the impact of different shared energy storage capacities on over-limit power export risk, different shared energy storage capacities are set for simulation. When other parameters remain unchanged, the total shared energy storage capacity is taken as 100 MWh to 150 MWh respectively. The value of VaR and CVaR, the energy storage allocation results, and the average daily power exceeding are shown in Figure 10.

When the total energy storage capacity reaches 110 MWh, the value of VaR in wind power base is 0. The power export of three wind farm groups will be over-limit at 90% confidence level. The average value of CVaR of the three wind farm groups is less than 20.38. With the increase of the total energy storage capacity, CVaR value of the three wind farm groups will gradually decrease, but the rate of reduction will be slower and slower. It can be seen that when the total energy storage capacity reaches 130 MWh, the energy storage allocated to wind farm 1 will be greater than 25 MWh. We can infer that the energy storage constraint with 10% capacity of the

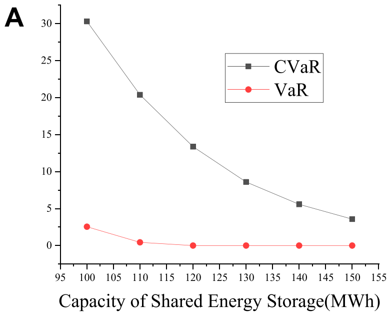

CVaR and VaR under different capacity of shared energy storage

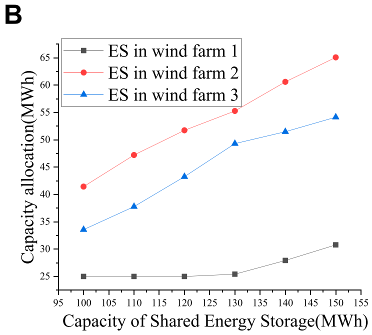

Capacity allocation under different capacity of shared energy storage

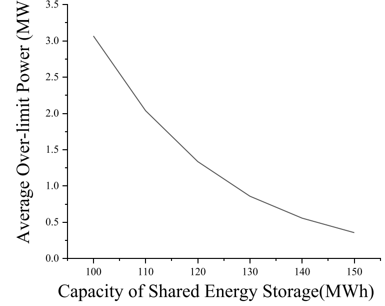

Average over-limit power under different capacity of shared energy storage

FIGURE 10
Solution results under different capacity of shared energy storage. **(A)** CVaR and VaR under different capacity of shared energy storage **(B)** Capacity allocation under different capacity of shared energy storage **(C)** Average over-limit power under different capacity of shared energy storage.

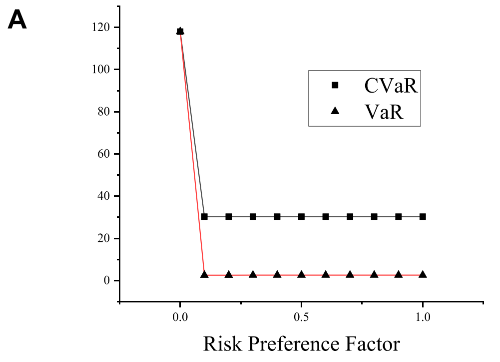

CVaR and VaR under different risk preference factors

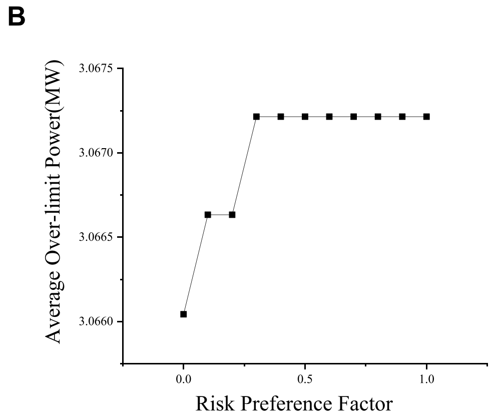

Average over-limit power under different risk preference factors

FIGURE 11
Solution results under different risk preference factors. **(A)** CVaR and VaR under different risk preference factors **(B)** Average over-limit power under different risk preference factors.

wind farm will no longer work when the total energy storage capacity exceeds 130 MWh. We define the daily over-limit power of the wind farm group as the total amount of over-limit power in a day. It also can be seen that when the total energy storage capacity increases, the average daily over-limit power of wind farm groups will decrease. With the increase of the total shared energy storage capacity, the average daily over-limit power will decrease more slowly. If the over-limit power cannot be connected to the grid, the wind abandonment rate of wind farm groups will decrease with the increase of the total shared energy storage capacity, but the marginal benefit of the total shared energy storage capacity will gradually decrease.

4.2.3 Risk preference factor

Figure 11 shows the value of VaR, CVaR, and daily average over-limit power of wind farm groups under different risk preference factors.

Different energy storage allocation methods under different risk preference factors lead to different values of CVaR. When the risk preference factor is larger, CVaR value of wind farm groups is smaller, and the shared energy storage allocation scheme tends to be more conservative; When the risk preference factor is less than 0.3, the average over-limit power of wind farm increased significantly with the increase of risk preference factor; When the risk preference factor is more than 0.3, the increase of risk preference factor had little impact on the average over-limit power of wind farm.

5 Conclusion

This paper proposes a method to allocate energy storage capacity for wind farm groups based on CVaR. A bilevel model with the objective function of minimizing the over-limit power export risk of wind farm groups is established. Then, a two-stage solution method for the bilevel model is proposed. The effectiveness of the two-stage method is proved. The model and solution algorithm proposed in this paper are used to allocate the energy storage of Belgian wind farm groups. The sensitivity of confidence level, total energy storage capacity and risk preference factors on the optimal allocation of shared energy storage are analyzed. The results show that the proposed method can significantly reduce the over-limit power export risk of wind farm groups and improve the utilization rate of wind energy.

Data availability statement

The raw data supporting the conclusion of this article will be made available by the authors, without undue reservation.

Author contributions

KS and ZL contributed to the conception and design of the study. WZ organized the simulation, analyzed the results and wrote parts of the manuscript. YL and YG gave suggestions in technical support. JS and HW contributed to write parts of the manuscript.

Conflict of interest

WZ and HW are employed by Zhejiang Huayun Electric Power Engineering Design & Consultation Co., Ltd. YG is employed by State Grid Zhejiang Electric Power Co., Ltd. YL and JS are employed by State Grid Ningbo Power Supply Co.

The remaining author declares that the research was conducted in the absence of any commercial or financial relationships that could be construed as a potential conflict of interest.

Publisher's note

References

Ben-Idris, M., Brown, M., Egan, M., Huang, Z., and Mitra, J. (2021). Utility-Scale Shared Energy Storage: Business models for utility-scale shared energy storage systems and customer participation. *IEEE Electrific. Mag.* 9, 47–54. doi:10.1109/mele.2021.3115558

Bitaraf, H., and Rahman, S. (2018). Reducing curtailed wind energy through energy storage and demand response. *IEEE Trans. Sustain. Energy* 9, 228–236. doi:10.1109/tste.2017.2724546

Cong, L., Chuanpu, Z., Kuan, W., Lizhu, S., Qingyu, W., and Wenhai, Z. (2021). "Multi-objective capacity optimal allocation of photovoltaic microgrid energy storage system based on time-sharing energy complementarity," in 2021 International Conference on Power System Technology (POWERCON), Kuala Lumpur, MALAYSIA, 14-16 September 2022, 1123–1129.

Cong, Y., Meng, X., Wang, L., and Wang, Y. (2018). "A power smoothing approach based on battery energy storage system for power fluctuations of wind power generation," in 2018 International Conference on Information Systems and Computer Aided Education (ICISCAE), Changchun, China, July 6-8, 2018, 331–334.

Gurobi Optimizer Reference Manual (2020). *Gurobi optimizer reference manual.* Beaverton, OR, USA: Gurobi Optimization Inc.

Ju, Y., Sun, G., Chen, Q., Zhang, M., Zhu, H., and Rehman, M. U. (2019). A model combining convolutional neural network and Light GBM algorithm for ultra-short-term wind power forecasting. *IEEE Access* 7, 28309–28318. doi:10.1109/access.2019.2901920

Kong, W., Dong, Z. Y., Jia, Y., Hill, D. J., Xu, Y., and Zhang, Y. (2019). Short-term residential load forecasting based on LSTM recurrent neural network. *IEEE Trans. Smart Grid* 10, 841–851. doi:10.1109/tsg.2017.2753802

Li, Z., Shahidehpour, M., Alabdulwahab, A., and Abusorrah, A. (2016). Bilevel model for analyzing coordinated cyber-physical attacks on power systems. *IEEE Trans. Smart Grid* 7, 2260–2272. doi:10.1109/tsg.2015.2456107

Lu, M. -S., Chang, C. -L., Lee, W. -J., and Wang, L. (2009). Combining the wind power generation system with energy storage equipment. *IEEE Trans. Ind. Appl.* 45, 2109–2115. doi:10.1109/tia.2009.2031937

Mussadiq, U., Kausar, T., Ahmed, S., and Kim, S. M. (2022). "A hybrid storage system for energy sharing and management within prosumers' community," in 2022 5th International Conference on Energy Conservation and Efficiency (ICECE), Pakistan, 16th and 17th March, 2022, 1–6.

Ren, X., Yang, N., Ye, B., Yao, Y., and Gao, C. (2019). "Stochastic planning model for incremental distributio network considering CVaR and wind power penetration," in 2019 IEEE Innovative Smart Grid Technologies - Asia (ISGT Asia), Chengdu, China, May 21 - Friday, May 24, 2019, 1358–1363.

Song, J., Hu, C., and Su, L. (2021). "Distributed wind power and photovoltaic energy storage capacity configuration method under big data," in 2021 International Conference on Electronic Communications, Internet of Things and Big Data (ICEIB), Xiamen, China, November 4-7, 2022, 318–322.

Taşcikaraoğlu, A., Erdinç, O., and Catalão, J. P. S. (2018). "Shared energy storage and direct load control for improved flexibility of distribution system operation," in 2018 53rd International Universities Power Engineering Conference (UPEC), Glasgow, United Kingdom, 4th-7th September 2018, 1–6.

Tian, X., Zheng, T., Chen, L., and Xue, X. (2021). "Capacity optimization for wind/photovoltaic prosumers and shared energy storage operator: A cooperative game approach," in 2021 IEEE 5th Conference on Energy Internet and Energy System Integration (EI2), Taiyuan, China, Held 22-24 October 2021, 2097–2103.

Wang, Q., Zhang, X., Yi, C., Li, Z., and Xu, D. (2022). A novel shared energy storage planning method considering the correlation of renewable uncertainties on the supply side. *IEEE Trans. Sustain. Energy* 13, 2051–2063. doi:10.1109/tste.2022.3179837

Weiss, T., and Schulz, D. (2013). "Development of fluctuating renewable energy sources and its influence on the future energy storage needs of selected European countries," in 2013 4th International Youth Conference on Energy (IYCE), Siófok. Hungary, Thu, 06/06/2013, 1–5.

XV, A., He, C., Zhang, M., and Wang, T. (2022). "Day-ahead scheduling with renewable generation considering shared energy storage," in 2022 4th Asia Energy and Electrical Engineering Symposium (AEEES), Chengdu, China, 25th to 28th March 2022, 492–497.

Zhang, X., Gu, J., Hua, L., and Ma, K. (2019). Enhancing performances on wind power fluctuation mitigation by optimizing operation schedule of battery energy storage systems with considerations of operation cost. *IEEE Access* 7, 94072–94083. doi:10.1109/access.2019.2928274

Zhang, Y., Han, X., Xu, B., Wang, M., Ye, P., and Pei, Y. (2018). Risk–based admissibility analysis of wind power integration into power system with energy storage system. *IEEE Access* 6, 57400–57413. doi:10.1109/access.2018.2870736

Zhang, Z., Zhang, Y., Huang, Q., and Lee, W. -J. (2018). Market-oriented optimal dispatching strategy for a wind farm with a multiple stage hybrid energy storage system. *CSEE J. Power Energy Syst.* 4, 417–424. doi:10.17775/cseejpes.2018.00130

Zhao, D., Wang, H., Huang, J., and Lin, X. (2020). "Virtual energy storage sharing and capacity allocation," in 2020 IEEE Power & Energy Society General Meeting (PESGM), Orlando, Florida, 16 – 20 July 2023, 1.

Zhu, H., Shi, L., and Wu, F. (2020). "Optimal allocation of energy storage capacity for stabilizing wind power fluctuation," in 2020 12th IEEE PES Asia-Pacific Power and Energy Engineering Conference (APPEEC), Nanjing, China, Sept. 20-Sept. 23, 2020, 1–5.

Zhu, K., Chowdhury, S., Sun, M., and Zhang, J. (2018). "Grid optimization of shared energy storage among wind farms based on wind forecasting," in 2018 IEEE/PES Transmission and Distribution Conference and Exposition (T&D), Denver, CO, 16-19 April 2018, 1–5.

frontiers | Frontiers in Energy Research

TYPE Original Research
PUBLISHED 10 January 2023
DOI 10.3389/fenrg.2022.1073194

OPEN ACCESS

EDITED BY
Yingjun Wu,
Hohai University, China

REVIEWED BY
Hongcai Zhang,
University of Macau, China
Tao Chen,
Southeast University, China
Changgang Li,
Shandong University, China
Yang Li,
Northeast Electric Power University,
China

*CORRESPONDENCE
Guobin He,
GuobinHe11@outlook.com

SPECIALTY SECTION
This article was submitted to Smart Grids, a section of the journal Frontiers in Energy Research

RECEIVED 18 October 2022
ACCEPTED 22 November 2022
PUBLISHED 10 January 2023

CITATION
Su R, He G, Su S, Duan Y, Cheng J, Chen H, Wang K and Zhang C (2023), Optimal placement and capacity sizing of energy storage systems *via* NSGA-II in active distribution network.
Front. Energy Res. 10:1073194.
doi: 10.3389/fenrg.2022.1073194

Optimal placement and capacity sizing of energy storage systems *via* NSGA-II in active distribution network

Rui Su[1], Guobin He[1]*, Shi Su[2], Yanru Duan[3], Junzhao Cheng[3], Hao Chen[1], Kaijun Wang[1] and Chao Zhang[1]

[1]Dali Power Supply Bureau of Yunnan Power Grid Co., Ltd., Dali, China, [2]Electric Power Research Institute of Yunnan Power Grid Co., Ltd., Kunming, China, [3]Grid Planning Research Center of Yunnan Power Grid Co., Ltd., Kunming, China

In recent years, with the rapid development of renewable energy, the penetration rate of renewable energy generation in the active distribution network (ADN) has increased. Because of the instability of renewable energy generation, the operation stability of ADN has decreased. Due to the ability to cut peak load and fill valley load, battery energy storage systems (BESSs) can enhance the stability of the electric system. However, the placement and capacity of BESSs connected to ADN are extremely significant, otherwise, it will lead to a further decline in the stability of ADN. To ensure the effectiveness of the BESSs connected to the grid, this work uses the fuzzy kernel C-means (FKCM) method for scene clustering. Meanwhile, a multi-objective optimization model of BESS configuration is established with the objective of BESS configuration cost, voltage fluctuation, and load fluctuation, and solved by non-dominated sorting genetic algorithm-II (NSGA-II). In this work, the grey target decision method based on the entropy weight method (EWM) is used to obtain the optimal compromise solution from the Pareto non-dominated set. Moreover, the proposed method is tested and verified in the extended IEEE-33 node system and the extended IEEE-69 node system. The results show that the BESSs configuration scheme obtained by NSGA-II can effectively reduce the fluctuation of voltage and load, and improve the stability of ADN operation.

KEYWORDS
battery energy storage systems, fuzzy kernel C-means, non-dominated sorting genetic algorithm-II, entropy weight method, active distribution network

1 Introduction

With the continuous development and progress of society and technology, traditional energy sources based on fossil fuels have become difficult to meet the needs of human society. Nowadays, thermal power generation is still the main way for people to obtain electric energy. However, the harmful gases emitted by the combustion of fossil fuels have become a problem, and the combustion of fossil fuels is aggravating environmental pollution and global warming (Company, 2021; Zandalinas et al., 2021). At present, energy storage and environmental pollution issues have become two serious challenges to the sustainable development of society. It is urgent to reduce carbon emissions and build a new type of power system with renewable energy sources as the main body (He et al., 2021; Dong et al., 2022).

The new power grid with photovoltaic and wind energy as the main energy structure has the advantage of a flexible power supply, so it is a better solution to the power supply problem of the grid (Bin et al., 2019; Li et al., 2022a). However, photovoltaic, wind power has obvious characteristics of randomness, volatility, and intermittency, its intermittency, and volatility will harm the quality of the power supply. And photovoltaic, wind power needs to go through the power electronic equipment to achieve energy control and does not have the power grid frequency, voltage regulation, and other functions. Renewable energy also has the characteristics of dispersion, when the renewable energy to a high penetration rate into the grid will aggravate the impact caused by the volatility, such as voltage deviation, power loss, etc. (Hu et al., 2022; Xiao and Pan, 2022).

Distributed generation (DG) and energy storage systems (ESSs) play an important role in power grids with high renewable energy generation penetration rates (Wu et al., 2021a; Shi et al., 2022). On the one hand, as an independent power supply compatible with the environment on the user side, DG can meet the peaking demand of the power system and supply power to remote users, and commercial and residential areas, it also can save transmission investment and reduce transmission losses. On the other hand, because the DG is mostly renewable energy generation, its output has obvious randomness and intermittency, which affects the voltage stability of the active distribution network (ADN), changes the direction of the ADN power flow, and causes the system power flow to be random. When large-scale renewable energy generation access to ADN will cause power flow and voltage over-limit, change the voltage characteristics, and reduce the stability of ADN. Furthermore, the role of DG in ADN is mostly used as a backup power supply, which is easy to cause the voltage and frequency of the ADN to drop and exceed the limit during the power switching process. Even so, DG is still considered by many energy and power system experts as the main way to increase the utilization of renewable energy and improve the stability and flexibility of ADN (Yang et al., 2021; Wu et al., 2022).

ESSs can effectively solve various energy supply and demand balance problems and improve energy utilization efficiency through their peak-shaving and flexible energy management capabilities. Meanwhile, the ESSs can effectively solve serious problems such as power flow reverse and voltage over-limit which occur in the ADN after DG access, and ensure the normal operation of the distribution network (Li et al., 2018). Battery energy storage systems (BESSs), which use batteries as energy storage carriers, have become a hot topic of current research due to their high energy density, fast response time, and modularity (Das et al., 2018; Wu et al., 2021b). BESS can effectively solve various supply-demand imbalance and power quality problems by using high energy density to cut peaks and fill valleys on the network and using high power density to smooth out random power fluctuation (Liu et al., 2016; Zheng, 2018; Ren et al., 2019; Yang et al., 2020).

After the ESSs are connected to the ADN, the operating state of the ADN and the ability of peak cutting are affected by the access mode, location, and capacity. In recent years, many scholars have studied the planning of ESSs, however, most of the research models are single-objective models, and these models are difficult to consider the stability of the network and the economics of energy storage at the same time. Reference (Yan et al., 2013) established an optimal value assessment model of BESSs with net income as the objective function. The reference (Su et al., 2016) established a planning model for the location and capacity of distributed power and energy storage devices with the cost input of ADN as the objective function. Literature (Lee and Chen, 1995) constructed an energy storage planning model with the cost of electricity purchased by customers as the objective function. Reference (Ghatak et al., 2019) established an energy storage planning model with battery storage life as the objective function and quantified the battery characteristic parameters by combining three characteristics of battery discharge depth, discharge rate, and effective discharge volume. In reference (Chen, 2020), an energy storage planning model has been established with the objective function of accurately tracking real-time meteorological conditions, and an improved logistic regression model was used to evaluate the impact of real-time numerical meteorological conditions on the device. All the above research models are single-objective planning models, which do not consider the coupling problem between ESSs planning and network operation conditions. The reference (Fu et al., 2022) established a multi-objective optimal configuration model with the economic benefits of ESSs and voltage quality as the optimization objectives. However, the voltage quality does not fully reflect the real operating condition of the network after accessing ESSs. Therefore, building a multi-objective optimal allocation model for ESSs can not only fully exploit the potential of ESSs, but also achieve a better balance between the economic benefits of ESSs and network stability.

In most papers, the multi-objective optimization problem is weighted into a single objective problem by the weighting method. However, it is difficult to guarantee the objectivity of the planning scheme solved by this method. In this regard, some studies used a bi-level planning model to solve the different problems of BESSs location and capacity sizing (Li et al., 2022b). The reference (Meng et al., 2021) proposed a bi-layer BESSs planning scheme considering renewable energy and load uncertainties. The optimal solution of this model can solve the problem of objectivity in the single-objective model, but the two-layer model is complex, and difficult to obtain the optimal solution. ESSs location and capacity sizing is a high-dimensional, multi-objective, complex constraints problem. The solution process of traditional planning methods is complex and easy to fall into local optimum. Therefore, it is very important to establish a Pareto-based multi-objective model. This model can well adjust the balance between various optimization variables in multi-objective optimization problems and ensure that the results have good objectivity.

This work is based on the non-dominated sorting genetic algorithm-II (NSGA-II), which shows a high optimization performance under several standard function test environments. The main content of this work is as follows:

(1) A multi-objective planning optimal location and capacity model based on the Pareto of BESSs is established with three objectives, and NSGA-II is used to solve this multi-objective model;
(2) The clustering algorithm is used to cluster the daily load, wind power, and photovoltaic (PV) output curves of the whole year, and the typical scenarios are obtained based on the combination of time series characteristics. Simulation calculations are performed in different typical scenarios to obtain the sum of each objective function throughout the year;
(3) The simulation based on the extended IEEE-33 node system and the extended IEEE-69 node system verifies that the proposed method can effectively obtain the optimal BESSs configuration method.

2 Battery energy storage systems configuration model

2.1 Objective function

In this work, the total investment operating cost of the BESSs, the total load fluctuation of ADN, the total voltage fluctuation of ADN, and the BESSs configuration optimization model based on Pareto can be established as follows:

$$\min \boldsymbol{F}(\boldsymbol{x}) = \min\{F_1,\ F_2, F_3\} \tag{1}$$

where $\boldsymbol{F}(\boldsymbol{x})$ consists of objective functions $\{F_1,\ F_2, F_3\}$, which are the total investment operating cost of the BESSs, total load fluctuation of ADN, and total voltage fluctuation of ADN; $\boldsymbol{x}$ represents the decision space consisting of the optimal installation node location, capacity, and hourly power optimization variables of BESSs and HESSs.

2.1.1 Total investment operating cost

The research object of this work is the ADN that has been built, so the total investment cost of BESS can be described as follow:

$$\min F_1 = \min\left(c_{\mathrm{TCC}} + c_{\mathrm{OM}} - I_{\mathrm{sub}} + (c_{\mathrm{c}} + I_{\mathrm{d}}) + c_{\mathrm{ab}} + c_{\mathrm{loss}} + c_{\mathrm{CE}}\right) \tag{2}$$

where c_{TCC} and c_{OM} are the investment cost, operation cost and maintenance cost of BESS respectively; c_{c}, I_{d} and I_{sub} represent the electricity purchase cost, electricity sales revenue, and government subsidies respectively; c_{ab}, c_{loss} and c_{CE} represent the wind power and solar power abandonment cost, the cost of ADN loss, and the cost of carbon emissions from peak shaving of conventional power sources.

(1) Equivalent investment cost

$$c_{\mathrm{TCC}} = \left[c_{\mathrm{inv}} \cdot N_{\mathrm{BESS}} + \sum\nolimits_{n=1}^{N_{\mathrm{BESS}}} \left(a \cdot P_{\mathrm{BESSs},n} + b \cdot E_{\mathrm{BESSs},n}\right)\right] \cdot \frac{r \cdot (1+r)^{y}}{(1+r)^{y} - 1} \tag{3}$$

where c_{inv} represents a fixed investment construction cost of one BESSs; N_{BESS} represents the number of BESS installed; $E_{\mathrm{BESSs},n}$ and $P_{\mathrm{BESSs},n}$ represent the configuration rated capacity and rated power of the n th BESS respectively; a and b represent the power cost of BESS and the capacity cost under different charging rates respectively; y represents the service life of BESSs. In this work y is 15 years; r represents the discount rate, which value is 6.332%.

(2) Operation and maintenance cost

$$c_{\mathrm{OM}} = \left[\sum\nolimits_{n=1}^{N_{\mathrm{BESS}}} \left(a \cdot P_{\mathrm{BESSs},n} + b \cdot E_{\mathrm{BESSs},n}\right)\right] \cdot \varepsilon_{\mathrm{OM}} \tag{4}$$

where $\varepsilon_{\mathrm{OM}}$ represents the coefficient of operation and maintenance. $\varepsilon_{\mathrm{OM}}$ takes 5% in this work.

(3) Government subsidies

$$c_{\mathrm{cha}} = \sum\nolimits_{m=1}^{M_{\mathrm{d}}} D_m \cdot \left[\sum\nolimits_{n=1}^{N_{\mathrm{BESSs}}} \sum\nolimits_{t=1}^{T} \left(\varepsilon_{\mathrm{p}}(t) \cdot P_{\mathrm{c},n}(t)\right)\right] \tag{5}$$

$$I_{\mathrm{dis}} = \sum\nolimits_{m=1}^{M_{\mathrm{d}}} D_m \cdot \left[\sum\nolimits_{n=1}^{N_{\mathrm{BESSs}}} \sum\nolimits_{t=1}^{T} \left(\varepsilon_{\mathrm{s}}(t) \cdot P_{\mathrm{d},n}(t)\right)\right] \tag{6}$$

$$I_{\mathrm{dis}} = \sum\nolimits_{m=1}^{M_{\mathrm{d}}} D_m \cdot \left[\sum\nolimits_{n=1}^{N_{\mathrm{BESSs}}} \sum\nolimits_{t=1}^{T} \left(\rho \cdot P_{\mathrm{dis},n}(t)\right)\right] \tag{7}$$

where M_{d} represents the number of scenarios; D_m represents the number of days corresponding to scenario m; $\varepsilon_{\mathrm{p}}(t)$ and $\varepsilon_{\mathrm{s}}(t)$ represent the electricity purchase and sale prices of BESSs in period t, respectively; $P_{\mathrm{c},n}(t)$ and $P_{\mathrm{d},n}(t)$ represent the charging and discharging power of the n th BESSs in period t, respectively; T represents the dispatching cycle, which is taken 24 h. ρ represents the operating subsidy given by the government for the electricity sales of BESSs.

(4) Wind and solar abandonment cost

$$c_{\mathrm{ab}} = \sum\nolimits_{m=1}^{M_{\mathrm{d}}} D_m \cdot \left[\sum\nolimits_{t=1}^{T} \Big(P_{\mathrm{wind}}(t) + P_{\mathrm{PV}}(t) - P_{\mathrm{c/d}}(t) - \Big|P_{\mathrm{load}}(t) - P_{\mathrm{loss}}(t)\big)\right] \cdot \delta \tag{8}$$

where $P_{\mathrm{load}}(t)$, $P_{\mathrm{wind}}(t)$ and $P_{\mathrm{PV}}(t)$ represent the load demand, wind power output, and PV output at time t, respectively; $P_{\mathrm{c/d}}(t)$ represents the charge/discharge power of BESSs in period t; $P_{\mathrm{loss}}(t)$ represents the line loss of power in t period; δ represents the cost of wind and solar abandonment on the renewable energy side of the ADN.

(5) Cost of power loss

$$c_{\mathrm{loss}} = \sum\nolimits_{m=1}^{M_{\mathrm{d}}} D_m \cdot \left[\sum\nolimits_{n=1}^{N_{\mathrm{BESSs}}} \sum\nolimits_{t=1}^{T} \left(\varepsilon_{\mathrm{s}}(t) \cdot P_{\mathrm{loss}}(t)\right)\right] \tag{9}$$

(6) Cost of carbon emissions from peak shaving of conventional power sources

$$c_{\mathrm{CE}} = \sum\nolimits_{m=1}^{M_{\mathrm{d}}} D_m \cdot \left[\sum\nolimits_{t=1}^{T} P_{\mathrm{grid}}(t) \cdot \sum\nolimits_{p=1}^{P} \left(U_p \cdot u_p\right)\right], \quad \text{if} \cdots P_{\mathrm{grid}}(t) > 0 \tag{10}$$

where $P_{\mathrm{grid}}(t)$ represents the amount of electricity purchased from the ADN at time t; P represents the number of pollutant types; U_p represents the pollutant p discharge penalty coefficient; u_p represents the emission penalty price of pollutant p.

2.1.2 Total load fluctuation of active distribution network

$$\min F_2 = \min \sum\nolimits_{m=1}^{M_{\mathrm{d}}} D_m \cdot \left[\sum\nolimits_{t=1}^{T} \sqrt{\left(F_{\mathrm{L}}(t) - F_{\mathrm{L}}(t-1)\right)^2}\right] \tag{11}$$

where $F_{\mathrm{L}}(t)$ represents the equivalent load power at time t.

2.1.3 Total voltage fluctuation of active distribution network

$$\min F_3 = \min \sum\nolimits_{m=1}^{M_{\mathrm{d}}} D_m \cdot \left[\sum\nolimits_{j=1}^{N_{\mathrm{nodes}}} \sum\nolimits_{t=1}^{T} \left|V_j(t) - V_{\mathrm{Rated}}\right|\right] \tag{12}$$

where $V_j(t)$ represents the voltage per unit value of j th node at time t; V_{Rated} represents the node-rated voltage, which is 1p.u.

3 Constraints

3.1 Node voltage

$$U_i^{\min} \leq U_i \leq U_i^{\max} \tag{13}$$

where $U_i^{\max}$ and $U_i^{\min}$ represent the maximum and minimum of the node voltage respectively.

$$E_{\mathrm{BESSs}}^{\min} \leq E_{\mathrm{BESSs}} \leq E_{\mathrm{BESSs}}^{\max} \tag{14}$$

where, $E_{\mathrm{BESSs}}^{\max}$and $E_{\mathrm{BESSs}}^{\min}$represent the maximum and minimum of the installed capacity of the BESSs, respectively.

3.2 Installation node

$$N_{\mathrm{BESSs}}^{\min} \leq N_{\mathrm{BESSs}} \leq N_{\mathrm{BESSs}}^{\max} \cdots N_{\mathrm{BESS},1} \neq N_{\mathrm{BESS},2} \tag{15}$$

where $N_{\mathrm{BESSs}}^{\max}$and $N_{\mathrm{BESSs}}^{\min}$represent the maximum and minimum of the location of the BESSs installation node, respectively.

3.3 Wind and solar abandonment

$$R_a = \frac{\sum_{m=1}^{M_{\mathrm{d}}} D_m \cdot \left[\sum_{t=1}^{T} \left(P_{\mathrm{wind}}(t) + P_{\mathrm{PV}}(t) - P_{\mathrm{c/d}}(t) - P_{\mathrm{load}}(t) - P_{\mathrm{loss}}(t)\right)\right]}{\sum_{m=1}^{M_{\mathrm{d}}} D_m \cdot \left[\sum_{t=1}^{T} \left(P_{\mathrm{wind}}(t) + P_{\mathrm{PV}}(t)\right)\right]} \tag{16}$$

$$R_a \leq R_{a,\max} \tag{17}$$

where R_a represents the rate of wind and solar abandonment, which can be calculated by Eq. 16; $R_{a,\max}$ represents the maximum rate of wind and solar abandonment.

4 Non-dominated sorting genetic algorithm-II for optimal battery energy storage systems placement and sizing

4.1 Non-dominated sorting genetic algorithm-II

NSGA-II has diverse populations and high-accuracy optimization results. Firstly, the algorithm uses a fast non-dominated sorting method to classify the population into different ranking levels. Secondly, the crowding distance between individuals with the same ranking level is calculated, and individuals with a larger crowding distance are selected. The results can be evenly distributed in the target space, thus maintaining the diversity of the population. Finally, the optimal solution in the Pareto solution set is effectively saved by the elite strategy (Wu et al., 2014).

(1) Non-dominated solution set ranking

The non-dominated solution in the population can be determined by calculating the value of the objective function. According to the non-dominated level of each individual in the population, the whole population is sorted hierarchically.

(2) Calculate the crowding distance

TABLE 1 The basic principles and procedures of NSGA-II.

```
1: Input the real-time electric power system data;
2: Initialize the parameters and population;
3: Calculate the objective function value $f(k)$ of all the searching individuals by Eqs 2, 3, 4, 5, 6, 7, 8, 9, 10, 11, 12;
4: Determine the non-dominated solution
5:    IF pop(i).DominatedCount = 0;
6:        ELSE q.Rank = $k$+1;
7:    END;
8:    Calculate the crowding distance;
9:    Updating the Pareto front;
10:     [~, RSO] = sort ([pop.Rank]);
11:     [~, CDSO] = sort ([pop.CrowdingDistance],'descend');
12:       For $Gen$ = 1: $Gen_{max}$;
13:           the population crossover, mutation operation to produce offspring populations;
14:           Merger of parent and offspring populations;
15:           According to steps (4)–(12), the non-dominated solutions are selected for the merged population, the crowding degree is calculated, and the Pareto front is updated;
16:           Select the appropriate individuals to form the new population;
17:       End
18:           Judge whether the decision variables exceed the upper and lower bounds, and verify the energy storage charging and discharging power;
19: Output the location and capacity of BESSs.
```

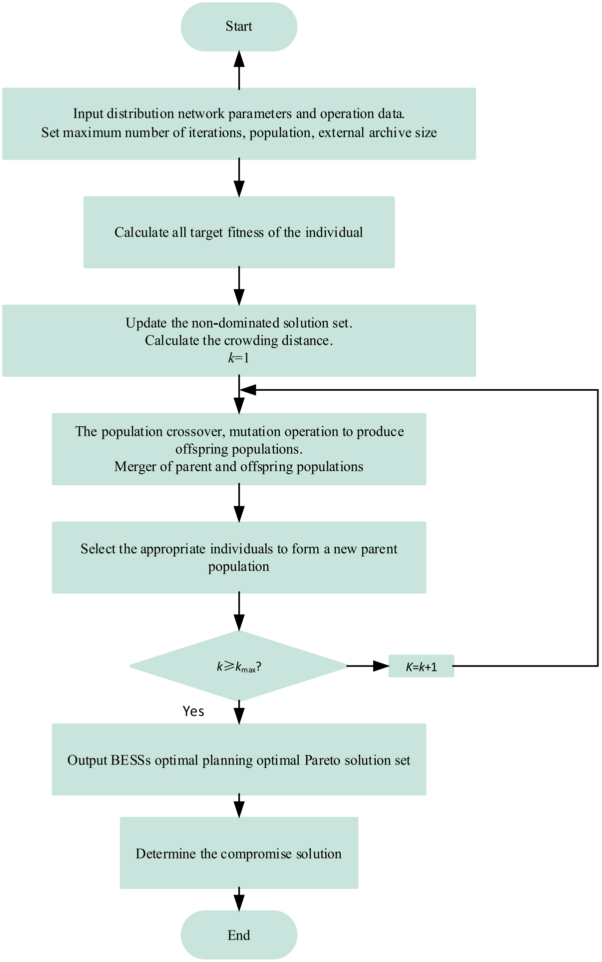

FIGURE 1
The flowchart diagram of the NSGA-II used for BESSs.

To further select individuals at the same non-dominated level, the crowding distance between individuals needs to be calculated.

$$L_d = L_d + \frac{\left[f_n(i+1) - f_n(i-1)\right]}{\left(f_n^{\max} - f_n^{\min}\right)} \tag{18}$$

where L_d represents the crowding distance; $f_n(i+1)$ and $f_n(i-1)$ represent the nth fitness value of the $(i+1)$ th and $(i-1)$ th individual at the same level, respectively; $f_n^{\max}$ and $f_n^{\min}$ represent the maximum and minimum value of the nth fitness function.

Then through the binary tournament selection method, two individuals are randomly selected, and the individuals with higher non-dominated levels can enter the next population. If the level is the same, choose the more crowded population.

(3) Elite strategy selection method

The simulated binary method is used to cross and polynomially mutate the population. Finally, the parent population and offspring population are combined to form a new population. The above steps should be repeated until the maximum number of iterations is reached, and output the Pareto optimal solution set.

4.2 Pareto solution set processing

In the process of NSGA-II algorithm optimization, the Pareto solution set will be continuously updated and put into a limited scale storage pool. When the algorithm iteratively obtains a new non-dominated solution, it needs to compare it with the non-dominated solution set in the storage pool, and then determine whether the new non-dominated solution is liberated into the storage pool. The judgment process is as follows (Faramarzi et al., 2020):

(1) If the new solution dominates the storage pool, it is replaced with the new solution;
(2) If the new solution is dominated by at least one solution in the storage pool, the new solution is discarded;
(3) If there is no dominant relationship between the new solution and the storage pool, the new solution is liberated into the storage pool.

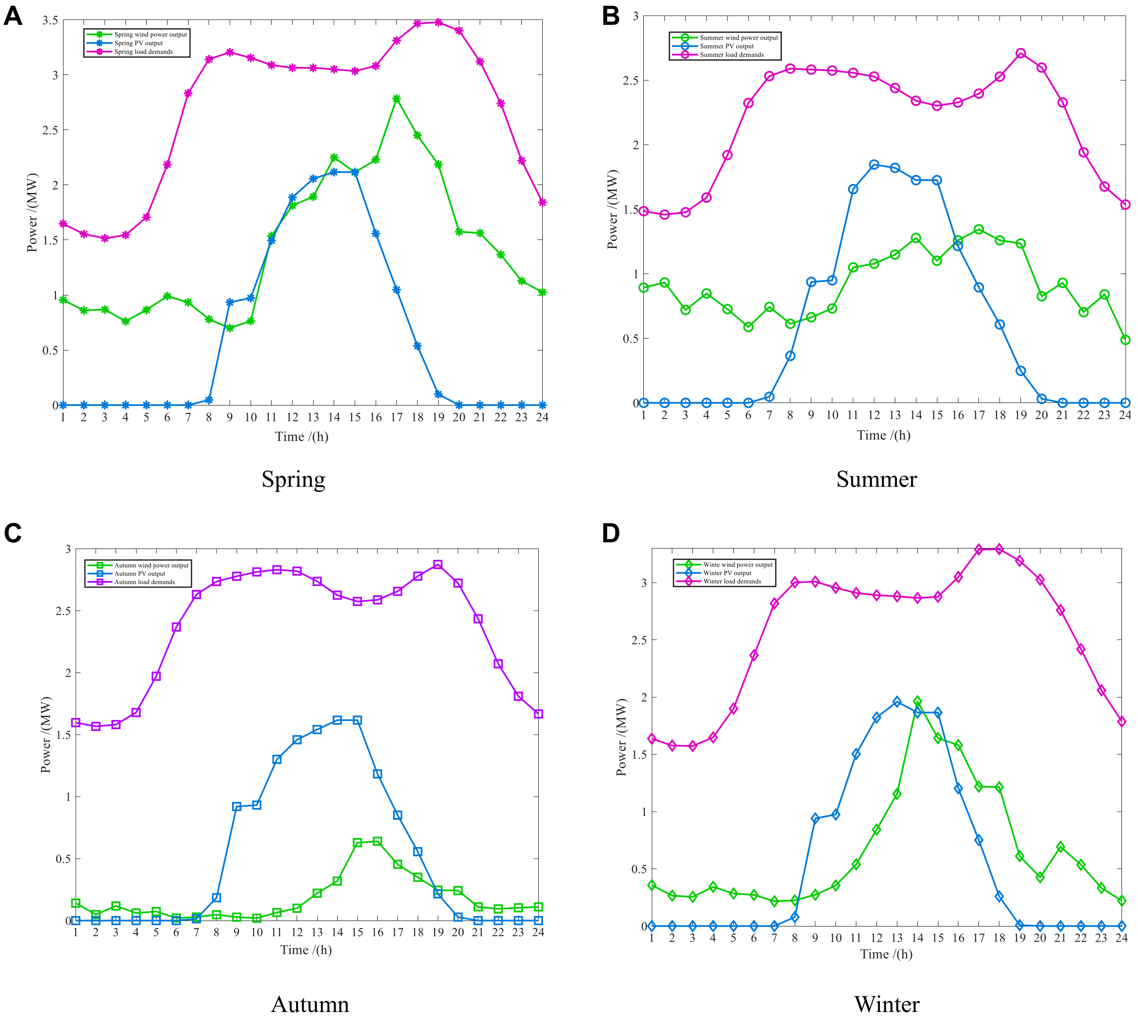

FIGURE 2
Typical diurnal curves of load, wind and PV power. **(A)** Spring. **(B)** Summer. **(C)** Autumn. **(D)** Winter.

TABLE 2 Main parameters of ADN.

ADN parameters	Value
ADN base capacity	10MVA
Total load power	(3.715 + j2.3) MVA
Wind power No. 1, No. 2, and No. 3 active power	0.75 MW
Photovoltaic No.1 Active Power	2.5 MW

To increase the diversity of solutions, when the number of non-dominated solutions in the archive set is higher than the upper limit, the redundant solutions must be removed. In this work, we use the crowded distance ranking method to select a densely distributed set of non-dominated solutions and eliminate redundant solutions by the roulette wheel method.

4.3 Multi-objective gray target decision based on entropy weight method

A multi-objective gray target decision based on the entropy weight method (EWM) is designed. Firstly, the evaluation indexes of each solution are set to build the sample matrix, and the decision matrix can be built by normalizing the sample matrix. Then, the weights of evaluation indexes of all Pareto non-dominated solutions and their distances from the target are obtained based on EWM and their distances from the target, and the solution with the closest distance to the target is determined as the best compromise solution for the BESS optimal allocation scheme (He et al., 2021).

(1) Establishing the sample matrix

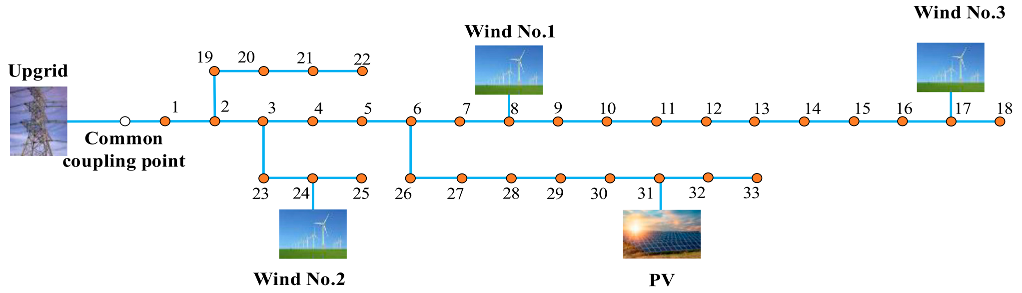

FIGURE 3
Topology of the extended IEEE-33 node test system.

TABLE 3 BESSs optimal configuration scheme.

BESS No.1			BESS No.2		
Node number	Rated capacity/MW·h	Rated power/MW	Node number	Rated capacity/MW·h	Rated power/MW
17	0.1	0.51	16	0.1	0.67

TABLE 4 Comparison before and after BESSs configuration.

	Before BESSs configuration	After BESSs configuration
Daily voltage fluctuation/p.u	12.58	7.7316
Daily load fluctuation/MW	6.604	4.1099
The total cost of BESSs/$		−1.92e+03

To evaluate the similarity and equilibrium of each solution, this method adds two indicators in the sample matrix. One is the Euclidean distance (ED) between each solution and the ideal point, and the other is the Mahalanobis distance (MD) between each solution and the equilibrium point. Therefore, the sample matrix of effects containing five evaluation metrics can be expressed as:

$$\mathbf{Z} = \left(v_g^k\right)_{n\times(m+2)} = [\mathbf{F}, \mathbf{E}, \mathbf{M}] = \begin{bmatrix} F_1^1 & \cdots & F_m^1 & E^1 & M^1 \\ F_1^2 & \cdots & F_m^2 & E^2 & M^2 \\ \cdots & \ddots & \cdots & \cdots & \cdots \\ F_1^n & \cdots & F_m^n & E^n & M^n \end{bmatrix} \tag{19}$$

where **E** and **M** denote the ideal point distance matrix and equilibrium point distance matrix of all solutions, respectively. The ED between the k th solution and the ideal point can be calculated by Eq. 20, and the MD between the k th solution and the equilibrium point can be calculated by Eq. 21.

$$E^k = \sqrt{\sum\nolimits_{g+1}^{m+2}\left(F_g^k - P_g\right)^2} \tag{20}$$

$$M^k = \sqrt{\sum\nolimits_{g=1}^{m}\left(F_g^k - u_g\right)^{\mathrm{T}}\sum\nolimits^{-1}\left(F_g^k - u_g\right)} \tag{21}$$

where P_g denotes the ideal point of the g th objective; u_g represents the average of all solutions under the g th objective; $\sum^{-1}$ is the covariance matrix.

(2) Design of decision matrix

According to the principle of rewarding good and punishing bad, the following operator is designed:

$$q_g = \frac{1}{n}\sum\nolimits_{g=1}^{n} X_g^k \tag{22}$$

where X_g^k represents the evaluation index of the k th solution at the g th objective.

Then the decision matrix is established, as follows:

$$\mathbf{V} = \left(v_g^k\right)_{n\times(m+2)} = \frac{q_g - F_g^k}{\max\left\{\max\limits_{1\le k\le n}\left\{F_g^k\right\} - q_g,\ q_g - \min\limits_{1\le k\le n}\left\{F_g^k\right\}\right\}} \tag{23}$$

The target is identified in the gray decision region formed by the decision matrix as follows:

$$v_g^0 = \max\left\{v_g^k | 1\le k\le n\right\} \tag{24}$$

(3) Grey target decision based on EWM

First, the target weight of the k th scenario under the g th objective can be calculated by Eq. 25

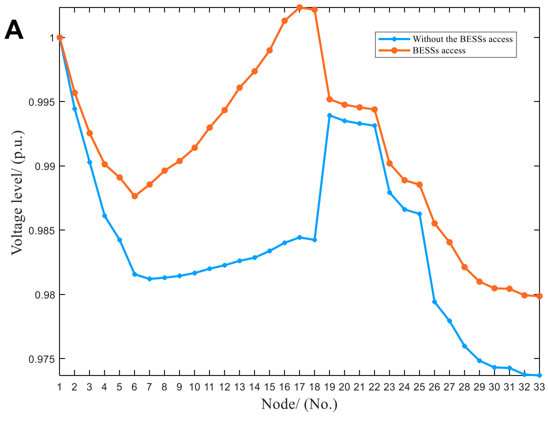

Node voltage level

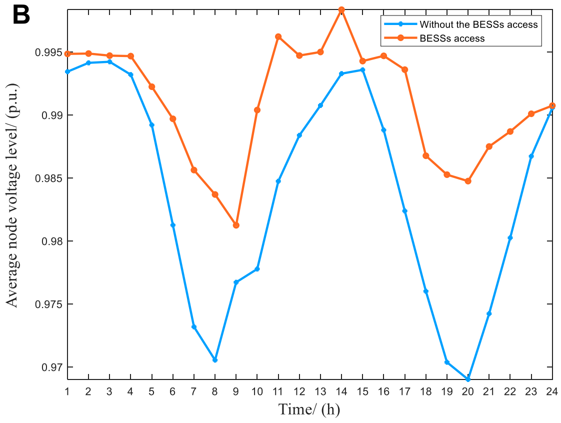

Average node voltage

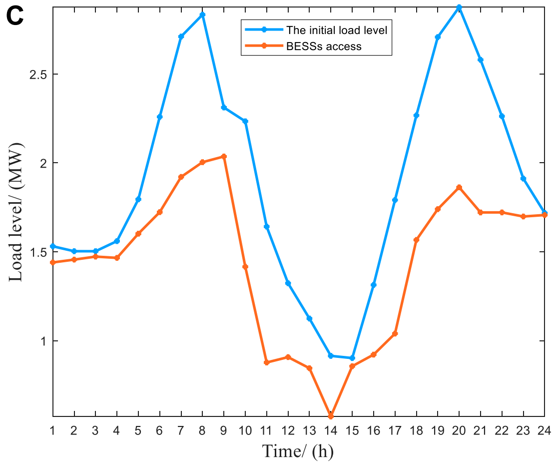

Load level

FIGURE 4
Optimization results of network obtained by NSGA-II in the extended IEEE-33 node test system. **(A)** Node voltage level. **(B)** Average node voltage. **(C)** Load level.

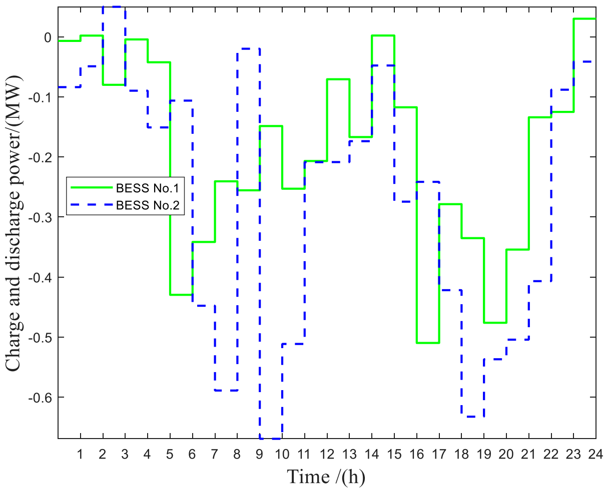

FIGURE 5
BESSs charge and discharge power in a day under IEEE-33 node system.

$$w_g^k = \frac{F_g^k}{\sum_{k=1}^{n} Z_g^k},\ \text{if } F_g^k \geq 0 \tag{25}$$

Next, the entropy values of the g targets can be calculated as follows:

$$EV_g = \frac{1}{\ln n}\sum_{k=1}^{n}\left(w_g^k \cdot \ln w_g^k\right),\ \text{if } EV_g > 0 \tag{26}$$

Among them, the smaller the entropy value of the indicator tends to contain more information, so the entropy weight is larger. The entropy weight of the g th target is calculated as follows.

$$w_g = \frac{1 - EV_g}{\sum_{g=1}^{m+2}\left(1 - EV_g\right)} \tag{27}$$

Then, the distance of each solution to the target can be calculated as follows:

$$MDB^k = \left|v^k - v^0\right| = \sqrt{\sum_{g=1}^{m+2} w_g\left(F_g^k - u_g\right)^{\mathrm{T}} \sum\nolimits^{-1}\left(F_g^k - u_g\right)} \tag{28}$$

Finally, the target distance of each solution is sorted, and the solution closest to the target is selected as the best decision. The specific process of Table 1 NSGA-II solving the optimization problem of BESSs is shown in Figure 1. The basic principles and procedures of NSGA-II are as follows:

5 Fuzzy kernel C-means-based scene clustering

The most well-known and commonly used clustering methods are the K-means (Kanungo et al., 2002) clustering algorithm and

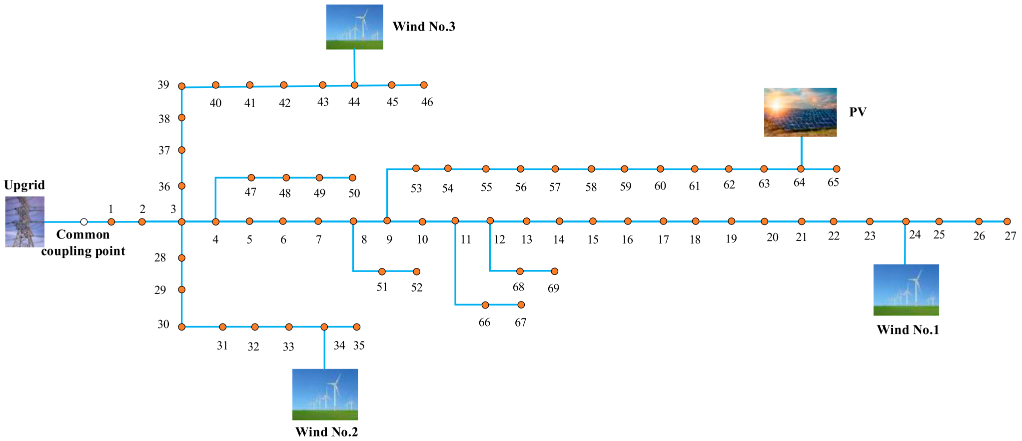

FIGURE 6
Topology of the extended IEEE-69 bus system.

TABLE 5 BESSs optimal configuration scheme.

BESS No.1			**BESS No.2**		
Node number	Rated capacity/MW·h	Rated power/MW	Node number	Rated capacity/MW·h	Rated power/MW
60	0.1	0.44049	62	0.1	0.54119

TABLE 6 Comparison before and after BESSs configuration.

	Before BESSs configuration	**After BESSs configuration**
Daily voltage fluctuation/p.u	36.7	28.605
Daily load fluctuation/MW	6.604	4.1559
The total cost of BESSs/$		−1.2e+03

the fuzzy C-means (FCM) clustering algorithm (Pal and Bezdek, 1995), (Askari, 2021). The K-means is simpler and more efficient, with the advantages of fast convergence and low linear complexity, but it is not applicable when the data set size is large and is sensitive to the initial clustering center. Moreover, its membership degree is either 0 or 1, which is a hard classification. In contrast, the membership degree of the FCM takes any value in the range of [0,1], and the criterion function is differentiable, which can The FCM clustering algorithm has any value in the range of [0, 1], and the criterion function is differentiable so that it can accurately cluster data with the non-convex distribution. To avoid the influence of non-uniform sample distribution on clustering results, this work uses a fuzzy kernel C-means (FKCM) clustering algorithm based on the Mercer kernel function to cluster ADN source-load scenarios.

The clustering principle of the FKCM clustering algorithm in the feature space is to minimize the weighted distance squared between a sample and its clustering center squared sum, which is described as follows:

$$J_m(U,v) = \sum_{i=1}^{c} \sum_{k=1}^{n} u_{ik}^{m} \| \Phi(x_k) - \Phi(v_i) \|^2, \cdots i = 1,2,\ldots,c; \quad k = 1,2,\ldots,n \tag{29}$$

where m represents a constant whose value is greater than 1; c and n are the numbers of clusters and the number of samples; x_k represents the k th sample; v_i represents the center of the i th cluster; u_{ik}^{m} represents the membership degree function of the k th sample in the i th cluster, which satisfies the $0 \le u_{ik}^{m} \le 1$ and $0 < \sum_{k=1}^{n} u_{ik} < 1$; U represents the membership degree matrix.

The typical days of wind power and photovoltaic in each season can be obtained by the FKCM clustering algorithm, and then the clustering results of typical days in each season are combined. Therefore, there are a total of 36 source-load combination scenario sets in the four seasons (for example, spring wind power output 1, spring photovoltaic output 2, and spring load can be combined into one scenario set). Although various ADN operation scenarios can make the planning results more reasonable, it will significantly increase the solution time of the configuration model.

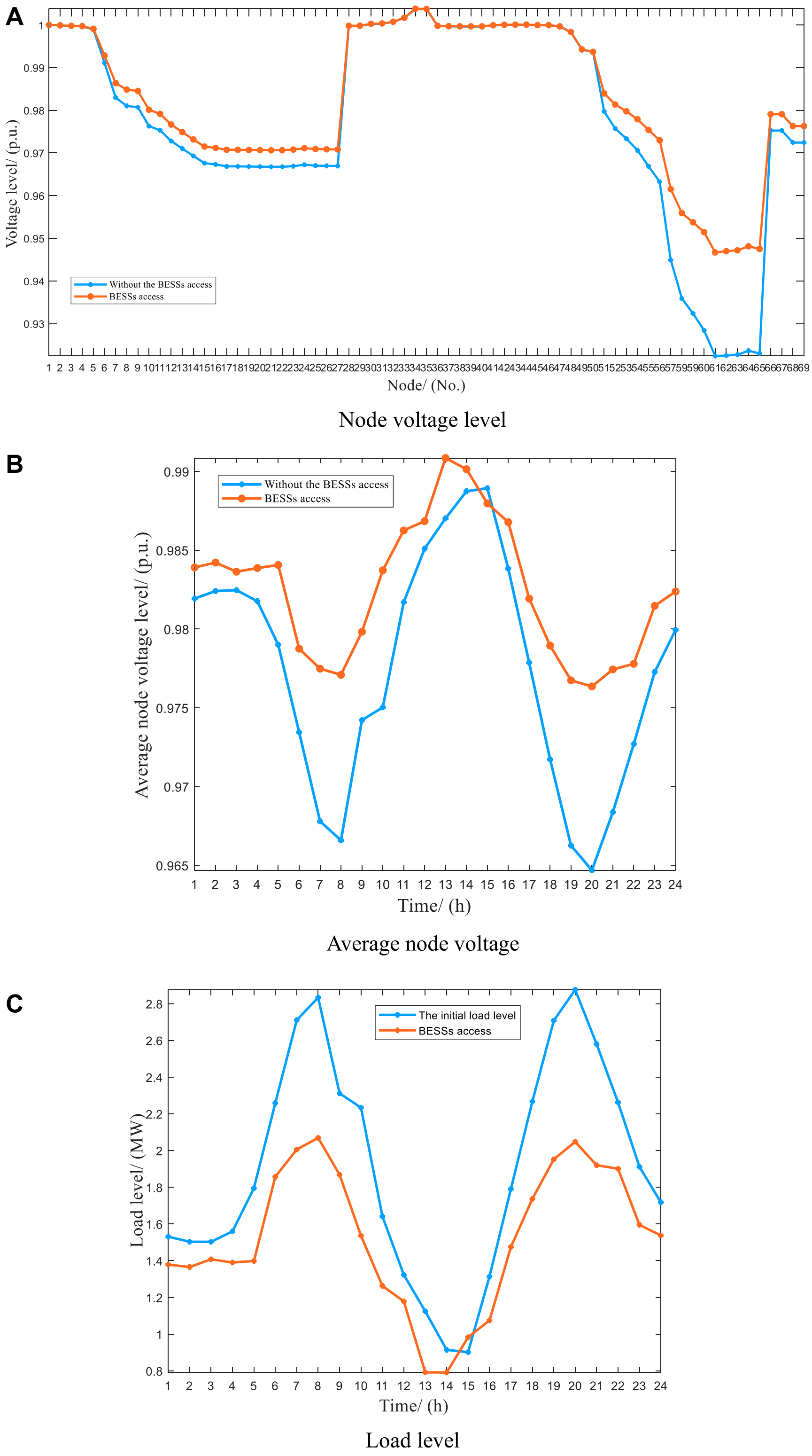

FIGURE 7
Optimization results of network obtained by NSGA-II under the extended IEEE-69 node test system. **(A)** Node voltage level. **(B)** Average node voltage. **(C)** Load level.

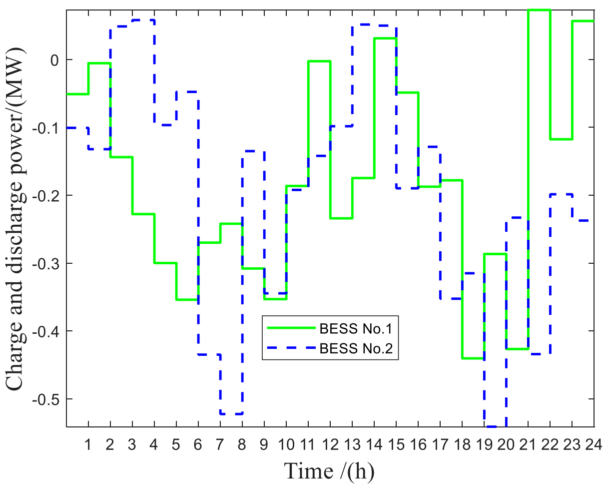

FIGURE 8
BESSs charge and discharge power in a day under the extended IEEE-69 node test system.

Therefore, this paper uses the probability distribution method to reduce the large number of operation scenarios generated based on the FKCM clustering algorithm, and finally fits out the source-load scenarios of four seasons.

First, the probability of each scenario in each season can be calculated as follows:

$$\rho_m = \frac{D_m}{\sum_{m=1}^{M} D_m} \tag{30}$$

where M represents the total number of all scenes in each season; D_m represents the number of days the m th scenario occurs during the season.

Then, based on the probability distribution of each scenario, the typical scenarios of each season are fitted to obtain four scenarios of spring, summer, autumn, and winter considering source-load uncertainty. The scenario fitting for each season is as follows:

$$\begin{cases} \boldsymbol{P}_{\mathrm{F}} = \left[P_{\mathrm{wind,F}}, P_{\mathrm{PV,F}}, P_{\mathrm{load,F}}\right] = \sum_{m=1}^{M} \rho_m \cdot \boldsymbol{P}_m \\ \boldsymbol{P}_m = \left[P_{\mathrm{wind},m}, P_{\mathrm{PV},m}, P_{\mathrm{load},m}\right] \end{cases} \tag{31}$$

where $\boldsymbol{P}_{\mathrm{F}}$ represents the fitted source-load timing power set; $P_{\mathrm{wind,F}}$, $P_{\mathrm{PV,F}}$ and $P_{\mathrm{load,F}}$ represent the wind power, photovoltaic output, and load power of the season after fitting, respectively. $\boldsymbol{P}_m$ represents the source-load sequential power set for scenario m; $P_{\mathrm{wind},m}$, $P_{\mathrm{PV},m}$, $P_{\mathrm{load},m}$ represent the wind power, PV output, and load power in m scenarios, respectively.

TABLE 7 Pareto optimization results of the model obtained by two algorithms.

Test system	Objective function	Value	NSGA-II	MOPSO
IEEE-33	The total cost of BESSs/$	Maximum	−1.72e+03	−22.63
		Minimum	−1.97e+03	−4.45e+03
		Mean	−1.87e+03	−2.34e+03
		Best compromise solution	−1.92e+03	**−2.41e+03**
	Daily voltage fluctuation/p.u	Maximum	7.8422	11.9381
		Minimum	7.6614	7.7188
		Mean	7.7310	9.6892
		Best compromise solution	**7.7316**	9.8524
	Daily load fluctuation/MW	Maximum	4.8069	15.4393
		Minimum	3.4900	4.6473
		Mean	3.9242	8.9457
		Best compromise solution	**4.1099**	6.3323
IEEE-69	The total cost of BESSs/$	Maximum	−841.37	−25.07
		Minimum	−1.35e+03	−1.74e+03
		Mean	−1.11e+03	−1.13e+03
		Best compromise solution	−1.20e+03	**−1.63e+03**
	Daily voltage fluctuation/p.u	Maximum	32.6083	34.1636
		Minimum	26.6522	29.1366
		Mean	28.4256	31.3895
		Best compromise solution	**28.605**	30.417
	Daily load fluctuation/MW	Maximum	5.2573	14.2594
		Minimum	3.9684	8.6910
		Mean	4.3019	10.9530
		Best compromise solution	**4.1559**	11.0400

The bold values represents a better result.

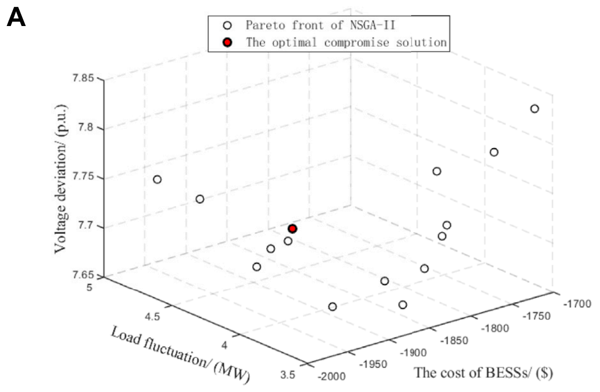

The Pareto front distribution based on the extended IEEE-33-node test system

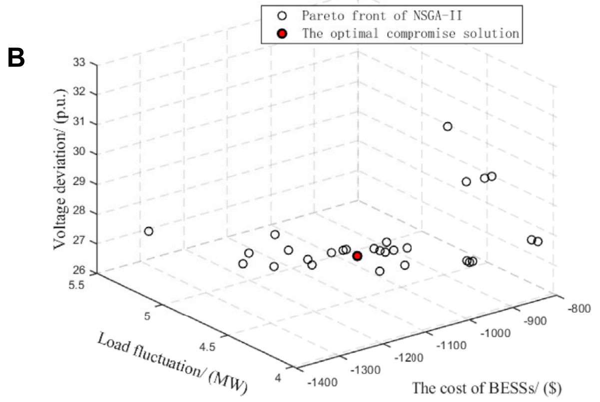

The Pareto front distribution based on the extended IEEE-69-node test system

FIGURE 9
The Pareto front distribution obtained by NSGA-II. **(A)** The Pareto front distribution based on the extended IEEE-33-node test system. **(B)** The Pareto front distribution based on the extended IEEE-69-node test system.

The fitted wind, photovoltaic, and load curves of four typical scenarios in spring, summer, autumn, and winter are shown in Figure 2.

6 Case studies

In this work, the extended IEEE-33 node test system and the extended IEEE-69 node test system are used to prove that NSGA-II can get the correct BESSs configuration scheme. And this scheme can effectively improve the voltage quality problem in ADN caused by the high renewable energy generation penetration rate. Table 2 shows the main parameters of the ADN.

6.1 IEEE-33 node test system

The extended IEEE-33 node test system topology is shown in Figure 3. Wind power No. 1, No. 2, and No. 3 are connected at nodes 8, 24, and 17, respectively, and PV is connected at node 31. Table 1 shows the main parameters of ADN.

Table 3 shows the specific configuration scheme of BESSs. Table 4 shows the numerical changes of specific indicators in ADN before and after the access of the BESSs configuration scheme obtained by NSGA-II. By comparing the data in Table 4, after accessing BESSs, specifically, daily voltage fluctuation decreased by 4.8484 p. u. (the improvement rate is 38.54%), and the load fluctuation decreased by 2.4941 MW (the improvement rate is 37.77%). The total cost of BESSs is $-1.92e+03, which means a profit of $ 1.92e+03 a year after BESSs configuration. Moreover, Figure 4 compares the changes of three technical indicators of the ADN before and after the access of BESSs. As shown in Figure 4A, after BESSs is connected to the active distribution network, the node voltage level generally has an upward trend (at 1p.u. nearby). Meanwhile, it can be seen from Figure 4B that the average voltage fluctuation of nodes in the

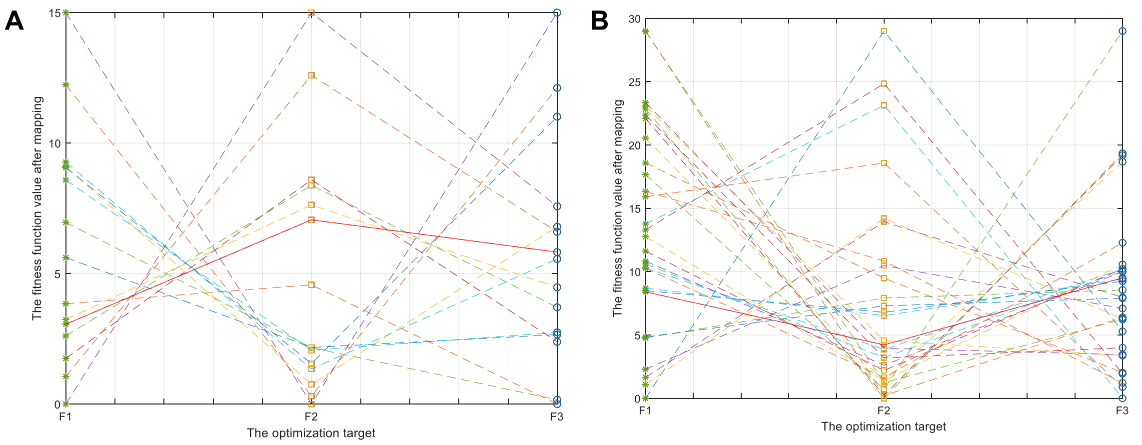

Pareto front after mapping under the extended IEEE-33 node system

Pareto front after mapping under the extended IEEE-69 node system

FIGURE 10
The Pareto front of the parallel coordinate system under the extended IEEE-33 node system and the extended IEEE-69 node system. **(A)** Pareto front after mapping under the extended IEEE-33 node system. **(B)** Pareto front after mapping under the extended IEEE-69 node system.

ADN decreases in 1 day. This means that BESSs can effectively improve the voltage quality of ADN. At last Figure 5 shows the charge and discharge power of BESSs in a day.

6.2 IEEE-69 node test system

The extended IEEE-69 node test system topology is shown in Figure 6. Wind power No. 1, No. 2, and No. 3 are connected at nodes 24, 34, and 44, respectively, and PV is connected at node 64.

Table 5 shows the specific configuration scheme of BESSs. By comparing the data in Table 6, after accessing BESSs, specifically, the daily voltage fluctuation decreased by 8.095 p. u. (the improvement rate is 22.058%), and the load fluctuation decreased by 2.4481 MW (the improvement rate is 37.07%). Moreover, Figure 7 compares the changes in three technical indicators of the ADN before and after the access of BESSs. The total cost of BESSs is $ -1.2e+03. Figure 7 shows the three technical indicators before and after the access of BESSs. In Figure 7A, the node voltage level of node 57-node 65 has been greatly improved, and the curve in Figure 7B also shows that the voltage fluctuation of ADN has been effectively reduced after BESSs access. It can be concluded that by installing BESSs in the ADN, the power quality in the ADN has been improved, and the revenue can be $1.2e+03. And Figure 8 shows the charge and discharge power in a day under the extended IEEE-69 node system.

6.3 Comparison of algorithms

In this section, we use multi-objective particle swarm optimization (MOPSO) as a comparison algorithm to verify the superiority of NSGA-II. Table 7 shows the result obtained by two algorithms.

By comparing the results in Table 7, it can be seen that NSGA-II has the smallest daily voltage fluctuation and daily load fluctuation except for the total cost of BESSs. Meanwhile, the cost results obtained by the two algorithms are not much different. Therefore, it can be concluded that NSGA-II can obtain a more reasonable Pareto non-dominated solution set and provide the best candidate for decision makers.

6.4 Discussion

Figure 9 shows the Pareto front distribution obtained by NSGA-II in the simulation experiments based on the extended IEEE-33 node test system and the extended IEEE-69 node test system. It can be seen from Figure 9 that the NSGA-II can obtain a widely distributed Pareto front. This proves the effectiveness and powerful optimizing ability of NSGA-II algorithm.

To verify the rationality of the EWM-based grey target decision, this work uses the method in Reference (Hu et al., 2014) to map the a th objective function corresponding to the b th non-dominated solution to the two-dimensional plane of (a $\times i$). The equation is as follows:

$$L_{i,a} = K\frac{f_{b,a} - f_a^{\min}}{f_a^{\max} - f_a^{\min}} \tag{32}$$

where K is a random parameter; $f_{b,a}$ represents the a th objective function of the b th non-dominated solution.

Figure 10 shows a two-dimensional plane ($a \times i$) mapped the Pareto front of the extend IEEE-33 node system and the extended IEEE-69 node system through the high-dimensional Cartesian coordinates. The abscissa is the optimized objective function, and the ordinate is the mapped objective function value. The objective functions are connected by a virtual line. The optimal compromise solution of the grey target decision based on EWM is represented by the red solid line. It can be seen that the compromise solution is in a reasonable range, which can avoid a greater preference for a certain goal due to subjective weight. And the distribution of the non-dominated solution set is more extensive, which indicates that NSGA-II algorithm has excellent optimization ability.

It should be noted that at 1 p.m. of Figure 4C and 1 and 2 p.m. of Figure 7C, the load level of the ADN with BESS drops to a very low level. This is because when configuring BESSs, the cost of configuring BESSs is considered an important factor. At 1 and 2 p.m. every day, it is in the peak load period. At this time, the load of the ADN increases, and the BESSs will deliver more electricity to the ADN to obtain more benefits while ensuring the stability of the ADN. The net load P_L of the ADN can be calculated by Eq. 33. As shown in Eq. 33, the increase of electric energy transmitted by BESSs to ADN will lead to a decrease in the net load level of the ADN.

$$P_L = P_{\text{load}} - P_{\text{wind}} - P_{\text{PV}} + P_{\text{BESSs}} \tag{33}$$

where P_{load}, P_{wind} and P_{PV} represent the load demand, wind poaxwer output, and PV output; P_{BESSs} represents the power of BESSs, and its value is negative when it outputs electricity to the ADN.

7 Conclusion

To deal with the low stability of the ADN caused by the high proportion of renewable energy generations, this work proposes a configuration method of a Pareto multi-objective battery ESSs based on NSGA-II to improve the stability of the ADN. The main contributions of this work are:

(1) The clustering algorithm based on FKCM is used to cluster the load and wind-solar output, and four clustering scenarios are obtained.
(2) The grey target decision based on EWM is used to obtain the optimal compromise solution from the Pareto front, to get rid of the unreasonable favoritism caused by weighting multiple objectives with subjective weights.
(3) The extended IEEE-33 node system and the extended IEEE-69 node system are used for simulation experiments. The experimental results show that NSGA-II can balance the economy of BESSs configuration and stabilize the power and voltage levels of the ADN. Therefore, the BESSs configuration scheme obtained by the method described in this work is effective and can improve the stability of ADN operation.

In practice, the scale of ADN is large and more constraints need to be considered, which is a great challenge to the performance of the algorithm. At the same time, the heuristic algorithm has strong randomness, and the best compromise solution obtained each time is different. Therefore, it is more subjective to select the final solution from multiple optimal compromise solutions. However, compared with traditional optimization methods, heuristic algorithms do not require accurate models and a large amount of data. The algorithm structure is simple and efficient, which greatly improves the calculation speed and efficiency, and it is easier to obtain the global optimal solution, making the configuration of ESSs more reasonable. Therefore, considering the accuracy, effectiveness and time cost of the algorithm, the heuristic algorithm has more advantages than other traditional methods.

In future research, the NSGA-II algorithm will be applied to the BESSs planning problem considering the demand side response and the optimization problem of the electricity-hydrogen hybrid ESSs.

Data availability statement

The original contributions presented in the study are included in the article/supplementary material, further inquiries can be directed to the corresponding author.

Author contributions

RS: writing the manuscript; GH: discussion of the objective functions; SS: discussion of the constrains; YD: discussion of the algorithm; JC and HC: completion of the experimental test; KW: editing; CZ: discussion of the topic.

Acknowledgments

The authors gratefully acknowledge the support of Enhancement Strategy of Multi-type Energy Integration of Active Distribution Network (YNKJXM20220113).

Conflict of interest

RS, GH, SS, YD, JC, HC, KW, and CZ were employed by Dali Power Supply Bureau of Yunnan Power Grid Co., Ltd., Electric Power Research Institute of Yunnan Power Grid Co., Ltd., Grid Planning Research Center of Yunnan Power Grid Co., Ltd.

Publisher's note

References

Askari, S. (2021). Fuzzy C-Means clustering algorithm for data with unequal cluster sizes and contaminated with noise and outliers: Review and development. *Expert Syst. Appl.* 165, 113856. doi:10.1016/j.eswa.2020.113856

Bin, Y., Xu, L., Wang, J., Zhu, S. Y., Qiu, X. F., Yin, C. X., et al. (2019). Research on investment input-output benefit of distribution network planning considering micro-grid and multi-load development under the new power reform. *IOP Conf. Ser. Earth Environ. Sci.* 237 (6), 062013–62013. doi:10.1088/1755-1315/237/6/062013

Chen, X. L. (2020). *Operational reliability evaluation of power generation and transmission combined system considering multiple meteorological elements and retired battery energy storage*. Chongqin, China: Chongqing University, doi:10.27670/d.cnki.gcqdu.2020.000145

Company, B. P. (2021). *Statistical review of world energy 2021*. https://www.bp.com/en/global/corporate/energy-economics/statistical-review-of-world energy.html.[R/OL]. [2021-07-09]

Das, C. K., Bass, O., Kothapalli, G., Mahmoud, T. S., Habibi, D., Hu, D. C., et al. (2018). Overview of energy storage systems in distribution networks: Placement, sizing, operation, and power quality. *Renew. Sustain. Energy Rev.* 91, 1205–1230. doi:10.1016/J.RSER.2018.03.068

Dong, X., Wu, J., Xu, Z. B., Liu, K., and Guan, X. (2022). Optimal coordination of hydrogen-based integrated energy systems with combination of hydrogen and water storage. *Appl. energy* 308, 118274. doi:10.1016/j.apenergy.2021.118274

Faramarzi, A., Heidarinejad, M., Stephens, B., and Mirjalili, S. (2020). Equilibrium optimizer: A novel optimization algorithm. *Knowl. Based. Syst.* 191, 105190. doi:10.1016/j.knosys.2019.105190

Fu, L., Dong, L. T., and Zhang, Y. (2022). Research on optimal configuration of energy storage system in distribution network considering voltage quality. *Electr. Autom.* 44 (1), 24–26. doi:10.3969/j.issn.1000-3886.2022.01.008

Ghatak, S. R., Sannigrahi, S., and Acharjee, P. (2019). Multi-objective approach for strategic incorporation of solar energy source, battery storage system, and DSTATCOM in a smart grid environment. *IEEE Syst. J.* 13, 3038–3049. doi:10.1109/JSYST.2018.2875177

He, T. Y., Li, S. N., Wu, S. J., Li, C., and Xu, B. (2021). Biobjective optimization-based frequency regulation of power grids with highparticipated renewable energy and energy storage systems. *Math. Problems Eng.* 2021, 1–16. doi:10.1155/2021/5526492

Hu, D. C., Zhang, S., Han, T., et al. (2022). Low-carbon transition path of power generation sector under carbon neutral target. *Clean. Coal Technol.* 28, 23–33. doi:10.13226/j.issn.1006-6772.cn22032102

Hu, W., Yen, G. G., and Zhang, X. (2014). Multiobjective particle swarm optimization based on Pareto entropy. *J. Softw.* 25 (5), 1025–1050. doi:10.13328/j.cnki.jos.004496

Kanungo, T., Mount, D. M., Netanyahu, N. S., Piatko, C., Silverman, R., and Wu, A. (2002). An efficient k-means clustering algorithm: Analysis and implementation. *IEEE Trans. Pattern Anal. Mach. Intell.* 24 (7), 881–892. doi:10.1109/TPAMI.2002.1017616

Lee, T. Y., and Chen, N. M. (1995). Determination of optimal contract capacities and optimal sizes of battery energy storage systems for time-of-use rates industrial customers. *IEEE Trans. energy Convers.* 10 (3), 562–568. doi:10.1109/60.464883

Li, J. L., Guo, Z. D., Ma, S. L., et al. (2022). Summary of "Source-Network-Load Storage" architecture and evaluation system in new power system. *High. Volt. Eng.*, 1003–6520. doi:10.13336/j.1003-6520.hve.20220532

Li, Y., Feng, B., Li, G. Q., Qi, J., Zhao, D., and Mu, Y. (2018). Optimal distributed generation planning in active distribution networks considering integration of energy storage. *Appl. Energy* 210, 1073–1081. doi:10.1016/j.apenergy.2017.08.008

Li, Y., Feng, B., Wang, B., and Sun, S. (2022). Joint planning of distributed generations and energy storage in active distribution networks: A Bi-level programming approach. *Energy* 245, 123226. doi:10.1016/j.energy.2022.123226

Liu, M. J., Li, W. R., and Wang, S. C. (2016). Reliability evaluation of microgrid with tidal power generation and battery storage in islanded mode. *Power Autom. Equip.* 36 (11), 33–39. doi:10.16081/j.issn.1006-6047.2016.11.005

Meng, Q. Q., Li, X. Q., Yu, H. F., et al. (2021). Optimal planning of energy storage power station considering source-charge uncertainty. *Acta Energiae Solaris Sin.* 42 (10), 415–423. doi:10.19912/j.0254-0096.tynxb.2019-1023

Pal, N. R., and Bezdek, J. C. (1995). On cluster validity for the fuzzy c-means model. *IEEE Trans. Fuzzy Syst.* 3 (3), 370–379. doi:10.1109/91.413225

Ren, Z. P., Lu, B. C., Zhao, Y. L., et al. (2019). Modeling and simulation of photovoltaic virtual synchronous generator. *Power Syst. Prot. Control* 47 (13), 92–99. doi:10.19783/j.cnki.pspc.180963

Shi, W. H., Qu, J. X., Luo, K., et al. Grid-integration and operation of high-proportioned new energy. *Strategic Study CAE* 2022, 1–12. doi:10.15302/J-SSCAE-2022.07.006

Su, H. F., Hu, M. J., and Liang, Z. R. (2016). Distributed power planning with energy storage device based on timing characteristics. *Power Autom. Equip.* 36 (6), 56–63. doi:10.16081/j.issn.1006-6047.2016.06.009

Wu, Q., Luo, J., and Lin, J. (2014). Production job multi-objective scheduling optimization based on set pair analysis and NSGA-II. *Appl. Res. Comput.* 31 (5), 1414–1417. doi:10.3969/j.issn.1001-3695.2014.05.031

Wu, Y. J., Liang, X. Y., Huang, T., Lin, Z., Li, Z., and Hossain, M. F. (2021). A hierarchical framework for renewable energy sources consumption promotion among microgrids through two-layer electricity prices. *Renew. Sustain. Energy Rev.* 145, 111140. doi:10.1016/j.rser.2021.111140

Wu, Y. J., Lin, Z. W., Liu, C. J., Chen, Y., and Uddin, N. (2021). A demand response trade model considering cost and benefit allocation game and hydrogen to electricity conversion. *IEEE Trans. Ind. Appl.* 58, 2909–2920. doi:10.1109/TIA.2021.3088769

Wu, Y. J., Lin, Z. W., Liu, C. J., Huang, T., Chen, Y., Ru, Y., et al. (2022). Resilience enhancement for urban distribution network via risk-based emergency response plan amendment for ice disasters. *Int. J. Electr. Power & Energy Syst.* 141, 108183. doi:10.1016/j.ijepes.2022.108183

Xiao, L. Y., and Pan, J. F. Suggestions on building a wide area virtual power plant based on photovoltaic power generation and physical energy storage. *Bull. Chin. Acad. Sci.* 2022, 549–558. doi:10.16418/j.issn.1000-3045.20220120001

Yan, Z. M., Wang, C. M., Zheng, J., et al. (2013). Value assessment model of battery energy storage system in distribution network. *Electr. Power Autom. Equip.* 33 (2), 57–61. doi:10.3969/j.issn.1006-6047.2013.02.010

Yang, B., Wang, J. T., Chen, Y. X., Li, D., Zeng, C., et al. (2020). Optimal sizing and placement of energy storage system in power grids: A state-of-the-art one-stop handbook. *J. Energy Storage* 32, 101814. doi:10.1016/j.est.2020.101814

Yang, B., Yu, L., Chen, Y. H., Ye, H., Shao, R., Shu, H., et al. (2021). Modelling, applications, and evaluations of optimal sizing and placement of distributed generations: A critical state-of-the-art survey. *Int. J. Energy Res.* 45 (3), 3615–3642. doi:10.1002/er.6104

Zandalinas, S. I., Fritschi, F. B., and Mittler, R. (2021). Global warming, climate change, and environmental pollution: Recipe for a multifactorial stress combination disaster. *Trends Plant Sci.* 26 (6), 588–599. doi:10.1016/j.tplants.2021.02.011

Zheng, Z. D. (2018). Analysis of application mode and control strategy of battery energy storage system to reduce light abandonment in photovoltaic power station. *Electr. Energy Effic. Manag. Technol.* 23, 58–61–78. doi:10.16628/j.cnki.2095-8188.2018.23.011

frontiers | Frontiers in Energy Research

TYPE Original Research
PUBLISHED 11 January 2023
DOI 10.3389/fenrg.2022.1035781

OPEN ACCESS

EDITED BY
Yingjun Wu,
Hohai University, China

REVIEWED BY
Cheng Chi,
Hong Kong University of Science and Technology, Hong Kong SAR, China
Qiang Xing,
Southeast University, China

*CORRESPONDENCE
Huang Kun,
634596964@qq.com

SPECIALTY SECTION
This article was submitted to Smart Grids, a section of the journal Frontiers in Energy Research

RECEIVED 03 September 2022
ACCEPTED 30 September 2022
PUBLISHED 11 January 2023

CITATION
Kun H, Rong C, Jingtao Z, Xundong G and Guodong H (2023), Analysis of current protection in distribution networks with clean energy access.
Front. Energy Res. 10:1035781.
doi: 10.3389/fenrg.2022.1035781

Analysis of current protection in distribution networks with clean energy access

Huang Kun[1,2]*, Cai Rong[3], Zhao Jingtao[2], Gong Xundong[3] and Huang Guodong[3]

[1]School of Electronic Science and Engineering, Southeast University, Nanjing, China, [2]NARI Technology Co., Ltd., NARI Group Corporation, Nanjing, China, [3]Suzhou Power Supply Company, State Grid Jiangsu Electric Power Co., Ltd., Suzhou, China

With the rapid development of the new energy industry, distributed generation (DG) is connected to the power grid on a large scale, and the traditional relay protection scheme is no longer suitable for modern power systems. In order to solve this problem, this paper establishes a mathematical model of the equivalent circuit of distributed photovoltaic power supply according to the external characteristics of photovoltaic cells, and analyzes its volt-ampmeter characteristics and voltage output characteristics of power supply. On this basis, it analyzes and puts forward the control mode of DG when the distribution network is faulty. On the basis of the study, this article has double feeder distribution network as an example, the analysis when the line fault occurring at different extents of DG connected to different position on the influence of the distribution network current protection, the results show that when answering DG side in the feeder bus for distribution network of current protection, pick a smaller effect on both ends of feeder, has a certain symmetry. Finally, the accuracy of theoretical analysis is verified by establishing a simulation model in PSCAD.

KEYWORDS

renewable energy sources, modern power system, distributed power supply, photovoltaic (pv) power supply, distribution network failure, current protection

1 Introduction

With the rapid development of society, economy and technology, the global ecological environment has been seriously damaged, and the climate issue has attracted great attention from all sides of society. Vigorously developing clean energy and improving energy use structure is one of the important ways to deal with environmental and climate problems. In 2021, China's photovoltaic power generation was 325.9 billion KWH, an increase of 64.8 billion KWH over the previous year, a year-on-year growth of 24.8%, accounting for about 4.0% of the country's total annual electricity generation. In 2021, China's cumulative installed capacity of photovoltaic power generation was 306.56 million kW, a year-on-year growth of 21%; China's newly installed PV capacity was 54.93 GW, up 14 percent year on year (Energy and the Environment, 2021). In the same time other clean energy technologies in our country have also been expanded and applied massively. Continuing to develop clean energy in the future will be an important contribution to optimizing energy structure, realizing "double carbon" target and promoting global environmental construction (Ming et al., 2014).

But as clean power sources, mainly photovoltaic, are connected to the distribution grid on a large scale, the structure of the distribution network has changed from the original single power supply radiant network to bidirectional multi-power network (Wu et al., 2021a), and the power flow and system short-circuit current of the power grid have changed. Therefore, the original protection scheme applicable to the traditional distribution network cannot be directly applied to the distribution network with distributed power access, so it is very necessary to analyze the influence of distributed power access on the protection device of distribution network.

In view of the above problems, researchers at home and abroad have carried out research and analysis from different aspects, and achieved good results. Literature (Calderaro et al., 2009; Liqun et al., 2020; Yin et al., 2020) takes the distribution system with a single distributed power supply as an example. By exploring the characteristics of photovoltaic output, voltage and current changes at the grid-connected end of photovoltaic are controlled based on island detection, so as to achieve the relay protection goal of distribution network. In literature (Alcala-Gonzalez et al., 2021; Ni et al., 2022), the equivalent model of photovoltaic power station was established and its short-circuit fault characteristics were simulated and analyzed to study the influence of different photovoltaic access capacity on the short-circuit level of regional power grid. Literature (Luning, 2019; Wu et al., 2022) proposed a new distributed power consumption model based on the dynamic reconstruction of distribution network. The model comprehensively considered the load demand change in each period, the uncertainty of distributed power output and the switching times, and established the optimization objective of maximizing the photovoltaic absorption ratio and minimizing the switching times. Literature (Yongfei et al., 2016; Xuekai et al., 2019) analyzes the transient process of inverter and the output characteristics of distributed power supply during reclosing operation based on the dynamic characteristics of distributed power lock loop during reclosing operation, and discusses the influence of photovoltaic access on reclosing. Finally, the reclosing configuration method considering distributed power supply access is given, which has good practical value. Based on the definition and characteristics of distributed power generation, literature (Yongfei et al., 2016; Xiao, 2018) explores the influence of distributed power access on relay protection of distribution network, but the content is theoretical and no specific simulation is used to verify the applicability of the proposed scheme. Literature (Azeroual et al., 2022) proposed a new method for fault location and autonomous recovery of distributed distribution system based on multi-agent system, and tested the proposed protection method by using the open-loop feeder distribution system in Kenitra, Morocco. In addition, the impact of DG integration on fault location and multiple faults is addressed. In this study, with suitable backup protection given *via* agent coordination.

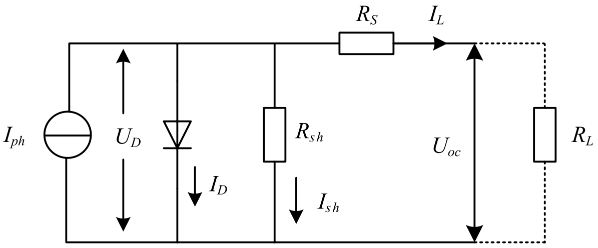

FIGURE 1
Equivalent circuit model of photovoltaic cell.

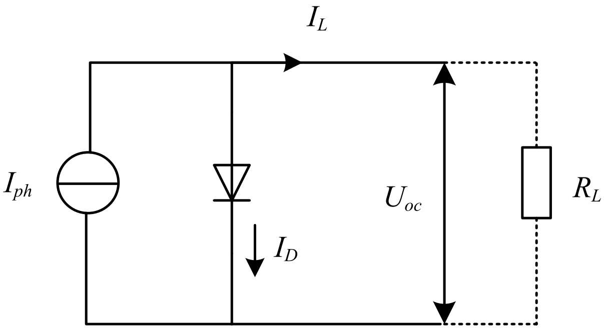

FIGURE 2
Simplified model of equivalent circuit of photovoltaic cell.

Through the above analysis we is not hard to find, after the DG interconnection of traditional relay protection scheme is not fully used and difficult to meet the requirements of the safe and stable operation of power grid, the current due to a variety of proposed methods in our study is limited by its own limitations, lack of strong general protection scheme is one of the important reasons, limit development of DG interconnection large-scale Therefore, it is very important to study the protection method of distribution network with DG access.

2 Modeling and operating characteristic analysis of distributed photovoltaic power generation

2.1 Structure modeling of distributed photovoltaic power generation

The smallest component unit of photovoltaic array of distributed photovoltaic power generation is photovoltaic cell, which generates current through photogenerating volt effect

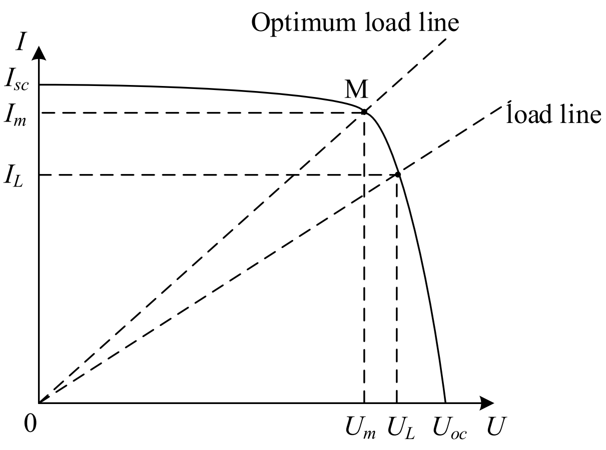

FIGURE 3
Voltammetric characteristic curve of photovoltaic cell.

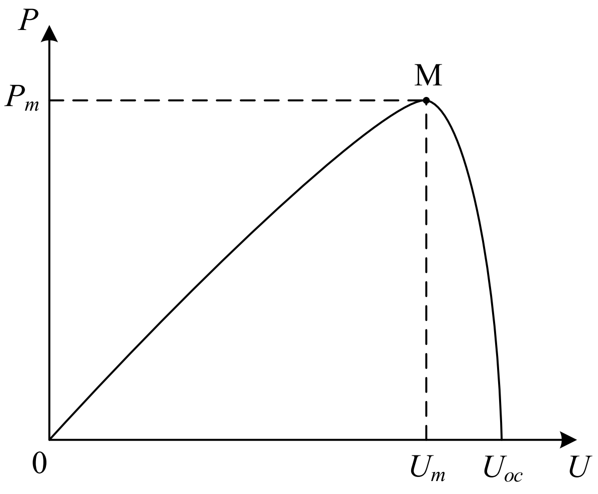

FIGURE 4
Pv cell power-voltage output characteristic curve.

(Mingjun, 2018; Hong and Hongbo, 2020). The equivalent circuit model of photovoltaic cell is established according to the external characteristics of photovoltaic cell, as shown in Figure 1.

Figure 1 shows that the equivalent circuit of photovoltaic cell consists of a current source in parallel with an ideal diode, and is connected with a series resistor and a parallel resistor. According to the characteristics of PN junction of the diode, the mathematical model of photovoltaic cell can be obtained as shown in Eqs 1–6:

$$\boldsymbol{I_L = I_{ph} - I_D - I_{sh}} \tag{1}$$

$$\boldsymbol{I_D = I_0\left[exp\left(\frac{qU_D}{AkT}\right) - 1\right]} \tag{2}$$

$$\boldsymbol{I_L = I_{ph} - I_0\left[exp\left(\frac{qU_D}{AkT}\right) - 1\right] - \frac{U_D}{R_{sh}}} \tag{3}$$

$$\boldsymbol{U_D = U_{oc} + I_L R_s} \tag{4}$$

$$\boldsymbol{I_{sc} = I_0\left[exp\left(\frac{qU_{oc}}{AkT}\right) - 1\right]} \tag{5}$$

$$\boldsymbol{U_{oc} = \frac{AkT}{q} ln\left(\frac{I_{sc}}{I_0} + 1\right)} \tag{6}$$

Where, I_L is the external output current of photovoltaic cell, I_{ph} is the current generated by photovoltaic cell through photogenerating volt effect, I_D is the internal dark current that photovoltaic cell flows through the diode, I_{sh} is the current that flows through the parallel resistor R_{sh}, I_0 is the reverse saturation current of the diode, q is the electronic load, $q = 1.6 \times 10^{-19}$C, U_D is the voltage at both ends of the diode, A is the fitting coefficient of the characteristic curve of the PN junction of the diode, k is the Boltzmann constant, $k = 1.38 \times 10^{-23}$ J/K, T is the absolute temperature of the operating environment, R_{sh} is the equivalent parallel resistance of the photovoltaic cell, U_{oc} is the open circuit voltage of the photovoltaic cell, R_L is the external load resistance of the photovoltaic cell, R_s is the equivalent series resistance of photovoltaic cells, and I_{sc} is the internal short-circuit current of photovoltaic cells.

Since the internal equivalent series resistance of photovoltaic cells is small (generally less than 1 Ω), while the resistance value of parallel resistance is large, the above resistance can be ignored under ideal conditions, and the equivalent circuit of photovoltaic cells can be further simplified into the model shown in Figure 2.

According to the simplified equivalent circuit model of photovoltaic cell, Eqs 1–6 are simplified, and the simplified mathematical model of photovoltaic cell can be obtained as follows:

$$\boldsymbol{I_L = I_{ph} - I_D} \tag{7}$$

$$\boldsymbol{P = U_L I_L = U_L I_{ph} - U_L I_0\left[exp\left(\frac{qU_L}{AkT}\right) - 1\right]} \tag{8}$$

Where U_L is the external output DC voltage of the photovoltaic cell, and P is the output power of the photovoltaic cell.

2.2 Operating characteristics of distributed photovoltaic power generation

Voltammetric characteristics of photovoltaic cells are shown in Figure 3. The intersection point of the curve with the current axis is the circuit current I_{sc} of photovoltaic cells, and the intersection point with the electric voltage axis is the open circuit voltage U_{oc}. The point M in the curve enables photovoltaic cells to output the maximum power when operating with the current and voltage at this point, which is called the maximum power point. The photovoltaic cell output current I_m is the best output current, and the voltage at this point

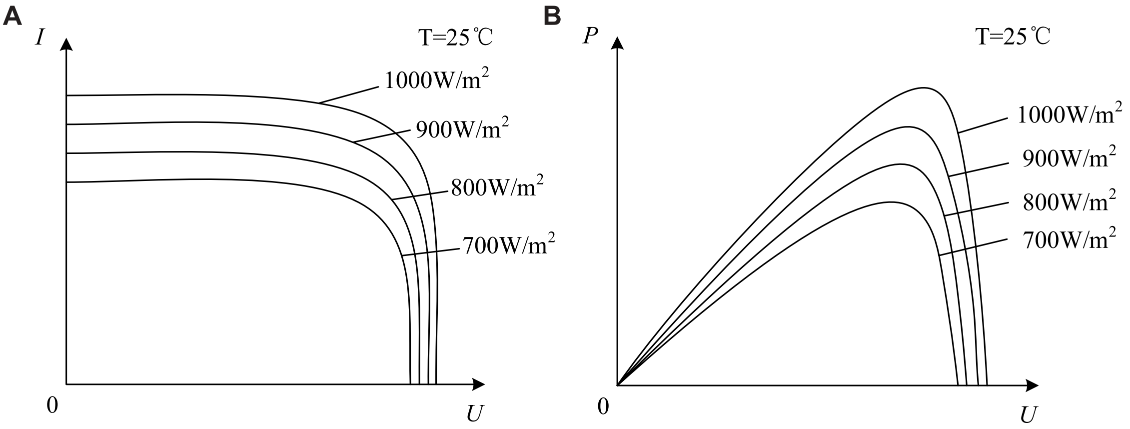

FIGURE 5
Output characteristics of photovoltaic cells under the same temperature and different light intensities. **(A)** Voltammetry characteristic curve. **(B)** Power voltage characteristic curve.

U_m is the best output voltage. From the origin, several lines can be drawn that intersect the I-U curve. These lines are called load lines with a slope of $1/R_L$. Among several load lines, there is only one line that intersects point M. The load line is called the optimal load line, and its slope is $1/R_m$. In this case, the external load resistance of the photovoltaic cell $R_L = R_m$.

The power-voltage output characteristics of photovoltaic cells are shown in Figure 4 (Yongfei et al., 2016). According to the figure, the output power and voltage transmission of photovoltaic cells have nonlinear characteristics. When the voltage is less than the maximum power point voltage, the output characteristics of photovoltaic cells are similar to current sources. When the voltage is greater than the maximum power point voltage, the photovoltaic cell output characteristics are similar to the voltage source.

To sum up, the maximum output power P_m of photovoltaic cells is expressed as:

$$\boldsymbol{P_m = I_m U_m} \tag{9}$$

Photovoltaic cells are easily affected by various external factors in actual operation, among which the solar illumination intensity and working environment temperature have a particularly significant impact on their output characteristics. Figure 5 for the different light intensity on pv cells at the same temperature volt-ampere characteristic and power—voltage output characteristic influence diagram, the output voltage is equal, with the increasing of light intensity, the photovoltaic battery output power and output current increase, at the same time, the light intensity has significant effects on short circuit current and open circuit voltage effect is relatively small.

Figure 6 for the same light intensity under different temperature on the pv cells volt-ampere characteristic and power—the influence of the voltage output characteristics, along with the temperature rising, the photovoltaic battery output power and output current showed a trend of decrease, but the overall degree of change is small, at the same time, the temperature has significant effects on the open circuit voltage and short circuit current effect is relatively small.

Through the above analysis shows that works in different light intensity and environment temperature the volt-ampere characteristic and power of the photovoltaic cells—voltage characteristic each are not identical, location of maximum power point is different also, in order to keep the pv cells can under different light and temperature can be maximum power output, you need to use the maximum power point tracking technology to control the pv cells.

2.3 Distributed photovoltaic grid-connected control mode

Because photovoltaic power generation outputs direct current by using the photogenerated volt effect of photovoltaic array solar cells, it must be converted into alternating current by inverters before it can be incorporated into the power grid. There are various control methods in the grid-connected inverter process of distributed photovoltaic power generation. In this paper, the PQ control method is adopted. The voltage and frequency are given by the grid, and the output power is guaranteed to be given by controlling the current. Therefore, in essence, PQ control is a kind of current control. Figure 7 shows the droop characteristics of system frequency and voltage under the PQ control mode. It can be seen that the active and reactive power of DG can be kept constant within the dynamic variation range of frequency and output voltage by using the PQ control mode. When the DG is connected to the power grid, the

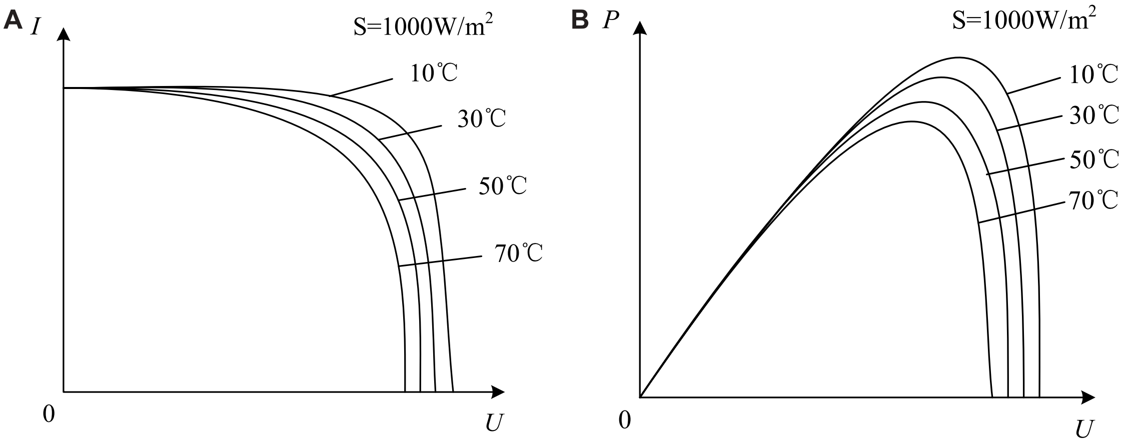

FIGURE 6
Output characteristics of photovoltaic cells at different temperatures under the same light intensity. **(A)** Voltammetry characteristic curve. **(B)** Power voltage characteristic curve.

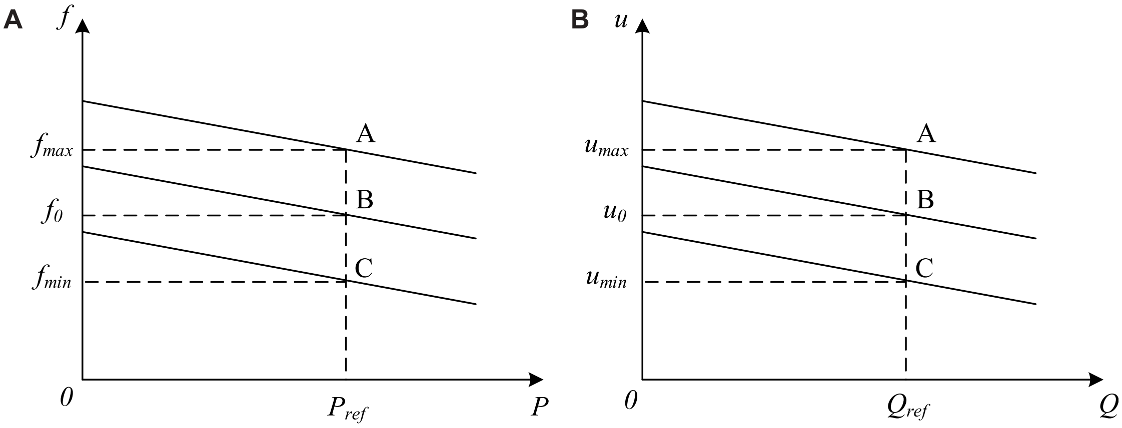

FIGURE 7
System frequency and voltage droop characteristics under PQ control. **(A)** Frequency droop characteristic. **(B)** Voltage droop characteristic.

frequency and voltage are maintained stable by the distribution network system itself.

The process of distributed photovoltaic grid-connected control using PQ control is shown in Figure 8. In Figure 8, the photovoltaic array first generates DC through the photovoltaic effect, and then converts DC to AC through the three-phase inverter after the voltage is raised by the Boost circuit. After the filtering is completed, it meets the power quality requirements of photovoltaic grid-connected, and then it is connected to the distribution network for operation. Among them, the inverter adopts PQ control strategy to make the active power and reactive power output of DG equal to the reference value given by the system. The instantaneous current i_{abc} and the instantaneous voltage e_{abc} of the common connection point are respectively subjected to Parker transform to obtain i_d, i_q, e_d, and e_q. The outer loop control is compared with the given reference power and PI is used to control the error, and then the reference currents i_{dref} and i_{qref} are obtained. Similarly, by comparing the inner loop control of the current with id and i_q, The difference is controlled by PI, and the output reference voltages u_{dref} and u_{qref} are obtained through Parker inverse transformation to obtain the three-phase component in the abc coordinate system. Finally, the three-phase inverter is controlled through PWM pulse width modulation.

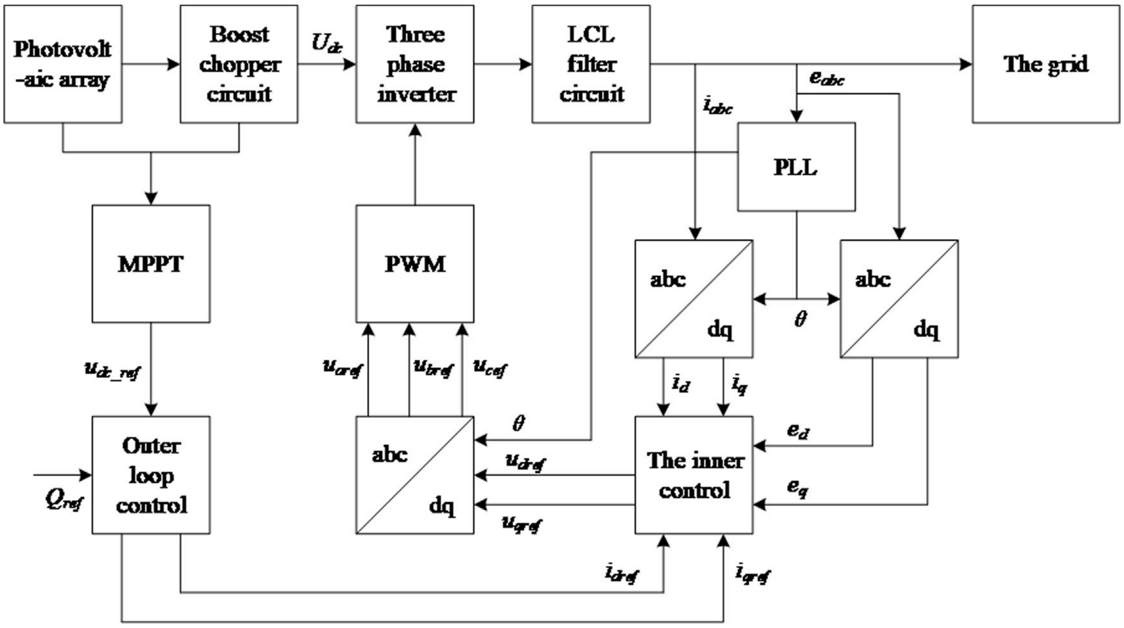

FIGURE 8
Schematic diagram of grid-connected operation control of distributed PV.

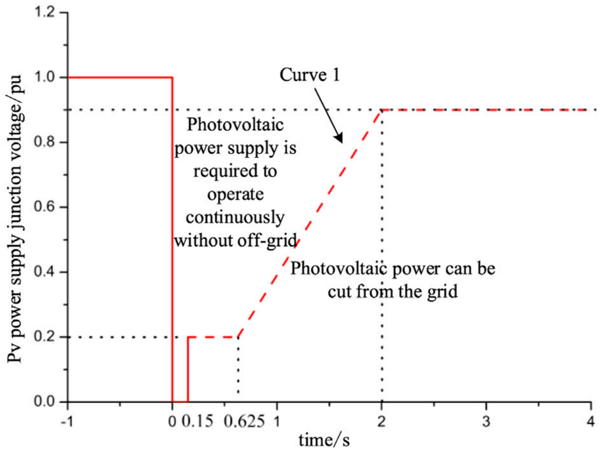

FIGURE 9
Low voltage traversal capability of distributed power supply.

2.4 Operating characteristics of distributed photovoltaic power generation

In case of distribution network failure, the distributed generation is required to have low-voltage crossing capability, that is, when the grid failure or disturbance leads to voltage sag of the distributed generation junction point, the distributed generation should be able to maintain the grid-connected state and continue to operate within the specified range and time of voltage sag. The low-voltage crossing capacity of DG should meet the requirements as shown in Figure 9. Specifically, when the voltage of the DG connection point drops to 0, the DG should be able to run continuously for 0.15 s without disconnecting from the grid, and when the voltage drops below curve 1, the DG can be cut off from the grid.

The reactive current output by DG during fault crossing satisfies Eq. 10. When the voltage of the connection point is too low, the DG is required to provide reactive current to the system to maintain the voltage level of the grid. Specifically, when the junction voltage is greater than 0.9 PU, no reactive current is output; When the junction point voltage is 0.2–0.9 PU, the reactive current is determined by the rated DG current and the junction point voltage. When the junction voltage is less than 0.2 PU, the output reactive current is 1.05 times of the rated current of DG.

$$\begin{cases} i_q = 0, U^* > 0.9 \\ i_q \geq 1.5\left(0.9 - U^*\right) I_N, 0.2 \leq U^* \leq 0.9 \\ i_q \geq 1.05 I_N, U^* < 0.2 \end{cases} \tag{10}$$

Where, U^* is the nominal voltage of DG connection point, and I_N is the rated current of DG.

DG should have certain operation adaptability, and it is required to run under the specified operating time requirements when the voltage and frequency of the distribution network connection point change. The specific requirements for the running time of DG within the voltage range of different connection points are shown in Table 1.

TABLE 1 Operating time requirements of photovoltaic power supply in different voltage range of junction points.

Voltage range	Operation requirements
Less than 0.9 pu	Meet the requirements of low voltage traversal
0.9–1.1 pu	The normal operation
1.1–1.2 pu	Run for at least 10 s
1.2–1.3 pu	Run continuously for at least 0.5 s

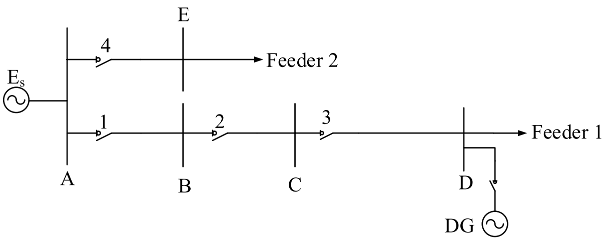

FIGURE 10
DG is connected to bus D at the end of feeder.

3 Analysis of the influence of distributed generation access on distribution network current protection

After the DG is connected to the distribution network, the system is transformed from the original simple single power supply network to the complex multi-power supply network. In case of short circuit fault, the direction of current is difficult to determine, and the influence of DG access to the distribution network varies with different capacity, quantity, location, (GB/T 19964-2012, 2012) type and other conditions (Chunlan et al., 2018; Wu et al., 2021b; Hongjuan et al., 2021).

In this paper, the dual-feeder distribution network is taken as an example to analyze the influence of DG on current protection when it is connected to the end busbar, middle busbar and head busbar of the feeder of the distribution network when faults occur in different sections of the line. In the fault analysis, DG is equivalent to the voltage controlled current source. Figure 10 shows the topological structure of DG connected to the terminal bus D of feeder 1.

3.1 Distributed power supply mode when distribution network failure

3.1.1 Distributed generation is connected to the head of the feeder

Figure 11 shows the schematic diagram of DG connected to bus A at the first end of feeder 1. The influence caused by DG access is discussed by analyzing the short circuit fault occurring at F1 and F2 at AE end of line AB, respectively.

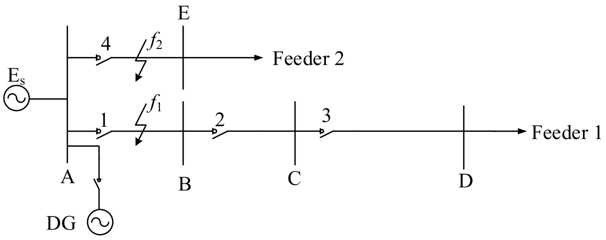

FIGURE 11
DG is connected to bus A at the beginning of feeder.

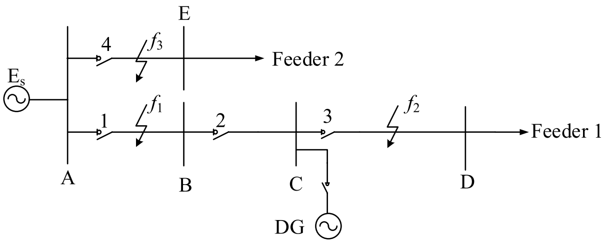

FIGURE 12
DG is connected to the terminal bus C of BC.

Head end when DG in the feeder bus, DG and original power supply system for line power supply, equivalent to increase the capacity of the power system, both when the end of the line AB f1 or f2 fault line AE end, compared to before the DG access, short circuit current changed little, the influence of various protection are in line of smaller.

3.1.2 Distributed generation is connected to the middle end of the feeder

Figure 12 shows the schematic diagram of DG connected to bus C in the middle section of feeder 1. The influence caused by DG access is discussed by analyzing the short circuit fault occurring at F1 of AB end, F2 of CD end and F3 of AE end, respectively.

3.1.2.1 A fault occurs at the end of AB upstream of DG

When a fault occurs at f_1 of AB terminal, the fault line is equivalent to the circuit diagram shown in Figure 13 for analysis in order to more intuitively analyze the current flowing through each protection.

$$\boldsymbol{I_1} = \frac{\boldsymbol{U_S}}{\boldsymbol{Z_S} + \boldsymbol{Z_{Af_1}}} \tag{11}$$

$$\left(\frac{\boldsymbol{1}}{\boldsymbol{Z_{CD}}} + \frac{\boldsymbol{1}}{\boldsymbol{Z_{Bf_1}} + \boldsymbol{Z_{BC}}}\right)\boldsymbol{U_{DG}} = \frac{\boldsymbol{P}}{\boldsymbol{U_{DG}}} \tag{12}$$

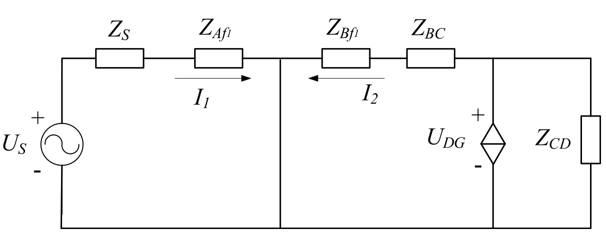

FIGURE 13
Equivalent circuit diagram of a fault at the end of line AB.

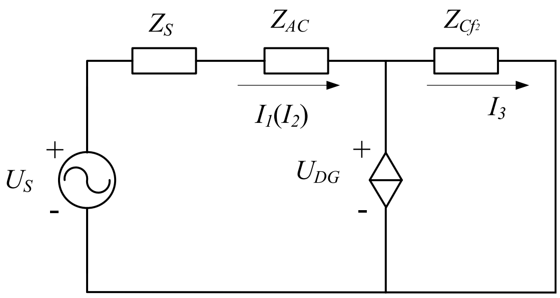

FIGURE 14
Equivalent circuit diagram of a fault at the end of line AB.

$$U_{DG} = \sqrt{\frac{P \cdot Z_{CD}\left(Z_{Bf_1} + Z_{BC}\right)}{Z_{CD} + Z_{Bf_1} + Z_{BC}}} \tag{13}$$

$$I_2 = \frac{U_{DG}}{Z_{Bf_1} + Z_{BC}} = \sqrt{\frac{P \cdot Z_{CD}}{\left(Z_{CD} + Z_{Bf_1} + Z_{BC}\right) \cdot \left(Z_{Bf_1} + Z_{BC}\right)}} \tag{14}$$

Where, I_1 is the current flowing through protection 1, I_2 is the reverse current output from DG to fault point f_1, U_s is the reference voltage of the system, Z_s is the system power supply impedance, is the equivalent impedance from bus A to fault point f_1, Z_{BC} is the equivalent impedance from bus B to bus C, Z_{CD} is the equivalent impedance from bus C to bus D, Is the equivalent impedance from bus B to the fault point f_1, U_{DG} is the voltage of DG, P is the power of DG. U_{DG} is solved through Eq. 12, and the calculation result is shown in Eq. 13.

According to Eqs 11–14, when a short-circuit fault occurs at f1 of AB terminal, DG provides fault current to the fault, and the short-circuit current flowing through protection 2 increases. When the short-circuit current is greater than the action value, protection 2 will misoperate, resulting in the extension of line outage range, while the current of protection 1 is not affected by DG access.

3.1.2.2 A fault occurs at the end of the downstream line CD of DG

When a fault occurs at f_2 at the end of line CD, the line can be equivalent to the simplified circuit model shown in Figure 14.

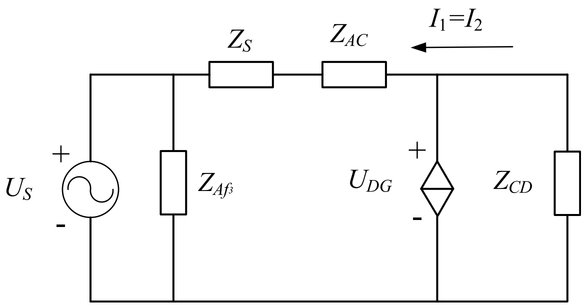

FIGURE 15
Equivalent circuit diagram of AE terminal fault.

According to the simplified circuit model diagram, the current I_1, I_2, and I_3 flowing through protection 1, protection 2 and protection 3 can be obtained.

$$I_1 = I_2 = \frac{U_S - U_{DG}}{|Z_S + Z_{AC}|} \tag{15}$$

$$I_3 = \frac{U_{DG}}{|Z_{Cf_2}|} \tag{16}$$

Where, U_s is the system reference voltage, Z_s is the system power supply impedance, Z_{AC} is the impedance of line AC, is the equivalent impedance of the distance between bus A and fault point f_2, and U_{DG} is the voltage of DG. U_{DG} is solved through Eq. 17, and the calculation result is shown in Eq. 18.

$$\left(\frac{1}{Z_S + Z_{AC}} + \frac{1}{Z_{Cf_2}}\right)U_{DG} = \frac{U_S}{Z_S + Z_{AC}} + \frac{P}{U_{DG}} \tag{17}$$

$$U_{DG} = \frac{U_S Z_{Cf_2} + \sqrt{U_S^2 Z_{Cf_2}^2 + 4\left(Z_{Cf_2} + Z_S + Z_{AC}\right) P Z_{Cf_2} \left(Z_S + Z_{AC}\right)}}{2\left(Z_S + Z_{AC} + Z_{Cf_2}\right)} \tag{18}$$

So, failure occurs when the end of the CD f_2, by protecting 3 I period of action to remove the fault, protect 2 as line CD backup protection, DG on bus C, increase of short circuit current protection 3, protection to improve sensitivity, of short circuit current protection 2 decreases, and protect the protection range of the two and lower sensitivity.

3.1.2.3 AE ends of adjacent feeders are faulty

When a fault occurs at f_3 of AE end, the fault line can be equivalent to the circuit diagram shown in Figure 15 for analysis.

$$\left(\frac{1}{Z_{CD}} + \frac{1}{Z_S + Z_{AC}}\right)U_{DG} = \frac{P}{U_{DG}} + \frac{U_S}{Z_S + Z_{AC}} \tag{19}$$

$$U_{DG} = \frac{U_S Z_{CD} + \sqrt{U_S^2 Z_{CD}^2 + 4\left(Z_S + Z_{AC} + Z_{CD}\right)\left(Z_S + Z_{AC}\right) \cdot Z_{CD} \cdot P}}{2\left(Z_S + Z_{AC} + Z_{CD}\right)} \tag{20}$$

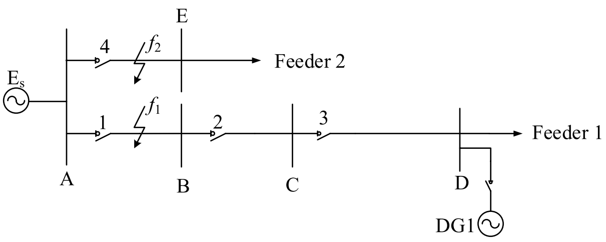

FIGURE 16
Equivalent circuit diagram of AE terminal fault.

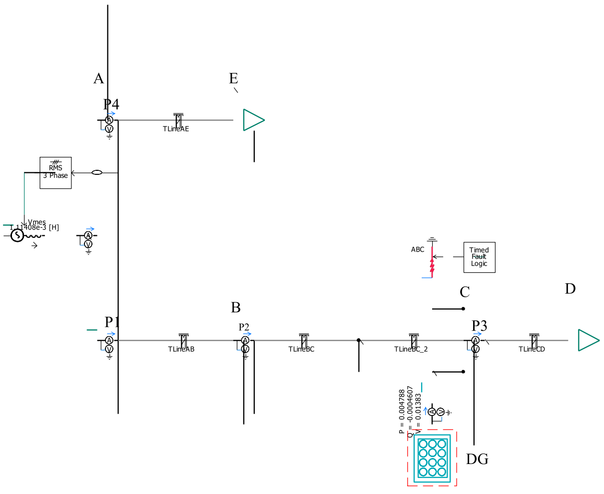

FIGURE 17
Equivalent circuit diagram of AE terminal fault.

$$\boldsymbol{I_1} = \boldsymbol{I_2} = \frac{\boldsymbol{U_S} - \boldsymbol{U_{DG}}}{\boldsymbol{Z_S} + \boldsymbol{Z_{AC}}} = \frac{(\boldsymbol{Z_S} + \boldsymbol{Z_{AC}})\boldsymbol{U_S} + \boldsymbol{U_S}\boldsymbol{Z_{CD}}}{(\boldsymbol{Z_S} + \boldsymbol{Z_{AC}} + \boldsymbol{Z_{CD}})(\boldsymbol{Z_S} + \boldsymbol{Z_{AC}})} - \frac{\sqrt{\boldsymbol{U_S^2}\boldsymbol{Z_{CD}^2} + 4(\boldsymbol{Z_S} + \boldsymbol{Z_{AC}} + \boldsymbol{Z_{CD}})(\boldsymbol{Z_S} + \boldsymbol{Z_{AC}}) \cdot \boldsymbol{Z_{CD}} \cdot \boldsymbol{P}}}{2(\boldsymbol{Z_S} + \boldsymbol{Z_{AC}} + \boldsymbol{Z_{CD}})(\boldsymbol{Z_S} + \boldsymbol{Z_{AC}})} \tag{21}$$

Where, U_s is the system reference voltage, Z_s is the system power supply impedance, Z_{AC} is the impedance of line AC, Z_{CD} is the impedance of line CD, Z_{Af3} is the equivalent impedance of the distance between bus A and fault point f_3, U_{DG} is the voltage of DG, I_1 is the reverse current output by DG through protection 1, I_2 is the reverse current output by DG through protection 2.

When a fault occurs at f_3 of AE terminal, the fault can be removed by the action of protection 4 before DG access. When DG access, the DG outputs reverse fault current to the fault point, and both protection 1 and protection 2 may misoperate. However, if DG is far enough away from the fault point, the fault current provided is not enough to cause the misoperation of protection.

3.1.3 Distributed generation is connected to the end of the feeder

Figure 16 shows the schematic diagram of DG connected to bus D at the end of feeder 1. The influence caused by DG access is discussed by analyzing the short circuit fault occurring at f_1 and F2 at AE end of line AB, respectively.

When a short circuit fault occurs at f_1 at the end of line AB, if the distribution network is not connected to DG, protection device one starts normally and the fault is removed. When DG is connected to the grid, f_1 has a short-circuit fault, and the fault current flowing through protection 2 and protection 3 becomes larger. When the short-circuit current exceeds the setting value of the operation, protection 2 and protection 3 misoperate. When a short circuit fault occurs at f_2 of AE end of line, the distance between DG position and fault point f_2 is far away, so the influence on protection 4 is small.

From the above theoretical analysis, we can figure out that when the distributed power supply is connected to the bus at the head of the feeder, it becomes a part of the overall power supply system because it is close to the power supply side of the line, and will not cause misoperation of protection basically when the fault occurs. When the distributed power supply is connected to the bus at the end of the feeder, if it is far enough away from the fault point, the influence on the fault point current is relatively small. However, when the distributed power supply is connected to the bus at the middle end of the feeder, different from the above two cases, the distributed power supply will have more or less influence on the current of the guard point, which is easy to lead to the misoperation of the guard device. The following is to verify the correctness of the conclusion by combining simulation analysis.

4 The simulation analysis

The simulation model as shown in Figure 13 is established on the PSCAD platform, and the specific parameters of the simulation are as follows:

(1) Power parameters on the system side

The reference voltage value of the distribution network system is 10.5 kV, the reference capacity is 100 MVA, and the impedance value of the system side is j0.35 Ω.

(2) Line parameters

The lines AB, BC, CD, and AF of the distribution network all adopt overhead lines, and the unit resistance and reactance are set as R = 0.26 Ω/km and X = 0.355 Ω/km. It can be seen from

TABLE 2 Maximum short-circuit current at different positions when a three-phase short-circuit fault occurs.

Fault location	**Current size (kA)**				
	Protection of 1	**Protection of 2**	**Protection of 3**	**Protection of 4**	**Fault current**
The ends of AB	4.388	0.360	0.293	0.347	4.438
The ends of BC	2.363	2.363	0.295	0.347	2.479
The ends of CD	0.842	0.842	0.978	0.347	1.031
The ends of AE	0.204	0.204	0.287	3.419	3.475

Figure 17 that the distribution network is a double-feeder system, and the specific parameters are set as follows:

Feeder 1: the length of AB is 3 km, and the impedance value is ZAB = 0.78 + j1.065 Ω; The length of BC is 3 km, and the impedance value is ZBC = 0.78 + j1.065 Ω; The length of CD is 10 km, and the impedance is ZCD = 2.6 + j3.55 Ω.

Feeder 2: the length of AF is 4 km, and the impedance value is ZAF = 1.04 + j1.42 Ω.

The load capacity of feeder 1 and feeder 2 ends is 6 MVA, and the power factor is 0.85.

DG output power range is adjustable in 0–10 MW.

The output power of DG is set as 5 MW, the simulation time is 3 s, and the time step of solution is set as 2 μs. Three-phase short-circuit fault is set at the end of AB, BC, CD, and AE, respectively, and it is permanent fault. The fault occurs when the simulation runs for 1 s. Record the current at the fault point when the fault occurs and the maximum short-circuit current flowing through each line protection as shown in Table 2.

The short circuit current and action changes before and after DG access are discussed respectively in the case of three-phase short circuit at the end of lines AB, BC, CD, and AE.

4.1 The upstream line of the distributed generation access point is faulty

Figures 18, 19 respectively show the simulation results of current size and protection action logic at each position of three-phase short-circuit fault of AB terminal.

According to the simulation results, when three-phase short-circuit fault occurs at the AB end of the line, the maximum a-phase current of the DG flowing through protection 1 (P1), protection 2 (P2), protection 3 (P3) and protection 4 (P4) before access is 4.39, 0, 0, 0.347 kA, respectively, and the current at the fault point is 4.438 kA. After DG access, the maximum a-phase currents flowing through P1, P2, P3, and P4 were 4.388, 0.36, 0.293, and 0.347 kA, respectively, and the current at the fault point was 4.438 kA. Compared with before DG access, P1 and P4 had little influence, while P2 and P3 currents increased. Before DG access, section ⅰ of P1 cannot protect the full length of the line, and the fault is removed by the protection of section ⅱ of P1, while the other protection does not misoperate and the protection selectivity is correct. After DG is connected, P2's ⅲ segment will act and P2 will misoperate. This is because when the end of AB line fails, DG will reverse current to the fault point, resulting in P2 misoperation.

When the BC terminal three-phase short-circuit fault occurs, the maximum a-phase current flowing through P1, P2, P3, and P4 before DG access is 2.364, 2.364, 0, 0.347 kA, respectively, and the current at the fault point is 2.41 kA. After DG access, the maximum a-phase current flowing through P1, P2, P3, and P4 was 2.363, 2.363, 0.295, and 0.347 kA, respectively, and the fault point current was 2.479 kA. Compared with DG access before, P1, P2, and P4 had little influence, while P3 current increased.

4.2 The downstream line of the distributed generation access point is faulty

Figures 20, 21 respectively show the simulation results of current size and protection action logic at each position of CD terminal three-phase short circuit fault.

According to the simulation results, when CD terminal three-phase short-circuit fault occurs, the maximum a-phase current flowing through P1, P2, P3, and P4 before DG access is 0.919, 0.919, 0.919, and 0.347 kA, respectively, and the fault point current is 0.973 kA. After DG access, the maximum a-phase currents flowing through P1, P2, P3, and P4 were 0.842, 0.842, 0.978, and 0.347 kA, respectively, and the current at the fault point was 1.031 kA. Compared with the current before DG access, P1 and P2 currents decreased, P3 currents increased, and P4 did not change, and all protection actions were normal.

4.3 The feeder adjacent to the distributed generation access point is faulty

Figures 22, 23 respectively show the simulation results of current size and protection action logic at each position of AE terminal three-phase short circuit fault.

According to the simulation results, when the AE terminal three-phase short-circuit fault occurs, the maximum a-phase current flowing through P1, P2, P3, and P4 before DG access is

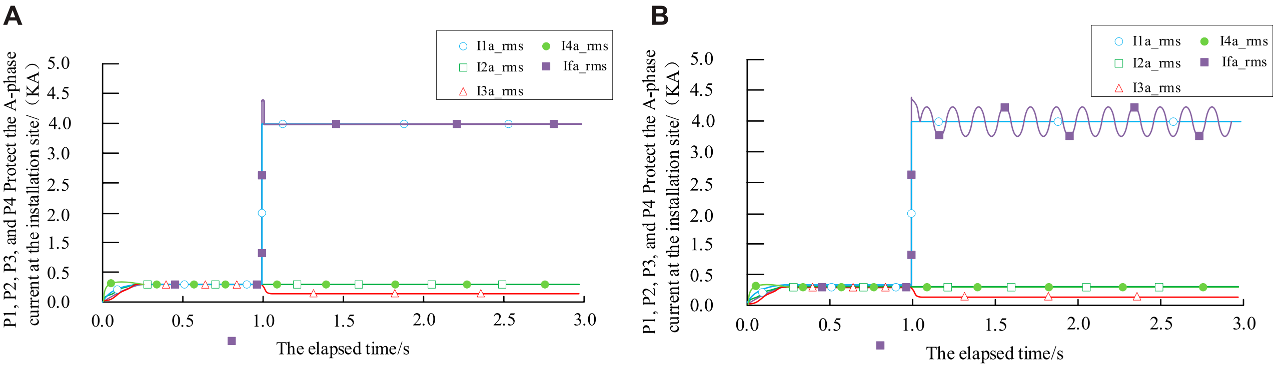

FIGURE 18
Current at each position of the AB terminal three-phase short-circuit fault. **(A)** Simulation results before DG access **(B)** Simulation results after DG access.

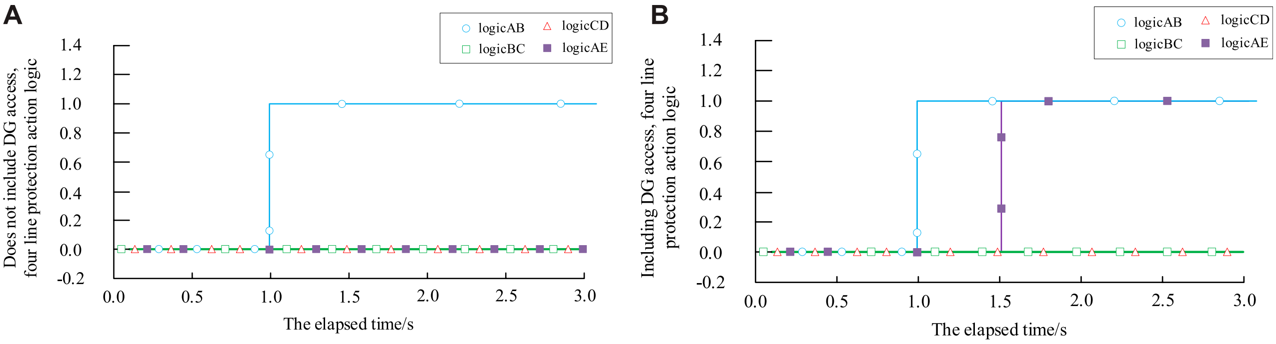

FIGURE 19
Three-stage protection action logic when three-phase short-circuit fault occurs at the AB terminal. **(A)** Simulation results before DG access **(B)** Simulation results after DG access.

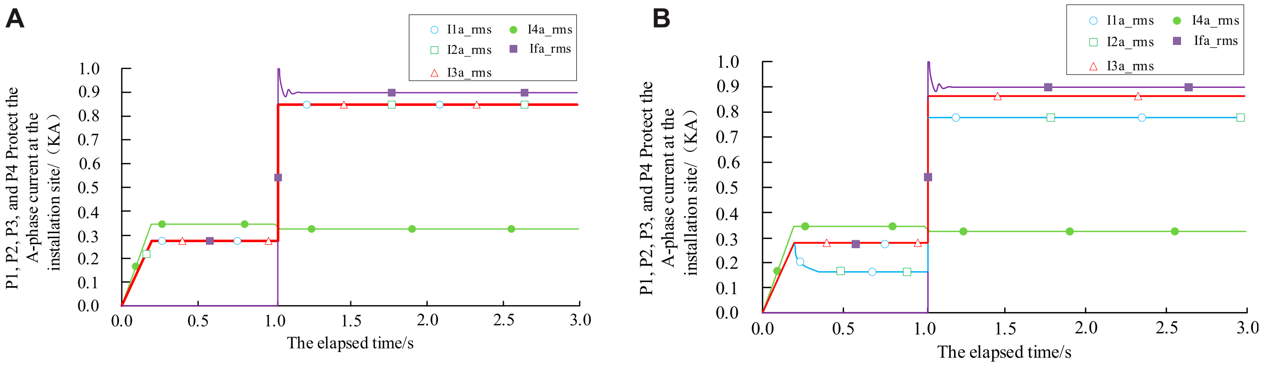

FIGURE 20
Current at each position of a CD terminal three-phase short-circuit fault. **(A)** Simulation results before DG access **(B)** simulation results after DG access.

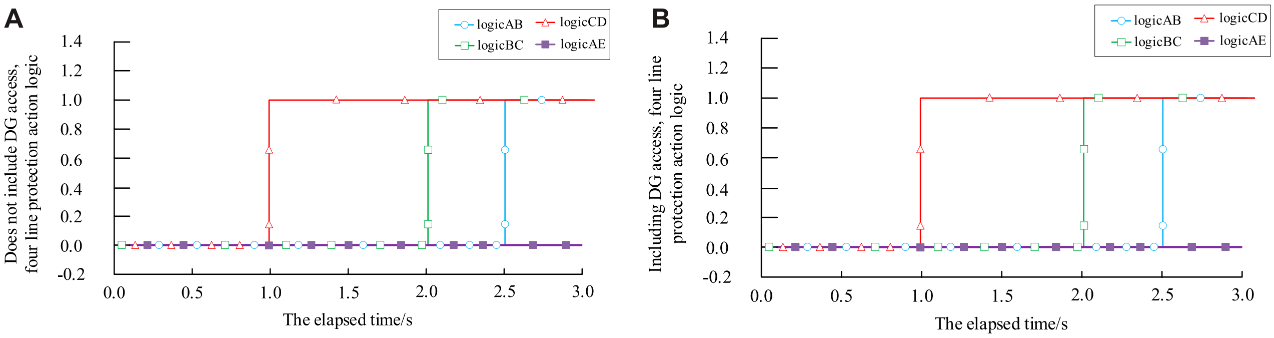

FIGURE 21
Three-stage protection action logic when three-phase short circuit fault occurs at the end of line CD. **(A)** Simulation results before DG access **(B)** simulation results after DG access.

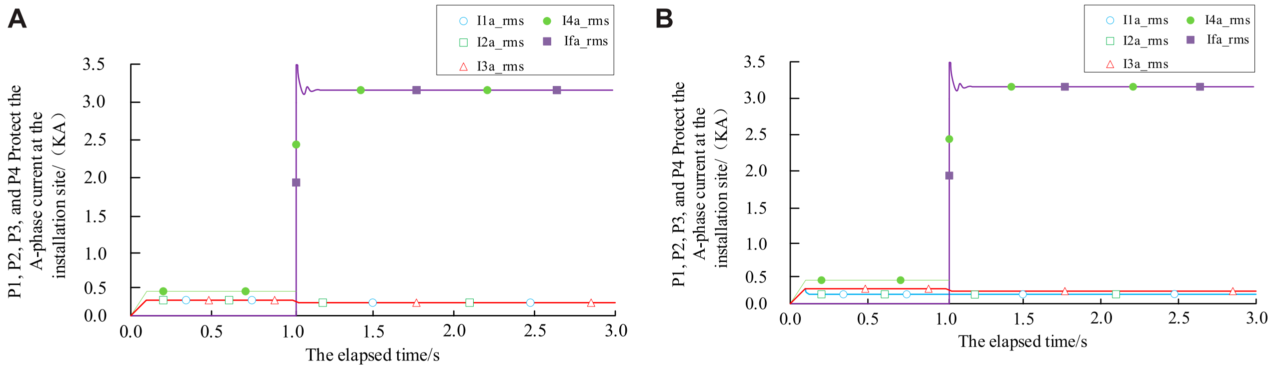

FIGURE 22
Current size at each position of AE terminal three-phase short-circuit fault. **(A)** Simulation results before DG access **(B)** simulation results after DG access.

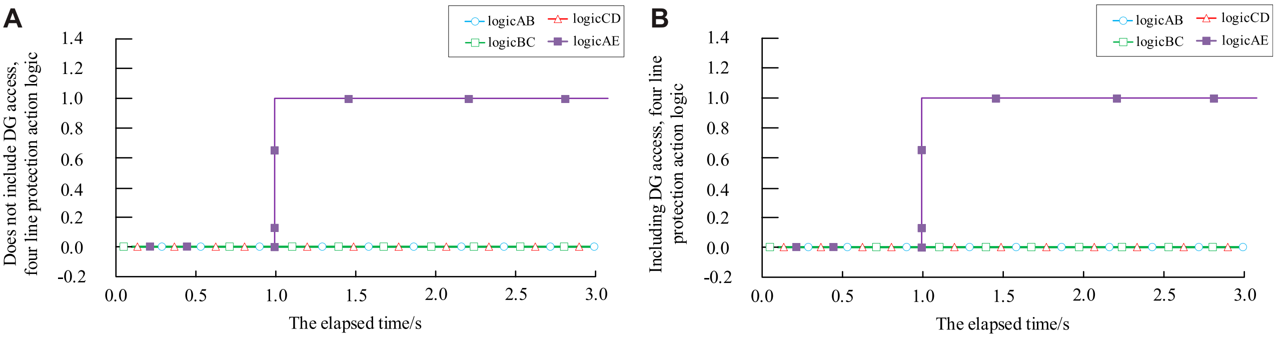

FIGURE 23
Three-stage protection action logic when AE terminal three-phase short circuit fault occurs. **(A)** Simulation results before DG access **(B)** simulation results after DG access.

TABLE 3 Influence of single DG access on three-phase short-circuit fault current.

The fault location	Protection type			
	Protection of 1	Protection of 1	Protection of 1	Protection of 1
The ends of AB	Less affected	Current increase	Current increase	Less affected
The ends of CD	Current decreases	Current decreases	Current increase	Less affected
The ends of AE	Less affected	Less affected	Less affected	Less affected

0.27, 0.27, 0.27, and 3.418 kA, respectively, and the fault point current is 3.475 kA. After DG access, the maximum a-phase current flowing through P1, P2, P3, and P4 was 0.204, 0.204, 0.287, and 3.419 kA, respectively, and the fault point current was 3.475 kA. Compared with before DG access, P1 and P2 currents decreased, while P3 and P4 had little influence. P4 works normally before DG access, and other protections do not misoperate. In the system with DG, because the access position of DG is far away from the fault point, the short circuit current of the reverse transmission is small, so the current protection of the distribution network is not affected.

Through the above theoretical analysis and simulation results verification, the influence of single DG access on the short-circuit fault current of each line in distribution network is shown in Table 3.

To sum up, the influence of single DG access on distribution network is related to the location of the fault. When the short-circuit fault occurs upstream of the DG access point, the protection three-phase short-circuit current downstream of the fault point will increase. When a short circuit fault occurs downstream of the DG access point, the short circuit current of the protection line located downstream of the DG increases, while the short circuit current of the protection line located upstream of the DG decreases. When short circuit fault occurs in adjacent feeder line of DG access point, it has little influence on each protection.

5 Conclusion

When clean energy is connected to the distribution network in the form of distributed power supply, if short-circuit fault occurs in the line, the fault direction is not easy to determine due to the transformation of the grid flow direction, so the formulation of relay protection scheme is different from that of traditional distribution network. In this paper, an equivalent circuit mathematical model with photovoltaic power supply as an example is established to analyze its volt-ampmeter characteristics and power-voltage output characteristics. At the same time, the control mode of distributed power supply is analyzed when the distribution network is faulty. Taking the dual-feeder distribution network with distributed power supply as the research object, when faults occur in different sections of the line, Influence on fault current and current protection when DG is connected to terminal bus, non-terminal bus and primary bus of distribution network feeder, respectively; It is concluded that when DG is connected in the middle of the feeder, it has the greatest influence on the protection device of the power grid, while when DG is connected in the head and end of the feeder, the influence is small. Finally, a simulation model is built in PSCAD to verify the accuracy of the theoretical analysis results.

Data availability statement

The original contributions presented in the study are included in the article/supplementary material, further inquiries can be directed to the corresponding author.

Author contributions

HK, CR, and ZJ contributed to conception and design of the study. HK organized the database. GX performed the statistical analysis. HG wrote the first draft of the manuscript. HK, CR, and ZJ wrote sections of the manuscript. All authors contributed to manuscript revision, read, and approved the submitted version.

Funding

This research was funded by Water port—ship multi-energy integration technology and integrated application, grant number 2021YFB2601600.

Acknowledgments

Thanks to the joint efforts of all the participants, the publication of this article could not have been done without the hard work of everyone.

Conflict of interest

Authors HK and ZJ were employed by the company NARI Group, Ltd. and authors CR, GX, and HG were employed by the company Suzhou Electric Power Company.

Publisher's note

References

Alcala-Gonzalez, D., García del Toro, E. M., Más-López, M. I., and Pindado, S. (2021). Effect of distributed photovoltaic generation on short-circuit currents and fault detection in distribution networks: A practical case study. *Appl. Sci.* 11 (1), 405. doi:10.3390/app11010405

Azeroual, M., Boujoudar, Y., Bhagat, K., El Iysaouy, L., Aljarbouh, A., Knyazkov, A., et al. (2022). Fault location and detection techniques in power distribution systems with distributed generation: Kenitra City (Morocco) as a case study. *Electr. Power Syst. Res.* 209, 108026. doi:10.1016/j.epsr.2022.108026

Calderaro, V., Milanovic, J. V., Kayikci, M., and Piccolo, A. (2009). The impact of distributed synchronous generators on quality of electricity supply and transient stability of real distribution network. *Electr. Power Syst. Res.* 79 (1), 134–143. doi:10.1016/j.epsr.2008.05.022

Chunlan, D., Yi, G., and Yao, X. (2018). Research on access location of distributed power based on complex network theory [J]. *Shandong Electr. power Technol.* 45 (05), 40–44.

Energy and the Environment (2021). Construction and operation of photovoltaic power generation in the first half of 2021 [J]. *Electr. Power Technol. Environ. Prot.* 37 (04), 46.

GB/T 19964-2012 (2012). *Technical Regulations for photovoltaic power station access to power system [S]*. Beijing: Standards Press of China.

Hong, L., and Hongbo, Y. (2020). Analysis of working principle and physical Modeling method of photovoltaic cell [J]. *Mech. Electr. Inf.* 3 (6), 3–4.

Hongjuan, G., Haiyun, W., and Jingxiang, H. (2021). Study on the influence of access location of distributed power supply on distribution network voltage. *J. Comput. Simul.* 38 (08), 113–117.

Luning, L. (2019). *Research on Multi-objective Reconfiguration of power generation and distribution network with distributed power [D]*. Nanchang, China: Journal of East China Jiaotong University.

Liqun, L., Tianbao, L., and Chunxia, L. (2020). Solutions for the distributed photovoltaic access distribution network relay protection. *J. Taiyuan Univ. Sci. Technol.* 41 (03), 165–169+175.

Ming, D., Weisheng, W., and Xiuli, L. (2014). Review of the influence of large-scale photovoltaic power generation on power system. *Proc. CSEE* 34 (01), 1–14.

Mingjun, D. (2018). Photovoltaic cell modeling and MPPT simulation analysis [J]. *Commun. power Technol.* 35 (07), 30–32.

Ni, Q., Yanan, S., and Zhenhua, T. (2022). Influence of short circuit characteristics of distributed power supply on distribution network protection. *Electr. Power Surv. Des.* 2, 39–45+53.

Wu, Y., Lin, Z., Liu, C., Huang, T., Chen, Y., Ru, Y., et al. (2022). Resilience enhancement for urban distribution network via risk-based emergency response plan amendment for ice disasters. *Int. J. Electr. Power & Energy Syst.* 141, 108183. doi:10.1016/j.ijepes.2022.108183

Wu, Y. J., Liang, X. Y., Huang, T., Lin, Z., Li, Z., and Hossain, M. F. (2021). A hierarchical framework for renewable energy sources consumption promotion among microgrids through two-layer electricity prices. *Renew. Sustain. Energy Rev.* 145, 111140. doi:10.1016/j.rser.2021.111140

Wu, Y., Lin, Z., and Liu, C. (2021). A bargaining strategy-based game model of power demand response considering hydrogen-to-electricity conversion of industrial users. *IEEE Trans. Industry Appl.* 99, 1. doi:10.1109/TIA.2021.3088769

Xiao, W. (2018). Influence of distributed power access on relay protection of distribution network [J]. *Electr. Equip. Econ.* 6, 14–15.

Xuekai, H., Gan, Z., and Wenping, H. (2019). Analysis of influence of distributed power supply on automatic reclosing of line [J]. *Power Syst. Prot. Control* 47 (17), 75–82.

Yin, Z., Wang, Z., and Xue, S. (2020). Analysis of the influence of distributed photovoltaic power station grid connection on distribution network relay protection. *J. Phys. Conf. Ser.* 1639 (1), 012042. doi:10.1088/1742-6596/1639/1/012042

Yongfei, M., Chunlai, L., and Yanjiao, H. (2016). "Analysis of the influence of distributed generation access on the operation and management of distribution network," in 2016 International Conference on Smart City and Systems Engineering (ICSCSE), Hunan, China, 25-26 November 2016 (IEEE), 194–196. doi:10.1109/ICSCSE.2016.0060

frontiers | Frontiers in Energy Research

TYPE Original Research
PUBLISHED 13 January 2023
DOI 10.3389/fenrg.2023.1109254

OPEN ACCESS

EDITED BY
Yingjun Wu,
Hohai University, China

REVIEWED BY
Can Huang,
Lawrence Livermore National Laboratory (DOE), United States
Haixiang Zang,
Hohai University, China
Shuzheng Wang,
Nanjing Institute of Technology (NJIT), China

*CORRESPONDENCE
Tang Chong,
✉ tc_tju1895@163.com

SPECIALTY SECTION
This article was submitted to Smart Grids, a section of the journal Frontiers in Energy Research

RECEIVED 27 November 2022
ACCEPTED 05 January 2023
PUBLISHED 13 January 2023

CITATION
Hao Z, Hai L, Enbo L, Yanting H, Zhi W, Chong T, Wenmeng Z and Guo X (2023), Research on power trade potential and power balance between Lancang-Mekong countries and southern China under long-term operation simulation.
Front. Energy Res. 11:1109254.
doi: 10.3389/fenrg.2023.1109254

Research on power trade potential and power balance between Lancang-Mekong countries and southern China under long-term operation simulation

Zhang Hao[1], Lu Hai[1], Luo Enbo[1], Huang Yanting[2], Wu Zhi[3], Tang Chong[2]*, Zhao Wenmeng[2] and Xie Guo[4]

[1]Electric Power Research Institute, Yunnan Power Grid Co., Ltd., Kunming, Yunnan, China, [2]Electric Power Research Institute, CSG, Guangzhou, Guangdong, China, [3]School of Electrical Engineering, Southeast University, Nanjing, Jiangsu, China, [4]Dehong Power Supply Bureau, Yunnan Power Grid Co., Ltd., Dehong, Yunnan, China

In order to further promote the interconnection development and construction of the power grids between the Lancang-Mekong countries and Southern China region and facilitate multilateral energy interaction, an assessment mechanism of the power balance and power trade potential between the two areas under long-term operation simulation is proposed. The mechanism first analyzes the energy supply structure, energy use forms, cross-border transmission capacity, and multi-area power trade potential of the power grids of the Lancang-Mekong countries and Southern China. Secondly, a power and electricity optimization model considering the long-period operation characteristics of generating units and regional interconnection transmission constraints is constructed, which can optimize the solution of a typical time-series operation scenario of 8760 h a year and improve the accuracy of regional power trade potential analysis. The results show that the Lancang-Mekong countries and the southern region of China have a significant potential for power trading, and the construction of a unified power trading market is vital for promoting the optimal allocation of power resources, achieving power balance, increasing the proportion of energy consumption, and reducing the cost of electricity consumption.

KEYWORDS

power trade potential, long-term operation simulation, power balance analysis, regional power system operation, joint optimization

1 Introduction

Cross-border cooperation and trade in energy have become an important grip for implementing the “Belt and Road” initiative. Southeast Asia is the world’s third most populous region, China’s third-largest trading partner, and the southern route of the “One Belt and One Road”. With the development of “China-Vietnam-Myanmar-Lao” economic cooperation, the contradiction between the fast-growing energy demand and the local energy infrastructure in the border areas and cities in the Lancang-Mekong countries has become more obvious. As the first domestic power grid enterprise to “go global” and the Chinese implementation unit of the Greater Mekong Sub-region (GMS) power cooperation authorized by the State Council, Southern Power Grid is responsible for promoting cross-border power interconnection and sharing the benefits of green energy among bilateral people (She et al., 2021). With the development and promotion of Vietnam's Vinh Tan coal-fired power plant Phase I BOT project, Laos' Namtha River No. 1 hydropower plant project, Chile's ETC equity acquisition project, and Laos' 230 kV northern power grid EPC project (Wu et al., 2020), while deepening the power trading between the two sides, many problems such as different energy market mechanisms for cross-border trading cooperation and difficulties in bilateral coordination and scheduling have also been revealed.

The Lancang-Mekong region is rich in hydropower resources. However, the degree of hydropower development is generally low, the scale of cross-border power transactions is small, and the potential for optimal allocation of power resources can be huge (Xing, 2017). Suppose the optimal allocation of power resources in the Lancang-Mekong region can be further promoted through cooperation to improve energy utilization efficiency. In that case, it will greatly ease the contradiction between the large power demand and scarce energy resources in the southern region of China, improve the proportion of energy consumption and reduce power consumption costs at the same time.

Europe, North America, and other regions have built a unified regional electricity market to solve the conflict between regional energy demand and shortage. Their market reform, trading scope integration, and expansion of relevant experience and practices can bring some inspiration and reference to constructing a unified electricity market in the southern region of China and the Mekong countries (Ngan, 2010). Taking European countries as an example (Amundsen and Bergman, 2006; Le et al., 2019; Zhang, 2019), Germany has achieved interconnection with seven neighboring countries, and the interconnection capacity exceeds 25% of the maximum system load and 33% of the installed landscape capacity. The complete interconnection with neighboring countries provides essential support for Germany's high proportion of new energy consumption. Portugal is connected to the Spanish grid with a maximum power exchange capacity of 3.1 million kilowatts, 59% of Portugal's installed landscape capacity. Spain is connected to France, Portugal, and Morocco grids, with a maximum power exchange capacity of 6.85 million kilowatts and 23.2% of Spain's installed landscape capacity. The Danish grid is interconnected with Norway, Sweden, and Germany through 14 liaison lines, with a connected capacity of more than 5 GW, close to the total installed capacity of scenery at the end of 2015, using the rich hydropower resources in Northern Europe to play a good regulating role in the consumption of wind power in Denmark. As an Independent System Operator ISO (Independent System Operator), the three main functions of the U.S. PJM power market are grid operation and management, market operation and management, and regional grid planning (Bushnell et al., 2007), which achieves resource complementarity while meeting power demand, improves power system efficiency and promotes the development and consumption of clean, low-carbon energy.

The source and load complement each other in the southern region of China, forming a closely connected grid system based on the hybrid AC/DC grid. From the perspective of the source-load complementary relationship, there is a continuous demand for a "west-east power supply". Guangdong and Guangxi have a strong electricity demand. At the same time, Yunnan and Guizhou in the west are important power bases, thus creating a stable demand for electricity from the west to the east. From the grid connection, the southern region has formed a 500 kV and above voltage level's primary grid of the west-east power transmission channel; the capacity of the west-east power transmission channel reached 58 million kilowatts, the annual scale of power transmission of more than 230 Terawatt hours, which also for the better realization of the optimal scheduling of resources, promote the construction of regional markets, especially to meet the fluctuation characteristics of new energy. In particular, it provides strong support for constructing a regional spot market that adapts to the volatile characteristics of new energy (Zhu et al., 2021).

This paper proposes a mechanism to evaluate the multi-stage power trading potential of the Lancang-Mekong countries and the Southern China region by setting different boundary conditions and considering different boundaries, such as whether the region is jointly optimized and whether the capacity constraints of the contact lines are taken into account, respectively. On this basis, a regional power balance analysis mechanism based on 8760 h of annual operation simulation is proposed, and power balance indexes and calculation methods reflecting power balance and power balance of all typical annual operation scenarios are designed to improve the accuracy of power balance analysis. Based on the actual data of Yunnan Power Grid and the five Lancang-Mekong countries, a long-period operation scenario for joint optimization of the regional power system is constructed. The simulation results show that the Lancang-Mekong countries and the southern region of China have a large potential for power trading, and the construction of a unified power trading market plays an important role in promoting the optimal allocation of power resources, achieving power balance, improving the proportion of energy consumption, and reducing the cost of electricity consumption.

2 Analysis of the characteristics of power coupling and complementary transactions between the Mekong countries and the southern China region

2.1 Power supply structure development status

In terms of power supply, the hydropower resources in the Lancang-Mekong countries are very abundant. However, the degree of hydropower development is generally low and the scale of cross-border power transactions is small. If a unified regional power market is established, the construction level of the power grids in the Lancang-Mekong countries can be significantly improved, and at the same time ease the power demand in the southern region of China with unexploited surplus water resources. The power supply structure of Lancang-Mekong countries is shown in Figure 1.

The five provinces of Southern China have apparent differences in power supply structures which can be seen in Figure 2, and have started to invest in the development of clean energy on a large scale. Facing the problem of energy consumption, the southern region has a large demand for electricity. Establishing a unified regional electricity market can help alleviate the contradiction between the

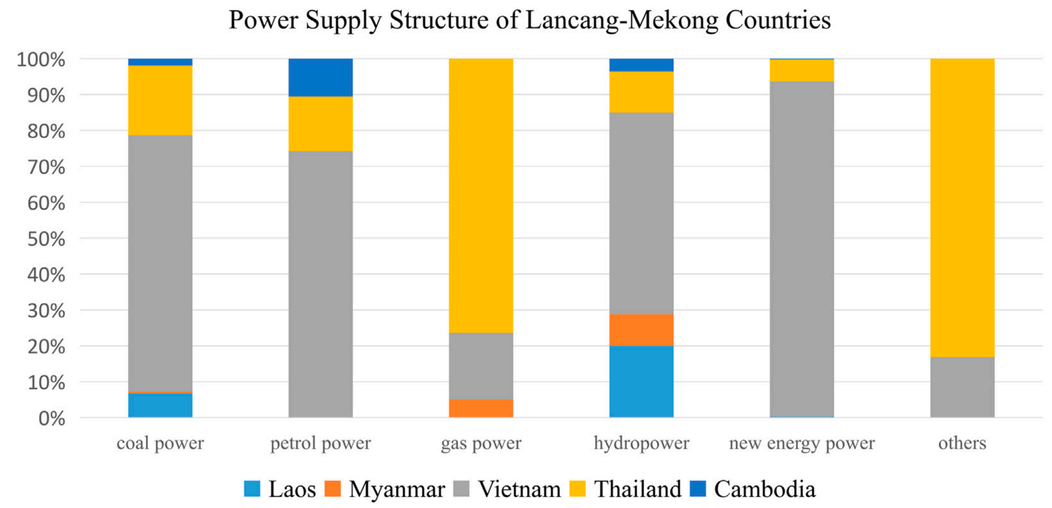

FIGURE 1
Power supply structure of Lancang- Mekong countries.

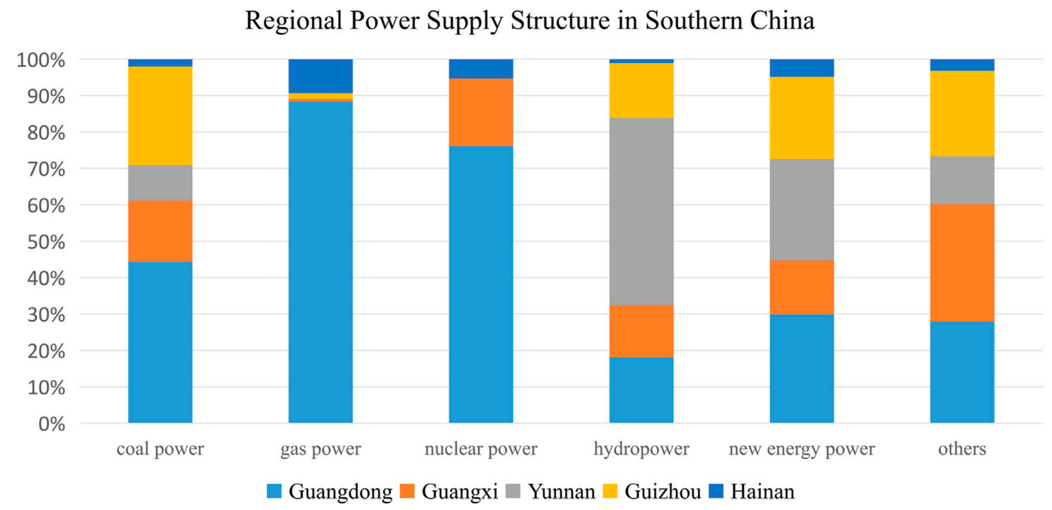

FIGURE 2
Regional power supply structure in southern China.

great demand for electricity and the scarcity of energy resources in the southern region of China, improve the proportion of energy consumption and reduce the cost of electricity.

2.2 Status of load structure development

In terms of load, the five Lancang-Mekong countries have been increasing the load level with social development. However, with the outbreak of the new crown epidemic, the degree of impact of the epidemic varies from country to country. The load forecast results shown in Figure 3 and Figure 4 are revised according to the degree of impact (Zhao, 2020).

The regional load level in southern China shows more stable growth; taking Yunnan as an example, the forecast results are shown in Table 1 as follows.

2.3 Multilateral complementary properties

The net load curves of Yunnan and the five Lancang-Mekong countries are shown in Figure 5 below. Net load is the rest part after subtracting photovoltaic and wind power from load. If sunshine or wind is abundant, then the net load can decrease. From April to September, the net load of Mekong continues to decline, while the net load of Yunnan shows an upward trend and reaches its peak in

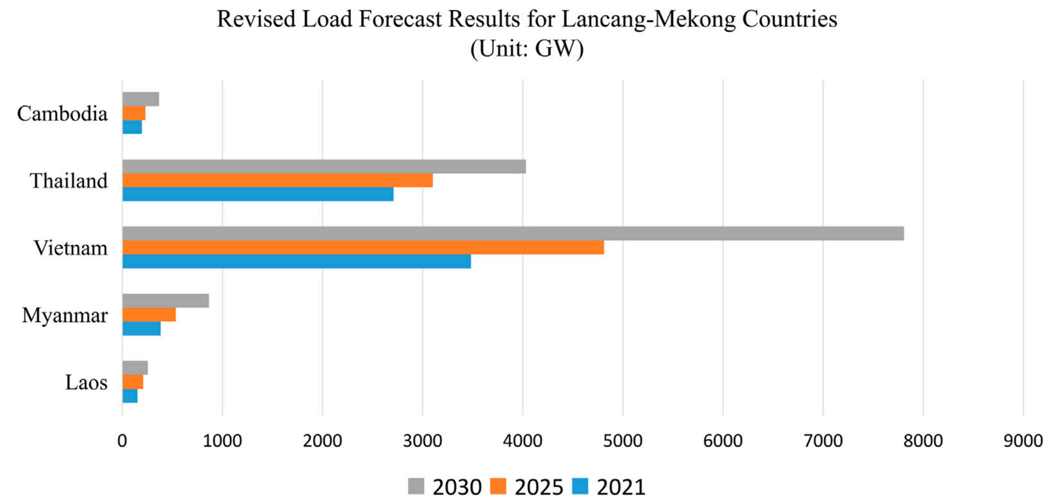

FIGURE 3
Revised load forecast results for Lancang- Mekong countries.

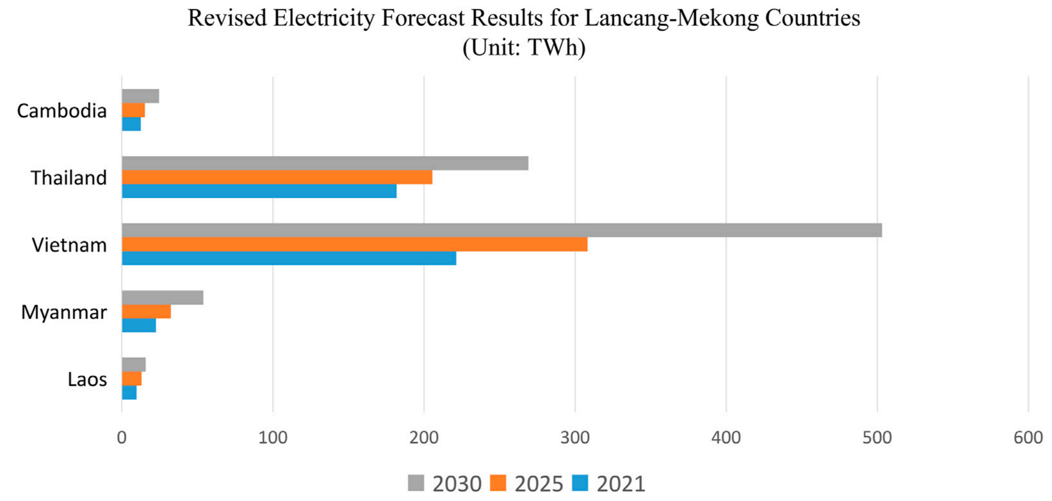

FIGURE 4
Revised electricity forecast results for Lancang- Mekong countries.

TABLE 1 Electricity demand of Yunnan in 2025 and 2030 (Unit: TWh/GW).

Projects	2025	2030
Electricity consumption	340	400
Maximum load	540	640

August and September, during which time the Lancang-Mekong countries can send electricity to Yunnan; from September to March, the net load of Yunnan shows a downward trend, while the net load of Lancang-Mekong countries shows a peak so that Yunnan can send electricity back to the Lancang-Mekong countries. The curve shows that Yunnan and the Lancang-Mekong countries have great potential to complement each other and have the first conditions to build a unified power trading market.

3 Model for assessing the complementary potential of the lancang-mekong countries and the southern China region

3.1 Assessment mechanism characteristics

The assessment mechanism of the power trading potential between the Mekong countries and the Southern China Power Grid under the long-period operation simulation takes into account

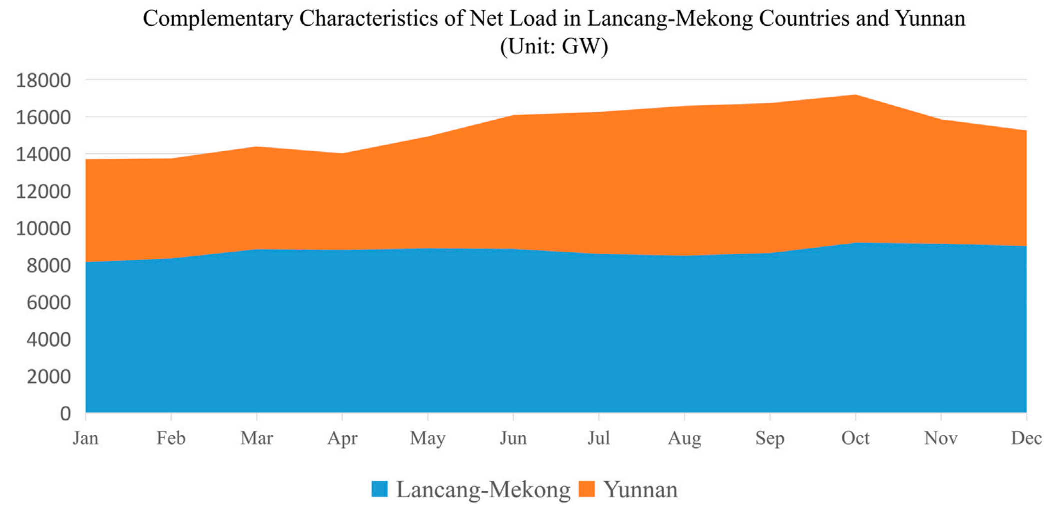

FIGURE 5
Complementary characteristics of net load in Lancang- Mekong countries and Yunnan.

the energy supply structure, energy use form, cross-border transmission capacity, and multi-area complementary potential of the Mekong countries and the Southern China Power Grid (Xiao et al., 2016), and realizes the assessment of the multi-stage power complementary potential between the Mekong countries and the Southern China Power Grid by setting different boundary conditions.

Its features are: 1) providing a variety of optimization objectives to meet different simulation needs; 2) considering long-term continuous unit combination models; 3) applicable to multi-area DC interconnection systems; 4) fully considering the supply structure and energy use forms of each country; 5) setting different boundary conditions to realize multi-stage power complementary potential assessment.

3.2 Mathematical model of the evaluation mechanism

1) Optimization objectives

The lowest operating cost is used as the objective function for the analysis. This objective function is a scheduling decision that integrates system generation economics, load shedding costs, and removal of new energy, and is expressed as

$$\begin{aligned}\min C &= \min C_1 + \min C_2\\ &= \lambda_{s1}C_{s1} + \lambda_{p1}C_{p1}\\ &\quad + \sum_{t\in T}\Big(C_{c1}\left({P_{c1}}^t\right) + C_{f1}\left({P_{f1}}^t\right) + C_{h1}\left({P_{h1}}^t\right)\\ &\quad + C_{n1}\left({P_{n1}}^t\right) + \alpha C_{cn1}{P_{cn1}}^t + \theta L_{d1}{D_{c1}}^t\Big)\\ &\quad + \sum_{l\in L} M_{l1}*P_{l1} + \lambda_{s2}C_{s2} + \lambda_{p2}C_{p2}\\ &\quad + \sum_{t\in T}\Big(C_{c2}\left({P_{c2}}^t\right) + C_{f2}\left({P_{f2}}^t\right) + C_{h2}\left({P_{h2}}^t\right)\\ &\quad + C_{n2}\left({P_{n2}}^t\right) + \alpha C_{cn2}{P_{cn2}}^t + \theta L_{d2}{D_{c2}}^t\Big)\end{aligned} \tag{1}$$

where: C is the lowest cost of the combined grid, C_1 is the lowest cost of the China Southern Power Grid, and C_2 is the lowest cost of the Lancang-Mekong Power Grid. Subscript 1 and 2 denote China Southern Power Grid and Lancang-Mekong Power Grid respectively. T is the number of optimization time periods, and $C_x(P_x^t)$ is the operating cost of each type of unit at time period t when the output power is P. The subscripts c, f, h, and n denote thermal power units which are not participating in intraday start-stop management, thermal power units which are participating in intraday start-stop management, hydropower units, and new energy units, respectively. C_{cn} is the cost of removing new energy. P_{cn}^t is the power of curtailing new energy in time period t. D_c^t is the power of load shedding in time period t. L_d is the cost of load shedding at each node. C_s、 C_p are the cost of start-stop management; and θ、 α、 λ are the weighting factors, which are usually 1 and can be adjusted as needed. M_l is the power line l's unit transmission price. P_l is the transmission power of the power line l. L is the set of power lines.

2) Constraints

To simplify the process, we divide the units in the Lancang-Mekong countries into thermal power units which are not participating in intraday start-stop management, thermal power units which are participating in intraday start-stop management, hydropower units, wind power units, and photovoltaic power units. Among them, wind turbines and PV units are introduced with a removal mechanism, so that the model removes part of the output when the system cannot achieve load balancing under extreme output conditions or when wind power or PV delivery is blocked. For the hydropower units, the short-term economic dispatch model of stepped hydropower is considered, and the operating constraints of hydropower units, reservoir operating constraints, and upstream and downstream reservoir water balance constraints are introduced in the model to precisely describe the operation process of hydropower units in detail.

1) Thermal power unit constraints

The thermal power unit constraints mainly include upper and lower thermal power unit output limits as well as creep constraints, denoted as

$$P_{c1\min} I_{c1} \le P_{c1} \le P_{c1\max} I_{c1} \tag{2}$$

$$P_{f1\min} I_{f1}{}^{t} \le P_{f1}{}^{t} \le P_{f1\max} I_{f1}{}^{t} \tag{3}$$

$$-\Delta P_{c1}{}^{down} \le \Delta P_{c1}{}^{\Delta t} \le \Delta P_{c1}{}^{up} \tag{4}$$

$$-\Delta P_{f1}{}^{down} \le \Delta P_{f1}{}^{\Delta t} \le \Delta P_{f1}{}^{up} \tag{5}$$

$$P_{c1}{}^{t}, P_{f1}{}^{t}, I_{c1}, I_{f1}{}^{t} \ge 0 \tag{6}$$

$$P_{c2\min} I_{c2} \le P_{c2} \le P_{c2\max} I_{c2} \tag{7}$$

$$P_{f2\min} I_{f2}{}^{t} \le P_{f2}{}^{t} \le P_{f2\max} I_{f2}{}^{t} \tag{8}$$

$$-\Delta P_{c2}{}^{down} \le \Delta P_{c2}{}^{\Delta t} \le \Delta P_{c2}{}^{up} \tag{9}$$

$$-\Delta P_{f2}{}^{down} \le \Delta P_{f2}{}^{\Delta t} \le \Delta P_{f2}{}^{up} \tag{10}$$

$$P_{c2}{}^{t}, P_{f2}{}^{t}, I_{c2}, I_{f2}{}^{t} \ge 0 \tag{11}$$

$$\forall t \in T \tag{12}$$

where: Subscript 1 and 2 denotes China Southern Power Grid and Lancang-Mekong Power Grid respectively. P_{cmax}, P_{cmin} are the maximum output and minimum output of the thermal power units which are not participating in intraday start-stop management, and P_{fmax}, P_{fmin} are the maximum output and minimum output of thermal power units which are participating in intraday start-stop management. $\Delta P_c^{down}, \Delta P_c^{up}$, $\Delta P_f^{down}, \Delta P_f^{up}$ are the downward and upward climbing rates of the unit, respectively. I_c is the state variable of thermal power units which are not participating in intraday start-stop management during the day, and I_f^t is the state variable of thermal power units which are participating in intraday start-stop management at time t during the day.

$$P_{h1}{}^{t} = f\left(q_{h1}{}^{t}, V_{R1}{}^{t}\right) \tag{13}$$

$$Q_{R1}{}^{t} = A_{h1} q_{h1}{}^{t} + Q_{R1}{}^{t,d} \tag{14}$$

$$R_{1\min} \le R_1{}^{t} \le R_{1\max} \tag{15}$$

$$R_1{}^{0} = R_1{}^{begin} \tag{16}$$

$$R_1{}^{T} = R_1{}^{end} \tag{17}$$

$$Q_{R1\min} \le Q_{R1}{}^{t} \le Q_{R1\max} \tag{18}$$

$$-\Delta Q_{R1} \le Q_{R1}{}^{\Delta t} \le \Delta Q_{R1} \tag{19}$$

$$Q_{R1}{}^{t,d} \ge 0 \tag{20}$$

$$R_1{}^{t} = R_1{}^{t-1} + Q_{in1}{}^{t} + I_{rain1}{}^{t} - Q_{R1}{}^{t} \tag{21}$$

$$y_{h1}{}^{t} \le I_{h1}{}^{t} \tag{22}$$

$$y_{h1}{}^{t} \ge I_{h1}{}^{t} - I_{h1}{}^{t-1} \tag{23}$$

$$\sum y_{h1}{}^{t} \le \tau \tag{24}$$

$$P_{h2}{}^{t} = f\left(q_{h2}{}^{t}, V_{R2}{}^{t}\right) \tag{25}$$

$$Q_{R2}{}^{t} = A_{h2} q_{h2}{}^{t} + Q_{R2}{}^{t,d} \tag{26}$$

$$R_{2\min} \le R_2{}^{t} \le R_{2\max} \tag{27}$$

$$R_2{}^{0} = R_2{}^{begin} \tag{28}$$

$$R_2{}^{T} = R_2{}^{end} \tag{29}$$

$$Q_{R2\min} \le Q_{R2}{}^{t} \le Q_{R2\max} \tag{30}$$

$$-\Delta Q_{R2} \le Q_{R2}{}^{\Delta t} \le \Delta Q_{R2} \tag{31}$$

$$Q_{R2}{}^{t,d} \ge 0 \tag{32}$$

$$R_2{}^{t} = R_2{}^{t-1} + Q_{in2}{}^{t} + I_{rain2}{}^{t} - Q_{R2}{}^{t} \tag{33}$$

$$y_{h2}{}^{t} \le I_{h2}{}^{t} \tag{34}$$

$$y_{h2}{}^{t} \ge I_{h2}{}^{t} - I_{h2}{}^{t-1} \tag{35}$$

$$\sum y_{h2}{}^{t} \le \tau \tag{36}$$

where: Subscript 1 and 2 denote China Southern Power Grid and Lancang-Mekong Power Grid respectively. Q_R^t is the column vector of water consumption in the reservoir for the time t period. $A_h q_h^t$ is the water consumption of all hydropower units in the reservoir. $Q_R^{t,d}$ is the column vector of the surplus water quantity in the reservoir at time *t*. R^t is the vector of reservoir capacity at time *t*. R_{max}, R_{min} are the upper and lower limits of the reservoir capacity. ΔQ_R is the creep rate of the unit. Q_{Rmin} depends mainly on the normal water supply and the limitation of downstream shipping. Q_{Rmax} depends mainly on the flood discharge capacity of the reservoir; Q_{in}^t represents the vector of water coming from the upstream reservoir at time t. I_{rain}^t denotes the column vector of incoming water from the reservoir at time period *t*. y_h^t denotes the column vector of hydropower unit start-up decision variables at time *t*. I_h^t is a vector of start-stop state variables for the time period *t*. τ is the allowed number of starts and stops.

2) Hydropower unit constraints
3) Renewable energy unit constraints (Li et al., 2019)

Since the renewable energy output is random, variable, and uncontrollable, the output of renewable energy is controlled to operate within the predicted value in the dispatching operation. At the same time, according to the requirement of energy conservation and environmental protection in the grid operation, the renewable energy generates as much as possible. The model proposed in this paper introduces a balance mechanism to curtail part of the output when the system cannot achieve load balancing under extreme output conditions or the renewable energy delivery is blocked. It is expressed as follows:

$$P_{n1}{}^{t} + P_{nc1}{}^{t} = P_{nf1}{}^{t}, \forall t \in T \tag{37}$$

$$0 \le P_{n1}{}^{t}, 0 \le P_{nc1}{}^{t}, \forall t \in T \tag{38}$$

$$P_{n2}{}^{t} + P_{nc2}{}^{t} = P_{nf2}{}^{t}, \forall t \in T \tag{39}$$

$$0 \le P_{n2}{}^{t}, 0 \le P_{nc2}{}^{t}, \forall t \in T \tag{40}$$

where: Subscript 1 and 2 denote China Southern Power Grid and Lancang-Mekong Power Grid respectively. P_n^t is the new energy output power in time period *t*. P_{nc}^t is the curtailing new energy power in time period *t*. P_{nf}^t is the predicted renewable energy output for time period *t*.

4) Load balance constraints

The balance constraint between load and generation is expressed as

$$\begin{aligned}\sum_{t\in T} D_1{}^{t} &= \sum_{t\in T} P_{c1}{}^{t} + \sum_{t\in T} P_{f1}{}^{t} + \sum_{t\in T} P_{h1}{}^{t} \\ &+ \sum_{t\in T} P_{n1}{}^{t} + \sum_{t\in T} D_{c1}{}^{t}, \forall t \in T\end{aligned} \tag{41}$$

$$\begin{aligned}\sum_{t\in T} D_2{}^{t} &= \sum_{t\in T} P_{c2}{}^{t} + \sum_{t\in T} P_{f2}{}^{t} + \sum_{t\in T} P_{h2}{}^{t} \\ &+ \sum_{t\in T} P_{n2}{}^{t} + \sum_{t\in T} D_{c2}{}^{t}, \forall t \in T\end{aligned} \tag{42}$$

5) Power line constraints

In performing the regional joint operation simulation, the regional power line transmission capacity constraint is expressed as

$$-L_{1i,\max} \le L_{1i}(t) \le L_{1i,\max} \tag{43}$$

$$-L_{2i,\max} \le L_{2i}(t) \le L_{2i,\max} \tag{44}$$

where: Subscript 1 and 2 denote China Southern Power Grid and Lancang-Mekong Power Grid respectively. $L_{i,max}, -L_{i,max}$ are the upper and lower limits of the transmission capacity of the power line *i*, respectively. The current reference direction is set to be positive for the inflow region and negative for the outflow region.

6) Spinning Reserve constraints

The positive and negative reserve constraints of the system are expressed as

$$\begin{aligned}&\sum_{t\in T} {D_1}^t + {r_{u1}}^t \sum_{t\in T} {D_1}^t \le \sum_{t\in T} {P_{c1\max}}^t I_{c1} + \sum_{t\in T} {P_{f1\min}}^t {I_{f1}}^t\\&+\sum_{t\in T} {P_{h1\min}}^t + \sum_{t\in T} {P_{nf1}}^t + \sum_{t\in T} {D_{c1}}^t, \forall t \in T\end{aligned} \tag{45}$$

$$\begin{aligned}&\sum_{t\in T} {D_2}^t + {r_{u2}}^t \sum_{t\in T} {D_2}^t \le \sum_{t\in T} {P_{c2\max}}^t I_{c2} + \sum_{t\in T} {P_{f2\min}}^t {I_{f2}}^t\\&+\sum_{t\in T} {P_{h2\min}}^t + \sum_{t\in T} {P_{nf2}}^t + \sum_{t\in T} {D_{c2}}^t, \forall t \in T\end{aligned} \tag{46}$$

where: Subscript 1 and 2 denote China Southern Power Grid and Lancang-Mekong Power Grid respectively. r_u^t is the positive reserve rate required for time period *t*.

$$\begin{aligned}&\sum_{t\in T} {D_1}^t - {r_{d1}}^t \sum_{t\in T} {D_1}^t \ge \sum_{t\in T} {P_{c1\min}}^t I_{c1}\\&+\sum_{t\in T} {P_{f1\min}}^t {I_{f1}}^t + \sum_{t\in T} {P_{h1\min}}^t + \sum_{t\in T} {D_{c1}}^t, \forall t \in T\end{aligned} \tag{47}$$

$$\begin{aligned}&\sum_{t\in T} {D_2}^t - {r_{d2}}^t \sum_{t\in T} {D_2}^t \ge \sum_{t\in T} {P_{c2\min}}^t I_{c2}\\&+\sum_{t\in T} {P_{f2\min}}^t {I_{f2}}^t + \sum_{t\in T} {P_{h2\min}}^t + \sum_{t\in T} {D_{c2}}^t, \forall t \in T\end{aligned} \tag{48}$$

where: Subscript 1 and 2 denote China Southern Power Grid and Lancang-Mekong Power Grid respectively. r_d^t is the negative reserve rate required for time period *t*.

In the calculation of the positive reserve rate, even if the output of new energy is curtailed, the curtailed portion is included in the reserve capacity. In the negative reserve rate calculation, new energy can be curtailed anytime, so it is not counted as reserve capacity.

In this paper, the values beyond the transmission capacity range are corrected. The corrected transmission curves are used as the designated output of the delivery units to conduct internal simulation runs in the Laos and Myanmar regions as well as the Yunnan region, respectively. According to the results, we obtain the power planning results for 2025 in both Laos and Myanmar as well as the Yunnan region.

4 Calculation method of regional power balance and trading potential assessment index

4.1 Power balance index and calculation method

The continuous, rapid, and uneven power demand growth and the rapid development of renewable energy sources have put forward higher requirements for achieving power balance in the regional unified power market. In order to achieve power balance and ensure regular regional power trading, this paper designs a calculation method for regional power balance and trading potential assessment, which not only gives the deterministic abandonment amount of wind power and photovoltaic power but also improves the accuracy of power balance analysis compared with the traditional power balance method (Hu et al., 2021), and provides a guarantee for regular trading in the power market (Zeng et al., 2017; Ji et al., 2021; Wang et al., 2021; Xu et al., 2022).

Power balance is the primary security issue of power system, which means that the power generation and load should be balanced in real time, otherwise the whole power system may oscillate or even collapse. By calculating the power surplus through our cases, it can be found that the power surplus level of the regional joint optimization is higher than that of the separate optimization, which indicates that the construction of a unified power market can alleviate the situation of insufficient power surplus and ensure the reliability and stability of power supply.

The specific calculation expression for power balance is as follows,

$$P^{sys} = P^{load} + P^{rotate} + P^{cease} + P^{s} + P^{A} \tag{49}$$

$$\begin{aligned}P^{avail} = {}& P^{thermal} + P^{pneumo} + P^{hydro} + P^{nuclear}\\&+P^{pump} + P^{stored} + P^{wind} + P^{photo}\end{aligned} \tag{50}$$

$$G^{power} = MIN\left(P^{\mathrm{avail}} - P^{sys}, 0\right) \tag{51}$$

where: P^{sys} is the system power demand, and P^{load} refers to the load. P^{rotate} is the spinning reserve, and P^{cease} is the shutdown reserve. P^{S} is the power delivered outside, P^{A} is the external power delivered inside, and P^{avail} is the available capacity of the power source. $P^{thermal}$ is the thermal generation power, P^{pneumo} is the gas power generation, P^{hydro} is the hydroelectric power generation, and $P^{nuclear}$ is the nuclear power generation. P^{pump} refers to the pumped storage availability, and P^{stored} refers to the energy storage. P^{wind} is the wind power generation, and P^{photo} is the photovoltaic power generation. G^{power} refers to the power shortage.

4.2 Energy balance index and calculation method

The energy balance is specifically expressed as follows,

$$G^{energy} = \sum_{t\in T} G^{power} * t, \forall t \in T \tag{52}$$

where: G^{energy} is the electric quantity shortage.

4.3 Peaking balance index and calculation method

The grid is often overloaded during peak consumption. At this time, it is necessary to put in the generator set outside the normal operation to meet the demand. These generating units are called peak shaving units, which is used to regulate the peak of electricity.

The peaking balance is expressed as follows [19]

$$G^{load} = MIN\left(P^{load} + P^{S} - P^{avail} - P^{sys}, 0\right) \tag{53}$$

where: G^{load} is the load shortage.

4.4 Electricity trading indicators and calculation methods

Electricity transaction costs are specifically expressed as follows.

$$C = P^{S} * C^{S} - P^{A} * C^{A} \tag{54}$$

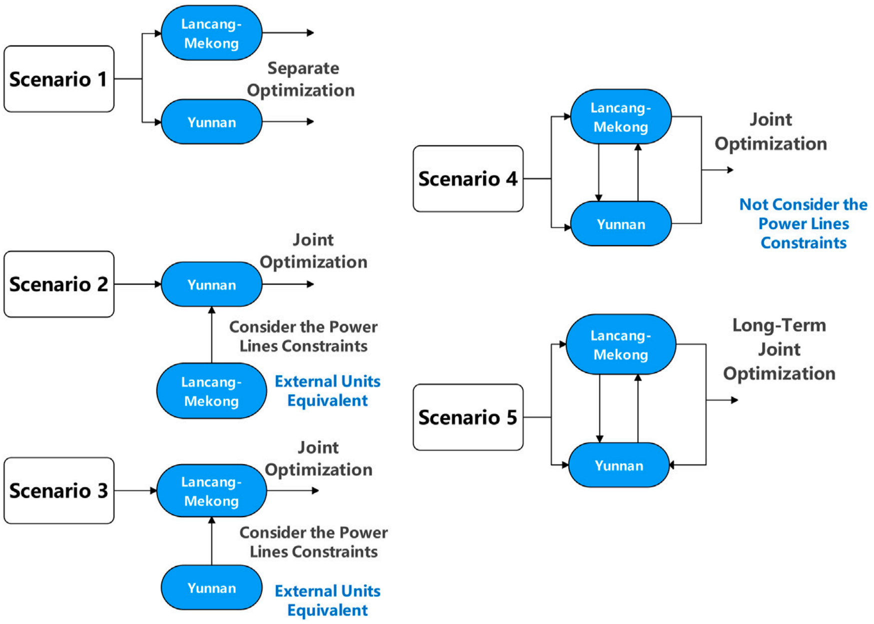

FIGURE 6
Boundary conditions under different scenarios.

where: C is the transaction cost, the C^S is the purchase price of electricity, and C^A is the price of electricity sold.

5 Case study

The daily operation curves derived from the operation simulations evaluate the trading potential and power balance analysis. Among them, the load 8760 curve is generated by planning the maximum annual power, annual electric quantity, historical load characteristics, and other parameters. The new energy 8760 curve is generated by using historical power output data and equal scaling of renewable energy planning installations. The reserve capacity in the simulation is taken as 12% of the highest load for the whole society, including 7% for spinning reserve and 5% for non-spinning reserve.

5.1 Operational simulation boundary conditions

Scenario 1(Benchmark Scenario): Without considering power trading, the existing interconnection Scenario between the Mekong countries and the southern region of China treats Laos and Myanmar as a whole and optimizes the power generation in the two regions of Laos and Myanmar and Yunnan, respectively according to the power and load characteristics in 2025, and obtains the power generation situation without power trading.

Scenario 2: Take Yunnan as the optimization subject, equate each of Laos and Myanmar into one out-of-area unit according to the existing interconnection Scenario between the Mekong countries and the southern region of China, set the maximum output constraint and generation capacity constraint, and simulate the power interconnection capacity of Laos, Myanmar, and Yunnan in 2025 under the state of constrained power lines.

Scenario 3: Take the Mekong countries as the optimization subject, equate Yunnan into an out-of-area unit according to the existing interconnection Scenario, set the maximum output constraint and generation capacity constraint, and simulate the power interconnection capacity of Yunnan and Mekong countries in 2025 under the state of constrained power lines.

Scenario 4: Set the installed capacity and load parameters of various power sources in Laos and Myanmar in 2025, and run them jointly with units and loads in Yunnan to simulate the interconnection capacity of Laos, Myanmar, and Yunnan under the ideal scenario of no power line constraint and "same unit bidding".

Scenario 5: Set the installed power and load parameters of various power sources in the five Mekong countries in 2025, and run them jointly with units and loads in Yunnan to simulate the power interconnection potential of the five Lancang-Mekong countries and Yunnan under the long-term plan.

All scenarios are concluded in Figure 6.

In non-joint operation cases, the calculation time for Yunnan and Lancang-Mekong countries operation are 401.45 s and 40.21 s separately, while in joint operation cases, the calculation time are 422.36 s and 56.31 s. Although joint operation seems more complex, its calculation time is acceptable.

In this paper, the transmission price between regions is a fixed parameter set manually. In the case of sufficient transmission capacity, the price difference between regions should be equal to the transmission price between those regions. If the transmission price is set reasonably, the price difference between regions will not be too large or too small.

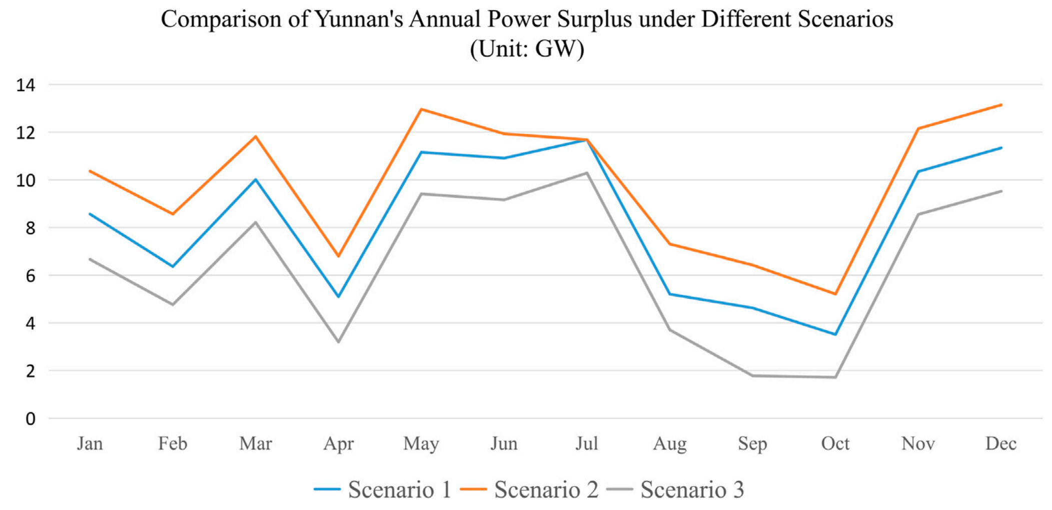

FIGURE 7
Comparison of Yunnan's annual power surplus under different scenarios.

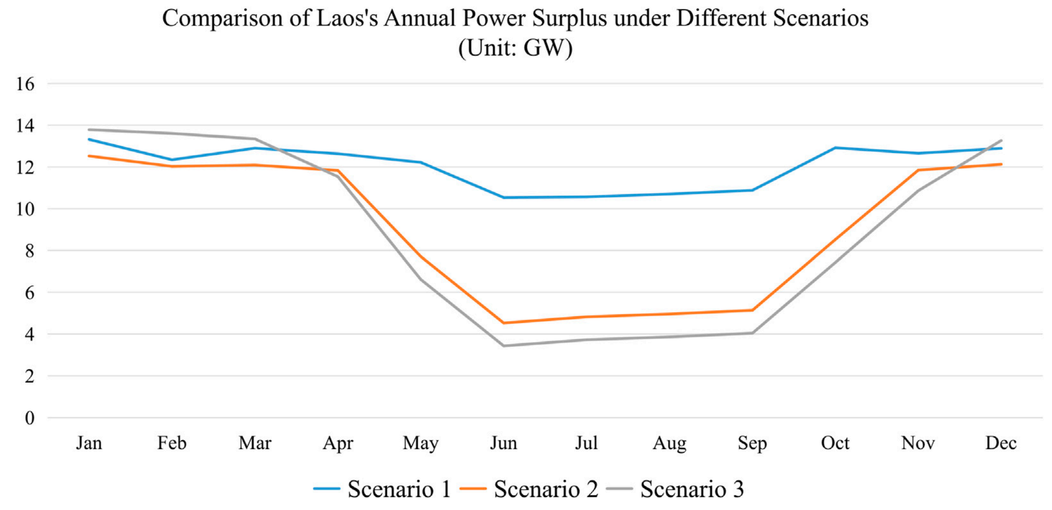

FIGURE 8
Comparison of Lao's annual power surplus under different scenarios.

5.2 Electricity balance analysis

The power surplus of Yunnan, Laos, and Myanmar under different scenarios is obtained using the power balance index calculation method in 4.1. In the benchmark scenario, Yunnan's power surplus is positive throughout the year and is greater than 3 GW per month with fluctuating values. It achieves a maximum value of 11.7 GW in July and a minimum value of 3.5 GW in October. From Yunnan's aspect, the power surplus curve is always above the power surplus curve of the benchmark scenario. The monthly power surplus increases, and the reliability of the power supply improves after trading. The minimum value of power surplus is 5.2 GW in October, which is 1.7 GW higher than Scenario 1. However, the maximum value of power surplus appears in December, reaching 13.1 GW, which is 1.8 GW higher than Scenario 1. Standing in the Lancang-Mekong perspective for power trading, the power surplus curve of Yunnan always lies below the power surplus curve of the benchmark Scenario because its delivery units deliver full power to both Lao and Myanmar. The power surplus appears at a minimum value of 1.7 GW in October, which is 1.8 GW less than Scenario 1, and at a maximum value of 10.2 GW in July, which is 1.4 GW less than Scenario 1. Results are shown in Figure 7.

In the benchmark scenario, Laos has a power surplus of more than 3 GW, which stays stable with high values from January to March, drops sharply from April to June, and gets a minimum power surplus of 10.5 GW in June. It has a small increase from July to September, and a larger increase from September to October, and then stays stable. The benchmark scenario has a maximum value of 13.3 GW in January.

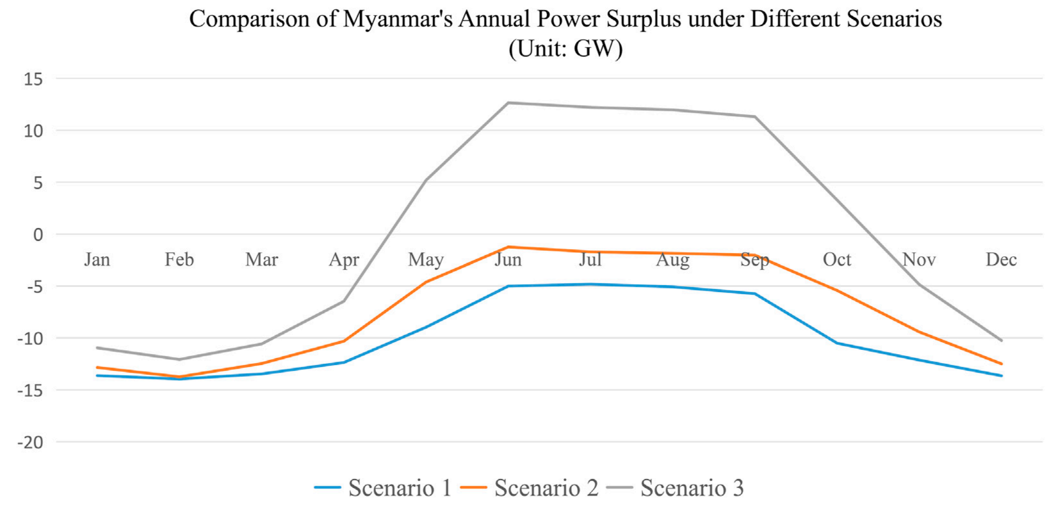

FIGURE 9
Comparison of Myanmar's annual power surplus under different scenarios.

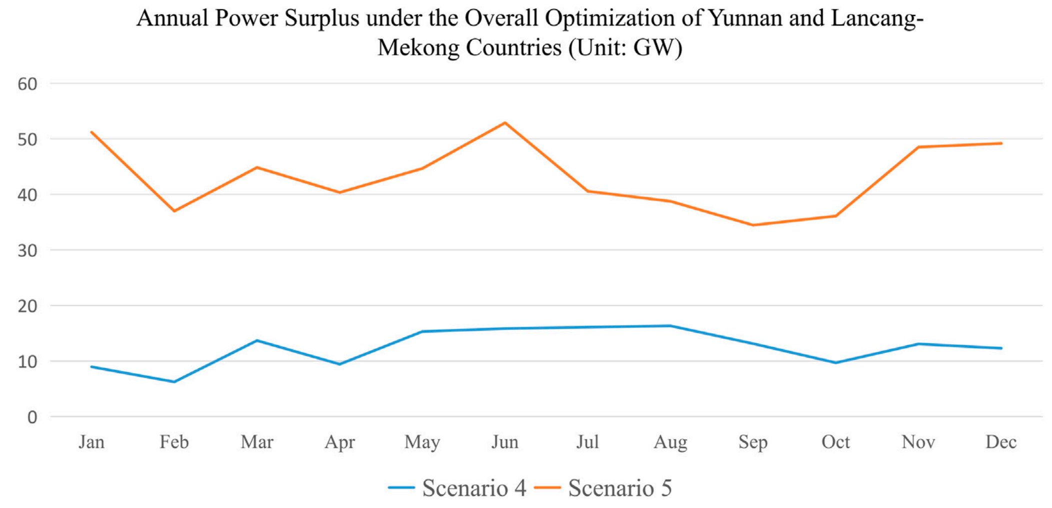

FIGURE 10
Annual power surplus under the overall optimization of Yunnan and Lancang- Mekong countries.

Scenario 2's and Scenario 3's trends are roughly the same as the benchmark. When seeing power trading from the Lancang-Mekong perspective, the power surplus also has a minimum value of 3.4 GW in February and a maximum value of 13.7 GW in January. From the Yunnan perspective, the power surplus shows a minimum value of 4.5 GW in June and a maximum value of 12.5 GW in January. Results are shown in Figure 8.

In the benchmark scenario, the power surplus in Myanmar is less than 0. The power surplus is seriously insufficient, with a minimum value of -13.9 GW in February, after which the power surplus starts to increase, approaching -5 GW in the flood season from June to September, with a maximum value of -4.82 GW in July. After September, the power surplus starts to decline significantly again. Scenarios 2 and 3 show roughly the same trend as the benchmark scenario. The overall curve is highest when power trading from the Lancang-Mekong perspective, as Yunnan's delivery units deliver full power to Myanmar. The power surplus also shows a minimum value of -12.1 GW in February and a maximum value of 13.7 GW in June. When seeing from Yunnan's perspective, the power surplus shows a minimum value of -14.2 GW in February and a maximum value of -1.24 GW in June. Results are shown in Figure 9.

Separately analyze Scenario 4 and Scenario 5, and show the results in Figure 10. Scenario 4 considers the power transactions between Yunnan and Lao-Myanmar without power line constraints. The minimum value occurs in February at 6.2 GW, which is larger than the sum of the power surpluses under Scenario 1 when Yunnan and Lao-Myanmar are optimized separately. The maximum value occurs in August, at 16.3 GW, which can maintain a surplus of more than

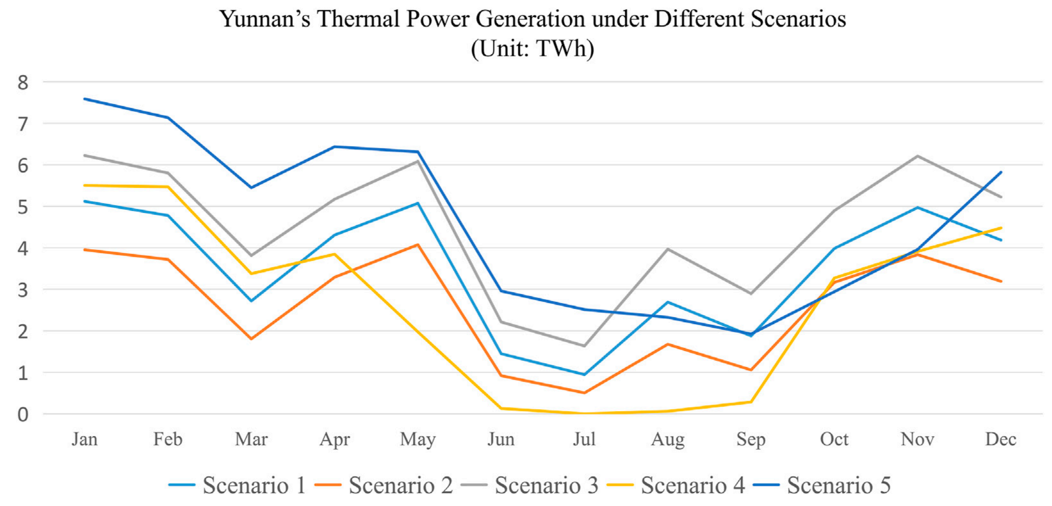

FIGURE 11
Yunnan's thermal power generation under different scenarios.

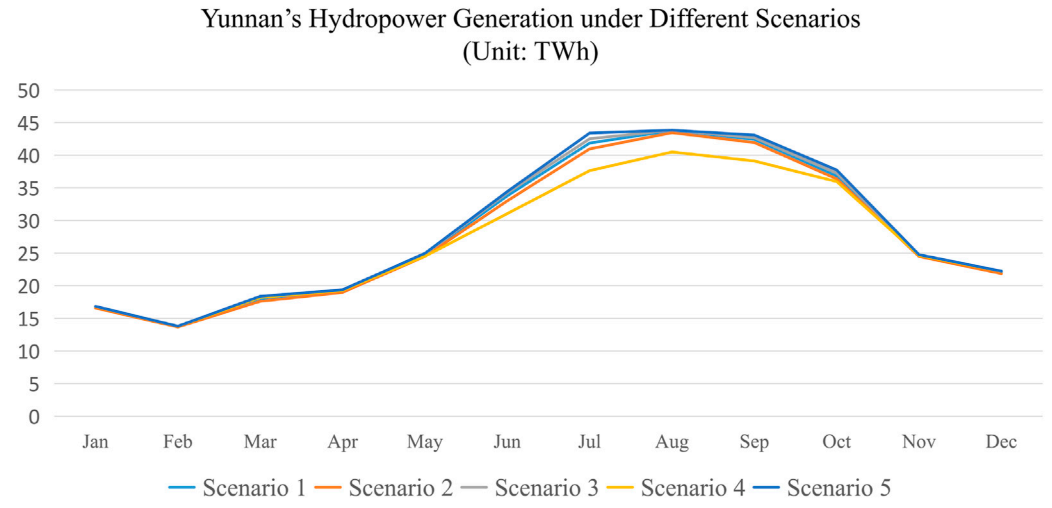

FIGURE 12
Yunnan's hydropower generation under different scenarios.

10 GW during the summer flood season. Scenario 5 considers the long-term power transactions between Yunnan and the five Lancang-Mekong countries. Its minimum value occurs in September at 34.4 GW, and the maximum value occurs in June at 52 GW, with an average power surplus of 43.2 GW. The curve proves that conducting long-term power interconnection is beneficial to increasing the regional power surplus and maintaining the stability of the power supply.

5.3 Energy balance analysis

Compare the month-by-month thermal power generation in Yunnan under different scenarios. In the benchmark scenario, the thermal power generation in Yunnan troughs during the summer hydro generation period, reaching a minimum of 0.9 TWh in July. January, May, and November witness three peaks concerning thermal power generation, reaching 5.1 TWh, 5.1 TWh, and 4.9 TWh, respectively. The thermal power generation in each month of Scenario 2 is lower than the benchmark scenario, proving that conducting power interconnection benefits the consumption of clean energy and reduces thermal power generation. It obtains a minimum value of 0.5 TWh in July and a maximum value of 3.9 TWh in January. Scenario 3 has a higher monthly thermal generation than the benchmark scenario due to the need for outbound transmission, obtaining a maximum value of 6.2 TWh in January and a minimum value of 1.6 TWh in July. Scenario 4 has thermal power output close to zero from June to September, but the

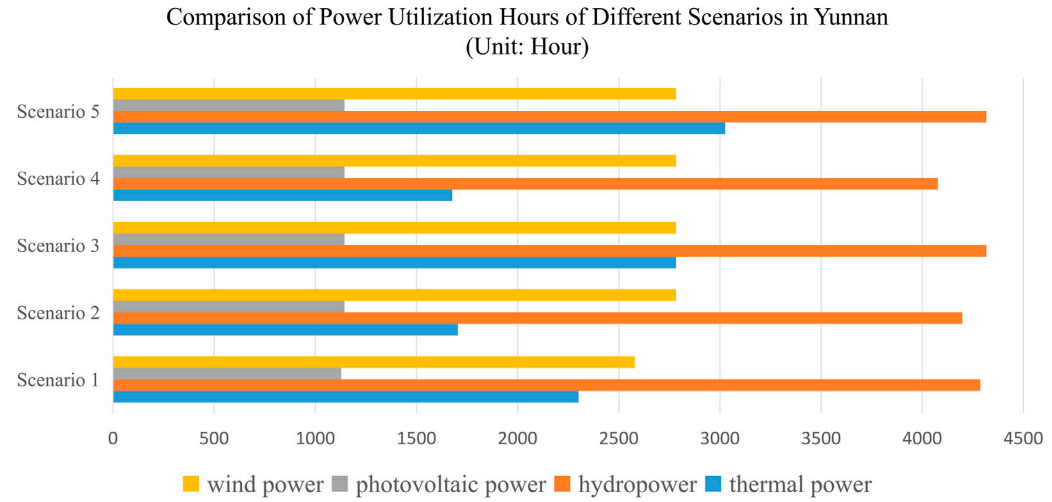

FIGURE 13
Comparison of power utilization hours of different scenarios in Yunnan.

TABLE 2 Power utilization hours of different scenarios in Yunnan (Unit: Hour).

Yunnan	Thermal power	Hydropower	Photovoltaic power	Wind power
Scenario 1	2300.46	4286.285	1127.629	2578.848
Scenario 2	1704.465	4197.528	1143.716	2782.334
Scenario 3	2782.334	4316.143	1143.716	2782.334
Scenario 4	1676.472	4075.702	1143.716	2782.334
Scenario 5	3025.138	4316.06	1143.716	2782.334

thermal power generation value is greater than the benchmark scenario during December and March. The trend of the generation curve of Scenario 5 tends to be consistent with the above four scenarios, obtaining a minimum value of 1.9 TWh in September and a maximum value of 7.5 TWh in January. Results are shown as Figure 11.

The following Figure 12 shows the level of hydropower generation in Yunnan. The curves of the five scenarios follow the same trend, with the minimum value of hydropower generation obtained in February, and the power generation has been on an upward trend since February, with the most obvious magnitude from May to July, all reaching the maximum value in August, and then starting to decline continuously in September. The curves from top to bottom are arranged in the order of Scenario 5, Scenario 3, Scenario 1, Scenario 2, and Scenario 4.

The power utilization hours for different scenarios in Yunnan shown as Figure 13 are obtained by counting the generation capacity of the units and the installed capacity. For thermal power, Scenario 2 has 596 fewer thermal power utilization hours than the benchmark scenario, i.e., a 25.9% decrease; Scenario 3 has 482 more thermal power utilization hours than the benchmark scenario, an increase of 21%; Scenario 4 has 624 less thermal power utilization hours than the benchmark scenario, a decrease of 27.1%. Scenario 5 has more thermal power utilization hours than the benchmark scenario at 3,025 h due to its vast area and heavy load. For hydropower, Scenario 2 has 89 h less than the benchmark scenario, a decrease of 2.1%; Scenario 3 has 30 h more than the benchmark scenario, an increase of 0.7%; Scenario 4 has 210 h less than the benchmark scenario, a decrease of 4.9%; and Scenario 5 has 30 h more than the benchmark scenario, an increase of 0.7%. Scenario 2 has the same number of wind power utilization hours for wind power as Scenarios 3, 4, and 5, all 203 h more than the benchmark scenario, i.e., an increase of 7.89%. For PV, Scenario 2 has the same wind power utilization hours as Scenarios 3, 4, and 5, which are 16 h more than the benchmark scenario, i.e., an increase of 1.43%. Except for the benchmark scenario, all other scenarios in Yunnan have no wind and light abandonment. Detailed data are shown in Table 2.

5.4 Complementary potential assessment

The curves of power delivered outside for Yunnan, Laos, and Myanmar under different scenarios are obtained by counting the output of the delivery units and the difference between the generation and load of each region.

Scenario 2 stands for power interconnection from Yunnan's perspective, where Yunnan gets full power from Lao and Myanmar units. Scenario 3 stands for power interconnection from Lancang-Mekong's perspective, where Yunnan's units send full power to Lao

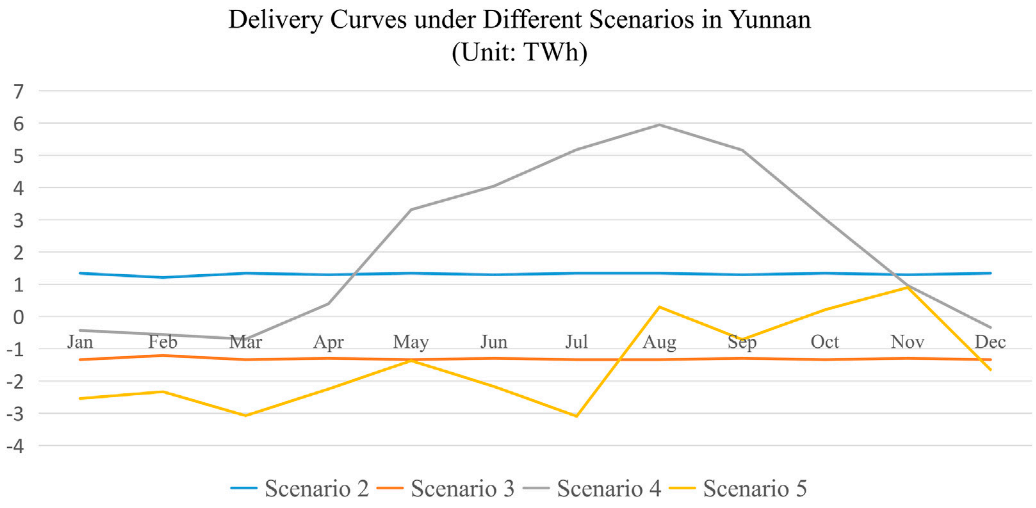

FIGURE 14
Delivery curves under different scenarios in Yunnan.

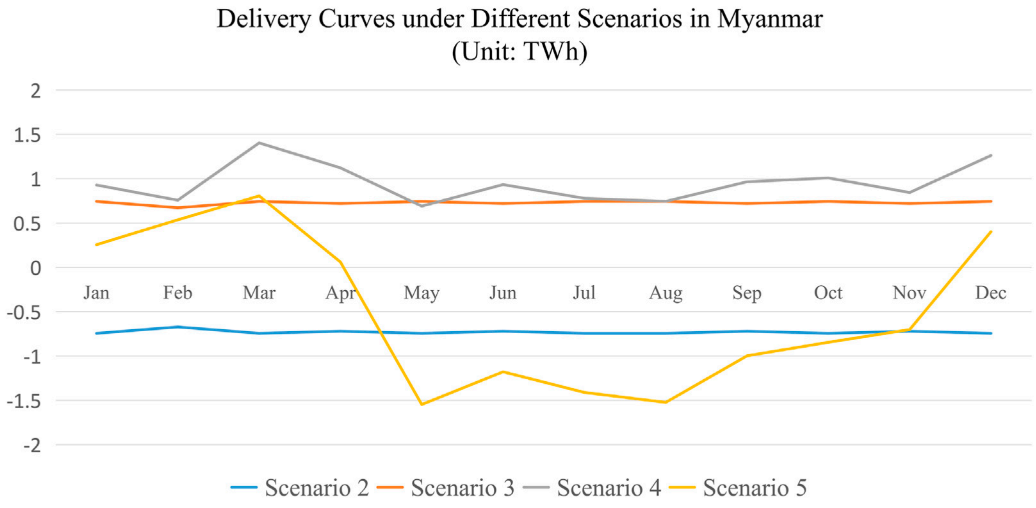

FIGURE 15
Delivery curves under different scenarios in Myanmar.

and Myanmar units. Hence, the curves of Scenarios 2 and 3 are basically in the form of straight lines opposite each other. The total amount of incoming power sold in Scenario 4 is 25.9 TWh. Yunnan sends power to Lancang-Mekong from January to March and December, gets power from Lancang-Mekong countries from April to November, and gets the maximum amount of incoming power sold in August of 5.9 TWh. The total power sent out from Scenario 5 is 17.7 TWh. Yunnan only needs power from Lancang-Mekong countries in August and November and can supply power to Lancang-Mekong countries in the rest of the months. The maximum amount of power available is 3.1 TWh in July. The delivery curves in Yunnan are shown in Figure 14.

Scenario 2 stands for power interconnection from Yunnan's perspective, with Myanmar's delivery units sending full power to Yunnan with a total of 8.8 TWh. Scenario 3 stands for power interconnection from Lancang-Mekong's perspective, with Yunnan's delivery units returning full power to Myanmar, with an opposite curve to Scenario 2. Scenario 4 sells 11.4 TWh of electric quantity, requiring monthly incoming power sales of more than 0.6 TWh, reaching a maximum of 1.4 TWh in March. Scenario 5 allows Myanmar to supply power to Yunnan from May to November, reaching a maximum of 1.5 TWh, and requires Yunnan to return power to Myanmar in other months. The delivery curves in Myanmar are shown in Figure 15.

Scenario 2 stands for power interconnection from the Yunnan perspective, where the Lao's delivery units send full power to Yunnan with a total delivery of 7.0 TWh. Scenario 3 stands for power interconnection from the Lancang-Mekong perspective, where the

TABLE 3 Total electricity interconnection and transaction amount under different scenarios (Unit: TWh/Million yuan).

	Yunnan		Myanmar		Laos	
	Total electricity interconnection amount	Transaction amount	Total electricity interconnection amount	Transaction amount	Total electricity interconnection amount	Transaction amount
Scenario 2	15.77	-47.30	-8.76	26.28	-7.01	21.02
Scenario 3	-15.77	47.30	8.76	-26.28	7.01	-21.02
Scenario 4	25.98	-77.94	11.44	-34.32	-36.75	110.24
Scenario 5	-17.79	53.39	-6.14	18.42	-43.44	130.33

Yunnan's delivery units return full power to Laos with an opposite curve to Scenario 2. Scenarios 4 and 5 have Laos returning power to Yunnan every month, reaching a maximum in the summer. The total amount of power delivered outside is 36.7 TWh for Scenario 4 and 43.4 TWh for Scenario 5, an increase of 18.2% over Scenario 4. Scenario 4 reached a maximum of 6.7 TWh in August, while Scenario 5 also reached a maximum of 7.2 TWh in August, an increase of 7.74% over Scenario 4.

The following Table 3 shows each country's electricity interconnection and transaction amount under different scenarios. The transaction price is determined with reference to the average level of inter-provincial transmission prices in the China southern region. When conducting the near-term transmission line interconnection, Yunnan, Myanmar, and Laos can receive roughly 4.7 billion yuan, 2.6 billion yuan, and 2.1 billion yuan, respectively. This transaction is essential to support the development of the Lancang-Mekong countries and also increases the revenue of the China Southern Power Grid. Under medium and long-term regional integration, each country can sell out more electricity, with Laos sending out a more significant proportion of its electricity, generating up to 13 billion yuan in revenue. Yunnan also has a corresponding revenue of 5.3 billion yuan. It can be seen that building a regional unified power market and improving market conditions have a positive impact on promoting power interconnection among countries.

6 Conclusion

This paper proposes a mechanism to evaluate the power balance and complementary potential of the regional power grids of the Lancang-Mekong countries and Southern China under long-period operation simulation. The mechanism takes into account the energy supply structure, energy use form, cross-border transmission capacity, and multi-area complementary potential of the power grids of the Lancang-Mekong countries and Southern China. It also assesses the multi-stage power balance and complementary potential of the power grids of the Lancang-Mekong countries and Southern China by setting different boundary conditions. The following conclusions are drawn from the case study.

1) Conducting power trading between the southern region of China and the Lancang-Mekong countries can reduce fossil energy generation and increase the rate of clean energy consumption, which is green and environmentally friendly. From Yunnan's perspective for power trading, Yunnan's thermal power utilization hours are reduced by 25.9%, and thermal power generation per month is lower than the benchmark scenario.
2) Electricity interconnection can alleviate the power surplus shortage and ensure the power supply's reliability and stability. The power trading scenarios have a higher overall surplus than the benchmark scenario. Myanmar has a negative surplus in the absence of trading, and the minimum monthly surplus shortfall is substantially improved after trading.
3) Long-term power interconnection has excellent economic benefits. Under medium and long-term regional integration, countries can send out more electricity, of which Laos sends out a larger proportion of electricity, with up to 13 billion yuan in revenue. Yunnan also has a corresponding revenue of 5.3 billion yuan. It can be seen that building a regional unified power market and improving market conditions have a positive impact on promoting power interconnection among countries.

Data availability statement

The original contributions presented in the study are included in the article/supplementary material, further inquiries can be directed to the corresponding author.

Author contributions

ZH, LH, and LE contributed to conception and design of the study. HY wrote sections of the manuscript. TC organized the database. ZW performed the statistical analysis. XG wrote the first draft of the manuscript. All authors contributed to manuscript revision, read, and approved the submitted version.

Funding

This work was supported by the Science and Technology Project of Yunnan Power Grid Co., Ltd (056200KK52210013). National Natural Science Foundation of China under Grant 52007029.

Conflict of interest

Authors ZH, LH, LE, and XG were employed by the Company Yunnan Power Grid Co., Ltd.

The remaining authors declare that the research was conducted in the absence of any commercial or financial relationships that could be construed as a potential conflict of interest.

The authors declare that this study received funding from Science and Technology Project of Yunnan Power Grid Co., Ltd. The funder had the following involvement in the study: offered the raw data of this work and made the decision to submit this paper for publication.

Publisher's note

References

Amundsen, E. S., and Bergman, L. (2006). Why has the Nordic Electricity Market worked so well? *Util. Policy* 14 (3), 148–157. Available at:. doi:10.1016/j.jup.2006.01.001

Bushnell, J., Mansur, E., and Saravia, C. (2007). Vertical arrangements, market structure, and competition an analysis of restructured U.S. Electricity Markets. *Am. Econ. Rev.* 98 (1), 237–266. doi:10.3386/w13507

Hu, S., Xiang, Y., Liu, J., Li, J., and Liu, C. (2021). A two-stage dispatching method for wind-hydropower-pumped storage integrated power systems. *Front. Energy Res.* 9, 65. doi:10.3389/fenrg.2021.646975

Ji, C., Chao, Y., Zhang, C., and Ma, H. (2021). A short-term power balance model for electricity considering the cost of abandoned water capacity[J]. *J. Hydropower Generation* 40 (03), 50–63. doi:10.11660/slfdxb.20210305

Le, H. L., Ilea, V., and Bovo, C. (2019). Integrated European intra-day electricity market: Rules, modeling and analysis. *Appl. Energy* 238, 258–273. Available at:. doi:10.1016/j.apenergy.2018.12.073

Li, M. J., Chen, G. P., Dong, C., Liang, C. F., Wang, W. S., and Fan, G. F. (2019). Research on the power balance problem of new energy power system [J]. *Power Grid Technol.* 43 (11), 3979–3986. doi:10.13335/j.1000-3673.pst.2019.0440

Ngan, H. W. (2010). Electricity regulation and electricity market reforms in China. *Energy Policy* 38 (5), 2142–2148. Available at:. doi:10.1016/j.enpol.2009.06.044

She, H., Han, X., Lu, D., and Du, B. (2021). Electricity "interconnection" to build "one belt and one road" [J]. *Guangxi Electr. Ind.* (09), 20–21.

Wang, X., Peng, P., and Chen, N. (2021). "Review and reflection on new energy participating in electricity spot market mechanism," in Proceedins of the IEEE Sustainable Power and Energy Conference (iSPEC), Perth Austrlia, 4-7th December-2022, 757–762. doi:10.1109/iSPEC53008.2021.9735730

Wu, H., Syed, M., Ali, S., Ahsan, N., Ali, A., Shahid, I., et al. (2020). The impact of energy cooperation and the role of the one belt and road initiative in revolutionizing the geopolitics of energy among regional economic powers: An analysis of infrastructure development and project management. *Complexity* 2020, 1–16. doi:10.1155/2020/8820021

Xiao, Y., Li, C. Y., Zhao, T. Y., and Liu, W. X. (2016). Credible capacity assessment of wind turbines considering grid constraints in Western water-rich areas[J]. *Power Constr.* 37 (06), 134–141.

Xing, W. (2017). Lancang-mekong river cooperation and trans-boundary water governance: A Chinese perspective. *China Q. Int. Strategic Stud.* 03 (03), 377–393. Available at:. doi:10.1142/s2377740017500233

Xu, J., Liu, A., Qin, Y., Xu, G., and Tang, Y. (2022). Research on power system joint optimal generation scheduling based on improved balance optimizer. *Front. Energy Res.* 10. doi:10.95838410.3389/fenrg.2022.958384

Zeng, X. T., Liu, T. Q., Li, X., He, C., Han, X., and Qin, H. T. (2017). Research on mixed integer quadratic programming model and algorithm for power balance of high hydropower specific gravity system [J]. *Chin. J. Electr. Eng.* 37 (04), 1114–1125. doi:10.13334/j.0258-8013.pcsee.152439

Zhang, Y. (2019). *Study on the impact of power futures on the dynamics of renewable energy returns and risks in China[D]*. Beijing: China University of Petroleum. doi:10.27643/d.cnki.gsybu.2019.000578

Zhao, D. (2020). *Annual power balance of hybrid power sources considering renewable energy consumption mechanism [D]*. China: Chongqing University. doi:10.27670/d.cnki.gcqdu.2020.003580

Zhu, S., Jiang, Y., and Huang, X. (2021). Reflections on the construction of southern regional electricity spot market under the new situation[J]. *China Energy* 43 (12), 46–51. doi:10.3969/j.issn.1003-2355.2021.12.006

frontiers | Frontiers in Energy Research

TYPE Original Research
PUBLISHED 13 January 2023
DOI 10.3389/fenrg.2022.1065405

OPEN ACCESS

EDITED BY
Nantian Huang,
Northeast Electric Power University, China

REVIEWED BY
Tao Chen,
Southeast University, China
Tao Huang,
Politecnico di Torino, Italy

*CORRESPONDENCE
Lixia Sun,
leexiasun@163.com

SPECIALTY SECTION
This article was submitted to Smart Grids, a section of the journal Frontiers in Energy Research

RECEIVED 09 October 2022
ACCEPTED 31 October 2022
PUBLISHED 13 January 2023

CITATION
Sun L, Tian Y, Wu Y, Huang W, Yan C and Jin Y (2023), Strategy optimization of emergency frequency control based on new load with time delay characteristics.
Front. Energy Res. 10:1065405.
doi: 10.3389/fenrg.2022.1065405

Strategy optimization of emergency frequency control based on new load with time delay characteristics

Lixia Sun*, Yiyun Tian, Yichao Wu, Wenzhe Huang, Chenhui Yan and Yuqing Jin

College of Energy and Electrical Engineering, Hohai University, Nanjing, China

With the development of modern communication technology and the large number of new controllable loads connected to the power grid, the new controllable loads with flexible regulation characteristics can participate in the emergency frequency stability control. However, the communication state differences and spatial distribution characteristics of controllable load will affect the actual effect of frequency control. In this paper, an emergency frequency control method based on deep reinforcement learning is proposed considering the response time of controllable load shedding. The proposed method evaluates response ability for emergency control of controlled loads through load response time, controllable load amount and controllable load buses. Then, the controllable load with smaller response time is cut out preferentially to ensure rapid control, and the Markov Decision Process (MDP) is used to model the emergency frequency control problem. Finally, Rainbow algorithm of Deep Reinforcement Learning (DRL) is used to optimize the emergency frequency stability control strategy involving controllable load resources. The formation of emergency load shedding instruction is directly driven by high-dimensional operation state data after power grid failure, so that, the aim of minimizing the economic cost is achieved under the constraint of system stability. The effectiveness of the proposed method is verified in the IEEE 39-bus system.

KEYWORDS

new controllable load, load delay characteristics, emergency frequency control, deep reinforcement learning, rainbow algorithm

1 Introduction

With the massive access of renewable energy and the interconnection of large-scale systems, the power grid has changed into a complex dynamic system, and it is difficult to establish accurate mathematical models for it (Fan et al., 2022; Ren et al., 2022). The increase of new energy penetration and the access of more electronic power equipment have brought new risks to the stability of frequency. When the power imbalance between the source and load occurs, it may lead to regional power outage and system collapse

(Cao et al., 2021b,a; Wen et al., 2020). On the other hand, there are massive flexible loads on the load side, such as electric vehicles and temperature-controlled air conditioners (Zhang et al., 2022), which, in combination with modern communication technology, can be controlled when the system is in an emergency state. It can improve the flexibility and economy of the emergency frequency control of the power system. Therefore, it is of great significance for the stability of power grid that the new controllable load participates in the emergency frequency stability control.

At present, controllable load participation in the emergency frequency stability control has become one of the hot research topics in power system. Reference (Xu et al., 2018) proposed the comprehensive contribution index of interruptible load according to the total amount of load excision and the user excision, and obtained the load reduction strategy through optimization. In addition, the large proportion of controllable load and rapid continuous regulation capacity are used to improve the refinement of emergency control on the premise of ensuring safety and stability (Li and Hou, 2016). Some researchers cooperatively optimized the decentralized emergency demand response to obtain the optimal emergency frequency stability control strategy (Wang et al., 2020). However, the above research on the participation of controllable load in emergency frequency control only considers the basic indicators such as the total amount of the load shedding, the controllable load bus and the cost, and considers that the load removal is instantaneous. However, in practice, due to the differences in communication states and response speeds of controllable loads, different loads have different delay characteristics, which will produce different control effects. However, the influence of load delay characteristics on emergency frequency control is not considered in the above conferences.

In order to solve the problem of emergency frequency control in power system, current research methods mainly include response driven and event driven. The former calculated the load shedding amount and its action rounds offline/online according to the frequency deviation and frequency change rate of the inertia center. The latter usually carries out pre-control after monitoring the fault event to prevent the further expansion of the impact. The response-driven emergency frequency control will adjust the load reduction and action rounds in advance according to a certain operation scenario of the system (Terzija, 2006; Banijamali and Amraee, 2019; Li et al., 2020), which may be deviated from the actual operation scenario and affect the control effect. Most of the studies on event-driven load shedding are based on the optimization of the mathematical model of the power system (Xu et al., 2017, 2016), and the effect of load shedding strategy is closely related to the accuracy of the system model. The new power system has a high degree of nonlinearity and uncertainty, and it is difficult to establish an accurate mathematical model, which poses a challenge to obtain an accurate load shedding strategy.

In recent years, Machine Learning (ML) has been applied to power system stability control. It does feature mining based on data and does not need accurate mathematical model. In reference (Singh and Fozdar, 2019), support vector machine was used to evaluate the stability of the power system, and the optimal load shedding scheme was obtained according to the evaluation results. The extreme learning machine can also be used to train the load shedding prediction model offline and predict the actual load shedding online (Dai et al., 2012). The above traditional ML algorithm model is simple and relies too much on expert experience. Its control effect is affected by the size and quality of knowledge database, resulting in poor adaptability of the control effect of the model.

Combined with deep learning technology, DRL can realize high-dimensional feature extraction and direct learning of complex action space. Meanwhile, Deep Learning Q Network (DQN) and other algorithms improve the scalability and robustness of DRL, making it suitable for solving control problems of large-scale systems (Mnih et al., 2015; Schulman et al., 2017). Double DQN algorithm is used to effectively screen out the line breaking faults which can easily lead to power grid instability, and formulate emergency stability control measures (Zeng et al., 2020). In conference (Liu et al., 2018), it obtained the optimal shedding strategy to ensure the transient stability of power grid through Double DQN and Dueling DQN model analysis. In addition, DRL algorithm was also used to optimize the emergency frequency control strategy, and a variety of regulation methods were aggregated to reduce the stable frequency fluctuation (Chen et al., 2021). The above emergency control strategy is used to shed the whole line directly from the substation, without considering the influence of the new controlled load and its delay characteristics on the emergency control effect. At the same time, the stability and robustness of some algorithms are poor, and it is difficult to ensure the control effect of the model. Rainbow algorithm is based on DQN and it integrates a variety of improved algorithms. The model has superior stability and robustness, and has been widely used in the field of control and decision making (Hessel et al., 2017). Therefore, Rainbow algorithm is adopted in this paper to optimize the control strategy for emergency control involving controllable load considering delay characteristics.

In order to solve the above problems, this paper proposes an emergency frequency control method based on deep reinforcement learning Rainbow algorithm that considers the delay characteristics of the controlled load. According to the different delay characteristics, the new controllable load resources are modeled and aggregated to form an emergency control process in which the new controllable load is graded, and the load with smaller control delay is preferentially removed to ensure rapid removal. Finally, the deep reinforcement learning Rainbow algorithm model is used to optimize the emergency frequency control strategy, suppress the frequency drop depth of the system, reduce the deviation of the stable frequency, and reduce the control cost as much as possible.

2 Emergency frequency control with new controllable load participation

2.1 Mathematical description of power grid emergency frequency stability control

In frequency stability analysis of power systems, the frequency of each generator oscillates around the inertial center of the system. When the system is stable, the frequency of each generator will eventually approach the center of inertia frequency of the system. The center of frequency inertia fCOI is defined as follows:

$$f_{\mathrm{COI}} = \sum_{j=1}^{m}\left(H_j f_j\right) / \sum_{j=1}^{m} H_j \tag{1}$$

where m is the number of generators, H_j and f_j are the inertia time constant and frequency of generator bus j.

Due to the complexity of components in large power systems, the emergency frequency control problem is the highly nonlinear optimal decision problem. The mathematical model is adopted:

$$\min F = \left|f_{\mathrm{tem}} - f_{\mathrm{tem.set}}\right| + \lambda \sum_{j=1}^{m} P_{\mathrm{sl}j} \tag{2}$$

$$x_t = g\left(x_t, y_t, d_t, a_t\right) \tag{3}$$

$$0 = h\left(x_t, y_t, d_t, a_t\right) \tag{4}$$

$$x_t^{\min} \le x_t \le x_t^{\max} \tag{5}$$

$$y_t^{\min} \le y_t \le y_t^{\max} \tag{6}$$

$$a_t^{\min} \le a_t \le a_t^{\max} \tag{7}$$

where f_{tem} is the center stable value of the frequency inertia, $f_{\mathrm{tem.\ set}}$ is the preset frequency inertia of the center steady-state threshold, $P_{\mathrm{sl}j}$ is the load shedding amount of bus j, λ is the weight coefficient, x_t is the state variable of the power grid, such as the angle and angular velocity of the generator rotor, y_t is the output variable of the power grid, such as the voltage of each bus, a_t is the control variable of the power grid, such as the emergency control to cut off generators or loads, d_t is a disturbance or fault that may occur in the power grid.

2.2 The aggregate modeling of new controllable load with delay characteristics

New power loads are constantly being integrated into new power systems, and demand-side loads are becoming more and more diversified, such as typical new loads such as electric vehicles, temperature-controlled air conditioning and intelligent buildings. These new loads have strong controllability, large volume and obvious time and space distribution characteristics, which can participate in emergency frequency stabilization control.

For different loads, the load amount is different, and their delay characteristics are different. In this paper, delay time refers to the time required from the decision of the control center to cut off the load from the main network, including the decision time of the control center, communication time and load response time. The delay time t_i of load bus i can be described as:

$$t_i = t_{i,\mathrm{dec}} + t_{i,\mathrm{down}} + t_{i,\mathrm{res}} \tag{8}$$

where $t_{i,\mathrm{dec}}$ is the decision time shedding the load i for the control center, $t_{i,\mathrm{down}}$ is the time required for the communication module to send the command to load i, $t_{i,\mathrm{res}}$ is the response time of load i.

The difference of the delay characteristics of controllable loads affects the effect of emergency frequency control, which is one of the important factors for the participation of controllable loads. Different from the traditional load, the time and space distribution characteristics of the controllable load slows down its control speed. Then, the drop depth of system frequency is increased. The spatial location of the load is dispersed, and the load granularity is small, so it is difficult to adjust by the traditional method. For different loads, it is necessary to establish models according to the location, the amount and the delay time of controllable loads. The modeling results are shown in **Table 1**.

In actual control, because the single load amount of the new load is small and the loads is numerous, modeling only the single

TABLE 1 Modeling results of controllable load with delay characteristics.

Controllable load	location	Load amount	Delay
Electric vehicle 1	$1-1$	P_{1-1}	t_{1-1}
Electric vehicle 2	$1-2$	P_{1-2}	t_{1-2}
…	…	…	…
Electric vehicle n	$1-n$	P_{1-n}	t_{1-n}
Smart Building 1	$2-1$	P_{2-1}	t_{2-1}
Smart Building 2	$2-2$	P_{2-2}	t_{2-2}
…	…	…	…
Smart building m	$2-m$	P_{2-m}	t_{2-m}
Other loads	other	other	other
…	…	…	…

load with delay characteristics will lead to too large amount of resource data, which is difficult to deal with. In order to optimize the strategy more conveniently, the modeled controllable loads should be aggregated, that is, it should be graded according to the control delay, and the controllable loads of the same level should be aggregated. At the same time, in order to ensure the security, the delay time of this stage is taken as the maximal actual control delay of this stage of load. Although this method has some errors, it can reduce the difficulty of model building under the premise of considering the influence of load delay characteristics. Therefore, the aggregate modeling process of controllable load is shown in **Figure 1**.

After aggregation, a hierarchical aggregate controllable load of multiple buses is formed. The model is also composed of load location, load amount and load delay time. The result is shown in **Table 2**.

2.3 The process of emergency frequency control with new controllable load participation

In order to uniformly control the new controllable load with spatial distribution and delay characteristics, the controllable resource control process should be divided into uplink and downlink parts, and the control center and controllable load resources should be connected. The controllable resource control process starts with the control center, including the upstream controllable load aggregation modeling results, power grid fault perception and downlink control instructions. The control process is shown in **Figure 2**.

After modeling the new controllable loads of different buses with delay characteristics, the modeling results are sent to the control center. According to the information of controllable load resources, the control center is trained off-line to obtain the emergency frequency stability control model which can adapt to the current load state.

TABLE 2 Results of controlled load aggregation.

location	Aggregate controllable loads	Load amount	Delay
Bus 1	level 1 controllable load	P_{11}	t_{11}
	level 2 controllable load	P_{12}	t_{12}
	…	…	…
	level n controllable load	P_{1n}	t_{1n}
Bus 2	level 1 controllable load	P_{21}	t_{21}
	level 2 controllable load	P_{22}	t_{22}
	……	……	……
	level n controllable load	P_{2n}	t_{2n}
…	…	…	…

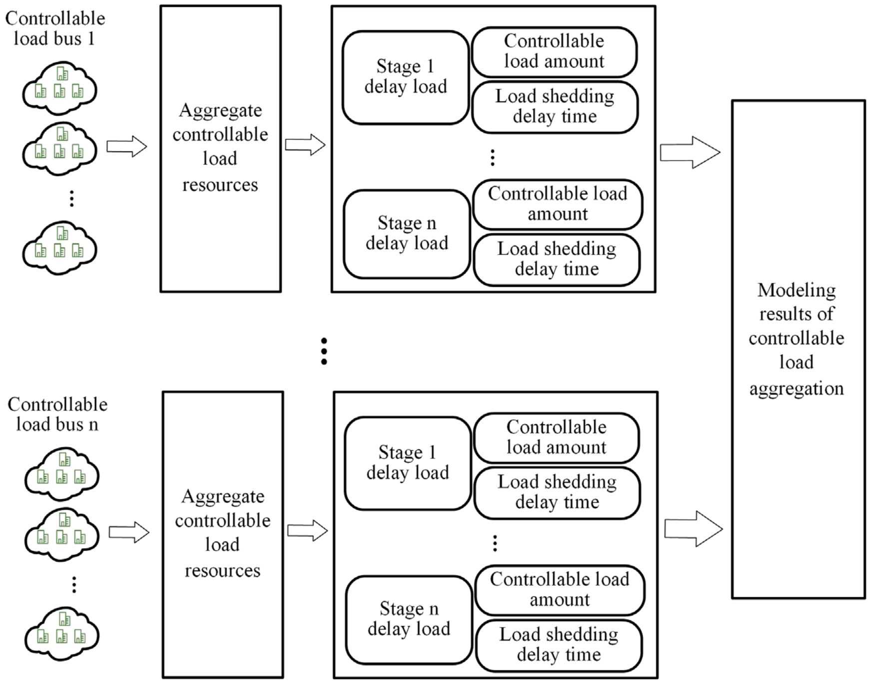

FIGURE 1
Controllable load aggregation modeling process.

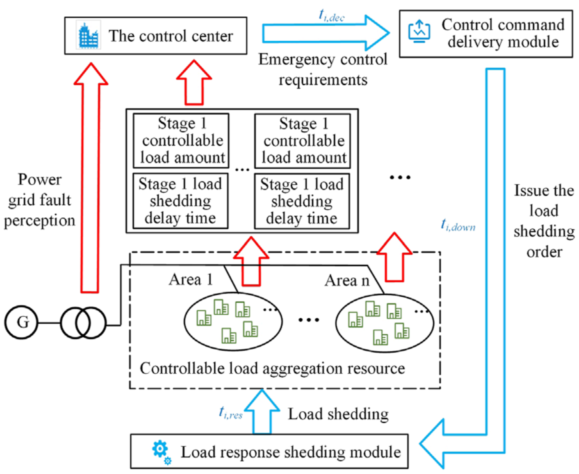

FIGURE 2
Emergency control process diagram of controllable load resources.

The control center monitors the power grid operation data in real time through the power grid fault perception. Once fault information or abnormal operation state of the power grid is found, the power grid operation state data will be put into the off-line training model to obtain the load shedding control instruction. After that, it transmits information through the control instruction delivery module to issue control actions to the controllable load resources on the demand side. The controllable load resources in each area complete the load shedding action response through the corresponding control components.

The new emergency control considering the controllable load resources is to implement cluster control on the controllable load before the traditional load shedding initial action, so as to avoid the whole line shedding caused by the traditional UFLS device. Therefore, the initial action of the new controllable load should take precedence over the traditional load shedding device, that is, the action frequency threshold of the controllable load control should be greater than the traditional initial action frequency threshold. When the system has power shortage, the method can quickly remove part of the new controllable load, achieve the purpose of load shedding in advance to restore the system frequency, without touching the traditional load shedding device. By controlling the aggregated new controllable load resources, the frequency recovery goal is achieved and the economy is higher than that of the traditional UFLS.

3 Deep reinforcement learning rainbow algorithm

The basic framework of Rainbow algorithm is the DQN algorithm. Therefore, this section first briefly introduces the DQN algorithm, and then explains the improvements and advantages of the Rainbow algorithm used in this article on its basis.

3.1 Deep learning Q network algorithm

The DQN algorithm uses deep neural networks to effectively extend the traditional tabular Q learning algorithm, which is a typical deep reinforcement learning algorithm. When training with the traditional Q learning method, it is necessary to use the Q table to record the status, action and corresponding Q value of each training sample, and the high-dimensional state and control action will cause the Q table to be too large and difficult to save. In order to solve the problem that it is difficult to deal with high-dimensional state space and control action set, the neural network is used to achieve direct prediction of Q values in the DQN method. This enables Q function to directly use the observed continuous states as input variables, which improves the ability of DQN to deal with complex problems. The process of using neural network to update Q value in DQN method can be described as:

$$Q(s_t,a_t;\theta_t) = Q(s_t,a_t;\theta_t) + \alpha\left(r_t + \gamma\max_{a_{t+1}} Q(s_{t+1},a_{t+1};\theta^-)\right. \\ \left. - Q(s_t,a_t;\theta_t)\right) \tag{9}$$

where $Q\ (s_t, a_t;\ q_t)$ is the Q value function for evaluating the action a_t taken by the neural network under state s_t, θ_t is the neural network parameter of the evaluation network, r_t is the immediate reward value of the action, θ^- is the neural network parameters of the target network, α is the learning rates, γ is the attenuation coefficient.

The target network is the stage replica of the evaluation network in the learning process. The two neural networks complete the iteration of Q value together, which makes the iteration process more stable and improves the convergence of the algorithm. After the iteration of Q value, DQN trains the evaluation network according to the difference of Q value before and after the iteration, which is called time difference deviation, and the expression is shown as follows:

$$H = r_t + \gamma\max_{a_{t+1}} Q(s_{t+1},a_{t+1};\theta^-) - Q(s_t,a_t;\theta_t) \tag{10}$$

The loss function $L\ (\theta_t)$ during the training of evaluation network is:

$$L(\theta_t) = H^2 \tag{11}$$

In order to improve the learning efficiency of DQN, two methods are usually adopted: experience replay and regular target network correction. First of all, neural network training requires independent input samples, while Markov decision process can only produce continuous procedural samples. To this end, DQN sets up an experience playback mechanism to shuffle the procedural samples, and specially stores the historical experience data and learns from it repeatedly, so as to update the policy. In addition, in order to avoid the divergence of neural network caused by unstable training, DQN adopts the method of target network, that is, it sets two independent neural network models: target network and evaluation network, which have the same structure but different parameters. The evaluation network constantly learns new samples to update parameters, which is fast, while the target network parameters are updated periodically by replication evaluation network parameters, which is slow. This method can effectively improve the stability of DQN algorithm training.

3.2 Rainbow algorithm

Although the traditional DQN algorithm can also solve the problem of emergency frequency control strategy, sometimes there are some problems such as poor generalization effect and difficult convergence of the model. These problems are mainly caused by the shortcomings of the algorithm itself, which is difficult to be improved by adjusting parameters and model design. Using its improved Rainbow algorithm can effectively accelerate the training process, and make the emergency frequency control strategy more stable and effective, so as to solve the above problems.

The Rainbow algorithm used in this paper is based on DQN and integrates three types of improved algorithms: priority playback caching mechanism, Double DQN and Dueling DQN.

3.2.1 Priority playback caching mechanism

In the DQN algorithm, the playback cache mechanism uniformly filters data from the cache pool and is used to evaluate the training of the network. However, it fails to measure the quality of samples, resulting in some important data not being selected quickly, which makes the training efficiency of the evaluation network low. There is a large gap between the output value of some data and the target value, which makes it difficult to train the network successfully. Therefore, the priority of its filtering should be increased. The priority playback cache mechanism determines the probability of sampling according to the time difference deviation of each sample. In order to make the sample access more efficient, the algorithm also introduces sum-tree structure to store the sample and its corresponding priority, which is shown as:

$$P_{\mathrm{sum},t} \propto \left| r_t + \gamma \max_{a_{t+1}} Q\left(s_{t+1}, a_{t+1}; \theta^-\right) - Q\left(s_t, a_t; \theta_t\right) \right|^{\omega} \qquad (12)$$

where $P_{\mathrm{sum},t}$ is the probability that the sample will be sampled, ω the influence degree of time difference deviation on sampling probability.

In the priority playback cache mechanism, M experience samples are selected from the experience pool according to the priority to train the neural network. The loss value is used to determine the degree of priority learning. The larger the error is, the larger the space for the prediction accuracy to rise, and the higher the priority of the sample is, as shown in **Figure 3**.

In fact, using a priority playback cache mechanism not only changes the process of filtering data, but also changes the method of parameter update. Therefore, it not only changes the distribution of selected data, but also changes the training method of the network. The priority playback cache mechanism extracts samples with larger time difference deviation more frequently, reduces the number of samples needed to evaluate the convergence of the network, significantly speeds up the convergence speed of the algorithm, and improves the learning efficiency of training.

3.2.2 Double deep learning Q network

Since the argmax function is included in the calculation formula of Q value, the estimation of Q value of DQN algorithm is often higher than the real value. If such overestimation is uniform, it will not affect the final optimal decision. However, the distribution of such overestimation in the environment is often complex and uneven, so different degrees of overestimation will lead to the final decision can only converge to the suboptimal solution instead of the optimal solution. The algorithm of Double DQN is proposed to solve this overestimation problem, which is an extension of DQN.

The difference between Double DQN and traditional DQN algorithms is mainly reflected in the estimation of the value of the next state. In DQN, the value estimation of the next state is done independently by the target Q network, and the target network outputs the Q value obtained by each action, and applies the action with the largest Q value to update formula. Double DQN uses two existing neural networks to improve the iterative

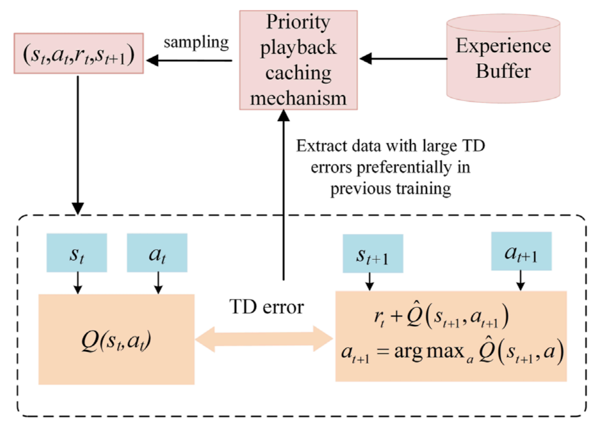

FIGURE 3
Schematic diagram of priority playback caching mechanism.

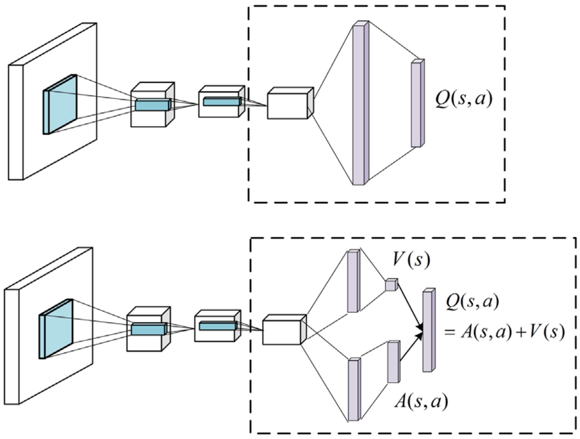

FIGURE 4
Schematic diagram of Dueling DDQN.

rules for Q values, with the time difference bias H expression:

$$H = r_{t+1} + \gamma_{t+1} Q\left(s_{t+1}, \text{argmax}_{a_{t+1}} Q_\theta\left(s_{t+1}, a_{t+1}\right); \theta^-\right) - Q\left(s_t, a_t; \theta_t\right) \tag{13}$$

3.2.3 Dueling deep learning Q network

Dueling DQN makes a change in the upper layer of the neural network output layer and divides the original output Q value into two parts, one is the value evaluation of the state and the other is the value evaluation of different actions. Two parts share parameters at the front end of the neural network, and only perform shunt when calculating their respective values. The state value $V(s_t)$ in the first part represents the value of the state, while the action dominance value $A(s_t, a_t)$ in the second part removes the influence of the state and calculates the value of each action separately. The final output Q value can be calculated as:

$$Q(s_t, a_t) = V(s_t) + A(s_t, a_t) \tag{14}$$

Dueling DQN provides a more accurate grasp of the environment by assessing the state and action separately, making decisions more realistic, as shown in Figure 4.

4 Emergency frequency control model based on deep reinforcement learning

When Rainbow algorithm is applied to the emergency frequency control of the power system, the emergency load shedding instructions can be directly generated by high-dimensional state data of power system, which avoids the disadvantages of traditional methods such as complex optimization and poor application effect. The power system emergency frequency control problem is formulated as MDP process, which has the elements of state, action and reward. In the process of MDP, the agent perceives the current system state and performs actions on the environment according to strategies, so as to change the state of the environment and get instant payoff. The accumulation of instant payoff over time is called reward. Thus, the MDP process combines the state space, action space and reward function of the emergency frequency control problem into a closed-loop whole. The MDP process of deep reinforcement learning algorithm is designed according to the mathematical model of the problem. The state control, action space and reward function correspond to each part of the mathematical model of the emergency control. Therefore, this paper introduces the mathematical description of emergency frequency stability control.

4.1 State space

In MDP, the state s_t represents the feedback of the environment to the agent, that is, the impact of the action of the previous step on the environment. This paper believes that the frequency stability of the power system is closely related to the active power of the generator, the load power and other factors, so the state space s_t is defined as:

$$s_t = s_1^t \cup s_2^t \cup s_3^t \cup s_4^t \tag{15}$$

$$\begin{cases} s_1^t = \left\{ f_1^t \quad f_2^t \quad \cdots \quad f_m^t \right\} \\ s_2^t = \left\{ (\mathrm{d}f/\mathrm{d}t)_1^t \quad (\mathrm{d}f/\mathrm{d}t)_2^t \quad \cdots \quad (\mathrm{d}f/\mathrm{d}t)_m^t \right\} \\ s_3^t = \left\{ P_{\mathrm{e}1}^t \quad P_{\mathrm{e}2}^t \quad \cdots \quad P_{\mathrm{e}m}^t \right\} \\ s_4^t = \left\{ P_{\mathrm{l}1}^t \quad P_{\mathrm{l}2}^t \quad \cdots \quad P_{\mathrm{l}n}^t \right\} \end{cases} \tag{16}$$

where f_i^t is the frequency of generator bus i at time t, $(df/dt)_i^t$ is the frequency change rate of generator bus i at time t, P_{ei}^t is the electromagnetic power of generator bus i at time t, P_{lj}^t is the active load of the load bus j at time t.

4.2 Action space

For power system emergency frequency stabilization problems, the action is defined as removing a certain amount of load on multiple controllable load buses. At each action moment, the control action on each controllable load bus is defined as 0 (the controlled load is not shed) or 1 (a controlled load of σ amount is shed). Therefore, the action space is discrete, the dimensionality is 2^n, where n is the number of load buses participating in emergency control.

4.3 Reward function

After an action is performed in a power system simulation environment, the model receives an immediate reward value to evaluate the corresponding state-action group at this time. For emergency frequency control problems, a larger reward value should be given if the action performed stabilizes the system frequency within the allowable range, keeps the system transient frequency nadir above the threshold, and shed less controllable load.

In order to quickly restore the system frequency to the allowable range, if the value of the frequency inertia center is still lower than the specified threshold in a certain period before the end of the simulation process, a large penalty value can be obtained. If the time does not reach the above moment, in order to keep the minimum frequency of the system higher than the threshold and remove less controllable load, the reward function consists of the following four parts:

1) The frequency inertia center deviation value of the system after the action;
2) The controllable load amount of shedding;
3) The penalty for crossing the threshold at the lowest point of the center of frequency inertia;
4) Invalid action penalty for removing unloaded buses.

Thus, the reward function r_t at time t can be defined as:

$$r_t = \begin{cases} -200, \ if\left(t > T_{\text{tem}}\right) \text{ and } \left(f(t) < f_{\text{tem.set}}\right) \\ \lambda_1 \Delta f(t) - \lambda_2 \sum_{j=1}^{n} P_{\text{sl}j} - H_1 - H_2, \text{ otherwise} \end{cases} \tag{17}$$

$$H_1 = \begin{cases} -100, \ if\left(f(t) < f_{\text{min.set}}\right) \\ 0, \text{ otherwise} \end{cases} \tag{18}$$

$$H_2 = \begin{cases} -100, \ if\left(P_{\text{l}j}{}^{t} = 0\right) \text{ and } \left(P_{\text{sl}j} \in a_t\right) \\ 0, \text{ otherwise} \end{cases} \tag{19}$$

where T_{tem} is the value at a certain moment before the end of the simulation process, $f_{\text{tem. set}}$ is the steady-state threshold of the frequency inertia center, $\Delta f(t)$ is the deviation value of the frequency inertia center at time t, $P_{\text{sl}j}$ is the excision amount of load bus j, λ_1 and λ_2 are the coefficients of each part of the reward function, $f_{\text{min. set}}$ is the threshold of the lowest point of the transient process frequency inertia center, H_1 is the penalty when the lowest point of the system frequency inertia center is less than the preset threshold, H_2 is the penalty when the load bus has been reduced to zero in the previous time step, and it still chooses the load shedding action.

The reward function design of deep reinforcement learning should combine the priori experience knowledge and automatic parameter search. Firstly, the priori experience about the emergency control problem is used to determine the approximate range of the coefficients of each part of the reward function. Secondly, once its rough range is determined, the model is automatically selected randomly in the range. The combination of selected parameters is used to train the model, and the combination with the best performance is selected as the coefficient of the reward function.

This reward function can quickly restore the system frequency to the allowable range, and the lowest frequency in the recovery process should not be lower than the threshold at the same time. It also ensures that the total amount of load shedding is small, and improve the economy.

5 Case study

In order to verify the effectiveness of the proposed method, Python and BPA simulation software are used to jointly build a deep reinforcement learning environment of IEEE 39-bus system, and Rainbow algorithm is used to solve the example. Tensorflow1.15 is used to build deep neural network in Python. The operating platform is Intel Core I5-11400H CPU, 16.00GB RAM, and RTX 3050.

5.1 Case data

In this paper, BPA is used to generate the failure scenario of IEEE 39-bus system. The generator model adopts the 6-order model. The load model is a mixed load model composed of constant impedance model and induction motor, both of which account for 50%. The failure scenario is that a generator loses part of the power, resulting in a certain power difference in the power system. The total simulation time is 40 s, and each cycle wave is a sampling point. In order to simulate fault states of different system and get enough samples, at the beginning of the simulation, one of the 10 generators is randomly selected to lose 0.5 p.u to 1 p.u of active power output. This random selection of fault location and fault size can improve the generalization ability of model. IEEE 39-bus topology is shown in **Figure 5**. In this paper, bus 3, 8, and 20 are considered as controllable load bus participating in emergency frequency control.

In IEEE 39-bus system, the deep reinforcement learning state space is composed of the frequency deviation, frequency change rate, active power output of 10 generators and the remaining controllable load buses participating in load shedding, with a size of 33 dimensions. The action space is composed of the combined excision actions of three loads. The control action at each load bus is defined as 0 (the controlled load is not shed) or 1 (the controlled load of 50 MW amount is shed), and the size of the action space is 8 dimensions.

5.1.1 Two-stage action

Emergency frequency control is divided into two stages: emergency control action process and recovery action process.

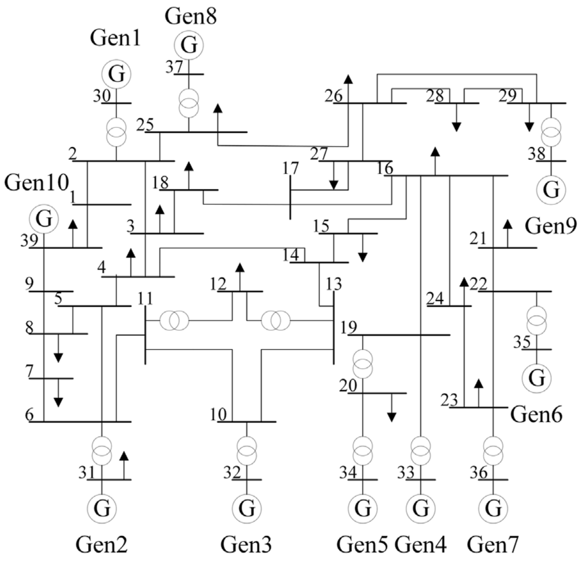

FIGURE 5
Topology of IEEE 39-bus.

When the center of inertia of the system frequency is lower than 49.5Hz, the initial emergency control action starts, and then the time interval of each action is 0.5 s. Continuing operate until the frequency change rate of the center of inertia of the system is positive, that is, when the center of frequency inertia begins to rise, enter the second stage. In the second stage, the recovery action is performed with an interval of 5 s each time, and the action is continued until the frequency stability is reached.

5.1.2 Graded shedding polymerization load

Considering the different delay characteristics of the new controllable load, the load is divided into three levels according to the delay time. The delay time within 100 ms is level 1 load, the delay time between 100 and 200 ms is level 2 load, and the delay time between 200 and 300 ms is level 3 load. After aggregation modeling, the controllable load ratio of each bus and the load ratio of different delay levels are shown in Table 3.

For loads of the same delay level, the actual control delay is calculated according to the maximum value, so as to ensure that the actual frequency drop depth is less than or equal to the ideal frequency drop depth and avoid frequency instability. Therefore, after aggregation, it is considered that the actual delay of level 1 load is 100 ms, level 2 load is 200 ms, and level 3 load is 300 ms. In each bus, the delay is shed in ascending order.

TABLE 3 Proportion of different grades of load.

Load bus number	Controllable load ratio	Level 1 load ratio	Level 2 load ratio	Level 3 load ratio
3	0.82	0.35	0.4	0.25
8	0.91	0.35	0.35	0.3
20	0.77	0.4	0.3	0.3

In this paper, the delay difference of less than 100 ms is small, and the influence on the control effect can be ignored. Therefore, the load delay is divided into three levels. If the delay level is too coarse, the delay difference within the same level cannot be ignored. If the delay level is too fine, the strategy optimization is too complicated and unnecessary.

5.2 Model training process

In this paper, different experimental scenarios are set to train the proposed Rainbow algorithm. The size of the input layer of the neural network is 33 dimensions, which is the same as the dimension of the state space, and there are two 64-dimension hidden layers in the middle. The size of the output layer is 8 dimensions, which is the same as the dimension of the action space, and the activation function adopts ReLU.

During training, the strategy of ε-greedy search action is adopted to balance the relationship between exploration and utilization. It can prevent the agent from falling into the local optimal solution or not getting the optimal solution. Policy selection is defined as:

$$a = \begin{cases} \arg\max_a Q(s,a), & \varepsilon \le \varepsilon_0 \\ \text{random}, & \varepsilon > \varepsilon_0 \end{cases} \tag{20}$$

Where ε is the random number evenly distributed within the interval [0,1], ε_0 is the fixed value of the specified greedy policy, satisfying $0 \le \varepsilon_0 \le 1$.

The ε_0 is small in the initial stage, which encourages DQN to explore more different load increase situations in the early stage of training, so as to avoid the problem of local optimum caused by insufficient exploration. With the progress of training, the value of ε_0 increases continuously and stabilizes at 0.95 finally, which requires DQN to learn and utilize the explored excellent strategies more in the later training period.

The training process of reinforcement learning model is the process of learning to obtain the maximum reward value. The reward change process in the training of this paper is shown in Figure 6.

As can be seen from Figure 6, at the beginning of training, the agent randomly selects actions to explore the environment, because the data cache pool is not full and the ε_0 is small. Therefore, the reward value at this stage is low and there is obvious oscillation. When the data cache pool is full, the model starts to train, the reward increases with the training, and the effect of load shedding strategy gradually becomes better. After about 700 rounds of training, the reward reaches a high value, and then the change is small, and the model is basically trained.

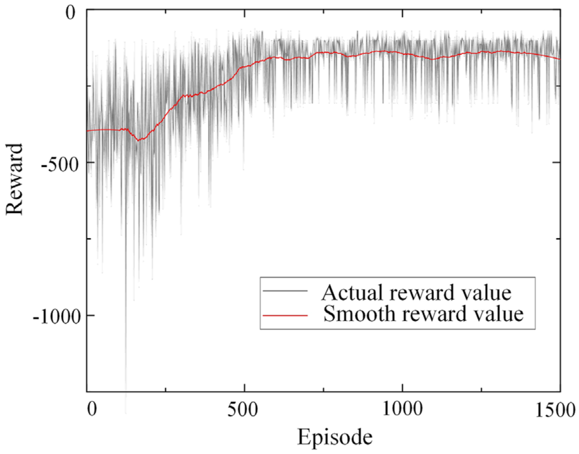

FIGURE 6
Change of reward value during training.

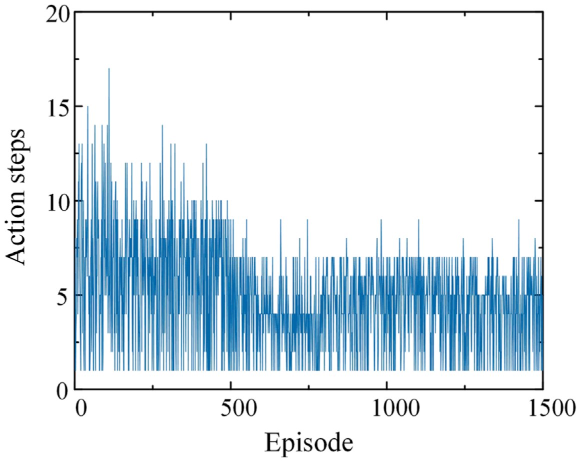

FIGURE 7
The number of excised movements in each training round.

In order to further show the process of model training, it is shown in Figure 7 that the change process of each round of shedding action step in the training process.

As can be seen from Figure 7, at the early stage of training, the effect of load shedding is not ideal because the optimal strategy is not explored, so there are many action steps in each round. After training, the well-trained agent only needs to take a few actions in each round to achieve the stability condition.

5.3 Rainbow model test results

After the training, in order to test the robustness and adaptability of the Rainbow agent, it was tested in different scenarios. The test scenario is that one of the 10 generators loses 0.5 p.u to 1 p.u of active power output, and the load level is randomly selected as 90%, 95%, 100%, 105%, or 110%. The frequency control strategies for the three scenarios are shown in Table 4.

As can be seen from Table 4, for various scenarios tested, the amount of load shedding is basically equal to the amount of power gaps, and the well-trained model can basically avoid overcutting or undercutting of load when applied online.

In order to further verify the superiority of the method, this paper compares the load shedding scheme obtained by the deep reinforcement learning Rainbow algorithm and the traditional UFLS algorithm, and Figure 8 shows the dynamic recovery process of frequency inertia center after the action of the two algorithms in scenario 2.

As can be seen from Figure 8, traditional UFLS is driven by multiple frequency stages, and the shedding action starts too slowly and is fixed, resulting in slow frequency recovery. However, Rainbow algorithm can effectively reduce the system frequency drop depth and speed up the process of frequency recovery. Within 10–60 s, the system frequency using Rainbow algorithm is much higher than that using UFLS, and the frequency recovery speed is accelerated. At the same time, when Rainbow algorithm is used, the lowest frequency of the system is around 49.4Hz, while the lowest frequency of the traditional UFLS algorithm is 49.3 Hz. It can be seen that the load shedding strategy in this paper can effectively improve the dynamic frequency nadir of the system and improve the frequency stability of the system.

TABLE 4 Frequency control strategy in three scenarios.

Scenario number	Load level (%)	Failed bus	Power gaps (MW)	Total amount of load shedding (MW)	Stage 1 load shedding (MW)	Stage 2 load shedding (MW)	Stage 3 load shedding (MW)
1	95	31	380	350	50	150	150
2	100	33	535	550	200	200	150
3	110	31	440	450	100	200	150

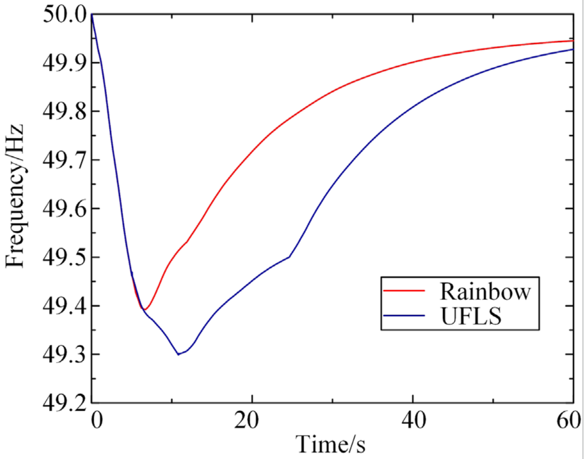

FIGURE 8
Curve of frequency inertia center after action of UFLS and Rainbow algorithm.

5.4 Effect comparison of different deep reinforcement learning algorithms

In order to comprehensively compare the effect of the proposed algorithm with other DRL algorithms, Rainbow algorithm is compared with various improved DQN algorithms. **Figure 9** shows the reward change process during training of different DRL algorithms.

As can be seen from **Figure 9**, the traditional DQN algorithm is basically stable after 600 rounds of training, but its algorithm has poor optimization ability, and the reward value obtained is lower than that of its improved algorithm. After using the improved Double DQN and D3QN algorithms, the model converges after 700 rounds, and the training effect is improved compared with the DQN algorithm, and a better control strategy can be calculated. The Rainbow algorithm in this paper converges after about 800 rounds of training, at which point the model reward value exceeds that of other algorithms. As a result, the Rainbow algorithm is able to obtain higher reward values than other algorithms, and although the training time is longer, it obtains a better control strategy at the expense of this.

Meanwhile, in order to verify whether Rainbow algorithm maintains its superior performance in the test scenario, this paper randomly tests four different algorithms for 100 times, and the test scenario is the same as that in 5.3. The distribution of reward value obtained in the test is shown in **Figure 10**.

As can be seen from **Figure 10**, the reward value obtained by DQN and Double DQN fluctuates greatly in the random test scenario, and the overall reward is low. It indicates that the model fails to find the optimal strategy at this time, and the generalization ability is poor, and the effect is poor for some test scenarios. The reward value of D3QN algorithm in the test is significantly higher than that of the previous two, but there is still a certain gap compared with Rainbow algorithm in this paper. Rainbow algorithm with successful training can obtain good reward values in various test scenarios and obtain the optimal action strategy.

Compared with other DRL algorithms, Rainbow algorithm can make the system frequency return to stable state faster, and minimize the total load shedding amount at the same time. In order to show the test improvement effect more intuitively,

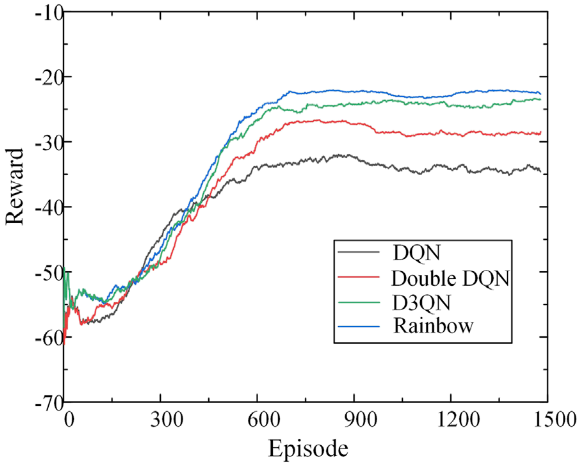

FIGURE 9
Reward value for DQN and its improved algorithm.

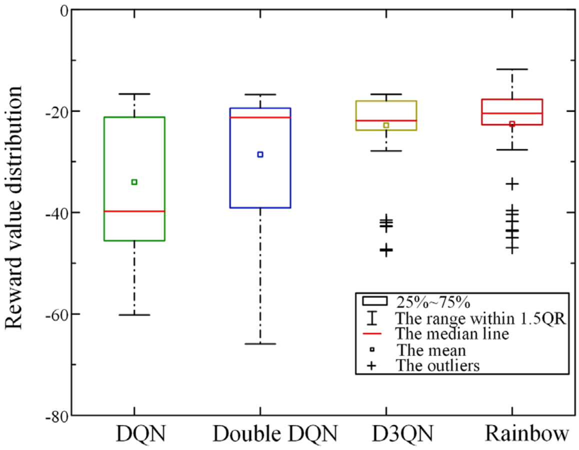

FIGURE 10
The distribution of reward values of different algorithms.

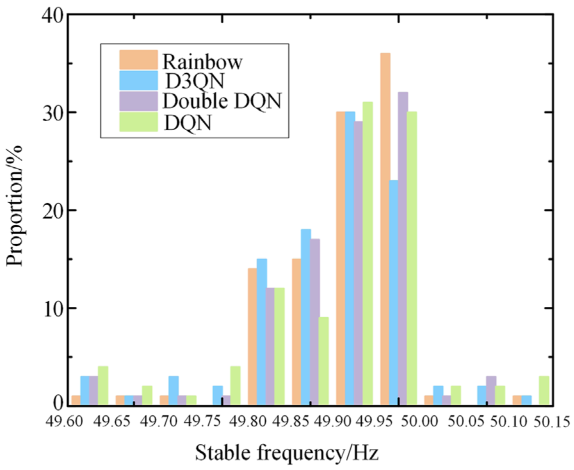

FIGURE 11
Frequency distribution at the time of system stability in different test scenarios.

Figure 11 shows the distribution of frequency inertia center values of system at a certain time before the end of simulation process after the implementation of random test strategy.

As can be seen from **Figure 11**, the model trained by the deep reinforcement learning algorithm can basically restore the system frequency above 49.8 Hz under various test scenarios, ensuring the stability of the system. However, compared with other traditional DQN algorithms, Rainbow algorithm can make the stable frequency deviation smaller, which reflects the superiority of Rainbow algorithm.

6 Conclusion

Considering the complexity and uncertainty of frequency stability of the new power system, and the feasibility of the new controllable load participating in the emergency control, this paper established a new controllable load participating in the emergency frequency stability control method based on Rainbow algorithm. Through the design of different operation scenarios for experimental verification, the conclusion is as follows.

1) In this paper, it comprehensively evaluates the response delay time of the new controllable load, and classifies and aggregates the controllable load according to the different delay time. At the same time, the simplified model makes the controllable load more accurate and effective when participating in the emergency control, and avoids the error of shedding effect due to the communication difference and spatial distribution of the controllable resources.
2) The emergency frequency control algorithm based on deep reinforcement learning can effectively maintain the balance between the system frequency stability and the emergency control cost. By designing the reward function, the model can learn the effective control strategy with the minimum control cost. It avoids the shortcomings of the traditional algorithm such as easy over-cutting, under-cutting and poor economy. In this paper, Rainbow algorithm improved by DQN algorithm is adopted to avoid the shortcomings of traditional UFLS method, such as slow control speed, slow frequency recovery and excessive frequency drop. At the same time, compared with other DRL algorithms, the strategy obtained by the proposed algorithm is more excellent and the stable frequency deviation is smaller.
3) In the subsequent study, the random fluctuation of system load will be added to simulate a more realistic power system environment and test the generalization ability of this method. In addition, Rainbow algorithm adopted in this paper can only deal with discrete action space. It is hoped that deep reinforcement learning algorithm based on policy gradient can be applied to emergency frequency control in subsequent studies, and its ability to deal with continuous action space can enable more controllable loads to participate in emergency control.

Data availability statement

The original contributions presented in the study are included in the article/Supplementary Material, further inquiries can be directed to the corresponding author.

Author contributions

LS: conceptualization, methodology, software; YT: software, data curation, writing-original draft preparation; YW: visualization, investigation; WH: supervision; CY: validation; JY: funding acquisition.

Funding

This work was supported by the National Natural Science Foundation of China (52077059).

Conflict of interest

The authors declare that the research was conducted in the absence of any commercial or financial relationships that could be construed as a potential conflict of interest.

Publisher's note

References

Banijamali, S. S., and Amraee, T. (2019). Semi-adaptive setting of under frequency load shedding relays considering credible generation outage scenarios. *IEEE Trans. Power Deliv.* 34, 1098–1108. doi:10.1109/TPWRD.2018.2884089

Cao, Y. J., Zhang, H. X., Xu, Q. W., Li, C. G., and Li, W. (2021a). Preliminary study on participation mechanism of large-scale distributed energy resource in security and stability control of large power grid. *Automation Electr. Power Syst.* 45, 1. doi:10.7500/AEPS2021021000

Cao, Y. J., Zhang, H. X., Zhang, Y., and Li, C. G. (2021b). Event-driven fast frequency response control method for generator unit. *Automation Electr. Power Syst.* 45, 148. doi:10.7500/AEPS20210426006

Chen, C., Cui, M., Li, F., Yin, S., and Wang, X. (2021). Model-free emergency frequency control based on reinforcement learning. *IEEE Trans. Ind. Inf.* 17, 2336–2346. doi:10.1109/TII.2020.3001095

Dai, Y., Xu, Y., Dong, Z. Y., Wong, K. P., and Zhuang, L. (2012). Real-time prediction of event-driven load shedding for frequency stability enhancement of power systems. *IET Gener. Transm. Distrib.* 6, 914–921. doi:10.1049/iet-gtd.2011.0810

Fan, S., Wei, Y. H., He, G. Y., and Li, Z. Y. (2022). Discussion on demand response mechanism for new power systems. *Automation Electr. Power Syst.*, 1. doi:10.7500/AEPS20210726010

Hessel, M., Modayil, J., Hasselt, H. V., Schaul, T., Ostrovski, G., Dabney, W., et al. (2017). . "Rainbow: Combining improvements in deep reinforcement learning," in 32nd AAAI Conference on Artificial Intelligence, AAAI 2018, 3215–3222.

Li, B. J., and Hou, Y. Q. (2016). Research of emergency load regulation for security and stability control. *Power Syst. Prot. Control* 44, 104. doi:10.7667/PSPC151194

Li, C., Wu, Y., Sun, Y., Zhang, H., Liu, Y., Liu, Y., et al. (2020). Continuous under-frequency load shedding scheme for power system adaptive frequency control. *IEEE Trans. Power Syst.* 35, 950–961. doi:10.1109/TPWRS.2019.2943150

Liu, W., Zhang, D. X., Wang, X. Y., Hou, J. X., and Liu, L. P. (2018). A decision making strategy for generating unit tripping under emergency circumstances based on deep reinforcement learning. *Proc. CSEE* 38, 109–119+347. doi:10.13334/j.0258-8013.pcsee.171747

Mnih, V., Kavukcuoglu, K., Silver, D., Rusu, A. A., Veness, J., Bellemare, M. G., et al. (2015). Human-level control through deep reinforcement learning. *NATURE* 518, 529–533. doi:10.1038/nature14236

Ren, K. Q., Zhang, D. Y., Huang, Y. H., and Li, C. (2022). Large-scale system inertia estimation based on new energy output ratio. *Power Syst. Technol.* 1, 0643. doi:10.13335/j.1000-3673.pst.2021.0643

Schulman, J., Wolski, F., Dhariwal, P., Radford, A., and Klimov, O. (2017). *Proximal policy optimization algorithms*, arXiv.

Singh, A. K., and Fozdar, M. (2019). Event-driven frequency and voltage stability predictive assessment and unified load shedding. *IET Gener. Transm. Distrib.* 13, 4410–4420. doi:10.1049/iet-gtd.2018.6750

Terzija, V. V. (2006). Adaptive underfrequency load shedding based on the magnitude of the disturbance estimation. *IEEE Trans. Power Syst.* 21, 1260–1266. doi:10.1109/TPWRS.2006.879315

Wang, L. P., Li, H. Z., and Xie, X. R. (2020). A decentralized and coordinated control of emergency demand response to improve short-term frequency stability. *Proc. CSEE* 40, 3462–3470. doi:10.13334/j.0258-8013.pcsee.191675

Wen, Y. F., and Yang, W. F. (2020). Review and prospect of frequency stability analysis and control of low-inertia power systems. *Electr. Power Autom. Equip.* 40, 211–222. doi:10.16081/j.epae.202009043

Xu, W., Li, Q., Yang, J. J., and Bao, Y. H. (2018). Multi-objective optimization method for emergency load shedding based on comprehensive contribution index. *Electr. Power Autom. Equip.* 38, 189–194. doi:10.16081/j.issn.1006-6047.2018.08.027

Xu, X., Zhang, H., Li, C., Liu, Y., Li, W., and Terzija, V. (2017). Optimization of the event-driven emergency load-shedding considering transient security and stability constraints. *IEEE Trans. Power Syst.* 32, 2581–2592. doi:10.1109/TPWRS.2016.2619364

Xu, X., Zhang, H. X., Li, C. G., Liu, Y. T., and Li, W. (2016). Emergency load shedding optimization algorithm based on trajectory sensitivity. *Automation Electr. Power Syst.* 40, 143. doi:10.7500/AEPS20151116002

Zeng, L. K., Yao, W., Ai, X. M., Huang, Y. H., and Wen, J. Y. (2020). Double q-learning based identification of weak lines in power grid considering transient stability constraints. *Proc. CSEE* 40, 2429–2441. doi:10.13334/j.0258-8013.pcsee.190305

Zhang, Z. Y., Zhang, N., Du, E. S., and Kang, C. Q. (2022). Review and countermeasures on frequency security issues of power systems with high shares of renewables and power electronics. *Proc. CSEE* 42, 1–25. doi:10.13334/j.0258-8013.pcsee.211425

frontiers | Frontiers in Energy Research

TYPE Original Research
PUBLISHED 16 January 2023
DOI 10.3389/fenrg.2022.1037874

OPEN ACCESS

EDITED BY
Yingjun Wu,
Hohai University, China

REVIEWED BY
Shuaishi Liu,
Changchun University of Technology, China
Xiaomeng Ai,
Huazhong University of Science and Technology, China

*CORRESPONDENCE
Dongxu Liu,
458162373@qq.com

SPECIALTY SECTION
This article was submitted to Smart Grids, a section of the journal Frontiers in Energy Research

RECEIVED 06 September 2022
ACCEPTED 31 October 2022
PUBLISHED 16 January 2023

CITATION
Yang M, Liu D, Su X, Wang J and Cui Y (2023), Ultra-short-term load prediction of integrated energy system based on load similar fluctuation set classification. *Front. Energy Res.* 10:1037874.
doi: 10.3389/fenrg.2022.1037874

Ultra-short-term load prediction of integrated energy system based on load similar fluctuation set classification

Mao Yang, Dongxu Liu*, Xin Su, Jinxin Wang and Yu Cui

Key Laboratory of Modern Power System Simulation and Control and Renewable Energy Technology, Ministry of Education, Northeast Electric Power University, Jilin, China

Due to the strong coupling characteristics and daily correlation characteristics of multiple load sequences, the prediction method based on time series extrapolation and combined with multiple load meteorological data has limited accuracy improvement, which is tested by the fluctuation of load sequences and the accuracy of Numerical Weather Prediction (NWP). This paper proposes a multiple load prediction method considering the coupling characteristics of multiple loads and the division of load similar fluctuation sets. Firstly, the coupling characteristics of multivariate loads are studied to explore the interaction relationship between multivariate loads and find out the priority of multivariate load prediction. Secondly, the similar fluctuating sets of loads are divided considering the similarity and fluctuation of load sequences. Thirdly, the load scenarios are divided by k-means clustering for the inter-set sequences of similar fluctuating sets, and the Bi-directional Long Short-Term Memory (BI-LSTM) models are trained separately for the sub-set of scenarios and prioritized by prediction. Finally, the effectiveness of the proposed method was verified by combining the multivariate load data provided by the Campus Metabolism system of Arizona State University.

KEYWORDS

load prediction, scenario set partitioning, Bi-LSTM, integrated energy system, meteorological factors

1 Introduction

Intergrated Energy System (IES) is a new energy system that integrates electricity, natural gas, heating and cooling energy supply, including various forms of energy production, energy conversion, energy distribution, energy storage and energy utilization, *etc.* (Valery et al., 2022). Compared with the traditional energy utilization system, IES can realize the coupling of different types of energy in different links such as source, network and load side, effectively improving the comprehensive utilization rate of energy (Wei et al., 2022). At present, as the basis for guiding the optimal scheduling of the system, IES load prediction is important for the accurate prediction of multivariate loads, considering the interaction of various relevant factors in IES and the complex mechanism (Wang et al., 2021; Jizhong et al., 2022).

On the energy supply side of the IES, the main focus is on wind power and PV power prediction. Among them, In Mao et al. (2022), proposed a composite prediction framework DC (DWT-DAE)-CNN consisting of dual clustering and convolutional neural network. Firstly, discrete wavelet transform (DWT) and deep self-encoder (DAE) are performed on the original data respectively to reduce data redundancy. Secondly, a pairwise clustering model based on dynamic time-bending distance clustering and fuzzy C-mean (FCM) clustering is proposed to gradually realize the dynamic characteristics of power curves and numerical clustering of weather information data. Finally, it is verified by arithmetic case analysis. In Mao et al. (2020), proposed an improved fuzzy (FCM) clustering algorithm, which can obtain better prediction results by using the principle of minimum distance to select relatively coarse initial cluster centers, and by dividing wind turbines with similar power output characteristics into several classes and selecting representative power curves as the equivalent curves of wind farms. The shortest distance method clustering is proposed to provide the initial clustering center for FCM, the use of validity analysis of the degree of similarity of samples within classes and the degree of independence between different classes to discriminate the superiority of clustering results, and the identification and elimination of noise points by data density are proposed to improve the performance of FCM clustering algorithm (Kai et al., 2022). In Yang et al. (2019), used set-pair analysis to assess the correlation between the power fluctuations of individual wind turbines and the power fluctuations of all aggregated wind turbines, and between the smoothing effect of aggregated wind farms and the prediction accuracy of the corresponding aggregated power output. The experimental results show that the wind power prediction accuracy varies with the smoothing effect index, which is influenced by the number of wind farms. In Wu et al. (2022a), proposed a multi-stage urban distribution network (UDN) resilience enhancement framework to cope with the substantial loss of UDN critical loads caused by high impact low probability events (HILP) in UDN. In the first stage, the distribution system operator forms typical failure scenarios based on historical data of electrical component damage under ice events and sets up specific response plans in each scenario to reduce the lost load and associated costs, in the second stage, the operator performs a risk assessment of the corresponding plans, and in the third stage, the operator revises the response plans to reduce the "second stage" impact. In Wu et al. (2021a), promotes distributed renewable energy consumption through a specially set price mechanism that incorporates supply and demand ratios into the dynamic price formation process to better accommodate highly penetrated renewable energy sources and small-scale energy markets. A two-way auction model is proposed in Wu et al. (2021b), first, to establish a participant-driven framework for distributed trading of electricity demand response, followed by a bargaining game for cost and benefit allocation, and finally, to form a co-optimization model for electricity and hydrogen considering production constraints to improve system capacity and economics. In Nantian et al. (2022), a multi-node charging load joint adversarial generation interval prediction method considering the charging load correlation between nodes is proposed to effectively predict the spatio-temporal distribution of EV charging load with respect to the time-space progressivity of EV charging load.

On the energy consumption side of the IES, the main focus is on multi-energy load prediction. Among them, a novel decomposition-ensemble model for short-term load prediction is proposed in Yang et al. (2019). (Xiaobo and Jianzhou, 2018) The singular spectrum analysis (SSA) decomposition and reconstruction strategy is introduced in the proposed model, and the cuckoo search algorithm is used to generate the ensemble results and thus improve the model prediction accuracy. In Abhishek et al. (2022), a seasonal partitioning method is proposed for day-ahead prediction of electrical loads, and corresponding prediction models are established for the transition season and the regular season, and in the transition season, the weighted output method of multiple seasonal prediction models is used to improve the prediction accuracy. In Mukhopadhyay et al. (2017), explore how to reasonably use meteorological factors for load prediction, use the meteorological factors of the day to determine the magnitude of load, and consider day type information to appropriately scale the forecast results for rest days to better approximate the actual load. In Luiz and Afshin (2015), a transfer function (TF) model was developed using measured hourly weather variables for the simulation and prediction of electric loads and compared with an autoregressive integrated moving average model (ARIMA) and an artificial neural network (ANN) based on exogenous variables, and finally, an arithmetic analysis concluded that the accuracy of the proposed method has good stability with the extension of the time series. The above research methods mainly focus on some single load type for prediction, compared to single load prediction, the research on multivariate load prediction is relatively new, and the multi-task structure is commonly used to accommodate multivariate output requirements. For example, a short-term prediction method for electricity and gas demand based on a radial basis function neural network (RBF-NN) model was proposed (Tang et al., 2019). A multivariate load prediction model based on kernel principal component analysis, quadratic modal decomposition, two-way LSTM and multiple linear regression was proposed (Jinpeng et al., 2021; Yingjun et al., 2022). In Ref. (Qingkai et al., 2021), a multi-task learning load prediction model with Long-Short-Term Memory (LSTM) as a shared layer is constructed, where the learning of single load features is first performed separately, and then the auxiliary coupling information is learned using the shared layer. In Ref. (Jixiang et al., 2019), a mixed-model short-term load prediction method based on convolutional neural networks and LSTM is proposed, in which a large amount of historical load data, meteorological data, date information, and peak and valley tariff data are used as inputs to construct a continuous fluctuation map by time-sliding windows, the eigenvectors are first extracted using convolutional neural networks. The eigenvectors are constructed in a time-series manner and used as input data for the LSTM network, and then the LSTM network is used for short-term load prediction. The method proposed in Ref. (Haohan et al., 2021), fails to explicitly consider the complex coupling interaction features between multi-energy loads, where LSTM as a recurrent neural network has its own limitations, and although it can better mine the data temporal features, it cannot fully explore the interaction coupling relationship between multi-energy loads. The key idea of load prediction is to exploit the cyclical nature of load demand behavior and its dependence on other influencing factors, such as multi-energy coupling and weather information. However, the analysis of historical data shows that some of these influences do not have a uniform impact on load demand throughout the year.

To sum up, this paper proposes a multivariate load ultra-short-term prediction method based on load similar fluctuation set division combined with multivariate load coupling characteristics. First, a gray correlation analysis is performed on the multivariate load series to explore the coupling characteristics of the multivariate load data. Secondly, based on the historical load data, the actual load sequence of the highest priority is divided into correlation and volatility to obtain the set of load similar fluctuations. Thirdly, the NWP strongly correlated features of inter-set load sequences are used as input for k-means clustering to classify load scenes and train BI-LSTM network by load scenes; Finally, the final prediction results are obtained by ranking the multivariate load prediction priorities one by one.

2 Coupling characteristics mining of multiple loads

Before carrying out the research work of IES multiple load prediction, the energy use characteristics of the system should be analyzed, i.e., starting from the mechanism of load composition and revealing the inherent change law of the system load itself. Multi-class energy coupling mechanism is the theoretical basis of IES, and all kinds of energy sources are interactively coupled with each other, so the coupling characteristics between all kinds of energy sources need to be considered in the process of multiple load prediction (Jizhong et al., 2021). Multi-Task Learning (MTL) is often used for joint prediction of multivariate loads. The idea is to use multiple types of loads as the object of study and other influencing factors as fluctuation data to predict multiple types of loads simultaneously, which is a method of multiple inputs accompanied by multiple outputs at the same time (Wang et al., 2021). Although this method is able to take into account the coupling characteristics between multiple types of energy sources, the output side of the method outputs the multivariate load forecasts simultaneously, and the coupling strengths between the various types of energy sources may be different.

Therefore, this paper takes the lead in exploring the coupling strength between multiple types of energy sources and analyzes the correlation between multiple load series by Grey Relation Analysis (GRA) method to portray the coupling strength between multiple loads by correlation degree (Xuexiang et al., 2022). The sum of the correlations between any two selected loads and the third load is set as a parameter indicator φ_i (cumulative correlation coefficient) that weighs the strength of the coupling of the two loads to the third load, $i = 1, 2, \cdots, i$ is the load type. The larger the value of φ_i, the greater the coupling strength of other kinds of loads to the i species load, and the more backward the prediction order, conversely, the smaller φ_i indicates that the coupling strength of other kinds of loads to that kind of load is smaller, then the prediction order is advanced. As a result, the magnitude of the cumulative correlation coefficient φ_i can be used to prioritize the prediction of multiple loads in an integrated energy system.

3 Load similar fluctuation set division

The average daily load distribution within a season follows almost a similar pattern. However, the classification of load characteristics by season alone is too subjective and is likely to ignore the load characteristics between non-contiguous months. Based on the above multiple load coupling characteristics mining, this paper divides the highest priority electrical loads into load similar fluctuation sets and analyzes the monthly average electrical load distribution of the integrated energy system under the complete seasonal sequence as shown in Figure 1. It can be seen that similar fluctuations exist between different seasons.

Firstly, the average monthly electric load distribution series under different months is obtained by taking the average value of parallel load points of the load series under different load days in the same month. Secondly, the obtained daily average electric load distribution series are then compared two by two using grey correlation analysis to form a correlation coefficient matrix D_α between different months of the same load with correlation coefficient $\xi_\alpha(i, j)$, where i and j are the number of sample series. The variance is used to portray the degree of volatility of the series, and the correlation coefficient is used to portray the similarity between the series. The variance of the daily average load series of different months is used to make the first-order difference, forming the variance first-order difference matrix D_β, and the correlation coefficient is $\xi_\beta(i, j)$. The smaller the value in the matrix, the more similar the degree of volatility between the two series is. Finally, the correlation thresholds of the parameters in the above matrix are selected separately to classify the multivariate load similar fluctuation fluctuation set, and the solution flow chart is shown in Figure 2.

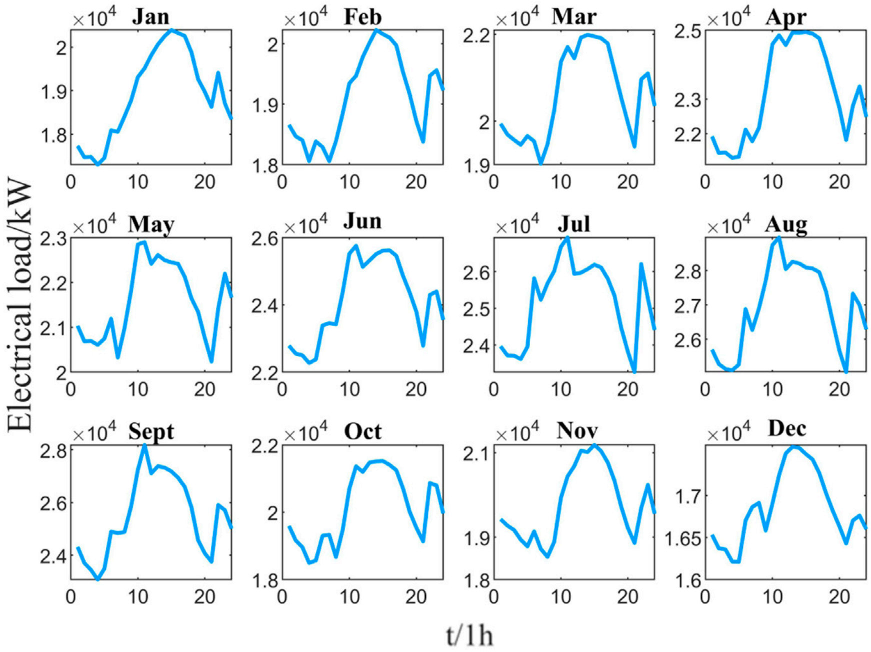

FIGURE 1
Monthly average electric daily load distribution chart.

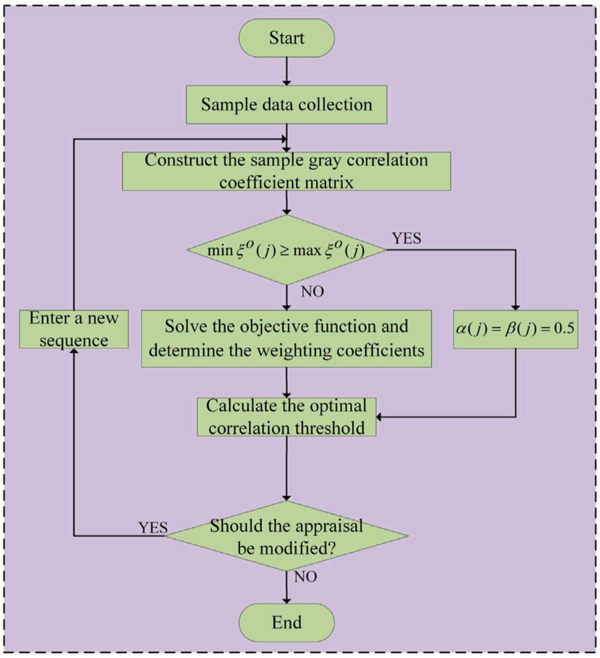

FIGURE 2
Flow chart of correlation coefficient threshold selection.

The correlation threshold $\xi^o(j)$ is actually the final criterion for the attribution of the sample to be examined. If the value of $\xi^o(j)$ is low, association misclassification will occur, i.e., sequences that are not originally part of the fluctuation set are classified, and the lower the value of $\xi^o(j)$, the higher the probability of misclassification. Conversely, if the value of $\xi^o(j)$ is high, the higher the probability of fault omission, the sequence that should have been classified into the fluctuation set is not classified in, and the higher the value of $\xi^o(j)$, the higher the probability of omission. We write down the minimum correlation threshold corresponding to the smallest correlation of the sequence as $\min \xi^o(j)$. Therefore, the maximum correlation threshold corresponding to the largest correlation is written down as $\max \xi^o(j)$. The best value of the correlation threshold $\xi^o(j)op$ should satisfy the following conditions.

$$\min \xi^o(j) < \xi^o(j)op < \max \xi^o(j),\ \min \xi^o(j) < \max \xi^o(j) \quad (1)$$

$$\min \xi^o(j) = \xi^o(j)op = \max \xi^o(j),\ \min \xi^o(j) = \max \xi^o(j) \quad (2)$$

$$\begin{aligned}\xi^o(j)op &= \alpha(j)\min \xi^o(j)\\ &\quad + \beta(j)\max \xi^o(j),\ \min \xi^o(j) > \max \xi^o(j)\end{aligned} \quad (3)$$

Where $\alpha(j)$ and $\beta(j)$ are weighting factors, $0 \le \alpha(j) \le 1$, $0 \le \beta(j) \le 1$, $\alpha(j) + \beta(j) = 1$.

Let the minimum correlation of the sequence j be $E_w(j)$ and the maximum correlation be $E_l(j)$. Establish the objective function on the sequence.

$$E(\alpha(j),\beta(j)) = E_w(j) + E_l(j) \tag{4}$$

Search for $\alpha(j)$ and $\beta(j)$ when this objective function is minimized, and find the corresponding correlation threshold, which we call the best correlation threshold at this time, and denote as $\xi^o(j)op$.

4 K-means clustering method for each fluctuation set sequence

4.1 Gray correlation analysis method

Electricity, heat and cold loads in IES have strong correlation for meteorological factors, and the usual prediction method is to artificially and subjectively select several meteorological factors as inputs, which does not seem to be logically sufficiently justified. Therefore, before carrying out multi load prediction of the regional integrated energy system, the various types of loads and the correlation strength between them and meteorological factors should be analyzed and screened, so as to analyze the coupling characteristics among electric, heat and cold loads, as well as the impact of each influencing factor on the multi loads.

GRA compensates for the shortcomings caused by the use of mathematical and statistical methods for systematic analysis. GRA is a multi-factor statistical analysis method, and its basic idea is to determine whether the association is strong or not based on the similarity of the geometry of the series curves. The closer the curves are to the response series, the greater the degree of association between them, and *vice versa*. The GRA method is suitable for analyzing the nonlinear relationship between multiple loads and influencing factors, which can largely reduce the loss due to information asymmetry, and this method does not need a large number of data sets as the basis, the calculation is small and fast, and there is no discrepancy between quantitative results and qualitative analysis results. Therefore, in this paper, GRA is selected to quantitatively analyze the degree of influence of meteorological factors on the multiplicative load, and the meteorological factors that have the greatest influence on the multiplicative load are selected as the influence factors to analyze the correlation between each influence factor and the multiplicative load.

4.2 Multivariate load and meteorological factor correlation analysis

The correlation coefficient and the correlation degree of the GRA method are two key parameters used to measure the correlation, and the magnitude of the correlation degree can visually reflect the degree of association between two factors, which are calculated by the following equations.

$$\xi_i = \frac{\min\limits_i \min\limits_k |x_0(k) - x_i(k)| + \rho \max\limits_i \max\limits_k |x_0(k) - x_i(k)|}{|x_0(k) - x_i(k)| + \rho \max\limits_i \max\limits_k |x_0(k) - x_i(k)|} \tag{5}$$

$$\gamma_i = \frac{1}{n}\sum_{k=1}^{n} \xi_i(k) \tag{6}$$

Where x_0 is the normalized weather factor sequence, x_i is the normalized load sequence, ρ is the resolution coefficient, generally taken as 0.5, n is the length of the sequence.

The correlation between the multiple loads of the integrated regional energy system and each meteorological influencing factor is analyzed. Let the sequence of electrical, heat and cold loads and each meteorological influence form the following matrix.

Based on the load prediction priorities derived from the above correlation analysis for multivariate loads, the NWP strongly correlated features are used as input for k-means clustering to classify load scenarios, and the BI-LSTM network is trained separately for each load scenario set for sub-scenario set prediction modeling.

$$X_s = \begin{bmatrix} x_E \\ x_H \\ x_C \\ x_{\mathrm{Temp}} \\ x_{HUM} \\ x_{WVEL} \\ x_{WD} \\ x_{GHI} \\ x_{\mathrm{PW}} \\ x_{Dp} \\ x_{atm} \\ x_{CT} \end{bmatrix}^T = \begin{bmatrix} x_E(1) & x_E(2) & \cdots & x_E(n) \\ x_H(1) & x_H(2) & \cdots & x_H(n) \\ x_C(1) & x_C(2) & \cdots & x_C(n) \\ x_{\mathrm{Temp}}(1) & x_{\mathrm{Temp}}(2) & \cdots & x_{\mathrm{Temp}}(n) \\ x_{HUM}(1) & x_{HUM}(2) & \cdots & x_{HUM}(n) \\ x_{WVEL}(1) & x_{WVEL}(2) & \cdots & x_{WVEL}(n) \\ x_{WD}(1) & x_{WD}(2) & \cdots & x_{WD}(n) \\ x_{GHI}(1) & x_{GHI}(2) & \cdots & x_{GHI}(n) \\ x_{\mathrm{PW}}(1) & x_{\mathrm{PW}}(2) & \cdots & x_{\mathrm{PW}}(n) \\ x_{Dp}(1) & x_{Dp}(2) & \cdots & x_{Dp}(n) \\ x_{atm}(1) & x_{atm}(2) & \cdots & x_{atm}(n) \\ x_{CT}(1) & x_{CT}(2) & \cdots & x_{CT}(n) \end{bmatrix}^T \tag{7}$$

Where x_E is electrical load, x_H is heat load, x_C is cold load, x_{Temp} is temperature, x_{HUM} is relative humidity, x_{WVEL} is wind speed, x_{WD} is wind direction, x_{GHI} is irradiance, x_{PW} is rainfall availability, x_{Dp} is dew point, x_{atm} is atmospheric pressure, and x_{CT} is cloud type.

5 Multivariate load prediction model

5.1 LSTM neural network prediction model

LSTM is an improved model of Recurrent Neural Network (RNN), which solves the gradient disappearance and explosion problems of RNN, enabling the network to effectively handle long-term time series data, improving the ability to handle samples with long time series intervals or delays, as well as the ability to handle non-linear data (Hongbo et al., 2022). The network

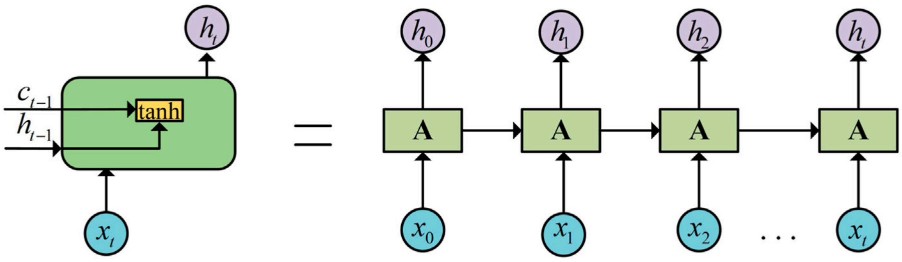

FIGURE 3
Single RNN hidden layer unit expansion structure diagram.

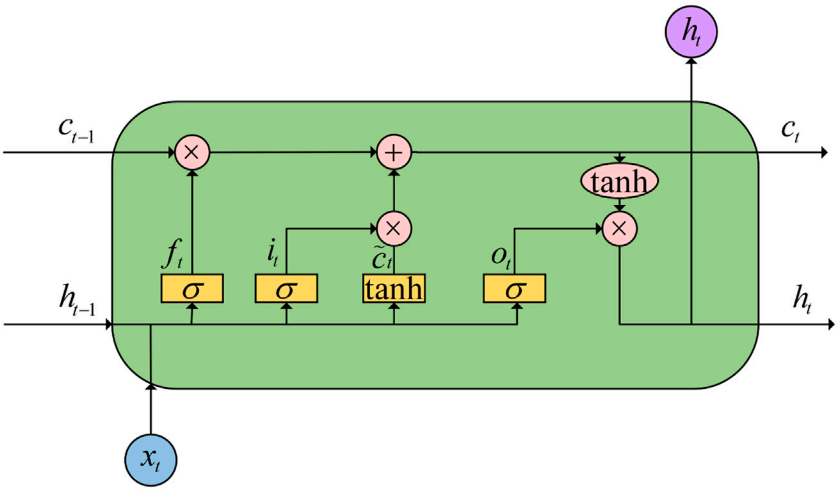

FIGURE 4
LSTM architecture.

structure of a typical RNN is shown in Figure 3. x_t is the input, h_t is the output, c_t is the memory state, A is the neural network module. The key is that it can be used to connect previous information to the current task, and to interact with information by stacking multiple neural networks, passing each neural network module corresponding information to the next one. However, the disadvantage is that as the network is extended, the distance between the relevant information and the current predicted location gradually increases, which makes the RNN lose the ability to learn information that is connected so far.

LSTM can learn long-term dependent information, the key of which is the transfer of cell states, and it has the same repetitive way as RNN, but redesigned memory units while retaining the original structure of RNN, The LSTM sets up three control gates, input gate i_t, output gate o_t, and forgetting gate f_t, which are used to select the correction parameters of the error function of the memory feedback with gradient descent, optimizing the weights of the self-loop and keeping the dynamic change of the weights (Fulong et al., 2022), the architecture is shown in Figure 4.

As shown in Figure 3, the output value h_{t-1} and the current moment input value x_t passed through the forgetting gate from the implicit layer of the previous moment, the forgetting gate reads the above information and outputs a value between 0 and 1 to each of the data in the cell state c_{t-1}. 1 means "complete retention" and 0 means "complete forgetting." Therefore, the forgetting gate can filter the previous data and discard the useless information. The calculation formula is as follows.

$$f_t = \sigma\left(W_f \cdot [h_{t-1}, x_t] + b_f\right) \tag{8}$$

Where W_f and b_f are the weight matrix and bias vector in the forgetting gate, respectively, σ is the activation function, and the sigmoid function is used.

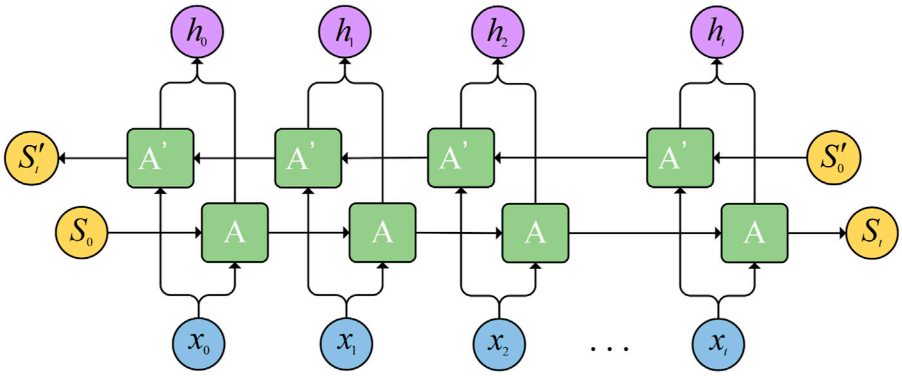

FIGURE 5
BI-LSTM architecture.

The new information is then subjected to a sigmoid function to determine the data that needs to be input into the memory cell, while a new candidate state $\tilde{c}_t$ is constructed through A. The calculation formula is as follows.

$$i_t = \sigma(W_i \cdot [h_{t-1}, x_t] + b_i) \tag{9}$$

$$\tilde{c}_t = \tanh(W_c \cdot [h_{t-1}, x_t] + b_c) \tag{10}$$

Where W_i and b_i are the weight matrix and bias vector in the input gate, respectively, W_c and b_c are the weight matrix and bias vector in the cell state, respectively.

Then, update the cell state, first multiply the old state c_{t-1} and f_t to complete the screening of useless information to delete, and then sum up the product of the calculated result i_t and the new cell state value $\tilde{c}_t$ with the input gate, then get the current moment cell state value, the calculation formula is as follows.

$$c_t = f_t c_{t-1} + i_t \tilde{c}_t \tag{11}$$

In addition, the implied layer data values h_t passed to the next moment are obtained using the new cell states $\tilde{c}_t$ processed by the tanh function and the data o_t classified by the sigmoid function, the calculation formula is as follows.

$$o_t = \sigma(W_o [h_{t-1}, x_t] + b_o) \tag{12}$$

$$h_t = o_t {}^* \tanh(c_t) \tag{13}$$

Where W_o and b_o are the weight matrix and bias vector in the output gate, respectively.

5.2 BI-LSTM prediction model

Both RNN and LSTM can only predict the output of the next moment based on the temporal information of the previous moment, but the output of the current moment is not only related to the previous state, but also may be related to the future state. BI-LSTM is a combination of a forward LSTM and a backward LSTM, and its architecture is shown in Figure 5. It can be viewed as a two-layer neural network, with the first layer serving as the starting input for the series from the direction of the input, and the second layer serving as the starting input from the direction of the output.

To splice and combine the backward-conducted information vector $[S_0', S_1', \cdots, S_t']$ with the forward-conducted information vector $[S_0, S_1, \cdots, S_t]$, so that the whole prediction process can take into account the bi-directional information, deepen the understanding of data features, and thus improve the prediction accuracy, and its splicing and combination structure is shown in Figure 6.

5.3 Step-by-step prediction of multiple loads

The prediction priority of the multiple loads in the IES can be determined based on the cumulative correlation coefficient φ_i. Take electric load as an example, select electric load as the benchmark, sum up the correlations of heat, cold and two loads for electric load to get the cumulative correlation coefficients φ_1 of hot and cold loads for electric load, and then select heat and cold loads as the benchmark respectively to get the cumulative correlation coefficients φ_2 and φ_3 of the selected loads relative to the other two loads. The smaller the value of cumulative correlation, the less coupling with other loads, and *vice versa*. Then, the priority of multiple load prediction can be determined according to the increasing order of the cumulative correlation coefficients.

On the basis of the load prediction method of the above priority, the idea of prioritized step-by-step prediction is adopted, as the electrical and cold loads have the weakest

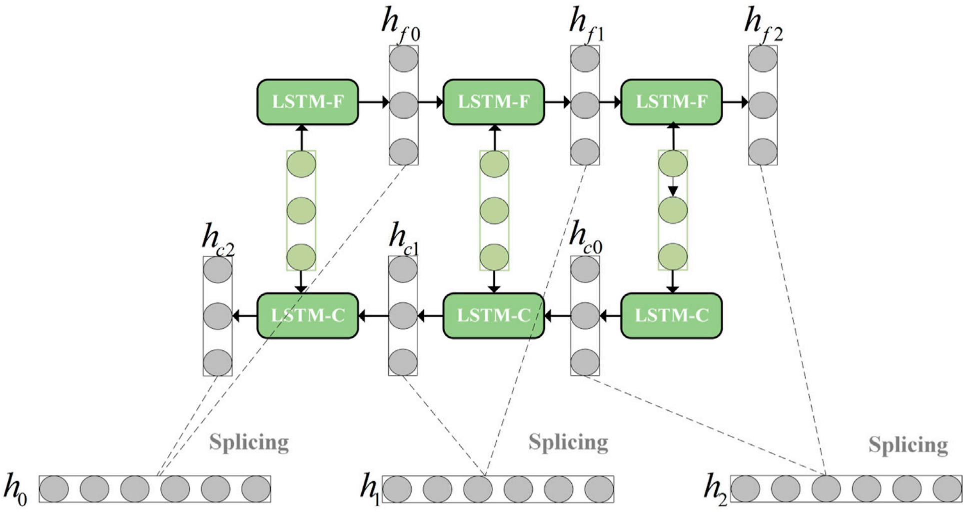

FIGURE 6
BI-LSTM bi-directional conductive splicing combinatorial architecture.

correlation for heat loads, followed by electrical and heat loads for cold loads, and again by heat and cold loads for electrical loads. Accordingly, the predicted heat load can be considered first, and the predicted heat load is first used as input combined with the NWP characteristics of the strong correlation of the cold load and the load mean value series of the first 16 time points of the prediction period for the prediction of the cold load in the set of sub-load sc. Secondly, the predicted hot load and cold load are used as the input combined with the strong correlation NWP characteristics of the electric load and the load mean value series of the first 16 time points of the prediction period to predict the electric load. Finally the overall prediction results of the multiple loads are obtained, where the overall prediction process is shown in Figure 7.

6 Example analysis

6.1 Data source

Example load data from Campus Metabolism for the Temp campus of Arizona State University from 1 January 2019 at 00:00 h to 31 December 2019 at 24:00 h for electricity, heat and cold (Arizona State University, 2022), Meteorological data were obtained from the National Climatic Resources website for the Tempe campus location (U.S. Department of Energy, 2022), including temperature, relative humidity, wind speed, wind direction, irradiance, rainfall availability, dew point, atmospheric pressure, and cloud type, at 15-min sampling intervals.

6.2 Model evaluation metrics

In this paper, Root Mean Square Error (RMSE), Mean Absolute Percentage Error (MAPE) and Mean Absolute Error (MAE) are selected as the evaluation indexes, and the expressions of the specific evaluation indexes are as follows.

$$RMSE = \sqrt{\frac{1}{N}\sum_{t=1}^{N}\left(y_t - y_t'\right)^2} \tag{14}$$

$$MAPE = \frac{1}{N}\sum_{t=1}^{N}\left|\frac{y_t' - y_t}{y_t}\right| \times 100\% \tag{15}$$

$$MAE = \frac{1}{N}\sum_{t=1}^{N}\left|y_t' - y_t\right| \tag{16}$$

Where y_t is the actual value, y_t' is the predicted value, t is the sampling moment, N is the sample size.

6.3 Load scenario set division results

Based on the results of gray correlation degree analysis in this paper, the highest priority electric load is used as the basis for the division of load scenarios, and the similar fluctuating sets of load for 12 months of a year are obtained according to the similarity and fluctuation division of load sequences. Among them, the load of a year is divided into four sets by month as shown in Table 1.

The correlation degree analysis of the strongly correlated NWP features of the multivariate loads is required before the load scenario set division, based on the results of the gray correlation degree analysis, as shown in Table 2. The results show that the strength of the correlation between each meteorological influence factor and the electric, heat and cold loads varies, so it is necessary to correspond the meteorological influence factors to the load types in a reasonable way when prediction.

Based on the results of the strong correlation NWP fluctuation analysis of multiple loads, the NWP features of each load are input into the k-means clustering model to obtain the clustering cluster division of each load under each fluctuation set and train the BI-LSTM model separately for each cluster to realize the sub-load scenario set prediction.

6.4 Multiple load prediction priorities

Since the paper is mainly based on the coupling characteristics of multiple loads to prioritize the single load sequence for load prediction, the coupling relationship of multiple loads obtained based on gray correlation analysis is shown in Table 3. The influence of day type information and meteorological influences on the degree of load coupling is taken into account. For the first predicted heat load, six meteorological factors with the highest correlation are selected for prediction, and then the cold load is predicted iteratively using the predicted heat load data and the corresponding meteorological influences on the cold load. And so on, ensuring that each load forecast from the second priority load forecast onwards iterates over the previous load forecast results and the newly added meteorological impact factors. The following results can be obtained from Table 3: $\varphi_1 = 1.4255$、 $\varphi_2 = 1.3561$、 $\varphi_3 = 1.3596$.

6.5 Analysis of experimental results

6.5.1 Prediction results for load scenario set partitioning

According to the idea of differentiated priority prediction, the heat load is first predicted. Prediction method 1: A sequence of meteorological factors strongly correlated with the heat load and a sequence of heat load history data are used as inputs, where the input meteorological factors are forecast data for the forecast period and the heat load history data are measured data for the 4 hours before the forecast period. Prediction method 2: Extract the strongly correlated meteorological element sequences within the similar fluctuation set with time interval of 1 hour by day as the input of k-means clustering model for load scenario set division, and train the model separately for prediction by load scenario set according to the division result, at which time the input is the same as prediction method 1. In order to highlight the

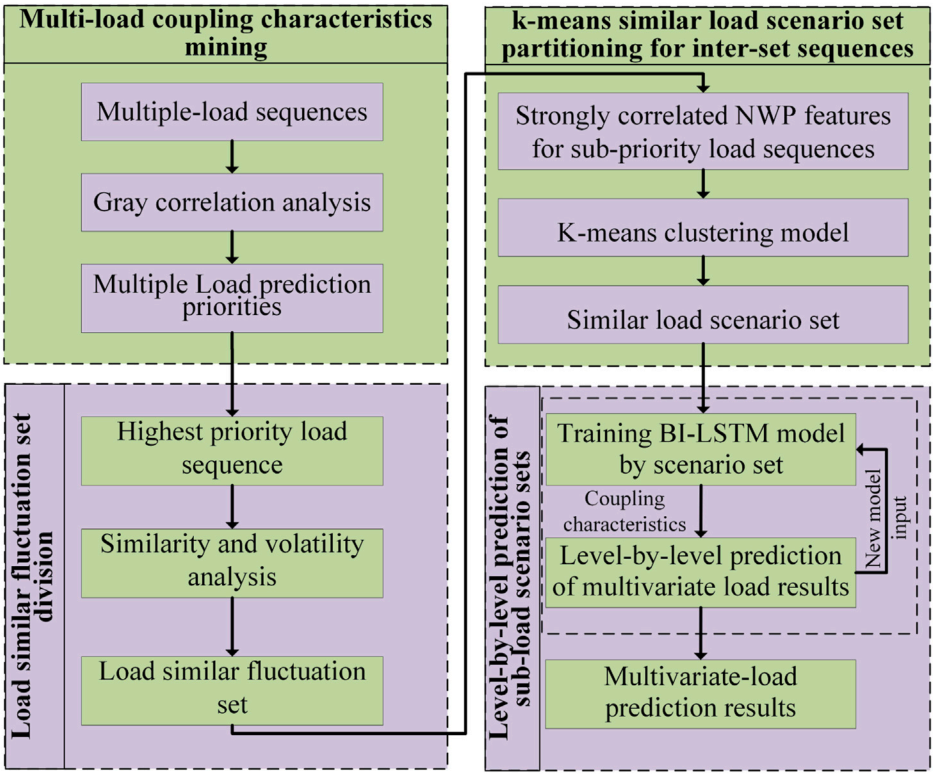

FIGURE 7
Flow chart of multivariate load data prediction.

TABLE 1 Results of load similar fluctuation set division.

Fluctuation set	Fluctuation set 1	Fluctuation set 2	Fluctuation set 3	Fluctuation set 4
Month	Jan Apr Jun	Feb Mar May	Jul Aug Sep	Oct Nov Dec

TABLE 2 Correlation analysis between multivariate load and NWP characteristics.

Meteorological factors	Data correlation							
	Temp	HUM	WVEL	WD	GHI	PW	Dp	atm
Electrical load	0.9468	0.8814	0.8963	0.9171	0.7887	0.9030	0.6315	0.9572
Heat load	0.8729	0.8975	0.8930	0.8811	0.7866	0.8587	0.6304	0.9339
Cold load	0.9522	0.8442	0.8707	0.8999	0.8010	0.9116	0.6362	0.8899

TABLE 3 Correlation analysis between multiple loads.

Load type	Data correlation		
	Electrical load	Heat load	Cold load
Electrical load	1.00	0.7110	0.7145
Heat load	0.7110	1.00	0.6451
Cold load	0.7145	0.6451	1.00

effect of clustering division, 2 days per month are selected for load prediction for similar fluctuation concentration at this time, and the load prediction results for 6 days are obtained, as shown in Figure 8, which shows that the prediction curve of the proposed prediction method in this paper is closer to the actual value curve.

Among them, the error evaluation indexes of the prediction results are shown in Table 4. The errors obtained by prediction method two based on load scenario set division are smaller compared with those obtained by prediction method 1, in which MAPE is reduced by 1.59% on average, RMSE is reduced by 0.14 MMBtu·h^{-1} on average, and MAE is reduced by 0.11 MMBtu·h^{-1} on average.

6.5.2 Prediction results for load scenario set partitioning

Prediction results base on heat load, the coupling characteristics are considered for the prediction of cold load taking into account the priority of multiple load prediction. In this case, due to the consideration of the coupling characteristics, the prediction results of the heat load, as well as the strongly correlated meteorological characteristic series and the actual cold load series of the first 4 hours of the prediction period are used as inputs. The prediction method 1 that directly predicts considering the coupling characteristics, the prediction method 2 that divides the set of load scenes without considering the coupling characteristics, and the prediction method 3 that considers both the coupling characteristics and the division of the set of load scenes are obtained. The prediction results are shown in Figure 9.

A comparison of the results of multiple prediction methods is shown in Table 5, where the prediction method 2 without considering the coupling characteristics is less effective, with the highest average absolute percentage error reaching 10.26%, prediction method 3 has the smallest prediction error because it considers the coupling characteristics of multiple loads and divides the set of load scenarios. Compared with the prediction method 1, the MAPE was reduced by 2.06%, RMSE by 278.93 Ton, and MAE by 188.82 Ton on average, compared to prediction Method 2, MAPE is reduced by 2.98% on average, RMSE by 219.30 Ton on average, and MAE by 389.47 Ton on average.

According to the above obtained heat and cold load prediction values, the electric load is predicted by considering the coupling characteristics. In this case, the electrical load forecast inputs include the forecasted hot and cold loads as well as strongly correlated meteorological characteristics and measured electrical load data for the first 4 hours of the forecast period. As the coupling characteristics and load scenario set division are considered, the same three prediction modes as the cold load are obtained, and the prediction results are shown in Figure 10. It can be seen that the average absolute percentage error of prediction method 3 decreases by 0.55% and 0.66% on average compared with prediction method 1 and prediction method 2. Respectively, which is due to the fact that prediction method 3 takes into account the characteristics of multi-energy

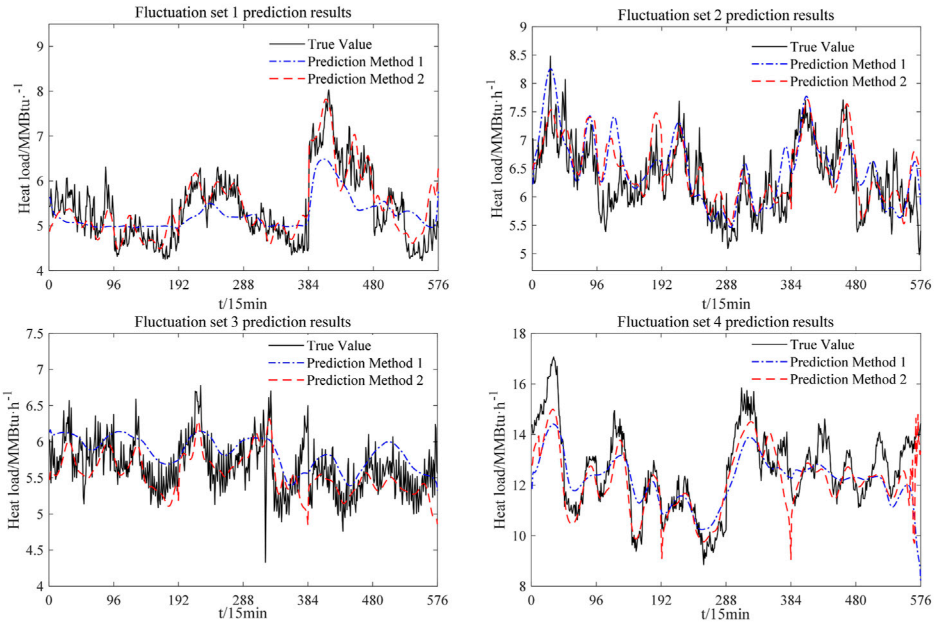

FIGURE 8
Heat load prediction results.

TABLE 4 Comparison of heat load prediction results.

Predictive models	MAPE%				RMSE/MMBtu·h^{-1}				MAE/MMBtu·h^{-1}			
	Set 1	Set 2	Set 3	Set 4	Set 1	Set 2	Set 3	Set 4	Set 1	Set 2	Set 3	Set 4
Prediction method 1	8.30	6.45	5.42	7.06	0.56	0.51	0.37	1.20	0.45	0.40	0.30	0.91
Prediction method 2	5.99	5.53	4.02	5.32	0.41	0.44	0.32	0.93	0.32	0.34	0.23	0.70

TABLE 5 Comparison of cold load prediction results.

Predictive models	MAPE/%				RMSE/Ton				MAE/Ton			
	Set 1	Set 2	Set 3	Set 4	Set 1	Set 2	Set 3	Set 4	Set 1	Set 2	Set 3	Set 4
Prediction method 1	10.25	4.96	2.91	6.38	1,588.35	507.95	405.03	182.63	1,098.61	387.25	298.79	137.25
Prediction method 2	5.65	6.30	5.97	10.26	807.49	602.23	729.67	294.12	601.08	445.95	581.71	218.56
Prediction method 3	4.22	4.07	2.96	5.00	623.17	411.43	391.35	142.28	454.17	294.21	302.75	115.49

coupling in IES and uses the remaining two loads as references, which in turn improves its prediction accuracy.

Due to the consideration of multivariate load coupling characteristics and the division method of load scenario set, the prediction results of prediction method 3 have less prediction error than the other two prediction methods, This is mainly reflected in the peak and valley hours of the load, and the prediction method 3 is more reflective of the actual load variation, which reflects that the prediction method considering the division of load scenarios and taking into account the coupling characteristics is more practical for IES multi load prediction. The electrical load

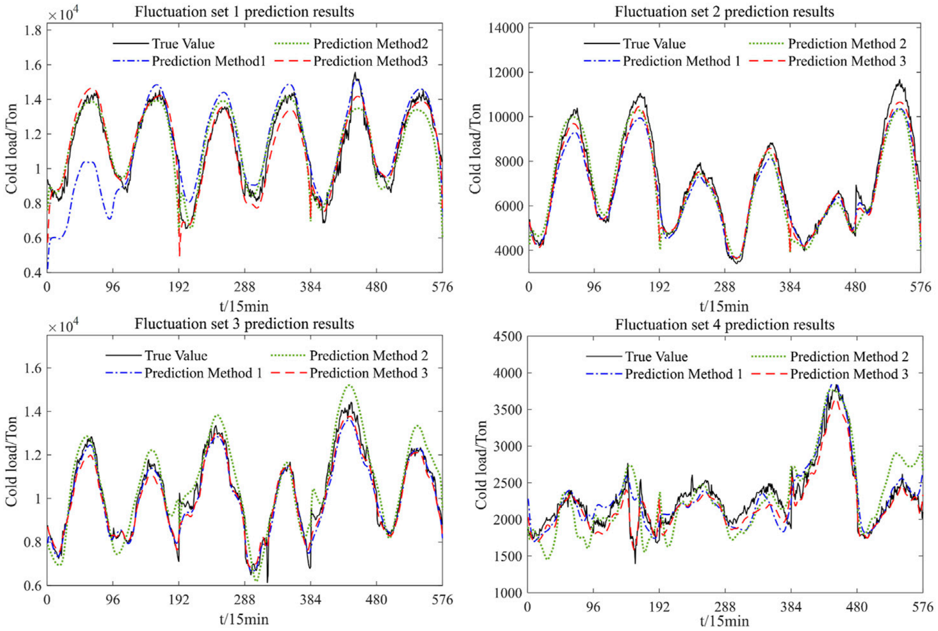

FIGURE 9
Cold load prediction results.

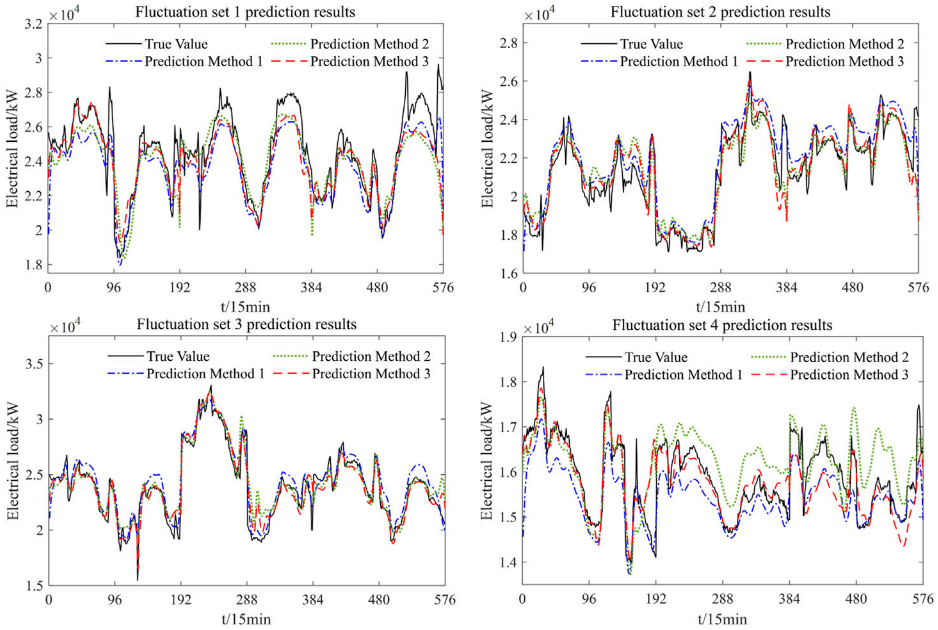

FIGURE 10
Electrical load prediction results.

forecast errors are shown in Table 6. Although the electric load prediction errors obtained by the three prediction methods are not significantly different, the prediction errors obtained by the prediction method considering coupling characteristics and load scenario set division are smaller.

TABLE 6 Comparison of electrical load prediction results.

Predictive models	MAPE/%				RMSE/kW				MAE/kW			
	Set 1	Set 2	Set 3	Set 4	Set 1	Set 2	Set 3	Set 4	Set 1	Set 2	Set 3	Set 4
Prediction method 1	3.93	3.53	3.27	2.85	1,215.23	892.00	945.34	552.68	998.04	750.63	760.40	463.27
Prediction method 2	4.14	3.04	3.39	3.47	1,493.70	951.83	1,145.31	663.33	1,034.97	643.35	752.23	541.11
Prediction method 3	3.51	2.73	3.00	2.14	1,330.08	919.35	949.03	486.67	897.73	588.18	686.75	337.22

7 Conclusion

1) In order to improve the accuracy of multivariate load prediction, this paper proposes a similar fluctuation feature set partitioning method considering the coupling characteristics of multivariate loads. By studying the coupling strength between multiple types of energy in IES to determine the prediction priority of multiple loads, the interactive coupling between electric, heat and cold loads is fully considered. The NWP features with strong correlation with multiple loads are obtained by gray correlation analysis, and k-means clustering is performed using the inter-set NWP as input, and fine-grained modeling is performed for each cluster. The analysis of the arithmetic examples leads to the following main conclusions.
2) Based on the load similar fluctuation set division method proposed in this paper, four fluctuation sets are obtained. The load fluctuation types within each fluctuation set are similar, and the load scenario set is divided based on the k-means clustering model for each load similar fluctuation set. And according to the results of the above analysis, the priority of load forecasting is considered, and the heat load, cold load and electric load are predicted step by step according to the fluctuation set and load scenario set respectively.
3) The prediction results based on multiple prediction methods show that the average absolute percentage errors of electric, heat, and cold loads are 2.85%, 5.22%, and 4.06% for the prediction methods considering the division of load scenario sets and coupling characteristics in the overall prediction results of four load similar fluctuation sets. The average absolute percentage error is reduced by 0.66%, 1.53% and 2.99% respectively compared to the prediction method considering only load scenarios, compared with the prediction method without considering load scenes, its average absolute percentage errors are reduced by 0.55%, 1.53%, and 2.07%, respectively, which verifies the effectiveness of the prediction method considering the division of load scenes set and coupling characteristics.

With the popularity of IES and the development of interconnected IES, the division of IES types can be considered in the subsequent study so as to realize the collaborative prediction among multiple IESs.

Data availability statement

The original contributions presented in the study are included in the article/supplementary material, further inquiries can be directed to the corresponding author.

Author contributions

MY: Writing—original draft. DL: Validation, Visualization. XS: Methodology. JW: Software, Supervision. YC: Data curation.

Funding

This work was supported by National Key R&D Program of China [Technology and application of wind power/photovoltaic power prediction for promoting renewable energy consumption (2018YFB0904200)].

Conflict of interest

The authors declare that the research was conducted in the absence of any commercial or financial relationships that could be construed as a potential conflict of interest.

Publisher's note

References

Abhishek, S., and Sachin, K. J. (2022). A novel seasonal segmentation approach for day-ahead load forecasting. *Energy* 257, 124752. doi:10.1016/j.energy.2022.124752

Arizona State University (2022). Campus metabolism. https://cm.asu.edu (Accessed August 11, 2022).

Fulong, Y., Wenju, Z., Mostafa, A. G., Yang, S., and Wanqing, Z. (2022). An integrated D-CNN-LSTM approach for short-term heat demand prediction in district heating systems. *Energy Rep.* 8 (13), 98–107. doi:10.1016/j.egyr.2022.08.087

Haohan, T., Zhisheng, Z., and Daolin, Y. (2021). Research on multi-load short-term forecasting of regional integrated energy system based on improved LSTM. *Proc. CSU-EPSA.* 33 (9), 130–137. doi:10.19635/j.cnki.csu-epsa.000726

Hongbo, R., Qifen, L., Qiong, W., Chunyan, Z., Zhenlan, D., and Jie, C. (2022). Joint forecasting of multi-energy loads for a University based on copula theory and improved LSTM network. *Energy Rep.* 8 (10), 605–612. doi:10.1016/j.egyr.2022.05.208

Jinpeng, C., Zhijian, H., and Weinan, C. (2021). Load prediction of integrated energy system based on combination of quadratic modal decomposition and deep bidirectional long short-term memory and multiple linear regression. *Autom. Electr. Power Syst.* 45 (13), 85–94. 10. 7500/AEPS20200829004.

Jixiang, L., Qipei, Z., Zhihong, Y., Mengfu, T., Jinjun, L., and Hui, P. (2019). Short-term load forecasting method based on CNN-LSTM hybrid neural network model. *Autom. Electr. Power Syst.* 43 (08), 131–137. doi:10.7500/AEPS20181012004

Jizhong, Z., Hanjiang, D., Shenglin, L., Ziyu, C., and Tengyan, L. (2021). Review of data-driven load forecasting for integrated energy system. *Proc. CSEE* 41 (23), 7905–7924. doi:10.13334/j.0258-8013.pcsee.202337

Jizhong, Z., Hanjiang, D., Weiye, Z., Shenglin, L., Yanting, H., and Lei, X. (2022). Review and prospect of data-driven techniques for load forecasting in integrated energy systems. *Appl. Energy* 321, 119269. doi:10.1016/j.apenergy.2022.119269

Kai, Z., Jian, F., Jianhua, L., Xinlei, B., Feixiang, G., Zudong, L., et al. (2022). Power consumption behavior pattern classification based on fuzzy C⁃mean clustering algorithm. *Power Demand Side Manag.* 24 (3), 98–103. doi:10.3969/j.issn.1009-1831.2022.03.016

Luiz, F., and Afshin, A. (2015). Short-term forecasting of the abu dhabi electricity load using multiple weather variables. *Energy Procedia* 75, 3014–3026. doi:10.1016/j.egypro.2015.07.616

Mao, Y., Chaoyu, S., and Huiyu, L. (2020). Day-ahead wind power forecasting based on the clustering of equivalent power curves. *Energy* 218, 119515. doi:10.1016/j.energy.2020.119515

Mao, Y., Meng, Z., Dawei, H., and Xin, S. (2022). A composite framework for photovoltaic day-ahead power prediction based on dual clustering of dynamic time warping distance and deep autoencoder. *Renew. Energy* 194, 659–673. doi:10.1016/j.renene.2022.05.141

Mukhopadhyay, P., Mitra, G., Banerjee, S., and Mukherjee, G. (December 2017). “Electricity load forecasting using fuzzy logic: Short term load forecasting weather parameter,” in Proccedings of the 2017 7th international conference on power systems (ICPS), Pune, India 812–819. doi:10.1109/ICPES.2017.8387401

Nantian, H., Qingkui, H., Jiajin, Q., Qiankun, H., Rijun, W., Guowei, C., et al. (2022). Multinodes interval electric vehicle day-ahead charging load forecasting based on joint adversarial generation. *Int. J. Electr. Power & Energy Syst.* 143, 108404. doi:10.1016/j.ijepes.2022.108404

Qingkai, S., Xiaojun, W., Yizhi, Z., Fang, Z., Pei, Z., and Wenzhong, G. (2021). Multiple load prediction of integrated energy system based on long short-term memory and multi-task learning. *Autom. Electr. Power Syst.* 45 (5), 63–70.doi:10.7500/AEPS20200306002

Tang, Y., Liu, H., Xie, Y., Zhai, J., and Wu, X. (2019). Short-term forecasting of electricity and gas demand in multi-energy system based on RBF-NN model. *IEEE Int. Conf. Energy Internet (ICEI)*, 542–547. doi:10.1109/ICEI.2019.00102

U.S. Department of Energy (2022). *NSEDB:National solar radiation database*. https://nsrdb.nrel.gov/ (Accessed August 11, 2022).

Valery, S., Evgeny, B., Dmitry, S., and Bin, Z. (2022). Current state of research on the energy management and expansion planning of integrated energy systems. *Energy Rep.* 8, 10025–10036. doi:10.1016/j.egyr.2022.07.172

Wang, X., Wang, S., Zhao, Q., Wang, S., and Fu, L. (2021). A multi-energy load prediction model based on deep multi-task learning and ensemble approach for regional integrated energy systems. *Int. J. Electr. Power & Energy Syst.* 126 (A), 106583. doi:10.1016/j.ijepes.2020.106583

Wei, W., Lin, X., Jierui, X., Chang, L., Xiaofeng, J., and Kai, L. (2022). Coupled dispatching of regional integrated energy system under an electric-traffic environment considering user equilibrium theory. *Energy Rep.* 8, 8939–8952. doi:10.1016/j.egyr.2022.07.008

Wu, Y., Liang, X., Huang, T., Lin, Z., Li, Z., and Hossain, M. (2021a). A hierarchical framework for renewable energy sources consumption promotion among microgrids through two-layer electricity prices. *Renew. Sustain. Energy Rev.* 145, 111140. doi:10.1016/j.rser.2021.111140

Wu, Y., Lin, Z., Liu, C., Chen, Y., and Uddin, N. (2021b). A demand response trade model considering cost and benefit allocation game and hydrogen to electricity conversion. *IEEE Trans. Ind. Appl.* 58, 2909–2920. doi:10.1109/TIA.2021.3088769

Xiaobo, Z., and Jianzhou, W. (2018). A novel decomposition-ensemble model for forecasting short-term load-time series with multiple seasonal patterns. *Appl. Soft Comput.* 65, 478–494. doi:10.1016/j.asoc.2018.01.017

Xuexiang, L., Haowen, L., Xudong, Z., Zhonghe, H., Yu, C., and Min, Y. (2022). A novel neural network and grey correlation analysis method for computation of the heat transfer limit of a loop heat pipe (LHP). *Energy* 259, 124830. doi:10.1016/j.energy.2022.124830

Yang, M., Zhang, L., Cui, Y., Zhou, Y., Chen, Y., and Yan, G. (2019). Investigating the wind power smoothing effect using set pair analysis. *IEEE Trans. Sustain. Energy* 11, 1161–1172. doi:10.1109/TSTE.2019.2920255

Yingjun, W., Zhiwei, L., Chengjun, L., Tao, H., Yuyang, C., Yingtao, R., et al. (2022). Resilience enhancement for urban distribution network via risk-based emergency response plan amendment for ice disasters. *Int. J. Electr. Power & Energy Syst.* 141, 108183. doi:10.1016/j.ijepes.2022.108183

Frontiers in Energy Research

TYPE Original Research
PUBLISHED 16 January 2023
DOI 10.3389/fenrg.2022.1044379

Research on data mining model of fault operation and maintenance based on electric vehicle charging behavior

Bin Zhu*, Xiaorui Hu, Min He, Lei Chi and Tingting Xu

State Grid Chongqing Electric Power Company Marketing Service Center Metrology Center, Chongqing, China

OPEN ACCESS

EDITED BY
Yingjun Wu,
Hohai University, China

REVIEWED BY
Srete Nikolovski,
Josip Juraj Strossmayer University of Osijek, Croatia
Haowei Yao,
Zhengzhou University of Light Industry, China

*CORRESPONDENCE
Bin Zhu,
sheep1055@163.com

SPECIALTY SECTION
This article was submitted to Smart Grids,
a section of the journal
Frontiers in Energy Research

RECEIVED 14 September 2022
ACCEPTED 31 October 2022
PUBLISHED 16 January 2023

CITATION
Zhu B, Hu X, He M, Chi L and Xu T (2023), Research on data mining model of fault operation and maintenance based on electric vehicle charging behavior. *Front. Energy Res.* 10:1044379.
doi: 10.3389/fenrg.2022.1044379

In recent years, with the development of new energy technology and the country's strong support for electric vehicles, there is a lack of effective electric vehicle charging fault analysis and diagnosis methods at this stage. A comprehensive analysis of the working principle of the charging process of electric vehicles, based on the clarification of the failure mechanism of the power battery and charging equipment, analyzes the fault-related factors affecting the power battery and charging equipment from multiple angles, and summarizes the relationship between the power battery and charging equipment. The feature parameters related to equipment failure are discretized by the k-means clustering algorithm. Using the optimized FP-Growth algorithm based on weights, the association rules between the power battery and charging equipment failures and the characteristic parameters of the failure factors are mined, and the correlation of the failures is analyzed based on the association rules, and the correlation between the failure factors and the failures is obtained relevant level.

KEYWORDS

association rules, charging equipment, renewable energy, data mining, electric car, fault correlation

---

Abbreviations: T, The transaction set; X, The item set in a transaction; ξ_{BU}, Battery charging overvoltage ratio; U_B, Power battery charging actual voltage; U_{B0}, Rated charging voltage of power battery; ξ_{ZU}, Charging voltage error rate of charging equipment; U_Z, Actual voltage of charging device; U_{Z0}, The demand voltage threshold set by the charging device controller; ξ_{ZI}, Error rate of charging output current of charging equipment; I_Z, Actual charging output current of the charging device; I_{Z0}, The demand current threshold set by the charging device controller; $SOC(t)$, The tth value on the SOC data sequence; $SOC_{dbi}(t)$, Forward I order difference of the t th value of battery SOC data sequence.

1 Introduction

1.1 Motivation and incitement

With the rapid development of social economy and science and technology, China has done a lot of work in the construction of transportation infrastructure. The developed transportation industry and the increasing living standards of residents have led to a gradual increase in residents' demand for automobiles as a means of transportation. However, the increasing number of motor vehicles means an increase in energy consumption, and at the same time it will cause continued environmental degradation. In this context, the country vigorously promotes the use of clean energy electric vehicles to replace traditional fuel vehicles in the field of transportation. At the same time, it has also issued a large number of preferential policies for electric vehicles to encourage residents to purchase and use electric vehicles as a means of family transportation (Zhu et al., 2021). In the charging process of electric vehicles, due to the operation of a large number of power electronic devices, various failures will occur, and in serious cases, safety accidents may even occur, threatening the personal and property safety of users (Tang and Cao, 2020).

1.2 Literature review

Research on the charging failure of electric vehicles is still in the preliminary stage, and the standards issued by the state and enterprises for the safety of electric vehicle charging also need to be improved. Wu Chao (Wu, 2019) designed an abuse experiment for lithium iron phosphate power batteries, summarized the failure mechanism of each component of the lithium battery, and proposed diagnostic methods and diagnostic strategies for typical failures of lithium iron phosphate batteries. However, the impact of charging facilities is not taken into consideration. Ma et al. (2020) constructed characteristic parameters that can characterize the characteristics of power batteries, and extracted the characteristic parameter thresholds for safe charging of power batteries by analyzing the changes of characteristic parameters, providing a basis for power battery failure mode identification. In this paper, the characteristic parameters of power battery characteristics and the characteristic parameters of charging facility operation characteristics are combined and analyzed to study their fault correlation and dig out the causes of charging faults of electric vehicles. Wilhelmiina Hämäläinen (Hämäläinen., 2016) used Fisher's exact test method to solve the problem of unreliable results in dependency rule mining. At the same time, the new solution-Fisher's exact test, has lower time complexity and higher accuracy. V. J. Rayward-Smith (Rayward-Smith, 2007) proposed a new technology to measure the correlation between real value data and nominal data, which relies on the definition of assigning nominal value to actual value. The proposed assignment is defined to be the most favourable of all such assignments and can be efficiently computed. Wu et al. (2020) applied the time series model to the fault diagnosis of the power battery of electric vehicles, using the principle of moving window deviation as an evaluation index for monitoring battery faults, and established a battery fault model on the MATLAB platform to conduct experiments. In order to adapt to the rapid increase in the number of electric vehicles, Western countries have begun to establish electric vehicle charging networks in the form of cooperation between traditional car companies and energy companies. At present, a series of standards have been formulated for the safety of charging equipment (IEC 62196-1-2014, 2014), which stipulate electric vehicles. Equipment related parameters and safety features involved in the process of car charging and discharging. Ru et al. (2017) conducted a safety evaluation on the electrical safety protection measures of electric vehicle charging equipment, established an evaluation index system for electrical safety, and verified the effectiveness of the evaluation method through experiments. Meng Jianzhong (Meng, 2018) designed the DC charging device and AC charging device of electric vehicles, and formulated the fault diagnosis strategy of the charging equipment using the finite state machine method, and verified the charging equipment's charging overvoltage fault, insulation fault, and insulation fault through experimental tests. Successfully realize fault diagnosis when communication faults and emergency stop faults occur. However, the correlation between faults is not deeply explored and the internal factors of faults cannot be accurately identified. Yu Chang (Yu, 2020) analyzed the safety influencing factors of electric vehicle charging equipment, developed an index system for evaluating the health of charging equipment from two aspects: electrical performance and safety performance, and designed the health of charging equipment based on the uncertainty analytic hierarchy process. Comprehensive evaluation method of state. In terms of artificial intelligence, the main idea is to make intelligent machines think and react in an artificial manner. In the field of equipment failure analysis, artificial intelligence technologies such as expert systems, neural networks, and data mining have also begun to have a large number of applications. It provides a thought for the analysis of fault correlation factors in this paper, but does not investigate the fault cause and mechanism. Zhao et al. (Zhao and Jiang, 2020) designed a fault diagnosis method for vehicle electronic accelerator pedal based on PNN and BP neural network methods, and verified the effectiveness of the method through experiments. Hu Jun (Hu et al., 2017) and others discovered the law of the state recording data of power transmission and transformation equipment through big data mining technology, and realized the fault diagnosis of power transmission and transformation equipment based on this. Qiu. (2020) analyzed EMU fault alarm data through data mining technology, and obtained the knowledge of EMU fault alarm correlation, which provided a basis for EMU fault location.

Zhang X C et al. proposed a fault analysis method for power distribution terminal units based on association rule mining algorithms, which can objectively and comprehensively analyze and diagnose faults (Zhang et al., 2021). Zhang Y L et al. (Zhang et al., 2020) proposed a Right-Hand Side Expanding Algorithm suitable for association rule mining, which can quickly and accurately process frequent itemsets and accurately find all maximal frequent itemsets. However, this method has some limitations. Inspired by this, we propose an FP-growth algorithm based on weighted optimization, which solves the problem that high-level faults may be missed if the minimum support is set too small.

1.3 Contribution and paper organization

In summary, it is important to make full use of the advantages of artificial intelligence technology, improve the research on the correlation analysis of electric vehicle charging faults, and obtain the correlation knowledge between different faults in the charging process of electric vehicles. This article first analyzes the working principles of power batteries and DC charging piles. Based on this, the fault-related factors are analyzed and the fault-related characteristic parameters are designed. The clustering method is used to discretize the fault-related characteristic parameter data, and the application is obtained. Transaction data set for mining association rules. Finally, the weighted optimized FP-Growth algorithm is used to mine the association rules between the power battery and charging equipment faults and their characteristic parameters, and the correlation between the power battery and charging equipment faults is analyzed based on the association rules, and the optimization is verified by experiments. Compared with the original FP-Growth algorithm, the method has superiority in algorithm performance.

The rest of this article is arranged as follows. Section 2 discusses the working principle of electric vehicle charging. Section 3 discusses the fault factor correlation model and proposes the FP-growth algorithm based on weighting, and then establishes the charging fault data mining model. Section 4 tests the data mining model and shows some fault association rules mined by the algorithm. Section 5 is the conclusion.

2 Working principle of electric vehicle charging

2.1 Working principle of power battery

2.1.1 Analysis of the working principle of lithium iron phosphate battery

The lithium iron phosphate battery relies on the transfer of lithium ions inside the battery to form current in the external circuit. Figure 1 shows the internal structure of the lithium iron phosphate battery. The internal structure of the lithium iron phosphate battery mainly has the following parts (Chang et al., 2020): First is the positive and negative electrodes of the battery. The lithium-ions inside the battery complete the deintercalation and intercalation reactions on the positive and negative electrodes. The main material of the positive electrode of the lithium-iron phosphate battery is lithium iron phosphate, and the negative electrode material is often graphite. Second is the

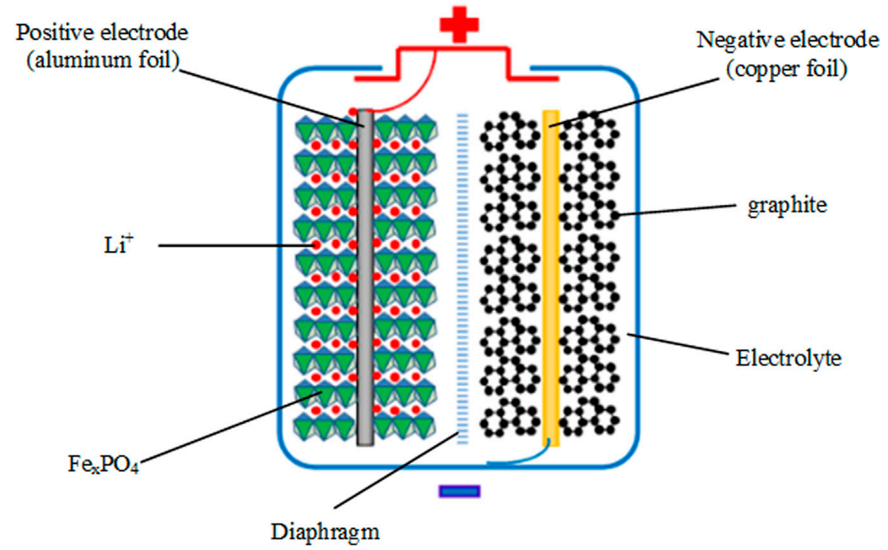

FIGURE 1
Internal structure of lithium iron phosphate battery.

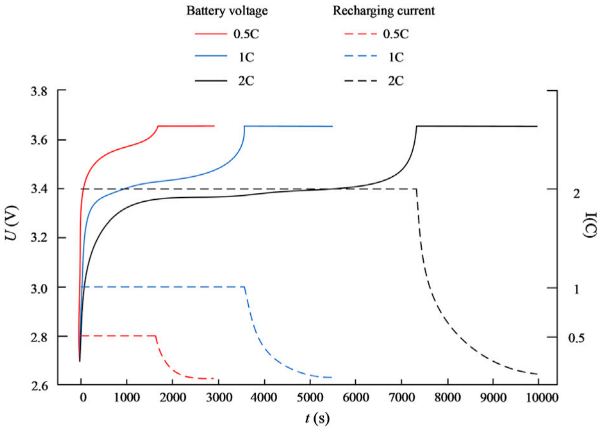

FIGURE 2
Changes in battery voltage and charging current under different charging rates.

positive and negative current collectors. The function of the positive and negative electrode current collectors of the battery is mainly to collect the current generated by the active material of the battery and output it to the outside. The positive electrode current collector material often uses aluminium foil, and the negative electrode current collector often uses copper foil. Third is the electrolyte. The migration of lithium ions inside a lithium iron phosphate battery requires electrolyte as a medium. Fourth is the diaphragm. In the lithium iron phosphate battery, it plays a role of isolating the positive and negative electrodes to prevent the internal short circuit of the battery.

When a lithium iron phosphate battery is charged, positively charged lithium ions are extracted from the positive electrode material of the battery into the electrolyte inside the battery, and are inserted into the negative electrode after passing through the diaphragm. Negatively charged electrons flow from the positive pole of the battery to the negative pole through an external circuit, so that the charge state of the positive and negative poles of the battery reaches a balance.

2.1.2 The working principle of ternary lithium battery

The composition structure of the ternary lithium battery is basically the same as that of the lithium iron phosphate battery. It is mainly composed of positive and negative electrodes, current collectors, separators, and electrolyte. The positive electrode material of the lithium battery is composed of three materials of lithium nickelate, lithium-cobaltate, and lithium manganate mixed in a certain proportion. The ternary lithium battery has a higher energy density, and more car companies apply it to their flagship models to obtain a higher cruising range.

When a ternary lithium battery is charged, positively charged lithium ions are extracted from the positive electrode material of the battery into the electrolyte inside the battery, and are inserted into the negative electrode after passing through the diaphragm. Negatively charged electrons flow from the positive pole of the battery to the negative pole through an external circuit, so that the charge state of the positive and negative poles of the battery reaches a balance.

2.1.3 Power battery charging characteristics

The electric vehicle power battery pack is composed of a certain number of single cells combined in series and parallel. The main performance parameters of the single power battery include nominal capacity, nominal voltage, internal resistance, charging voltage range, etc. The performance parameters of single power batteries produced by different manufacturers also have certain differences. This article selects a single battery with a nominal voltage of 3.2 V and a charging voltage range of 2.5V–3.65 V to show its own parameter changes and charging characteristics during charging.

Generally, the charging of lithium-ion batteries is a dynamic process of constant current, then constant voltage and then constant current (Guo, 2020). At the beginning of the charging process, the voltage of the battery is quickly raised to the cut-off voltage with a constant current, and then the battery is charged with a constant cut-off voltage until the charging current drops to a certain level (Li, 2015). After this process is completed, the battery has completed most of the charge, and then keeps a small current constant current charge to continue to replenish the power (Tan, 2020). Figure 2 shows the change curve of battery voltage with time during the charging process of a single lithium-ion battery at different charging rates.

2.1.4 Working principle of DC charger

The DC charger can output DC power to directly charge the power battery of the electric vehicle. Its charging power is large, also called a fast-charging pile. Since the fast-charging speed of DC chargers can meet the charging needs of more users, DC chargers have begun to become the mainstream of electric vehicle charging methods. The National Energy Administration has formulated an industry standard for DC chargers (NB/T 33001-2010, 2010), which stipulates that the DC charger is composed of the following parts. Figure 3 shows the composition and electrical structure of the DC charger.

The DC charging pile includes four modules: power unit, control unit, metering unit and human-computer interaction interface. Among them, the power unit realizes the rectification and power factor correction of the AC power of the grid and then converts it into charging DC. The control unit can receive the user's operation instructions to control the power unit, and then complete the charging start and stop control of the charging pile, power unit output control and other functions. The metering unit can record the electrical energy output by the DC charger to the power battery. The human-computer interaction interface can monitor the operating data of the charging process in real time and display

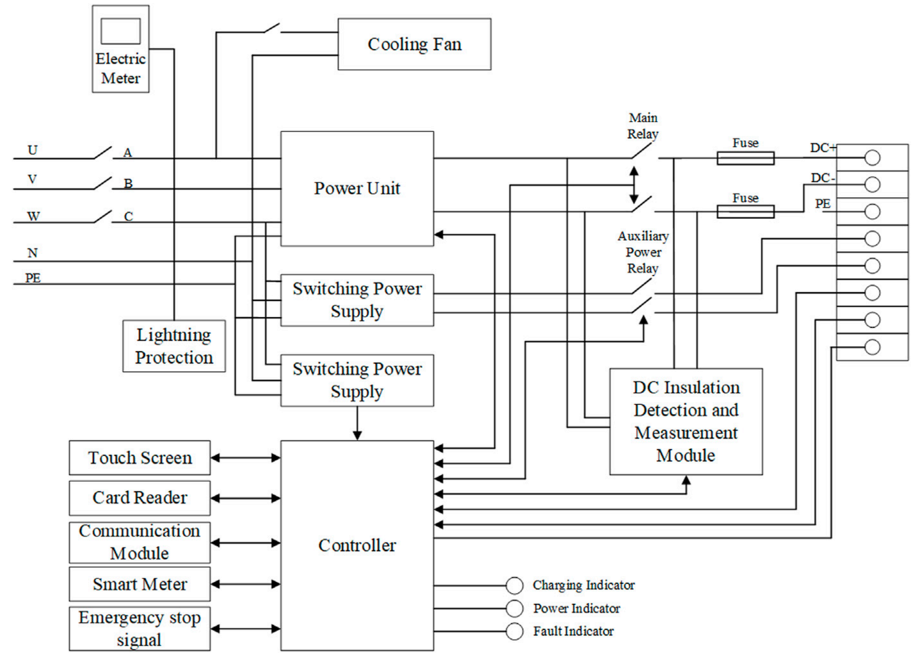

FIGURE 3
Electrical structure diagram of DC charger.

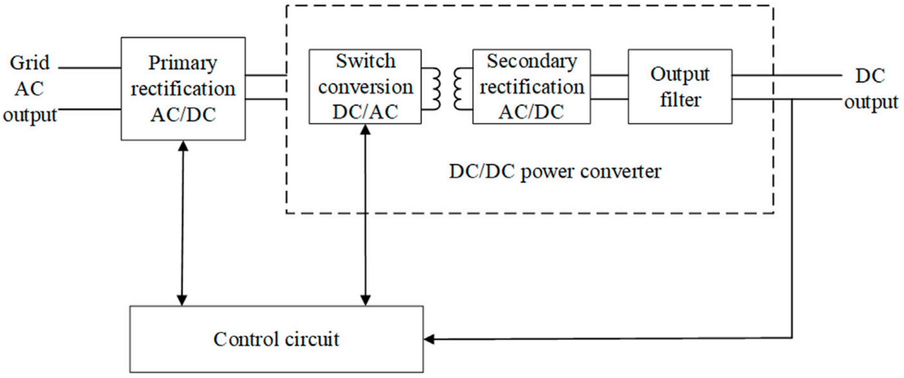

FIGURE 4
Basic structure diagram of DC charger power unit.

the information on the screen to the user. At the same time, it supports the user's operation instruction input and parameter setting, and informs the control. The unit completes the control of the start and stop of the charging process and the charging state.

The most critical part of the structure of the DC charger is the power unit, which can realize the rectification function from alternating current to direct current. The basic structure of the power unit is shown in Figure 4. The front part of the power unit has a rectification function to rectify the AC power of the grid into a direct current. The latter part has a DC conversion function to achieve electrical isolation and voltage conversion.

At present, the pre-stage circuit of the DC charger power unit is mainly selected as the VIENNA rectifier circuit. The

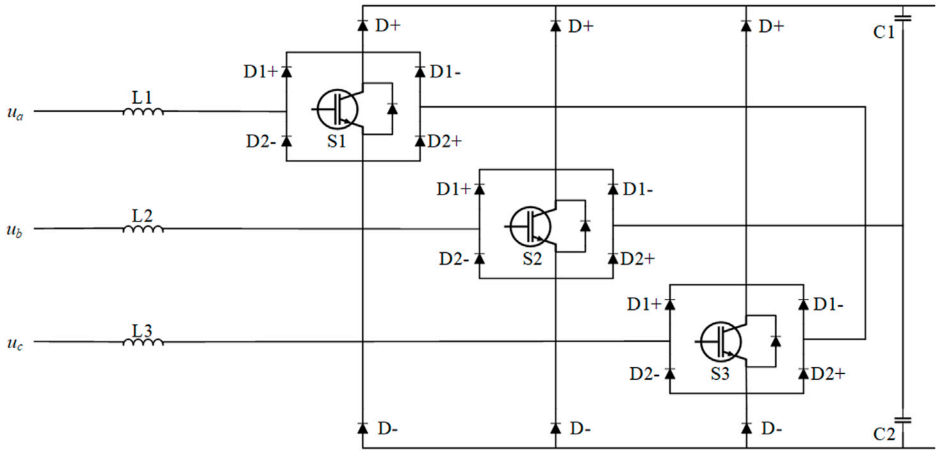

FIGURE 5
Topological structure of VIENNA rectifier circuit of front-end circuit.

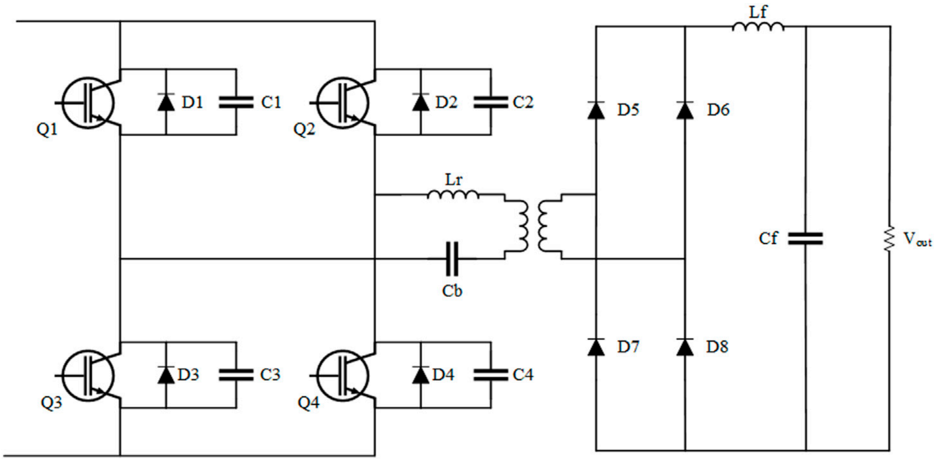

FIGURE 6
The circuit topology structure of the phase-shifted full-bridge converter of the back-stage circuit.

voltage stress of the switch tube is half of the DC side bus voltage, which is suitable for high-voltage environments. The topological structure of VIENNA rectifier circuit of the front stage circuit is shown as in Figure 5.

The back-stage circuit of the DC charger power unit mainly adopts a phase-shifted full-bridge converter, which can realize electrical isolation and voltage conversion at the same time to realize soft switching of the circuit, thereby improving the transmission efficiency of electric energy. The circuit topological structure of the phase-shifted full-bridge converter of the latter stage circuit is shown as in Figure 6.

2.2 Analysis of failure mechanism and correlation factors of electric vehicle charging process

2.2.1 Analysis of power battery failure mechanism and related factors

Lithium-ion battery cathode material is lithium alloy metal oxide. The temperature at which the positive electrode of the lithium iron phosphate battery reacts with the electrolyte is around 230°C, and the temperature at which the other positive electrode materials react with the electrolyte is lower than this level. Therefore, the lithium iron phosphate battery has

TABLE 1 Failure phenomena and causes of power battery.

Fault phenomenon	Cause of failure
Battery pack capacity reduced	Inconsistent voltage of single battery
	Battery pack temperature protection
	High energy consumption load in peripheral circuit
	Long term shallow charging and discharging of battery, with memory effect
Charging voltage is too high	Battery cell overcharged
	Low battery or charging ambient temperature
	At the end of battery life, the internal resistance increases
	Charging at the original rate after capacity attenuation
	The charge of the battery pack is already very high
	Charger fault, high charging current

a higher temperature and thermal stability than other types of lithium-ion batteries. The excessive intercalation and deintercalation of lithium ions in the positive electrode, that is, overcharge will damage the lattice of the positive electrode material to accommodate the lithium ions, thereby reducing the capacity of the lithium-ion battery.

The anode material of lithium-ion battery is mainly graphite. In the pre-charging stage of the lithium-ion battery, the graphite of the negative electrode of the battery can react with the electrolyte to form a solid electrolyte interface (SEI) film on the surface. The SEI film can prevent the battery performance due to the continuous decomposition of the electrolyte in the battery. Decreases, but the formation of the SEI film consumes lithium-ions. During the charging process of a lithium-ion battery, the negative electrode of the battery will continuously insert lithium ions. If the speed of lithium-ion insertion into the negative electrode material is lower than the speed at which the negative electrode receives lithium-ions, this part of the lithium metal will be permanently withdrawn from the lithium cycle inside the battery, and decrease lithium-ion battery capacity.

The speed at which lithium ions are inserted into the negative electrode material is lower than the speed at which the negative electrode receives lithium-ions, which often occurs in the low-temperature charging and overcurrent charging conditions of lithium-ion batteries. It is necessary to strictly control the charging rate of lithium-ion batteries and reduce the charging current. Table 1 shows the phenomena and causes of power battery failure.

In summary, the factors related to the failure of the power battery pack can be summarized as battery overcharge, ambient temperature, and charge rate.

2.2.2 Analysis of DC charger failure mechanism and related factors

Under the strong power input of the power distribution system, the insulating material of the charging equipment may break down, which will lead to the loss of insulation of the charging equipment. The insulation fault of the charging equipment is a serious fault, which may endanger personal safety. Once the insulation fault of the charging pile occurs, the charging pile will be shut down immediately and wait for professional maintenance personnel to repair.

The same environment will have different effects on the working conditions of the charging equipment such as excessive ambient temperature may cause over-temperature failure of charging equipment under normal use, higher humidity can affect the electrical insulation of charging equipment, the smoke and dust environment will affect the heat dissipation function of the charging and discharging equipment, etc. During the working process of the charging equipment, it is inevitable that abnormality will occur. For example, the failure of the temperature sensor may cause the charging and discharging equipment to generate an over-temperature false alarm. If the output current threshold of the charging and discharging equipment is set too small, it may cause an output over-current alarm. The circuit breaker of the charging and discharging equipment, contactor and other devices will trigger the protection of charging and discharging equipment to stop working when there is a failure.

The protection measures of charging equipment include equipment detection function, which can monitor the real-time operation status of the pile during the charging and discharging process, and also need to have protection against problems such as over-temperature of the pile, abnormal input and output, and short circuit. Insufficient protection measures for charging and discharging equipment will lead to equipment failures of different severity. Table 2 shows the fault phenomena and causes of DC charger.

In summary, the fault factors related to charging equipment are summarized as electrical insulation of charging and discharging equipment, environmental factors Charging and discharging equipment itself factors and pile protection measures.

TABLE 2 Fault phenomenon and cause of DC charger.

Fault phenomenon	Cause of failure
Charging output overvoltage	Low control accuracy of charging module
	Damaged charging module
Charge output undervoltage	Overload
	Damaged charging module
Charge output overcurrent	Abnormal battery
	Damaged charging and discharging module
Insulation monitoring failure	The insulation of the charging output circuit to the ground is damaged
	Damaged insulation monitoring module
Charge input overvoltage	Power distribution system failure
Charge input undervoltage	Power distribution system failure
Charging module over temperature	Too much dirt inside the charger pile
	The charger runs at high power for a long time

3 Data mining model of electric vehicle charging failure

3.1 Page layout

In the field of electric vehicle charging, my country has initially formed a systematic standard and system. With reference to various national standards, industry standards, and related engineering and scientific research materials, we determine the temperature change rate of power battery packs, ambient temperature, battery charging overvoltage rate. The parameters of battery internal resistance, battery pack historical failure times, battery state of charge SOC, battery internal resistance change rate, charging voltage error rate and charging current error rate are used as characteristic parameters to characterize the correlation factors of charging equipment failures. Among them, the calculation formulas for battery charging overvoltage rate, charging voltage error rate and charging current error rate are expressed as follows:

3.1.1 Battery charging overvoltage rate

The normal power battery charging process has a specified charging voltage. Charging the power battery with a voltage exceeding the specified charging voltage will affect the battery. The charging overvoltage rate is calculated by the following formula.

$$\xi_{BU} = \frac{U_B - U_{B0}}{U_{B0}} \times 100\% \tag{1}$$

3.1.2 Charge voltage error rate

The charging output error rate reflects the electrical performance of the charging equipment. Normal charging equipment requires that the charging output voltage error should not exceed ± 5%, and it indicates that the charging equipment may be abnormal. The charging output error rate is calculated by the following formula.

$$\xi_{ZU} = \frac{|U_Z - U_{Z0}|}{U_{Z0}} \tag{2}$$

$U_Z > U_{Z0}$ indicates that the charging output of the charging device is over-voltage, and $U_Z < U_{Z0}$ indicates that the charging output of the charging device is under-voltage.

3.1.3 Charging current error rate

The charging output current error rate also reflects the electrical performance of the charging equipment. Normal charging equipment requires that the charging output current error should not exceed ± 5%, and it indicates that the charging equipment may be abnormal. The charge output current error rate is calculated by the following formula.

$$\xi_{ZI} = \frac{|I_Z - I_{Z0}|}{I_{Z0}} \tag{3}$$

$I_Z > I_{Z0}$ indicates that the charging output of the charging device is overcurrent, and $I_Z < I_{Z0}$ indicates that the charging output of the charging device is undercurrent.

Electric vehicle charging data is measured by sensor equipment, and various abnormalities will inevitably occur during the actual operation of the sensor. In view of this situation, this article deals with the data in consideration of the integrity and accuracy of the data.

First of all, from the perspective of data integrity, we should focus on checking for data lack of value. For missing data, calculate the mean of the two data points before and after the missing data point, and replace the missing data with the mean. Secondly, considering the accuracy of the data, selectively find out the wrong data points in the original data. This paper uses the calculation of the forward and backward third-order difference of the power battery SOC to determine whether the current data is wrong. The specific process is as follows:

Calculate the forward and backward third-order differences of all SOC data in turn:

$$SOC_{db1}(t) = SOC(t) - SOC(t-1) \tag{4}$$

$$SOC_{db2}(t) = SOC(t) - SOC(t-2) \tag{5}$$

$$SOC_{db3}(t) = SOC(t) - SOC(t-3) \tag{6}$$

$$SOC_{da1}(t) = SOC(t) - SOC(t+1) \tag{7}$$

$$SOC_{da2}(t) = SOC(t) - SOC(t+2) \tag{8}$$

$$SOC_{da3}(t) = SOC(t) - SOC(t+3) \tag{9}$$

The $SOC_{da1}(t)$, $SOC_{da2}(t)$, and $SOC_{da3}(t)$ respectively represent the backward one of the tth value in the battery SOC data sequence, second and third order difference.

For the data of the charging process, the following judgments are made:

$$\begin{cases} SOC_{db1}(t) \geq 0 \\ SOC_{da1}(t) \leq 0 \\ SOC_{db2}(t) \geq 0 \\ SOC_{da2}(t) \leq 0 \\ SOC_{db3}(t) \geq 0 \\ SOC_{da3}(t) \leq 0 \end{cases} \tag{10}$$

If the current SOC data meets this condition, it is judged to be normal data, otherwise it is wrong data. For the SOC data judged to be wrong, the average value method is used for all the data collected this time, that is, the average value of the preceding and following items replaces this data point.

3.2 Association rule model

Life Science Identifiers (LSIDs) for ZOOBANK registered names or nomenclatural acts should be listed in the manuscript before the keywords with the following format:

Association rule mining is based on a large amount of data. By analyzing which data items appear together frequently, a collection of data items with many frequent items appearing together can be obtained (Nalini, 2016). In a transaction set, the frequency of the data item set can be represented by the concept of support. Suppose there is an item set X in the transaction set T. Define the number of occurrences of the item set X in the transaction set T as $\sigma(X)$. Suppose the total number of transactions in transaction set T is N, then the support of item set X is defined as:

$$\sup(X) = \frac{\sigma(X)}{N} \tag{11}$$

With the definition of support, we can show how frequently the itemset X appears in the transaction set T. Here we introduce a definition of minimum support min sup. The criterion for item set X as a frequent item set is that its support is not less than min sup.

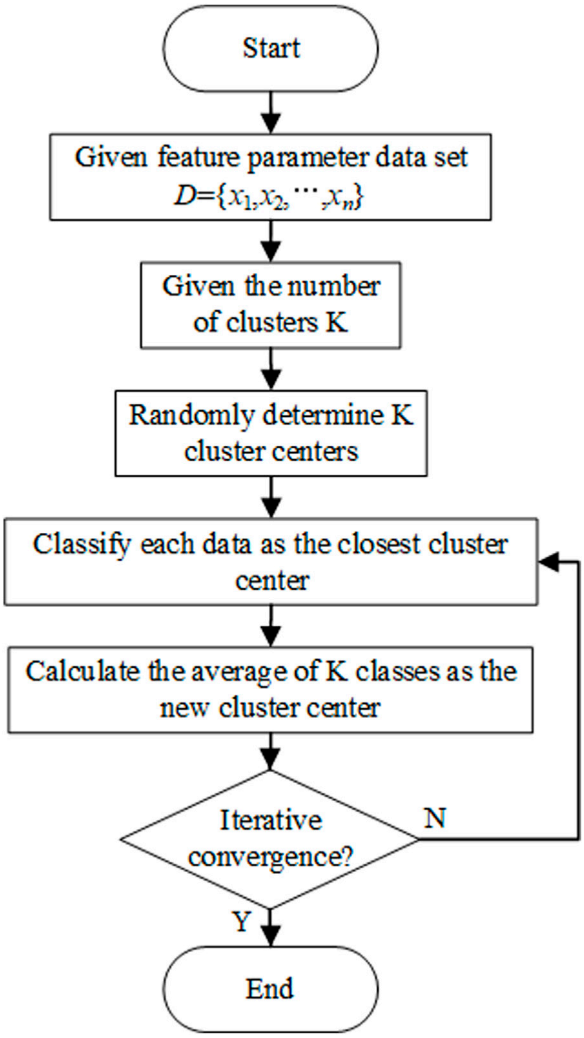

FIGURE 7
Process of discretizing feature data using K-means clustering algorithm.

Use expressions $A \rightarrow B$ to represent association rules. Support for association rules:

$$\sup(A \rightarrow B) = \frac{\sigma(A \cup B)}{N} \tag{12}$$

Both non-empty subsets $A \subset X$ and $B = X - A$ of frequent itemset X constitute association rule $A \rightarrow B$, and then the association rule of interest is determined based on the confidence of another index that measures the association rule.

$$\operatorname{con}(A \rightarrow B) = \frac{\sigma(A \cup B)}{\sigma(A)} \tag{13}$$

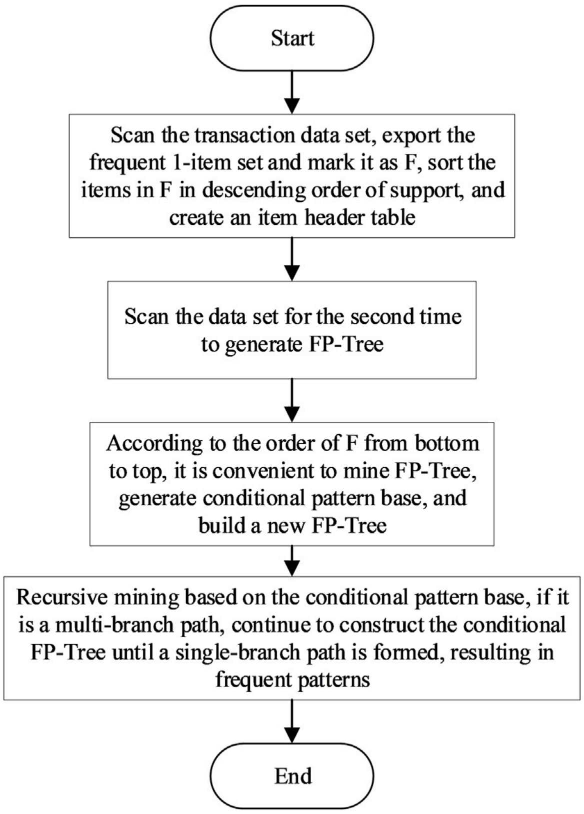

FIGURE 8
FP-Growth algorithm flow chart.

After setting a minimum degree of confidence, the association rules can be filtered through the minimum support and minimum confidence. When applying the association rule model to fault correlation analysis, you can choose the preceding item of the association rule as a symptom, and the latter item of the association rule as the failure phenomenon. Such an association rule can reflect the correlation between the symptom and the failure phenomenon, and the confidence level reflects. The credibility of fault association rules (Peng et al., 2019; Wang, 2020; Zhao and Su, 2021). In this paper, the association rule model is used in the analysis of the relevance of electric vehicle charging failures. The first item of the association rule is the characteristic parameter obtained after the K-means clustering algorithm is used to discretize the characteristic parameter data. It can be reflected by using the association rule mining algorithm. Fault association rules for the correlation between characteristic parameters and fault phenomena in the charging process of electric vehicles. The specific process of discretization is shown in Figure 7.

TABLE 3 Example table.

Transaction ID	Item set
1	A, B, C, D, E, F
2	D, E, F, G, H, C
3	I, H, J, D, F, K
4	I, H, A, B, D, F
5	I, H, A, C
6	A, H, K, D, E, F

TABLE 4 Transaction set in descending order of support.

Transaction ID	Item set
1	F, D, E, A, C
2	F, H, D, E, C
3	F, H, D, I
4	F, H, E, A, I
5	H, A, C, I
6	F, H, D, E, A

3.3 Optimized FP-growth algorithm model based on weight

3.3.1 FP-growth algorithm model

FP-Growth uses frequent itemset growth to conduct correlation mining. By recursively searching for frequent patterns on the FP tree, add a suffix to each frequently mined pattern to obtain all frequent patterns suffixed with a frequent item (Zeng et al., 2019). FP-Growth algorithm has better efficiency when mining a large amount of data, so it is suitable for complex charging fault data mining. The flow of the FP-Growth algorithm is shown in Figure 8.

Take the transaction set in Table 3 as an example to introduce the principle of the FP-Growth algorithm.

Set the minimum support to 3, the first step of the algorithm is to scan the transaction set to obtain frequent 1-itemsets, and arrange the itemsets according to the support to form the item header table $F = \{\{F{:}5\}, \{H{:}5\}, \{D{:}4\}, \{E{:}4\}, \{A{:}4\}, \{C{:}3\}, \{I{:}3\}\}$. Scan all transactions in the transaction set T, access each item in the order in F, and do not deal with infrequent items. The sorted transaction set is shown in Table 4.

The root node of FP-Tree is marked as Null, and each sorted transaction record is scanned in turn to form each branch of FP-Tree. The final FP-Tree is shown in Figure 9. It can be seen that FP-Tree contains all the information needed to mine frequent itemsets in the transaction set T.

The item header table has been arranged according to item support, so in each frequent pattern, the item with high support

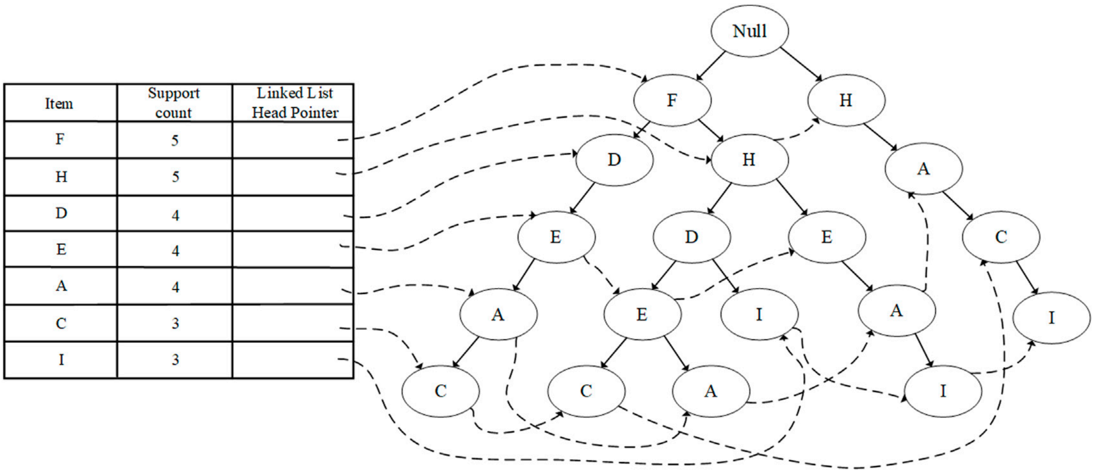

FIGURE 9
Complete FP-Tree.

TABLE 5 Conditional pattern library.

Transaction ID	Conditional mode	Conditional mode for removing infrequent items
1	F, H, D:1	H:1
2	F, H, E, A:1	H:1
3	H, A, C:1	H:1

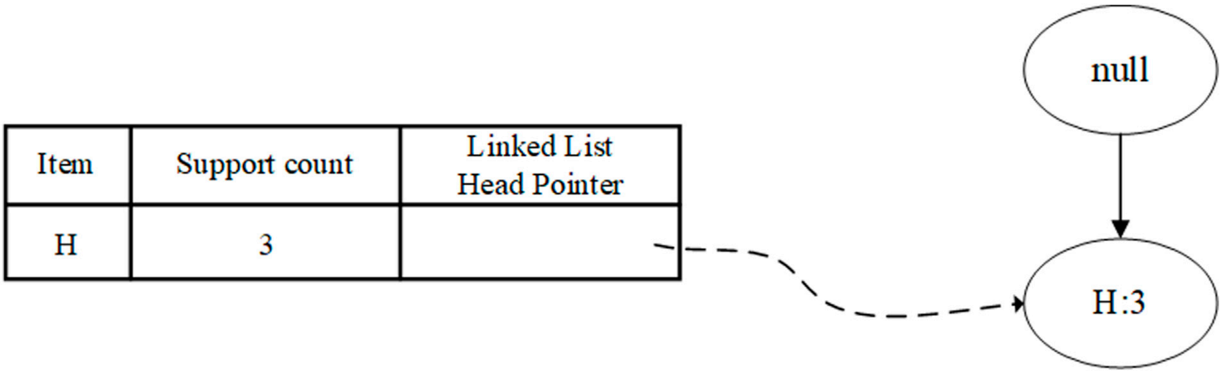

FIGURE 10
I's condition FP-Tree.

must be in front of the item with low support, so that the divide and conquer strategy can be used to mine all frequent items. First, mine the frequent patterns suffixed with I to obtain the conditional pattern library of I. After removing the infrequent items from the conditional pattern library, the database and its corresponding conditional FP-Tree are shown in Table 5; Figure 10.

FP-Tree is composed of a path. The combination mode of all nodes on the path is only {H:3}. After adding the conditional

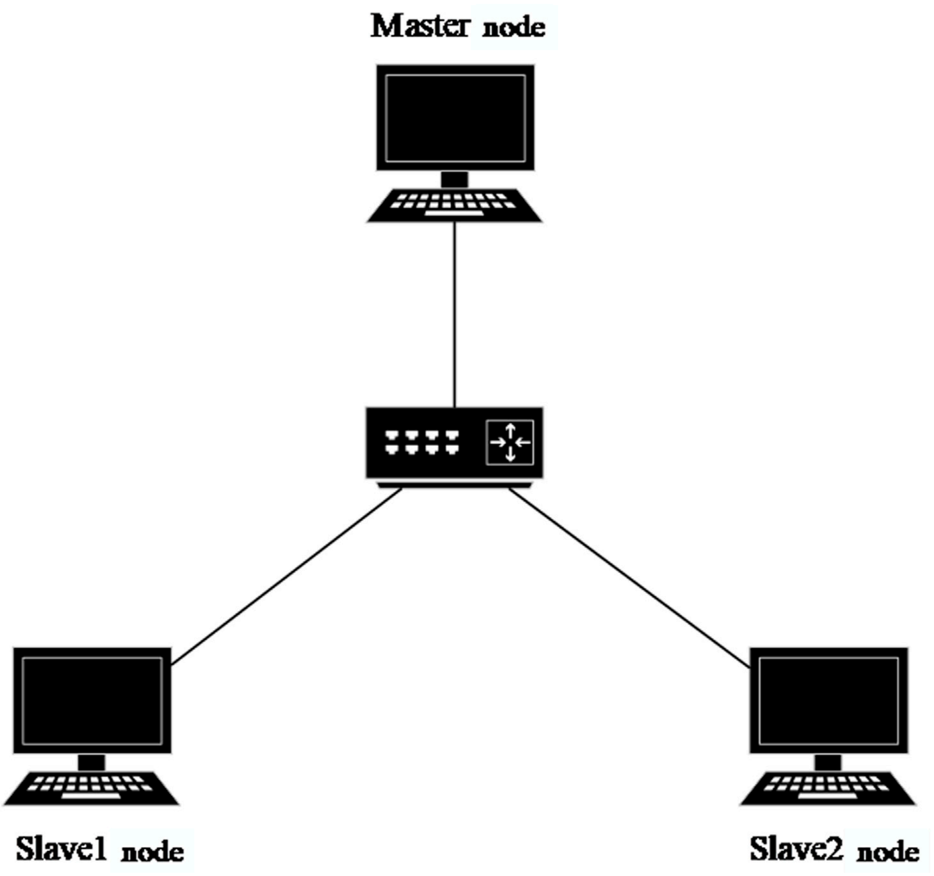

FIGURE 11
Cluster structure diagram.

TABLE 6 Power battery failure association rules.

Pre-rule	Rule post	Weighted support (%)	Weighted confidence (%)
The internal resistance change rate is greater than 0.2 mΩ/s	Battery pack is over temperature	2.7	94
The temperature change rate is greater than 0.2 ℃/s	Battery pack is over temperature	3.1	88
Battery charging overvoltage rate is greater than 12%	Battery pack is over temperature	1.7	74
The battery charging overvoltage rate is greater than 12%, and the ambient temperature is greater than 38.5°C	Battery pack is over temperature	1.5	81
The ambient temperature is less than −5°C	High charging voltage	1.2	62
The internal resistance of the battery is greater than 5 mΩ	High charging voltage	2.3	79
The internal resistance of the battery is greater than 5 mΩ	Reduced battery pack capacity	2.3	91
The ambient temperature is less than −5°C, and the number of historical failures of the battery pack is greater than 3	Reduced battery pack capacity	2.5	81

TABLE 7 Correlation level of power battery failure factors.

Failure related factors	Correlation level (%)
Temperature change rate in battery	86
Ambient temperature	67
Battery charging overvoltage rate	83
Battery internal resistance	81
Change rate of battery internal resistance	89
Battery state of charge SOC	73
The number of historical failures of the battery pack	84

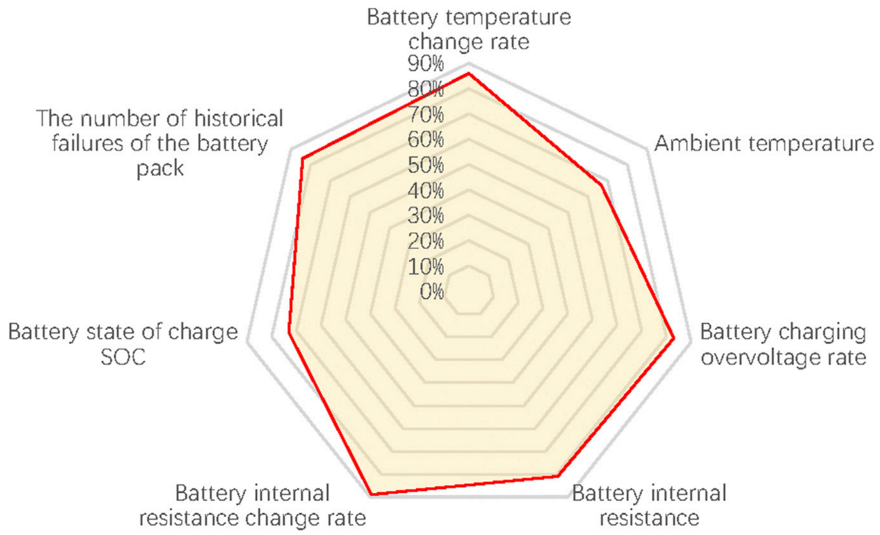

FIGURE 12
Correlation level of power battery failure factors.

suffix I and outputting, all frequent patterns {H, I:3} with I as the suffix can be obtained, which is the association rule H → I. Continue to mine frequent patterns with the remaining items as suffixes, and finally get all the association rules H → I, F, E → A, F → A, H → A, E → A, F, D → E, F, H → E, F → E, D → E, H → E, F, H → D, F → D, H → D, F → H.

3.3.2 Optimization of FP-growth algorithm based on weight

Electric vehicle charging faults are divided into levels. The national standard divides electric vehicle charging faults into three levels: personal safety level faults, equipment safety level faults, alarm prompt level faults (GB/T 27930, 2015), the higher the level of faults charging electric vehicles, the greater the impact of normal progress. In the actual working conditions of the equipment, the number of high-level faults is often very small, which will lead to the failure of the FP-Growth algorithm to mine fault association rules. If the minimum support is set too small, high-level faults may be missed. To solve this problem, this paper uses the idea of weighting to optimize the FP growth algorithm, comprehensively considering the weight of the characteristic data of fault correlation factors, which can increase the support of fault factors with large weight to a certain extent, avoid the omission of association rules, and reduce the support of fault factors with low weight. In this way, some useless feature data with high degree of occurrence may be deleted, so as to reduce the useless association rules mined by the algorithm.

Aiming at the shortcomings of the original FP-Growth algorithm, this paper uses the weighting idea to optimize the algorithm. With feature parameter data set $D = \{x_1, x_2, \cdots, x_n\}$, and all discretized feature parameter transaction item sets $I = \{i_1, i_2, \cdots, i_m\}$, the feature parameter types contained in each fault correlation factor feature data x_n belong to I, that is, each fault factor characteristic data x_n is a subset of I.

Define the discretized feature parameter type. All feature parameter types in the transaction item set I have a

TABLE 8 DC charger fault association rules.

Pre-rule	Rule post	Weighted support (%)	Weighted confidence (%)
The ambient temperature is greater than 38°C, and the continuous working time exceeds 300 min	Charger over temperature fault	1.9	79
The number of historical failures exceeds 4	Charger over temperature fault	1.5	66
The charging voltage error rate is greater than 4.3%	DC output overvoltage fault	1.7	83
BMS response rate is less than 94%	DC output overvoltage fault	1.2	76
The charging voltage error rate is less than −4.5%	DC output undervoltage fault	1.6	82
The number of historical failures exceeds 4	DC output undervoltage fault	1.5	62
Charging current error rate is greater than 4.1%	DC output overcurrent fault	1.5	77
BMS response rate is less than 94%	DC output overcurrent fault	1.4	83
The number of historical failures exceeds 4	The charging module is damaged	1.1	61
The ambient temperature is greater than 38°C, and the continuous working time exceeds 300 min	Charging module over temperature	2.1	74

TABLE 9 Correlation level of DC charger failure factors.

Failure related factors	Correlation level (%)
Charging current error rate	84
Charge voltage error rate	85
Ambient temperature	68
Charger and BMS response rate	91
Continuous working time of charger	74
The number of historical failures of the charger	66

corresponding weight, and the weight set corresponding to I is $W = \{\omega_1, \omega_2, \cdots, \omega_m\}$.

Each piece of feature data is composed of k-dimensional feature parameters, and the weight of each piece of feature data is defined as the average value of all parameter weights under that piece of data:

$$\omega(x_n) = \frac{1}{k} \sum_{I_m \in x_n} \omega_{I_m} \tag{14}$$

Define the weighted support degree of the characteristic parameter transaction item:

$$\mathrm{Wsup}(i_m) = \sup(i_m) \times \omega_{i_m} \tag{15}$$

Define the weighted support of feature parameter data x_n:

$$\mathrm{Wsup}(x_n) = \sup(x_n) \times \frac{1}{k} \sum_{I_m \in x_n} \omega_{I_m} \tag{16}$$

Define the weighted support of association rule $A \to B$, suppose A contains a feature parameter type, B contains b feature parameter types, and the weighted support of association rule $A \to B$ is:

$$\mathrm{Wsup}(A \to B) = \sup(A \cup B) \times \frac{1}{a+b} \sum_{I_m \in A \cup B} \omega_{I_m} \tag{17}$$

Define the weighted confidence of association rule $A \to B$ as:

$$\mathrm{Wcon}(A \to B) = \frac{\mathrm{Wsup}(A \cup B)}{\mathrm{Wsup}(A)} \tag{18}$$

After defining the weighted support and weighted confidence, replace all support and confidence calculations with weighted support and weighted confidence in FP growth algorithm, so as to increase the support of fault correlation factor characteristic data with large weight to a certain extent and avoid the omission of association rules due to too small minimum support setting. At the same time, it can reduce the support of feature data with low weight, which may delete some feature data with high degree of occurrence but useless, so as to reduce the useless association rules mined by the algorithm.

4 Example analysis

4.1 Examples

This paper uses the Hadoop distributed computing platform as the basic platform of this experiment to build an experimental environment for the correlation analysis of electric vehicle charging failures. Hadoop is a distributed system infrastructure, which is currently widely used in various academic research and industrial applications (Ragaventhiran and Kavithadevi, 2020). Its core components are the Hadoop Distributed File System (HDFS) and the MapReduce engine. Using the operating

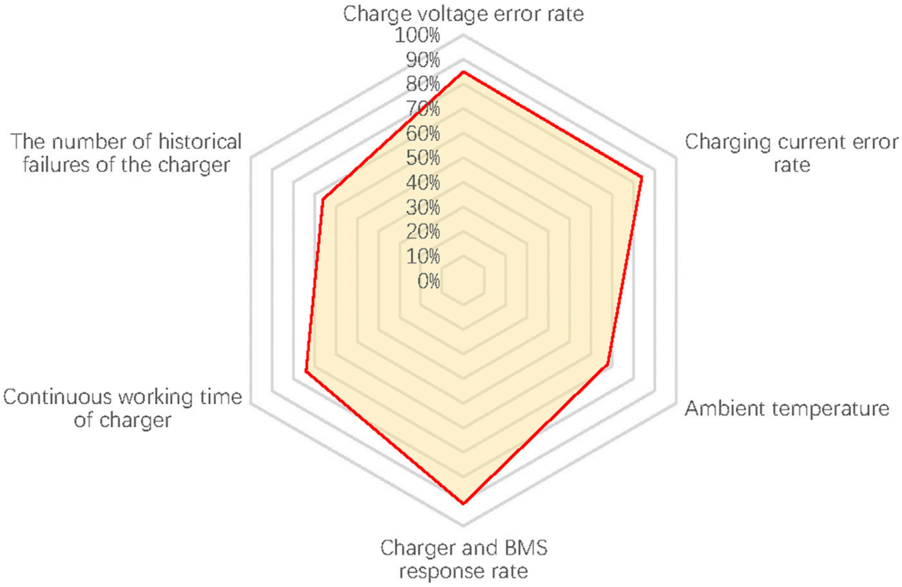

FIGURE 13
Correlation level of DC charger failure factors.

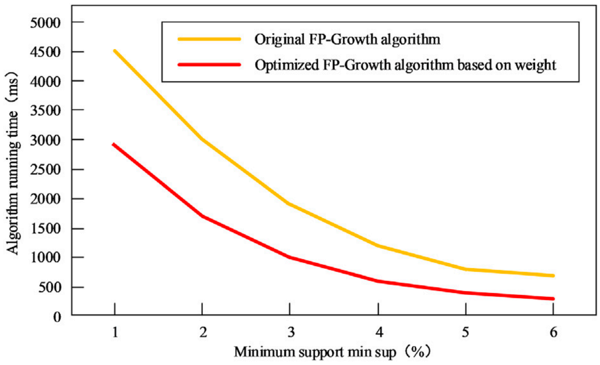

FIGURE 14
Variation of algorithm running time with minimum support.

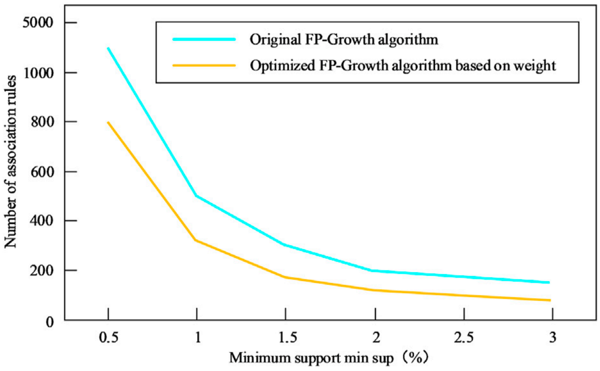

FIGURE 15
The number of association rules changes with the minimum support.

data provided by a company in Nanjing, Jiangsu Province when the charging of electric vehicles failed, the characteristic data was extracted and processed to obtain characteristic data that can reflect the factors related to the failure of the power battery and the charging equipment.

This experiment uses three computers to form a cluster to build a three-node distributed computing environment. One of the master nodes is used as the name node, the NameNode is responsible for cluster scheduling and data storage and calculation, and the two slave nodes are used as the data nodes, and the DataNode is responsible for data storage. And computing, the cluster structure is shown in Figure 11.

4.1.1 Fault association rules and correlation analysis

The weighted optimized FP growth algorithm is applied to mine association rules for the characteristic data of power battery fault correlation factors of electric vehicles. The minimum weighted support is set to min Wsup = 1% and the minimum weighted confidence is set to min Wcon = 60% to obtain power battery fault association rules. Some representative association rules are selected, as shown in Table 6, and the correlation analysis of power battery fault is carried out.

Table 6 shows some strong association rules based on power battery charging fault data mining. They describe the relationship between power battery fault related factors and fault forms. For example, the first association rule indicates that when the internal resistance conversion rate of the battery is greater than 0.2 mΩ/s, there is a 94% chance that the battery pack may cause over-temperature failure. The second association rule indicates that when the temperature change rate in the battery is greater than 0.2 ℃/s, there is an 88% chance that the battery pack may cause over-temperature failure, and so on.

These association rules are only a small part of the mining results. All the association rules obtained are counted, and the temperature change rate in the battery, the ambient temperature, the battery charging overvoltage rate, the battery charging overcurrent rate, and the battery internal resistance, battery internal resistance change rate, battery state of charge SOC, battery pack failure history related to the average level of confidence in association rules to evaluate the correlation level of factors and failures. The results are shown in Table 7, and the radar chart of the correlation level is shown in Figure 12.

The weighted optimized FP growth algorithm is applied to mine the association rules of the characteristic data of DC charger fault correlation factors, and the minimum weighted support is set to $\min Wsup = 1\%$ and the minimum weighted confidence is set to $\min Wcon = 60\%$ to obtain the DC charger fault association rules. In this section, some representative association rules are selected as shown in Table 8 below, and the DC charger fault correlation analysis is carried out.

Table 8 shows some strong association rules based on DC charger charging fault data mining, which describe the association relationship between DC charger fault correlation factors and fault forms. For example, the first association rule indicates that when the ambient temperature is greater than 38 ℃ and the continuous working time of the charging pile exceeds 300 min, 79% may lead to the over temperature fault of the charger. The second association rule indicates that when the number of historical faults exceeds 4, 66% may lead to over temperature fault of charger, and so on.

All the obtained association rules are counted, and the correlation level between factors and faults is evaluated by calculating the average confidence level of association rules related to DC charger fault related factors, such as charging voltage error rate, charging current error rate, ambient temperature, charger and BMS response rate, charger continuous working time and charger historical fault times. The results are shown in Table 9, and the correlation level values are drawn into the radar diagram, as shown in Figure 13.

In order to verify the optimization effect of the proposed weighted FP-Growth algorithm, this paper conducts experiments on both the optimized FP-Growth algorithm and the original FP-Growth algorithm.

Figure 14 shows the changes in the running time of the original FP-Growth algorithm and the optimized FP-Growth algorithm under different minimum support degrees. It can be seen that when the minimum support setting is small, the running time of the algorithm is relatively long due to the large number of transactions that need to be calculated. With the increase of the minimum support degree, the running time of the two algorithms is decreasing. However, when the minimum support is the same, the weighted optimized FP-Growth algorithm has a significant computational time advantage compared to the original FP-Growth algorithm, which shows that the weighted optimized FP-Growth algorithm improves the efficiency of association rule mining.

Figure 15 shows the changes in the number of association rules mined by the original FP-Growth algorithm and the optimized FP-Growth algorithm under different minimum support degrees. It can be seen that when the minimum support setting is small, the number of association rules mined by the algorithm is relatively large, and there may be more invalid rules and duplicate rules among them. As the minimum support increases, the number of association rules mined by the two algorithms is decreasing. However, when the minimum support is the same, the number of association rules mined by the weighted optimized FP-Growth algorithm is significantly smaller than that of the original FP-Growth algorithm, which shows that the weighted optimized FP-Growth algorithm has achieved the expected reduction. The support of feature data with lower weight can reduce the useless association rules mined by the algorithm and avoid the omission of association rules due to the too small minimum support setting.

5 Conclusion

Aiming at the problems that the failure forms of power battery and charging and discharging equipment involved in the charging process of electric vehicles are diverse, and the failure mechanism load is difficult to analyze and diagnose, this paper analyzes and summarizes the common failure forms and failure mechanisms of power battery and charging equipment based on the working principle and failure mechanism of power battery and charging equipment, The correlation factors that may affect the failure of EV charging are analyzed at the two levels of EV power battery and charging equipment, and the characteristic parameters that can reflect the failure correlation of EV power battery and charging equipment are extracted. Discretize the characteristic parameter data of the K-means clustering algorithm, and then use the weight-based optimized FP-growth algorithm to mine the association rules of the discretized data, and obtain the fault association rules for the charging process of electric vehicles. The association rule analysis obtains the correlation level of the correlation factor to the failure, which provides certain technical support for realizing the intelligent diagnosis of the charging process of electric vehicles.

Data availability statement

The original contributions presented in the study are included in the article/Supplementary Material, further inquiries can be directed to the corresponding author.

Author contributions

Conceptualization, BZ; methodology, BZ; software, XH; validation, LC and TX; formal analysis, BZ; resources, BZ; data curation, XH; writing—original draft preparation, BZ and MH; writing—review and editing, BZ; supervision, LC and TX.; project administration, BZ; funding acquisition, BZ, MH, and XH. All authors have read and agreed to the published version of the manuscript. All authors have read and agreed to the published version of the manuscript.

Funding

This research was funded by the State Grid Chongqing Electric Power Company Technology Project, grant number 5220002000C1.

Conflict of interest

BZ, XH, MH, LC, and TX were employed by State Grid Chongqing Electric Power Company Marketing Service Center Metrology Center.

The authors declare that this study received funding from the State Grid Chongqing Electric Power Company Technology Project. The funder had the following involvement in the study: collection, analysis, the study design.

Publisher's note

References

Chang, B., Li, Y. E., and Ma, Z. Y. (2020). Study on the heat generation characteristics of ternary lithium-ion power battery. *Power Technol.* 44 (12), 1729–1731+1739. doi:10.3969/j.issn.1002-087X.2020.12.005

GB/T 27930 (2015). *The communication protocol between the electric vehicle off-board conductive charger and the battery management system.*

Guo, H. (2020). Research on fast charging method of lithium battery of electric vehicle. *Intern. Combust. Engine Accessories* 13, 212–213. doi:10.3969/j.issn.1674-957X.2020.13.098

Hämäläinen., W. (2016). New upper bounds for tight and fast approximation of Fisher's exact test in dependency rule mining. *Comput. Statistics Data Analysis* 93, 469–482. doi:10.1016/j.csda.2015.08.002

Hu, J., Yi, L. Q., and Li, Z. (2017). Fault diagnosis method of power transmission and transformation equipment based on big data mining technology. *High. Volt. Technol.* 43 (11), 3690–3697. doi:10.13336/j.1003-6520.hve.20171031026

IEC 62196-1-2014 (2014). *Plugs, electrical sockets, vehicle connectors and vehicle lead-in wires. Conductive charging of electric vehicles*. China: Part 1 General requirements.

Li, C. J. (2015). *Research on intelligent evaluation method of lithium-ion battery health*. Nanjing: Nanjing University of Aeronautics and Astronautics. MS thesis.

Ma, Y. Y. (2020). *Li-ion battery system fault diagnosis and software development*. Beijing: Beijing Jiaotong University. MS thesis.

Meng, J. Z. (2018). *State detection and fault diagnosis technology of intelligent charging device for electric vehicle*. Heifei: Hefei University of Technology. MS thesis.

Nalini, C. (2016). Correlation associative rule induction algorithm using ACO. *Circuits Syst.* 7 (10), 2857–2864. doi:10.4236/cs.2016.710244

NB/T 33001-2010 (2010). *Technical requirements for off-board conductive chargers for electric vehicles.*

Peng, G., Tang, S. P., and Zeng, L. (2019). Research on association rules of power grid faults based on data mining. *Comput. Digital Eng.* 47 (9), 2369–2374.

Qiu, Y. (2020). *Research on the correlation of EMU fault warning based on data mining*. Beijing: Beijing Jiaotong University. MS thesis.

Ragaventhiran, J., and Kavithadevi, M. K. (2020). Map-optimize-reduce CAN tree assisted FP-growth algorithm for clusters based FP mining on Hadoop. *Future Gener. Comput. Syst.* 103, 111–122. doi:10.1016/j.future.2019.09.041

Rayward-Smith, V. J. (2007). Statistics to measure correlation for data mining applications. *Comput. statistics data analysis* 51 (8), 3968–3982. doi:10.1016/j.csda.2006.05.025

Ru, Y., Yin, Z., and Zhang, K. (2017). Quantitative assessment of electric safety protection for electric vehicle charging equipment. *J. Electr. Eng.* 12 (10), 25–30.

Tan, M. X. (2020). *Study on electrochemical and thermal characteristics of lithium iron phosphate battery during charge and discharge*. Guangzhou: South China University of Technology. MS thesis.

Tang, Y., and Cao, Z. P. (2020). Explore new energy vehicles and motor drive control technology. *Electron. World* 10 (20), 200–201.

Wang, W. J. (2020). Research on fault diagnosis technology of monitoring equipment based on FP-growth algorithm. *Electron. Test.* 22 (2).

Wu, C. (2019). *Research on typical failure mechanism and diagnosis method of lithium iron phosphate power battery*. Harbin: Harbin Institute of Technology. PhD thesis.

Wu, Y. W. (2020). *Fault monitoring and diagnosis of power battery of electric vehicle*. Zhejiang Institute of Technology. MS thesis.

Yu, C. (2020). *Research on comprehensive evaluation method of health state of electric vehicle charging pile*. Harbin: Harbin University of Science and Technology. MS thesis.

Zeng, W., Li, Q., and Zhang, Y. F. (2019). UAV flight fault diagnosis based on improved FP-Growth algorithm. *Technol. Innovation Appl.* 13, 16–19.

Zhang, X. C., Tang, Y., Liu, Q., Liu, G. F., Ning, X., and Chen, J. K. (2021). a fault analysis method based on association rule mining for distribution terminal unit. *Appl. Sci.* 11 (11), 5221–3982. doi:10.3390/app11115221

Zhang, Y. L., Yu, W., Zhu, Q. Q., Ma, X., and Ogura, H. (2020). ECLAT algorithm for frequent item set generation with association rule mining algorithm. *Int. J. Sci. Res. Comput. Sci. Eng. Inf. Technol.* 11 (21), 306–309. doi:10.32628/cseit206247

Zhao, G. C., and Su, J. Y. (2021). Research on association rules of aircraft system faults based on data mining. *J. Civ. Aviat. Flight Univ. China* 32 (2), 10–14.

Zhao, X. H., and Jiang, Y. X. (2020). PNN and BP neural network fault diagnosis research on electronic accelerator pedal detection. *Recent Pat. Eng.* 14 (2), 205–220. doi:10.2174/1872212113666190911124334

Zhu, D. Y., Deng, Y. S., and Deng, H. W. (2021). Current status and development trend of electric vehicle charging facilities. *Time Car* 7 (4), 22–23.

frontiers | Frontiers in Energy Research

TYPE Original Research
PUBLISHED 16 January 2023
DOI 10.3389/fenrg.2022.1046140

Techno-economic assessment of electrolytic hydrogen in China considering wind-solar-load characteristics

Gang Lu[1], Bo Yuan[1], Zhongfan Gu[2]*, Haitao Chen[1], Cong Wu[1] and Peng Xia[1]

[1]State Grid Energy and Power Planning Laboratory, State Grid Energy Research Institute Co., Ltd., Beijing, China, [2]School of Electrical Engineering, Southeast University, Nanjing, China

OPEN ACCESS

EDITED BY
Yingjun Wu,
Hohai University, China

REVIEWED BY
Kaiqi Sun,
Shandong University, China
Haiyang Lin,
Harvard University, United States

*CORRESPONDENCE
Zhongfan Gu,
gzf2206@163.com

SPECIALTY SECTION
This article was submitted to Smart Grids, a section of the journal Frontiers in Energy Research

RECEIVED 16 September 2022
ACCEPTED 31 October 2022
PUBLISHED 16 January 2023

CITATION
Lu G, Yuan B, Gu Z, Chen H, Wu C and Xia P (2023), Techno-economic assessment of electrolytic hydrogen in China considering wind-solar-load characteristics.
Front. Energy Res. 10:1046140.
doi: 10.3389/fenrg.2022.1046140

Hydrogen production by electrolysis is considered an essential means of consuming renewable energy in the future. However, the current assessment of the potential of renewable energy electrolysis for hydrogen production is relatively simple, and the perspective is not comprehensive. Here, we established a Combined Wind and Solar Electrolytic Hydrogen system, considering the influence of regional wind-solar-load characteristics and transmission costs to evaluate the hydrogen production potential of 31 provincial-level regions in China in 2050. The results show that in 2050, the levelized cost of hydrogen (LCOH) in China's provincial regions will still be higher than 10 ¥/kg, which is not cost-competitive compared to the current hydrogen production from fossil fuels. It is more cost-effective to deploy wind turbines than photovoltaic in areas with similar wind and solar resources or rich in wind resources. Wind-solar differences impact LCOH, equipment capacity configuration, and transmission cost composition, while load fluctuation significantly impacts LCOH and electricity storage configuration. In addition, the sensitivity analysis of 11 technical and economic parameters showed differences in the response performance of LCOH changes to different parameters, and the electrolyzer conversion efficiency had the most severe impact. The analysis of subsidy policy shows that for most regions (except Chongqing and Xizang), subsidizing the unit investment cost of wind turbines can minimize LCOH. Nevertheless, from the perspective of comprehensive subsidy effect, subsidy cost, and hydrogen energy development, it is more cost-effective to take subsidies for electrolysis equipment with the popularization of hydrogen.

Abbreviations: CWSEHs, Combined wind and solar electrolytic hydrogen system; LCOH, Levelized cost of hydrogen; CF, Capacity factor; WT, Wind turbine; PV, Photovoltaic; ES, Electricity storage; ELY, Electrolysis; OM, Operation and maintenance; P2H, Power to hydrogen.

KEYWORDS

electrolytic hydrogen, renewable energy, transmission cost, wind-solar-load characteristics, techno-economic assessment (TEA), sensitivity analysis A(t), subsidy policy analysis

1 Introduction

With the depletion of traditional fossil energy and the increasingly severe environmental problems it brings, countries worldwide are gradually falling into the dilemma of traditional fossil energy, and it is imminent to promote the reform of traditional energy structure (Pan et al., 2021a; Bertram et al., 2021; Wu et al., 2022). Countries have promulgated regulations and policies to promote the vigorous development of renewable energy sources such as wind and solar to achieve the goal of carbon neutrality (Holdmann et al., 2019; O'Malley et al., 2020; Yang et al., 2021). The International Energy Agency (IEA) states that renewable energy generation needs to grow at an annual rate of nearly 12% over the 2021–2030 period to put the world on track for net-zero emissions by 2050 (International Energy Agency, 2021). How to absorb a high proportion of renewable energy power generation will become a fundamental research problem (Yang et al., 2018; Wu Y et al., 2021).

As one of the essential means of consuming renewable energy, electrolytic hydrogen has received extensive attention worldwide in recent years (Wang et al., 2021; Wu Y J et al., 2021). Compared with electricity, the advantage of hydrogen energy is that it can be used as long-term energy storage to achieve cross-regional and cross-season energy mutual assistance (Pan et al., 2020; Zhang et al., 2021). Currently, the research on hydrogen production from renewable energy focuses on feasibility (Fereidooni et al., 2018; Lin et al., 2021; Lucas et al., 2022) and cost analysis (Glenk and Reichelstein, 2019; Guerra et al., 2019; Pan et al., 2021b), multi-subject cooperation (Wu et al., 2020; Ma et al., 2021), and the operation planning and marketization of systems such as electric-hydrogen hybrid energy storage and hydrogen-mixed natural gas (Xiao et al., 2017; Tao et al., 2020). However, at present, the evaluation of hydrogen production potential from renewable energy is mainly based on specific regions, and only independent evaluation of hydrogen production from wind power or photovoltaic hydrogen production is conducted. For example, Lucas et al. (2022) and Lin et al. (2021) analyzed the feasibility of hydrogen production from wind power. Fereidooni et al. (2018) analyzed the feasibility of solar hydrogen production and evaluated the potential of photovoltaic hydrogen production in Iran. Pan et al., 2021a) analyzes China's cost and low-carbon competitiveness of hydrogen production from grids and photovoltaics. (Guerra et al. (2019). and (Glenk and Reichelstein, 2019) focus on the economics and cost competitiveness of hydrogen production from renewable energy sources. In addition, the current research is relatively simple in considering the electrolytic hydrogen model, lacks comprehensive system modeling, and lacks the analysis of the wind-solar combination and regional load characteristics.

Because of the above shortcomings, this paper predicts and evaluates the levelized hydrogen production cost of 31 provincial-level regions in China in 2050 and establishes a Combined Wind and Solar Electrolytic Hydrogen system (CWSEHs). On this basis, we thoroughly evaluate the impact of the combination of wind and solar and the energy consumption characteristics of each provincial region on the CWSWHs and give a system sensitivity analysis and a variety of subsidy policy evaluations. In particular, based on the characteristics of future marketization and the consideration of promoting the development of hydrogen production from renewable energy, wind and solar power generation is expected to use the existing power network to transmit and supply electricity to the hydrogen production system by paying a transmission fee, which can not only promote the process of marketization but also significantly reduce the investment cost of the line. Therefore, we have established a more refined model for the CWSEHs and fully consider the influence of factors such as transmission fee and inflation rate in the calculation of levelized cost of hydrogen (LCOH), hoping to provide a helpful reference and thinking for hydrogen production from renewable energy in 2050.

2 Materials and methods

2.1 Wind and solar capacity factor and electrical load data

To obtain the capacity factor (CF) of wind and solar power generation in each provincial region, we simulated through the renewables. ninja platform jointly developed by ETH Zurich and Imperial College of Technology (Pfenninger and Staffell, 2016), and obtained 8760 h of wind and solar power generation CF in each provincial region throughout the year, as the upper limit of wind turbine (WT) and photovoltaic (PV) power generation output. Specifically, for different provincial-level regions, we select five cities distributed in five directions to calculate the CF of wind energy and solar energy, respectively, and take the

TABLE 1 China's 31 provincial-level regions and their abbreviations.

Provincial area	Abbreviation	Provincial area	Abbreviation	Provincial area	Abbreviation
Beijing	BJ	Shaanxi	SA	Fujian	FJ
Tianjin	TJ	Ningxia	NX	Zhejiang	ZJ
Shanghai	SH	Gansu	GS	Jiangxi	JX
Chongqing	CQ	Qinghai	QH	Anhui	AH
Liaoning	LN	Xinjiang	XJ	Jiangsu	JS
Jilin	JL	Sichuan	SC	Hubei	HB
Heilongjiang	HL	Yunnan	YN	Henan	HY
Inner Mongolia	IM	Guangxi	GX	Hainan	HI
Shanxi	SX	Guizhou	GZ	Xizang	XZ
Hebei	HZ	Hunan	HN		
Shandong	SD	Guangdong	GD		

average value as the CF of wind energy and solar power generation in the provincial-level region. Similarly, the national average wind and solar CFs were averaged across 31 provincial-level regions. Due to data limitations, hourly provincial electric loads were obtained from provincial power grid companies or fitted based on typical provincial daily and annual load curves (National Energy Administration, 2020).

In addition, in order to make the article easy to understand and without losing rigor, we use abbreviated form for the names of 31 provincial-level regions in China. The specific correspondence is shown in Table 1 below.

2.2 Optimization model of CWSEHs

2.2.1 Objective function

In this paper, we define LCOH as the hydrogen production cost obtained after the cost of wind and solar power generation equipment, electrolysis-related equipment investment, operation and maintenance, and transmission fee and hydrogen production amount are levelized. A series of factors such as investment, operation, and maintenance costs, transmission fees, equipment life, wind and solar power generation CF, electrolyzer conversion efficiency, discount rate, inflation rate, and electrical load in the system will affect LCOH. Among the above parameters, the parameters with regional differences are the CF of wind and solar power generation and the regional electricity load. The following optimization model can be established based on this, with the objective function of minimizing LCOH.

$$\text{Min LCOH} = \frac{C_{\text{inv}} + \sum_{n=1}^{N} \frac{(C_{\text{om}}+C_{\text{tp}})(1+i)^n}{(1+r)^n}}{\sum_{n=1}^{N} \frac{\eta^{\text{ELY}} \sum_{t=1}^{T} P_t^{\text{ELY}} (1+i)^n}{LHV\,(1+r)^n}} \tag{1}$$

$$C_{\text{inv}} = \frac{\lambda}{1+\lambda}\left(c_{\text{inv}}^{\text{PV}} C^{\text{PV}} + c_{\text{inv}}^{\text{WT}} C^{\text{WT}} + c_{\text{inv}}^{\text{ES}} C^{\text{ES}}\right) + c_{\text{inv}}^{\text{ELY}} C^{\text{ELY}} \tag{2}$$

$$C_{\text{om}} = \frac{\lambda}{1+\lambda}\left(c_{\text{om}}^{\text{PV}} C^{\text{PV}} + c_{\text{om}}^{\text{WT}} C^{\text{WT}} + c_{\text{om}}^{\text{ES}} C^{\text{ES}}\right) + c_{\text{om}}^{\text{ELY}} C^{\text{ELY}} \tag{3}$$

$$C_{\text{tp}} = \frac{\lambda}{1+\lambda}\left(\sigma^{\text{PV}} \sum_{t=1}^{T} P_t^{\text{PV}} + \sigma^{\text{WT}} \sum_{t=1}^{T} P_t^{\text{WT}}\right) \tag{4}$$

As shown in Eq. 1, the established optimization model aims to minimize the LCOH of the system, where C_{inv} is the annual investment cost of PV, WT, electricity storage (ES), and electrolysis (ELY) equipment. C_{om} is the annual operation and maintenance cost of the system. C_{tp} is the transmission fee paid for transmitting photovoltaic and wind turbine power generation through the grid. N is the system's life, i is the inflation rate, r is the discount rate, η^{ELY} is the conversion efficiency of ELY, *PELY t* is the electric power consumed by electrolysis at time t, and *LHV* is the low calorific value of hydrogen.

C_{inv}, C_{om} and C_{tp} are given by Eqs 2–4, where λ is the hydrogen to electricity ratio and represents the power consumed by hydrogen production to the power consumed by the electrical load. C^{PV}, C^{WT}, C^{ES} and C^{ELY} are PV, WT, ES, and ELY's optimal configuration capacities. cPV inv, cWT inv, cES inv and cELY inv are the unit investment costs of PV, WT, ES, and ELY, respectively. cPV om, cWT om, cES om and cELY om are the unit annual fixed operation and maintenance costs of PV, WT, ES, and ELY, respectively. σ^{PV} and σ^{WT} are the unit power transmission fees paid by PV and WT, respectively, and *PPV t* and *PWT t* are the actual power generated by PV and WT at time t.

2.2.2 Constraints

The optimization model also needs to satisfy the investment and equipment operation constraints of Eqs 5–17:

2.2.2.1 Electric power balance constraint

$$P_t^{\mathrm{PV}} + P_t^{\mathrm{WT}} - P_t^{\mathrm{ES+}} + P_t^{\mathrm{ES-}} = P_t^{\mathrm{LOAD}} + P_t^{\mathrm{ELY}}, \forall t \in \Phi^T \tag{5}$$

Equation 5 ensures the hour-level electric power balance of the CWSEHs, where $PES+\ t$ and $PES-\ t$ respectively represent ES's charge and discharge power at time t, and $PLOAD\ t$ represents the regional electrical load at time t. $PELY\ t$ represents the electrical power consumed by ELY at time t, Φ^T is the time series set, $\Phi^T = \{1,2,3,...,8760\}$.

2.2.3 Hydrogen production power constraint

$$\sum_{t=1}^{T} P_t^{\mathrm{ELY}} = \lambda \sum_{t=1}^{T} P_t^{\mathrm{LOAD}}, \forall t \in \Phi^T \tag{6}$$

Equation 6 ensures that ELY's electricity consumed is λ times the electric load daily. According to Hydrogen Council (2017) and Institute of Climate Change and Sustainable Development, Tsinghua University (2021), it is estimated that hydrogen energy and electric energy will account for 18% and 55% of the final energy demand in 2050, respectively. Based on this, we calculated the value of λ.

2.2.4 Equipment investment capacity constraints

$$0 \le C^{\mathrm{PV}} \tag{7}$$

$$0 \le C^{\mathrm{WT}} \tag{8}$$

$$0 \le C^{\mathrm{ES}} \tag{9}$$

$$0 \le C^{\mathrm{ELY}} \tag{10}$$

Equations 7–10 ensure that the investment capacity of PV, WT, ES and ELY equipment is non-negative.

2.2.5 PV and WT operating constraints

$$0 \le P_t^{\mathrm{PV}} \le p_t^{\mathrm{PV}} C^{\mathrm{PV}}, \forall t \in \Phi^T \tag{11}$$

$$0 \le P_t^{\mathrm{WT}} \le p_t^{\mathrm{WT}} C^{\mathrm{WT}}, \forall t \in \Phi^T \tag{12}$$

Equations 11 and 12 and ensure that the output electric power of PV and WT is non-negative and not greater than the upper limit of output power, where $pPV\ t$ and $pWT\ t$ are the upper limits of output electric power of unit capacity PV and unit WT at time t, respectively.

2.2.6 ES operating constraints

$$0 \le P_t^{\mathrm{ES+}} \le C^{\mathrm{ES}}, \forall t \in \Phi^T \tag{13}$$

$$0 \le P_t^{\mathrm{ES-}} \le C^{\mathrm{ES}}, \forall t \in \Phi^T \tag{14}$$

$$0 \le S_t^{\mathrm{ES}} \le C^{\mathrm{ES}}, \forall t \in \Phi^T \tag{15}$$

$$S_0^{\mathrm{ES}} = S_T^{\mathrm{ES}} = \frac{C^{\mathrm{ES}}}{2}, S_t^{\mathrm{ES}} = S_{t-1}^{\mathrm{ES}} + \eta^{\mathrm{ES+}} P_t^{\mathrm{ES+}} - \frac{P_t^{\mathrm{ES-}}}{\eta^{\mathrm{ES-}}}, \forall t \in \Phi^T \tag{16}$$

Equations 13 and 14 respectively ensure that the ES charge and discharge power is non-negative and not greater than the ES configuration capacity. Eq. 15 ensures that the actual storage capacity of the ES is not greater than the upper limit of the storage capacity, where $SES\ t$ is the actual storage capacity of the ES at time t. Eq. 16 simulates ES's charging and discharging process and ensures the same storage capacity at the beginning and end of ES, where $\eta^{\mathrm{ES+}}$ and $\eta^{\mathrm{ES-}}$ are ES's charging and discharging efficiencies, respectively.

2.2.7 ELY operating constraint

$$0.1\varepsilon_t^{\mathrm{ELY}} C^{\mathrm{ELY}} \le P_t^{\mathrm{ELY}} \le \varepsilon_t^{\mathrm{ELY}} C^{\mathrm{ELY}}, \forall t \in \Phi^T \tag{17}$$

Equation 17 is the ELY operating constraint, which limits the minimum operating power of ELY, where $\varepsilon ELY\ t$ is the operating state of ELY at time t, its value 1 means ELY is working, and 0 means ELY is not working.

2.3 Model parameters

In this model, the relevant techno-economic parameters of CWSEHs are unified in 2050, and the specific data are given in Table 2 below. Among them, the annual operation and maintenance (OM) cost of PV, WT, and ES are 0.01 of the unit investment cost of each piece of equipment, and the annual OM cost of ELY is 0.04 of the unit investment cost of it.

3 Results

3.1 System structure

Figure 1 shows the schematic diagram of the CWSEHs structure. On the energy supply side, renewable energy power generation, such as wind and solar energy, and electric energy storage modules are considered dispatchable electric power to compensate for the imbalance between supply and demand. The network side considers wind and solar power generation through the existing power network for transmission and pays a certain transmission fee. On the load side, we consider that electric energy can be used to simultaneously meet the electrical load and the operation of power to hydrogen (P2H) equipment. The produced hydrogen energy can be

TABLE 2 Predicted values of system-related technical and economic parameters in 2050.

Parameters	Symbols	Values
Unit Investment Cost of PV (¥/kW)	c_{inv}^{PV}	1900 State Grid Energy Research Institution. (2019)
Unit Operation and Maintenance Cost of PV (¥/kW)	c_{om}^{PV}	19
Unit Investment Cost of WT (¥/kW)	c_{inv}^{WT}	4000 State Grid Energy Research Institution. (2019)
Unit Operation and Maintenance Cost of WT (¥/kW)	c_{om}^{WT}	40
Unit Investment Cost of ES (¥/kW)	c_{inv}^{ES}	1000 State Grid Energy Research Institution. (2019)
Unit Operation and Maintenance Cost of ES (¥/kW)	c_{om}^{ES}	10
Unit Investment Cost of ELY (¥/kW)	c_{inv}^{ELY}	1273.4 Pan et al. (2021b)
Unit Operation and Maintenance Cost of ELY (¥/kW)	c_{om}^{ELY}	50.93
System Lifetime (years)	N	20 Pan et al. (2021a)
Low Heating Value of Hydrogen (kWh/kg)	LHV	33.3
Hydrogen to Electricity Ratio	λ	18/55 Hydrogen Council. (2017); Institute of Climate Change and Sustainable Development, Tsinghua University. (2021)
Conversion Efficiency of ELY	η^{ELY}	74% International Renewable Energy Agency. (2020)
Discount Rate	r	7% Gu et al. (2022)
Inflation Rate	i	1.9% Kempler et al. (2022)
Transmission Cost of PV (¥/kWh)	σ^{PV}	0.028 Qiu (2022)
Transmission Cost of WT (¥/kWh)	σ^{WT}	0.028 Qiu (2022)
Charge Efficiency of ES	η^{ES+}	95% Gu et al. (2022)
Discharge Efficiency of ES	η^{ES-}	95% Gu et al. (2022)

used as fuel in transportation, power generation, and heating and can also be used as raw materials for oil refining and steel production.

3.2 LCOH assessment of wind solar electrolytic hydrogen in China

Figure 2 shows the LCOH of wind-solar combined hydrogen production in 31 provincial-level regions in China. The darker the background color of each region, the higher the LCOH (See Supplementary Figure S1 in Supplementary Material for the composition of LCOH in each provincial region). Overall, there are significant regional differences in the LCOH of wind-solar combined hydrogen production in 31 provincial-level regions. It is estimated that in 2050, the highest provincial LCOH in China will be CQ and the lowest is Inner Mongolia, and the span between the two can reach 16 ¥/kg. The eight provinces with the highest LCOH are CQ, ZJ, HB, SC, XJ, GD, YN, and FJ, all of which are greater than 15 ¥/kg, and the main parts are located in the eastern coastal areas and central areas. While northern regions such as HL, LN, JL, and IM have lower LCOH, it can be found that the LCOH of different provincial regions has significant geographic differences, which are essentially related to the level of wind and solar resources and power generation in each region.

The above results show that the differences between LCOH and wind and solar resources are significantly correlated. In order to further study the impact of the two on LCOH, Figure 3 shows the relationship between LCOH and the proportion of PV and WT configuration capacity in each provincial region. The definition of PV and WT capacity ratio is shown in Eq. 18. It can be found that compared with WT, there is a higher correlation between the PV capacity ratio and LCOH. Moreover, regions with higher PV capacity ratios have higher LCOH. The results show that from the perspective of reducing LCOH to a certain extent, the configuration of WT is more cost-effective than the configuration of PV. Of course, this is also related to the wind and solar CF in each provincial area, and the configuration of WT in areas with low wind power CF will be of limited significance.

$$Capacity\ ratio\,(i) = \frac{C^{i}}{C^{PV} + C^{WT}}, i \in \{\mathrm{PV}, \mathrm{WT}\} \tag{18}$$

3.3 The influence of wind and solar characteristics on CWSEHs

In order to compare the impact of wind and solar characteristics on the system, we selected four representative provinces for typical analysis to ensure that they are under similar load fluctuations, as shown in the first four rows in Table 3.

Figure 4A shows that HB has the highest LCOH of 17.38 ¥/kg, SH has the lowest LCOH of only 8.48 ¥/kg, the difference is nearly 10 ¥/kg, and the LCOH of TJ and XZ are in the middle. Comparing the data in Table 3, we can see that HB has the lowest wind and solar CF, SH has the highest wind and wind CF, and TJ and XZ have higher wind and photovoltaic CF, respectively has a significant correlation with their LCOH. In addition, comparing TJ and XZ again shows that wind resources can reduce LCOH more than solar resources.

Figure 4B shows the configuration capacity of PV and WT in four regions. The configuration capacity of PV and WT has a positive relationship with the CF of PV and WT. The CF of TJ wind power is higher, so its WT configuration capacity is larger, XZ can configure

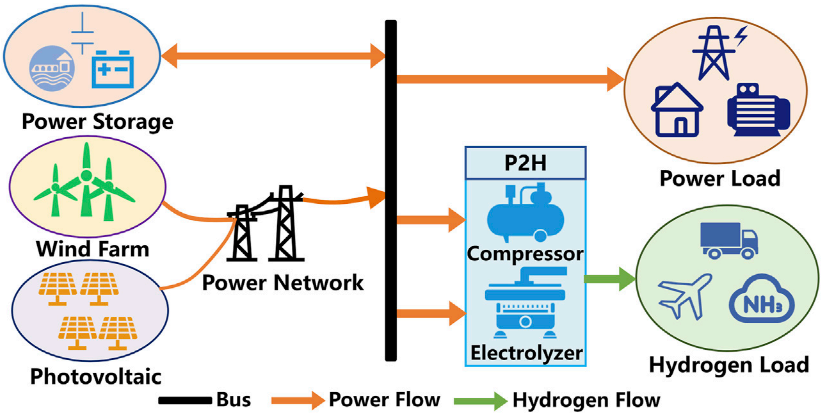

FIGURE 1
Structure diagram of CWSEHs.

more PV because of higher PV power generation CF. It is worth noting that the CF of wind and solar power generation of HB and SH are both higher or lower, and the system is more inclined to configure WT instead of PV at this time, which is consistent with the above analysis. The PV and WT transmission cost in Figure 4C is similar to the equipment configuration capacity in Figure 4B. Because the more WT or PV equipment capacity is equipped, the greater the power generation and the higher the transmission cost. Wind and solar differences significantly impact LCOH, WT, and PV capacity allocation and transmission costs. In areas with similar wind and solar resources, prioritizing WT equipment can further reduce LCOH, making it more competitive than PV equipment.

3.4 The influence of power load volatility on CWSEHs

When studying the influence of regional electrical load fluctuations on system parameters, in order to avoid the influence of dimensions, we have normalized the electrical loads in different regions and selected two regions with similar wind and solar resources and significant differences in electrical load fluctuations as shown in the last two rows in Table 3.

The left panel in Figure 5A shows that the LCOH of XJ is higher than that of SA, but in Figure 5B, it is shown that the ES configuration capacity of SA is significantly higher than that of XJ, even more than two times that of XJ, which is due to the electrical load fluctuation of SA is bigger than XJ. Specifically, when the electrical load is low, the PV and WT power generation can meet the electrical load and the P2H system, and only a small amount or no ES is needed for compensation. While at a high electrical load, most or all of the PV and WT power generation is absorbed by the electrical load, and the P2H system needs to be compensated by ES. In addition, regardless of the fluctuation of the electrical load, the WT configuration capacity is higher than the PV configuration capacity (Figure 5B), and WT also occupies an absolute advantage in the transmission fee (Figure 5A), which highlighted that the configuration of WT has significant advantages and universality compared to PV again.

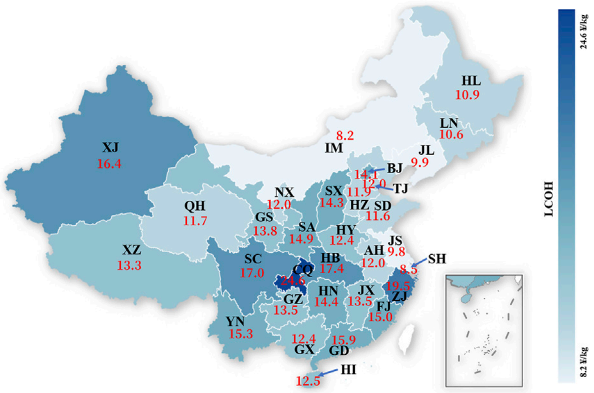

FIGURE 2
LCOH of wind-solar electrolytic hydrogen in 31 provincial-level regions in China.

3.5 LCOH sensitivity analysis

Figure 6 presents the LCOH sensitivity analysis of CWSEHs under different parameters. We calculated the LCOH at this time by making each parameter ±25% based on the benchmark scenario. It can be seen from Figure 6 that the average LCOH in China under the benchmark scenario is 9.82 ¥/kg, and the change in electrolyzer

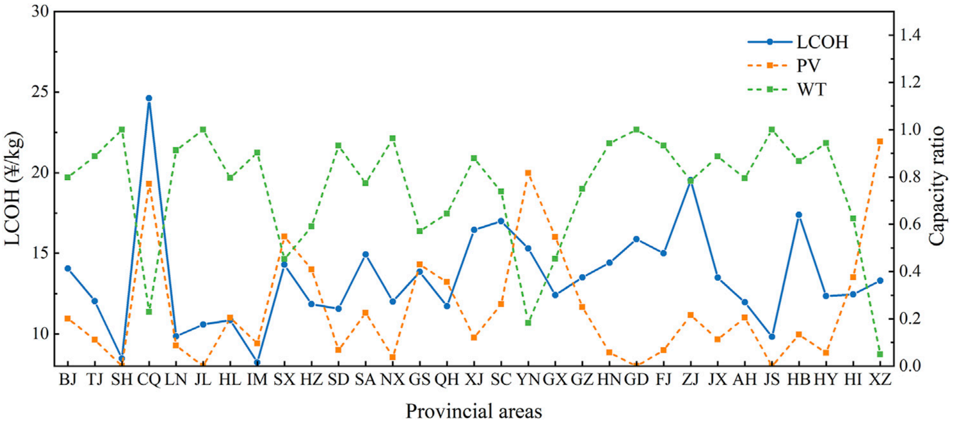

FIGURE 3
The relationship between LCOH and PV, WT configuration capacity ratio.

TABLE 3 Wind, solar and load characteristics of representative provinces.

Province	Wind capacity factor (%)	Solar capacity factor (%)	Load peak-valley difference
HB	17.72	11.07	0.6013
TJ	35.97	13.07	0.6565
XZ	28.86	18.10	0.7073
SH	45.70	14.18	0.7130
XJ	20.14	15.78	0.2468
SA	21.69	14.71	0.5648

conversion efficiency has the most significant impact on LCOH, and a ±25% fluctuation will cause LCOH to change from 7.86 ¥/kg to 13.10 ¥/kg. The impact of the unit investment cost of WT, system lifetime, and discount rate on LCOH is gradually reduced but still has a significant impact. Changes in other parameters have a limited impact on LCOH, especially the unit investment cost of PV, and the transmission costs of PV can hardly make LCOH change, which is also related to the low PV configuration capacity. It is worth noting that as λ increases, the LCOH will gradually decrease, which means that when the hydrogen demand (electric power consumed by hydrogen production) increases, the LCOH will further decrease, which is consistent with the scale effect of system development. In addition, system lifetime, electrolyzer conversion efficiency, inflation rate, and λ remain negatively correlated with LCOH changes, which is also consistent with common sense.

3.6 Subsidy policy analysis

Currently, the LCOH of hydrogen production using traditional fossil energy (such as coal and natural gas) is about 10 ¥/kg (National Alliance of Hydrogen and Fuel Cell, 2019), and according to our prediction in 2050, 27 of China's 31 provincial-level regions have LCOH higher than 10 ¥/kg. It means that even by 2050, the competitiveness of renewable energy electrolysis hydrogen production is still limited compared with traditional fossil energy hydrogen production. Therefore, we considered six different subsidy policies, adopting a 50% investment cost subsidy for PV, WT, ELY, ES, and a 50% cost subsidy for PV and WT transmission costs. The subsidy effect is shown in Figure 7. The results show that, except for the two regions of CQ and XZ, subsidizing WT can reduce LCOH to the greatest extent, so that the LCOH in most regions is reduced to less than 10 ¥/kg, while CQ and XZ have the best subsidy effect on PV, which is mainly closely related to the landscape resources in different regions. Generally, the effect of subsidizing ES and PV is better than the other three subsidy policies except for the WT subsidy, which can significantly reduce LCOH. The ELY subsidy and the PV and WT transmission cost subsidy have the worst effect on reducing LCOH, which can only reduce about 0.5 ¥/kg.

Further, Figure 8 (the upper part) shows the annual cost of the six subsidy policies. Overall, the annual cost of various

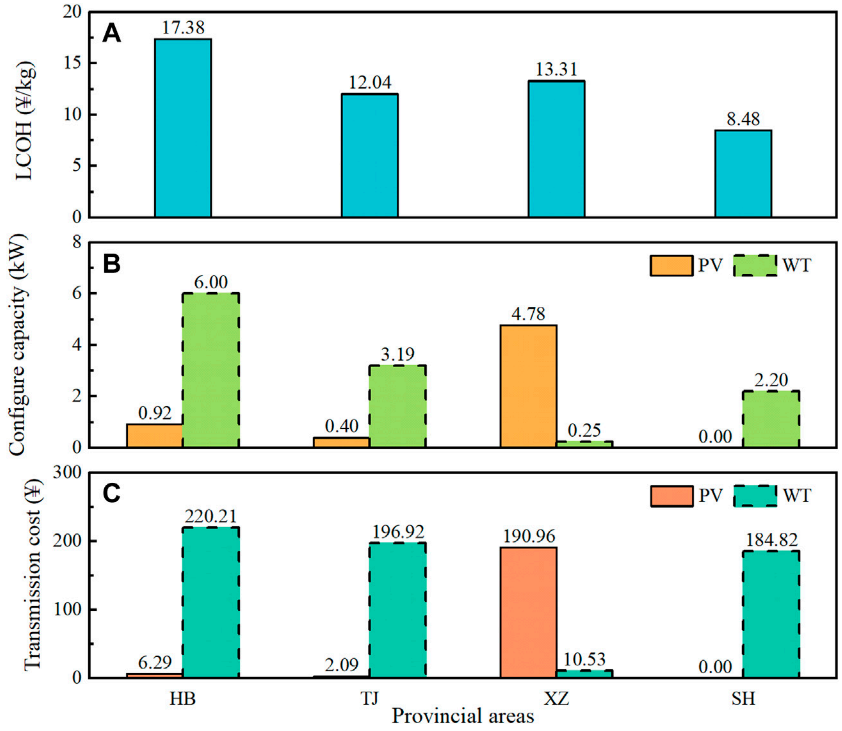

FIGURE 4
Comparison of **(A)** LCOH **(B)** PV and WT configuration capacity **(C)** PV and WT transmission costs in four representative regions.

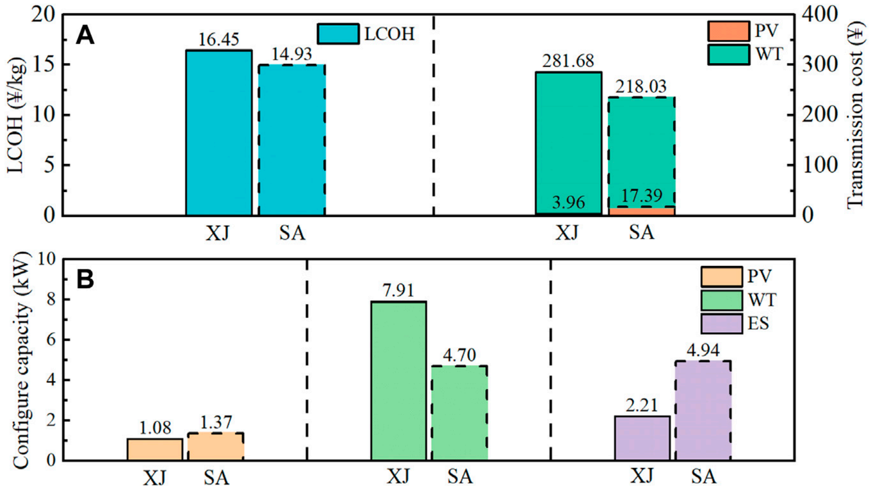

FIGURE 5
Comparison of **(A)** LCOH and PV and WT transmission costs **(B)** PV, WT and ES configuration capacity for two representative regions.

subsidy policies is proportional to the subsidy effect. The better the subsidy effect, the higher the annual subsidy cost. It is worth noting that CQ subsidizes PV with the best effect, but the annual cost of PV subsidy is less than that of WT subsidy, which is a very shocking situation because it shows that adopting PV subsidy in CQ can not only minimize LCOH, but also it can ensure that the annual subsidy cost is not the highest, which is a very cost-effective subsidy policy.

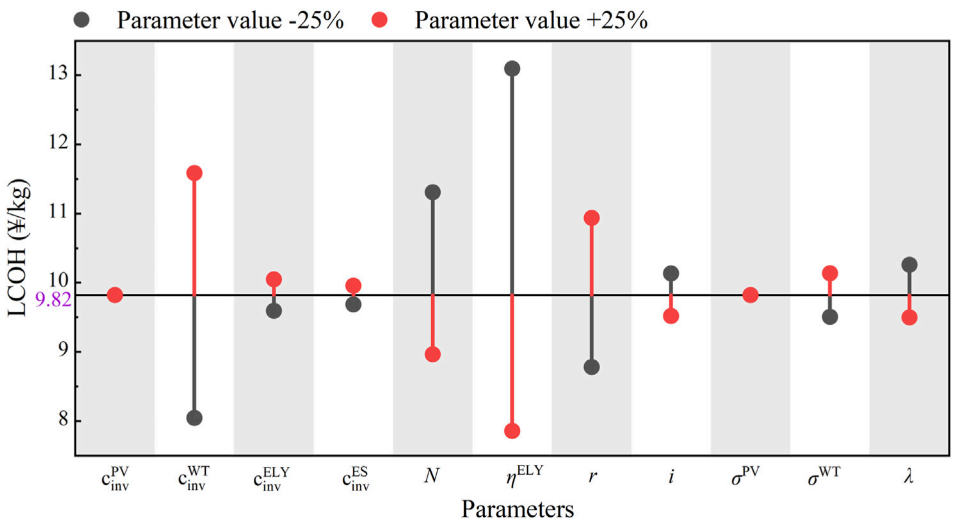

FIGURE 6
Sensitivity analysis of the LCOH under the different parameters.

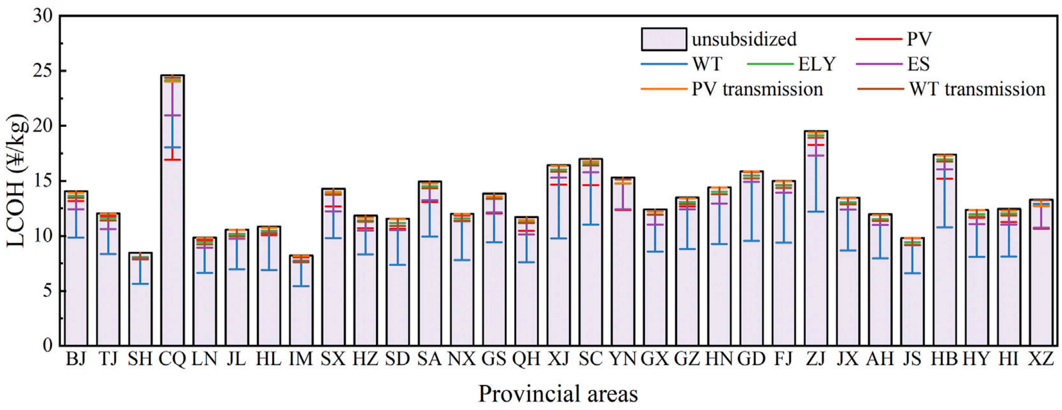

FIGURE 7
LCOH in provincial-level regions under six subsidy policies.

In response to the particular situation of CQ, we comprehensively considered the subsidy effect of various policies and the annual subsidy cost and proposed the concept of unit LCOH decrease cost, whose definition is shown in Eq. 19. In the equation, UM,i LCOH, $Cost^{M,i}$, and $\Delta LCOH^{M,i}$ are the unit LCOH decrease cost, annual subsidy cost, and LCOH decrease of the i^{th} provincial region under the M^{th} subsidy policy, respectively, Φ^{COMP} and Φ^{PRO} are the subsidy policy set and the provincial set, respectively. Figure 8 (the lower part) shows each provincial region's unit LCOH decrease cost. It can be found that PV, WT, and ES subsidies have their advantages and disadvantages in different regions, but generally, the U_{LCOH} subsidized by PV, WT, and ES will be higher than that subsidized by ELY and transmission costs. In particular, although subsidizing ELY can obtain lower U_{LCOH}, it still has a limited effect on reducing LCOH because the predicted terminal hydrogen demand in 2050 is still small, and the required ELY equipment configuration capacity is limited. However, in the long run, there is excellent potential to subsidize ELY after the terminal hydrogen demand increases in the future. In addition, if the PV and WT transmission costs can be further reduced, this will benefit LCOH.

$$U_{LCOH}^{M,i} = \frac{Cost^{M,i}}{\Delta LCOH^{M,i}}, \forall M \in \Phi^{COMP}, i \in \Phi^{PRO} \qquad (19)$$

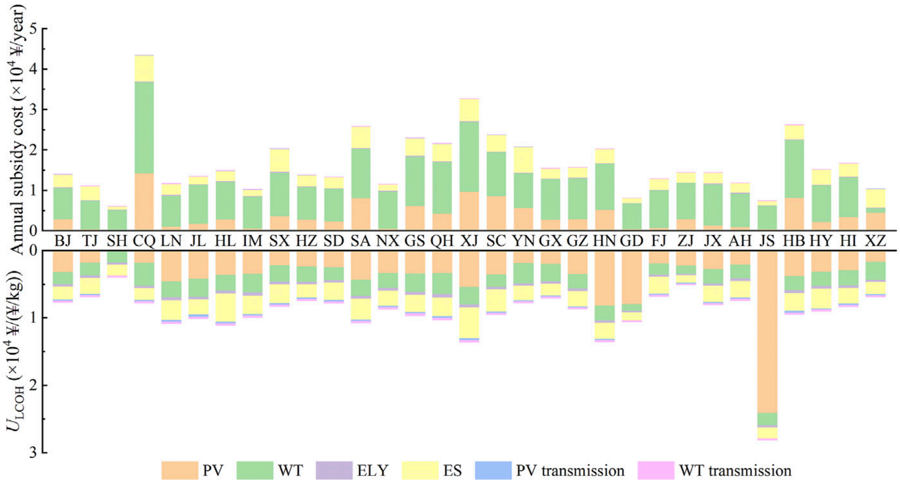

FIGURE 8
Annual subsidy costs and unit LCOH reduction costs for each provincial-level region under six subsidy policies.

4 Discussion

In the context of emission reduction, hydrogen production from renewable energy electrolysis has received extensive attention from countries worldwide. In this paper, we build CWESHs, evaluate the LCOH of 31 provincial-level regions in China in 2050, and analyze the advantages and disadvantages of using PV or WT power generation in detail. Starting from regional wind and solar energy characteristics and load characteristics, we evaluate the impact of regionally differentiated resource characteristics and load characteristics on CWESHs. Finally, the system sensitivity is analyzed, and the differences between the six subsidy policies are compared from different aspects, which is expected to provide helpful guidance for developing and popularizing hydrogen energy.

In China's provincial-level LCOH assessment, 27 of the 31 provincial-level regions are expected to have still LCOH higher than 10 ¥/kg in 2050, which is limited compared to traditional fossil energy hydrogen production. In this context, if a specific carbon tax is charged for hydrogen production from fossil energy at the policy level, it will further enhance the cost competitiveness of hydrogen production from renewable energy. In addition, we also found that deploying WT is more cost-effective than deploying PV and can widely promote wind power development in areas with abundant wind resources. In particular, when analyzing the influence of wind and solar characteristics and regional electrical load characteristics on the system, it was once again found that the configuration of WT in areas with similar wind and solar resources or areas with abundant wind resources is more cost-effective than PV, and the analysis of 31 provincial-level regions shows that the results are generalizable.

Finally, in the analysis of the system's sensitivity, it is pointed out that the conversion efficiency of the electrolyzer, the unit investment cost of WT, the system lifetime, and the discount rate are the four most critical factors affecting LCOH. With the further development of electrolyzer-related technologies in the future, even a slight increase in electrolysis efficiency can significantly impact reducing LCOH. Subsidy policy analysis shows that WT subsidies can reduce LCOH to the greatest extent in most provinces, but the annual cost is also the highest, but CQ and XZ are exceptional cases. With the further development of hydrogen energy in the future, subsidies for ELY equipment will have more tremendous application potential.

The above research has comprehensively assessed China's future renewable energy electrolysis hydrogen business, which is of great significance for promoting the development and popularization of hydrogen energy. In the future, we will further explore the unique role of hydrogen energy in carbon reduction from the perspective of deep coupling between the power system and the hydrogen energy system.

Data availability statement

The original contributions presented in the study are included in the article/Supplementary Material, further inquiries can be directed to the corresponding author.

Author contributions

GL and ZG conceived and designed the research. GL, BY, and ZG developed the framework and formulated the theoretical model. GL, BY, and ZG conducted the data search. GL, BY and ZG performed the simulations and analyses. All authors contributed to the discussions on the methods and the writing of this article.

Funding

This work was supported by State Grid Corporation of China Headquarters Science and Technology Project (1400-202257460A-2-0-ZN).

Conflict of interest

Authors GL, BY, HC, CW, and PX were employed by the company State Grid Energy Research Institute Co., Ltd.

The remaining author declares that the research was conducted in the absence of any commercial or financial relationships that could be construed as a potential conflict of interest.

The authors declare that this study received funding from State Grid Corporation of China Headquarters Science and Technology Project. The funder had the following involvement in the study: data collection, interpretation, analysis and the writing of this article.

Publisher's note

Supplementary material

The Supplementary Material for this article can be found online at: https://www.frontiersin.org/articles/10.3389/fenrg.2022.1046140/full#supplementary-material

References

Bertram, C., Riahi, K., Hilaire, J., et al. (2021). Energy system developments and investments in the decisive decade for the Paris Agreement goals. *Environ. Res. Lett.* 16, 074020. doi:10.1088/1748-9326/ac09ae

Fereidooni, M., Mostafaeipour, A., Kalantar, V., and Goudarzi, H. (2018). A comprehensive evaluation of hydrogen production from photovoltaic power station. *Renew. Sustain. Energy Rev.* 82, 415–423. doi:10.1016/j.rser.2017.09.060

Glenk, G., and Reichelstein, S. (2019). Economics of converting renewable power to hydrogen. *Nat. Energy* 4, 216–222. doi:10.1038/s41560-019-0326-1

Gu, Z., Pan, G., and Gu, W. (2022). "Portfolio of wind-photovoltaic-loads toward green hydrogen development," in 2022 IEEE 5th International Electrical and Energy Conference (CIEEC).

Guerra, O. J., Eichman, J., Kurtz, J., and Hodge, B. M. (2019). Cost competitiveness of electrolytic hydrogen. *Joule* 3, 2425–2443. doi:10.1016/j.joule.2019.07.006

Holdmann, G. P., Wies, R. W., and Vandermeer, J. B. (2019). Renewable energy integration in Alaska's remote islanded microgrids: Economic drivers, technical strategies, technological niche development, and policy implications. *Proc. IEEE* 107, 1820–1837. doi:10.1109/jproc.2019.2932755

Hydrogen Council (2017). Hydrogen, scaling up. Available at: https://hydrogencouncil.com/en/study-hydrogen-scaling-up/(Accessed September 14, 2022).

Institute of Climate Change and Sustainable Development, Tsinghua University (2021). *Research on China's long-term low-carbon development strategy and transformation path*. Beijing: Tsinghua University.

International Energy Agency (IEA) (2021). Renewable power. Available at: https://www.iea.org/reports/renewable-power (Accessed September 14, 2022).

International Renewable Energy Agency (IRENA) (2020). Green hydrogen cost reduction: Scaling up electrolysers to meet the 1.5°C climate goal. Available at: https://www.irena.org/publications/2020/Dec/Green-hydrogen-cost-reduction (Accessed September 14, 2022).

Kempler, P. A., Slack, J. J., and Baker, A. M. (2022). Research priorities for seasonal energy storage using electrolyzers and fuel cells. *Joule* 6, 280–285. doi:10.1016/j.joule.2021.12.020

Lin, H., Wu, Q., Chen, X., Yang, X., Guo, X., Lv, J., et al. (2021). Economic and technological feasibility of using power-to-hydrogen technology under higher wind penetration in China. *Renew. Energy* 173, 569–580. doi:10.1016/j.renene.2021.04.015

Lucas, T. R., Ferreira, A. F., Pereira, R. S., and Alves, M. (2022). Hydrogen production from the WindFloat atlantic offshore wind farm: A techno-economic analysis. *Appl. Energy* 310, 118481. doi:10.1016/j.apenergy.2021.118481

Ma, T., Pei, W., Xiao, H., Li, D., Lyu, X., and Hou, K. (2021). Cooperative operation method for wind-solar-hydrogen multi-agent energy system based on Nash bargaining theory. *Proceeding CSEE* 41, 25–39.

National Alliance of Hydrogen and Fuel Cell (2019). *White paper of China's hydrogen energy and fuel cell industry (2019 Edition)*. Beijing: National Alliance of Hydrogen and Fuel Cell.

National Energy Administration (NEA) (2020). Notice on doing a good job in the signing of medium- and long-term electric power contracts in 2021. Available at: https://www.ndrc.gov.cn/xwdt/tzgg/202012/t20201202_1252095.html?code=&state=123 (Accessed September 14, 2022).

O'Malley, M. J., Anwar, M. B., Heinen, S., Kober, T., McCalley, J., McPherson, M., et al. (2020). Multicarrier energy systems: Shaping our energy future. *Proc. IEEE* 108, 1437–1456. doi:10.1109/jproc.2020.2992251

Pan, G., Gu, W., Hu, Q., Wang, J., Teng, F., and Strbac, G. (2021a). Cost and low-carbon competitiveness of electrolytic hydrogen in China. *Energy Environ. Sci.* 14, 4868–4881. doi:10.1039/d1ee01840j

Pan, G., Gu, W., Lu, Y., Qiu, H., Lu, S., and Yao, S. (2020). Optimal planning for electricity-hydrogen integrated energy system considering power to hydrogen and heat and seasonal storage. *IEEE Trans. Sustain. Energy* 11, 2662–2676. doi:10.1109/tste.2020.2970078

Pan, G., Hu, Q., Gu, W., Ding, S., Qiu, H., and Lu, Y. (2021b). Assessment of plum rain's impact on power system emissions in Yangtze-Huaihe River basin of China. *Nat. Commun.* 12, 6156–6210. doi:10.1038/s41467-021-26358-w

Pfenninger, S., and Staffell, I. (2016). Long-term patterns of European PV output using 30 years of validated hourly reanalysis and satellite data. *Energy* 114, 1251–1265. doi:10.1016/j.energy.2016.08.060

Qiu, C. (2022). Analysis and suggestions on the pricing mechanism of transmission and distribution Fee of pilot distributed power generation nearby trading. *Water Power*, 1. doi:10.3969/j.issn.0559-9342.2022.09.020

State Grid Energy Research Institution (2019). *China energy & electricity outlook*. Beijing: China Electric Power Press.

Tao, Y., Qiu, J., Lai, S., and Zhao, J. (2020). Integrated electricity and hydrogen energy sharing in coupled energy systems. *IEEE Trans. Smart Grid* 12, 1149–1162. doi:10.1109/tsg.2020.3023716

Wang, W., Huang, S., Zhang, G., Liu, J., and Chen, Z. (2021). Optimal operation of an integrated electricity-heat energy system considering flexible resources dispatch for renewable integration. *J. Mod. Power Syst. Clean Energy* 9, 699–710. doi:10.35833/mpce.2020.000917

Wu, X., Li, H., Wang, X., and Zhao, W. (2020). Cooperative operation for wind turbines and hydrogen fueling stations with on-site hydrogen production. *IEEE Trans. Sustain. Energy* 11, 2775–2789. doi:10.1109/tste.2020.2975609

Wu, Y., Lin, Z., Liu, C., Huang, T., Chen, Y., Ru, Y., et al. (2022). Resilience enhancement for urban distribution network via risk-based emergency response plan amendment for ice disasters. *Int. J. Electr. Power & Energy Syst.* 141, 108183. doi:10.1016/j.ijepes.2022.108183

Wu, Y, Y., Lin, Z., Liu, C., Chen, Y., and Uddin, N. (2021). A demand response trade model considering cost and benefit allocation game and hydrogen to electricity conversion. *IEEE Trans. Ind. Appl.* 58, 2909–2920. doi:10.1109/tia.2021.3088769

Wu, Y. J, Y. J., Liang, X. Y., Huang, T., Lin, Z. W., Li, Z. X., and Hossain, M. F. (2021). A hierarchical framework for renewable energy sources consumption promotion among microgrids through two-layer electricity prices. *Renew. Sustain. Energy Rev.* 145, 111140. doi:10.1016/j.rser.2021.111140

Xiao, Y., Wang, X., Pinson, P., and Wang, X. (2017). A local energy market for electricity and hydrogen. *IEEE Trans. Power Syst.* 33, 3898–3908. doi:10.1109/tpwrs.2017.2779540

Yang, J., Zhang, N., Wang, Y., and Kang, C. (2018). Multi-energy system towards renewable energy accommodation: Review and prospect. *Automation Electr. Power Syst.* 42, 11. doi:10.7500/AEPS20171002004

Yang, Y., Wu, W., Wang, B., Li, M., and Zhu, T. (2021). Optimal decomposition of stochastic dispatch schedule for renewable energy cluster. *J. Mod. Power Syst. Clean Energy* 9, 711–719. doi:10.35833/mpce.2020.000620

Zhang, C., Liu, L., Cheng, H., Liu, D., Zhang, J., and Li, G. (2021). Frequency-constrained Co-planning of generation and energy storage with high-penetration renewable energy. *J. Mod. Power Syst. Clean Energy* 9, 760–775. doi:10.35833/mpce.2020.000743

frontiers | Frontiers in Energy Research

TYPE Review
PUBLISHED 17 January 2023
DOI 10.3389/fenrg.2022.1080882

OPEN ACCESS

EDITED BY
Nantian Huang,
Northeast Electric Power University,
China

REVIEWED BY
Leijiao Ge,
Tianjin University, China
Tao Huang,
Politecnico di Torino, Italy

*CORRESPONDENCE
Chengwei Peng,
1221056301@njupt.edu.cn

SPECIALTY SECTION
This article was submitted to Smart Grids, a section of the journal Frontiers in Energy Research

RECEIVED 26 October 2022
ACCEPTED 08 November 2022
PUBLISHED 17 January 2023

CITATION
Liu K, Zeng Y, Xu J, Jiang H, Huang Y and Peng C (2023), Multi-source electricity information fusion methods: A survey. *Front. Energy Res.* 10:1080882.
doi: 10.3389/fenrg.2022.1080882

Multi-source electricity information fusion methods: A survey

Kunling Liu[1,2], Yu Zeng[1,2], Jia Xu[1,2], He Jiang[1,2], Yan Huang[3] and Chengwei Peng[4]*

[1]Sichuan New Electric Power System Research Institute, Chengdu, China, [2]State Grid Sichuan Information and Communication Company, Chengdu, China, [3]NARI-TECH Nanjing Control Systems Co., Ltd., Nanjing, China, [4]College of Automation & College of Artificial Intelligence, Nanjing University of Posts and Telecommunications, Nanjing, China

With the vigorous development of the global economy, the demand for electricity quality from all walks of life is also increasing, so it is essential to ensure the electric power grid's safe, stable, and efficient operation. Multi-source electric power information fusion, as the core technology of electric power grid data processing, has become the foundation to promote the intelligent and automatic development of the electric power grid. This paper presents the first work on the survey of the methods of electricity information fusion. It first gives an overview of the process of electricity information fusion and shows the types of electricity data. Then, we provide different classifications of existing methods in view of communication annotation and electric power data, and conduct a thorough comparison and analysis of them. Moreover, we introduce the relevant data sets and evaluation criteria of electric power information and summarize the corresponding evaluation scenarios. Finally, we conclude the maturity of existing works and provide an outlook on future multi-source electric power information fusion methods.

KEYWORDS

smart grid, electricity information, communication standard fusion, electricity data fusion, representation learning

1 Introduction

Electricity is an essential foundation for social development. As the global energy situation is becoming increasingly severe, every country has devoted itself to developing and practicing smart grids (Yao and Lai, 2010; Zhang et al., 2013). With the rapid development of the global economy, the demand for quality electricity in all walks of life is also increasing. Therefore, it is essential to ensure the electric power grid's safe, stable, and efficient operation.

There are many kinds of electric power data, including structural attributes (e.g., signal indicators, charging equipment, and external environment), unstructured text descriptions (e.g., operating instructions, operating mechanisms, and principles), and various topological graphs (e.g., electric power station topological information and internal lines of equipment). Therefore, the challenges faced by data processing technology in data storage, processing, and display of smart grids have become the constraints of the intellectual development of smart grid (Xue and Lai, 2016), in which the method of multi-source electric power information fusion has become the core research topic in this field.

Several fusion methods for multi-source electric power information have been proposed and achieved some encouraging results. For example, Han et al. (2019) formulated a series of standards for substation communication networks and systems according to the International Electrotechnical Commission (IEC), called the IEC 61850 communication protocol, by which the standardization of electric power data in related systems was established. Furthermore, researchers explored the fusion methods in the view of the physical topology node (Han et al., 2019; Wang et al., 2020) and external protocol (He et al., 2019; Kong et al., 2021) based on IEC 61850. Benefiting from these fusion methods, fault detection, and information interconnection requirements could be solved to some extent. On the other hand, several intelligent algorithms have been employed to integrate and optimize information from the electric power data level to meet business needs for electricity, such as badness data identification (Pan et al., 2022), fusion efficiency improvement (Xia et al., 2022), and electric power consumption prediction (Shao et al., 2020).

Although current works of multi-source electric power information fusion have obtained significant progress, the complexity of electric power system not only lies in its massive data rules and attributes, the non-linearity of the topological electric power grid structure but also depends on temperature, humidity, time, space and many physical quantities collected in the environment (Xue and Lai, 2016). Therefore, no single fusion method can flexibly satisfy all the practical needs and overcome the challenges of smart grid data processing.

In this paper, we comprehensively survey the research works of electric power information fusion methods, especially the research progress of machine learning and deep learning for multi-source electric power information fusion in recent years. Precisely, we first present the overview of the fusion process for electric power information and list the related data types. Then, we provide two classifications of existing methods in view of communication annotation and electric power data, further introduce their critical ideas, and thoroughly compare them. Moreover, we introduce the relevant data sets and evaluation metrics of electric power information and summarize the corresponding evaluation scenarios. Finally, we conclude the maturity of existing works and give an outlook to future methods for multi-source electric power information fusion.

2 Background knowledge of electric power information fusion

2.1 Electric power information fusion process

Currently, electric power grid enterprises worldwide are starting to build integrated data platforms, and digital electric power grids as lots of measurement data can be immediately acquired and quickly shared, which can provide multi-source and heterogeneous information sources for fault diagnosis and other applications. In electric power systems, tedious data and a large amount of information are inconvenient for dispatchers to analyze and operate, so it is important to employ data fusion method to solve these issues. When some failures happen in the electric power grid, its data information reflects the abnormal changes in electrical quantity, protection, and circuit breaker, which can provide valid data information for electric power grid fault diagnosis. The reason is that the methods based on multi-source information fusion can make a comprehensive diagnosis according to the switching information and electrical information provided by different data sources, which can overcome the problem of fault diagnosis error caused by the uncertainty of fault information compared to employing a single data source. In addition, effective integration of multi-source can not only realize the standardization and unification of interfaces and real-time data-sharing requirements under the inter-operability of different devices and systems but also aggregate distributed energy storage with similar controllable potential and functional space. Benefiting from the fusion methods, the demand response capability of distributed energy storage can be fully dispatched in the scheduling process. Although the fault diagnosis algorithms of electric power grid based on multi-source information fusion are still in the stage of rapid development, they still have several limitations in practical application scenarios.

Shui et al. (2013) applied the information fusion method to the intelligent warning system of electric power, in which three data fusion architectures are proposed. According to the information sharing, interactivity, and high efficiency of the electric power system, the general integration framework is constructed, by which the electric power system can map data three-tier structure to one of the electric power systems. The data layer corresponds to the sensing measurement layer, the characteristic layer corresponds to the electric power data management layer, and the decision layer corresponds to the electric power system application layer. Moreover, Li et al. (2016) employed the three-layer structure for the massive monitoring data of the energy Internet. They further proposed a data fusion schema based on a multi-layer mode.

As shown in Figure 1, we give a flow chart of electric power information fusion. We combine the electric power system to map the unique three-layer data fusion structure to the electric power

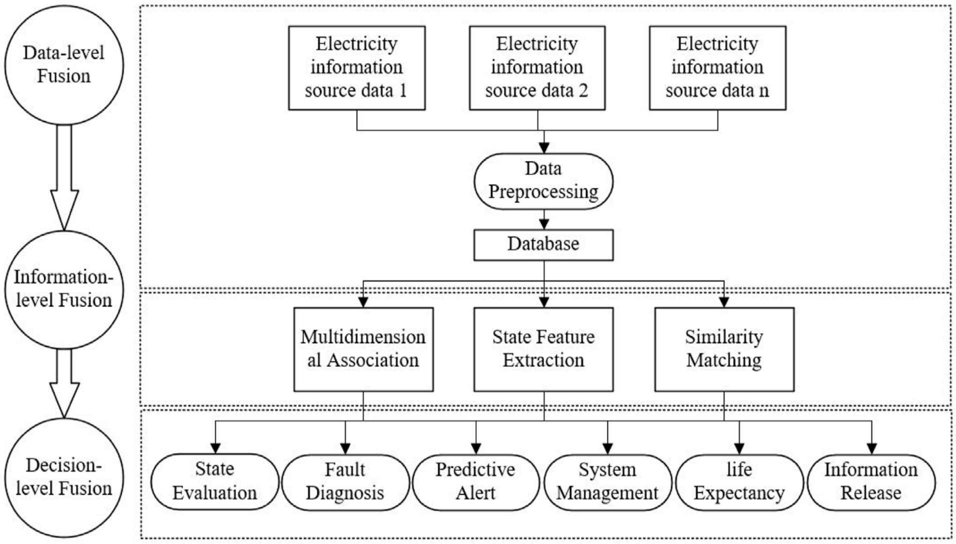

FIGURE 1
The flow chart of electric power information fusion.

system's three-layer structure. The fusion process has three levels, including data level, information level, and decision level. The data-level fusion is employed to the sensor measurement layer, and the electric power data measured by the sensor is transmitted to the data fusion center through the network line to complete the analysis, processing, and storage. The information-level fusion is utilized to the electric power data management layer, which extracts the state feature phasor from the original data source and then performs correlation analysis and similarity matching with the primary fusion feature extracted by the previous layer. The decision-level fusion is used to the electric power system application layer. The obtained decision vector can be combined with related algorithms to make classification, reasoning, identification, judgment, and other applications.

2.2 The flow chart of electric power information fusion the data type of electric power fusion

The data collected by the system has the characteristics of a diversified structure due to the distribution network's different types of power equipment. It is the basis of data fusion to understand the distribution of heterogeneous data in the electric power system. According to the internal structure type, the types of electric power data can be divided into structured, unstructured, and topological data. More precisely, the structured data includes photovoltaic, energy storage, voltage, electric power, electricity, illuminance, temperature, and other structural attributes of charging piles, as well as monitoring data of action signal switches. Unstructured data mainly contains unstructured text descriptions such as user manuals, operation introductions, maintenance records, operation mechanisms, and principles. Topological data mainly includes topological information on plants and stations and wiring diagrams of internal equipment, as shown in Table 1.

3 The methods of multi-source electric power information fusion

According to the characteristics and applications of existing methods, we mainly divide them into communication standard-based fusion methods and electric power data-based fusion methods, as shown in Figure 2.

In the upper classification of Figure 2, electric power information fusion methods are divided based on communication standards, which can be divided into the ones based on physical topology nodes, fusion the ones based on external protocol standards, and the ones based on model feature extraction as follow.

Fusion methods based on physical topology nodes: It models the topological structure of physical nodes with IEC 61850–90-6 protocol. These logical nodes are employed for fault location.

Fusion methods based on external protocol standards: It establishes a unified information model from the standard model level and the data type level.

Fusion methods based on model feature extraction: It integrates the related data from the electric power platform to extract the critical features of electrical equipment.

From another point of view in Figure 2, existing fusion methods can also be classified based on electric power data,

TABLE 1 Data type of electric power fusion.

Types	The list of electric power data type
Structural data	Voltage, electric power, electric quantity, irradiance, temperature, and other data of photovoltaic, energy storage, charging pile, etc., electric quantity information, operation state monitoring data such as protection action signal and switch tripping information, control data such as control instruction etc.
Unstructured data	Various text data include report data, video/audio data, image data, sensor flow data, instructions for use, technical documents, operation and maintenance records, operation mechanisms and principles etc.
Topological data	Plant topology information diagram, equipment internal wiring diagram etc.

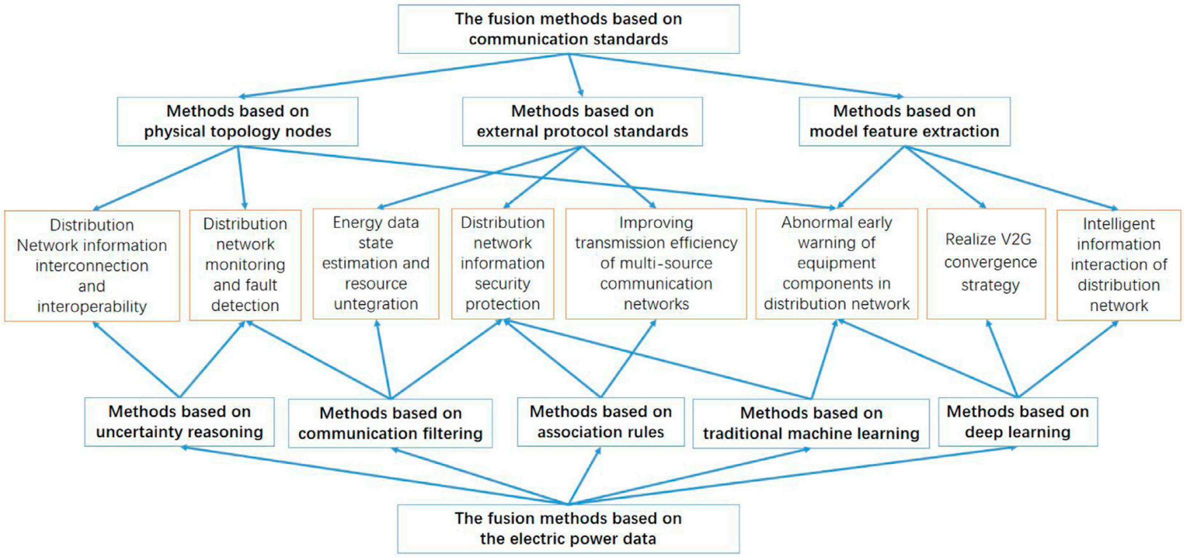

FIGURE 2
The classification of the fusion method for multi-source electric power information.

including the ones based on association rules, the ones based on communication filtering, the ones based on uncertainty reasoning, the ones based on traditional machine learning and the ones based on deep learning.

Fusion method based on association rules: It employs the clustering method to convert data into the one that is suitable for association rules, and the periodic association among converted data will be obtained, and then the data will be fused through ensemble methods (e.g., random forest).

Fusion methods based on communication filtering: It compresses multi-global information so that the error of heterogeneous data fusion and delay time can be reduced.

Fusion methods based on uncertainty reasoning: It employs Dempster-Shafer to converge the components' physical model and fault characteristics so that the influence of information quality changes can be overcome.

Fusion methods based on traditional machine learning: It uses machine learning methods (e.g., Bayesian-based method) to learn the feature from the limited annotation, which can ensure the reliability and fusion efficiency of the results.

Fusion methods based on deep learning: It employs deep learning to integrate and learn the features from the platform data, by which the learning features are more robust for fusion.

Next, we will introduce these methods because of communication annotation and electric power data.

3.1 The fusion methods based on a communication standard

Data mapping is the foundation of communication mapping. Information fusion needs to ensure the safe transmission of information under specific criteria. To promote the standardization of intelligent substations, IEC TC57 has formulated standards for substation communication networks and systems-IEC 61850. The release of the IEC 61850 standard solves the problem that the traditional telecontrol communication protocol is complicated to realize interconnection and interoperability, which needs the heavy workload of installation and debugging between the distribution terminals of different manufacturers. It realizes the standardization of the distribution automation information model (Han et al., 2019). IEC 61850 series standards play an essential role in substation automation informatization, whose goal is realizing unified modeling and seamless communication of electric power systems. With the migration of public utilities to substations and other network solutions, IEC61850 has become the preferred protocol which is the first standardization work to solve the communication problems of intelligent electronic devices (IEDs) (Xyngi and Popov., 2010).

At present, there are lots of studies related to the application of the IEC 61850 standard. Liu D et al. (2020) studied the source-side maintenance technology of substation autonomous systems according to the IEC 61850 standard to improve the real-time information exchange between the electric power grid. Shantanu et al. (2021) evaluated the feasibility of applying unconventional high-voltage transformers in future digital substations under the IEC 61850 standard. The simulation results showed that unconventional high-voltage transformers were better than conventional transformers in key performance indicators such as ETE, time delay, DC offset, and frequency response. With the introduction of the substation automation system and advanced network and communication technology, the complexity of the electric power system increases dramatically, which may make the whole electric power grid vulnerable to hackers. To solve this problem, Suleman et al. (2021) proposed a network model developed in OPNET, demonstrating the results of various denial of service (DoS) attacks on digital substations based on IEC 61850. It was of great significance to understand the influence of these factors on the performance of digital substations.

Zhu et al. (2017) aimed at the configuration problem of a distributed intelligent application using the IEC 6185 standard in a distribution automation system. The authors presented a configuration solution from two aspects: the semantic model and the processing method. Taha and Suhail. (2020) proposed a communication technology based on IEC 61850 and XMPP. They developed the IEC 61850 information model of the UPFC controller to coordinate the stable operation of UPFC and DERs in the microgrid. With the international standard IEC 61850 and IEEE 2030 reference models, Leitea et al. (2016) proposed a voltage regulation optimization method based on the communication architecture model that coordinated the interaction between DGPV units to meet the connectivity and interoperability requirements.

Therefore, studying electric power information fusion technology based on communication standards is imperative. We divide the electric power information fusion technology based on communication standards into three categories: fusion based on physical topology nodes, fusion based on external protocol standards, and fusion based on model feature extraction.

Fusion methods based on physical topology nodes: Han et al. (2019) employed the IEC 61850–90-6 standard to divide the fault indication into two parts according to the mapping of logical nodes: fault detection and fault indication. The release of the IEC 61850 standard solved the problem that the traditional telecontrol communication protocol is hard to realize the interconnection, interoperability, and heavy workload of installation and debugging between distribution terminals of different manufacturers and the central station and distribution terminals so that the standardization of distribution automation information model is realized. Taking fault indication, fault location isolation, and electric power supply restoration as examples, the author analyzed the establishment process of fault detection and protection information model of the distribution network. Fault indication information was needed to convert the transient impulse control signal output by fault detection information into a continuous position indication signal. New logic nodes needed to be added to a unique distribution automation function. The new logical nodes added in IEC 61850–90-6 are shown in Table 2.

Wang et al. (2020), aimed at the problem that there was no physical link model in the IEC 61850 protocol, modeled the corresponding physical information nodes in the secondary communication of the process layer and constructed the physical topology of the secondary device communication. The authors put forward an intelligent warning and fault diagnosis schema for the secondary circuit of the smart substation and established a fault diagnosis method that combined a virtual circuit with an actual physical link according to the information flow characteristics in the smart substation. Through comprehensive analysis of configuration file information in the substation, link alarm information of protection measurement, and status information, of the control device, the probability of all the possible fault points would be calculated when the communication abnormality occurs is given. According to the failure point probability given by the system, the operation and maintenance engineer can find out the failure point by troubleshooting the corresponding equipment in turn, which could improve the operation and maintenance efficiency. This method makes full use of the state information given by each piece of equipment in the station and various data flowing on the network and automatically and intelligently analyzes and judges the fault points in the secondary circuit by relying on the correlation and coupling characteristics in each virtual circuit. It satisfied the

TABLE 2 New logical nodes for fault indication in IEC 61850–90-6.

Functional requirements	Logical node
Error indication	SFPI
Voltage indication generates a persistent "presence" signal and a "non-presence" signal according to the input from PTOV and PTUV	SVPI
Current indication generates a persistent "presence" signal and a "non-presence" signal according to the input from PTOC and PTUC	heSCPI
Calculation and statistics of faults in a given period	SFST

IEC, 61850–90-6 mainly solves the problems of fault location and isolation of distribution lines (feeders) and the establishment of electric power supply recovery logic nodes in non-fault sections in distribution automation. The logic nodes added for electric power supply restoration in IEC, 61850–90-6 are shown in Table 3.

TABLE 3 New logic nodes for electric power supply restoration in IEC 61850–90-6.

Functional requirements	Logical node
Detect the faults on the feeder based on overcurrent or Undervoltage	ASWI
Detects that the voltage on one side disappears and closes	AATS
Error indication	SFPI
Voltage presence indication	SVPI
When no voltage is detected on both sides of the segmentary, turn on the segmentary. After a voltage is detected on one side, the segmentary is closed after a specified delay	
If the voltage is not detected within the predetermined blocking time, it will block the segmentary and not close it again	RRFV
Current presence indication	SCPI
Fault status	AFSL
Fault isolation after indication completed	AFSI
Control of the electric power during the recovery process	ASRC

requirement of standardized information transmission and sharing in intelligent substations, and the developed system could achieve good results in real applications.

Fusion methods based on external protocol standards: He et al. (2019) analyzed the hybrid measurement architecture of an intelligent distribution network and compared the differences between D-PMU data, AMI data, and SCADA data in data composition, data accuracy, and time scale information. Based on the IEC 61850 standard and IEC 61968–301 (CIM) static mapping and dynamic mapping of SCADA interaction with new systems, the authors put forward a unified information model, which unified the equipment descriptions of IEC 61850 standard and IEC 61968–301 (CIM) standard, made up for the defect that the modeling standards followed by the wide-area measurement and control systems of smart distribution networks were not uniform in construction, and realized the data exchange among all systems. Kong et al. (2021) proposed an external protocol standard of IEC 61850 communication protocol called MQTT, which could be adopted in the cloud edge communication of distribution Internet of Things. The MQTT protocol is regarded as the application layer communication protocol for the information interaction between the cloud master station and edge devices, which could enhance interoperability and solve the problems of standardization of data transmission and data description model between the cloud master station and the edge devices of distribution Internet of Things. The communication mapping methods from the communication service subset to the MQTT protocol are summarized, including the direct and indirect mapping methods. The authors concluded that the direct mapping method was more applicable and economical than complex ones on cloud-side communication of distribution Internet of Things.

Fusion methods based on model feature extraction: Zhao et al. (2021) proposed a fault diagnosis method based on the confidence fusion of the Dempster-Shafer theory, which could effectively and comprehensively utilize the redundant features of multi-source data information and thoroughly mined the fault features of related switching information and electrical information. The authors implemented the effective integration of multi-source alarm information, which was of great help in improving the accuracy of fault diagnosis and quickly identifying fault components. Lu et al. (2020) constructed the fault optimization detection model of substation equipment, combined with the collaborative fault method, to improve the fault optimization diagnosis ability of substation equipment. They put forward the collaborative fault diagnosis method of substation equipment based on the information fusion technology of the sampling and feature extraction model. The experimental analysis showed that this method could obtain good synergies in fault diagnosis of substation equipment operation and own a high precision of detecting fault features. GOOSE message is a vital part of the IEC 61850 protocol, which embeds selection logic and simulation data. Li J et al. (2021) studied the measurement method based on the specification part of the IEC 61850 protocol. They analyzed the behavior characteristics of CPS from many GOOSE and manufacturing message specifications based on a digital substation network and system management scheme. To solve the problem of low accuracy of existing detection methods, the authors proposed an anomaly detection method based on difference sequence variance combined with the message characteristics of a digital substation, including the determination of membership function of traffic anomaly and CPS parameters of fusion.

3.2 The fusion methods based on electric power data

With the development and maturity of global electric power big data multi-source information fusion technology, fusion algorithms are gradually diversified. The multi-modal data fusion is an effective way to implement the collaborative analysis of multiple heterogeneous networks that pushes forward observable and controllable power grids (Wang B et al., 2022). We divide the electric power information fusion methods based on electric power data into five categories: the ones based on association rules, the ones based on communication filtering, the ones based on uncertainty reasoning, the ones based on traditional machine learning, and the ones based on deep learning.

Fusion methods based on association rules: Pan et al. (2022) applied the data mining method of association rules to the energy system and employed random forest to establish the training network of big energy data for data fusion. Inspired by incremental learning and offline learning, the authors proposed the MCS-RF framework of energy big data. By converting discrete data into data suitable for association rules, the accuracy of wrong data identification and energy data state estimation was improved. Compared with the traditional algorithms based on residual error, the proposed method can save time in identifying lousy energy data and obtain higher accuracy. Similarly, Liu B et al. (2021) adopted the extensive data analysis method based on random forest. The authors proposed a regional priority business screening model for the multi-station fusion project that could satisfy the concept of sustainable development and reliability.

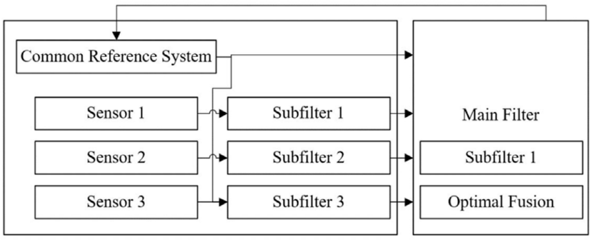

FIGURE 3
Structure diagram of joint Kalman filter algorithm.

Fusion methods based on communication filtering: Wen and Li (2018) proposed an information fusion method combining compressed sensing with global forwarding data. According to the communication range of network nodes, the clusters are divided into multiple areas. Each node selects the communication mode to transmit global information to the communication cluster head according to its location to reduce the global information fusion delay. In the process of global information collection in the multi-source communication network, the model employed the compressed sensing model to compress the global information and forward the global information according to the number of sub-nodes of network nodes. The fusion of global information in a multi-source communication network effectively improves its transmission efficiency.

As the traditional methods do not register the time during the collection of multi-source heterogeneous data in the distribution network, it leads to significant errors and low efficiency for the fusion of multi-source heterogeneous data. Xia et al. (2022) proposed a multi-source heterogeneous data fusion method in a distribution network based on a joint Kalman filter to solve this issue. The authors employed the joint Kalman filtering algorithm to implement heterogeneous data fusion. The structure diagram of the joint Kalman filtering algorithm is shown in Figure 3. We can observe that the data process of joint Kalman filtering algorithm is mainly divided into two ones: the primary filter and the local sub-filter. In the calculation, each sub-filter works independently. That is, the time update and the measured value update run separately. This method can improve data fusion efficiency and reduce data fusion error compared with traditional methods.

3.3 Structure diagram of joint kalman filter algorithm

Fusion methods based on uncertainty reasoning: Zhao et al. (2021) proposed a multi-layer fault diagnosis model of the electric power grid and used the Dempster-Shafer theory to analyze the data information in the multi-source information fusion diagnosis layer. The authors considered various information, such as switching value and electrical quantity, which provided the basis for fault diagnosis to obtain the probability value of the possible fault components for each fault component. In addition, they further analyzed the related protection and the action of circuit breakers. Traditional fusion methods for fault diagnosis may reduce the confidence of fault components and affect the fault diagnosis results. Therefore, the author improved the multi-source information fusion diagnosis method based on the Dempster-Shafer theory. It could solve the problem that the uncertain factors (e.g., misoperation, refusal of protection, circuit breaker, transmission error of alarm information) could affect the accuracy of fault diagnosis results.

Fusion methods based on traditional machine learning: Electricity data fusion methods have broad applications in electric vehicles and the grid. Rik and Willett (2008) put forward a model of electric vehicles with three control types. The authors added electric and V2G vehicles into the energy system to integrate higher-level wind electric power without generating excess electric power and significantly reduce carbon dioxide emissions. Wang Y et al. (2022) employed the entity alignment of the Bayesian model to implement the fusion method for related attribute mapping. It was a highly reliable and low-complexity knowledge fusion method that combined a concept drift detection algorithm with an unsupervised reverse verification algorithm. The experiments showed that the proposed method was superior to the conventional machine learning algorithm regarding knowledge fusion efficiency and algorithm complexity.

Fusion methods based on deep learning: The forecast of electric power consumption is an essential task of smart grid construction. Related works pay attention to weather, holidays, and temperature for electric power forecasts. It is necessary to use lots of sensors to collect these data, which increases the cost of time and resources. Darudi et al. (2015) proposed a new data fusion algorithm based on an artificial neural network and adaptive neuro-fuzzy inference system, modified ordered weighted average (OWA). Shaxiaorui et al. (2020) proposed a hybrid depth prediction model based on CNN and LSTM, which could learn fusion features in parallel. As corresponding statistics were considered, the method could obtain more robust features even if some original information was lost. To predict electric power consumption, the authors incorporated the advantages of each model. Similarly, Liu and Meng (2020) adopted the depth-limited Boltzmann machine to encode all data into the same vector space. They applied the time series method to implement the effective fusion of power network communication service data and improve the accuracy of fusion results. Wang et al. (2021) proposed a universal fusion framework suitable for structured multiple time series and unstructured images, which could achieve the deep fusion for heterogeneous multi-parameter under the power Internet of Things. Li G et al. (2021) proposed a multi-source log comprehensive feature extraction method based on Restricted Boltzmann Machine (RBM) to excavate security threats in the electric power grid by entirely using heterogeneous data sources in the electric power information system.

3.4 Method review

This section summarizes the fusion methods of multi-source electric power information listed in Table 4, including the core models, characteristics, and limitations.

For the fusion methods of electric power information based on a communication standard, the methods based on physical topology mainly depend on IEC 61850. These methods establish new logical and line nodes so that loops can be detected for the equipment in the station (Han et al., 2019; Wang et al., 2020). Although these methods have strong engineering, the hardware and maintenance costs for establishing physical topology nodes are high in the early stage. The fusion methods based on external protocol standards mainly construct the unified information model from the levels of a standard model and the data type. For these methods, the communication protocol standards are layered, and different mapping strategies are formulated according to the characteristics of protocol files (He et al., 2019; Kong et al., 2021). However, these methods lack scalability and depend on manual construction and maintenance. For the methods based on model feature extraction, the associated data in the data platform are integrated to extract the critical feature quantities of electrical equipment. The statistical probability is automatically calculated for the fault diagnosis or abnormal electrical equipment data (Lu et al., 2020; Li Y et al., 2021; Zhao et al., 2021). Although the methods are automatic and real-time, they are only suitable for single-task scenarios.

For the fusion methods of electric power information based on electric power data, the methods based on association rules are inspired by unsupervised learning, in which the clustering method is employed to transform the data to mine the association rules. Then, the periodic correlations among data are obtained. This way, random forest can further fuse the transformed data (Pan et al., 2022). Although the accuracy of related tasks is high, these methods can only deal with discrete data, and the subjective factors might influence the clustering results. The fusion methods based on communication filtering employ collaborative Kalman filtering (Wen and Li, 2018) and compressed sensing (Xia et al., 2022). These methods can effectively compress global information and reduce errors and delays during the process of heterogeneous data fusion. Therefore, they can improve the efficiency of signal fusion and forwarding. However, high requirements exist for the hardware storage space of network acquisition nodes, which sacrifice the fusion accuracy. The methods based on uncertain reasoning employed the Dempster-Shafer theory to model the

TABLE 4 Comparison of multi-source electric power information fusion methods.

Method name	Core ideas/models	Method characteristics	Limitations	Representative literature
Fusion methods based on physical topology nodes	Logical nodes in fault location, isolation, and non-fault areas are established based on IEC 61850–90-6 protocol, and the topological structure of physical nodes is modeled	Detecting the equipment in the station from the line nodes and loops has strong engineering practicability	The hardware and maintenance costs for establishing physical topology nodes are high in the early stages	Han et al., (2019); Wang et al., (2020)
Fusion methods based on external protocol standards	Establish a unified information model from the levels of the standard model and the data type	The communication protocol standards are layered, and different mapping strategies are drawn up according to the characteristics of protocol files	The scalability of the method is weak, and they depend on manual construction and maintenance	He et al., (2019); Kong et al., (2021)
Fusion methods based on model feature extraction	Integrate the related data of the data platform to extract the critical characteristic quantities of electrical equipment	The statistical probability can be automatically calculated for fault diagnosis or abnormal electrical equipment data	They are only suitable for the of single-scenarios	Zhao et al., (2021); Lu et al., (2020); Li Y et al., (2021)
Fusion methods based on association rules	K-Means Periodic Association Rule Random Forest Model	The clustering method transforms the data for mining the association rules. Data fusion is carried out through the periodic association rule and the random forest	Only discrete data can be processed, and subjective factors might influence clustering results	Pan et al., (2022)
Fusion methods based on communication filtering	Joint Kalman Filtering Compressed Sensing	The global information can be effectively compressed, and the efficiency and real-time performance of signal fusion and forwarding can be improved	High requirements for the hardware storage space of network acquisition nodes sacrifice the fusion accuracy	Wen and Li, (2018); Xia et al., (2022)
Fusion methods based on uncertainty reasoning	Dempster-Shafer theory	Modeling the physical model and fault characteristics of components based on Dempster-Shafer. It can overcome the influence of information quality change and realize uncertain reasoning	Limited by how objects are fused pairwise, their time complexity is extensive	Zhao et al., (2021)
Fusion methods based on traditional machine learning	Bayesian Estimation	It can ensure results' reliability and fusion efficiency with limited labeled data	They cannot realize the effective combination of features and further mine the hidden feature association between data	Wang B et al., (2022)
Fusion methods based on deep learning	Recurrent Neural Network Convolutional Neural Networks Boltzmann Machine	They can make the fusion features obtained by representation learning more robust and perform better	They heavily rely on lots of labeled data and the actual hardware	Jiang et al., (2019); Lin et al., (2020)

components' physical model and fault characteristics, which can overcome information quality change and realize uncertain reasoning (Zhao et al., 2021). Nevertheless, these methods are limited by how objects are fused pairwise, so their time complexity is extensive. Traditional machine learning of fusion methods is represented by Bayesian estimation (Wang B et al., 2022). Although these methods can ensure the reliability and fusion efficiency of results with limited labeled data, they cannot realize the effective combination of features and further mine the hidden feature association between data. Therefore, there exists a bottleneck to improving the accuracy of specific tasks such as fault detection. The methods based on deep learning mainly utilize the recurrent neural network. This kind of method makes the fusion features obtained by representation learning more robust and perform better. Nevertheless, these methods heavily rely on lots of labeled data and the actual hardware.

After a comprehensive comparison of the above existing methods, we discover that the fusion method of electric power information based on a communication standard is a well-established methodology because the IEC 61850 standard has been published for nearly 20 years. The requirement of information interconnection for fault detection and electric power consumption prediction is still a hot research topic. This kind of research works already accounts for about 30% of the fusion works. One of the main reasons is the business's need for electricity. In recent years, more than half of fusion works have been devoted to exploring machine learning and deep learning to learn rich features and meet the requirements of smart grid. Nevertheless, there is room for making progress in optimizing existing solutions. We conclude the test datasets of electric power information fusion and their data processing methods listed in Table 5.

TABLE 5 Datasets and data processing methods.

Datasets	Dataset size	Data processing method
Electric power flow Dataset system (Pan et al., 2022)	1,440 samples	The clustering method is employed discretization
Phasor Measurement Unit (PMU) Dataset (Xia et al., 2022)	Thousands of meteorological data, equipment data, and photovoltaic data	The original data is stored in a temporary table, and a processing thread corresponding to the data type is established
American Electric Company (AEP) Dataset[1] (Shao et al., 2020)	121,273 pieces of data from December 2004 to January 2018	Normalization processing
Commonwealth Edison (COMED) Dataset[2] (Shao et al., 2020)	66,497 data from December 2011 to January 2018	Normalization processing
Dayton Electric power and Light Company (DAYTON) Dataset[3] (Shao et al., 2020)	121,275 pieces of data from December 2004 to January 2018	Normalization processing
Public Data Set of University of California Machine Learning and Intelligent Systems Center (Wang Y et al., 2022)	Environmental data of 12 areas of Beijing from 2014 to 2017 including air quality, temperature/dew point temperature, wind direction/speed, air pressure, rainfalletc.	Ontology association
A data set composed of defective texts of an electric power company in a China province (Jiang et al., 2019)	23,409 data from 2015 to 2017, all from the operation and maintenance records of AC 220 kV oil-immersed transformers	Convert original text data into continued vectors

Evaluation metrics of electric power information fusion method.

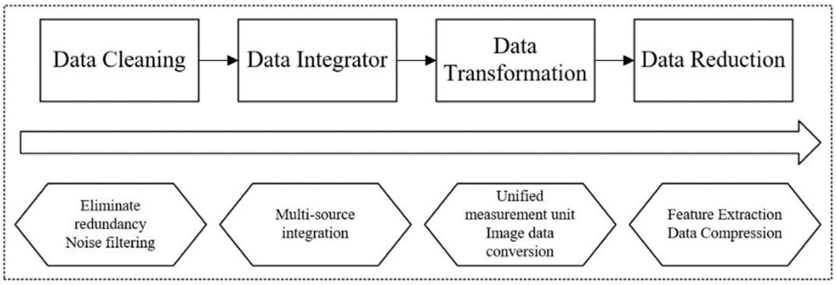

FIGURE 4
The workflow for pre-processing multi-source heterogeneous data.

4 Evaluation of electric power information fusion methods

4.1 Test dataset for electric power information fusion method

This section will introduce the test[1] datasets of electric power information fusion in detail. First, the standard pre-processing techniques for datasets are introduced in this paper[2]. Then, we list the statistic of corresponding datasets for electric power information fusion.

There are several kinds and quantities of electric power data, but their interrelated relationships are vague as the initially collected data has high redundancy and noise content. Therefore, preliminary signal processing and data classification are essential. The function of data fusion is to ensure that the electric power information acquisition equipment can accurately provide feedback on the current electric power network data and store[3] the historical data completely. In this way, the original data of heterogeneous electric power information systems can be processed by eliminating invalidity, filtering redundancy, and data interpolation. Afterward, the researchers could carry out the operations of feature extraction and feature matching operations among heterogeneous datasets, which facilitate the next big data fusion

---

[1] https://www.kaggle.com/datasets/robikscube/hourly-energy-consumption?select=AEP_hourly.csv

[2] https://www.kaggle.com/datasets/robikscube/hourly-energy-consumption?select=COMED_hourly.csv

[3] https://www.kaggle.com/datasets/robikscube/hourly-energy-consumption?select=DAYTON_hourly.csv

and decision analysis. Figure 4 shows the concrete workflow for pre-processing multi-source heterogeneous data.

4.2 The workflow for pre-processing multi-source heterogeneous data

Several pre-processing methods exist for electric power data, such as the average, the least square methods, and so on.

Dai et al. (2017) proposed a non-parametric method (kernel density-mean). By comparing the average and the least square methods, the calculation results show that the kernel density-mean method could obtain better results in terms of the robustness of sampling frequency.

Pan et al. (2022) regarded the electric power flow data in the SCADA system as the samples, for which the standard deviation of the measured value was set to 0.02 and the standard deviation of the phase angle was set to 0.005. The authors simulated and analyzed the electric power flow data change from April to June. These data were discretized by the clustering method to obtain the discrete level of active electric power.

Xia et al. (2022) synchronized the dataset with Phasor Measurement Unit data, meteorological data, equipment data, and photovoltaic data. The pre-processing of data contains two steps. Firstly, extracted data from the data source and stored the original data in the corresponding temporary table. Therefore, it must establish a processing thread corresponding to the data type. Then, traverse the acquired data from the temporary table, and judge whether there is any abnormal situation in the data according to the rectification rules. If any abnormal situation exists, it needs to process the data and generate rectification records.

Zhao et al. (2021) employed electrical data and switching records as samples. Furthermore, the authors measured the confidence of samples after data and records were normalized.

Lin et al. (2020) analyzed that the same type of multi-source heterogeneous data fusion is meaningful for correlation analysis. Therefore, the authors concluded that Euclidean distance and Pearson correlation coefficient were the most common metrics methods for correlation analysis. The Euclidean distance of any two points x_i , x_j in m-dimensional space was defined in Eq. 1:

$$d\left(x_i, x_j\right) = \sqrt{\sum_{k=1}^{m}\left(x_{ik} - x_{jk}\right)^2} \tag{1}$$

where x_{ik}, x_{jk} are the coordinates of two points in m-dimensional space.

Zhao et al. (2021) employed a local electric power system for simulation analysis. The confidence was calculated by synthesizing evidence based on the Dempster-Shafer theory. Then, the effectiveness of the proposed method was verified by comparing the confidence levels as shown in Eq. 2, where p is the probability value of the i-th possible faulty element, and the fault confidence value of the possible faulty element p_i^* is calculated in Eq. 3. After then, the authors would set a confidence threshold and compare the predicted results with the real samples.

$$\sum\nolimits_{Fault,end} = \left\{p_1, p_2, \ldots, p_n\right\} \tag{2}$$

$$p_i^* = p_i \Big/ \max\left\{p_i \middle| p_i \in \sum\nolimits_{Fault,end}\right\} \tag{3}$$

To fairly evaluate the effectiveness of the proposed models based on deep learning, Shao et al. (2020) adopted Root Mean Square Error (RMSE), Mean Absolute Error (MAE), and Mean Absolute Percentage Error (MAPE) composed of multiple evaluation indicators for evaluation. The specific formulas are as follows Eqs 4–6:

$$RMSE = \sqrt{\frac{\sum_{n=1}^{N}\left(forecast_n - real_n\right)^2}{N}} \tag{4}$$

$$MAE = \frac{\sum_{n=1}^{N}\left|forecast_n - real_n\right|}{N} \tag{5}$$

$$MAPE = \frac{100\%}{n}\sum_{n=1}^{N}\left|\frac{forecast_n - real_n}{real_n}\right| \tag{6}$$

Where N is the number of test samples, f is the predicted value, and real is the ground truth. RMSE evaluated the model by the standard deviation of the residuals between the ground truth and predicted values; MAE is the average vertical distance between the ground truth and predicted values, which is more robust to more significant errors than RMSE. RMSE and MAE increase significantly and rapidly when using extensive data for model training and evaluation. Hence, the authors employ MAPE to evaluate the fusion methods comprehensively.

Wang Y et al. (2022) used the calculation of Precision, Recall, and F1 to verify the feasibility of the proposed method for the evaluation of heterogeneous datasets. The calculation formula is shown in Eqs 7–9:

$$Precision = \frac{TP}{TP + FP} \tag{7}$$

$$Recall = \frac{TP}{FP + FN} \tag{8}$$

$$F1 = 2 \times \frac{Precision \times Recall}{Precision + Recall} \tag{9}$$

where TP (True Positive), FP (False Positive), and FN (False Negative) represent the entity alignment indicators of the fused ontology.

In addition, Jiang et al. (2019) found that there are three types of fault defect include general defects, severe defects, and critical defects, and they used macro-P macro precision (represented by $A_{macro-P}$), macro-R macro recall (represented by $A_{macro-R}$), macro-F1 macro comprehensive index (represented by

$A_{macro-F1}$) to evaluate. Eq. 10 lists their expression, where the precision rate p and recall rate R are the two-class evaluation indexes. Their definitions of p and R are shown in Eq. 11, where P_T represents the number of positive cases that are correctly judged as positive cases; N_F indicates the number of positive examples that are wrongly judged as counterexamples; P_F represents the number of negative examples that are wrongly judged as positive examples. For the three-classification problem, there exist three different positive examples and three values that correspond to p and R.

$$\begin{cases} A_{macro-P} = \frac{1}{n}\sum_{i=1}^{n} P_i \\ A_{macro-R} = \frac{1}{n}\sum_{i=1}^{n} R_i \\ A_{macro-F1} = \frac{2A_{macro-R} \times A_{macro-R}}{A_{macro-R} + A_{macro-R}} \end{cases} \tag{10}$$

$$\begin{cases} P = \frac{P_T}{P_T + P_F} \\ R = \frac{P_T}{P_T + N_F} \end{cases} \tag{11}$$

Wen and Li (2018) utilized the global information reconstruction error ε to evaluate the feasibility of the proposed methods. The defined formula is as follows:

$$\varepsilon = \|\bar{f} - f\|_2 / \|f\|_2 \tag{12}$$

f and $\bar{f}$ represent the original and restored global information sequences, respectively.

4.3 Evaluation scenarios of electric power information fusion method

For the above test data sets and evaluation metrics, we summarize three types of test scenarios listed as follows:

Information interconnection of Electric power grid: It is suitable to evaluate the fusion methods based on communication standards. Through the mapping operation and standard specification between different protocols, the multi-type protocol signal transmission can be employed to verify the proposed model's compatibility and delay of signal transmission (Han et al., 2019; He et al., 2019; Kong et al., 2021).

Anomaly detection of substation data: It is also suitable for evaluating the fusion methods based on communication standards, which can verify the performances of the model in terms of accuracy, and missed detection rate by labeled signal datasets based on specific standard protocol (Wang et al., 2020; Li Y et al., 2021).

Fault detection of charging equipment: It is suitable for evaluating fusion methods based on electric power data. On the one hand, the effect of the models can be verified from the waveform of the running equipment (Lu et al., 2020). On the other hand, this scenario can be modeled as a classification problem given machine learning. The methods can be verified by precision, recall, and F1 value and the corresponding variants of these metrics (Wang et al., 2022).

5 Conclusion and future work

Multi-source electric power information fusion, as the core technology of electric power grid data processing, has become the foundation to promote the intelligent and automatic development of the electric power grid. However, there does not exist survey of existing methods to discuss their limitation for this topic. This paper overviewed information fusion methods for multi-source electricity information. We thoroughly reviewed current methods regarding communication annotation and electric power data and further introduced their critical ideas. Then, we introduced the relevant datasets and evaluation criteria of electric power information and summarized the corresponding evaluation scenarios. We further evaluated the maturity of existing fusion methods and analyzed that the fusion method of electric power information based on a communication standard was a well-established methodology. Relatively, there is room for making progress on optimizing fusion methods of electric power information based on machine learning and deep learning, which could achieve the goal of information interconnection for satisfying the requirements in smart grid (e.g., fault detection, electric power consumption prediction). We believe that future research for multi-source electric power information fusion can be carried out from the following four aspects:

The fusion methods are based on multi-modal. Currently, the existing models mainly refine the features from the properties of electric systems or communication standards. However, these methods are not mature enough to contain text information and image data such as fault descriptions recorded by engineers and equipment pictures. The methods based on multi-modal are helpful to improve further the accuracy of electric power information fusion and other related tasks (Yang et al., 2021). On the one hand, the relation extraction models can extract more useful information from the textual descriptions, which can assist the electric power information fusion method; on the other hand, the image recognition technology can be used to improve the granularity for equipment fault type identification. Then, the performances of electric power information fusion can be further enhanced.

The fusion methods are based on federated learning. As the system data associated with charging piles and photovoltaic equipment has a certain degree of privacy, a set of electric power specification systems can be formed based on all levels through consultation among various electric power companies and related platforms. Then, the high-quality data in electric power companies can be encrypted and shared using federal learning (Liu & Meng, 2020). Finally, a high-quality mapping relationship is constructed among electric power grid systems to satisfy more smart grid requirements.

The incremental dynamic information fusion strategy. As too many standards and attributes are increasing in the electric power grid system, it is hard for existing methods to immediately respond to the requirements for updating and iterating electric power systems because the cost of training and fusion of these models is high. In addition, it may not better satisfy the real-time tasks of electric power information. Therefore, incremental dynamic fusion technology (Yu et al., 2020) can be explored to reduce the cost of information fusion and ensure the real-time performance of the system.

The fusion methods are based on an interactive strategy. Considering application scenarios such as equipment fault monitoring requiring high precision, follow-up correction by domain experts is indispensable. Therefore, the interactive fusion strategy (Liu F et al., 2021c; Liu Q et al., 2021) could be adopted so that domain experts can screen the results of fusion methods in each iteration. This way, experts could mark the results that can be reused as training samples for feeding the models. It can not only ensure the reliability of the model results but also improve the fusion accuracy of the electric power information.

Author contributions

KL and YZ contributed to the conception and design of the study. KL and JX wrote parts of the manuscript. HJ gave suggestions to technical support. YH and CP contributed to the improvement of the study design.

Conflict of interest

Authors KL, YZ, JX, and HJ were employed by State Grid Sichuan Information and Communication Company. Author YH was employed by NARI-TECH Nanjing Control Systems Co., Ltd.

The remaining author declares that the research was conducted in the absence of any commercial or financial relationships that could be construed as a potential conflict of interest.

Publisher's note

References

Dai, J., Cao, J., Zhang, F., Liu, D., and Shen, X. (2017). Data pre-processing method and its evaluation strategy of SCADA data from wind farm. *Acta Energiae Solaris Sin.* 38 (9), 2597–2604. doi:10.19912/j.0254-0096.2017.09.038

Darudi, A., Bashari, M., and Javidi, M. H. (2015). Electricity price forecasting using a new data fusion algorithm. *IET Gener. Transm. &amp. Distrib.* 9 (12), 1382–1390. doi:10.1049/iet-gtd.2014.0653

Han, G., Chen, Y., and Xu, B. (2019). Information model for distribution network fault detection and protection based on IEC 61850. *Distribution Util.* 36 (07), 8–12. doi:10.19421/j.cnki.1006-6357.2019.07.002

He, X., Tu, C., and Li, P. (2019). Research on multi-source data fusion for smart distribution network. *South. Power Syst. Technol.* 13 (04), 42–47. doi:10.13648/j.cnki.issn1674-0629.2019.04.007

Henrik, L., and Willett, K. (2008). Integration of renewable energy into the transport and electricity sectors through V2G. *Energy policy* 36 (9), 3578–3587. doi:10.1016/j.enpol.2008.06.007

Jiang, Y., Peng, M., Ma, K., and Li, L. (2019). Evaluation method for power transformer conditions based on multi-source heterogeneous data fusion. *Guangdong Electr. Power* 32 (09), 137.

Kong, C., Chen, Y., and Zhao, Q. (2021). Research on cloud-side communication mapping of the distribution internet of things based on MQTT protocol. *Power Syst. Prot. Control* 49 (08), 168–176. doi:10.19783/j.cnki.pspc.200775

Leitea, L., Boaventuraa, W., Erricoa, L., Cardosoa, E., Dutra, R., and Lopes, B. (2016). Integrated voltage regulation in distribution grids with photovoltaic distribution generation assisted by telecommunication infrastructure. *Electr. Power Syst. Res.* 136, 110–124. doi:10.1016/j.epsr.2016.02.016

Li, G., Yang, L., Liu, F., Yu, M., Song, Y., and Wen, F. (2016). A mutual information method for associated data fusion in energy internet. *Electr. Power Constr.* 37 (09), 22.

Li, G, G., Zhang, X., Wu, T., and Zhang, F. (2021). Research on the maintenance technology of substation autonomous system source end based on IEC 61850. *Process Autom. Instrum.* 42 (07), 68–72. doi:10.16086/j.cnki.issn1000-0380.2020090028

Li, J, J., Li, X., Gao, T., Zhang, J., and Zhang, B. (2021). Research and application of fault handling based on power grid multivariate information knowledge graph. *Electr. Power Inf. Commun. Technol.* 19 (11), 30–38. doi:10.16543/j.2095-641x.electric.power.ict.2021.11.005

Li, Y, Y., Gao, B., Xu, L., Ding, J., Tang, H., and Shan, R. (2021). An anomaly detection method for digital substation abnormal data based on fusion of difference sequence variance and CPS. *Power Syst. Clean Energy* 37 (02), 30.

Lin, Y., Chen, R., and Jin, T. (2020). Research on multi-source heterogeneous data fusion technology for complex information system. *China Meas. Test* 46 (07), 1.

Liu, J., and Meng, X. (2020). Survey on privacy-preserving machine learning. *J. Comput. Res. Dev.* 57 (2), 346. doi:10.7544/issn1000-1239.2020.20190455

Liu, B, B., Scells, H., Zuccon, G., Hua, W., and Zhao, G. (2021). *ActiveEA: Active learning for neural entity alignment.* arXiv preprint arXiv:2110.06474.

Liu, D, D., Kong, D., Chang, Y., Ma, L., and Wang, R. (2020). Multi-source log comprehensive feature extraction based on restricted Boltzmann machine in power information system. *Comput. Syst. Appl.* 29 (11), 210–217. doi:10.15888/j.cnki.csa.007667

Liu, F, F., Chen, M., Roth, D., and Collier, N. (2021). Visual pivoting for (unsupervised) entity alignment. *Proc. AAAI Conf. Artif. Intell.* 35 (5), 4257–4266. doi:10.1609/aaai.v35i5.16550

Liu, Q, Q., Liu, P., Sun, Y., and Zhang, C. (2021). Screening mechanism for priority business of multi-station integration project based on random forest algorithm. *Smart Power* 49 (06), 32

Liu, Q, Q., Liu, X., Tang, W., Jin, H., and Yuan, H. (2020). Analysis of fusion technology of grid communication service data. *Inf. Technol.* 44 (03), 153–158. doi:10.13274/j.cnki.hdzj.2020.03.030

Lu, Z., Yang, Z., Du, C., and He, G. (2020). Research cooperative diagnosis method of substation equipment operation fault based on information fusion technology. *Automation Instrum.* 10, 207–210. doi:10.14016/j.cnki.1001-9227.2020.10.207

Pan, J., Zhang, F., Wang, L., Zhang, J., and Hao, B. (2022). Research on energy data processing technology based on multi-source heterogeneous. *Electron. Des. Eng.* 30 (16), 143–147. doi:10.14022/j.issn1674-6236.2022.16.031

Shantanu, K., Ahmed, A., Narottam, D., and Syed, I. (2021). Toward a substation automation system based on IEC 61850. *Electronics* 10 (3), 310. doi:10.3390/electronics10030310

Shao, X., Kim, C. S., and Sontakke, P. (2020). Accurate deep model for electricity consumption forecasting using multi-channel and multi-scale feature fusion CNN–LSTM. *Energies* 13 (8), 1881. doi:10.3390/en13081881

Shen, J., Cao, R., Su, C., Cheng, C., Li, X., Wu, Y., et al. (2019). Big data platform architecture and key techniques of power generation scheduling for hydro-thermal-wind-solar hybrid system. *Proc. CSEE* 39 (1), 43–55. doi:10.13334/j.0258-8013.pcsee.181546

Shui, Y., Lv, L., and You, B. (2013). Application of data fusion to power system intelligent early warning. *East China Electr. Power* 41 (03), 554.

Suleman, A., Mohammad, H., Haris, M., and Muyeen, S. (2021). Denial-of-service attack on IEC 61850-based substation automation system: A crucial cyber threat towards smart substation pathways. *Sensors* 21 (19), 6415. doi:10.3390/s21196415

Taha, S., and Suhail, S. M. H. (2020). IEC 61850 Modeling of UPFC and XMPP communication for power management in microgrids. *IEEE Access* 8, 141696–141704. doi:10.1109/access.2020.3013264

Wang, H., Wang, B., Dong, X., Yao, L., Zhang, R., Ma, F., et al. (2021). Heterogeneous multi-parameter feature-level fusion for multi-source power sensing terminals: Fusion mode, fusion framework and application scenarios. *Nat. Cell. Biol.* 36 (07), 1314–1328. doi:10.1038/s41556-021-00796-6

Wang, T., Liu, H., Shao, Q., and Yu, B. (2020). Research on intelligent early warning and fault diagnosis technology for the secondary loop of smart substation. *Electr. Meas. Instrum.* 57 (08), 59–63+98. doi:10.19753/j.issn1001-1390.2020.08.010

Wang, B, B., Wang, H., Yao, L., Dong, X., Ma, H., and Ma, F. (2022). Multi-modal data fusion mode for power system and its key technical issues. *Automation Electr. Power Syst.* 46 (19), 188.

Wang, Y, Y., Wang, X., Zhang, S., Zheng, G., Zhao, L., and Zheng, G. (2022). Research on efficient knowledge fusion method for heterogeneous big data environments. *Comput. Eng. Appl.* 58 (06), 142.

Wen, H., and Li, Z. (2018). Simulation of global information fusion for multi-source communication networks. *Comput. Simul.* 35 (01), 188.

Xia, W., Cai, W., Liu, Y., and Li, H. (2022). Multi-source heterogeneous data fusion of a distribution network based on a joint Kalman filter. *Power Syst. Prot. Control* 50 (10), 180–187. doi:10.19783/j.cnki.pspc.211485

Xue, Y., and Lai, Y. (2016). Integration of big energy thinking and big data thinking (1) big data and electric power big data. *Automation Electr. Power Syst.* 40 (01), 1. doi:10.7500/AEPS20151208005

Xyngi, I., and Popov, M. (2010). IEC61850 overview-where protection meets communication." in 10th IET International Conference on Developments in Power System Protection (DPSP 2010). Managing the Change IET.

Yang, Y., Zhan, D., Jiang, Y., and Xiong, H. (2021). Reliable multi-Modal learning: a survey. *J. Softw.* 32 (4), 1067–1081.

Yao, J., and Lai, Y. (2010). The essential cause and technical requirements of the smart grid. *Automation Electr. Power Syst.* 34 (02), 1.

Yu, H., He, D., Wang, G., Li, J., and Xie, Y. (2020). Data for intelligent decision making. *Acta Autom. Sin.* 46 (05), 878. doi:10.16383/j.aas.c180861

Zhang, D., Yao, L., and Ma, W. (2013). Development strategies of smart grid in China and abroad. *Proc. CSEE* 33 (31), 1–15. doi:10.13334/j.0258-8013.pcsee.2013.31.001

Zhao, W., Xiong, N., Ning, N., Li, Y., Gu, Z., and Li, H. (2021). Multi-layer intelligent fault diagnosis method of power grid based on multi-source information fusion. *South. Power Syst. Technol.* 15 (09), 9–15. doi:10.13648/j.cnki.issn1674-0629.2021.09.002

Zhu, Z., Xu, B., Christoph, B., Tony, Y., and Yu, C. (2017). IEC 61850 configuration solution to distributed intelligence in distribution grid automation. *Energies* 10 (4), 528. doi:10.3390/en10040528

frontiers | Frontiers in Energy Research

TYPE Original Research
PUBLISHED 18 January 2023
DOI 10.3389/fenrg.2022.1053498

EDITED BY
Yingjun Wu,
Hohai University, China

REVIEWED BY
Jianli Yu,
Weifang University, China
Qiushi Cui,
Arizona State University, United States
Na Li,
Delft University of Technology,
Netherlands

*CORRESPONDENCE
Yonghui Nie,
✉ nieyonghui@neepu.edu.cn

SPECIALTY SECTION
This article was submitted
to Smart Grids,
a section of the journal
Frontiers in Energy Research

RECEIVED 25 September 2022
ACCEPTED 30 November 2022
PUBLISHED 18 January 2023

CITATION
Lv G, Ji Y, Zhang Y, Wang W, Zhang J, Chen J and Nie Y (2023), Optimization of building microgrid energy system based on virtual energy storage. *Front. Energy Res.* 10:1053498. doi: 10.3389/fenrg.2022.1053498

Optimization of building microgrid energy system based on virtual energy storage

Guangxian Lv[1], Yu Ji[1], Ying Zhang[1], Wenbo Wang[1], Jie Zhang[2], Jikai Chen[2] and Yonghui Nie[2]*

[1]State Grid Shanghai Energy Interconnection Research Institute, Shanghai, China, [2]School of Electrical Engineering, Northeast Electric Power University, Jilin, China

With the continuous development of building microgrids, it is crucial to explore and study the energy-saving potential of buildings to resolve energy shortages and environmental protection problems. Therefore, to realize the efficient and economical operation of a building microgrid, a new multi-objective optimization method is proposed for the planning and operation of building microgrid considering virtual energy storage. First, virtual energy storage model of the building microgrid is established based on the heat storage characteristics of the building itself. Second, a multi-objective optimization model of the building microgrid considering virtual energy storage is constructed by considering the investment cost and the comprehensive operation benefits as the objectives as well as the constraints of cooling, heating, power balance. Finally, based on the original gray wolf swarm algorithm, the niche processing mechanism and gray weighted correlation method are introduced to optimize the configuration and operation of the building microgrid. For a typical building microgrid in summer and winter, the simulation results reveal that the proposed method improves the overall economy of planning the building microgrid system and its operation and user experience *via* virtual energy charge and discharge management.

KEYWORDS

building heat storage characteristics, building microgrid, gray weighted correlation degree, multi-objective optimization, virtual energy storage

1 Introduction

Promoting the development of clean energy systems based on distributed energy is a major strategic choice worldwide. At present, research has shown that the proportion of energy consumption in the end-use energy systems of buildings is increasing annually, which has significant potential for energy conservation and emission reduction. Therefore, energy-saving solutions for mining buildings have become crucial approaches to solve the shortage of energy demand and achieve the double carbon goal (Dounis et al., 2009; Zhao et al., 2015).

A building microgrid system is a multi-energy joint energy supply system formed by integrating natural gas, heating, energy storage, and distributed energy systems along with related technologies into the building energy supply system. To ensure the safe and reliable operation of the system, it is effective to use the diversity of energy supply modes to satisfy the diversified needs of users and use the energy storage system and related control technologies to reduce the impact of fluctuations in the output of clean energy (Guan et al., 2010; Hca et al., 2021). Owing to the integration of supply side energy supply, renewable energy, and demand side cold/heat/electricity load demand, and other elements in the system, new requirements are proposed as follows: 1) ensure the consumption of renewable energy. 2) realize the complementary advantages of various forms of energy on the supply side and cooperative configuration operation to reduce the operation cost of the microgrid. 3) and ensure the energy optimization management for safe and economic operation of the building microgrid system (Wang et al., 2021; Chang et al., 2022).

At present, there has been research progress on the optimal configuration strategy of microgrid energy systems. Liu et al. (2019) proposed a comprehensive energy planning strategy based on the improved kriging model, which rapidly and accurately obtained the optimal capacity allocation scheme of the system. Bahmani et al. (2021) established a cooperative method in which a network of energy hubs collaborates to share adjustable energy. Each hub comprises a combined heat and power unit, electrical chiller, renewable sources, absorption chiller, and boiler. Mixed integer linear programming was used to determine the optimal comprehensive economic cost of the system. Li et al. (2020) considered the uncertainty of wind power and proposed a comprehensive energy system planning strategy based on a scenario method, aiming at investment and wind curtailment costs. Qiu et al. (2015) developed a microgrid energy system planning model to minimize the total investment cost based on the electrical-pneumatic coupling phenomenon. To obtain both the optimal structural configuration and energy management dispatch for multi-energy systems, a generic optimal planning framework was proposed in (Ma et al., 2018) and mixed-integer linear programming was employed to minimize the overall cost. Han et al. (2018) considered the volatility of distributed energy resources, net income of the entire operation cycle, penetration of renewable energy, and reliability of the power supply, and established a three-objective two-stage planning model. Lin et al. (2021) considered the economy and reliability of an integrated energy system and proposed a planning model based on an improved collaborative algorithm to coordinate the complex relationship between the two performance indexes, and they verified the effectiveness of the model using a practical example. Based on the above literature, it is evident that for integrated energy system research, the minimum operating cost of the system is usually selected as the optimization objective, and there are several deterministic constraints, such as power balance and equipment output. However, load changes caused by environmental costs and temperature constraints is given less priority.

Simultaneously, by exploiting the complementary characteristics of various power sources in the building microgrid energy system, peak shaving and valley filling can be realized and the energy utilization rate can be improved through the charge and discharge regulation of the energy storage system. However, the initial investment in configuring energy storage equipment is high, and virtual energy storage technology provides a potential solution to the problem. Wang et al. (2020) conducted a detailed study on the virtual energy storage technology of an air conditioning load, established a virtual energy storage energy model, and verified the feasibility of using the virtual energy storage of an air conditioning load for power grid regulation. Zhu et al. (2019) considered virtual energy storage on the user side and established a comprehensive energy system scheduling model including the temperature control load and electric vehicle with consideration of the uncertainty of weather. The simulation results reveal that virtual energy storage has a positive significance in reducing the capacity of energy storage equipment. Jin et al. (2017) considered the characteristics of virtual energy storage and battery-coordinated operation and proposed a control strategy for stabilizing the power fluctuation of a microgrid tie line. Currently, research on the joint optimization of the energy storage optimization link and other energy supply equipment in building microgrid energy systems needs more in-depth analysis.

In summary, this paper proposes a method for capacity configuration and operation optimization of building microgrid systems considering virtual energy storage through the optimal adjustment of temperature. The main contributions of this study are the following.

1) Based on the thermal storage characteristics of buildings, a virtual energy storage system model of the building microgrid is constructed. The charge and discharge management of virtual energy storage is realized to achieve low-carbon operation of building microgrid systems.
2) The proposed strategy considers the principle of virtual energy storage to construct a multi-objective optimization model to improve the operation economy of the building microgrid.
3) The comprehensive benefits and user satisfaction are introduced as the objectives. Under meeting customer satisfaction index, the proposed strategy increases comprehensive benefits through virtual energy storage charging and discharging management.
4) The gray wolf algorithm based on niche technology was employed to solve the optimization problem. Based on the non-dominated solution set, the optimal solution of the system configuration and operation was obtained using the gray-weighted correlation degree evaluation index.

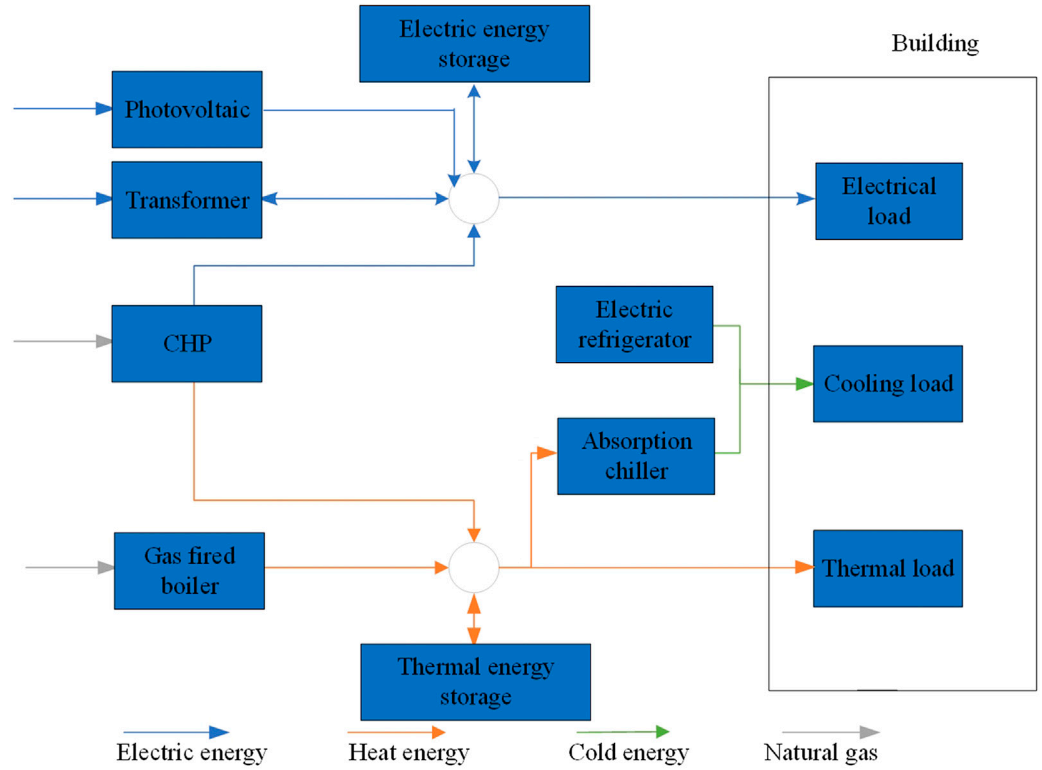

FIGURE 1
Schematic of the building microgrid system.

5) Structure and mathematical model of building microgrid system

2 Structure of building microgrid system

With the continuous development of distributed energy technology, various energy equipment, such as refrigeration units, gas turbines, heat storage tanks, energy storage equipment, and PV equipment, are connected to buildings. This energy equipment can realize complementary and cooperative effects among energy sources to satisfy the diversified needs of users and improve the overall operational efficiency of the system (Favre-Perrod, 2005; Pazouki et al., 2014).

In this study, a variety of energy devices were applied to a building microgrid system, the structure of which is illustrated in Figure 1. Absorption chillers and electric chillers satisfy the cooling demand of buildings, and the cooling power of absorption chillers originates from gas turbines. The thermal power demand originates from the gas turbine, thermal storage system, and virtual energy storage system in the building. The virtual thermal energy storage is the indoor energy change caused by the temperature change. The electric load power originates from photovoltaics, energy storage equipment, and the external power grid. From the above process, it is evident that the building microgrid system formed by the cold thermal–electrical structure and the external power grid are interconnected.

3 System modeling

3.1 Photovoltaic device

Photovoltaic equipment can convert solar radiation energy into electrical energy *via* photovoltaics, and the conversion efficiency primarily depends on the illumination and ambient temperature, which can be expressed as follows (Ma et al., 2016):

$$P_{pv,t} = \eta \times Y_{pv}\left(\frac{I_T(t)}{I_S}\right), \tag{1}$$

where η represents the energy conversion efficiency (%), Y_{pv} indicates the capacity of the photovoltaic panel (kW), $I_T(t)$

represents the solar radiation intensity (kW/m^2) received by the photovoltaic panel at time t, and $I_s = 1$ kW/m^2.

3.2 Electric refrigerator

The refrigerator was cooled by consuming electric energy, and its cooling power was as follows:

$$Q_{EC,t} = P_{EC,t} I_{COP}^{EC}, \tag{2}$$

where I_{COP}^{EC} indicates the ratio of the rated cooling capacity to the rated power of the electric refrigerator, $Q_{EC,t}$ corresponds to the refrigeration power (kW), and $P_{EC,t}$ denotes the electric power consumed (kW).

3.3 Micro gas turbine

The active power output of the micro gas turbine is as follows:

$$P_{mt,t} = \eta_{mt} P_{gas}, \tag{3}$$

where η_{mt} indicates the power generation efficiency of the micro gas turbine, $P_{mt,t}$ denotes the active output (kW), and P_{gas} represents the natural gas power consumed (kW).

3.4 Absorption chiller

The small gas turbine drives the absorption chiller through the residual energy in the industrial production process, and its cooling power is as follows:

$$Q_{AC,t} = H_{AC,t} I_{COP}^{AC}, \tag{4}$$

where $H_{AC,t}$ indicates the heat consumption power (kW), I_{COP}^{AC} denotes the ratio of the rated cooling capacity to the rated power of the absorption chiller, and $Q_{AC,t}$ represents the cooling power (kW).

3.5 Energy storage device

We adopted the conventional battery model, and the change relationship of the state of charge is as follows:

$$SOC_{bt}(t) = SOC_{bt}(t-1) + \frac{\left[S_{ch}(t) P_{ch}(t) \eta_{ch} - \left(S_{dis}(t) P_{dis}(t) / \eta_{dis}\right)\right] \Delta t}{S_{bt}^{max}}, \tag{5}$$

where $SOC_{bt}(t)$ represents the state of charge of the battery, P_{ch} and P_{dis} denote the charging and discharging powers of the battery (kW), respectively, η_{ch} and η_{dis} denote the charging and discharging efficiencies, respectively, and $S_{sh}(t)$ and $S_{dis}(t)$ represent the charge and discharge states of the battery, respectively.

3.6 Heat storage device

The heat-storage model is similar to the energy-storage battery model, and the relationship between the state of charge and heat power is as follows (Lu et al., 2015):

$$SOC_H(t) = SOC_H(t-1) + \frac{\left[P_{ch,H}(t) \eta_{ch,H} - \left(P_{dis,H}(t) / \eta_{dis,H}\right)\right] \Delta t}{S_H^{max}}, \tag{6}$$

where SOC_H(t) indicates the state of charge, $P_{ch,H}$ and $P_{dis,H}$ denote the heat charging and discharging power (kW), respectively, and $\eta_{ch,H}$ and $\eta_{dis,H}$ refer to the heat charging and discharging efficiencies, respectively, $S_H{}^{max}$ denotes the capacity of the heat storage device (kW).

3.7 Building virtual energy storage system

A building can be regarded as a heat storage body because of its thermal inertia and heat storage characteristics of indoor air. Thus, when the indoor temperature changes within a certain range are compared with the constant set temperature, the heating or cooling capacity of the building also changes correspondingly relative to the cooling and heating capacity at a constant set temperature. This change can be regarded as the characteristics of the virtual energy storage of the building, and the difference in the value of this heat change can be regarded as the storage and discharge power of the virtual energy storage (the heat change caused by the difference between the set value and the actual value of the temperature).

The relationship between heat inside and outside the building and temperature is:

$$\begin{aligned} Q_H - Q_d &= C \times \rho \times V \times \frac{d(T_{out} - T_{in})}{dt}, \\ Q_d - Q_{AC} &= C \times \rho \times V \times \frac{d(T_{in} - T_{out})}{dt}. \end{aligned} \tag{7}$$

Eq. 7 represents the two operating conditions of heating in winter and cooling in summer: where Q_H indicates the heating power in winter (kW), Q_d denotes the heat dissipation power of the building (kW), Q_{AC} corresponds to the cooling power in summer (kW), ρ symbolizes the air density (kg/m^3), C denotes the specific heat capacity of the air (J/(kg.°C)), V refers to the indoor volume (m^3), and T_{out} and T_{in} are the indoor and outdoor temperatures (°C), respectively.

Taking summer cooling as an example, the key factors affecting the heat change in the building include three parts:

the indoor heat change caused by solar radiation, difference between the heating power, and the cooling equipment power in the building, as shown below:

$$\begin{aligned} &K_{\mathrm{wa}} S_{\mathrm{wa}} \left(T_{\mathrm{out}} - T_{\mathrm{in}}\right) + K_{\mathrm{wi}} S_{\mathrm{wi}} \left(T_{\mathrm{out}} - T_{\mathrm{in}}\right) \\ &+ I S_{\mathrm{wi}}\, SC + Q_{\mathrm{in}} - Q_{\mathrm{cl}} = \Delta Q, \end{aligned} \tag{8}$$

where ΔQ indicates the indoor heat change value of the building (kW), K_{wa} and K_{wi} denote the heat transfer coefficients of the outer wall and the outer window (W/(m^2 K)), respectively, S_{wa} and S_{wi} denote the area of outer wall and outer window (m^2), respectively, I indicates the solar radiation intensity (kW/m^2), SC denotes the shading coefficient, Q_{in} denotes the heating power in the building (kW), and Q_{cl} indicates the cooling power (kW).

4 Operation model of building optimal configuration

4.1 Objective function

In the capacity allocation process, with the goal of minimizing the comprehensive benefit of building equipment and equipment investment costs, a multi-objective optimization function is constructed as follows:

$$\min \begin{cases} F_1 = \dfrac{1}{C_1 + C_3 - C_2}, \\ F_2 = C_4, \end{cases} \tag{9}$$

where F_1 indicates the comprehensive income of the building micro network (1/yuan), C_1 represents the operation and maintenance cost of the equipment in the building (yuan), C_2 represents the comprehensive income and user satisfaction of the building (yuan), C_3 represents the environmental and fuel costs of the building microgrid system (yuan), and F_2 refers to the investment cost of each piece of equipment of the building microgrid system (yuan), expressed by C_4.

4.2 Objective function F_1

4.2.1 Operation and maintenance cost

$$\begin{aligned} C_1 = \sum_{t=1}^{N} \big(& C_{\mathrm{pv}} P_{\mathrm{pv,t}} + C_{\mathrm{bt}} P_{\mathrm{bt,t}} + C_{\mathrm{ec}} P_{\mathrm{ec,t}} + C_{\mathrm{gas}} P_{\mathrm{gas},t} \\ & + C_{\mathrm{H}} P_{\mathrm{H,t}} + C_{\mathrm{ac}} P_{\mathrm{ac,t}} + C_{\mathrm{ph},t} P_{\mathrm{ex},t} \big) \Delta t, \end{aligned} \tag{10}$$

where C_{pv}, C_{bt}, C_{ec}, C_{gas}, C_{H}, and C_{ac} denote the unit time operation and maintenance costs (yuan/kWh) of photovoltaic devices, batteries, electric refrigerators, micro gas turbines, heat storage tanks, and absorption chillers, respectively, $P_{\mathrm{ex,t}}$ indicates the electric power exchanged between the building microgrid and the external power grid (kW); $C_{\mathrm{ph,t}}$ denotes the unit power purchase cost at t (yuan/kWh), which adopts the time-of-use price to guide the user's power consumption behavior, $P_{\mathrm{pv,t}}$, $P_{\mathrm{bt,t}}$, $P_{\mathrm{ec,t}}$, $P_{\mathrm{mt,t}}$, $P_{\mathrm{H,t}}$, and $P_{\mathrm{ac,t}}$ refer to the outputs (kW) of photovoltaic device, storage battery, electric refrigerator, micro gas turbine, heat storage tank, and absorption refrigerator, respectively, at time t; $N = 24$, $\Delta t = 1$.

4.2.2 Comprehensive income and user satisfaction

$$C_2 = \sum_{t=1}^{N} \Big(\left(C_{\mathrm{pvsu}} P_{\mathrm{pv,t}} + C_{\mathrm{btsu}} P_{\mathrm{bt.t}} \right) \Delta t + \lambda \left| T_{\mathrm{in,t}} - T_{\mathrm{set}} \right| \Big), \tag{11}$$

where the first item indicates the photovoltaic consumption income, and C_{pvsu} denotes the photovoltaic subsidy price (yuan/kWh). The second item corresponds to the peak-shaving income from energy storage, and C_{btsu} refers to the peak-shaving auxiliary service price, $P_{\mathrm{bt,t}}$ indicates the battery power participating in the peak-shaving period t (kW). The energy storage device was charged at the low-load valley and discharged at a high load peak. Through the low storage and high discharge mechanism, it can fill the valley and cut the peak, and increase the peak regulation income of the system. The third item is user satisfaction; λ denotes the energy penalty factor, $T_{\mathrm{in,t}}$ indicates the actual temperature in the building, and T_{set} represents the set temperature (°C).

4.2.3 Environmental cost and fuel cost

$$C_3 = \sum_{t=1}^{N} \left(K_{\mathrm{SP}} C_S + K_{\mathrm{NP}} C_N + K_{\mathrm{CP}} C_C \right) P_{\mathrm{mt},t} \Delta t + \sum_{t=1}^{N} C_{\mathrm{mt}} P_{\mathrm{mt},t} \Delta t, \tag{12}$$

where the first term indicates the environmental cost, and K_{sp}, K_{np}, and K_{cp} denote the emission intensities of SO_2, NO_x, and CO_2, respectively, produced by the gas turbine, which are 0.01026, 0.01702, and 0.000928 kg/kWh, respectively (Zhang et al., 2017; EPA et al., 2021). $P_{\mathrm{mt,t}}$ indicates the output (kW) of the gas turbine at time t, and C_{s}, C_{n}, and C_{c} represent the unit treatment costs of SO_2, NO_x, and CO_2 produced by the gas turbine, which are 0.21, 0.13, and 14.824 yuan/kg, respectively (Zhang et al., 2017; EPA et al., 2021). The second item indicates the fuel cost; C_{mt} denotes the fuel cost per hour of the unit gas turbine, which is 0.3894 yuan/kWh.

4.2.4 Objective function F_2

$$C_4 = \left(S_{\mathrm{mt}} c_{\mathrm{mt}} + S_{\mathrm{bt}} c_{\mathrm{bt}} + S_{\mathrm{ec}} c_{\mathrm{ec}} + S_{\mathrm{pv}} c_{\mathrm{pv}} + S_{\mathrm{ac}} c_{\mathrm{ac}} + S_{\mathrm{H}} c_{\mathrm{H}} \right), \tag{13}$$

where S_{mt}, S_{bt}, S_{ec}, S_{pv}, S_{ac}, and S_{H} denote the installation capacities (kW) of the micro gas turbine, battery, electric refrigerator, photovoltaic device, absorption refrigerator, and heat storage tank, respectively, and c_{mt}, c_{bt}, c_{ec}, c_{pv}, c_{ac}, and c_{H} denote the unit capacity installation costs (yuan/kW) of the micro gas turbine, battery, electric refrigerator, photovoltaic device, absorption chiller, and heat storage tank, respectively.

4.3 Constraints

4.3.1 Electric power balance constraint

$$P_{\mathrm{ex},t} + P_{\mathrm{PV},t} + P_{\mathrm{bt},t} = P_{\mathrm{el},t} + P_{\mathrm{EC},t}, \tag{14}$$

where $P_{\mathrm{el},t}$ indicates the electric power load (kW) at time t and $P_{\mathrm{ex},t}$ represents the power (kW) of the connecting line; that is, the electric power exchanged between the building microgrid and the external power grid.

4.3.2 Cooling power constraint

$$Q_{\mathrm{AC},t} + Q_{\mathrm{EC},t} = Q_{\mathrm{cool},\,t}, \tag{15}$$

where $Q_{\mathrm{cool,t}}$ is the cooling power load (kW) at time t.

4.3.4 Thermal power balance constraint

$$Q_{\mathrm{heat},t} - Q_{\mathrm{out},t} - \eta_{\mathrm{eh}} P_{\mathrm{mt},t} = \Delta Q, \tag{16}$$

where $Q_{\mathrm{heat},t}$ denotes the thermal power load (kW) at time t, $Q_{\mathrm{out},t}$ represents the thermal power output (kW) of the thermal storage device at time t, and η_{eh} denotes the electric heating ratio of the micro-gas turbine.

4.3.5 Equipment configuration and operating output upper and lower limit constraints

$$\begin{cases} S_{\mathrm{EC}}^{\min} \le S_{\mathrm{EC}} \le S_{\mathrm{EC}}^{\min}, \\ S_{\mathrm{mt}}^{\min} \le S_{\mathrm{mt}} \le S_{\mathrm{mt}}^{\max}, \\ P_{\mathrm{ex}}^{\min} \le P_{\mathrm{ex}} \le P_{\mathrm{ex}}^{\max}, \\ P_{\mathrm{EC}}^{\min} \le P_{\mathrm{EC}} \le P_{\mathrm{EC}}^{\min}, \\ P_{\mathrm{mt}}^{\min} \le P_{\mathrm{mt}} \le P_{\mathrm{mt}}^{\max}, \end{cases} \tag{17}$$

where Smin * and Smax * represent the lower and upper capacity limits of each device (kW), respectively, and Pmin * and Pmax * denote the lower and upper output limits of each device (kW), respectively.

4.3.6 Constraints related to energy storage system

Charging and discharging power constraint:

$$\begin{cases} 0 \le P_{\mathrm{dis}}(t) \le P_{\mathrm{dis}}^{\max} S_{\mathrm{dis}}(t), \\ 0 \le P_{\mathrm{ch}}(t) \le P_{\mathrm{ch}}^{\max} S_{\mathrm{ch}}(t). \end{cases} \tag{18}$$

Charging and discharging state transition constraint:

$$S_{\mathrm{ch}}(t) + S_{\mathrm{dis}}(t) = 1. \tag{19}$$

Power storage constraints:

$$SOC_{\mathrm{bt}}^{\min} \le SOC_{\mathrm{bt}}(t) \le SOC_{\mathrm{bt}}^{\max}. \tag{20}$$

Configure capacity constraints:

$$S_{\mathrm{bt}}^{\min} \le S_{\mathrm{bt}}(t) \le S_{\mathrm{bt}}^{\max}, \tag{21}$$

where P_{ch} max and P_{dis} max denote the maximum power (kW) of the charge and discharge, respectively; $SOC_{\mathrm{bt}}^{\max}$ and $SOC_{\mathrm{bt}}^{\min}$ represent the upper and lower limits of the state of charge of the battery, respectively; and $S_{\mathrm{bt}}^{\max}$ and $S_{\mathrm{bt}}^{\min}$ represent the upper and lower limits of the configuration capacity (kW), respectively.

4.3.7 Indoor temperature expectation interval constraint

$$T_{\mathrm{in}}^{\min} \le T_{\mathrm{in}} \le T_{\mathrm{in}}^{\max}, \tag{22}$$

where Tmax and Tmin denote the expected upper and lower limits of the indoor temperature (°C), respectively.

5 Multi-objective solution strategy

We optimize the configuration of various types of equipment in a building based on virtual energy storage. The optimal mathematical model is established with the state of charge of the battery, output of the refrigerator, input and output power of the heat storage system, and indoor temperature of the building as the decision variables. The constraints include the power balance of the cooling, heating, and power loads; the upper and lower limits of the equipment; and the constraints of the equations and inequalities related to the energy storage system. It is difficult to solve complex problems with many variables and constraints using traditional algorithm strategies; therefore, this study introduces an improved multiparticle swarm wolf optimization (MPSWO) to optimize the solution. Based on the original swarm wolf algorithm, the niche processing mechanism and gray weighted correlation index are introduced, and the population diversity and self-regulation ability are introduced into the PSWO algorithm (Mirjalili et al., 2014).

5.1 Niche technology

Niche technology forms a niche for each wolf based on the distance between wolves. Using the update iteration principle of particle swarm optimization algorithm, the wolves in the wolf group are also regarded as a group of particles.

Subsequently, the PSO algorithm is employed to update each group of particles once in speed and position. For the updated particle swarm returning to the wolf swarm, a sharing mechanism is employed to improve the hunting ability of the wolves and provide the best location according to the distance between the wolves. The crowding distance of the gray wolf is improved based on the notion of particle swarm optimization and can be expressed as

$$d_{ij} = \|x_i - x_j\| = \sqrt{\sum_{k=1}^{N}\left(x_{ik} - x_{jk}\right)^2}, \tag{23}$$

where x_i and x_j represent any 2 Gy wolves. For a given parameter, the fitness can be expressed as

$$f_i^1 = \frac{f_i}{\sum_{j=1}^{N} S\left(d_{ij}\right)}, \tag{24}$$

where f_i represents the original fitness and $S\ (d_{ij})$ represents the sharing function. When the distance between the gray wolves is less than the radius R of the small mirror, the sharing function can be calculated as follows:

$$S\left(d_{ij}\right) = 1 - \left(\frac{d_{ij}}{R}\right)^{\lambda}, \tag{25}$$

where λ symbolizes the shape parameter.

5.2 Non-dominated sorting selection strategy based on gray weighted correlation degree

The gray correlation degree analysis method is based on the similarity between the obtained non-dominated solution set curve and optimal dominated curve. The closer the curve, the higher the degree of correlation between the corresponding sequences and the higher the ranking priority. The gray weighted correlation degree was obtained by combining the analytic hierarchy process to select the optimal solution. The steps are as follows (Si et al., 2019).

5.2.1 Preprocessing of objective function matrix

The objective function data matrix is calculated. Because the dimensions of each objective of the proposed optimization strategy are inconsistent, it is necessary to conduct dimensionless processing; thus, the following matrix can be obtained:

$$F = \left[f_i(k)\right]_{N\times m}, \tag{26}$$

where $f_i(k) = (\tilde{f}_i(k)/f_i(1))\,(k = 1, 2, \ldots m, i = 1, 2, \ldots N)$, $\tilde{f}_i(k)$ indicates the original value, and $f_i(1)$ the first element of the vector f_i.

5.2.2 Calculating the gray relational degree

First, the intermediate difference matrix is obtained to obtain the minimum difference a and maximum difference b. Then, according to the correlation coefficient formula, the correlation coefficient matrix is calculated as follows:

$$\begin{cases} a = \min_i \min_k \left|f_0(k) - f_i(k)\right|, \\ b = \max_i \max_k \left|f_0(k) - f_i(k)\right|, \\ Y = \left[y_i(k)\right]_{N\times m}, \\ y\left(f_0(k), f_i(k)\right) = \dfrac{a + \mu b}{\left|f_0(k) - f_i(k)\right| + \mu b}, \end{cases} \tag{27}$$

where μ is the resolution coefficient, usually taken as 0.5.

1) Determining the corresponding weight of each optimization objective

The corresponding weight ω_k of the kth optimization index is determined based on the analytic hierarchy process, as shown in Eqs 28, 29:

$$R = \begin{bmatrix} r_{11} & r_{12} & \cdots & r_{1m} \\ r_{21} & r_{22} & \cdots & r_{2m} \\ \vdots & \vdots & \ddots & \vdots \\ r_{m1} & r_{m2} & \cdots & r_{mm} \end{bmatrix}, \tag{28}$$

$$\omega_k = \frac{1}{m}\sum_{j=1}^{m}\frac{r_{kj}}{\sum_{l=1}^{m} r_{lj}}\,(k = 1, 2, \ldots, m), \tag{29}$$

where r_{ij} indicates the relative importance of optimization objectives i and j.

5.2.3 Determining the gray weighted correlation degree

The gray weighted correlation degree of the ith optimal solution of the Pareto solution set is calculated using Eq. 30

$$\xi_i = \sum_{k=1}^{n}\omega_i y\left(x_0(k), x_{\mathrm{i}}(k)\right). \tag{30}$$

According to the size of the gray weighted correlation degree, the solution set is sorted, and a compromise solution is selected. The higher the degree of correlation, the higher is the ranking priority.

5.3 Solution procedure

Initialization algorithm parameters: The population size of the gray wolf was $N = 50$, and the maximum iteration number was iterax = 100. The initial populations that meet the upper and lower limit constraints of each equipment inequality in the building were randomly generated. Each individual is represented as the feasible value of all control

TABLE 1 Equipment electrical parameters.

Parameter	Value
Micro-turbine efficiency	0.3
Micro gas turbine thermoelectric ratio	1.47
Micro gas turbine power upper and lower limit (kW)	650/0
Electric refrigerator energy efficiency ratio	4
Upper and lower limit of state of charge (pu)	0.9/0.1
Upper and lower limit of battery configuration capacity (kWh)	850/0
Maximum charge and discharge power (kW)	300
Battery charging efficiency	0.95
Battery discharge efficiency	0.95
Photovoltaic use and maintenance cost (yuan/kWh)	0.06
Battery maintenance cost (yuan/kWh)	0.03
Maintenance cost of electric refrigerator (yuan/kWh)	0.01
Maintenance cost of micro gas turbine (yuan/kWh)	0.04
Photovoltaic subsidy electricity price (yuan/kWh)	0.45
Electricity price for peak shaving auxiliary services (yuan/kWh)	0.35
Use energy penalty factor	0.5
Set temperature (°C)	22.5–25

variables and coded according to real numbers. Vector u_{ij} represents the jth equipment control variable of the ith individual, and $u_{ij}{}^{\max}$ and $u_{ij}{}^{\min}$ represent their upper and lower limits, respectively.

1) Calculate the fitness value of each wolf in the population, and select the first three best wolves to save them as α, β, and γ.
2) According to the four steps of the gray wolf algorithm, including encirclement, hunting, attack, and search, update the current gray wolf individual position and relevant algorithm parameters.
3) Randomly add M new gray wolves to maintain population diversity.
4) According to niche technology and fitness-sharing mechanisms (23)–(25), adjust the fitness of individuals in the niche.
5) Adopt roulette strategy to select N excellent gray wolves to enter the next-generation and calculate the fitness to obtain the global optimal value.
6) Determine whether the number of iterations is satisfied; if the number of iterations iter is greater than the maximum number of iterations iter$^{\max}$, end the loop and output the result, and obtain the compromise solution by sorting according to the gray weighted correlation degree; otherwise, proceed to step 2).

6 Case study

6.1 Input data and assumptions

The commercial complex is located at 37°54′N, 112°33′E. The building is a single-family building with a length of 70 m, width of 50 m, a 3-storey height, and a total of 33 floors. The exterior walls of the building are made of cement bricks, the windows are made of PVC material and plastic, and double-layer sound insulation vacuum glass is used. The location of the commercial complex is a provincial capital city facing north. Based on the survey data and the relationship between the building windows and the direct angle of the Sun, this study approximately takes $\mathrm{IS}_{win}SC$ as $0.45IS_{\mathrm{win}}$, and the air density ρ and air specific heat capacity C are respectively considered as 1.2 kg/m^3 and 1000 J/kg°C; centralized office hours are from 8:00 to 20:00.

When the time-of-use electricity price is adopted, the electricity price and load changes can be effectively transmitted to the user side to guide and change the electricity consumption behavior of users, thereby improving the economic level of the building microgrid operation. In this study, the time-of-use electricity price is utilized to purchase the electricity shortage of the microgrid from the external power grid to guide the electricity consumption behavior of users in the building. The electricity price is 0.65 yuan/kWh from 10 to 20 h, and the electricity price is 0.45 yuan/kWh from 0 to 9 h and 21–24 h. The price of natural gas is 2.68 yuan/m^3, and the price of its equivalent unit calorific value is 0.45 yuan/kWh. The upper limit of the tie line power between the building microgrid and the external grid is set to 400 kW, while the other simulation-related parameters are listed in Table 1.

6.2 Simulation example and result analysis

To verify the effectiveness of the building comprehensive energy optimization model and optimization algorithm proposed in this study, the initial values of the optimization variables are obtained according to a uniform distribution within the constraint range, and the following two scenarios are set for calculation and analysis:

Case 1. Optimization of a single scene in winter (December);
Case 2: Optimization of a single scene in summer (June);

6.3 Typical scenarios in winter

For the Case 1 scenario, December is winter in the north, the solar light intensity is low, and the temperature difference between day and night is large. To improve the energy-saving

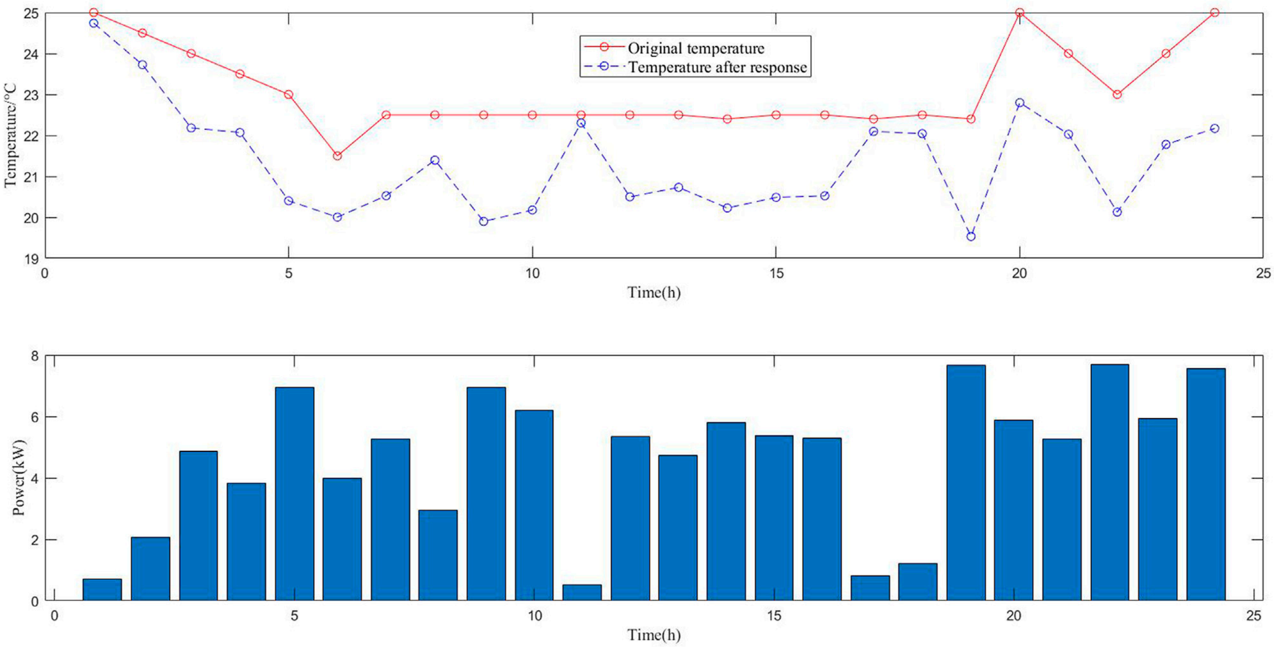

FIGURE 2
Building virtual energy storage and temperature change.

TABLE 2 Optimization results of building microgrid system for Case 1.

Equipment name	Capacity	Investment cost/yuan	Operation and maintenance cost/yuan
Battery	375/kWh	562,500	180
Gas Turbine	650/kW	130,000	468
Photovoltaic	60/kW	60,000	115.2
Heat storage tank	200/kW	14,400	57.6
Electric refrigerator	50/kW	20,000	48
Absorption chiller	200/kW	16,000	120

level of the building microgrid system, based on the principle of virtual energy storage in buildings, the temperature in the building is actively reduced in winter, forming a virtual energy storage thermal load response of the building, as illustrated in Figure 2. Based on the virtual energy storage of this building, the optimal configuration calculation in the typical scenario of Case 1 is performed, and the typical daily operation results are listed in Table 2.

It is evident from the results in Table 2 that solar energy resources are not particularly abundant in winter, and the photovoltaic configuration capacity is small, as presented in Figure 3. The primary function of the electric energy storage system is to cooperate with the photovoltaic system to enhance the utilization rate of photovoltaics simultaneously, play the role of peak shaving and valley filling and emergency load support, and improve the economic level of the comprehensive energy system of the building. The capacity of the battery energy storage system is configured to 375 kWh.

As the main energy supply equipment of the building system, the gas turbine provides electricity and thermal power to the building system, and is the main adjustment method for the building microgrid integrated energy system. Ensuring a reliable supply of heat load is also one of the reasons for the larger configuration of gas turbines.

The absorption refrigeration unit converts the heat generated by the gas turbine power generation into the

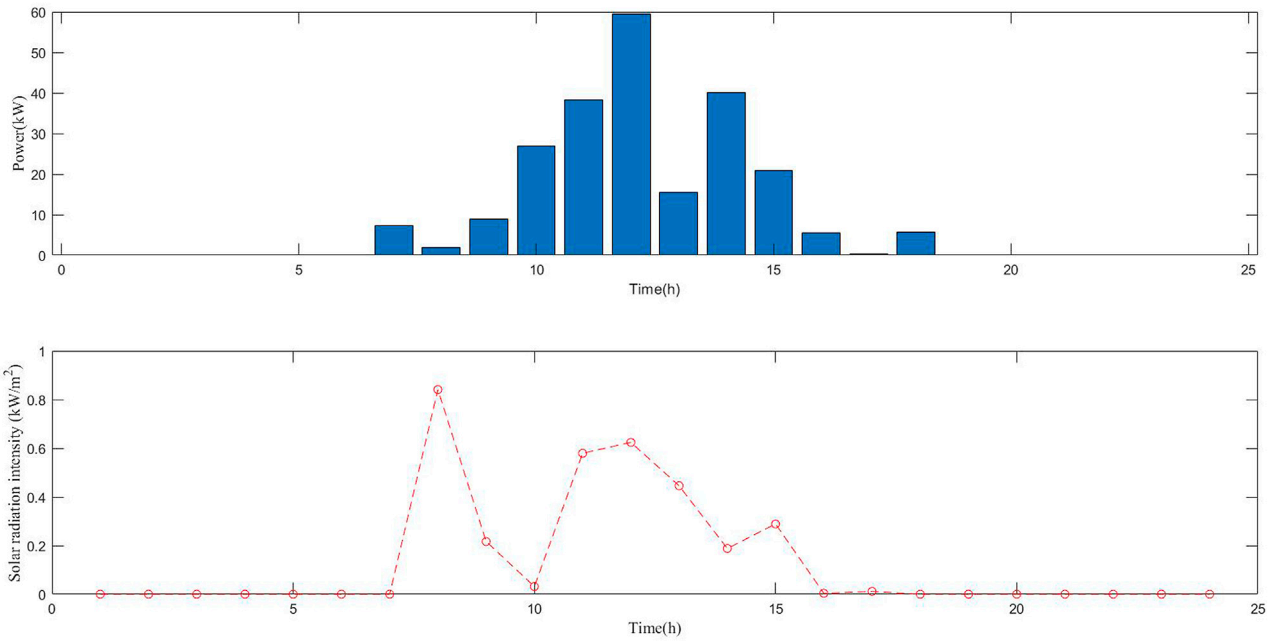

FIGURE 3
Photovoltaic output and light curve under Case 1.

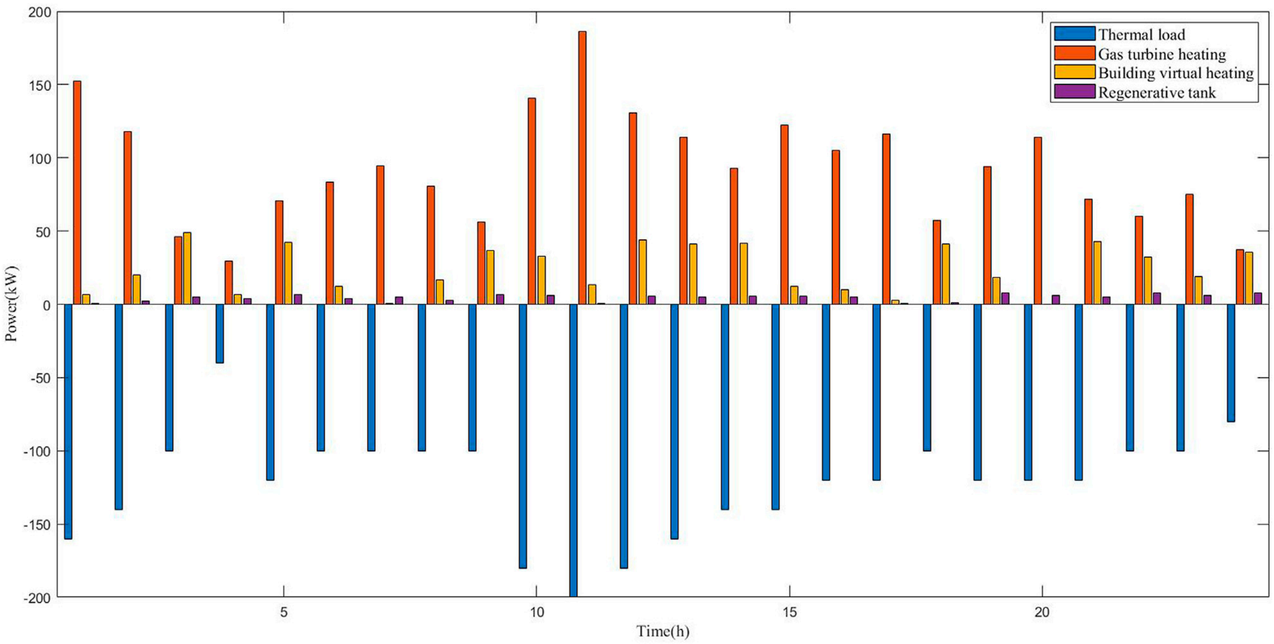

FIGURE 4
Optimization results of the heat load under Case 1.

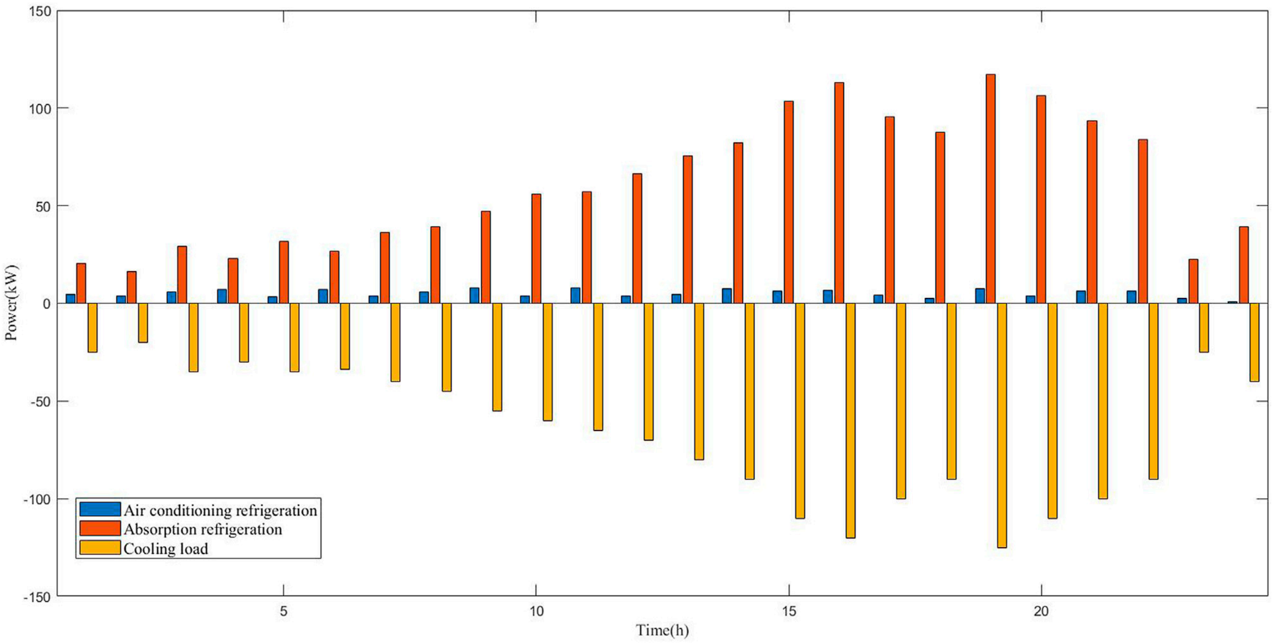

FIGURE 5
Optimization results of cooling load under Case 1.

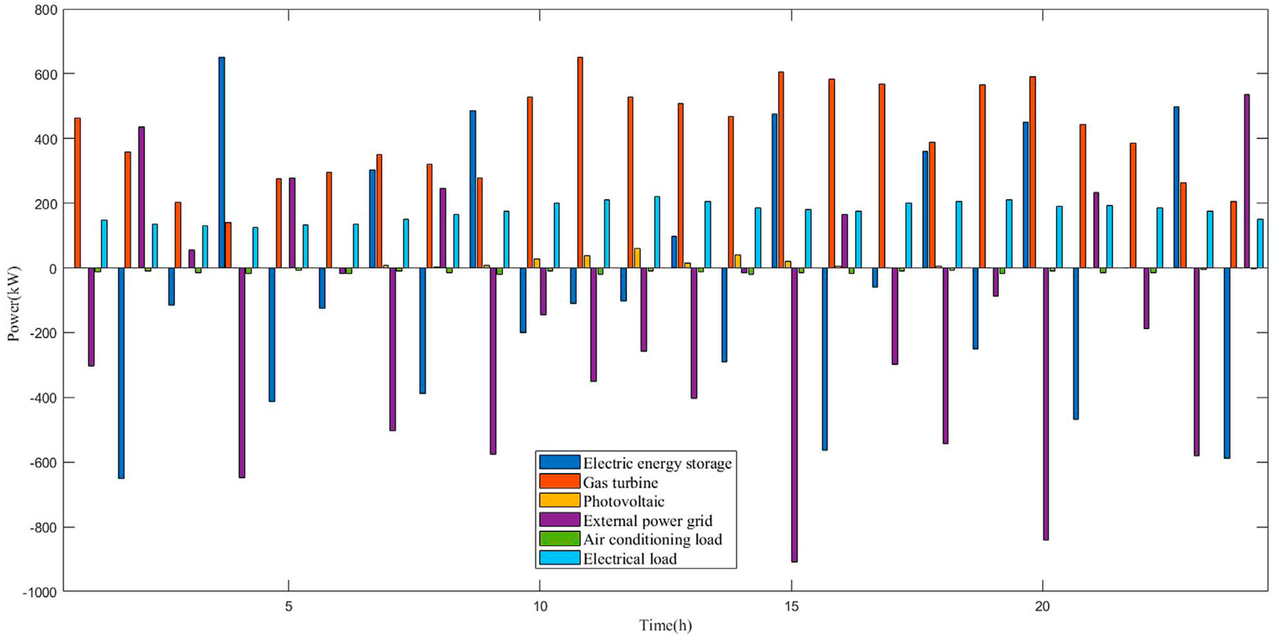

FIGURE 6
Optimization results of power load under Case 1.

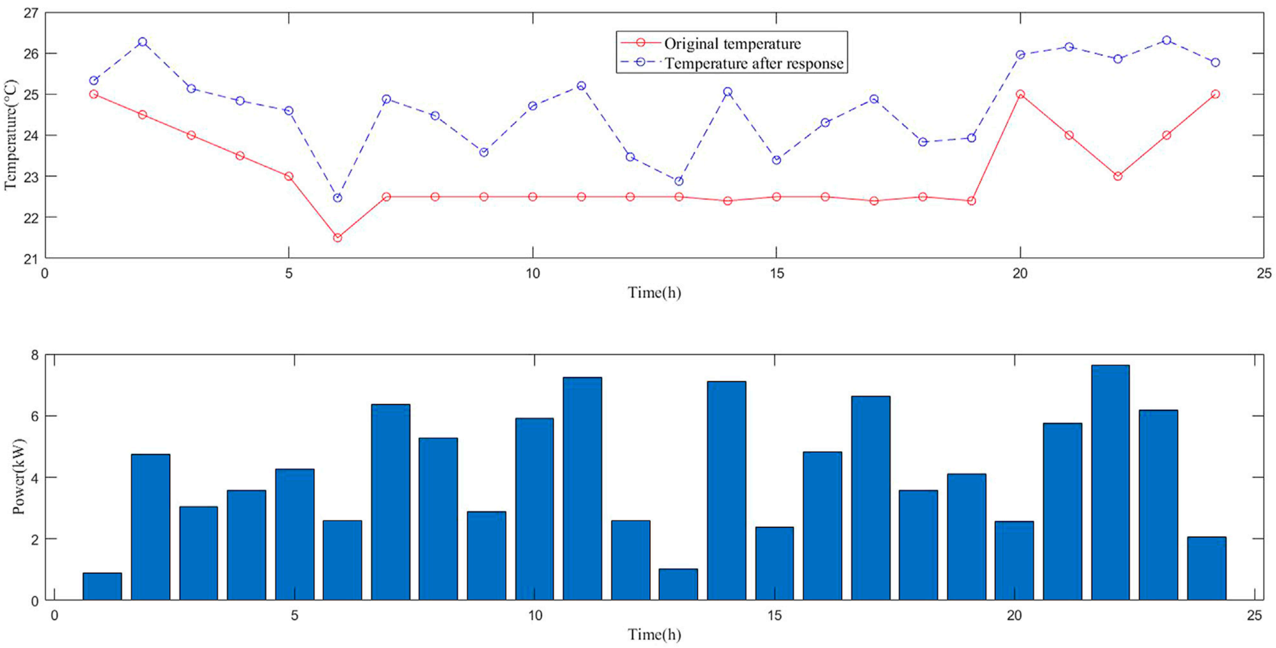

FIGURE 7
Photovoltaic output and light curve under Case 2.

TABLE 3 Optimization results of the building microgrid system under Case 2.

Equipment name	Capacity	Investment cost/yuan	Operation and maintenance cost/yuan
Battery	800/kWh	1200000	384
Gas Turbine	350/kW	70,000	252
Photovoltaic	80/kW	80,000	153.6
Heat storage tank	80/kW	5,760	23.04
Electric refrigerator	150/kW	60,000	144
Absorption chiller	250/kW	20,000	150

cooling load; however, it needs to effectively cooperate with the heat storage tank to ensure reliable operation of the heat load system of the building integrated system. Therefore, under the conditions of a typical winter day, the facility configuration capacity in relation to the heat load is higher. In contrast, the cooling load of electric refrigeration and air conditioners is low in winter, and refrigeration equipment is configured according to the lower limit in typical winter scenarios.

Under the calculation conditions of Case 1, to make the configuration capacity of the building microgrid system more reasonable, the optimal scheduling of each piece of equipment on a typical day is performed. The results are presented in Figures 4–6, and the cost-effectiveness of the economical operation is as follows: the environmental cost, fuel cost, photovoltaic consumption benefit, and building virtual energy storage benefit are 309, 2,360, 137, and 189 yuan, respectively. As shown in the figure, owing to the active reduction in indoor temperature in winter, the virtual energy storage of the building has a charging effect to reduce the operating cost of the system. However, in winter, owing to the small amount of heat transferred by sunlight, the operation mode of heat storage and heat storage systems is relatively simple. To ensure a heat supply, gas turbines make the operation mode of the entire integrated energy system inflexible, and the unbalanced power in the microgrid is adjusted by the external grid.

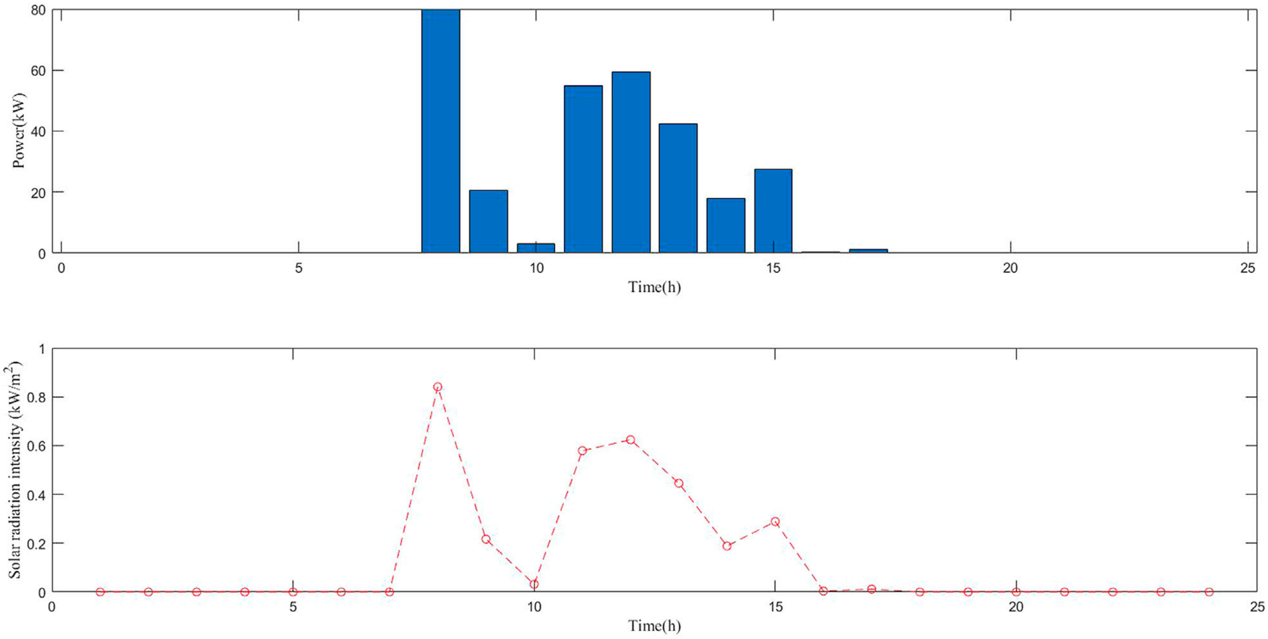

FIGURE 8
Building virtual energy storage and temperature change.

6.4 Typical scenarios in summer

For the Case 2 scenario, June is summer in the north, the solar light intensity is high, and the temperature difference between day and night is small. To enhance the energy-saving level of the building microgrid system, based on the principle of virtual energy storage in the building, the temperature in the building is actively increased in summer, and the virtual energy storage and cooling load response of the building is formed, as illustrated in Figure 7. Based on the virtual energy storage of the building, the optimization calculation is performed under the typical scenario of Case 2, and the typical daily operation results are listed in Table 3.

As indicated in Table3, considering that solar energy resources are particularly abundant in summer, the photovoltaic capacity configuration is relatively high, as depicted in Figure 8. The primary function of an electric energy storage system is to cooperate with the photovoltaic system to improve the utilization rate of photovoltaics. Simultaneously, the economic level of the building's comprehensive energy system can be improved as much as possible through the strategy of low storage and high discharge. The capacity configuration is 800 kWh. In summer, the cooling load demand is primarily considered, and the heating load is small. The gas turbine supplies a small amount of cooling load to the system *via* the absorption chiller; therefore, the gas turbine is configured to 350 kW in a typical summer scenario. In contrast, cooling load-related facilities have a higher configuration capacity to ensure a reliable supply of the cooling load of the building integrated system.

Under the calculation conditions of Case 2, the optimal scheduling results for the building microgrid system are presented in Figures 9–11, and the cost-effectiveness of the economical operation is as follows: the environmental cost, fuel cost, photovoltaic consumption benefit, and building virtual energy storage benefit are 259, 1,640, 337 and 209 yuan, respectively. It is evident from the figure that, owing to the strong sunlight in summer and the small heating load of the gas turbine, the electric energy storage system participates in the energy storage adjustment, which makes the operation mode of the entire integrated energy system more flexible, and the balance of the electric heating and cooling load does not depend on the external power grid. Therefore, in a typical summer scenario, the time-of-use electricity price mechanism of the external power grid can maximize the effect of low storage and high discharge in the building microgrid system to maximize the economic benefit of the building microgrid.

6.5 Algorithm convergence analysis

We proposed an improved multi-objective gray wolf optimization algorithm based on niche technology, and the

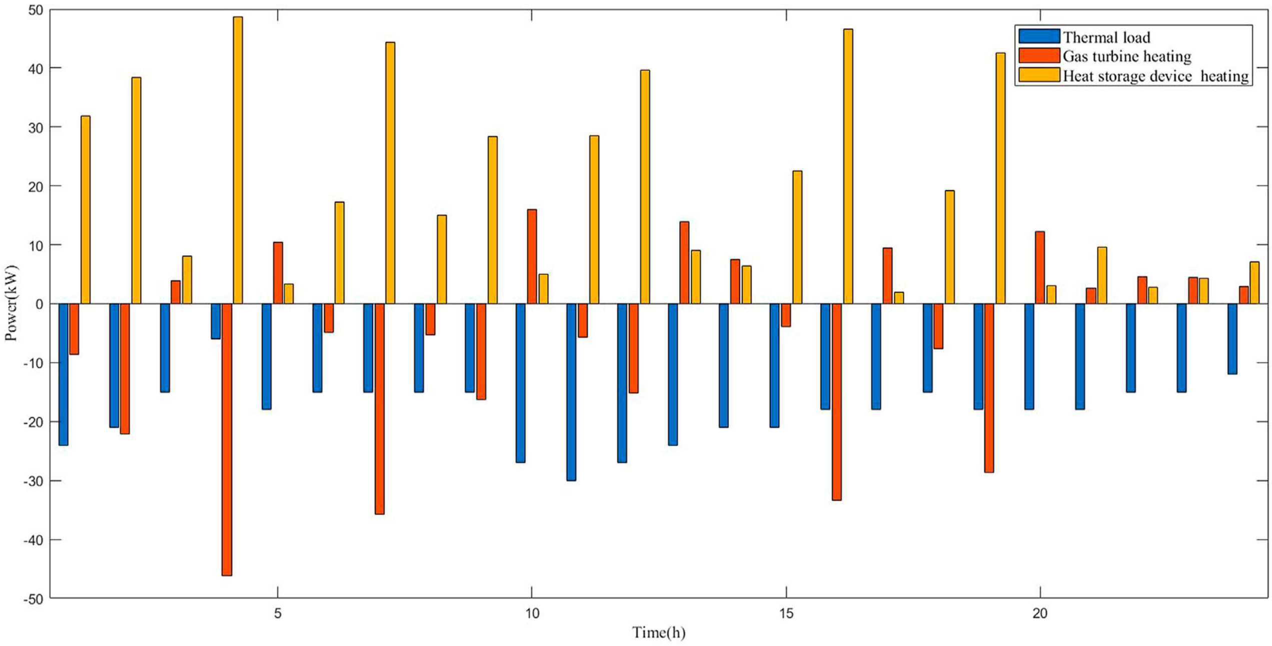

FIGURE 9
Optimization results of heat load under Case 2.

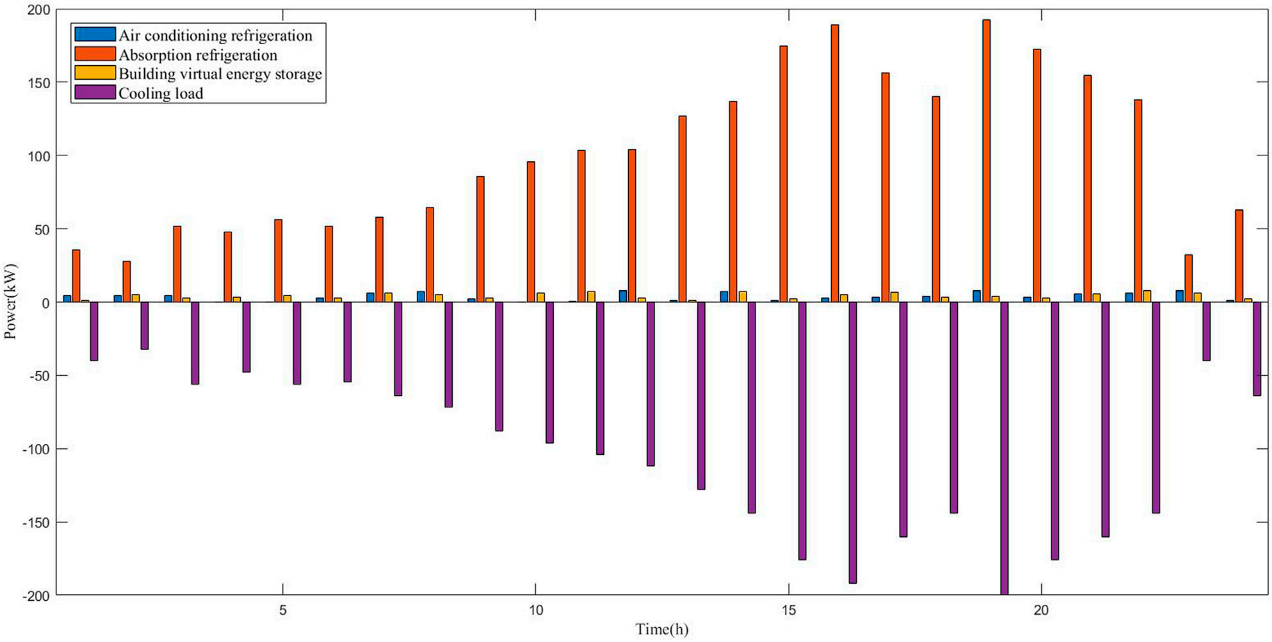

FIGURE 10
Optimization results of cooling load under Case 2.

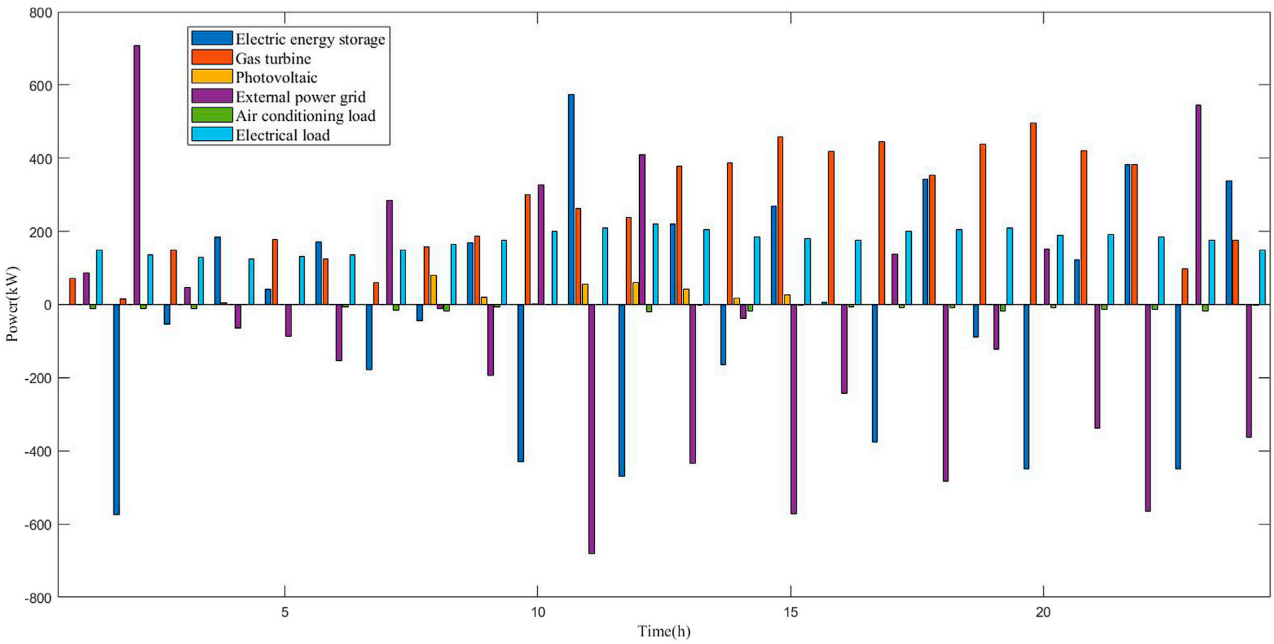

FIGURE 11
Optimization results of power load under Case 2.

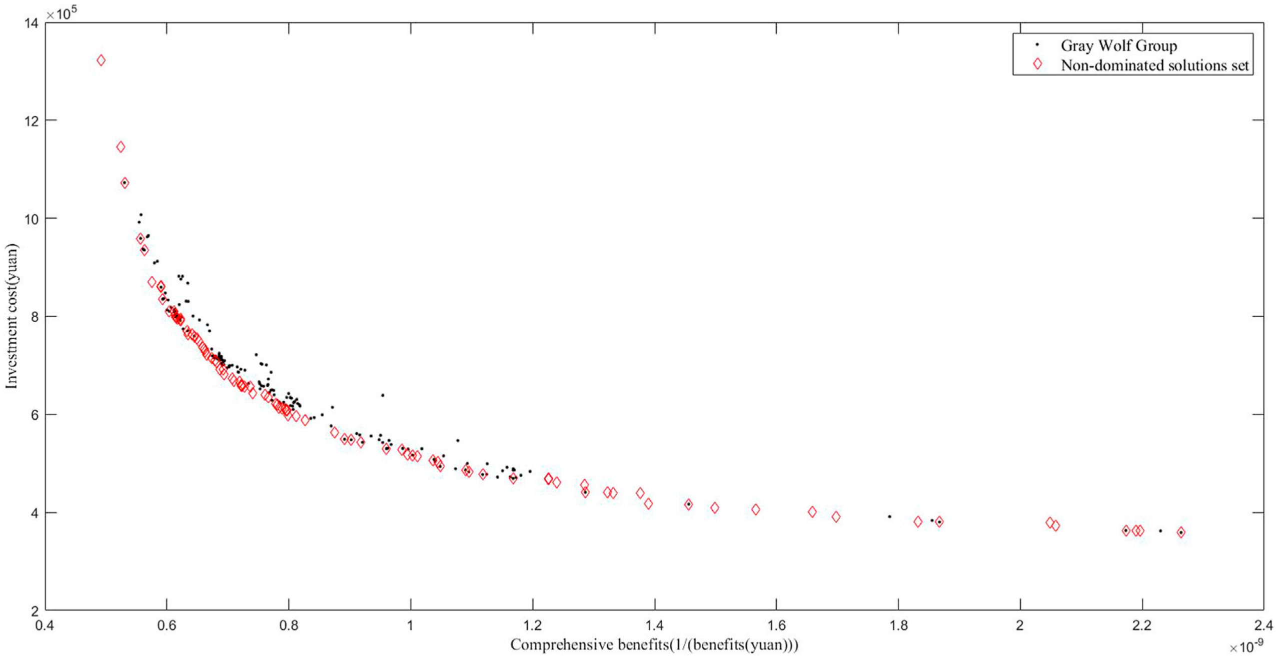

FIGURE 12
Pareto Frontier solution set under Case 1.

gray weighted correlation index was employed to evaluate and analyze the optimization results. Figure 12 illustrates the multi-objective convergence curve of a typical winter day. The convergence curve was relatively smooth and stable. The 100 fitness function values (non-dominated solutions) obtained by optimization were closely distributed around the gray wolf population (dominated solution set), indicating that the niche technique used in this study effectively improved the ability of non-dominated solutions to approach optimal solutions. Simultaneously, multiple non-dominated solutions improved the selectivity of users and obtained the optimal proportion of investment costs and comprehensive benefits through the gray-weighted correlation value. In summary, the multi-objective gray wolf optimization algorithm based on niche technology proposed in this paper exhibits good convergence in the optimization and solution of a building microgrid system.

7 Conclusion

In this study, we constructed a virtual energy storage system model based on the thermal storage characteristics of a building. On this basis, a capacity configuration and operation optimization method for a building microgrid integrated energy system that considers virtual energy storage was proposed. Through theoretical analysis and simulation, the following conclusions were drawn:

1) Virtual energy storage technology was integrated into the optimization model of the building microgrid energy system. By adjusting the indoor temperature of the building to satisfy user requirements, energy management based on virtual energy storage improved the operating economy of the building microgrid system.
2) User satisfaction reflected the control effect of virtual energy storage to a certain extent. The larger the indoor temperature control range, the more obvious the virtual energy storage control effect, which indicated that the system had general requirements for user satisfaction and lower operating costs. In contrast, the system had higher requirements for user satisfaction and higher operating costs.
3) The improved multi-objective gray wolf optimization algorithm based on niche technology effectively coordinated the optimization relationship between comprehensive benefits and investment costs, improving the ability of non-dominated solutions to approach the optimal solution, and effectively determining the optimal solution through the gray-weighted correlation degree evaluation method, reducing the investment cost of the building microgrid system, and enhancing the comprehensive operation benefit of the building system.

The virtual energy storage system can better respond to the power system to fill valleys and cut peaks, and reduce operating costs of integrated energy systems. At the same time, it improves new energy digestion capacity to reduce carbon emissions. These provide new ideas for green and low-carbon operation of integrated energy system.

Data availability statement

The raw data supporting the conclusion of this article will be made available by the authors, without undue reservation.

Author contributions

GL and YJ conceived of and designed the study. YZ and YN translated the articles and prepared the tables. JZ constructed and solved the model. JC and YN wrote the first draft of the manuscript. WW drew the microgrid system diagrams. All authors contributed to the revision of the manuscript and read and approved the submitted version.

Funding

This work is supported by the Science and Technology Project of State Grid Corporation of China (Grant No. 5100-202155289A-0-0-00) “Research on implementation path of new-type power system with new energy as the main body”. The funder was not involved in the study design, collection, analysis, interpretation of data, the writing of this article, or the decision to submit it for publication.

Acknowledgments

The authors would like to thank the sponsorship of Science and Technology Project of State Grid Corporation of China.

Conflict of interest

The authors declare that the research was conducted in the absence of any commercial or financial relationships that could be construed as a potential conflict of interest.

Publisher’s note

References

Bahmani, R., Karimi, H., and Jadid, S. (2021). Cooperative energy management of multi-energy hub systems considering demand response programs and ice storage. *Int. J. Electr. Power & Energy Syst.* 130, 106904. doi:10.1016/j.ijepes.2021.106904

Chang, J., Yang, X., Zhang, Z., Zheng, S., and Cui, B. (2022). Multi-objective optimal source–load interaction scheduling of combined heat and power microgrid considering stable supply and demand. *Front. Energy Res.* 10, 901529. doi:10.3389/fenrg.2022.901529

Dounis, A. I., and Caraiscos, C. (2009). Advanced control systems engineering for energy and comfort management in a building environment—a review. *Renew. Sustain. Energy Rev.* 13, 1246–1261. doi:10.1016/j.rser.2008.09.015

Favre-Perrod, P. (July 2005). A vision of future energy networks," in Proceedings of the 2005 IEEE power eng. soc. inaugural conference and exposition in Africa, Durban, South Africa.

Guan, X., Xu, Z., and Jia, Q. S. (2010). Energy-efficient buildings facilitated by microgrid. *IEEE Trans. Smart Grid* 1, 243–252. doi:10.1109/TSG.2010.2083705

Hca, B., Lin, G., and Zhong, Z. C. (2021). Multi-objective optimal scheduling of a microgrid with uncertainties of renewable power generation considering user satisfaction. *Int. J. Electr. Power & Energy Syst.* 131, 107142. doi:10.1016/j.ijepes.2021.107142

Hedman, B. A., and Hampson, A. C., (2021). *Fuel and carbon Dioxide emissions savings calculation methodology for combined heat and power systems*, American Society of Heating, Refrigerating, and Air-Conditioning Engineers, Inc, Atlanta, Georgia, USA.

Jin, X., Mu, Y., Jia, H., Wu, J., Jiang, T., and Yu, X. (2017). Dynamic economic dispatch of a hybrid energy microgrid considering building based virtual energy storage system. *Appl. Energy* 194, 386–398. doi:10.1016/j.apenergy.2016.07.080

Li, Z., Wang, C., Li, B., Wang, J., Zhao, P., Zhu, W., et al. (2020). Probability-interval based optimal planning of integrated energy system with Uncertain wind power. *IEEE Trans. Ind. Appl.* 18, 4–13. doi:10.1109/TIA.2019.2942260

Liu, D., Wu, J., Lin, K., and Wu, M. (2019). Planning of multi energy-type micro energy grid based on improved kriging model. *IEEE Access* 7, 14569–14580. doi:10.1109/access.2019.2894469

Lu, Y., Wang, S., Sun, Y., and Yan, C. (2015). Optimal scheduling of buildings with energy generation and thermal energy storage under dynamic electricity pricing using mixed-integer nonlinear programming. *Appl. Energy* 147, 49–58. doi:10.1016/j.apenergy.2015.02.060

Ma, L., Liu, N., Wang, L., Zhang, J., Lei, J., Zeng, Z., et al. (2016). Multi-party energy management for smart building cluster with PV systems using automatic demand response. *Energy Build.* 121, 11–21. doi:10.1016/j.enbuild.2016.03.072

Ma, T., Wu, J., Hao, L., Lee, W., Yan, H., and Li, D. (2018). The optimal structure planning and energy management strategies of smart multi energy systems. *Energy* 160, 122–141. doi:10.1016/j.energy.2018.06.198

Mirjalili, S., Mirjalili, S. M., and Lewis, A. (2014). Grey wolf optimizer. *Adv. Eng. Softw.* 69, 46–61. doi:10.1016/j.advengsoft.2013.12.007

Pazouki, S., Haghifam, M. R., and Moser, A. (2014). Uncertainty modeling in optimal operation of energy hub in presence of wind, storage and demand response. *Int. J. Electr. Power & Energy Syst.* 61, 335–345. doi:10.1016/j.ijepes.2014.03.038

Qiu, J., Yang, H., Dong, Z. Y., Zhao, J. H., Meng, K., Luo, F. J., et al. (2015). A linear programming approach to expansion co-planning in gas and electricity markets. *IEEE Trans. Power Syst.* 31, 3594–3606. doi:10.1109/TPWRS.2015.2496203

Si, Q., and Ma, Z., (2019). DEA cross-efficiency ranking method based on grey correlation degree and relative entropy. *Entropy* 21, 966. doi:10.3390/e21100966

Wang, D., Lai, C. S., Li, X., Wu, R., Gao, X., Lai, L. L., et al. (2021). Smart coordination of virtual energy storage systems for distribution network management. *Int. J. Electr. Power & Energy Syst.* 129, 106816. doi:10.1016/j.ijepes.2021.106816

Wang, Y., Hu, C., Wu, B., Zhang, J., Zi, Z., and Kang, L. (2020). Matching characteristic research of building renewable energy system based on virtual energy storage of air conditioning load. *Energies* 13 (135), 1269. doi:10.3390/en13051269

Yin, B., Li, Y., Miao, S., Lin, Y., and Zhao, H. (2021). An economy and reliability co-optimization planning method of adiabatic compressed air energy storage for urban integrated energy system. *J. Energy Storage* 40, 102691. doi:10.1016/j.est.2021.102691

Yuhui, H., Jiandong, D., Xinyu, Q., and Hao, H. (November 2017). Research on Dispersed wind generation planning in distributed system based on Voltage maximum Correntropy. IEEE Publications. Proceedings of the 2017 IEEE Conference on Energy Internet and Energy System Integration (EI2), Beijing, China.

Zhang, X., Zhao, X., Jiang, Z., and Shao, S. (2017). How to achieve the 2030 Co2 emission-reduction targets for China's industrial sector: Retrospective decomposition and prospective trajectories. *Glob. Environ. Change* 44, 83–97. doi:10.1016/j.gloenvcha.2017.03.003

Zhao, Y., Lu, Y., Yan, C., and Wang, S. (2015). MPC-based optimal scheduling of grid-connected low energy buildings with thermal energy storages. *Energy Build.* 86, 415–426. doi:10.1016/j.enbuild.2014.10.019

Zhu, X., Yang, J., Liu, Y., Liu, C., Miao, B., and Chen, L. (2019). Optimal scheduling method for a regional integrated energy system considering joint virtual energy storage. *IEEE Access* 7, 138260–138272. doi:10.1109/ACCESS.2019.2942198

Frontiers in
Energy Research

Advances and innovation in sustainable, reliable and affordable energy

Explores sustainable and environmental developments in energy. It focuses on technological advances supporting Sustainable Development Goal 7: access to affordable, reliable, sustainable and modern energy for all.

Discover the latest Research Topics

See more →

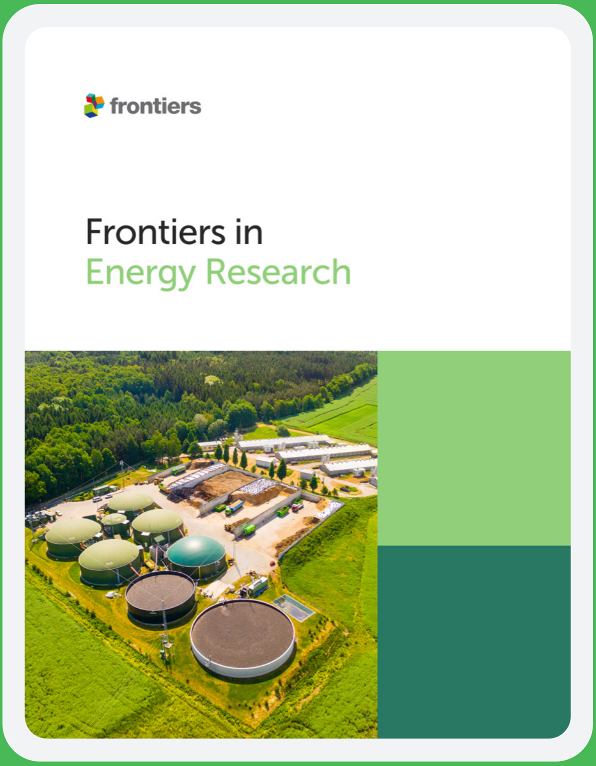

frontiers

Frontiers in
Energy Research

Frontiers

Avenue du Tribunal-Fédéral 34
1005 Lausanne, Switzerland
frontiersin.org

Contact us

+41 (0)21 510 17 00
frontiersin.org/about/contact